H
TL
798
M4
C62
1984

Preprints

CONFERENCE ON SATELLITE/REMOTE SENSING AND APPLICATIONS

Clearwater Beach, Fla. June 25–29, 1984

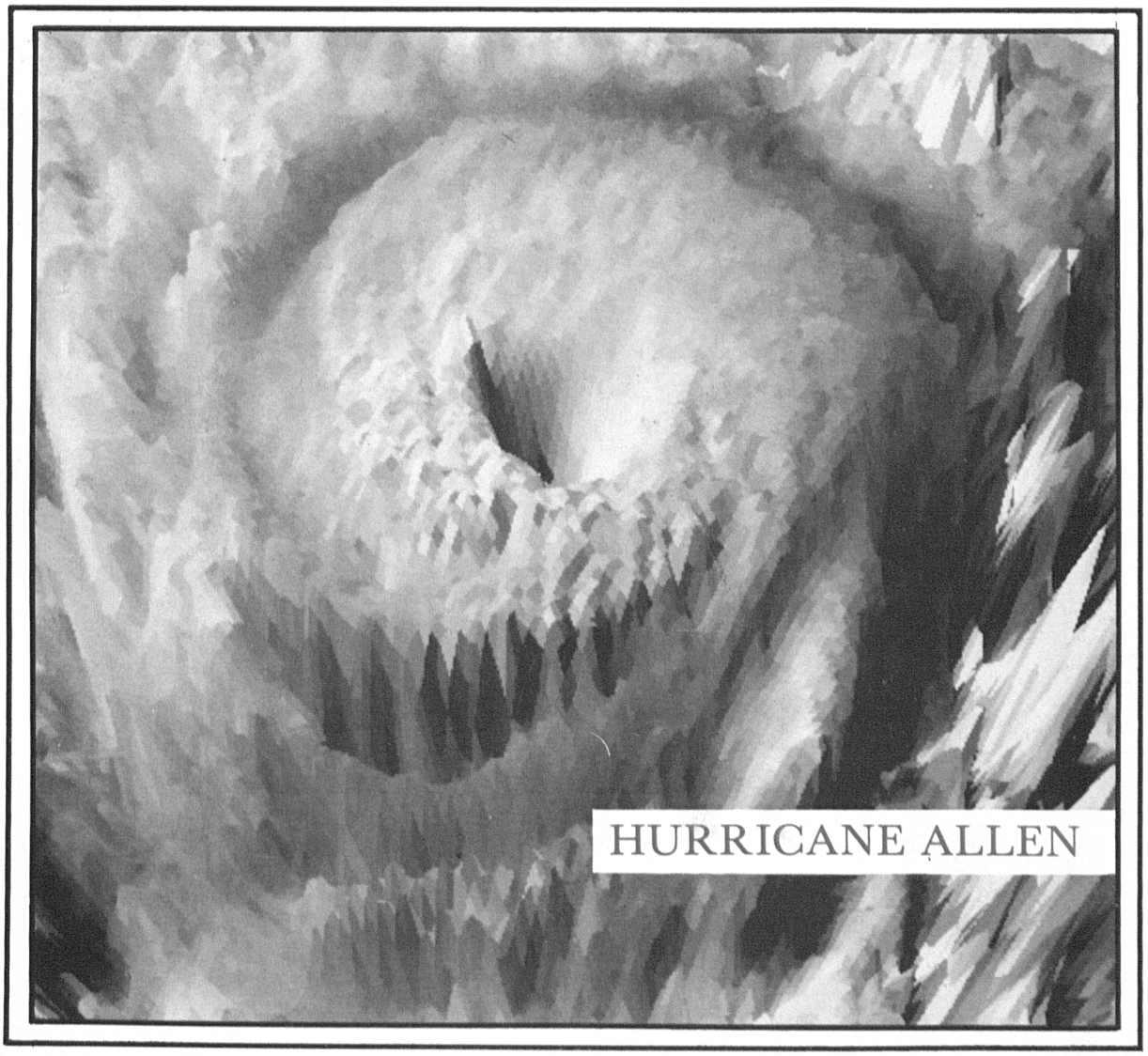

AMERICAN METEOROLOGICAL SOCIETY

AMERICAN METEOROLOGICAL SOCIETY

45 BEACON STREET, BOSTON, MASSACHUSETTS 02108

PERIODICALS—1984

	Nonmember Prices
JOURNAL OF THE ATMOSPHERIC SCIENCES (ISSN 0022-4928)	$200.00*
Volume 41, 1984. Semi-monthly	$30.00†

Original research papers and critical surveys related to the atmospheres of the earth and other planets with emphasis on the quantitative and deductive aspects of the physics and dynamics of atmospheric processes and phenomena.

JOURNAL OF CLIMATE AND APPLIED METEOROLOGY (ISSN 0733-3021)	$120.00*
Volume 23, 1984. Monthly	$15.00†

Original papers and critical surveys concerned with all aspects of climate and the socioeconomic impacts of a changing climate; and with the applications of the atmospheric sciences to operational and practical goals. Its editorial scope encompasses interdisciplinary climate studies and the full range of applications of meteorology to safety, health, industry, the economy, and general well-being of the human community.

JOURNAL OF PHYSICAL OCEANOGRAPHY (ISSN 0022-3670)	$120.00*
Volume 14, 1984. Monthly	$15.00†

Original research and survey papers devoted to the communication of knowledge concerning the physics and chemistry of the oceans and of the processes coupling the sea to the atmosphere. Papers will deal with the theoretical and observational aspects of topics such as: ocean circulation, surface waves, internal waves, inertial oscillations, oceanic turbulence, interpretive regional studies, and oceanic tides and other long-wave phenomena.

MONTHLY WEATHER REVIEW (ISSN 0027-0644)	$120.00*
Volume 112, 1984. Monthly	$15.00†

Original papers, survey papers, and synoptic and climatological summaries and features pertaining to weather observation, analysis, and forecasting.

JOURNAL OF ATMOSPHERIC AND OCEANIC TECHNOLOGY (ISSN 0739-0572)	$80.00*
Volume 1, 1984. Quarterly	$5.00†

Original research and survey papers related to instrument system descriptions, exploratory measurement techniques, calibration methods, and performance analyses for the mainstream of atmospheric and oceanic technology, including the development of data-acquisition hardware, real-time and post-analysis software, and signal processing techniques.

BULLETIN OF THE AMERICAN METEOROLOGICAL SOCIETY (ISSN 0003-0007)	$60.00*
Volume 65, 1984. Monthly	$15.00†

The official organ of the Society, devoted to editorials, topical reports to members, articles, professional and membership news, conference announcements, programs, and summaries, book reviews, and Society activities.

METEOROLOGICAL & GEOASTROPHYSICAL ABSTRACTS (ISSN 0026-1130)	$450.00*
Volume 35, 1984. Monthly	$15.00†

Abstracts of current world literature in meteorology, climatology, aeronomy, planetary atmospheres, solar-terrestrial relations, hydrology, oceanography, glaciology, cosmic rays, and radioastronomy. The abstracts of books, articles, and reprints are arranged by subject categories with extensive cross-referencing. Monthly author, subject, and geographical indexes. Information on the computerized MGA data base, 1970–1984 may be obtained by writing to the Society.

Back issues of periodicals

The availability and the prices of back issues of AMS periodicals will be furnished on request.

* Subscriptions are accepted on calendar year basis only. † Surface postage and handling for foreign subscriptions.

For additional information, write to the American Meteorological Society.

TL
798
M4C62
1984

CONFERENCE ON SATELLITE/REMOTE SENSING AND APPLICATIONS

Sponsored by
AMERICAN METEOROLOGICAL SOCIETY

JUNE 25-29, 1984 CLEARWATER BEACH, FLA.

PHOTO/COVER CAPTION: Perspective view of Hurricane Allen showing the eye, central dense overcast, and intense convective regions. The image was generated at the Goddard Space Flight Center using the Atmospheric and Oceanic Information Processing System (AOIPS-II) by Dr. A. F. Hasler and Harold Pierce using 1 km resolution Advanced Very High Resolution Radiometer (AVHRR) visible and IR imagery from the NOAA polar orbiting satellite. Apparent height in this image is proportional to the IR radiance. New software techniques allow selective perspectives, variable illumination angles, and image sequences representing a low-angle simulated aircraft circumnaviagtion of the hurricane.

Copyright © 1984, American Meteorological Society. This copyright notice applies to only the overall collection of papers; authors retain their individual rights and should be contacted directly for permission to use their material separately. Contact AMS for permission pertaining to the overall collection.

The manuscripts reproduced in this collection of preprints are unrefereed papers presented at the Conference on Satellite Meteorology/Remote Sensing and Applications; their appearance in this collection does not constitute formal publication.

AMERICAN METEOROLOGICAL SOCIETY
45 Beacon Street, Boston, Massachusetts 02108
U.S.A.

LIBRARY
OCT 1 1984
N.O.A.A.
U. S. Dept. of Commerce

National Oceanic and Atmospheric Administration
TIROS Satellites and Satellite Meteorology

ERRATA NOTICE

One or more conditions of the original document may affect the quality of the image, such as:

Discolored pages
Faded or light ink
Binding intrudes into the text

This has been a co-operative project between the NOAA Central Library and the Climate Database Modernization Program, National Climate Data Center (NCDC). To view the original document contact the NOAA Central Library in Silver Spring, MD at (301) 713-2607 x124 or Library.Reference@noaa.gov.

HOV Services
Imaging Contractor
12200 Kiln Court
Beltsville, MD 20704-1387
January 26, 2009

H TL 798 .M4 C62 1984
Conference on
Satellite/Remote Sensing
Conference on
Satellite/Remote Sensing
I/3004

11/14/85	Lew Adams GAO 443-8691
5/12/86	David M. Harris Falcon Assoc 703-356 4445

DEMCO 32-209

H TL 798 .M4 C62 1984
Conference on
Satellite/Remote Sensing
Conference on
Satellite/Remote Sensing
I/3004

11/14/85	Lew Adams GAO 443-8691
5/12/86	David M. Harris Falcon Assoc. 356-4445

DEMCO 32-209

I/3004

FOREWORD

Our ability to observe and measure the atmosphere using space-based sensor systems has improved many fold since the first meteorological satellite was flown as TIROS-I in April 1960 (see footnote). In addition, we have made significant improvements in our ability to assimulate the data into the operational weather services of not only the United States but other countries throughout the world. We now take for granted the importance of the satellite observations made on a routine basis. Measurements are now routinely utilized in numerical models. New techniques continue to be developed for the practical use of these data in global regional and local forecasts. Sensor technology developments also continue to improve and provide even greater opportunities for future space-based measurements of the atmosphere.

The conference was organized to focus on the development of space-borne remote sensing techniques (instrumentation and interpretation) and the application of satellite observation to meteorological problems, both present and future. Papers have been contributed in the areas of new observation and techniques, retrieval techniques, applications, information retrieval, ground truth and validation, data assimilation and diagnosis, and observing system simulation studies.

This conference proceedings provide the interested researcher and active forecaster with an up-to-date status of this important new element of meteorological observations and measurements. We are convinced the future will see even more dramatic improvements and contributions by satellite meteorology to our understanding and ability to predict the atmosphere.

John S. Theon, General Chairman
Walter Frost, Technical Chairman
William W. Vaughan
Thomas Vonder Haar

AMS 1983 Committee on

Meteorological Aspects of Aerospace Systems

Walter Frost, Chairman	Kenneth R. Hardy	Thomas H. Pries
George H. Fichtl	Arthur F. Hasler	John S. Theon
Frank Globaker	Roland E. Nagle	Thomas H. Vonder Haar

Program Committee

Mr. John S. Theon, NASA Headquarters, Washington, D.C., is the General Chairman for the conference with Dr. Walter Frost, University of Tennessee Space Institute, Tullahoma, Tennessee, serving as Technical Chairman. In addition, the conference planning committee consisted of Dr. William W. Vaughan, NASA-Marshall Space Flight Center, Huntsville, Alabama; and Dr. Thomas Vonder Haar, Colorado State University, Ft. Collins, Colorado.

Local Hosts

West Central Florida Chapter of the AMS

Footnote:

The NASA Conference Publication 227, "Meteorological Satellite--Past, Present, and Future" 1982 provides an excellent review of the growth and development of the meteorological satellite program. Copies are available from the NASA Scientific and Technical Information Branch, NASA Headquarters, Washington, D.C., 20546.

TABLE OF CONTENTS

		Page
FOREWORD		i
AUTHOR INDEX		viii
SESSION A: NEW SATELLITE OBSERVATIONS AND TECHNIQUES		
Chairperson: Thomas H. Vonder Haar, Colorado State Univ., Ft. Collins, Colo.		
A.1	AGEOSTROPHIC MOTIONS IN THE STRATOSPHERE FROM SATELLITE OBSERVATIONS. L. S. Elson, Jet Propulsion Laboratory, Pasadena, Calif.	1
A.2	SATELLITE MEASUREMENT OF AEROSOL MASS OVER LAND. R. S. Fraser, Goddard Space Flight Center(GSFC)/NASA, Greenbelt, Md.;Y. J. Kaufman, Univ. of Maryland, College Park, Md.; and R. L. Mahoney, Science Systems and Applications, Inc., Seabrook, Md.	4
A.3	MARINE AEROSOL OPTICAL DEPTH FROM SATELLITE-DETECTED RADIANCE. P. A. Durkee, E. E. Hindman, T. H. Vonder Haar, Colorado State Univ., Ft. Collins, Colo.; and D. R. Jensen, Naval Ocean Systems Center, San Diego, Calif.	11
A.4	RADIATION CHARACTERISTICS OF MARINE BOUNDARY LAYER CLOUDS DERIVED FROM MULTI-SATELLITE OBSERVATIONS. C. Gautier and R. Frouin, California Space Institute, La Jolla, Calif.	*
A.5	METEOROLOGICAL SATELLITE DATA USEFUL FOR AGROCLIMATE. P. K. Rao, J. D. Tarpley, R. A. Scofield and J. F. Moses, (NESDIS)/NOAA, Washington, D.C.	15
A.6	OVERSHOOTING CLOUD TOP, VARIATION OF TROPOPAUSE AND SEVERE STORM FORMATION. R. J. Hung, Univ. of Alabama, Huntsville, Ala.; and R. E. Smith, Marshall Space Flight Center (MSFC)/NASA, Huntsville, Ala.	22
A.7	A STATISTICAL EVALUATION AND COMPARISON OF VISSR ATMOSPHERIC SOUNDER (VAS) DATA AND CORRESPONDING RAWINSONDE MEASUREMENTS. G. J. Jedlovec, MSFC/NASA, Huntsville, Ala.	29
A.8	GROUNDBASED DEMONSTRATION OF A 0.5 MICROMETER WIND SENSOR. J. T. Sroga, L. S. O'Hara and A. Rosenberg, RCA Astro Electronics, Princeton, N.J.; P. B. Hays, B. Kennedy and V. Abreu, Univ. of Michigan, Ann Arbor, Mich.	35
SESSION B: RETRIEVAL TECHNIQUES		
Chairperson: M. T. Chahine, Jet Propulsion Laboratory, Pasadena, Calif.		
	CONFERENCE KEYNOTE ADDRESS: AN ASSESMENT OF THE FUTURE IMPACT OF METEOROLOGICAL SATELLITES ON THE ATMOSPHERIC SCIENCES. Dr. J. H. McElroy, Assistant Administrator for Satellites, National Oceanic and Atmospheric Administration.	*
B.1	DESIGN AND SIMULATION OF NEW SATELLITE PRECIPITATION MEASUREMENT SYSTEMS. A. Mugnai, E. A. Smith and T. H. Vonder Haar, Colorado State Univ., Ft. Collins, Colo.	*
B.2	THE IMPROVED INITIALIZATION INVERSION ("3I") METHOD: A HIGH RESOLUTION PHYSICAL METHOD FOR TEMPERATURE RETRIEVALS FROM THE SATELLITES OF THE TIROS-N SERIES. A. Chedin, N. A. Scott, C. Wahiche, P. Moulinier, N. Husson, and I. Cohen-Hallaleh, Laboratoire de Meteorologie Dynamique de CNRS, Palaiseau, France	39
B.3	IMPROVED VERTICAL SOUNDINGS FROM AN AMALGAMATION OF POLAR AND GEOSTATIONARY RADIANCE OBSERVATIONS. W. L. Smith, and H. M. Woolf, NESDIS/NOAA, Madison, Wis.	45

* Manuscript not available; if paper received in time, it will appear in back of book.

B.4 THE CLOUDS AND VAS. C. M. Hayden, NESDIS/NOAA Development Laboratory, Madison, Wis; W. P. Menzel, NESDIS/NOAA Satellite Applications Laboratory, Madison, Wis.; and A. J. Schreiner, Space Science and Engineering Center, Madison, Wis. 49

B.5 PHYSICAL RETRIEVAL OF PRECIPITABLE WATER USING THE SPLIT WINDOW TECHNIQUE. T. J. Kleespies, Naval Environmental Prediction Research Facility (NEPRF), Monterey, Calif.; and L. M. McMillin, NESDIS/NOAA, Washington, D.C. 55

B.6 A NEW TECHNIQUE TO INFER CONVECTIVE RAINFALL INFORMATION FROM SATELLITE INFRARED CLOUD OBSERVATIONS. A. J. Negri, and R. F. Adler, GSFC/NASA, Greenbelt, Md. 58

B.7 PASSIVE MICROWAVE RAIN ESTIMATION OVER LAND AND OCEAN AT 37 GHZ. R. W. Spencer, Space Science and Engineering Center, Madison, Wis. 64

B.8 EFFECT OF INSTRUMENT PARAMETERS ON SATELLITE RETRIEVAL ACCURACY. L.M. McMillin, NESDIS/NOAA, Washington, D.C. 68

SESSION C: ESTIMATION OF SURFACE AND ATMOSPHERIC PROPERTIES

Chairperson: Owen E. Thompson, Univ. of Maryland, College Park, Md.

C.1 SURFACE ALBEDO OVER THE SAHEL FROM METEOSAT RADIANCES. B. Pinty and J. Stum, L.A.M.P., Univ. de Clermont II, Aubiere, France; and G. Szejwach, L.M.D., Ecole Polytechnique, Paliseau, France 73

C.2 INVESTIGATION OF SURFACE ALBEDO VARIATIONS OVER WEST AFRICA FROM METEOSAT. B. Pinty, L.A.M.P. Univ. de Clermont II, Aubiere, France; G. Szejwach and M. Desbois, L.M.D., Ecole Polytechnique, Palaiseau, France 76

C.3 DERIVATION OF SURFACE PROPERTIES FROM SATELLITE OBSERVATIONS. E. Ruprecht and G. Nacke, Institut fur Geophysik und Meteorologie, Cologne, Federal Republic of Germany *

C.4 A CASE STUDY ON THE APPLICATION OF GEOSYNCHRONOUS SATELLITE INFRARED DATA TO ESTIMATE SOIL MOISTURE. R. H. Woodward, General Software Corp., Landover, Md.; and P. J. Wetzel, D. A. Atlas, GSFC/NASA, Greenbelt, Md. 80

C.5 VERTICAL DISPLACEMENTS OF THE MID-TROPOSPHERIC WATER VAPOR BOUNDARY IN THE TROPICS DERIVED FROM THE VISSR ATMOSPHERIC SOUNDER (VAS) 6.7 MICROMETER CHANNEL. J. Stout and J. Steranka, General Software Corp., Landover, Md.; and Ralph A. Petersen, GSFC/NASA, Greenbelt, Md. 86

C.6 NIGHTTIME CLOUDINESS ESTIMATION FROM AVHRR HIGH RESOLUTION IMAGERY. T. Phulpin and A. Brard, Centre de Meteorologie Spatiale, Lannion, France *

C.7 ON A SIMPLE METHOD FOR DETERMINING THE RELATIVE SHIFT BETWEEN THE VISIBLE AND INFRARED GOES IMAGES. A. A. Tsonis, Atmospheric Environment Service, Downsview, Ontario, Canada 90

SESSION D: SATELLITE APPLICATIONS: MESOSCALE, CLOUD, AND WATER RELATED STUDIES

Chairperson: James R. Scoggins, Texas A&M Univ., College Station, Tex.

D.1 MESOSCALE APPLICATIONS OF VAS IMAGERY. R. M. Zehr and R. N. Green, NESDIS/NOAA, Ft. Collins, Colo. 94

D.2 DIAGNOSING THE SEVERE THUNDERSTORM ENVIRONMENT BY MESOSCALE CLOUD TRACKING - A NEW APPROACH AND NEW INFORMATION. J. F. W. Purdom, NESDIS/NOAA, Ft. Collins, Colo.;J. K. Steward, N. E. Leary and T. H. Vonder Haar, Colorado State Univ., Ft. Collins, Colo. 100

* Manuscript not available; if paper received in time, it will appear in back of book.

D.3 USING SATELLITE IMAGERY TO UNDERSTAND MESOSCALE WEATHER DEVELOPMENT. J. F. W. Purdom, NESDIS/NOAA, Ft. Collins, Colo. 106

D.4 APPLICATIONS OF CUMULUS CLOUD FIELD STATISTICS FROM GOES DATA. J. L. Behunek and T. H. Vonder Haar, Colorado State Univ., Ft. Collins, Colo. 112

D.5 THUNDERSTORM CLOUD TOP DYNAMICS AS INFERRED FROM SATELLITE OBSERVATIONS AND MODELS. R. F. Adler, GSFC/NASA, Greenbelt, Md.; and R. A. Mack, General Software Corp., Landover, Md. 115

D.6 ESTIMATING PRECIPITATION AREAS OVER THE EASTERN PACIFIC USING GOES SATELLITE IMAGERY. L. K. Neil, Atmospheric Environment Service, Vancouver, Canada 121

D.7 NIMBUS 7 SMMR DERIVED SEASONAL VARIATIONS IN THE WATER VAPOR, LIQUID WATER, AND SURFACE WINDS OVER THE GLOBAL OCEANS. C. Prabhakara and D. A. Short, GSFC/NASA, Greenbelt, Md. 127

D.8 ARCTIC ATMOSPHERE - ICE INTERACTION STUDIES USING NIMBUS-7 SMMR. M. R. Anderson and R. G. Crane, Cooperative Institute for Research in Environmental Sciences, Boulder, Colo. 132

SESSION E: DIAGNOSIS OF WEATHER SYSTEMS

Chairperson: Gary L. Achtemeier, Illinois State Water Survey, Champaign, Ill.

E.1 ANALYSIS OF TROPICAL SYNOPTIC DISTURBANCES USING SATELLITE-DERIVED SOUNDINGS AND RADIANCE DATA FROM SELECTED CHANNELS. A. H. Thompson, J. P. McGuirk, L. L. Anderson, Jr., and N. R. Smith, Texas A&M Univ., College Station, Tex. 137

E.2 A CLOUDINESS STUDY OF THE EASTERN EQUATORIAL PACIFIC USING GEOSTATIONARY SATELLITE DATA. C. F. Shih, T. H. Vonder Haar, and G. G. Campbell, Colorado State Univ., Ft. Collins, Colo. 294

E.3 SATELLITE DERIVED ATMOSPHERIC WATER VAPOR AS A TRACER OF LARGE SCALE INTERACTIONS BETWEEN THE ATMOSPHERE AND OCEAN. D. A. Short, and C. Prabhakara , GSFC/NASA, Greenbelt, Md. 143

E.4 DETECTION OF TROPOPAUSE FOLDS USING BOTH WATER VAPOR AND OZONE SATELLITE DATA. J. Tournadre, D. Ramond, IOPG du Puy de Dome,; and S. Muller, CNRM/EERM, Clermont-Ferrand, Toulouse, France 149

E.5 SATELLITE CLOUD AND PRECIPITATION ANALYSIS USING INTERACTIVE COMPUTER SYSTEM. C. Wash, L. Chou, C. Nelson, C. Moren, and L. Spray, Naval Postgraduate School, Monterey, Calif. 155

E.6 AIRCRAFT PENETRATIONS OF ARC CLOUD LINES. P. C. Sinclair, Colorado State Univ., Ft. Collins, Colo.; and J. F. W. Purdom, NESDIS/NOAA, Ft. Collins, Colo. 160

E.7 APPLICATIONS OF GOES DATA IN FORECASTING AND ANALYSIS OF MARINE AIR PENETRATION IN WESTERN OREGON. P. H. Ruscher, Texas A&M Univ., College Station, Tex. *

SESSION F: INFORMATION RETRIEVAL

Chairperson: P. K. Rao, NESDIS/NOAA, Washington, D.C.

F.1 AUTOMATED MESOSCALE WIND FIELDS DERIVED FROM GOES SATELLITE IMAGERY. G. S. Wilson, MSFC/NASA, Huntsville, Ala. 164

F.2 STRUCTURE FUNCTION ANALYSES OF MESOSCALE VAS RETRIEVALS. P. J. Meyer and H. E. Fuelberg, St. Louis Univ., St. Louis, Mo. 172

F.3 APPLICATIONS OF AUTOMATIC CLOUD DETECTORS TO INTERACTIVE METEOROLOGICAL OPERATIONS. J. F. Moses, NESDIS/NOAA, Washington, D.C. 178

* Manuscript not available; if paper received in time, it will appear in back of book.

F.4 MESOSCALE ANALYSIS OF 6.7 MICROMETER IMAGE DATA FROM THE VISSR ATMOSPHERIC SOUNDER (VAS) FOR SEVERAL CASE STUDIES. G. J. Jedlovec, MSFC/NASA, Huntsville, Ala. 185

F.5 REMOTE SENSING OF TEMPERATURE PROFILES BY A COMBINATION OF GROUND-BASED PROFILER AND SATELLITE-BASED MSU RADIOMETRIC OBSERVATIONS. E. R. Westwater, W. Zhenhui, Wave Propagation Laboratory ERL/NOAA, Boulder, Colo.; and N. C. Grody, and L. M. McMillin, NESDIS/NOAA, Washington, D.C. 191

F.6 ATMOSPHERIC AND SURFACE SHORT-WAVE ENERGY BALANCE FROM COMBINED SATELLITE AND GROUND-BASED DATA. C. G. Justus, Georgia Institute of Technology, Atlanta, Ga. 197

F.7 THE DETECTION AND LOCATION OF LIGHTNING FROM SPACE. H. J. Christian, W. W. Vaughan, MSFC/NASA, Huntsville, Ala.; and J. C. Dodge, NASA Headquarters, Washington, D.C. 202

F.8 OBJECTIVE SCATTEROMETER WIND AMBIGUITY REMOVAL USING SMOOTHNESS AND DYNAMICAL CONSTRAINTS. R. N. Hoffman, Atmospheric and Environmental Research, Inc., Cambridge, Mass. 206

SESSION G: GROUND TRUTH AND VALIDATION

Chairperson: William W. Vaughan, Marshall Space Flight Center, Huntsville, Ala.

G.1 A COMPARISON OF REAL-TIME SATELLITE RAIN ESTIMATES AND RADAR DATA. J. A. Augustine, and C. G. Griffith, Weather Research Program ERL/NOAA, Boulder, Colo. 210

G.2 A COMPOSITE LOOK AT A PRECIPITATION REGION USING DIGITAL RADAR, GOES VISIBLE AND INFRARED IMAGES, SURFACE CLIMATOLOGICAL RAINFALL DATA, NIMBUS 7 SMMR INFORMATION AND 3 HR RAWINSONDE MEASUREMENTS, J. E. Arnold, MSFC/NASA, Huntsville, Ala.; and G. Huebner, Texas A&M Univ., College Station, Tex. *

G.3 OBSERVATIONS OF DEEP CONVECTION FROM AN AIRBORNE HIGH FREQUENCY (92 and 183 GHz) PASSIVE MICROWAVE RADIOMETER. I. Hakkarinen and R. F. Adler, GFSL/NASA, Greenbelt, Md. 216

G.4 RELATIVE ERRORS OF SATELLITE SOUNDINGS AND RADIOSONDES. H. J. Brodrick and A. Thomasell, Jr., NESDIS/NOAA, Washington, D.C. 222

G.5 THE ACCURACY OF MESOSCALE TEMPERATURE AND DEWPOINT FIELDS RETRIEVED FROM VAS SATELLITE AND CONVENTIONAL SURFACE DATA. D. Chesters, GSFC/NASA, Greenbelt, Md.; T. H. Lee, Computer Sci. Corp., Silver Spring, Md.; A. Mostek, and D. A. Keyser, General Software Corp., Landover, Md. 226

G.6 VERIFICATION AND ANALYSIS OF TOVS SATELLITE DATA. M. E. Gelman and A. J. Miller, NWS/NOAA, Camp Springs, Md.; and F. J. Schmidlin, GSFC/NASA, Wallops Island, Va. 232

G.7 EFFECT OF WIND AND MOISTURE GRADIENTS ON THE ARBITRARY ASSIGNMENT OF CLOUD MOTIONS TO A VERTICAL COORDINATE SYSTEM IN TWO SESAME CASES. C. A. Peslen, S. E. Koch, and L. W. Uccellini, GSFC/NASA, Greenbelt, Md. 234

G.8 A COMPOSITE STUDY OF MID-LATITUDE CYCLONES BASED ON SATELLITE IMAGERY. F. H. Carr, and J. P. Millard, Univ. of Oklahoma, Norman, Okla. *

G.9 PREDICTION OF FROST NIGHT TEMPERATURES THROUGH USE OF GOES EAST SATELLITE DATA AND TEMPERATURE PREDICTION MODELS. P. H. Heinemann and J. D. Martsolf, Univ. of Florida, Gainesville, Fla. 240

* Manuscript not available; if paper received in time, it will appear in back of book.

SESSION H: DATA ASSIMILATION AND DIAGNOSTICS

Chairperson: Kenneth Hardy, Air Force Geophysics Laboratory, Hanscom AFB, Mass.

H.1 DEVELOPMENT OF MANUALLY DIGITIZED RADAR AND GOES IR COMPOSITE PRODUCTS. P. H. Heinemann, J. D. Martsolf, and J. F. Gerber, Univ. of Florida, Gainsville, Fla.; D. L. Smith, NWS, Fort Worth, Texas 242

H.2 THE DIURNAL CYCLE IN COLD CLOUD IN THE TROPICS DURING 1982-83. P. A. Arkin, NMC/NOAA, Washington, D.C. 245

H.3 SATELLITE IMAGERY AS AN AID FOR DERIVING 300 MB AND 1000/300 MB GEOPOTENTIAL HEIGHTS. S. D. Swadley, NEPRF, Monterey, Calif. 250

H.4 VAS DATA ASSIMILATION INTO A MESOSCALE MODEL. J.M. Cram and M.L. Kaplan, Systems and Applied Sciences Corp., Hampton, Va. 254

H.5 A DIAGNOSTIC NUMERICAL MODEL FOR THE APPLICATION OF SATELLITE DATA FOR THE STUDY OF GLOBAL WEATHER SYSTEMS. G. L. Achtemeier and H. T. Ochs, Illinois State Water Survey, Champaign, Ill.; and Stanley Q. Kidder, Univ. of Illinois, Urbana, Ill. 260

H.6 THE UTILIZATION OF SEASAT-A DATA IN NUMERICAL WEATHER PREDICTION. D. G. Duffy and R. Atlas, GSFC/NASA, Greenbelt, Md. 261

SESSION I: PART I. WIND SIMULATION STUDIES

Chairperson: Milton Halem, Goddard Space Flight Center/NASA, Greenbelt, Md.

I.1 ANALYSIS OF A 0.5 MICRON SPACEBORNE WIND SENSOR. P. B. Hays, V. J. Abreu, Univ. of Michigan, Ann Arbor, Mich.; J. Sroga and A. Rosenberg, RCA Astro Electronics, Princeton, N.J. 266

I.2 OBSERVING SYSTEM SIMULATION EXPERIMENTS RELATED TO SPACE-BORNE LIDAR WIND PROFILING. PART I: FORECAST IMPACTS OF HIGHLY IDEALIZED OBSERVING SYSTEMS. M. Halem, GSFC/NASA,; and R. Dlouhy, M/A COM Sigma Data Corp., Greenbelt, Md. 272

I.3 OBSERVING SYSTEM SIMULATION EXPERIMENTS RELATED TO SPACEBORNE LIDAR WIND PROFILING. PART II: SENSITIVITY TO ATMOSPHERIC AND INSTRUMENTAL INFLUENCES. R. Dlouhy, M/A COM Sigma Data Corp.; and M. Halem, GSFC/NASA, Greenbelt, Md. 280

I.4 SIMULATION STUDIES OF THE IMPACT OF ADVANCED OBSERVING SYSTEMS ON NUMERICAL WEATHER PREDICTION. R. Atlas, E. Kalnay, J. Susskind, D. Reuter, W. E. Baker, and M. Halem, GSFC/NASA, Greenbelt, Md. 283

PART II: OBSERVING SYSTEM SIMULATION STUDIES

I.5 METHOD FOR ESTIMATING ERRORS FOR RADIATION BUDGET BASED ON A SCANNING RADIOMETER. G. L. Smith, L. M. Avis, R. N. Green, and B. A. Wielicki, Langley Research Center/NASA, Hampton, Va. 288

I.6 EFFECT OF THE UPPER ATMOSPHERE ON INFERRED CONCENTRATIONS OF STRATOSPHERIC TRACE GASES IN SOLAR OCCULTATION EXPERIMENTS. M. P. Weinreb, NESDIS/NOAA, Washington, D.C.; and I. Chang, American Univ., Washington, D.C. *

* Manuscript not available; if paper received in time, it will appear in back of book.

AUTHOR INDEX

		Paper	Page
A	Abreu, V.J.	A.8	35
		I.1	266
	Achtemeier, G.L.	H.5	260
	Adler, R.F.	B.6	58
		D.5	115
		G.3	216
	Anderson, L.L., Jr.	E.1	137
	Anderson, M.R.	D.8	132
	Arkin, P.A.	H.2	245
	Arnold, E.	G.2	*
	Atlas, D.A.	C.4	80
	Atlas, R.	H.6	261
		I.4	283
	Augustine, J.A.	G.1	210
	Avis, L.M.	I.5	288
B	Baker, W.E.	I.4	283
	Behunek, J.L.	D.4	112
	Brard, A.	C.6	*
	Brodrick, H.J.	G.4	222
C	Campbell, G.G.	E.2	294
	Carr, F.H.	G.8	*
	Chang, I.	I.6	*
	Chedin, A.	B.2	39
	Chesters, D.	G.5	226
	Chou, L.	E.5	155
	Christian, H.J.	F.7	202
	Cohen-Hallaleh, I.	B.2	39
	Cram, J.M.	H.4	254
	Crane, R.G.	D.8	132
D	Desbois, M.	C.2	76
	Dlouhy, R.	I.2	272
		I.3	280
	Dodge, J.C.	F.7	202
	Duffy, D.G.	H.6	261
	Durkee, P.A.	A.3	11
E	Elson, L.S.	A.1	1
F	Fraser, R.S.	A.2	4
	Frouin, R.	A.4	*
	Fuelberg, H.E.	F.2	172
G	Gautier, C.	A.4	*
	Gelman, M.	G.6	232
	Gerber, J.F.	H.1	242
	Green, R.N.	D.1	94
		I.5	288
	Griffith, C.G.	G.1	210
	Grody, N.C.	F.5	191
H	Hakkarinen, I.	G.3	216
	Halem, M.	I.2	272
		I.3	280
		I.4	283
	Hayden, C.M.	B.4	49
	Hays, P.B.	A.8	35
		I.1	266
	Heinemann, P.H.	G.9	240
		H.1	242
	Hindman, E.E.	A.3	11
	Hoffman, R.N.	F.8	206
	Huebner, G.	G.2	*
	Hung, R.J.	A.6	22
	Husson, N.	B.2	39
J	Jedlovec, G.J.	A.7	29
		F.4	185
	Jensen, D.R.	A.3	11
	Justus, C.G.	F.6	197
K	Kalnay, E.	I.4	283
	Kaplan, M.L.	H.4	254
	Kaufman, Y.J.	A.2	4
	Kennedy, B.	A.8	35
	Keyser, D.	G.5	226
	Kidder, S.Q.	H.5	260
	Kleespies, T.J.	B.5	55
	Koch, S.E.	G.7	234
L	Leary, N.E.	D.2	100
	Lee, T.H.	G.5	226
M	Mack, R.A.	D.5	115
	Mahoney, R.L.	A.2	4
	Martsolf, J.D.	G.9	240
		H.1	242
	McGuirk, J.P.	E.1	137
	McMillin, L.M.	B.5	55
		B.8	68
		F.5	191
	Menzel, W.P.	B.4	49
	Meyer, P.J.	F.2	172
	Millard, J.P.	G.8	*
	Miller, A.J.	G.6	232
	Moren, C.	E.5	155
	Moses, J.F.	A.5	15
		F.3	178
	Mostek, A.	G.5	226
	Moulinier, P.	B.2	39
	Mugnai, A.	B.1	*
	Muller, S.	E.4	149
N	Nacke, G.	C.3	*
	Negri, A.J.	B.6	58
	Neil, L.	D.6	121
	Nelson, C.	E.5	155
O	Ochs, H.T.	H.5	260
	O'Hara, L.S.	A.8	35
P	Petersen, R.A.	C.5	86
	Peslen, C.A.	G.7	234
	Phulpin, T.	C.6	*
	Pinty, B.	C.1	73
		C.2	76
	Prabhakara, C.	D.7	127
		E.3	143
	Purdom, J.F.W.	D.2	100
		D.3	106
		E.6	160
R	Ramond, D.	E.4	149
	Rao, P.K.	A.5	15
	Reuter, D.	I.4	283
	Rosenberg, A.	A.8	35
		I.1	266
	Ruprecht, E.	C.3	*
	Ruscher, P.H.	E.7	*
S	Schmidlin, F.J.	G.6	232
	Schreiner, A.J.	B.4	49
	Scofield, R.A.	A.5	15

* Manuscript not available; if received in time, it will appear in back of book.

		Paper	Page
	Scott, N.A.	B.2	39
	Shih, C.F.	E.2	294
	Short, D.A.	D.7	127
		E.3	143
	Sinclair, P.C.	E.6	160
	Smith, D.L.	H.1	242
	Smith, E.A.	B.1	*
	Smith, G.L.	I.5	288
	Smith, N.R.	E.1	137
	Smith, R.E.	A.6	22
	Smith, W.L.	B.3	45
	Spencer, R.W.	B.7	64
	Spray, L.	E.5	155
	Steranka, J.	C.5	86
	Stewart, J.K.	D.2	100
	Stout, J.	C.5	86
	Sroga, J.	A.8	35
		I.1	266
	Stum, J.	C.1	73
	Susskind, J.	I.4	283
	Swadley, S.D.	H.3	250
	Szejwach G.	C.1	73
		C.2	76
T	Tarpley, J.D.	A.5	15
	Thomasell, A., Jr.	G.4	222
	Thompson, A.H.	E.1	137
	Tournadre, J.	E.4	149
	Tsonis, A.A.	C.7	90
U	Uccellini, L.W.	G.7	234
V	Vaughan, W.W.	F.7	202
	Vonder Haar, T. H.	B.1	*
		A.3	11
		D.2	100
		D.4	112
		E.2	294
W	Wahiche, C.	B.2	39
	Wash, C.	E.5	155
	Weinreb, M.P.	I.6	*
	Westwater, E.R.	F.5	191
	Wetzel, P.J.	C.4	80
	Wielicki, B.A.	I.5	288
	Wilson, G.S.	F.1	164
	Woodward, R.H.	C.4	80
	Woolf, H.M.	B.3	45
Z	Zehr, R.M.	D.1.	94
	Zhenhui, W.	F.5	191

* Manuscript not available; if paper received in time, it will appear in back of book.

AGEOSTROPHIC MOTIONS IN THE STRATOSPHERE FROM SATELLITE OBSERVATIONS

Lee S. Elson

Jet Propulsion Laboratory/California Institute of Technology
Pasadena, California

1. INTRODUCTION

The winter polar stratosphere is frequently disturbed by sudden warmings. These events have been modeled extensively, with a recent example being that of Dunkerton et al. (1981). As satellite observations of the stratosphere have become available, sudden warmings, such as that which occurred in February of 1979, have been studied using a diagnostic approach, (Palmer, 1981) with an emphasis on the comparison of model results to observations. Such an approach is extremely valuable in understanding these events, however careful consideration of the limitations of the observations must be made before firm conclusions can be drawn.

2. THE DIAGNOSTIC APPROACH

2.1 The Generalized Equations of Momentum Conservation

In spherical coordinates, the zonally averaged zonal and meridional components of the momentum equation can be written as:

$$\bar{u}_t + \bar{v}\bar{u}_\phi/a - 2\,\omega_o \sin\phi\,\bar{v} - \bar{u}\bar{v}\tan\phi/a = -(\overline{u'v'})_\phi/a + 2\,\overline{u'v'}\tan\phi/a \qquad (1)$$

$$\bar{v}_t + \bar{v}\bar{v}_\phi/a + 2\,\omega_o \sin\phi\,\bar{u} + \bar{u}^2\tan\phi/a = -(\overline{v'^2})_\phi - (\overline{u'^2}-\overline{v'^2})\tan\phi/a - \bar{\Phi}_\phi/a \qquad (2)$$

where $\bar{u}$ and $\bar{v}$ are the zonal and meridional components of velocity, Φ is the geopotential, t is time, ϕ is latitude, a and ω_o are the earth's radius and rotation rate, and a subscript variable denotes a derivative with respect to the variable. An overbar indicates a zonal average, a prime a deviation from that average, and vertical velocity and dissipation have been neglected in this treatment.

2.2 Quasi-geostrophic Assumptions

As discussed by Palmer (1981), the usual approach to determining the mean circulation is to calculate $\bar{u}$ by assuming strict geostrophy in (2). $\bar{\Phi}$ is determined from satellite temperature observations together with a boundary value of $\bar{\Phi}$. This approach can be expected to give reasonable results as long as $\bar{u}$ or $\sin\phi$ are not small. As will be shown, the first condition is occasionally violated in the stratosphere. For completeness, it should be mentioned that either $\bar{v}$, or the residual version of this quantity can be calculated by assuming that the first and third terms on the left side of (1) are balanced by the first and second terms on the right side of that equation. In addition, the thermodynamic equation can be used to define the Eliassen-Palm (E-P) flux which is important to an understanding of the interaction between the waves and the mean flow. Since these quantities have not yet been calculated for the data data set which will be examined here, their formulation will not be discussed.

It is obvious from (1) and (2) that u' and v' must be specified. This is done by assuming that these quantities are related geostrophically to Φ' by the following:

$$2\,\omega_o \sin\phi\, v' = \Phi'_\lambda/(a\cos\phi) \qquad (3)$$

$$2\,\omega_o \sin\phi\, u' = -\Phi'_\phi/a \qquad (4)$$

Once the velocities have been determined, it is possible to substitute them back into (1) and (2) to check for consistency in the scaling assumptions.

3. SUDDEN WARMINGS

Much of the discussion of sudden warmings in the literature centers on the role of the focusing of planetary waves into a small polar area where mean flow deceleration is accompanied by a warming. One way for such focusing to occur is through a partial reflection of the upward propagating waves by a critical line. Since critical lines are determined by the location where these slowly moving waves have Doppler shifted phase speeds of zero, one would expect that regions of zero mean zonal wind might have an effect on the E-P fluxes (Dunkerton et al., 1981). Such an effect or its absence should be readily observable from the analysis discussed above. An important result of Palmer's work is that the diagnostically determined evolution of the zero wind line during the warming of February, 1979, did not agree with the behavior suggested by the model of Dunkerton et al. In particular, no encroachment of easterlies from the equatorial regions into the mid-latitudes, was implied by the data. Such behavior played an important role in the model evolution of the mean zonal wind.

4. LIMS DATA

The data used in this study come from the Limb Infrared Monitor of the Stratosphere (LIMS)

instrument which has been described by Gille and Russell (1984). This instrument has a vertical resolution less than 4 km and the spacecraft (Nimbus 7) orbit provided good daily global coverage. One of the data products from the experiment consists of Fourier components of both temperature and geopotential mapped as a function of latitude and pressure altitude. The geopotential was used in (2) - (4) as input data. Although these data have been compared favorably with other sources, and the data appear to be self-consistent, the usual caveats concerning accuracy limitations should be kept in mind during the discussion that follows.

Derived quantities from LIMS will be compared with the same quantities which Palmer derived from the Stratospheric Sounding Unit (SSU) on TIROS-N. Both data sets have been interpolated to one synoptic time: for LIMS, it is 12:00 GMT, and for the SSU, it is 00:00 GMT. As a result, direct comparisons are difficult during times of rapidly changing conditions.

5. RESULTS AND DISCUSSION

Fig. 2 shows the mean zonal wind versus pressure and latitude for Feb. 16 and 17 at 12:00 GMT as derived from LIMS data. For comparison, Fig. 1, which has been taken from Palmer (1981), shows the same quantity for 00:00 on Feb. 17. Although the scales are a little different in the two figures, it can be seen that the LIMS data indicate greater extremes in the values of $\bar{u}$. The westerly jet at 75° shows maximum values in excess of 50 m/s, and perhaps as large as 65 m/s. In the SSU data, the maximum is less than 50 m/s. Perhaps more significant, the LIMS data show the existence of a zero wind line and a small region of easterlies in Fig. 2a near 40°. Even though this zero wind line has disappeared 24 hours later, as shown by Fig. 2b, the LIMS data indicate a more extensive region of low values of $\bar{u}$ at this time, than do the SSU data. As will be shown below, the easterlies indicated by the LIMS data are more prevalent at earlier times. One suspects that the reason for the differences between the two data sets arises from the higher vertical resolution of the LIMS instrument.

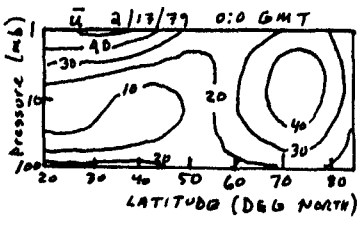

Fig. 1. Height/latitude cross section of the zonally averaged zonal wind, in m/s, as determined from SSU data by Palmer (1981). Data have been interpolated to Feb. 17, 1979 at 00:00 GMT.

As mentioned, once $\bar{u}, \bar{v}, u'$ and v' have been calculated using the approximations described above, they can be substituted into (1) and (2) to determine the importance of the neglected terms. It has been found that for many days

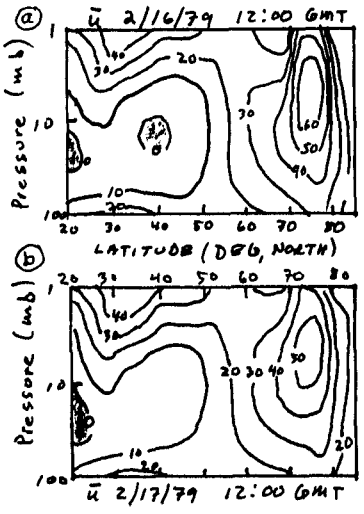

Fig. 2. As in Fig. 1, but using LIMS data for 12:00 GMT on Feb. 16 (a) and 17 (b), 1979. Figure scale is slightly different from Fig. 1. Negative (shaded) regions indicate areas of easterlies.

where disturbed conditions exist in the polar regions, $\bar{u}$ is not well approximated by the geostrophic relationship at some locations. Both the centrifugal term {4th on the left side of (2)} and the wave flux convergence terms {1st and 2nd terms on the right side of (2)} can be relatively large. As an example, the Coriolis term {3rd term on the left side of (2)} and the wave flux term are compared in Fig. 3 for 2 days in February. The increased coverage in latitude over the earlier figures, allows one to see that there is an encroachment of easterlies on Feb. 13 that looks remarkably like the early stages of the model of Dunkerton et al. It should be noted, however, that the subsequent evolution of $\bar{u}$ in the model does not resemble the diagnostically determined evolution. On both of the days shown in Fig. 3, the wave flux terms are large enough to alter the balance of momentum in the 50° to 55° region and their tendency would be to bring the mean zonal wind closer to zero in that region. In the polar regions, the wave flux tends to reinforce the westerlies and the centrifugal term (not shown) tends to reduce the westerlies.

6. FUTURE WORK

An analysis of the meridional momentum balance on a day to day basis shows that the mid-latitude region of easterlies or near easterlies is a persistent feature over several days. A proper determination of $\bar{u}$ would involve the inclusion of the two terms discussed above and would be expected to indicate that a large area in the mid-latitudes could, within the errors of the LIMS measurements, be surrounded by a zero wind line. A more complete understanding of the role of critical lines and upward propagating waves will result from the calculation of the E-P fluxes as well as the residual mean meridional circulation.

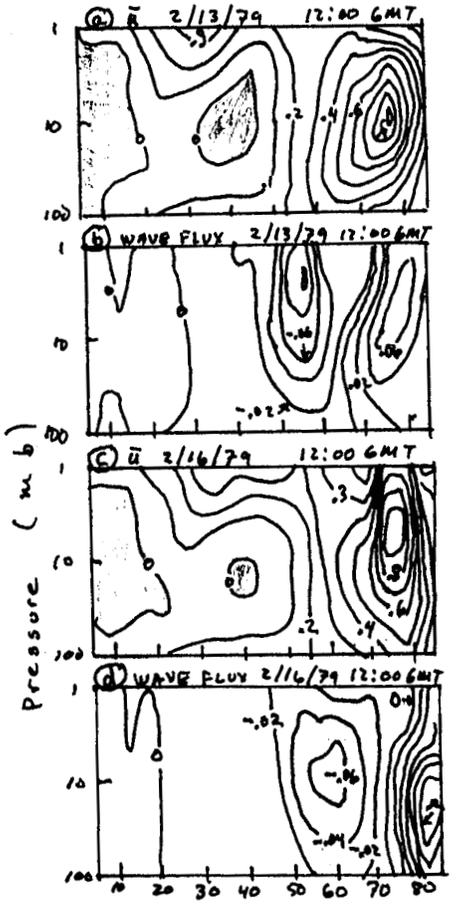

Fig. 3. Height/latitude cross sections of Coriolis terms for Feb. 13 (a) and Feb. 16 (c), and wave flux terms for those dates (b and d respectively). Note increase in latitude scale coverage from Figs. 1 and 2. Units are cm/s^2.

7. REFERENCES

Dunkerton, T., C.-P. Hsu, and M. E. McIntyre, 1981: Some Eulerian and Lagrangian diagnostics for a model stratospheric warming. J. Atmos. Sci., 38, 819-843.

Gille, J. C., and J. M. Russell III, 1984: The Limb Infrared Monitor of the Stratosphere (LIMS): An overview of the experiment and its results. Submitted to J. Geophys. Res.

Palmer, T. N., 1981: Diagnostic study of a wavenumber-2 sudden warming in a transformed Eulerian-mean formalism. J. Atmos. Sci., 38, 844-855.

Satellite Measurement of Aerosol Mass over Land

Robert S. Fraser
Goddard Laboratory for Atmospheric Sciences
NASA/Goddard Space Flight Center
Greenbelt, MD, U.S.A. 20771

Yoram J. Kaufman
University of Maryland
in collaboration with
Goddard Laboratory for Atmospheric Sciences
NASA/Goddard Space Flight Center
Greenbelt, MD, U.S.A. 20771

R. L. Mahoney
Science Systems and Applications, Inc.
10210 Greenbelt, Road
Seabrook, MD, U.S.A. 20706

1. INTRODUCTION

The aerosol transport, source, and sink strengths are important for understanding tropospheric chemistry. Controls and legislation concerning gaseous emission depend on such knowledge. Data are required on specific constituents such as aerosol sulfate, sulfur, water, etc., rather than on only total mass.

Measurements from satellites of the radiance of sunlight scattered from the earth and its atmosphere have been used to derive properties of aerosols. Methods are most successful where the surface reflection is weak and fairly uniform. Many investigators have been involved in making measurements of aerosol optical thickness (Griggs 1975, 1979; Mekler et al., 1977; Carlson, 1979; Koepke and Quenzel, 1979; Kaufman and Joseph, 1982) and mass (Fraser, 1976) over oceans. Attempts to make such measurements over land do not seem to have been reported. The emphasis in this report is on satellite measurements of aerosol optical thickness and mass over land.

Measurements from the Geostationary Operational Environmental Satellite (GOES) by the Visible Infrared Spin-Scan Radiometer (VISSR) are used. Since VISSR is not calibrated after launch, a post-launch calibration method was developed and is presented. A discussion of the algorithm follows for deriving the aerosol optical thickness over land from the measured radiance of scattered sunlight by means of a radiative transfer model in which the optical characteristics of the aerosol are assumed. The surface reflectance values are required and are measured on days when the optical thickness is small. Values of the optical thickness measured from the ground and satellite are compared. Finally, the flux divergence of particulate sulfur during an air pollution incident is given.

2. CALIBRATION

GOES stationed near 75° W longitude provides radiance measurements of Eastern United States and the Atlantic Ocean every one-half hour. The effective wavelength of the visible light channels is 610 nm. The nadir spatial resolution is about 1 km. Unfortunately, VISSR is uncalibrated after launch. Furthermore, the gains of the eight channels are changed aperiodically to reduce striping that appears in images of the earth. Hence, VISSR should be calibrated on each day that its measurements are used quantitatively.

Earlier investigators attempted post-launch calibrations of VISSR. The prelaunch calibration between radiance (L) and voltage counts (C) was

$$L = a+bC^2, \tag{1}$$

with possible small contributions from higher order terms. L is a relative radiance in this report and is expressed in reflectance units:

$$L = \pi L'/F \cos\theta_0,$$

where L' is the absolute radiance, F is the solar irradiance, and θ_0 is the solar zenith angle. In the following discussion C refers to the adjusted counts made available to users of the VISSR measurements. Norton et al. (1980) calibrated VISSR with direct sunlight that illuminated only a small fraction of the area of the optical surfaces. They assumed that the small prism collecting the sunlight maintained the same tramissivity as measured before launch. Muench (1981) showed that the post-launch calibration of VISSR could differ significantly from the prelaunch values. For example, the responsivity of the VISSR on the SMS 2 satellite, whose measurements are used in this study, decreased 40 percent during one year.

Because of post-launch instrumentation changes and aperiodic adjustments to the VISSR gain, a procedure was developed to calibrate

VISSR on each day that its measurements were used. The voltage counts were collected from many cloud-free regions of an Atlantic Ocean image. These counts were related to radiances computed for models of the ocean-atmosphere system. An additional description of the method follows.

The radiances were calculated for a model of the ocean-atmosphere system (Ahmad and Fraser, 1982). The ocean surface was rough, but the radiances were calculated for regions far removed from the bright glitter pattern of the sun. The gain b in Eq. (1) changed by only one percent for a likely range of wind speeds between 2 and 10 m/s. An additional reflectance of 0.005 accounts for the light scattered from below the ocean surface. This reflectance is small, since the effective wavelength was 610 nm.

The model atmosphere contains the standard gases, the absorbing gas ozone, and aerosols. The maritive aerosol of Shettle and Fenn (1979) at a relative humidity of 80 percent was used. The size distribution over the optically effective range follows a power law:

$$(2) \qquad dn/d \log r^{-2.48},$$

where n is the number density of spheres with radius r. Their index of refraction was 1.35-1.1×10^{-8} i. The aerosol optical thickness was 0.1. The gain b in Eq (1) decreases 17 percent for a 0.1 decrease in aerosol optical thickness.

The VISSR responses to the ocean radiances in one image was developed from a collection of histograms of 15-40 regions of the Atlantic Ocean that seemed to be cloud free. Each histogram consisted of voltage counts for arrays as small as 80 rows and 80 columns to large arrays of 400 x 400 high-resolution pixels. Because the radiance varies approximately as $L \sim \cos\Theta$, where Θ is the zenith angle of array at a point of where observation to VISSR, the histograms were obtained for a range of Θ between 20° to 80° in order to obtain a large range of radiances. Inasmuch as the radiances over land during very hazy conditions attain twice the ocean values, the final calibration curves were extrapolated to cover the highest radiances over land.

A representative count C for each histogram was obtained from the following relation:

$$(3) \qquad C = \overline{C'} + \Delta C',$$

where $\overline{C'}$ is the mean of the lowest 10 to 30 percent of the counts, and $\Delta C'$ accounts for the difference between that mean and the median value of a uniform scene. C is an estimate of the counts if no clouds were present. A representative histogram of C' and a calculation of C are given in Fig. 1. 953 values of C' are included in this histogram. The numbers of the lowest 10 and 30 percent of all counts are 95 and 286, respectively. The calculation of $\overline{C'}$ is shown.

Before counts are related to radiance, Eq. (1) is put in a different form:

$$(4) \qquad L = \alpha (C^2 - C_0^2)/(255)^2,$$

where α is the gain, C is the count obtained from a histogram, C_0 is the count for zero radiance, and the VISSR counts are suplied as an 8-bit number. C_0 is obtained by viewing black space beyond the limb of the earth. The gain α

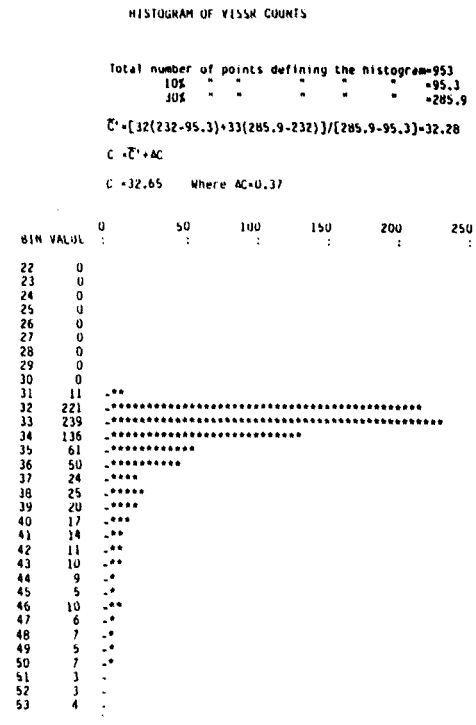

Fig. 1. Histograms of VISSR counts over the Atlantic Ocean where it seemed to be without clouds.

is obtained from the slope of a regression line of the radiance L on C^2. Many samples of L, C^2 pairs for one image were chosen by a booststrap statistical inference method (Diaconis and Efron, 1983). For a particular image, 15-40 pairs of L, C^2 values were available. A sample point was assigned a number. The numbers were selected randomly until as many pairs were available as were present initially. A pair L, C^2 could be chosen more than once. A thousand such sets were constructed. L was regressed linearly on C^2 for each of the 1000 sets. The slope of each line gave the value of gain α for an image.

The regression values of the gain that were computed for July and August 1980 are given in Fig. 2. The error bars include 68 percent of

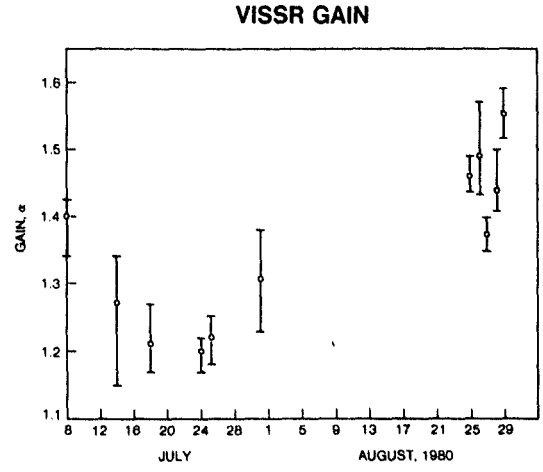

Fig. 2 The SMS 2 VISSR gain for 7 weeks.

the gains computed by the bootstrap method. The gains (α) for the SMS2 VISSR changed by 25 percent over a six week period.

3. ALGORITHM

The algorithm for deriving aerosol properties is given in Fig. 3. The VISSR counts from

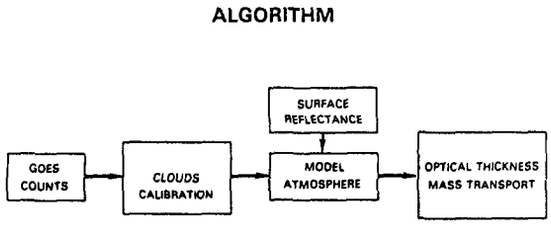

Fig. 3 Algorithm for deriving the aerosol properties from satellite measurements.

a GOES are taken for regions that are expected to be free of clouds. Infrared images screen out thin cirrus clouds. These operations take place on an Atmospheric Oceanic Information Processing System (AOIPS). The surface reflectance is derived from VISSR observations on days with small amounts of haze. The aerosol optical thickness is derived from the calibrated VISSR radiances by means of a radiative transfer model. The last box on the right indicates that variables well correlated with the aerosol optical thickness are available also, or can be calculated with additional data, such as winds, which are not derived from satellite observations.

A somewhat different radiative transfer model was developed for eastern United States. The ground is assumed to reflect light according to Lambert's law with a reflectance value derived from VISSR observations. The atmospheric model is the same as described previously, except for the aerosol properties. The size distribution was given by Whitby (1978) for the accumulation mode, which is the strongly dominate mode for aerosol optical properties in the visible spectrum. It is a log normal function with a mean and standard deviation of the logarithm of the diameter in micrometers of -2.40 and 0.693, respectively. The index of refraction of the assumed sperical particles was 1.43-0.0035 i, resulting in an albedo of single scattering of 0.96. Tables of radiance are calculated for this model as a function of the coordinates of the sun, satellite, and points of observation, the surface reflectance, and the aerosol optical thickness.

An error budget for satellite measurments of aerosol optical thickness is given in Fig. 4. The unperturbed model is representative for VISSR measurements of Eastern United States during the morning. A surface reflectance error ΔR of only 0.01 causes an optical thickness error of 0.04 to 0.05. The precision ΔL_p of the radiance measurements was determined by taking the difference in the mean pixel counts over an ocean area of 250,000 km^2 on days when the gain α (Eq. (4)) changed only slightly. The bias radiance error ΔL_B is difficult to establish. It could have several sources: an error in water reflectance, wrong

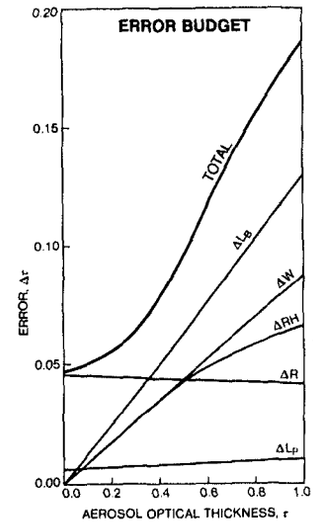

Fig. 4. Results of a sensitivity study for the effect of several error sources on the error in the VISSR measurement of aerosol optical thickness (ΔL_p = 0.001, precision in the calibration; ΔL_B = 0.05 L, bias error in the relative radiance; ΔRH= 10%, error in relative humidity; ΔW = 0.01, error in the dry aerosol albedo of single scattering; ΔR=0.01, error in surface reflectance). The unperturbed model parameters are: λ= 550 nm, solar zenith angle = 60°, observation polar angle = 60° and azimuth angle from principal plane = 150°, aerosol index of refraction = 1.43- 0.0035 i, aerosol albedo of single scatter = 0.96, and RH = 80%.

aerosol models, nonlinear response by VISSR, and computations. An estimate of the bias error is 5 percent of the relative radiance, which results in an optical thickness error that increases almost linearly with wavelength, as is the case with the relative humidity and albedo of single scattering errors. The total error is 20 percent of the aerosol optical thickness for values exceeding 0.3. The validity of these error estimates is shown next with experimental data.

The accuracy of both the calibration and the algorithm for the optical thickness is demonstrated with Fig. 5. The aerosol optical thicknesses measured by the satellite are compared with values derived from solar transmission measurements made from the ground near Washington, D.C., Columbus, Ohio, and Miami, Florida. In order to estimate the accuracy of the regression line, its equation was calculated for 1000 sets of data according to the bootstrap statistical method (Diaconis and Efron, 1983). The dashed lines include 68 percent of the regression lines. The deviation of the dashed lines from the mean regression line ranges from $\pm$ 0.04 to $\pm$ 0.08 as the optical thickness increases from 0.2 to 0.7. These values are about one-half of the estimated total error in Fig. 4. The measured errors indicate the accuracy of calibrating the satellite radiometer and algorithm for deriving optical thickness from the satellite radiances.

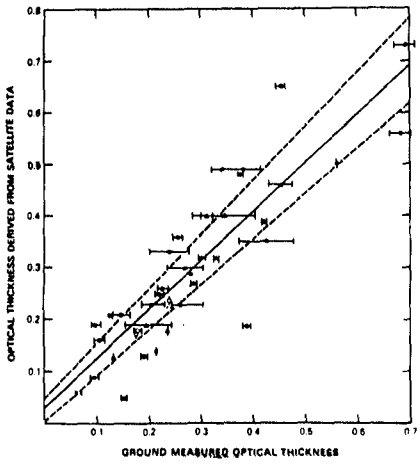

Fig. 5. The aerosol optical thicknesses derived from satellite observations are compared with the values for a vertical column measured from the ground.

4. AEROSOL MASS

Mass density at a point

The total mass of an aerosol constituent is based on a linear relation between its point mass (ρ) and the aerosol scattering coefficient (b_s^d):

$$(5) \qquad b_s^d = a + b\ \rho,$$

where a and b are constants. In the following discussion ρ may be the mass density of the fine particles (FPM), sulfate ($SO_4^=$), or sulfur (S) in the aerosol: and b_s^d is a scattering coefficient measured in the visible spectrum of air at low relative humidity. The values of the constants depend on the region and season (Pierson et al., 1980; Waggoner and Weiss, 1980; Wolff et al., 1982). The correlation between ρ and b_s^d usually exceeds 0.9.

The data of Ferman et al. (1981) and Wolff et al. (1982) are used for estimating the mass density of $SO_4^=$. They found the following empirical relationship:

$$(6) \qquad \frac{b_s^d}{FPM} = 7.32\ \frac{SO_4^=}{FPM} + 2.26,$$

where FPM includes $SO_4^=$, and their units are gm^{-3} and those of b_s^d are m^{-1}. The correlation between b_s^d/FPM and $SO_4^=$/FPM was 0.98. Equation (6) can be written in the following form:

$$(7) \qquad b_s^d = 9.58\ SO_4^= + 2.26\ R,$$

where R is the remaining mass in the fine particle mode ($R = FPM - SO_4^=$). Since the R-term of Eq. (7) contributes only one-fourth of the total scattering coefficient b_s^d, and the concentration of R is not known, a constant ratio $R/SO_4^=$ is assumed. The $SO_4^=$/FPM ratio for the eastern United States usually falls within the range of 0.3 to 0.6 (Stevens et al., 1978: Trijonis, 1982). Therefore, an average values of $R/SO_4^= = 1.27$. Substition of this ratio in (3) results in the following equation for sulfate mass:

$$(8) \qquad SO_4^= = \left(0.080\ {}^{+0.009}_{-0.014}\right) b_s^d$$

The satellite measurement of radiance is not related directly to b_s^d, but is related to the extinction coefficient b_{ext} for the aqueous aerosol. The relation between between b_s^d and b_{ext} was discussed by Fraser et al. (1983):

$$(9) \qquad b_s^d\ (\lambda_1) = g(\lambda)\ f(RH) W b_{ext}(\lambda_2),$$

where W is the aerosol albedo of single scatter, f reduces the scattering coefficient of the wet aerosol to that of a dry aerosol, and $g \sim \lambda^{-1.6}$ to relate the field measurements of b_s^d at λ_1, to the satellite measurements at λ_2. The mass of $SO_4^=$ and S are obtained by substitution of Eq (9) in Eq. (8):

$$SO_4^= = 0.12\ f(RH) W\ b_{ext}\ (610)$$
$$S = 0.04\ f\ w\ b_{ext},$$

where the units of b_{ext} and mass density are m^{-1} and $g\ m^{-3}$, respectively.

B. Columnar Mass

The aerosol mass in a vertical column (M) is obtained by integration of Eqs. (5) or (10) with respect to height (z):

$$M_i = \int_{surface}^{30\ km} \rho\ (z)dz\ ,\ i = 1, 2$$

$$= c_i \int f(z) w(z) b_{ext}(z)\ dz.$$

$$= c_i\ \overline{f\ w} \int b_{ext}(z) dz$$

$$(11) \qquad M(S) = 0.04\ \overline{fw}\ \tau(610)\ g\ m^{-2},$$

where $C_1 = 0.04$ and $C_2 = 0.12$ for S and $SO_4^=$, respectively, and τ is the total vertical optical thickness of aerosol. A weighted product $\overline{fw}$ is taken outside of the integral, because none of the vertical profiles are known from the satellite observations.

The weighted mean $\overline{fw}$ is difficult to estimate accurately. As an example, a vertical profile of humidity and scattering coefficient of ambient air (b_s) measured over Chesapeake Bay are shown in Fig. 6. The dry aerosol scattering coefficient is obtained from the aqueous coefficient from the following relation:

$$(12) \qquad b_s^d = 1.4\ (1-RH)^{0.7}\ b_s$$

The strong scattering by the aqueous aerosol with high relative humidity at 1200 m vanishes for the dry aerosol. On the other hand, the strong scattering by the aqueous aerosol at lower relative humidity at 400 m remains strong for the dry aerosol. Such vertical profiles of b_s^d can not be derived from current satellite data. Hence, the correct weighting of the relative humidity ($\overline{fw}$) is uncertain. Perhaps such profiles of the dry aerosol can be derived in the future from lidar and humidity data.

The relative error in the columnar mass (Eq. 11) is given by the approximate relation

$$(13) \qquad \frac{\Delta M}{M} = \pm\left[\left(\frac{\Delta C_i}{C_i}\right)^2 + \left(\frac{\Delta f}{f}\right)^2 + \left(\frac{\Delta w}{w}\right)^2 + \left(\frac{\Delta \tau}{\tau}\right)^2\right]^{1/2}$$

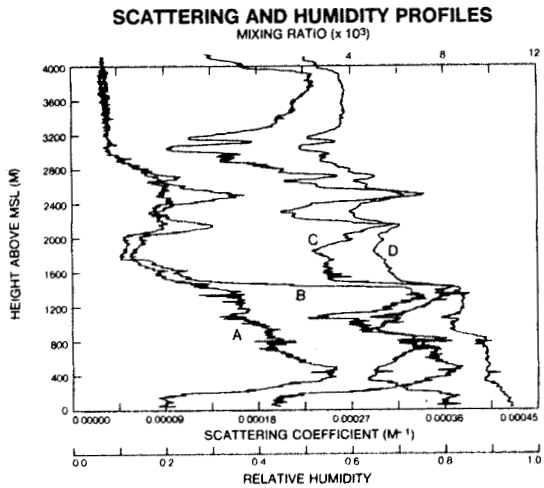

Fig. 6. The scattering coefficient of dry air (A) derived from the scattering coefficient of moist air (B). The relative humidity is given by C and mixing ratio by D. The time of measurements is 1344 to 1424 GMT, Sept. 1982. Kaufman et al., 1983, made the measurements.

The relative errors in c_i, f, and w were estimated in percent by Fraser et al. (1983) as ± 25, +20, and ± 10 respectively. The error of measuring the aerosol optical thickness is $\pm$ 15 percent Fig. 5). The resultant error in estimating the columnar mass $\Delta M/M = \pm 37$ percent. The error in estimating the mass of sulfur results more from lack of knowledge about the optical properties of hazes rather than measurement of the satellite optical thickness.

5. ANALYSIS OF SATELLITE OBSERVATIONS

The mass of aerosol sulfur is desrived from GOES observations taken at 1300 GMT on 31 July 1980. The sun had been shining for 3 hours over the eastern U.S. This day was chosen because a large effort was made by many other experimenters to measure and analyze the properties of the air pollution for this day. A weak cyclone with accompanying rain was located over Lake Michigan. South of this region weak, anticyclonic flow, which is associated with elevated air pollution, prevailed.

The columnar mass density of aerosol sulfur is calculated by means of Eq. (11) and given in Fig. 7. The maximum concentrations above 0.045 g m^{-2} occur over the Atlantic Ocean and West Virginia. No other measurements of the columnar mass have been published, but surface measurements can be used to estimate columnar mass. If it is assumed that the volume density is independent of height within the layer extending 1500 m above the ground and zero above that, then the average mass of aerosol sulfur is between 0.005 and 0.008 g/m^2 east of the Mississipi River during the summer (Husar and Patterson, 1980). The maximum value found in publications was 0.040 g/m^{-2} over West Virginia (Hidy et al., 1978). The satellite values measured at a particular instant with a spatial resolution of 100 km lies within the range of previous data, except for values that exceed 0.04gm^{-2}. The total mass of aerosol sulfur within the outlined region is 0.036 Tg.

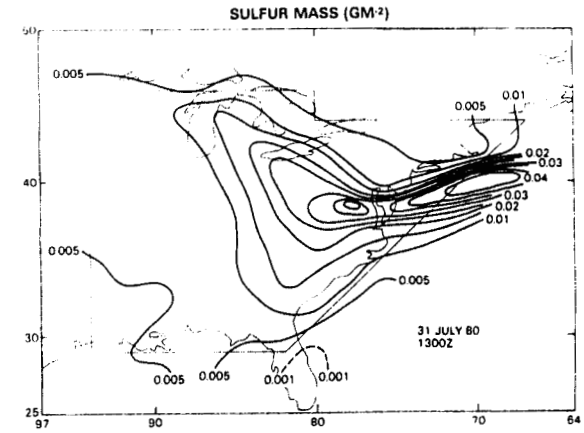

Fig. 7. The columnar density of aerosol sulfur. The borders through which the transport of sulfur are computed are given by the continuous, straight lines.

The horizontal divergence of aerosol mass is computed with the wind velocity at the 925 mb level measured by rawins one hour before the satellite observations. The streamlines in Fig. 8 show the direction of flow: southerly in the

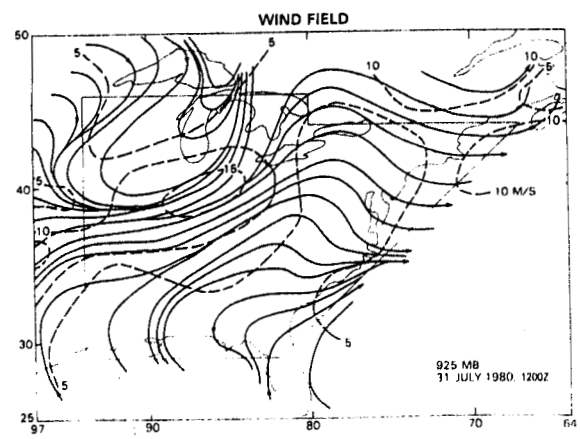

Fig. 8. The wind field at the 925 mb level. The continuous lines are the streamlines, and the dashed lines give the wind speed in m s^{-1}.

south, westerly in midlatitudes, and cyclonically around a low pressure over Lake Michigan. The wind speed is given by the dashed lines. The maximum speed is 15 m/s south of Lake Michigan and less than 5 m/s over a large region of eastern region of eastern U.S.

The divergence of sulfur mass is shown in Fig. 9. The strongest divergence is associated with the east-west belt of maximum aerosol concentration, which coincides with the strongest winds. There do not seem to be similar published data for comparison. The annual anthropogenic source strength of SO_2, however, forms a basis for comparison in Fig. 10. The production of S is 0.5 of that of SO_2. The belt of maximum production is similar to the satellite values in magnitude and location.

MASS DIVERGENCE OF SULFUR

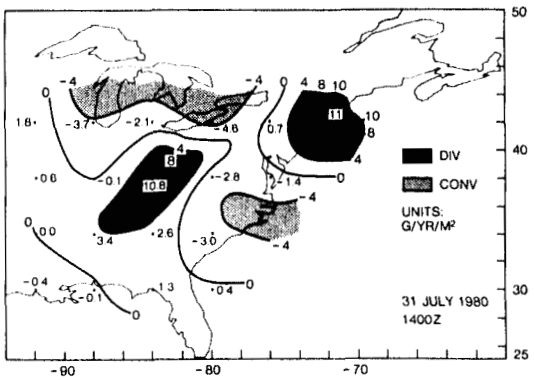

Fig. 9. Horizontal mass divergence of particulate sulfur in units of g/yr/m2. The time is 1400 GMT, 31 July 1980.

ANTHROPOGENIC PRODUCTION SO_2

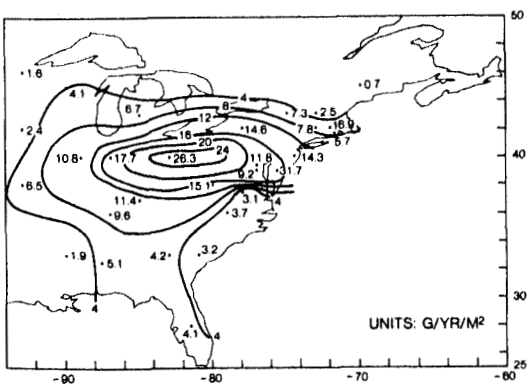

Fig. 10. Annual rate of production of SO_2 in units of g/yr/m^2 (Acid Deposition Processes in Eastern North America, 1983).

5. CONCLUSION

A method has been presented for calibrating satellite measurements of the radiance of scattered sunlight. The calibrated radiances are then used to measure the aerosol optical thickness over land. Optical thicknesses derived from solar transmission measurements were then used to validate the calibration and algorithm for deriving the aerosol optical thickness from satellite measurements. The standard error of estimate was 15 percent.

Since the mass of aerosol sulfur species is well correlated with the scattering coefficient of the aerosols at low relative humidity, the total mass of sulfur in a vertical column was estimated from the measurement of optical thickness. The accuracy of the columnar mass was estimated to be 40 percent. An example of the horizontal mass divergence of the sulfur at one instant was similar to the annual anthropogenic production of gaseous sulfur. The satellite measurements of aerosol mass, transport, and divergence require validation with an independent set of data.

References

Acid Deposition Atmospheric in Eastern North America, 1983: Academy Press, Washington, DC., 373 p.

Ahmad, Z., and R. S. Fraser, 1982: An iterative radiation transfer code for ocean-atmosphere systems. J. Atmos. Sci., 39, 656-665.

Carlson, T. N., 1979: Atmospheric trubudity in Saharan dust outbreaks as determined by analyses of satellite brightness data. Mon. Wea. Rev., 107. 322-335.

Diaconis, P., and B. Efron, 1983: Computer-intensive methods in statistics. Sci. Amer., 249, 116-129.

Ferman, M. A., G. T. Wolff and N. A. Kelly, 1981: The nature and sources of haze in the Shenandoah Valley/Blue Ridge Mountains area. J. Air Pollution control Assoc., 31, 1074-1083.

Fraser, R. S., 1976: Satellite measurements of mass of Sahara dust in the atmosphere. Appl. Opt., 15, 2471-2479.

Fraser, R. S., Y. J. Kaufman and R. L. Mahoney, 1983: Satellite measurements of aerosol mass and transport. Submitted to Atmos. Environ.

Griggs, M., 1975: Measurements of atmospheric aerosol optical thickness over water using ERTS-1 data. J. Air Poll. Contr. Assoc., 25, 622-626.

_____, 1979: Satellite observations of atmospheric aerosols during the EOMET cruise. J. Atmos. Sci., 36, 695-698.

Hidy, G. M., P. K. Mueller and E. Y. Tong, 1978: Spatial and temporal distributions of airborne sulfate in parts of the United States. Atmos. Environ., 12, 735-752.

Husar, R. B., and D. E. Patterson, 1980: Regional scale air pollution: sources and effects. Annals New York Acad. Sci., 338, 399-417.

Kaufman, Y. J., T. W. Brakke and E. Eloranta, 1983: Field experiment to measure the radiative characteristics of a hazy atmosphere. Preprints Fifth Conf. on Atmos. Radiation, Amer. Meteor., Soc., Boston, Mass., 224-227.

Kaufman, Y. J., and J. H. Joseph, 1982: Evaluation of surface albedos and extinction characteristics of the atmosphere from satellite images, J. Geoph. Res., 87, 1287-1299.

Koepke, P., and H. Quenzel, 1979: Turbidity of the atmosphere determined from Satellite: Calculation of optimum viewing geometry. J. Geophys. Res., 84, 7847-7855.

Mekler, Yu., H. Quenzel, G. Ohring and I. Marus, 1977: Relative atmospheric aerosol content from ERTS observations. J. Geophys. Res., 82, 967-970.

Muench, H. S., 1981: Calibration of Geosynchronous Satellite Video Sensors. Air Force Geophysics Laboratory, Hanscom AFB, Mass., 19 pp.

Norton, C. C., F. R. Mosher, B. Hinton, D. W. Martin, D. Santek and W. Kuhlow, 1980: A model for calculating desert aerosol turbidity over the oceans from geostationary satellite data. J. Appl. Meteor., 19, 633-644.

Pierson, W. R., W. W. Brachaczek, T. J. Truex, J. W. Butler and T. J. Korniski, 1980: Ambient sulfate measurements on Allegheny Mountain and the question of atmospheric sulfate in the northeastern United States. Annals New York Acad. Sci., 338, 145-173.

Shettle, E. P., and R. W. Fenn, 1979: Models for the aerosols of the lower atmosphere and the effects of humidity variations on their optical properties. Air Force Geophysics Laboratory Report No. AFGL-TR-79-0214. Hanscom AFB, Mass., 94 pp.

Stevens, R. K., T. G. Dzubay, G. Russwarm and D. Rickel, 1978: Sampling and analysis of atmospheric sulfates and related species. Atmos. Environ., 12, 55-68.

Trijonis, J., 1982: Existing and natural background levels of visibility and fine particles in the rural east. Atmos. Environ., 16, 2431-2445.

Waggoner, A. P., and R. E. Weiss, 1980: Comparison of fine particle mass concentration and light scattering extinction in ambient aerosol. Atmos. Environ., 14, 623-626.

Whitby, K. T., 1978: The physical characteristics of sulfur aerosols. Atmos. Environ., 12, 135-159.

Wolff, G. T., M. A. Ferman, N. A. Kelly, D. A. Stroup and M. S. Ruthkosky, 1982: The relationships between the chemical composition of fine particles and visibility in the Detroit metropolitan area. J. Air Pollution Control Assoc., 32, 1216-1220.

A.3

MARINE AEROSOL OPTICAL DEPTH FROM SATELLITE-DETECTED RADIANCE

P. A. Durkee [1], E. E. Hindman [1], D. R. Jensen [2], and T. H. Vonder Haar [1]

[1] Department of Atmospheric Science
Colorado State University
Fort Collins, CO 80523
(303) 491-8398

[2] Ocean and Atmospheric Sciences Division
Naval Ocean Systems Center
San Diego, CA 92152

1.0 INTRODUCTION

Recent improvements of the sensitivity of satellite-borne sensors have made it possible to detect variations of aerosol optical depth from space. These variations may be caused, in part, by relative humidity variations through growth of particles by water vapor condensation. The variations also may be caused by particle population variations at constant humidity. To examine these hypotheses, a set of near-simultaneous satellite images and aircraft measuresments was collected between 20 September to 7 October, 1982 off-shore of southern California. The satellite images were from the NIMBUS-7 Coastal Zone Color Scanner (CZCS) and the NOAA-7 Advanced Very High Resolution Radiometer (AVHRR). The airborne measurements consisted of aerosol particle sizes, numbers and compositions and atmospheric state variables. Extinction due to scattering was calculated from the measured particle size distributions. Then, the vertical and horizontal distributions of extinction were compared with the satellite-detected radiance values. The results show a positive relationship between scattering by marine aerosol particles and satellite-detected radiance. Also, scattering by marine particles is shown to be related positively to variations of relative humidity. Therefore, satellite sensors appear to be able to yield information on relative humidity variations as well as boundary layer optical properties.

2.0 THE EXPERIMENT

Satellite images were collected and analyzed in real-time at the Scripps Satellite Oceanography Facility (SSOF). During the experiment period, NIMBUS-7 CZCS and NOAA-7 AVHRR images were collected. The AVHRR sensor provides imagery in one visible and one near-infrared band. Below are the spectral responses of the AVHRR channels:

Channel 1 0.58-1.68 μm (yellow-red visible)
Channel 2 0.725-1.10 μm (near-infrared)

The CZCS sensor provides imagery in 4 visible bands and 1 near-infrared band. In this paper only data from CZCS channels 4 and 5 will be presented:

Channel 4 0.66-0.58 μm (red visible)
Channel 5 0.70-0.80 μm (near-infred)

For a description of meteorological satellite sensors as they relate to marine haze detection see Durkee et al. (1982).

3.0 RESULTS

3.1 5 October 1982 Case

The experimental results from the flights executed on 5 October 1982 have been presented by Durkee et al. (1984). We summarize those results here and incorporate them with more recent findings from the experiment. Figure 1 shows the satellite-detected radiance (AVHRR channel 1) values plotted against calculated values of aerosol optical depth from aircraft-measured particle size distributions. The slope of the relationship in figure 1 has been shown by Durkee et al. (1984) to be that which is expected for marine particles. These results confirm and expand the preliminary results of Hindman et al. (1983).

The relationship between extinction due to scattering by marine particles and ambient relative humidity was also investigated by Durkee et al (1984). The results from the 5 October flights are shown in figure 2. The relationship in figure 2 has the same shape as that reported by Covert et al. (1972) and Fitzgerald et al. (1982) from their surface humidified nephelometer measurements. Thus, it appears that extinction is related to relative humidity throughout and perhaps even above the marine boundary layer.

3.2 Spirial measurements

During the experiment, 25 vertical spirals were flown within 1 hour of a satellite overpass. Due to various problems (eg. loss of satellite or aircraft data), data from 13 of the spirals are available for presentation here.

The direct comparison between satellite-detected radiance and aerosol optical depth shows a high correlation on a single day within a small region as demonstrated in figure 1. To compare aerosol properties to upwelling radiance with measurements made on different days, the variations due to sun-earth-satellite geometry differences need to be accounted for.

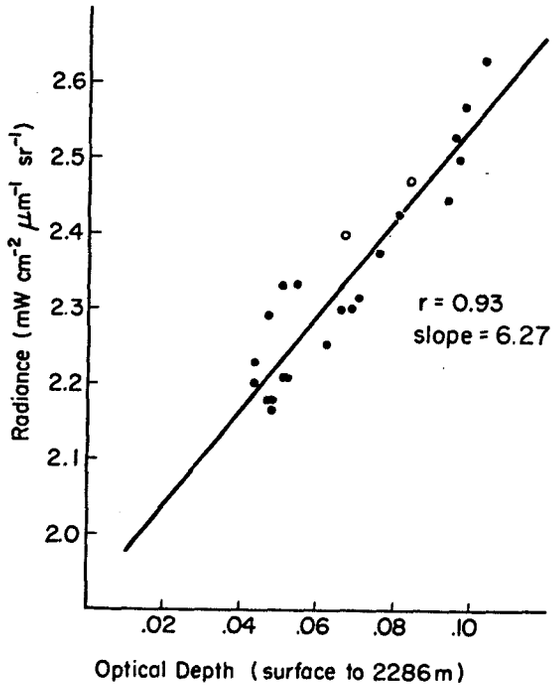

Figure 1. Satellite-detected radiance vs. aerosol optical depth from the surface to 2286 m. The solid line is the estimated linear relationship; r is the correlation coefficient.

If single scattering is assumed, upwelling radiance is given by

$$L = \frac{\omega_0 \mu_0 F_0}{4(\mu+\mu_0)} p(\theta)\left\{1 - \exp\left[-\tau_A\left(\frac{1}{\mu}+\frac{1}{\mu_0}\right)\right]\right\} \qquad (1)$$

where ω_0 is the single scattering albedo, F_0 is the solar flux density, μ_0 and μ are the cosine of the solar and satellite zenith angles, $p(\theta)$ is the single scattering phase function, and τ_A is the aerosol optical depth. If $\tau_A\left(\frac{1}{\mu}+\frac{1}{\mu_0}\right)$ is small, equation (1) may be further simplified to

$$L \sim \frac{\omega_0 F_0}{4\mu} p(\theta)\tau_A \qquad (2)$$

Finally, separating satellite-dependent terms from aerosol-dependent terms gives

$$\frac{4\mu L}{F_0} \sim \omega_0 p(\theta)\tau_A \qquad (3)$$

Equation (3) provides a first-order method for comparing satellite-detected radiance with aerosol optical depth while accounting for geometry affects.

Figure 3 illustrates the results of plotting values from the left- and right-hand sides of equation (3) for the spiral measurements made within 1 hour of an AVHRR overpass. Figure 4 illustrates the same plot as figure 3 but for values from CZCS overpasses. The vertical error bars in figures 3 and 4 are due to the uncertainty in the satellite measurements of radiance. The horizontal error bars are due to uncertainties in assumptions about the composition of particles above the boundary layer.

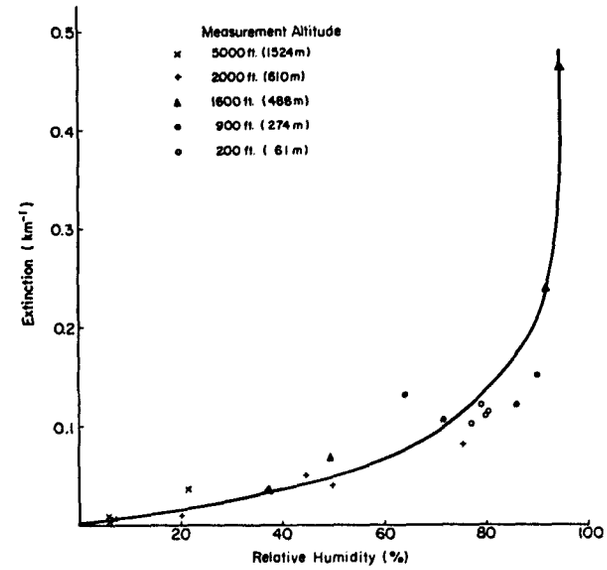

Figure 2. Scattering extinction coefficient vs. relative humidity. Points are 18.5 km averages from 5 October 1982 aircraft measurements.

A positive relationship between values from satellite-dependent terms and aerosol-dependent terms is apparent in figures 3 and 4. The correlation for the CZCS cases is higher than for the AVHRR cases. One major cause of this difference is the fact that the spiral data collected near the AVHRR overpasses were significantly affected by aerosol particles above the boundary layer. These upper level particles also account for the larger horizontal error bars for the AVHRR cases than for the CZCS cases (compare figures 3 and 4).

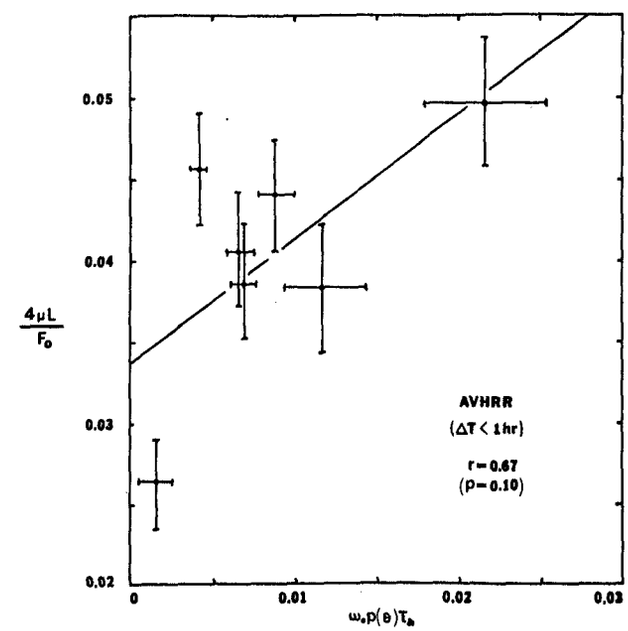

Figure 3. Satellite-dependent terms vs. aerosol-dependent terms from equation (3) for vertical spiral measurements made within 1 hour of an AVHRR overpass.

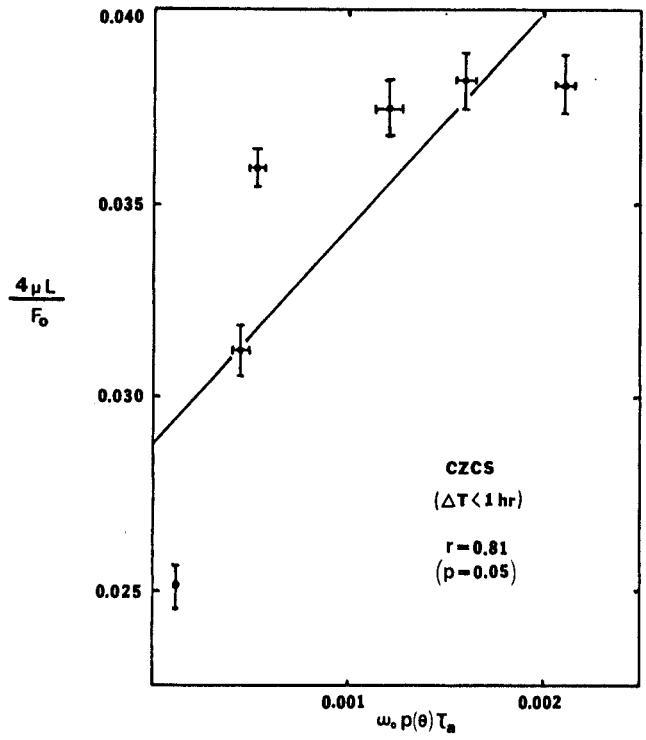

Figure 4. Same as figure 3 except for CZCS overpasses.

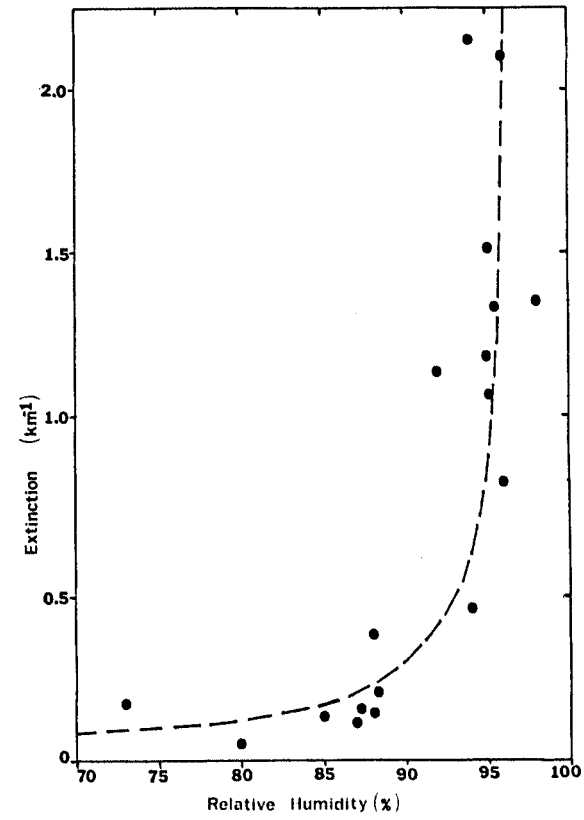

Figure 5. Averages over the marine boundary layer of extinction plotted against relative humidity.

Figure 5 presents values of extinction plotted against relative humidity; the values were averaged through the marine boundary layer. The results in figure 5 and figure 2 are in qualitative agreement. Consequently, the relationship described in figure 2 apparently holds over several days within the marine boundary layer.

3.3 Upper level particles

The presence of significant numbers of particles above the marine boundary layer limits the extent to which upwelling radiance depends on characteristics of the marine boundary layer. A method to detect the presence of significant amounts of upper level particles is therefor needed if satellite-detected radiance is to be used to characterize the marine boundary layer.

The parameters in equation (2) all vary with wavelength. Particles above the boundary layer, which result from transport off-shore of continental and urban type particles, differ from marine particles in that they are smaller in size and absorb more radiation. The parameters on the right hand side of equation (2) therefor vary more with wavelength for upper level particles than marine particles. A ratio can be formed of equation (2) applied at red and near-infrared wavelengths such that:

$$\frac{L_{Red}}{L_{nIR}} \propto \frac{(\omega_0 p \tau_A)_{Red}}{(\omega_0 p \tau_A)_{nIR}}$$

The right-hand side of (4) will be larger for upper level particles than for marine particles because of a larger variation with wavelength. The ratio of red radiance to near-infrared radiance should therefor be larger in cases where the total optical depth has significant contribution from upper level particles.

Figure 6 illustrates values of the ratio of red radiance to near-infrared radiance during the experiment period. The ratio decreases after 26 September. The decrease coincided with the passage of a precipitating cold front through the experiment area. The bracketed values indicate the fraction of the total optical depth which is due to upper level particles. The sharp decrease in these values at frontal passage indicates the front removed the upper level particles present at the beginning of the experiment.

4.0 CONCLUSIONS

The conclusions from the results presented here are as follows:

1. Satellite detected radiance is positively correlated with aerosol optical depth; a result consistent with Griggs (1975).

2. Extinction is related to relative humidity within the marine boundary layer. The relationship follows that which is expected from previous measurements and particle growth theory.

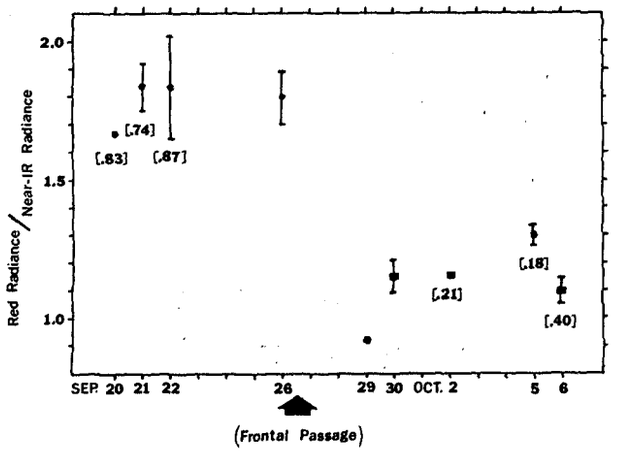

Figure 6. The ratio of red to near-infrared radiance from 20 September to 6 October 1982. Circles refer to AVHRR cases and squares refer to CZCS cases. Bracketed values indicate the fraction of the total optical depth which is due to upper level particles (missing values are due to missing aircraft data).

3. Since satellite-detected radiance is related to extinction and extinction is related to relative humidity, satellite-detected radiance may be used to investigate variations of marine boundary layer relative humidity.

4. The presence of significant numbers of particles above the marine boundary layer limits the relationship between satellite-detected radiance and boundary layer relative humidity. The ratio of satellite-detected radiance at red and near-infrared wavelengths can be used to detect the presence of significant amounts of upper level particles.

5.0 *ACKNOWLEDGEMENTS*

The work was sponsored jointly by ONR Contract No. N00014-c-79-0793 (administered through the Research Institute of Colorado) and Program Element 61153N, Project No. WR03302 of the Naval Air Systems Command.

6.0 REFERENCES

Covert, D. S., R. J. Charlson and N. C. Ahlquist, 1972: A study of the relationship of chemical composition and humidity to light scattering by aerosol. J. Appl. Meteor., 11, 968-976.

Durkee, P. A., E. E. Hindman and T. H. Vonder Haar, 1982: The detection of marine haze with the meteorological satellites. Hygroscopic Aerosols in the Planetary Boundary Layer. In press. Also, Special Report for the Research Institute of Colorado.

Durkee, P. A., D. R. Jensen, E. E. Hindman and T. H. Vonder Haar, 1984: A field study to relate marine aerosol particles with satellite-detected radiance. Submitted to J. Geophys. Res.

Fitzgerald, J. W., W. A. Hoppel and M. A. Vietti, 1982: The size and scattering coefficient of urban aerosol particles at Washington, DC as a function of relative humidity. J. Atmos. Sci., 39, 1838-1852.

Griggs, M., 1975: measurements of atmospheric aerosol optical thickness over water using ERTS-1 data. J. Air Pollut. Control Assoc., 25, 662-626.

Hindman, E. E., P. A. Durkee, P. C. Sinclair and T. H. Vonder Haar, 1983: Detection of marine aerosol particles in coastal zones using satellite imagery. Intl. J. Remote Sens., In press.

METEOROLOGICAL SATELLITE DATA USEFUL FOR AGROCLIMATE

P. K. Rao
J. D. Tarpley
R. A. Scofield
J. F. Moses

Satellite Applications Laboratory, NOAA/NESDIS
Washington, D.C. 20233

1. INTRODUCTION

The most important and variable determinant of agricultural conditions is the weather. Crop forecast models make use of conventional weather observations to estimate soil moisture, crop yield, and detect crop stress. The accuracy of these models decreases when weather observations are sparse or not received in a timely manner. In many countries of agricultural importance, reported meteorological observations are not adequate for agricultural monitoring.

Part of the AgRISTARS effort under way at NESDIS is to develop products from operational meteorological satellite data that will supplement ground-based weather observations for agricultural monitoring. Meteorological quantities that are needed for crop models and that can be produced from satellite data include estimates of precipitation, daily temperature extremes, canopy temperatures, insolation, and snowcover. In addition, there is a direct measure of the condition of vegetation called a "vegetation index" that is derivable directly from satellite measurements.

2. SATELLITE-DERIVED AGROCLIMATE PRODUCTS

Vegetation Index:

The NOAA polar orbiting satellites have Advanced Very High Resolution Radiometers (AVHRR) onboard that make observations in the visible band (Channel 1, 0.58 to 0.90 μm) and in the near infrared band (Channel 2, 0.73 to 1.10 μm). The spectral response for these bands is similar to bands 5 and 7 on the Landsat Multispectral Scanner (MSS). The AVHRR scans with a ground resolution of 4 km; selected areas can be observed at 1 km resolution.

The reflectance of green vegetation in the visible part of the spectrum is low (20% or less) but is much higher (50-60%) in the near infrared. Other surfaces, such as water, bare ground, and clouds have reflectances that are nearly the same in the two bands, so the difference between measurements in Channels 1 and 2 is a sensitive indicator of vegetation (Hoffer and Johannsen, 1969). The differential reflectance of vegetation in the visible or near infrared was used with MSS data to estimate crop acreage, study the distribution and condition of vegetation and detect plant stress (Myers, 1975, Tucker, 1979). The advantage of the NOAA satellites for monitoring vegetation is that they provide daily observations while Landsat has a repeat time of 18 days. Cloud obscuration of the areas of interest is much less of a problem with daily observations. The trade-off for daily coverage is resolution. Only a small part of the earth can be observed daily at the full 1 km resolution of the AVHRR; daily global coverage is obtained at 4 km resolution.

Examples of an experimental vegetation index product are shown in Figures 1 and 2. These are northern hemisphere polar stereographic mapped images of the normalized difference (CH2-Ch1)/(Ch2+Ch1) vegetation index. The greener the scene, the darker the image and the higher the vegetation index, which ranges between 0.1 and 0.6 for most vegetation. The images are generated from 4 km AVHRR observations made during the week of August 23-29, 1982 and March 21-27, 1983. The data were mapped each day into a 1024 x 1024 polar stereographic array and composited over a 7-day period by saving the greenest observation for each array point. Atmospheric effects such as Rayleigh and Mie scattering and subpixel clouds all reduce the radiance in channel 2 relative to channel 1 and reduce the value of the vegetation index. Saving the greenest observation over the 7-day period minimizes cloud and atmospheric effects and throws out high nadir angle observations in favor of straight down looks. The disadvantage of saving the greenest observation is that it can bias the sampling toward the greener vegetation (forest, irrigated land, etc.). The usefulness of this product for monitoring global agriculture is being evaluated by units of NESDIS and USDA.

Other vegetation index products being studied include use of full resolution AVHRR for regional monitoring of vegetation, land use, and surface climate.

Insolation Received at the Surface:

Insolation is the primary energy source for growing crops and is used in numerical models for estimating crop yield, potential evapotranspiration, and soil moisture. The amount of solar radiation reaching the surface is determined by the transmittance of the atmosphere, and clouds are the most important factor affecting transmittance. Under overcast conditions up to 60 or 70 percent of incident solar radiation may be reflected to space and another 10 or 15 percent absorbed within the cloud. The satellite directly observes the reflected component of the incident radiation, so satellite measurements in the visible part of the spectrum are directly related to insolation reaching the surface. GOES is the preferred data

source for satellite estimates of insolation because its repeat observation throughout a day allows tracking of changing cloud conditions. Where geostationary data are not available, techniques using polar orbiter data have been developed (Davis and Penn, 1981).

An insolation method has been developed (Tarpley, 1979; Justus and Tarpley, 1983) that uses hourly GOES visible data to estimate hourly insolation. The technique involves regression against observed target brightness as measured by GOES, and the known brightness of the target under clear conditions. The difference between these two quantities is a measure of cloudiness. Hourly estimates are summed to give a daily total insolation which is the measure used in agricultural models. Figure 3 shows a comparison of satellite estimates of daily insolation against pyranometers. These data are for satellite estimates colocated with selected sites in the NOAA pyranometer network. Insolation estimates are being currently made and archived for all of the U.S. and agriculturally important areas in Mexico and South America. The average daily values could be used to provide weekly, monthly, or seasonal values which should be useful for climate and energy studies. An example is shown in Figure 4.

Temperature:

Canopy temperature, shelter temperature, dewpoint temperature, and daily maximum and minimum temperature are all needed for use in crop and soil moisture models. Surface temperature has a high spatial variability which contributes to crop forecasting errors where observations are sparse and not representative of the whole region. Quantities derived from satellite data are by their nature, area averages. For large agricultural areas a single satellite estimate may be more representative than a few conventional observations within the area.

The approach selected to obtain temperatures for agricultural monitoring is through the operational atmospheric soundings derived from satellite observations. The enhanced sounding processing provides temperature and moisture soundings for 3x3 pixel arrays of HIRS/2 instantaneous fields of view (IFOV) giving a ground resolution of about 75 km at nadir. Canopy temperature is simply the moisture corrected brightness temperature observed in an atmospheric window channel (11 μm) of the HIRS/2. If the radiating surface of the earth is covered with vegetation then the surface is a plant canopy. Since the IFOV for the HIRS/2 is so large, the observed radiance is from a mixture of various surface types (water, bare soil, crops, native vegetation).

Shelter and dewpoint temperatures are obtained by regression using TOVS data and sounding products as predictors in the equations (Davis and Tarpley, 1983). Figure 5 shows a comparison between satellite estimates of shelter temperature compared against observed values from NOAA-6 soundings. The results shown are for clear and partly cloudy conditions during spring and summer. The error is large for cloudy retrievals (microwave) and during the winter.

Estimates of maximum and minimum temperatures are obtained by regression against shelter temperature, local solar zenith angle and cloud cover. The satellite overpass times of the daytime polar orbiter (NOAA-7) at 0230 and 1430 local time are near optimum for estimating the daily maximum and good for estimating minimum. Regression for max/min adds another 1 to 1.5°C to the expected error in the shelter temperature retrieval.

Since the max/min temperature estimates are liable to considerable error, the experimental temperature product currently prepared for USDA is a blend of satellite and surface temperature observations, with greater weight given to the conventional measurements. The satellite values enter the field where conventional data are sparse.

Precipitation:

Precipitation is a key meteorological variable that is needed to determine soil moisture and evaluate crop yield. Precipitation observations are required to specify land surface conditions for climate simulation models and climate prediction models. In many parts of the globe synoptic raingauge reports are sparse and sporadic. For data void regions, weather satellite observations of cloud cover provide valuable additional information which can be used to infer the distribution of rainfall.

As part of the AgRISTARS program, interactive computer techniques are being developed for analysis and estimation of precipitation over major crop growing regions in USSR and South America. A cloud history technique that utilizes GOES hourly images was developed by the Environmental Research Laboratories over South America. A cloud indexing technique developed by Barrett at University of Bristol that utilizes NOAA polar orbiter data is being utilized to estimate precipitation over USSR. The following example shows the Bristol-NOAA technique that is currently being evaluated.

The NOAA-7 AVHRR IR data is mapped to a polar stereographic projection with a resolution of 6.7 km at 60°N. The NOAA enhanced IR image for 0113Z May 14, 1981, is shown in Figure 6. The enhancement shows the area of coldest clouds and heaviest precipitation. These are interpreted as cumulonimbus with cirrus on top and are associated with a low centered between the Black and Caspian Seas. The NOAA enhanced IR image at 104Z May 14, is shown in Figure 7. Wind field analysis confirmed that the cumulonimbus area with warmer tops just northeast of the Caspian Sea is associated with the wave feature previously observed between the Black Sea and Caspian Sea. Plots of the few available reporting stations indicate showers and precipitation associated with the wave feature. In addition, Figure 7 shows extensive area of cumulonimbus clouds over the southern Caspian Sea.

An analysis of rain producing cloud areas was performed on the 0113Z and 1140Z images on the interactive computer. The 0113Z and 1140Z cloud type analyses were summed and analyzed further to account for cloud movement and development. The most significant cloud movement linked the cumulonimbus cloud mass west and northeast of the Caspian Sea. A broad corridor of rain cloud was analyzed along the path of the wave feature according to the pressure and wind fields.

The cloud field analysis was combined with station observations, climatic and morphoclimatic fields to produce the final rainfall estimate for the 12-hour period ending at 12Z May 14, 1981 (Figure 8). The estimates are in millimeters and represent the average rainfall over an area of approximately 47 km x 47 km at 60°N on a polar stereographic projection.

This technique will be evaluated further by using the dense raingauge network over the USA. The operational US raingauge network will be separated into two independent sets of observations, one to represent the density of observations in USSR and it will be used for calibration of the satellite derived estimates. The remaining stations will serve as the verification set for comparison with the satellite derived and improved analysis.

Conclusions:

Examples of satellite-derived agroclimate products that are currently produced on a routine basis have been shown. These products are being provided to USDA and other users for evaluation and assessment. When adequate feedback is received from the user community improvements and requirements are expected. Improvements are also expected with the introduction of new sensors on future satellite systems. The examples shown above were primarily developed for agricultural monitoring, however, the same parameters could be utilized for climate applications with minor modifications.

References

Davis, P.A. and L.M. Penn, 1981, Development of a Surface Insolation Estimation Technique Suitable for Application of Polar-Orbiting Satellite Data, NOAA AgRISTARS Contract No. NA-80-SAC-00741, Washington, D.C.

Davis, P.A. and J.D. Tarpley, 1983, Estimation of shelter temperatures from operational satellite sounder data, J. Climate and Applied Meteorol., 22, 369-376. Hoffer, R.M. and C. J. Johannsen, 1969: Remote Sensing in Ecology (University of Georgia Press, Athens, Georgia, p. 1.)

Justus, C.G. and J.D. Tarpley, 1983, Accuracy and availability of solar radiation data from satellites and from forecast estimates, AMS Atmospheric Radiation Conference, Baltimore, Maryland, Oct.-Nov. 1983.

Myers, V.I., 1975: Manual of Remote Sensing, Ch. 5 (American Society of Photogrammetry). Tarpley, J.D., 1979, Estimating incident solar radiation at the surface from geostationary satellite data, J. Appl. Meteorol., 18, 1172-1181. Tucker, C.J., 1979: Remote Sensing of the Env., 8, 127.

Yates, H.W., J.D. Tarpley, S.R. Schneider, D.F. McGinnis, and R.A. Scofield, 1984, The role of meteorological satellites in agricultural remote sensing, Remote Sensing of Environment, 14, (in press).

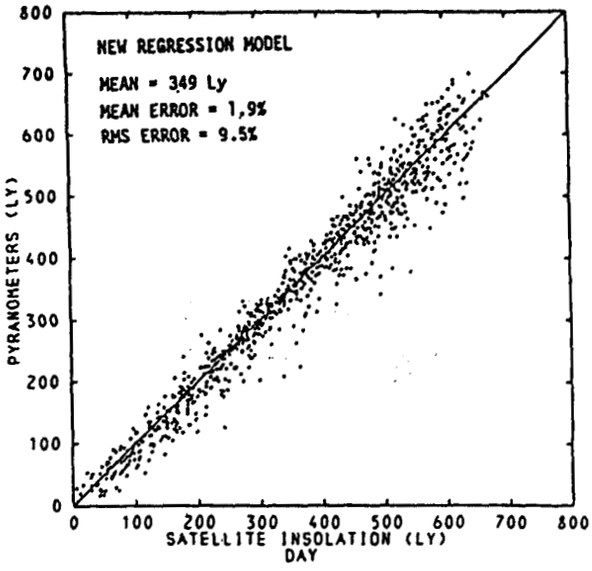

Fig. 3. *Observed daily total insolation vs. satellite estimate, using regression against GOES visible data.*

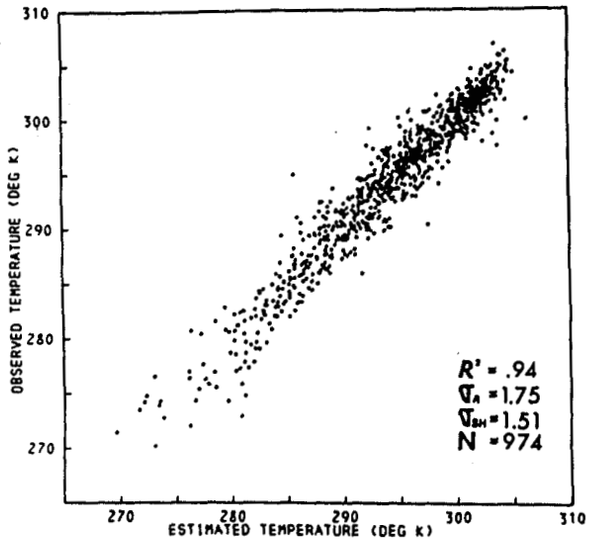

Fig. 5. *Shelter temperature estimated from satellite soundings compared against ground observations. Data are from eastern two-thirds of U.S. for April through July, 1981.*

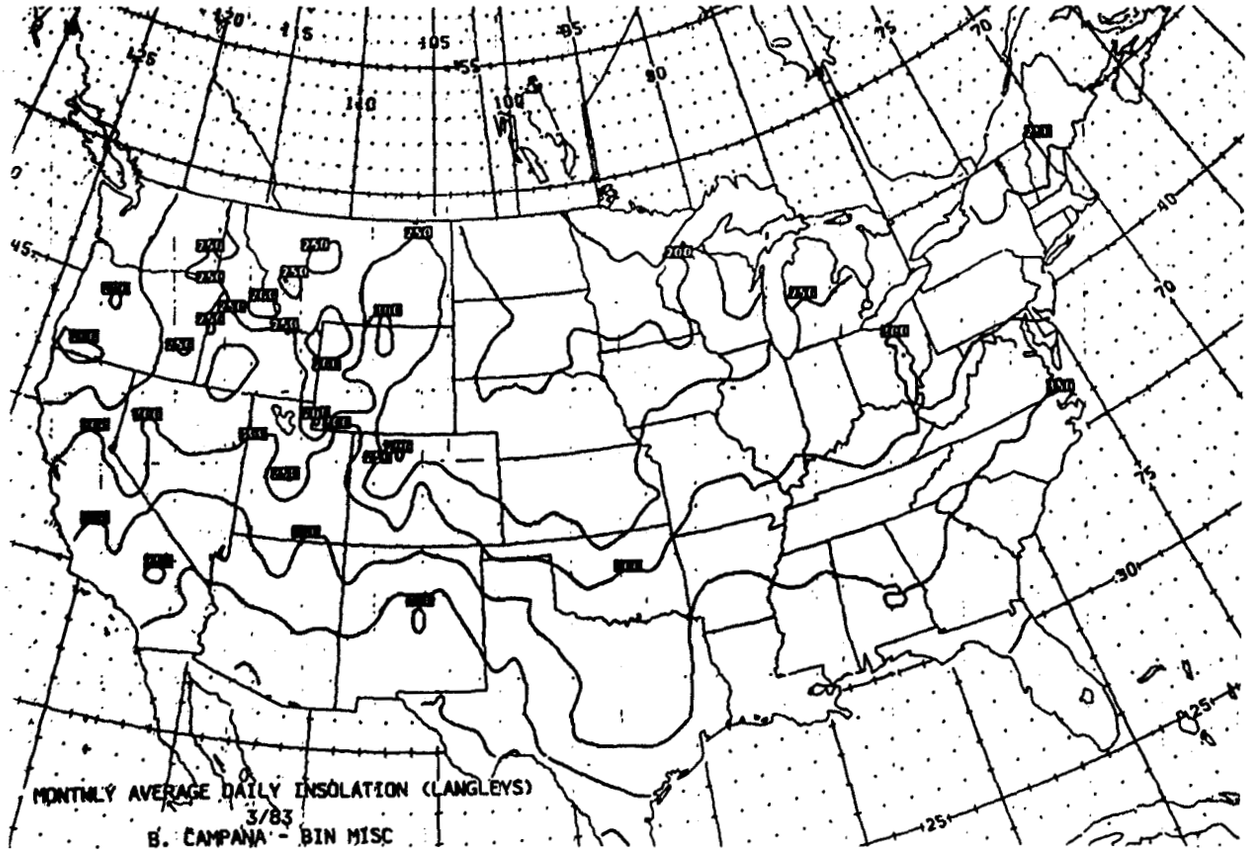

Fig. 4. *Map of monthly mean of daily insolation estimated from GOES data in March 1983. Contour interval is 50 langleys.*

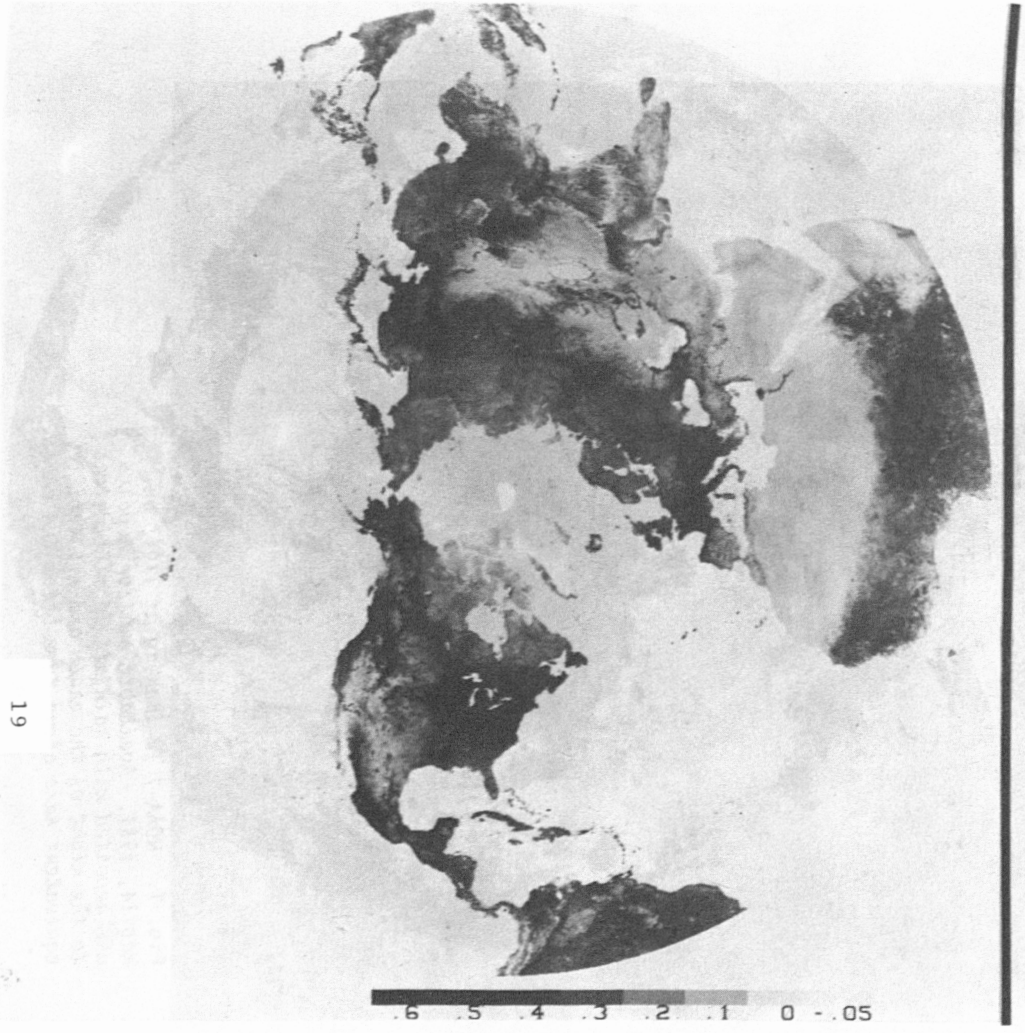

Fig. 1. *Northern hemisphere polar stereographic vegetation index maps for the week of August 23-29, 1982. Produced from 4 km data sampled at 20 km resolution.*

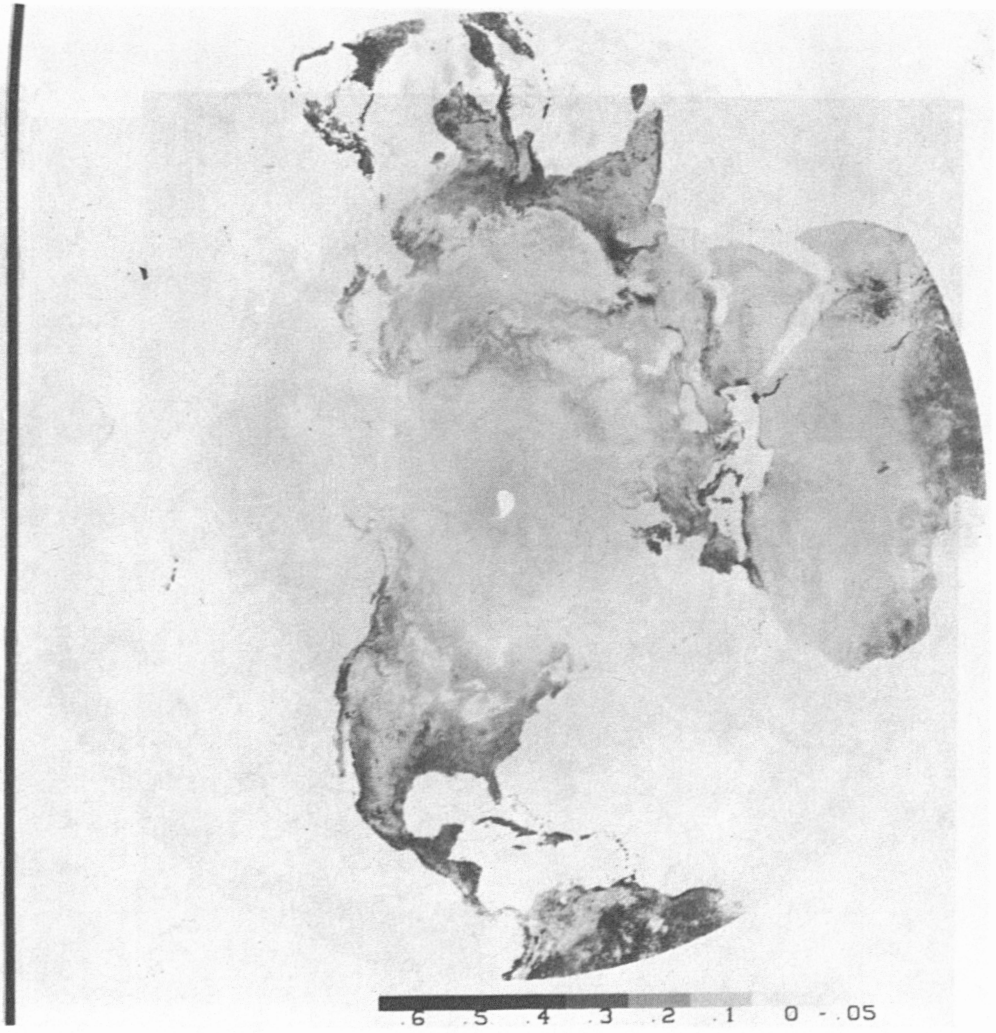

Fig. 2. *Same index as Figure 1 except for March 21-27, 1983.*

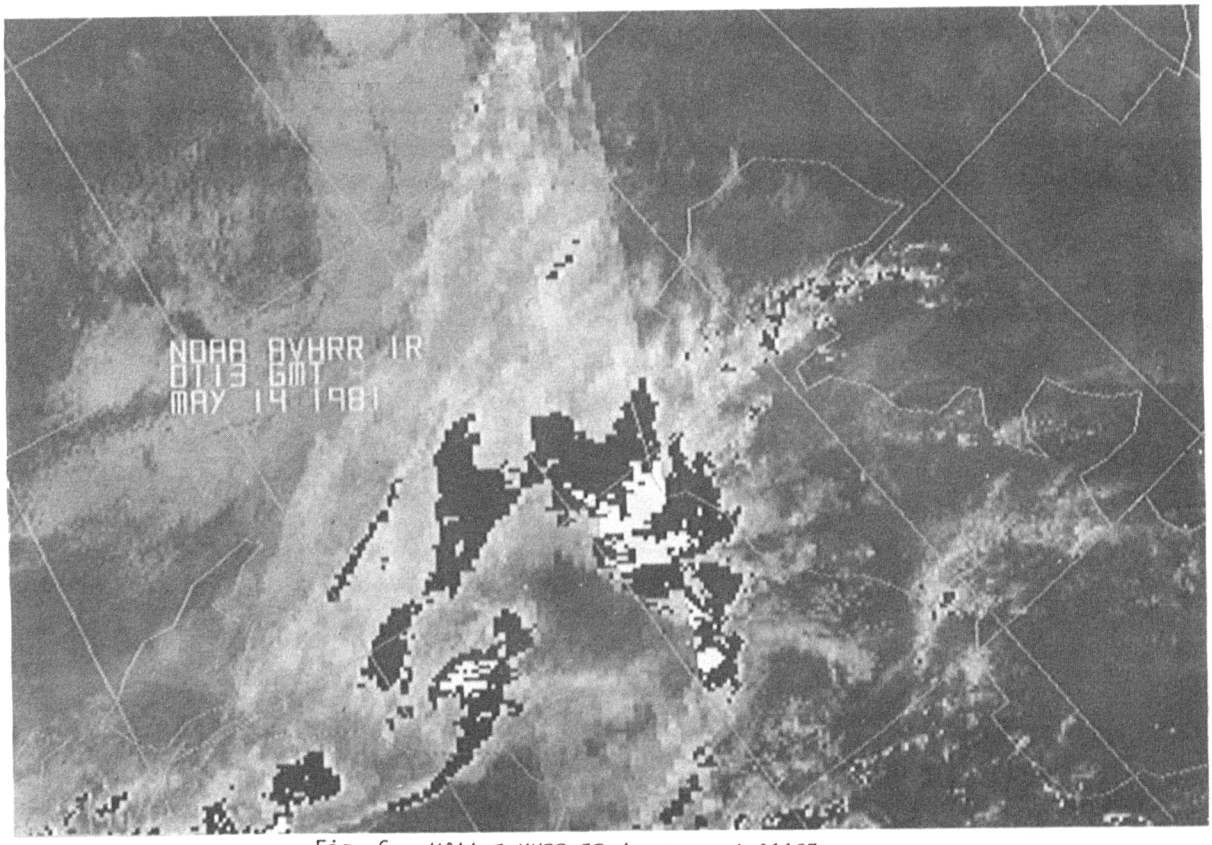

Fig. 6. *NOAA-7 VHRR IR imagery at 0113Z on May 14, 1981. The IR data was mapped to a polar stereographic projection and enhanced at -50°C and -60°C.*

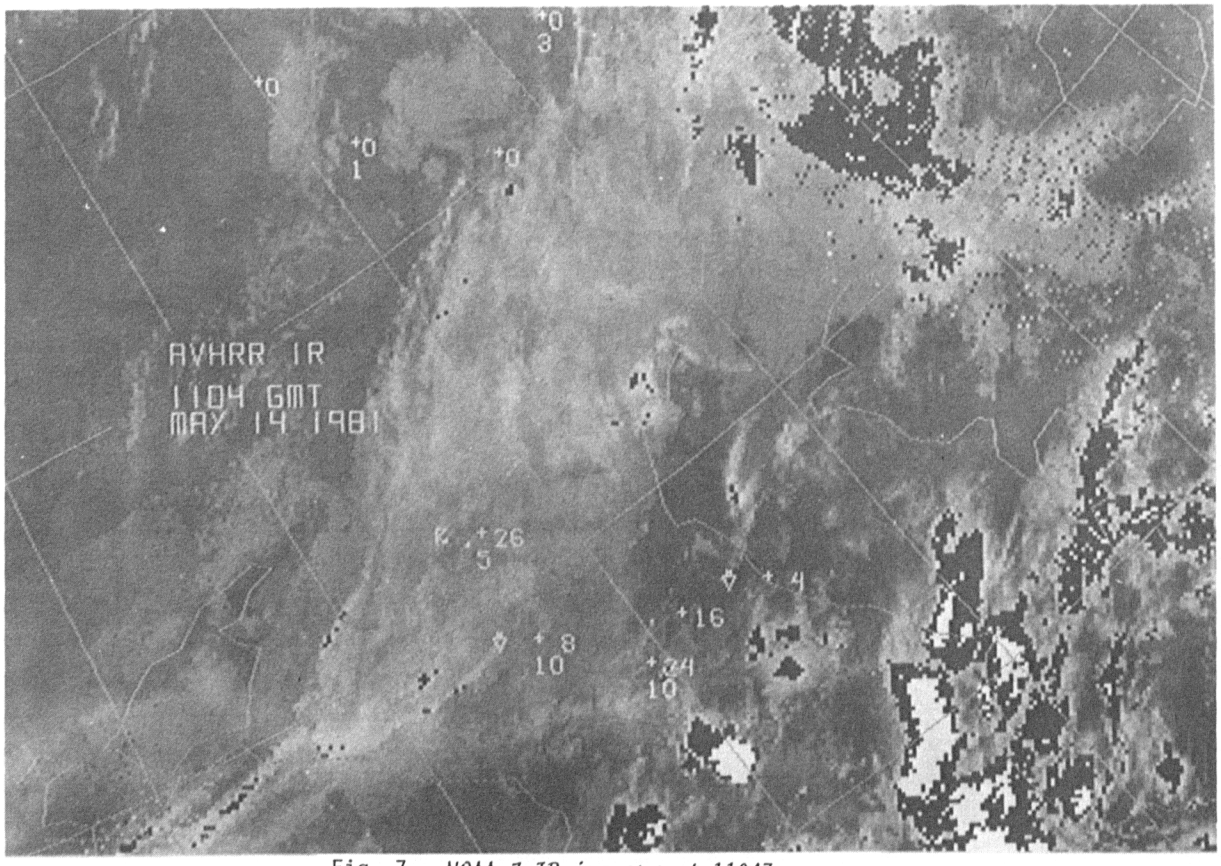

Fig. 7. *NOAA-7 IR imagery at 1104Z on May 14, 1981. Available station reports are reported with rainfall in millimeters to the right of the cross and a satellite equivalent rain cloud type below the cross.*

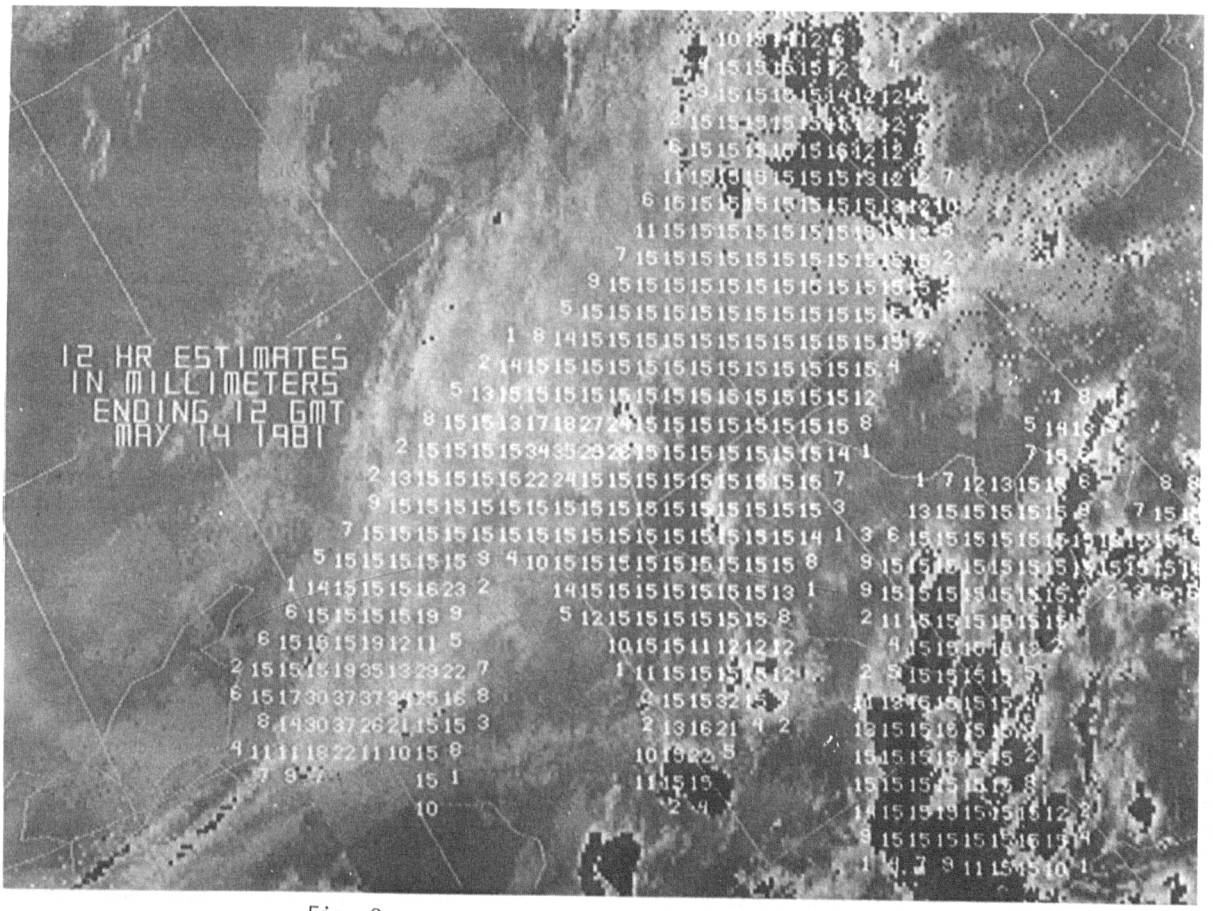

Fig. 8. *Estimates of precipitation in millimeters for the 12-hour period ending 12Z May 14, 1981. Estimates are plotted at the product resolution over the NOAA-7 image.*

OVERSHOOTING CLOUD TOP, VARIATION OF TROPOPAUSE AND SEVERE STORM FORMATION

R. J. Hung

The University of Alabama in Huntsville
Huntsville, Alabama

and

R. E. Smith

Atmospheric Science Division
NASA/Marshall Space Flight Center
Huntsville, Alabama

1. INTRODUCTION

Most thunderstorms are composed of short-lived units of convection, referred to as cells. The cumulus stage in cell development is characterized by updrafts throughout. As the cell builds up, a large amount of moisture condenses and precipitation particles grow (Barnes, 1976).

The lifetime of an individual cell averages about an hour. A storm consisting of a sequence of such cells may, however, persist for several hours.

In the presence of favorable vertical distributions of temperature, humidity, and wind velocity encountered in some frontal regions, a much more vigorous unit of convection may develop (Browning, 1964). These convections are important because they are responsible for a disproportionate amount of severe weather, especially damaging tornadoes and hail (Nelson, 1976). Perhaps its basic distinguishing feature is a circulation that is not only large and intense, but also virtually steady state, with updraft and downdraft coexisting to each other's advantage for periods of 30 minutes or more (Browning and Foote, 1976).

In this study we are particularly interested in the multicell thunderstorms (Newton and Fankhauser, 1975) near Pampa, Texas, in which 6 tornadoes touched down on May 19-20, 1982.

It has long been recognized that severe storm initiation and development are enhanced by strong convective instability, abundant moisture at low levels, strong wind sheer, usually veering considerably with height, and a dynamical lifting mechanism that can release the instability (Newton, 1963).

Convective instability can be induced by proper vertical profiles of temperature and moisture. It also can be released by the presence of gravity waves (Curry and Murty, 1974; Uccellini, 1975; Hung et al., 1978; Hung and Smith, 1981). In this study, weather maps, radar summaries, and rawinsonde data are used to study the background meteorological conditions and the conditions which favor the initiation of severe storm development.

Geosynchronous satellite data is a potentially powerful tool for studying enhanced convection and mesoscale systems. Purdom (1976) has noted that intersecting cloud lines observed on GOES imagery can be used in forecasting mesoscale convection and thunderstorms. Sikdar et al. (1970) have used ATS-3 visible data to measure thunderstorm anvil expansion rates. Hung et al. (1980) employed GOES infrared data for studying the May 29, 1977, Oklahoma tornado, to show that both cloud top equivalent blackbody temperature, T_{BB}, and the growth rate of the area enclosed by the cloud top T_{BB} isotherm can be used to distinguish between thunderstorms which eventually spawn tornadoes and those that do not. Adler and Fenn (1981) examined cloud top temperature variations from geosynchronous infrared satellite data relative to 11 tornado touchdown times. In 8 of the 11 cases there was a period of rapid cloud top ascent 30-45 min. prior to the tornado touchdown. This upward growth appears to be associated with the formation of a mesocyclone.

In this study, rapid-scan infrared imagery at 15 minute intervals from GOES are used in the analysis of Pampa, Texas multicell storms.

In a study of severe storm intensity using satellite data, Hung and Smith (1982) show that the difference between the cloud top T_{BB} and the temperature at the tropopause could serve as an indicator of the intensity of the storm rather than the absolute value of the cloud top T_{BB}. The possibility of the conversion of a severe thunderstorm into a tornadic thunderstorm depends on this difference rather than either the absolute value of the T_{BB} or the height of the top of the overshooting turret (Hung and Smith, 1983).

In this study, the role of the variation of the tropopause height in severe storm formation is introduced and discussed.

2. METEOROLOGICAL BACKGROUND

Surface meteorological data show a cold front extending from Arizona, Utah, to Wyoming at 0000 GMT 19 May 1982. This cold front gradually moved eastward and approached the Pampa, Texas area. The meteorological data below 850 mb indicates that warm moist air from the Gulf of Mexico had been moving into the area ahead of the front. The wind direction gradually changed from a south wind at 850 mb, to a west wind at 500 mb where a short wave pressure disturbance in eastern Texas indicated an instability in the higher altitude troposphere. Figure 2 shows the vertical wind profile in the Amarillo, Texas panhandle at 0000 GMT 20 May 1982.

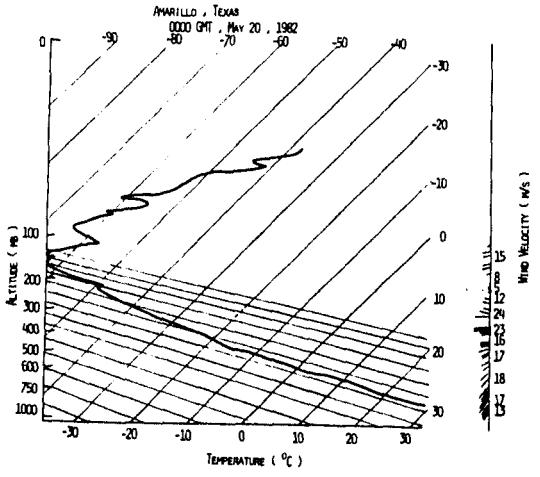

Fig. 1 Skew-T log-P diagram of Amarillo, Texas at 0000 GTM, 20 May 1982.

The 1200 GMT 19 May 1982 surface weather map shows the eastward moving cold front approaching New Mexico and Colorado. The low pressure zone extended from the surface to 850 mb, with warm and moist air coming from the Gulf of Mexico. There was a trough line extending from 850 to 500 mb in the area of interest.

A radar summary shows no radar echoes in the Pampa area before 1935 GMT 19 May 1982. The first radar echo was observed at 2035 GMT, indicating that the cloud formed between 1935 and 2035, in agreement with the satellite observations. This rapidly-growing cloud, in the presence of favorable vertical distributions of temperature, humidity, and wind velocity (see rawinsonde analysis in Section 3 for detailed description) in the frontal region, created a multicell thunderstorm (Browning, 1964). This multicell thunderstorm, which is responsible for the outburst of 6 Pampa tornadoes, persisted for more than 6 hours.

3. ANALYSIS OF RAWINSONDE DATA

Available temperature, moisture and wind profiles from rawinsonde observations all over the United States were fed into the McIDAS system at the NASA Marshall Space Flight Center (NASA/MSFC). Barnes (1964) scheme was used to maximize detail in numerical map analysis.

As an example, Figure 1 shows skew-T log-P diagrams from rawinsonde observations in Amarillo, Texas, the closest to Pampa, Texas, at 0000 GMT, 20 May; which are representative of the atmosphere in the vicinity of the thunderstorms. In the temperature profile, there were temperature inversions at 850 and 480 mb altitudes at 1200 GMT 19 May, that had disappeared by 0000 GMT 20 May. The temperature lapse rates were dry adiabatic between 800 and 480 mb altitudes at 1200 GMT 19 May, and also at 0000 GMT 20 May. The presence of temperature inversions assures the occurrence of a deep convection when the potential energy for overcoming these inversions becomes available (Beebe, 1958). By the time of formation of the tornadoes, the inversions no longer existed.

The wind profile at Amarillo had strong winds that veered with height, with a maximum wind speed of 27 m/sec at 170 mb (0000 GMT 19 May), and 25 m/sec at 260 mb (1200 GMT 19 May), parallel to the movement of the cold front. Also, there was a zone of low wind speeds (5 m/sec or less) at the tropopause height (180 mb) at 0000 GMT 20 May, during the cloud formation time period. This condition is favorable for the development of overshooting turrets.

Time-dependent, three dimensional analysis of the mixing ratio in the Texas panhandle and surrounding areas are plotted with a 12 km spacing using the Barnes (1964) scheme with input from rawinsonde observations all over the United States. As an example, Figure 2 shows the geographical distribution of the mixing ratio at 700 mb height at 1200 GMT, 19 May.

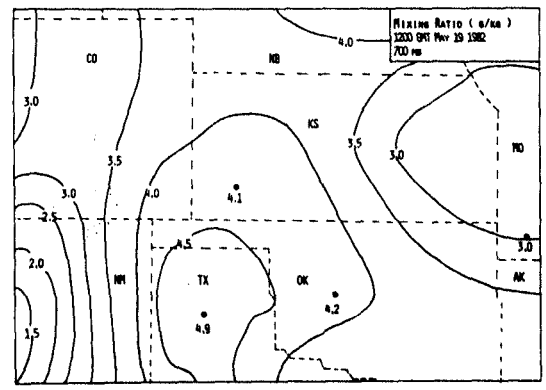

Fig. 2 Geographical distribution of the mixing ratio at 700 mb level, 1200 GMT, 19 May 1982, in the area of south central United States.

The figures show that there was a strong horizontal convergence of moisture at the 850 mb height. Approximately 24 hours before the formation of the tornadic cloud (0000 GMT, 19 May), a mixing ratio of 10 g/kg appeared in eastern Kansas and west central Missouri. The horizontal convergence of moisture shifted to the northwestern Oklahoma and Texas panhandle (location of tornado touchdown) areas, with a mixing ratio of 12 g/kg about 12 hours before the touchdown of the tornadoes. This horizontal convergence of

moisture moved northward to the southwestern Kansas and northwestern Oklahoma areas, with a mixing ratio of 12 g/kg at the time of the tornado touchdown at 850 mb heights.

The Figures of horizontal convergence of moisture also show much stronger horizontal convergence of moisture at the 700 mb level. There was horizontal convergence of moisture with a mixing ratio of 7 g/kg in the Texas panhandle area approximately 24 hours before the touchdown of the tornadoes. The horizontal convergence of moisture still remained in the same area when the mixing ratio dropped to about 5.0 g/kg about 12 hours before the touchdown of tornadoes. The horizontal convergence of moisture at the 700 mb level disappeared at the time of the tornado touchdown.

The horizontal convergence of moisture at the 500 mb height at different times has been compared. There was horizontal convergence of moisture with a mixing ratio of 2 g/kg in central Colorado approximately 24 hours before the touchdown of tornadoes. This horizontal convergence of moisture shifted to the Texas panhandle, north central Oklahoma, and southwestern Kansas areas with a mixing ratio of 2 - 3 g/kg about 12 hours before the touchdown of the tornadoes. The horizontal convergence of moisture smoothed out at the time of the tornado touchdown. The zigzag shaped oscillations in the temperature profiles are disturbances caused by the propagation of gravity waves (Rice and Sharp, 1977; Spencer et al., 1976). Figure 1 shows that gravity waves appeared (at the top of the tropopause) during the time periods between 1200 GMT 19 May and 0000 GMT 20 May, another indication of the initiation of enhanced convection (Hung et al., 1978 and 1980; Hung and Smith, 1981).

In the study of severe storm environments, Darkow (1964) shows that the tornado proximity sounding has substantially higher total energy values in the lower troposphere (850 mb height) and lower values in the mid-troposphere (500 mb height), than nearby stations. With similar consideration in mind, it is possible to formulate a Mixing Ratio Index which is nothing more than the algebraic difference between the mixing ratio of the air at the 850 and 500 mb levels. The time dependent Mixing Ratio Index at the location of the tornado touchdown (Pampa, Texas in this case) is shown in Figure 3. The Mixing Ratio Index may be expressed as:

$$\text{Mixing Ratio Index} = (\text{Mixing Ratio})_{850mb} - (\text{Mixing Ratio})_{500mb} \quad (1)$$

The Mixing Ratio Index provides an indicator of the availability of local latent heat which is necessary for the development of convective clouds. It can be seen from Figure 3 that the Mixing Ratio Index increased from 7.5 g/kg approximately 24 hours before the formation of the severe storms to 10.5 g/kg 12 hours before the touchdown of tornadoes. The Mixing Ratio Index finally decreased to 3.5 g/kg at the time of tornado touchdown.

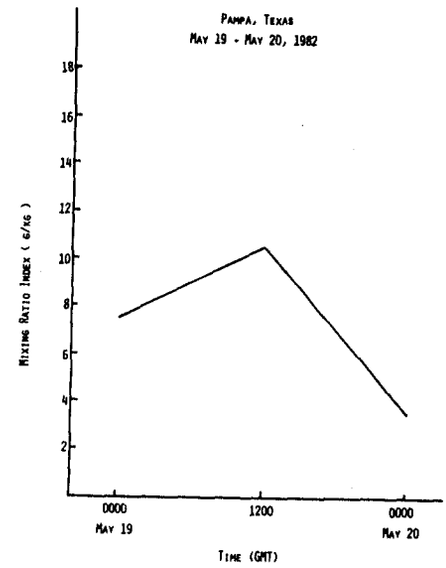

Fig. 3 Time-dependent variation of the Mixing Ratio Index in the Pampa, Texas area during May 19-20, 1982.

The difference between the overshooting cloud-top height and the tropopause height, a measure of how much the cloud has penetrated above the tropopause, rather than the height of the top of the overshooting turret, is important in the development of severe storms (Hung and Smith, 1982 and 1983). The high mass density overshooting turret can only exist as long as it is dynamically supported by intense vertical convection; therefore, as the intense vertical convection disappears, the overshooting turret collapses. The magnitude of force per unit area supporting the weight of the high mass density overshooting turret is proportional to the volume of the cloud top above the tropopause and the difference between the temperature of the turret and the ambient environment. The downward collapsing rate of the overshooting turret is, therefore, proportional to the volume of the cloud top above the tropopause and the temperature differential. This makes the volume of the cloud top above the tropopause and the temperature differential critical in studying the initiation of the downdraft motion which produces the funnel cloud.

On the other hand, the difference between the overshooting cloud-top height and the tropopause height may increase if the tropopause height decreases during the time period of the storm formation. Similar to Figure 2, the time-dependent geographical distribution of tropopause height in the south central United States is plotted by using the Barnes (1964) scheme with inputs from rawinsonde observations all over the United States into the McIDAS system at NASA/MSFC. Figures 4, 5, 6, and 7 show the tropopause temperature distribution at 0000 GMT, 19 May; 1200 GMT, 19 May; 0000 GMT, 20 May; and 1200 GMT, 20 May, respectively. The location of the warmest tropopause temperature (lowest height tropopause) of -58°C shifted from Missouri at 0000 GMT, 19 May, to a tropopause temperature of -58°C in the Texas panhandle area, at 1200 GMT, 19 May. This warmest

tropopause temperature became even warmer, -56°C, in the Texas panhandle and southwestern Oklahoma area at 0000 GMT, 20 May. Finally, the warmest tropopause temperature cooled to -58°C and shifted to the Colorado area, at 1200 GMT, 20 May. The study of tropopause temperature distribution during this 36-hour period indicates that the lowest tropopause height was located in the Texas panhandle area at 0000 GMT, 20 May.

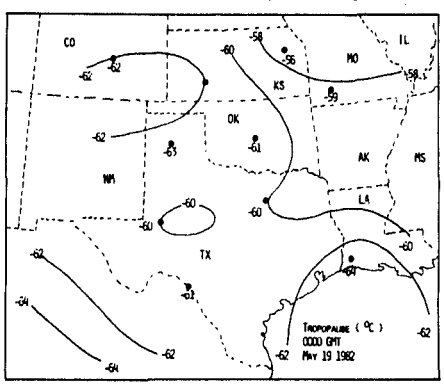

Fig. 4 Geographical distribution of tropopause temperature at 0000 GMT, 19 May 1982, in the area of south central United States.

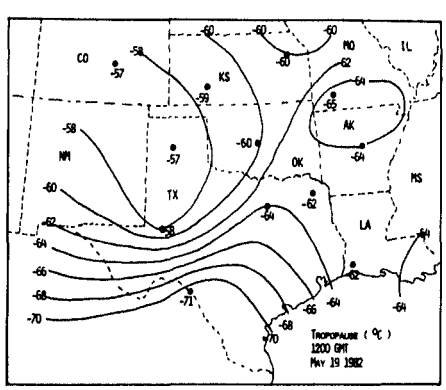

Fig. 5 Geographical distribution of tropopause temperature at 1200 GMT, 19 May 1982, in the area of south central United States.

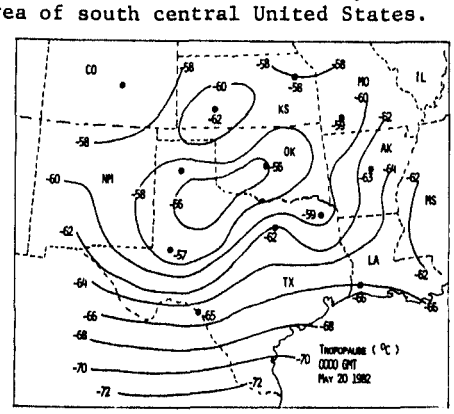

Fig. 6 Geographical distribution of tropopause temperature at 0000 GMT, 20 May 1982, in the area of south central United States.

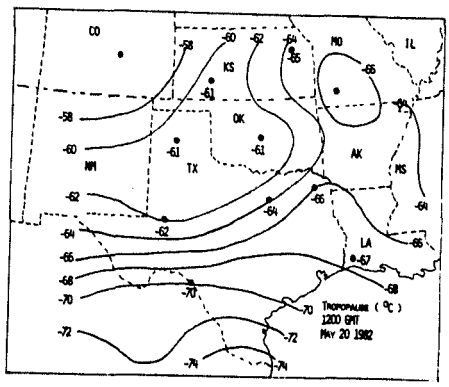

Fig. 7 Geographical distribution of tropopause temperature at 1200 GMT, 20 May 1982, in the area of south central United States.

Figure 8 shows that the tropopause heights over Pampa, Texas during this 36-hour period decreased from a temperature of -63°C at 0000 GMT 19 May to -58°C at 1200 GMT 19 May and then to a minimum temperature of -57°C at 0000 GMT 20 May, the severe storm formation time period. The tropopause height increased to a temperature of -61°C at 1200 GMT 20 May, after the dissipation of the severe storms. Figure 8 suggests that the decrease of the tropopause height may be an additional indication of the possibility of severe storm formation.

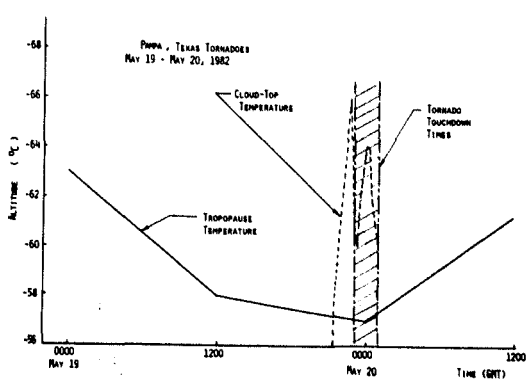

Fig. 8 Variations of tropopause temperature (height), overshooting cloud-top temperature and tornado touchdown time in the Pampa, Texas area.

The values of the mixing ratio, shown in Figure 2; and temperature, expressed in Figure 1, may be combined in energy units to yield the total energy of the ascending low-level air. Darkow (1968) suggests that the total energy variations are useful and meaningful parameters in the analysis of potential-convective instability associated with severe storm activity. In the present study, the time-dependent variation of the vertical profile of total energy over Pampa, Texas, was investigated to study the evolution of a storm environment.

The total energy E_T of a unit mass of air may be expressed as:

$$E_T = C_p T + gz + Lq + \frac{V^2}{2} \qquad (J/g) \qquad (2)$$

which is the sum of the specific enthalpy (or heat energy processed at constant pressure), geopotential energy (or energy associated with elevation), latent energy, and kinetic energy. In Eq. (2), C_p is the specific heat of air at constant pressure; T, the absolute temperature; g, the gravitational acceleration; z, the height of the air parcel above sea level; L, the latent heat; q, the specific humidity (or mass of water vapor per unit mass of moist air); and V, the scalar velocity of the unit mass of air.

Darkow (1968) suggests the applicability of the Energy Index as an indicator of the severe storm environment of latent and potential convective instability by using the algebraic difference between the total energy of the air at the 850 and 500 mb levels. This may be expressed as:

$$\text{Energy Index} = (E_T)_{850mb} - (E_T)_{500mb} \qquad (3)$$

The time-dependent Energy Index in Pampa, Texas, and the location of the tornado touchdown, is plotted in Figure 9. The Energy Index was at its maximum value of 14 J/g about 12 hours before the touchdown of tornadoes, and decreased to the value of 3.5 J/g at the time of the tornado touchdown. The Energy Index even decreased to the value of 2 J/g, 12 hours after the touchdown.

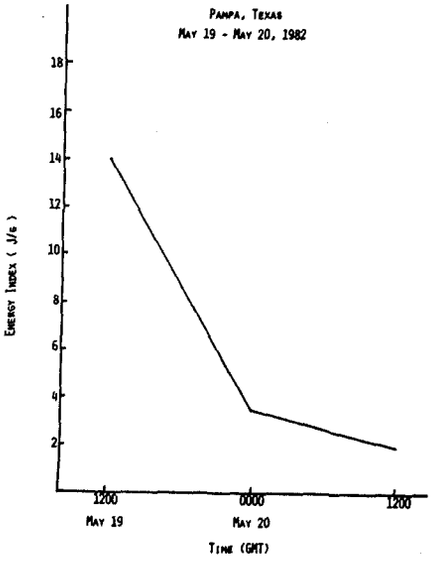

Fig. 9 Time-dependent variation of the Energy Index in the Pampa, Texas area during May 19-20, 1982.

4. ANALYSIS BASED ON SATELLITE IMAGERY

Rapid-scan imagery from GOES was used in this study. Rawinsonde analysis shows that the air mass in the Pampa area was extremely unstable and very moist in the layer below 500 mb. Cloud formation was initiated after 1945 GMT 19 May. Figure 10 shows the evolution of the cloud, from the initiation of cloud condensation to the outbreak of the second tornado, in terms of the change of cloud-top temperature. Figure 1 (temperature profile), Figure 2 (horizontal convergence of moisture at different altitudes), Figure 3 (evolution of the Mixing Ratio Index), Figures 4 to 7 (evolution of the geographical distribution of tropopause temperature), and Figure 9 (evolution of the Energy Index) show how the horizontal convergence of moisture provided the energy and momentum which initiated the deep convection through the release of latent heat during the condensation process. This convective cloud started to penetrate above the tropopause at 2130 GMT, while the local tropopause height was lowest during a 36-hour period, less than two hours after the initiation of the cloud formation.

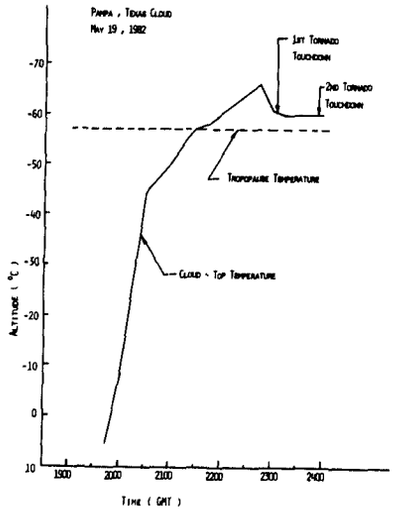

Fig. 10 History of Pampa storm cloud top temperature.

Figure 8 shows the change in cloud top temperature just prior to and during the time-span of the touchdowns of the six Pampa tornadoes. The multicell severe storms were formed during the time period with the lowest tropopause heights about 20 minutes before the touchdown of the first tornado. A histogram of the growth and collapse of each individual multicell Pampa storm was traced based on the outburst and touchdown of each individual tornado, and is illustrated in Figure 11 as an example for the first tornado.

Figure 11 shows the changes in the areas (in terms of pixel numbers) of the cloud top at different temperatures during the 2115-2315 GMT time period for the 2305 GMT tornado touchdown. The overshooting cloud top started to penetrate above the tropopause with an equivalent blackbody temperature $T_{BB} \leq -57^{\circ}C$ at 2130 GMT. By 2145 GMT, the cloud top had reached an altitude with a temperature $\leq -58^{\circ}C$; by 2200 GMT, the cloud top had reached a temperature $\leq -60^{\circ}C$; and by 2245 GMT, the cloud top had finally reached its highest altitude where the temperature was $-66^{\circ}C$. Then, the growth rate started decreasing and the cloud collapsed about 20 minutes before the tornado touchdown, in good agreement with the results of our earlier investigation (Hung et al., 1980; Hung and Smith, 1982; Hung et al., 1983) and those of Fujita and his associates (Fujita and Caracena, 1977; Fujita and Byers, 1977).

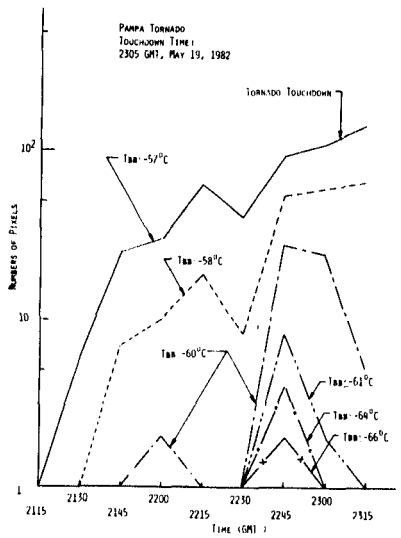

Fig. 11 Cloud area expansion and vertical growth of the cloud top in terms of time change of number of pixels with temperatures for multicell Pampa storms touchdown at 2305 GMT, 19 May 1982.

In this study the overshooting cloud top temperautre is more than 9°C below the temperature of the surrounding air; therefore, the overshooting turret is much denser than the surrounding air. For the reasons expressed earlier, this makes the height of the cloud-top above the tropopause and the temperature differential critical in studying the initiation of the downdraft motion which produces the funnel cloud.

The growth and collapse patterns of the rest of the other 5 tornadoes are similar to the tornado which touched down at 2305 GMT.

5. DISCUSSIONS AND CONCLUSIONS

Multicell Pampa storms were investigated using weather maps, radar summaries, rawinsonde data, and rapid-scan satellite imagery. Weather maps, radar summaries, and rawinsonde data provided the following background information 12 hours before the development of the multicell Pampa storms:

(1) Strong horizontal convergence of moisture appeared at the 850, 700, and 500 mb levels in the Texas panhandle area before the storm formation.

(2) Mixing Ratio Index with a maximum value before storm formation in the Texas panhandle area.

(3) During a 36-hour period, a tropopause height in the Texas panhandle area that was the lowest in the southeast United States at the time of tornadic cloud formation.

(4) During a 36-hour period, the variation of tropopause height in the area of the tornadic cloud formation was lowest at the time of the multicell cloud formation.

(5) The Energy Index with a maximum value in the area of the tornadic cloud formation before the formation of clouds.

(6) A train of gravity waves which was detected before and during the cloud formation period.

Rapid-scan infrared imagery provided near real-time information of the life cycle of the multicell Pampa storm formation, development, and dissipation as follows:

(1) The cloud started to form at 1945 GMT and penetrated above the tropopause at 2130 GMT.

(2) The multicell storm cloud was formed at the location of the highest horizontal convergence of moisture, lowest tropopause height in the southeast United States.

(3) The cloud-top reached its maximum height at 2245 GMT which was 9°C below the tropopause temperature.

(4) The cloud-top collapsed about 20 minutes before the touchdown of the first tornado.

(5) The relationship between the cloud-top height and the tropopause height shows that the most favorable conditions for severe storm development occur at minimum tropopause height.

It is true that all the overshooting cloud tops will eventually collapse regardless of the association with tornadoes. However, the dissipation rate of the non-tornado-associated clouds is much slower, and the cloud can persist for several hours after the cloud top penetrates above the tropopause and reaches the highest altitude; the tornado-associated clouds collapse in a very short time, about 10-40 minutes (Hung and Smith, 1983).

This research suggests that the combination of weather maps, radar summaries, rawinsonde data, and rapid-scan satellite imagery is useful for studying the environment favoring the severe storm formation, the life cycle of the multicell severe storm formation, development and dissipation. In the study of the background severe storms triggering mechanisms, observations of vertical profiles of temperature, humidity, and winds at shorter time intervals and more dense grid points than the current rawinsonde setup are necessary. It is very difficult to obtain the information critical in studying short-lived mesoscale phenomena using regular 12-hourly rawinsonde observations. Improvement of the present system depends upon obtaining the necessary profile data from satellites such as GOES-VAS.

ACKNOWLEDGEMENTS

R. J. Hung would like to thank the Office of Space Sciences and Applications, National Aeronautics and Space Administration Headquarters, and NASA/Marshall Space Flight Center through contract NAS8-33726, which supported the present research.

REFERENCES

Adler, R. F., and Fenn, D. D., J. Appl. Meteor., 20, 1369-1372, 1981.

Barnes, S. L., J. Appl. Meteor., 3, 396-409, 1964.

Barnes, S. L., Bull. Am. Meteor. Soc., 57, 412-419, 1976.

Beebe, R. G., Bull. Am. Meteor. Soc., 39, 195-201, 1976.

Browning, K. A., J. Atmos. Sci., 21, 634-639, 1964.

Browning, K. A., and Foote, G. B., Q. J. R. Meteor. Soc., 102, 499-533, 1964.

Curry, M. J., and Murty, R. C., J. Atmos. Sci., 31, 1402-1408, 1974.

Darkow, G. L., J. Appl. Meteor., 7, 199-205, 1968.

Fujita, T. T., and Byers, H. R., Mon. Wea. Rev., 105, 129-146, 1977.

Fujita, T. T., and Caracena, F., Bull. Amer. Meteor. Soc., 58, 1164-1181, 1977.

Hung, R. J., Dodge, J. C., and Smith, R. E., AIAA J., 21, 1217-1224, 1983.

Hung, R. J., Phan, T., and Smith, R. E., J. Atmos. Terr. Phys., 40, 831-843, 1978.

Hung, R. J., Phan, T., Lin, D. C., Smith, R. E., Jayroe, R. R., and West, G. S., Mon. Wea. Rev., 108, 456-464, 1980.

Hung, R. J., and Smith, R. E., Il Nuovo Cimento, 4C, 339-358, 1981.

Hung, R. J., and Smith, R. E., Int. J. Remote Sensing, 3, 69-81, 1982.

Hung, R. J., and Smith, R. E., Int. J. Remote Sensing, 4, 617-630, 1983.

Nelson, S. P., Preprints, International Conference on Cloud Physics, Boulder, Co., American Meteorological Society, Boston, Mass., 335-340, 1976.

Newton, C. W., In Severe Local Storms, Meteor. Mongr. 5, American Meteorological Society, Boston, Mass., 33-58, 1963.

Newton, C. W., and Fankhauser, J. C., Pure Appl. Geophys., 113, 747-764, 1975.

Purdom, J. F. W., Mon. Wea. Rev., 104, 1474-1483, 1976.

Rice, C. J., and Sharp, L. R., Geophys. Res. Lett., 4, 315-319, 1977.

Sikdar, D. N., Suomi, V. E., and Anderson, C. E., Tellus, 22, 521-532, 1970.

Spencer, N. W., Theis, R. F., Wharton, L. E., and Carrignan, G. R., Geophys. Res. Lett., 3, 313-317, 1976.

Uccellini, L. W., Mon. Wea. Rev., 103, 497-513, 1975.

A STATISTICAL EVALUATION AND COMPARISON OF VISSR ATMOSPHERIC SOUNDER (VAS) DATA AND CORRESPONDING RAWINSONDE MEASUREMENTS

Gary J. Jedlovec

Universities Space Research Association
Marshall Space Flight Center
Huntsville, Alabama

1. INTRODUCTION

In the fall of 1980, the first VISSR Atmospheric Sounder (VAS) was launched into geostationary orbit onboard the GOES-4 spacecraft bringing new remote sounding capabilities into existence. Since then, two more VAS instruments have been launched with the last two being operational at this writing. VAS measures radiation emitted by the atmosphere in 12 infrared spectral bands and is capable of collecting sounding quality radiances at frequent time intervals (see Chesters, et al., 1982; Smith, et al., 1981; or Menzel, et al., 1981 for instrument description and operating modes). These radiances can be used to produce vertical profiles of temperature and moisture in the cloud-free environment by inverting the radiative transfer equation.

The usefulness of multispectral imagery and sounding products has been demonstrated recently by several groups (e.g., Smith, 1983; Anthony and Wade, 1983; and Petersen, et al., 1982,1983) without much regard for the accuracy and representativeness of these products in describing mesoscale atmospheric features. This is mainly because of the lack of verifying measurements. In the spring of 1982, Marshall Space Flight Center conducted an experiment aimed at collecting rawinsonde measurements of similar resolution to those available from VAS. This paper presents some results of a comparison study between VAS soundings produced using various retrieval algorithms and corresponding ground truth rawinsonde data from the AVE/VAS experiment.

2. DATA AND PROCEDURES

Two basic types of data were used in the study; namely, three-hourly rawinsonde and VAS sounding data for the 6 - 7 March 1982 experiment day. Details of this and other experiment periods in the spring of 1982 may be found in Greaves, et al., (1982) and Hill and Turner (1983). The rawinsonde data used in the evaluation consisted of the basic thermodynamic parameters at 50mb increments from the surface up to 100mb. The rawinsonde locations of interest are shown in Fig. 1. The spacing of these sites is roughly 125km over central Texas providing detailed mesoscale resolution of atmospheric features.

The VAS sounding data available for this period consisted of three data sets. The first satellite data set contained soundings produced using

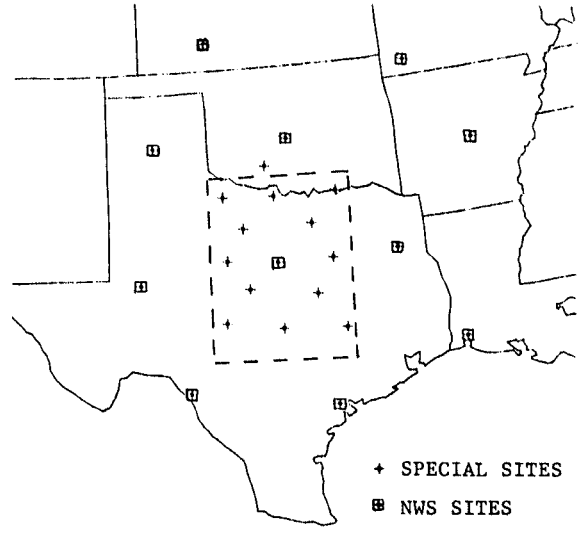

Figure 1. Rawinsonde sites used in the analysis on 6 March 1982. The grid area for both the satellite and rawinsonde data is located in central Texas (dashed box).

a scheme similar to the one used by Smith (1970). The scheme is a physical one, where an iterative solution is employed and LFM model output is used as first guess information. These soundings will be referred to as "physical" retrievals. The second data set is similar to the previous one except an analytic solution is employed after the iterative physical retrievals are obtained in order to improve the vertical structure of the satellite profiles (Smith, 1983). These soundings will be called "modified physical" retrievals. The third set of VAS soundings was produced using a linear regression scheme as described by Lee, et al. (1983). This method uses a local rawinsonde data set to determine statistical relationships between the radiance measurements and the structure of the atmosphere. These relationships are then applied to the observed radiance measurements to derive temperature and moisture profiles. This data set will be denoted as "regression" soundings. In all three data sets, soundings had a horizontal spacing of 75 - 100km over the entire cloud-free region of Texas, Oklahoma, and surrounding states. The location of the soundings varied with time due to the

extent and variation of the cloud cover.

Rawinsonde and satellite soundings are rarely co-located in space nor taken at the same time, thus making comparisons between them difficult to interpret. To overcome this problem, special procedures were used to make these data sets more consistent. First, the ground truth rawinsonde data were adjusted to a common release time (10 minutes after the beginning satellite scan time) using a scheme described by Fuelberg and Jedlovec (1982). The adjusted rawinsonde times in the study are 1100, 1445, 1745, 2045, and 2345 GMT 6 March 1982. The rawinsonde and satellite data were both objectively analyzed to a uniform grid (Fig. 1) with the balloon position (radiosonde) being recalculated at every level in the vertical. This procedure eliminated any spatial discrepancies between the two data types since the same grid was used for all data sets. The same objective analysis scheme weighting parameters were utilized with all data sets so that the potential for detail in the gridded fields was similar in each case.

The procedures followed in this evaluation and described above have provided three sets of satellite data at constant pressure surfaces from the surface to 100mb. Utilizing identically gridded rawinsonde data, mean differences, standard deviations of the differences, and root-mean-square differences between the rawinsonde and each satellite grid were calculated. In section 4, mean differences, along with analyzed fields and vertical profiles of rawinsonde and satellite data will be presented.

3. SYNOPTIC CONDITIONS

The 6 - 7 March 1982 case was used for extensive ground truth comparisons because of a large region of predominately cloud-free skies over the special network region. Showers and thundershowers associated with a cold front moved through central Texas during the night (Fig. 2). Behind this front, a shallow high pressure area was centered over western Oklahoma. To the north, another cold front, extenting from a low up in Canada, was pushing south through the upper plain states. The thermal gradient over the central portion of the region was quite strong with a 15°C gradient over Texas and a similar one over the central plains. Serval inches of snow were present on the ground in portions of Oklahoma and west Texas but melted during the afternoon hours. Further details of the synoptic conditions may be found in Greaves, et al. (1982) or Jedlovec (1982).

4. RESULTS

Figure 3 displays the mean temperature difference between the rawinsonde and satellite data sets as a function of pressure and time. Since the rawinsonde is considered "ground truth" in this study, the satellite grid point values were subtracted from the rawinsonde values ($T_{rao} - T_{sat}$). Several main features are noticeable and common to all three satellite data sets. First, there is a low level warm bias ($T_{rao} - T_{sat} < 0$) in the satellite grids from the surface to about 800mb. It ranges in magnitude from 3 - 5°C and is strongest at 1745 GMT. Above this level, there exists a cold bias up to around 600mb which is present in all satellite data sets for the first three time periods. At the last two time periods, the cold bias gives way to slight warm bias for the physical (dotted line) and regression (dashed line) sounding sets. The modified physical soundings (solid line) maintains a cold bias at these times. Undoubtably, this pattern is directly related to the low level frontal inversion present over the region (Fig. 4) which weakens as a result of boundary layer heating during the day. There is a tendency for the biases to become smaller as the frontal inversion weakens. The inability of the VAS retrievals to capture this feature is a result of the broad weighting functions in the lower troposphere.

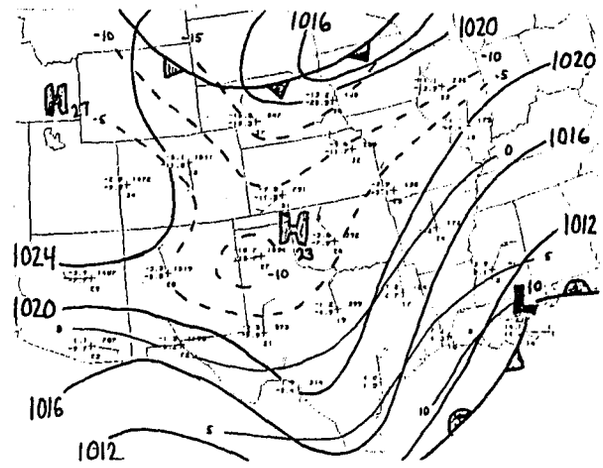

Figure 2. Surface pressure and temperature analysis at 1100 GMT 6 March 1982. Units are in millibars and °C respectively.

In the middle and upper troposphere, the temperature biases in the satellite soundings are not extremely large until 1745 GMT when biases of 2 - 5°C are present and persist through 2345 GMT. Again, all three satellite data sets show this bias with physical retrieval biases being smallest in this layer (600 - 300mb). Above 300mb there seems to be a compensating cold bias up to about 150mb. This bias pattern is related to the lowering of the tropopause onto the frontal boundary at 1745 GMT creating a strong temperature inversion near 350mb (Fig. 4). This inversion continues to lower, strengthens during the next two time periods, and the corresponding warm satellite biases get worse. Maximum values approach 6°C at 2345 GMT for the regression scheme (dashed line).

In order to properly evaluate the vertical structure resolved with the VAS soundings, grid mean profiles of the satellite and rawinsonde data sets are presented in Fig. 5 for 2045 GMT. The rawinsonde profile (solid line) is somewhat smoother than normal since it is a grid mean profile but contains the two major inversions previously discussed (Fig. 4). All three satellite grid mean profiles at 2045 GMT indicate biases (previously discussed) and misassign the levels of the inversions. This could be due to the broad weighting functions, the low signal-to-noise ratio of the radiance values in the upper levels, or to the dependency of the retrievals on first guess and apriori information.

The dewpoint profiles indicate a rather dry environment with some residual moisture in the lower and upper levels. This structure is only grossly captured by the satellite soundings, which might be expected since there are only three moisture channels on VAS. The regression retrievals (dotted line) do a good job of representing the rawinsonde profile while the physical (dot-dashed line) and modified physical (dashed line) schemes seem to over-estimate the low level moisture and under-

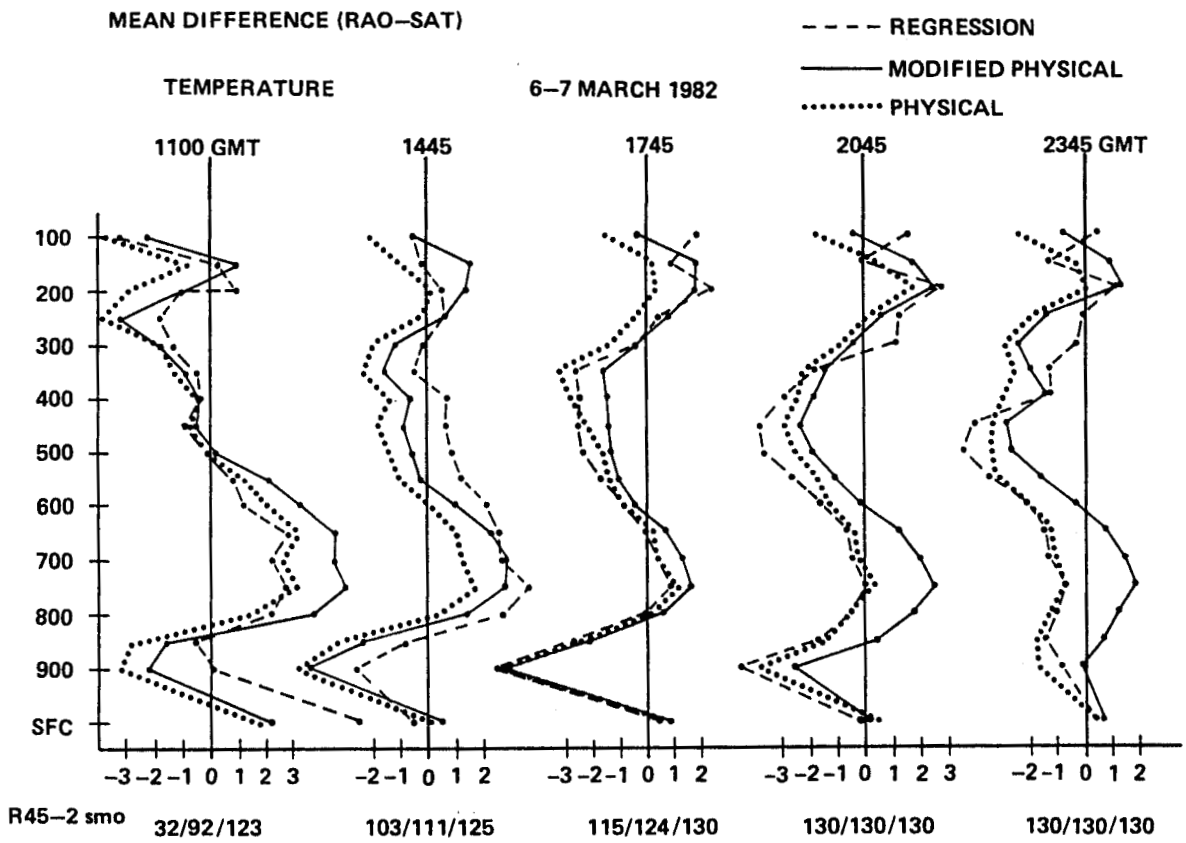

Figure 3. Mean temperature difference profiles as a function of pressure and time for each retrieval method. Units are in °C (horizontal axis). The numbers at the bottom are the number of grid points used in the calculations for the regression, modified physical, and the physical schemes, respectively.

estimate the upper level amounts.

Gridded fields of 500mb geopotential height values derived from the temperature and moisture

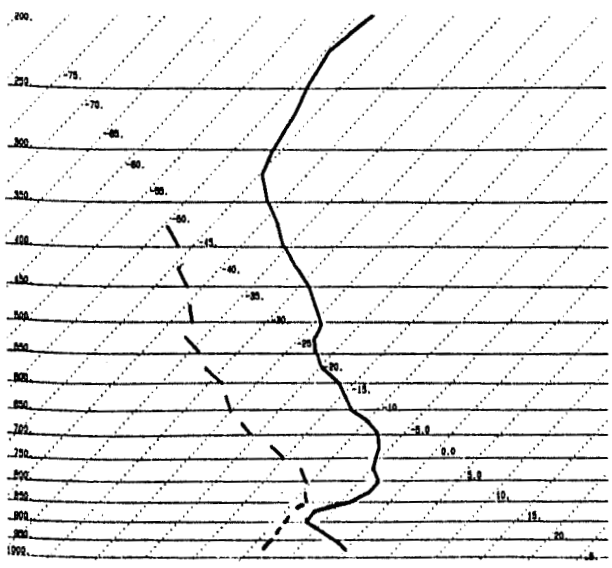

Figure 4. Skew-T diagram indicating the temperature (solid) and dewpoint temperature (dashed) profiles for Stephenville, Texas at 1745 GMT 6 March 1982.

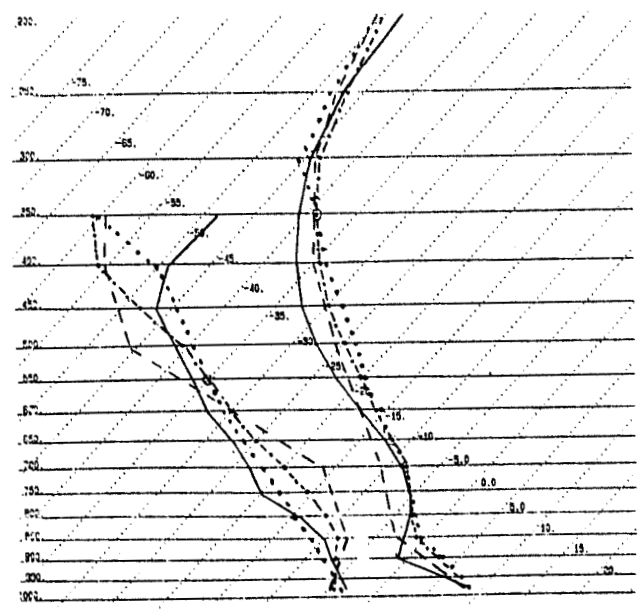

Figure 5. Grid mean skew-T profiles of temperature and dewpoint temperature for the rawinsonde (solid), regression (dotted), physical (dash-dotted), and modified physical (dashed) data sets at 2045 GMT 6 March 1982.

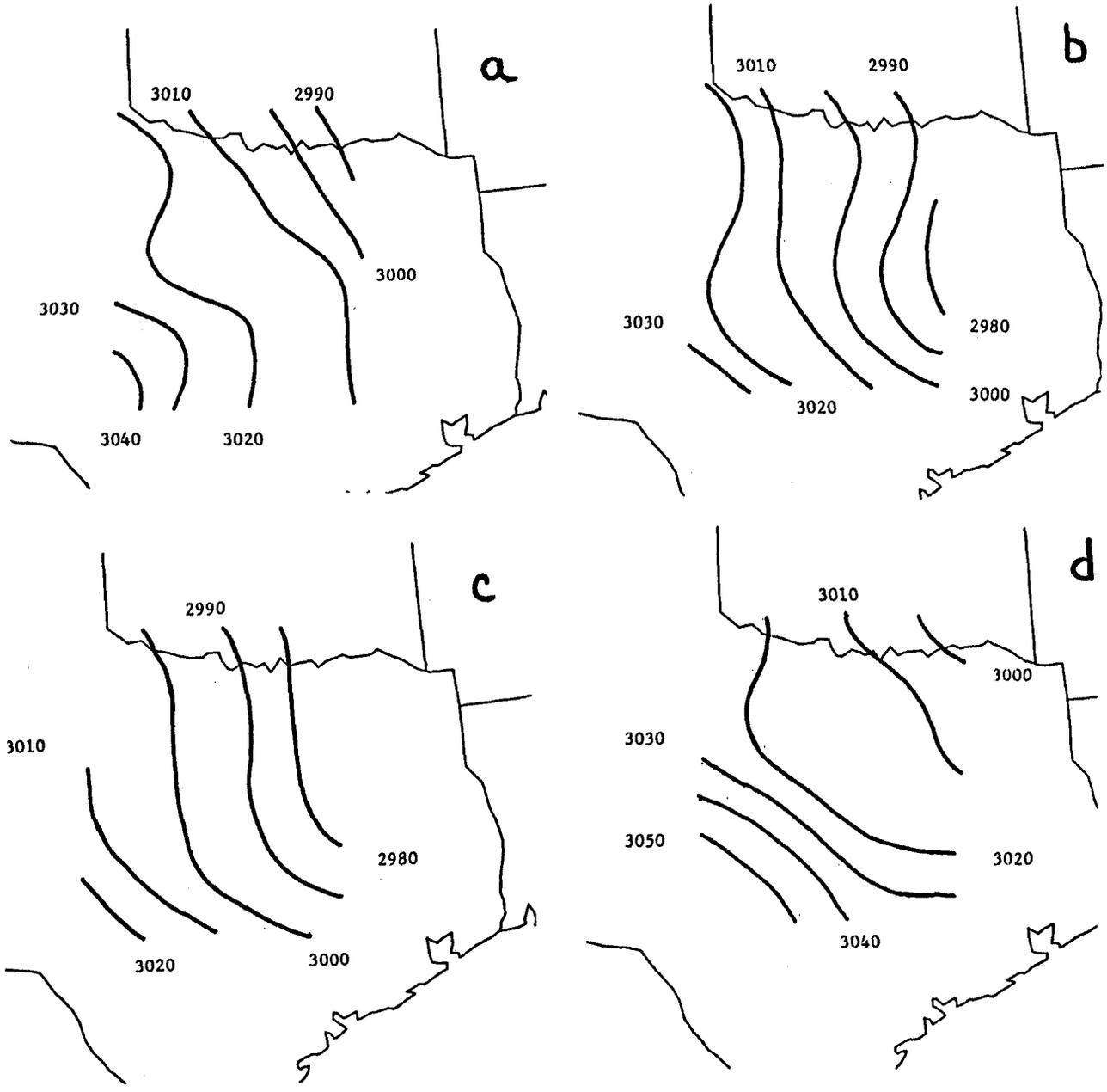

Figure 6. Geopotential height analyses at 500mb over the mesoscale grid region at 2345 GMT 6 March 1982 for the rawinsonde (a), physical (b), modified physical (c), and the regression (d) retrievals. Contours are labeled in meters.

data are presented in Fig. 6 at 2345 GMT. Biases discussed in the previous paragraphs will influence the height fields, however, alternating levels of warm and cold biases may cancel some accumulation of error in these derived fields. Figure 6a shows the rawinsonde height field over the special network. A fairly strong gradient exists in the northeast-southwest direction with a magnitude of about 50m. There is a small perturbation in this field making the gradient non-uniform. All three of the satellite derived height analyses capture some portion of the rawinsonde features. The physical sounding analysis (Fig. 6b) and the modified physical analysis (Fig. 6c) present a uniform gradient which is orientated more in the east-west direction than the rawinsonde feature. The regression analysis (Fig. 6d) presents a non-uniform field similar to the rawinsonde. In all three satellite analyses, the magnitude of the gradient across the network is similar, however, absolute values indicate that the physical and modified physical schemes are roughly 10m too low while the regression soundings are a similar amount too high. This can be traced back to the temperature biases presented in Fig 3. These satellite analyses are definitely quite good and represent the "cream of the crop" so to speak. The accuracy of the satellite analyses and gradient indicated here however, does not always represent the real atmosphere this well.

Figure 7 indicates the mean precipitable water differences as a function of time over the special network. As was pointed out with the dewpoint

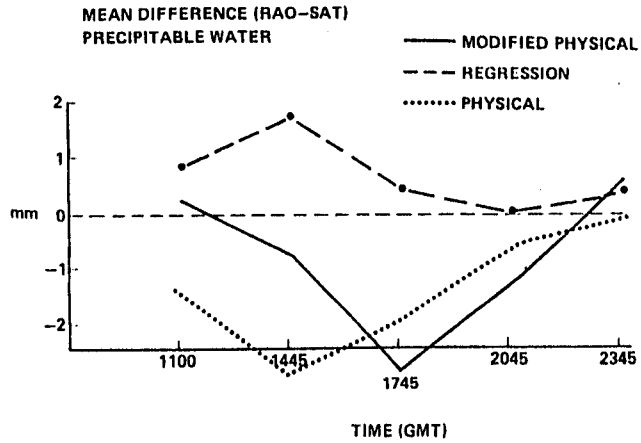

Figure 7. Mean precipitable water differences as a function of time for the satellite data sets. Units of the vertical axis are in millimeters. The number of grid points used at each time are the same as in Fig. 3.

profiles (Fig. 5), the physical soundings (dotted line) and the modified physical soundings (solid line) are too moist, particularly in the lowest layers, with mean precipitable water differences approaching 3.0mm at 1445 GMT and 1745 GMT, respectively. Although this may not seem excessive, it represents over 30% of the total precipitable water in the column over the mesoscale region. The regression soundings (dashed line) have relatively small difference values except at 1445 GMT when they approach 2.0mm. Although this is quite good, horizontal fields of this quantity (not shown) indicate very little precipitable water gradient despite a significant gradient in the rawinsonde measurements.

5. CONCLUSIONS

In general, all three VAS retrieval sets, produce similar temperature bias patterns when compared to the rawinsonde data. The bias patterns alternate between warm and cold in the vertical and are centered around the level of major inversions. Apparently systematic moisture biases are prominent in both of the physical retrieval data sets while the regression scheme produces horizontally bland but relatively unbiased moisture products. The magnitude of the temperature and moisture biases vary with time and to some degree with each retrieval scheme. This suggests that two factors may control the quality of VAS soundings for a particular situation. First, the vertical structure of the atmosphere is a major factor for the biases in the retrievals. The broadness of the weighting functions plus the poor signal-to-noise ratio in the upper levels limits the detail in the satellite profiles and may also affect the horizontal resolution of atmospheric features. Second, a particular retrieval scheme might produce soundings which are less biased that others for a particular synoptic situation. It is not apparent from this research however, that any one scheme consistently produces better results in the grid mean.

Horizontal analyses presented indicate success in deriving geopotential height fields at a single time and level. Other analyses show less consistency in space and with time and the horizontal gradients are generally weaker than those of the corresponding rawinsonde observations. The 6 March 1982 experiment day, with a strong frontal inversion and horizontal gradient, is just one type of situation in which VAS soundings should be evaluated in detail. Results for other synoptic settings may or may not be the same, depending on the vertical and horizontal structure of the sounding environment.

Acknowledgements. The author wishes to express his thanks to Drs. Bill Smith and Kit Hayden of NESDIS at the University of Wisconsin for providing both of the physical retrieval data sets and for several discussions of the results. Thanks also goes to Drs. Louis Uccellini and Harry Montgomery at NASA Goddard Space Flight Center for their cooperation in providing the regression soundings used in this study. This work was performed under the Universities Space Research Association's Visiting Scientist Program at Marshall Space Flight Center under NASA contract NAS8-34767. NASA's support of this program is appreciated.

REFERENCES

Anthony, R. W., and G. S. Wade, 1983: VAS operational assessment findings for Spring 1982/1983. Preprints 13th Conference on Severe Local Storms, AMS, Boston, J23-J28.

Chesters, D., L. W. Uccellini, and A. Mostek, 1982: VISSR Atmospheric Sounder (VAS) simulation experiment for a severe storm environment. Mon. Wea. Rev., 110, 198-216.

Fuelberg, H. E., and G. J. Jedlovec, 1982: A subsynoptic-scale kinetic energy analysis of the Red River Valley tornado outbreak (AVE-SESAME I). Mon. Wea. Rev., 110. 2005-2024.

Greaves, J. R., H. E. Montgomery, L. W. Uccellini, and D. L. Endres, 1982: 1982 AVE/VAS ground truth field experiment: Satellite data acquisition summary and preliminary meteorological review. NASA report X-903-82-17, 27pp, available from Goddard Space Flight Center.

Hill, C. K., and R. E. Turner, 1983: NASA's AVE/VAS Program. Bull. Amer. Meteor. Soc., 64, 796-797.

Jedlovec, G. J., 1982: AVE/VAS experiment: Synoptic summary and preliminary results. VISSR Atmospheric Sounder (VAS) Research Reveiw. NASA Conference Publication 2253, Goddard Space Flight Center, Greenbelt, Md., 39-42.

Lee, T., D. Chesters, and A. Mostek, 1983: The impact of conventional surface data upon VAS regression retrievals in the lower troposphere. J. Appl. Meteor., 22, 1853-1874.

Menzel, W. P., W. L. Smith, and L. D. Herman, 1981: Visible Infrared Spin Scan Radiometer Atmospheric Sounder radiometric calibration: An inflight evaluation from intercomparisons with HIRS and radiosonde measurements. Appl. Opt., 20, 3641-3644.

Petersen, R. A., L. W. Uccellini, D. Chesters, A. Mostek, and D. Keyser, 1982: The use of VAS satellite data in weather analysis, prediction, and diagnosis. Preprints 9th Conference on Weather Forecasting and Analysis, AMS, Boston, J29-J32.

Petersen, R. A., D. Keyser, A. Mostek, and L. W. Uccellini, 1983: Techniques for diagnosing mesoscale phenomena affecting aviation using VAS satellite data. Preprints 9th Conference on Aero. and Aeron. Meteorology, AMS, Boston, 12-17.

Smith, W. L., 1983: The retrieval of atmospheric profiles from VAS geostationary radiance observa-

tions. J. Atmos. Sci., 40, 2025-2035.
Smith, W. L., V. E. Soumi, W. P. Menzel, H. M. Woolf, L. A. Sromovsky, H. E. Revercomb, C. M. Hayden, D. N. Erickson, and F. R. Mosher, 1981: First sounding results from VAS-D. Bull. Amer. Meteor., 62, 232-236.
Smith, W. L., 1970: Iterative solution to the radiative transfer equation for the temperature and absorbing gas profile of an atmosphere. Appl. Opt., 9, 1993-1999.

GROUNDBASED DEMONSTRATION OF A 0.5μm WIND SENSOR

J. T. Sroga, L. S. O'Hara, A. Rosenberg
RCA Astro Electronics
Princeton, NJ

P. B. Hays, B. Kennedy, V. Abreu
Space Physics Research Laboratory
University of Michigan
Ann Arbor, MI

I. INTRODUCTION

Laser based sensor have recently been receiving increased attention as possible satellite system to improve measurements of the atmospheric base state. One technique for determining the wind velocity is to measure the Doppler shift of light backscatter from naturally occuring aerosol particles. Beneditti-Michelengeli et al., 1972 have demonstrated the feasibility of such Doppler shift measurements using a scanning interferometer system operating at a visible wavelength (.488μm).

Spaceborne applications of the scanning interferometer technique are severly limited by the time required to obtain a spectral scan. This paper describes a ground based lidar system to measure the Doppler spectrum simultaneously using incoherent detection. The 0.5μm Wind Sensor described here consists of a frequency doubled, Nd;YAG laser producing single frequency, narrow band pulses and a Fabry Perot Interferometer (FPI) using an Image Plane Detector (IPD) to spatially scan the FPI spectral transmission. A block diagram of the .5μm Wind Sensor is shown in Fig 1. Since each channel measures a separate wavelength interval of the backscatter spectrum, the relative displacement of the backscatter spectrum from the reference signal is a direct measure of the Doppler shift.

The capabilities of a spaceborne .5μm Wind Sensor is described in a companion paper, "Analysis of a 0.5μm Spaceborne Wind Sensor" by Hays, et al., 1984. A ground based Wind Sensor based upon this feasibility study is currently being assembled. This paper will concentrate on the description of the ground based Wind Sensor with prelimenary results to be presented.

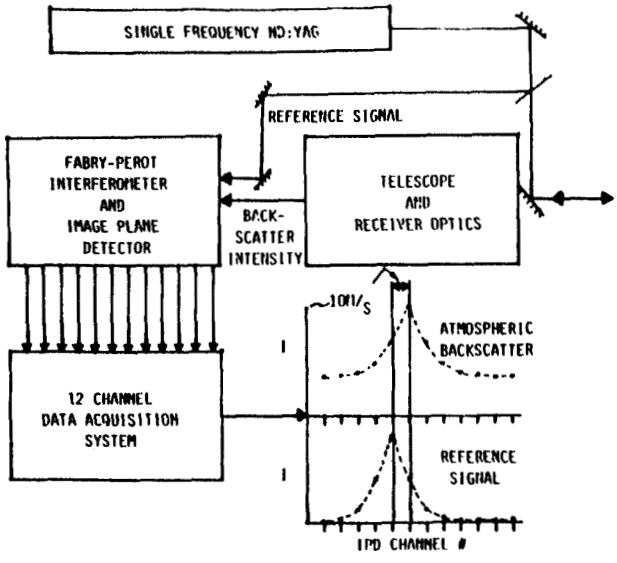

Figure 1 .5μm Wind Sensor Block Diagram.

II TRANSMITTER

The transmitter for the .5μm Wind Sensor, shown schematically in Fig 2, consists of a frequency doubled, Q switch Nd;YAG oscillator amplifier system. Since laser cavity resonator consisting of only mirrors, lasing medium and Q switching device simultaneously oscillate at a number of different frequencies (called longitudinal modes), additional steps must be incorporated in the oscillator cavity design to meet the single frequency narrow band width requirements for the Wind Sensor transmitter.

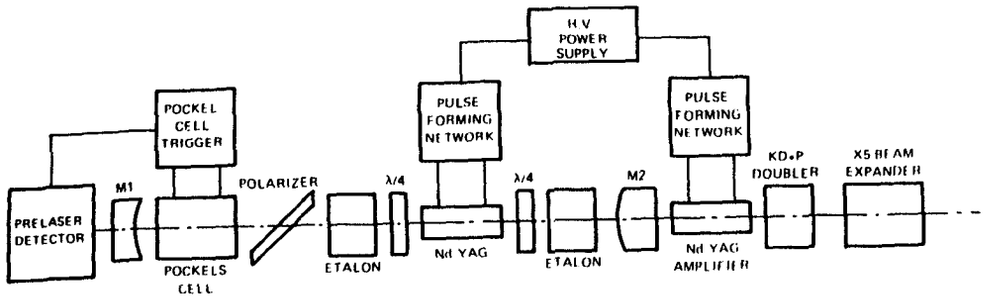

Figure 2 Nd;YAG Transmitter Schematic

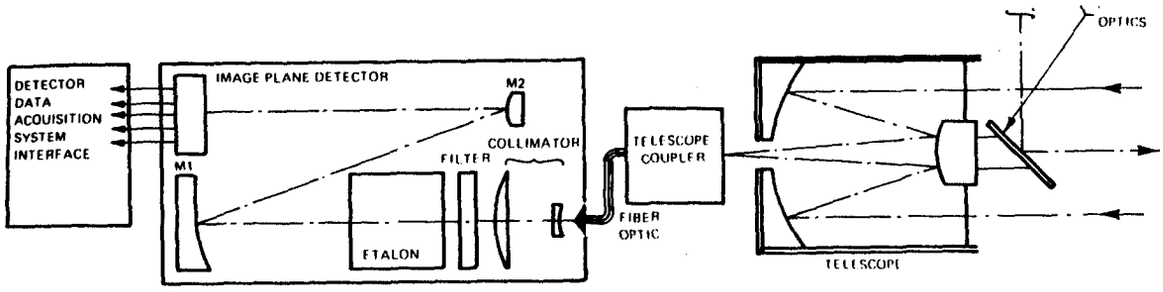

Figure 3 Schematic of Receiver Optics

Two techniques are employed in the oscillator design to constrain the laser frequency to a single longitudinal mode (SLM). A minimal cavity length was chosen to maximize the longitudinal mode spacing while allowing accessibility to the intercavity components. An intercavity etalon reduces the number of longitudinal modes which experience gain in the oscillator to a few modes (Smith, 1965). The etalon is tilted from the cavity optical axis to prevent lasing from the reflective surface and to adjust the transmission maxima to coincide with a cavity longitudinal mode. Because temperature fluctuation, which occur during optical pumping, will cause the relative spectral positions of the mode selecting elements and the longitudinal mode to change with respect to each other, adjacent modes can possibly be above the oscillation threshold and experience amplification.

A second technique is used to further reduce the possibility of multimode operation. A prelasing technique (Berry et al 1981) consisting of slowly reducing the optical losses in the laser cavity preferentially amplifies the longitudinal mode experiencing the most gain. These optical cavity lasers are controlled by adjusting the voltage on the Pockels cell. Once the buildup of a single mode has been detected by the photodiode, the Pockel cell is triggered and the entire Q-switched pulse energy is channeled into the single longitudinal mode. Quarter wave plates are used to eliminate spatial hole burning in the laser rod to further reduce competition between adjacent modes.

The 1.06μm output from the oscillator is amplified before being frequency doubled by the KD*P crystal. The output beam is expanded by a 5x telescope before being transmitted into the atmosphere via steering optics.

Table I lists the operating parameters of the transmitter.

Table I : Transmitter Parameters.

Operating wavelength	.53 μm
Expected output energy	50mj/pulse
Pulse width	20ns FWHM
Bandwidth (Transform Limit)	50 mHz
Beam Divergence	.37 mrad

III Receiver

The receiver optics for the .5μm Wind Sensor are shown schematically in Figure 3. A 30cm diameter f/16 Cassegrain telescope is used to collect the light backscattered from the atmosphere. Additional optics are used to conserve the etendue of the FPI and couple in additional calibrations light sources. A fiber optic cable is used to simplify optical alignment and eliminate any systematic angular dependence of the backscattered light.

The design of the FPI which has been optimized to measure the aerosol backscatter Doppler spectrum is described in a companion paper (Hays, et al,1984)

Table II lists the design parameters of the FPI. The combination of large spacer length and low plate reflectively is the optimum condition to obtain maximum signal throughput for the necessary high spectral resolution. The design and construction of the etalon holder and chamber is similar to that of the FPI flown on the Dynamics Explorer Satellite (Hays, et al,1981). This design and construction yield a very stable and rugged FPI for space flight applications. The FPI Transmission fringes are focused on to an image plane detector (IPD) to simultaneously measure the Doppler backscatter spectrum.

Table II Reciever Paremeter

FPI	
Prefilter (Interference)	30A° FWHM
Etalon Spacer(Zerodur)	30.48cm
Plate Reflectively(Dielectric	70 %
Nominal Bandwidth/Channel	41 MHz
Plate Coated Area	5 cm/Dia
IPD	
Photocathode	S-20, 1.2 cm/dia
Amplification	3 microchannel plate Z configuration
Anode Type	12 concentric equal area rings
Electric Gain	10^6 max

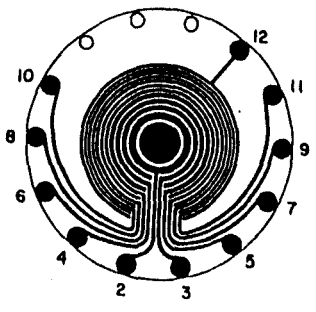

Figure 4 IPD Anode Schematic
Killeen et al, 1983

The .5μm Wind Sensor IPD is similar to one for the Dynamic Explorer Satellite described by Kileen, et al., 1983. This device has a S-20 photocathode, three microchannel plate electron multiplication stage and a segmented anode consisting of 12 equal area, concentric rings. Figure 4 schematically illustrates the anode layout which is designed to imitate the transmission fringe pattern of the FPI. This segmented anode design simultaneously monitors equal and continuous wavelength intervals of the backscatter spectrum. Table II also lists some of the Wind Sensor IPD specifications. The IPD signal outputs are converted to a voltage and interfaced to a data acquisition system for storage and analysis.

IV Data Acquisition System.

A LeCroy Model 3500 microcomputer with two floppy disk devices, graphics terminal printer and Tektronics 4632 video hard copy unit is the basis for acquisition, storage and analysis of Wind Sensor data. Several digitizers located in a CAMAC module are used to convert the analog signal from the IPD digital values for storage and processing by the computer. Expansion of the data acqusition system will include additional digitizers for all 12 channels and a data logger to monitor operating parameters of the system.

V Conclusions.

A ground based lidar system designed to derive atmospheric wind measurements from the aerosol backscatter Doppler Spectrum, has been described in this paper. The system consists of a single line, narrow band, frequency doubled Nd;YAG laser transmitter utilizing incoherent detection with a Fabry Perot interferometer. An Image Plane Detector allows simultaneous sampling of the backscattered spectrum. The individual subsystem components have been fabricated and are currently being integrated into a system. Preliminary results of initial system performance will be presented at the conference.

VI References.

Benedetti-Michelangeli,G., F. Congeduti and G. Fiocco, 1972: Measurements of Aerosol Motion and Wind Velocity in the lower Troposphere by Doppler Optical Radar. J. Atmos. Sci. V29 pp. 906-910.

Berry, A. J., D. C. Hanna and C. G. Sawyer 1981: High Power Single Frequency Operation of a Q-Switched TEM_{00} Mode Nd:YAG Laser. Opt. Comm. V40 pp 54-58.

Hays, P. B., T. L. Killeen, and B. C. Kennedy, 1981: The Fabry-Perot Interferometer on Dynamics Explorer. Space. Sci. Inst. V5 pp 395-416.

Hays, P. B., V. Abreu, D. B. Hogan and A. Rosenberg, 1984: Analysis of a 0.5 μm Spaceborne Wind Sensor Conference on Satellite Meteorology, Remote Sensing and Applications. June 25-29, 1984 Clearwater Beach, FLA.

Killeen, T. L., B. C. Kennedy, P. B. Hays D. A. Symanow and D. H. Ceckowski, 1983: An Image Plane Detector for the Dynamics Explorer Fabry-Perot Interferometer, Appl. Opt., V22 pp 3508-3513.

Smith, P. W., 1965: Stabilized, Single Frequency Output from a long laser Cavity. IF-EE J. Quart. Elect. V QE-1, pp 343-348.

THE IMPROVED INITIALIZATION INVERSION ("3I") METHOD : A HIGH RESOLUTION PHYSICAL METHOD FOR TEMPERATURE RETRIEVALS FROM THE SATELLITES OF THE TIROS-N SERIES

A. Chédin, N.A. Scott, C. Wahiche, P. Moulinier,
N. Husson and I. Cohen-Hallaleh

Laboratoire de Météorologie Dynamique du C.N.R.S.
Ecole Polytechnique, Palaiseau, France

1. INTRODUCTION

The "3I" (Improved Initialization Inversion) Procedure is a physical algorithm for retrieving meteorological parameters from the satellite data of the TIROS-N series at a spatial resolution of 100 km x 100 km. Accounting for the physics of the phenomena involved, this procedure explicitly takes into consideration local properties of each terrain observed like surface elevation, surface emissivity, percentage of water, viewing angle. Considerable effort is paid to the optimization of the initial guess solution which is retrieved owing to a large precomputed data set, the "TIGR" (TOVS Initial Guess Retrieval) data set, which describes the physical and statistical properties of a large number of well sampled atmospheric situations to which the observed situation may be compared. Retrieval of the initial guess also relies upon operational forecasts of the temperature and of the geopotential altitude of the lowest atmospheric level. The quality of the initial solution obtained is demonstrated by the fact that only one iteration with the retrieval scheme is required to get the final solution. Preliminary comparisons, in the case of the ALPEX Intensive Observing Period of March 4 and 5, 1982, show a satisfactory agreement with conventional data and, in particular, a much better agreement in the 500 mb to 1000 mb pressure range.

2. GENERALITIES ON THE IMPROVED INITIALIZATION INVERSION ("3I") PROCEDURE

The "3I" procedure is based upon the constitution, once and for all, of a synthetic data set (the "TIGR" - TOVS Initial Guess Retrieval - data set) which comprises, for a large number of atmospheric situations (presently around 400 for the middle latitudes, and close to 1400 for all latitude zones, extracted from a much larger set owing to a careful statistical analysis) :

a) the description of each atmospheric situation through radiosonde rocketsonde reports : pressure, temperature, moisture, and, when available, ozone mixing ratio profile, latitude, longitude, date, etc... ;

b) computed values of the transmittance at each of the 40 pressure levels in which the atmosphere is divided, from the surface pressure to 0.05 mb, and for all the HIRS-2 channels (except the visible channel) and the MSU channels. These values are obtained owing to a fast line-by-line transmittance code, the "Automatized Atmospheric Absorption Atlas" (see Scott et al. (1981, 1984)) hereafter referred to as the "4A" model ;

c) computed values of the corresponding radiances and their associated brightness temperatures for the channels above mentioned. Actually, these numbers are divided into two components : surface contribution and atmospheric contribution ;

d) two Jacobian matrices representing the partial derivatives of radiances (or brightness temperatures) with respect to temperature and with respect to moisture ;

e) in addition to these physical data, statistical data corresponding to the sample are computed once and for all : temperature and radiance means and covariance matrices, "coordinates" of each atmospheric situation in an axis system defined by the eigenvectors of the radiance covariance matrix, etc...

These computations are made for 6 zenith angles and extended to 10 angles owing to an interpolation procedure so as to sample correctly the interval covered by the scanning instruments of TOVS. They are also carried out for several values of the surface pressure, actually 11 values ranging from 1013 mb (or more) to 725 mb (for land observations). In addition, for each channel, two surface emissivities are considered, one for land observations and one for sea observations.

Given observed clear column radiances (see § 3.c), the "3I" procedure follows two principal steps :

a) retrieval of the initial guess solution : the observed clear column radiances are first used

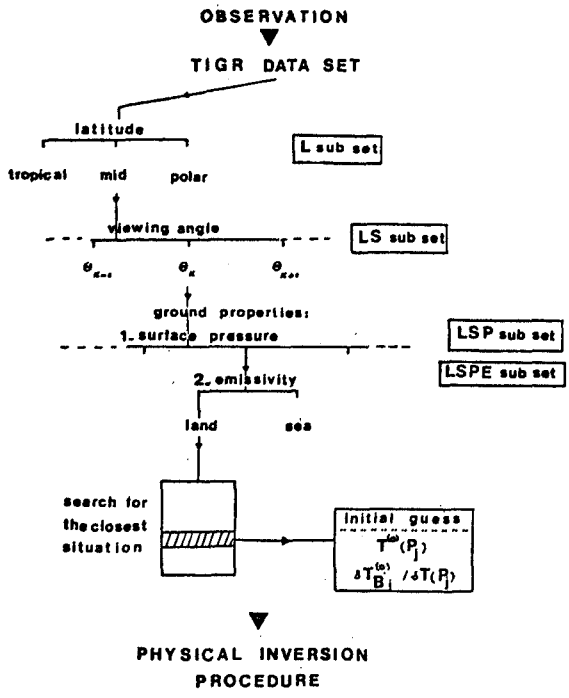

Figure 1

Organization of the TIGR data set. From a selected set of n observations (radiances or brightness temperatures) to the retrieval of the initial guess solution, $T^0(P_j)$, there are three main steps : search for the L sub-set corresponding to the latitude of the observations, search for the LS sub-set (closest viewing angle), search for the closest ground properties (LSPE sub-set), and search for the closest archived situation in the sample corresponding to the right secant, to the right latitude and to the right surface properties. The quantity $\partial T_{Bi}(0)/\partial T$ symbolizes the Jacobian associated with the retrieved archived situation.

to retrieve the "best" initial guess solution in a statistical sense. The procedure makes use of the "TIGR" data set (see Fig. 1). The selected set of observed radiances is "compared" to each of the computed sets of radiances and the "closest" is retained. The distance between two sets of radiances is calculated in the axis system defined by the eigenvectors of the normalized radiance covariance matrix. This search for the closest archived situation may be carried out by considering either all the HIRS-2 and MSU channels or more restricted radiance sets emphasizing such or such property in the atmosphere, for example : a set of channels almost insensitive to clouds ;

b) the basis for the retrieval of the "exact" solution is a least squares procedure aiming at minimizing the differences between the radiances associated with the initial guess and the observed radiances. Use is made of the Jacobian associated with the retrieved initial guess, in the "TIGR" data set. Actually, this procedure is applied to the brightness temperatures rather than to the radiances and makes use of prior data (Bayesian estimate).

3. INVERSION SCENARIO

3.a Observations and ancillary data. Spatial resolution.

The structure of the observed data set is closely connected to the spatial resolution which has been adopted for analysing the satellite measurements in terms of atmospheric parameters through the inversion of the radiative transfer equation. Here, HIRS-2 spots are grouped into boxes of 4x3 to 2x3 spots according to the viewing angle. One box covers 3 scan lines and 2 consecutive boxes share two scan lines resulting in an over-sampling along the sub-satellite track. HIRS-2 and MSU sounding data are processed according to the following procedure :

- MSU sounding data are first interpolated taking into account the six MSU spots the closest to the box considered. The interpolation scheme is linear in the angle and inversely proportional to the square of the distance of each MSU spot to the center of the box (more details are given in Wahiche (1983)).

- The ECMWF (European Centre for Middle Range Weather Forecasting) high resolution US Navy topography is then interpolated within each HIRS-2 spot resulting in a mean altitude value and a mean percentage of water for each HIRS-2 spot.

- Forecasts from the ECMWF (European area grid, 1.5° x 1.5°) are implemented into each HIRS-2 spot after interpolation (the scheme uses spline functions). Are considered : temperature and geopotential altitude at 1000, 850 and 700 mb ; pressure at the surface. Corrections are brought to surface pressure and temperature so as to account for the difference between the spatial resolution of the ECMWF grid and the spatial resolution associated with each HIRS-2 spot.

This procedure takes care of the only HIRS-2 spots finally considered in each box (see below).

3.b Cloud tests

Cloud tests are conducted for each box, and in each box, for each HIRS-2 spot. Seven tests are considered which follow very closely the procedure by McMillin (1982) except that, in our case, observations are not angle corrected. The regressions or the test-limits defined in this reference had consequently to be extended or modified, to make them apply to non-nadir observations, using the TIGR data set described above. One regression is defined for one angle (10 angles are considered), one ground emissivity (land or sea), one surface pressure (six surface pressures are considered in that case, among the 11 archived in the TIGR data set : every other one). Thus, one regression in McMillin (1982) is replaced by 120 sets of coefficients computed once and for all. It may be noted that, for day time observations, use is made

of the albedo in a way similar to Hillger et al. (1981). A box is "clear" if at least one spot has passed all tests. If several spots are clear, variance tests are made on channels HIRS 5, 7 and 13 similarly to McMillin (1982). For "not clear" boxes, the half containing the highest brightness temperatures for channel 18 (corrected for water vapor attenuation) for night time observations or for channel 8 for day time observations is considered and variance tests are made on channel 7. For clear and not-clear boxes, remaining spots are averaged and the mean values of the latitudes and longitudes of these spots are assigned to the box.

3.c Inversion scenario

The procedure used to retrieve thermal profiles from HIRS-2 and MSU observations depends upon the flag "clear" or "not clear" attributed to the box. The first operation, however, is the same for the two cases and consists in isolating the TIGR sub-set within which the initial guess is to be retrieved. That part of the data set is reached after analysis of the values of the latitude, of the viewing angle, of the flag emissivity (sea/land) and of the surface pressure.

i. "Not clear" boxes. A cloud clearing technique : the Ψ-method.

For not-clear boxes, the initial guess is obtained in two steps. The first step consists in searching, in the right sub-set of the TIGR data set, a preliminary initial guess which is the closest among the archived situations when reference is made to channels HIRS-2 n° 1, 2, and MSU n° 2, 3 and 4, to forecast of either the temperature at 1000 mb or at 850 mb, or at 700 mb, according to the surface pressure, and to the mean temperature between two specific levels of the "4A" model atmospheric stratification. These two levels vary with the latitude zone considered. For mid-latitudes, the boundary levels correspond respectively to 160 mb and 275 mb and represent approximately the lowest part of the stratosphere. This mean temperature, hereafter referred to as T(LS) is archived in the TIGR data set for each situation. The "observed" value is obtained through a regression of the type :

$$T(LS) = a_0 + a_1 T^{HIRS}(1) + a_2 T^{HIRS}(2) + a_3 T^{HIRS}(3) + a_4 T^{MSU}(2) + a_5 T^{MSU}(3) + a_6 T^{MSU}(4) \qquad (1)$$

where $T^{HIRS}(i)$ is the brightness temperature associated with channel i of HIRS-2. The coefficients of this regression are obtained from the data archived in eachTIGR data sub-set. Applied to the synthetic data of the TIGR data set, the regression provides T(LS) values with no bias and a standard deviation close to 1 K.

This first step provides the "preliminary initial guess". From this first solution is started the cloud clearing algorithm which provides the brightness temperatures one would have obtained under clear sky conditions for several "contaminated" channels, and, in particular, channels 14 and 15. In addition to the well-known fact that their associated weighting functions are narrower than for example at 15 µm, channel 14 has also the advantage of peaking close to the surface (950 to 920 mb) while the satellite-surface transmittance is close to zero (typically 0.1), which means that contamination by surface characteristics is small. The clear brightness temperatures for channels 3 to 6, 14 and 15, that we will call "pseudo-channel", are obtained owing to a method that will be referred to as the "Ψ-method" in the following.

The clear equivalent brightness temperature for the pseudo-channel 15, $\Psi^{HIRS}(15)$, is simply obtained by the expression :

$$\Psi^{HIRS}(15) = T_{OBS}^{MSU}(2) + \left(T_{closest}^{HIRS}(15) - T_{closest}^{MSU}(2) \right) \qquad (2)$$

where $T_{closest}^{HIRS}(15)$ and $T_{closest}^{MSU}(2)$ are the brightness temperatures for channels HIRS-2 n° 15 and MSU n° 2 associated with the preliminary initial guess. This expression means that we rely upon the difference of two channels peaking approximately at the same level and obtained for a situation relatively close to the observed one. This difference is small and less dependent on small atmospheric changes than $T_{closest}^{HIRS}(15)$ itself. The Ψ-method is also applied to channels HIRS n° 4, 5 and 6 : the clear equivalent brightness temperature for the pseudo-channel 4, $\Psi^{HIRS}(4)$, is obtained by the expression :

$$\Psi^{HIRS}(4) = T_{OBS}^{MSU}(3) + \left(T_{closest}^{HIRS}(4) - T_{closest}^{MSU}(3) \right)$$

where the symbols have the same meaning as in Eq. (2), when the clear equivalent brightness temperature for the pseudo-channels 5 and 6 are obtained by an expression similar to that of Eq. (2). Finally, a pseudo-channel HIRS n°3 is obtained from an expression similar to Eq. (2) where $T_{OBS}^{MSU}(2)$ and $T_{closest}^{MSU}(2)$ are respectively replaced by :

$0.5 * \left(T_{OBS}^{MSU}(3) + T_{OBS}^{MSU}(4)\right)$ and

$0.5 * \left(T_{closest}^{MSU}(3) + T_{closest}^{MSU}(4)\right)$

and where $T_{closest}^{HIRS}(15)$ is replaced by $T_{closest}^{HIRS}(3)$.

The brightness temperature of the pseudo-channel 14, $\Psi^{HIRS}(14)$ is obtained through a regression of the type :

$$\Psi^{HIRS}(14) = b_o + \sum_i b_i T^{HIRS}(i) + \sum_j c_j T^{MSU}(j) \qquad (3)$$

where i takes the values 2 to 6 and 15 and j the values 2 and 3.

The coefficients of this regression are, like those of Eq. (1), obtained from the data archived in each TIGR data sub-set. Applied to the synthetic data of the TIGR data set, the regression provides values of $\Psi^{HIRS}(14)$ which, when

compared to the true $T^{HIRS}(14)$ values, show no bias and a standard deviation varying from 0.1 K to 0.3 K according to the viewing angle and the surface pressure.

"Observed" values of $\Psi^{HIRS}(14)$ are obtained by replacing the brightness temperature appearing in Eq. (3) by their observed values :

$$T_{OBS}^{HIRS}(2),\ \Psi_3 \text{ to } \Psi_6,\ \Psi_{15},\ T_{OBS}^{MSU}(2),\ T_{OBS}^{MSU}(3)$$

The Ψ-method has two important advantages. First, it allows, quite simply, to accurately eliminate the effects of the clouds and the departure from the exact values (over-corrections or under-corrections) are relatively small. Second, no "smoothing" of the cleared brightness temperatures is required when it may be the case for the so-called N* method by Smith (1968) as explained in Fleming et al. (1982). Although the results presented in this reference are interesting, any smoothing procedure applied to geophysical fields will hardly make the distinction between errors of erratic nature and real characteristics of the field itself like boundaries between oversea and overland observations, or like the occurence of a moutain in the field of view. We have verified that these features are preserved by the Ψ-method.

The second step consists in searching the actual initial guess which is the closest among the archived situations when considering channels HIRS-2 n°1,2,Ψ_4,Ψ_{14},Ψ_{15}, MSU n°2,3 and 4, forecast of either the temperature at 1000 or 850 mb, or at 700 mb, depending on the surface pressure, and T(LS). From the initial guess obtained at the end of the second step, the physico-statistical inversion algorithm (see below) is activated with channels HIRS-2 n° 1, 2, 4, 14, 15, and MSU n° 3 and 4. One iteration is enough to provide the final solution.

ii. "Clear" boxes

After having isolated the right sub-set of the TIGR data set, the situation the closest to the observed situation is searched, within this sub-set, by making reference to channels HIRS-2 n° 1, 2, 3, 4, and MSU n° 2, 3, 4, and to forecast of either the temperature at 1000 mb or to the temperature at 850 mb or at 700 mb according to the surface pressure. From this initial solution, the physico-statistical inversion algorithm (see below) is activated with channels HIRS-2 n° 1, 2, 5, 14, 15, and MSU n° 3, 4. One iteration (one inversion) is enough to provide the final solution.

3.d Inversion algorithm : a simple Bayesian approach

Since it starts from an optimum initial guess, which is the situation the closest to the observed situation among those archived in the TIGR data set, the "3I" method aims at estimating the difference between the parameters and their values for the closest situation rather than the parameters themselves (or the difference between the parameters and their mean values). Writing the radiative transfer equation under the form :

$$y(\nu_i) = \int X(\nu_i,z)\ \beta(z)\ dz$$

where y represents the measurements and β the parameters (here the temperature profile), and where the ν_i's summarize the conditions of observations (frequencies, viewing angles, surface properties, ..), $X(\nu_i,z)$ is the kernel including transmittances and z is directly related to the altitude, a linear model may be established using an appropriate quadrature formula giving the matrix equation :

$$y_e = X\,\beta + e$$

where $y_e = y+e$, e being the associated error. Following a simple Bayesian approach, a least-squares type estimate of β,b, may be written as :

$$b-\beta_{IG} = [\ X'\ S_e^{-1} + S_{\beta*}^{-1}\ ]^{-1}\ X'\ S_e^{-1}\ (y_e-y_{IG})$$

where $S_{\beta*}$ is the covariance matrix of $\beta-\beta_{IG}$ and β_{IG} is the initial guess solution. $S_{\beta*}$ may be easily computed from the TIGR data set. More details are given in Chedin et al. (1984).

In our approach to meteorological parameters retrievals from the satellites of the TIROS-N series, the matrix X has as many rows as channels used in the inversion process. Its number of columns is determined by the altitude range for which the temperature is retrieved : here, from the lowest "4A" stratification level, up to approximately 10 mb. It is easily shown that a matrix element of X, for channel ν_i and layer l_j, may be written as (see for example Susskind et al. 1980) :

$$X(\nu_i,l_j) = \left(\frac{T_{\nu_i}}{T(P_j)}\right)^2 \exp\left(a\omega_i\left(\frac{1}{T(P_j)} - \frac{1}{T_{\nu_i}}\right)\right) \left(\frac{\exp\left(\frac{a\omega_i}{T_{\nu_i}}\right)-1}{\exp\left(\frac{a\omega_i}{T(P_j)}\right)-1}\right)^2 \frac{\delta\tau}{\delta\ \ln P}$$

where a=hc/k, $T(P_j)$ is the temperature of the layer, T_{ν_i} the brightness temperature of channel ν_i and the last factor is the derivative of transmittance τ with respect to lnP at the pressure P_j of layer l_j. The brightness temperature T_{ν_i} of channel ν_i which transmittance to the ground τ_{ν_i} is supposed not to be zero, is also affected by a variation of the surface temperature, T_G. the partial derivative of T_{ν_i} with respect to T_G is obtained by replacing, in the above equation, $T(P_j)$ by T_G and the last factor by τ_{ν_i}. This new expression is used to correct the channels involved in the inversion process for eventual deviations between the true surface temperature and that associated with the initial guess solution. Since no very transparent channels are used, a high accuracy of the retrieved surface temperature is not necessary. For "clear boxes", the surface temperature is obtained from channels HIRS n° 8, 18 and 19 observations. For night time passes, the three channels, corrected for atmospheric attenuation, are used ; for day time passes, only channel 8 is used. For "not-clear" boxes, no corrections are brought to the surface temperature of the initial guess.

4. APPLICATION OF THE "3I" PROCEDURE TO ALPEX - THE 4-5 MARCH 82 INTENSIVE OBSERVING PERIOD

We have applied the "3I" procedure described in the preceding sections to the ALPEX (Alpine Experiment) IOP of March 4-5 1982. Satellite data have been prepared by NOAA/NESDIS Development Laboratory, Madison, USA. They represent 4 satellite passes : March 4, 2 orbits (at 12h00 and 13h45) ; March 5, 2 orbits (at 2h00 and 3h45).

4.a Preliminary evaluation of the "3I" temperature retrieval accuracy by comparison with radiosoundings measurements

For the period considered, a preliminary assessment of the quality of the "3I" procedure can be made by comparing retrievals to the available radiosounding measurements. These data were obtained from ECMWF. A total of 171 radiosondes collocated to approximately 100 km in space and 3 h in time were used for this comparison. Cloud tests performed on the 100 x 100 km^2 boxes resulted in 66 boxes declared "clear" and 105 declared "not-clear". A total of 81 % of the retrievals collocated with the radiosondes were declared acceptable, 77 % of the clear cases and 84 % of the not-clear cases. Rejections are made on the basis of an automatic procedure evaluating the quality of the initial guess and its distance to the observations.

Results of this comparison between radiosondes and retrievals are illustrated on Fig. 2. On this figure, we have used the standard levels stratification instead of that of the "4A" model for the sake of simplicity in comparing with other algorithms. One of the most salient features of this figure is the good quality of the retrievals in the lower part of the troposphere (500-1000 mb). The agreement is significantly better than what has been recently published in the literature (see Gruber and Waktins, 1982, for example). If we consider the lowest layer, 1000-850 mb, we obtain a RMS value of 1.6 K for the clear case (instead of "usual" values varying from 2.5 to 3 K) and of 1.9 K for the not-clear case (instead of values varying from 3.5 to more than 4 K). The present results must however be taken as very preliminary indications since the samples (51 for the clear case and 88 for the not-clear case) are obviously too small. They are certainly encouraging and may be tentatively explained as follows : a) a good proximity of the initial solution to the final solution ; b) a good elimination of the influence of the clouds by the "Ψ-method" ; c) the fact that surface pressures, emissivities are correctly taken into account jointly with the viewing angle ; d) the high stability and convergence of the inversion algorithm used, which only requires one iteration to get the final solution ; e) the impact of forecast temperature values at 1000 mb or 850 mb, or 700 mb, according to surface pressure, which help in the retrieval of the initial guess.

4.b Results for the four satellite passes of the ALPEX IOP of March 4-5, 1982.

These results have been obtained using the method described above : retrieval of the initial solution in the TIGR data set ; inversion of the radiative transfer equation ; rejection of "bad" retrievals. Table 1 gives, for each pass, the maximum number of possible retirevals with the spatial resolution of the "3I" procedure and the number of retrievals rejected. One full retrieval cycle requires 0.10 seconds with the NAS-9080 computer of the CIRCE (Centre Inter-Régional de Calcul Electronique du CNRS).

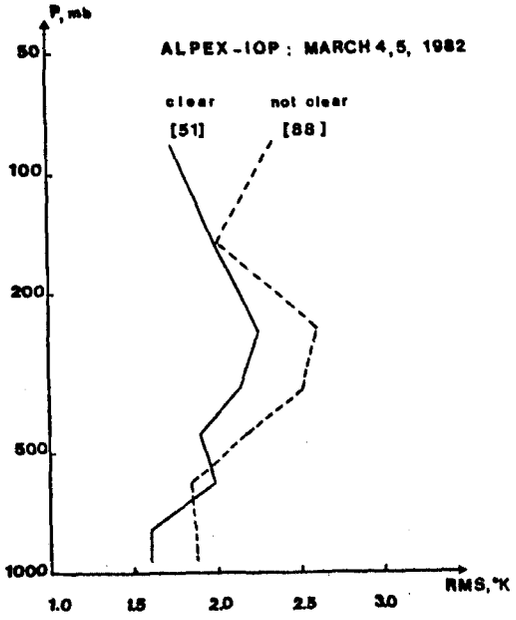

Figure 2
RMS error of retrieved mean layer temperature (standard levels) compared to collocated radiosonde for the ALPEX IOP, March 4-5, 1982. Dashed curve : not-clear boxes ; solid curve : clear boxes.

The numbers in Table 1 are remarkably small in consideration of the numerous heavily cloudy areas encountered during the ALPEX IOP of March 4-5. Both these small numbers of rejections and the over sampling in the boxes along the satellite track produce retrievals with a high spatial density.

Orbit n°	Maximum number of retrievals	Effective number of retrievals	Rejected %
3586	1240	1083	13
3587	1217	1007	17
3594	1184	1111	6
3595	1190	948	20

Table 1
Number of retrievals, orbit by orbit

One example of the results obtained is presented on Figure 3. Comparisons between conventional analysis chart and the results of the "3I" procedure show a good agreement. More details are given in Chedin et al. (1984).

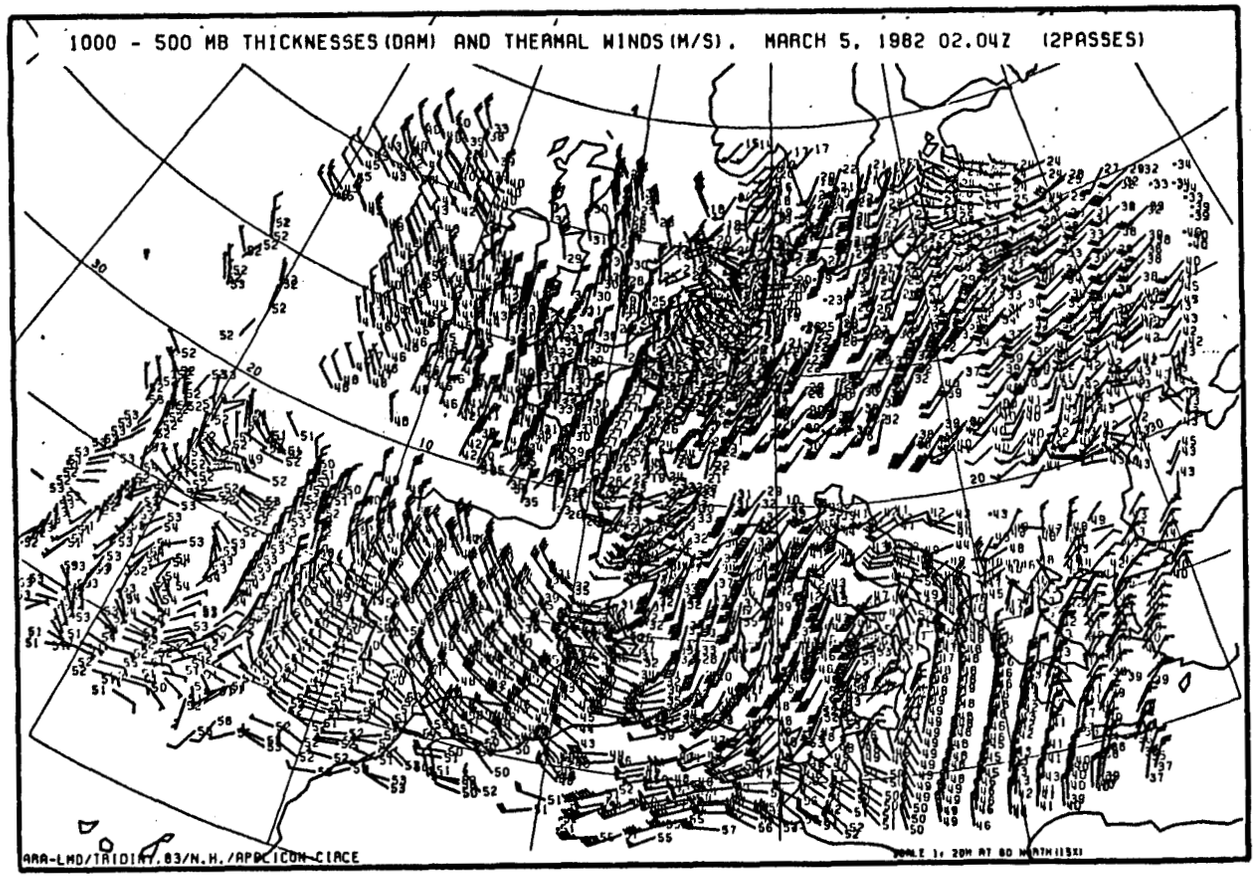

Fig. 3 Thermal winds and thicknesses between 1000 and 500 mb for the two night-passes - orbits 3594 and 3595 - of March 5th, 1982. Areas where data are missing are either regions where the calibration of the radiometer occured or regions where the rejection tests have a significant impact. Winds are in m/s. ; thicknesses are in dam minus 500.

5. PERSPECTIVES AND CONCLUSION

The key feature of the "3I" method is to supply accurate values of the atmospheric temperatures or thicknesses after only one iteration (one inversion) with a relatively high spatial density. The quality of the initial guess solution, retrieved by comparing the observations to similar synthetic data, pre-computed for a large set of atmospheric situations, together with the use of forecast values for the temperature at the lowest level, explains this rapid convergence. It must be pointed out that, in the present approach, forecasts are used solely to improve surface pressure determinations and to help in the retrieval of the initial guess solution. From a good estimation of the atmospheric temperature structure, other geophysical parameters may be obtained and the "3I" method now currently supplies cloud parameters like the cloud top pressure and the percentage of cloud cover, surface parameters like the temperature and the microwave emissivity and profiles of atmospheric water vapor.

References

Chedin,A., N.A.Scott, C.Wahiche and P.Moulinier, 1984 : The Improved Initialization Inversion method : a high resolution physical method for temperature retrievals from the satellites of the TIROS-N series. Submitted to J. Atmos. Sci.

Fleming, H.E., and M.L. Hill, 1982. J. Geophys. Res., 87, 7312-7324.

Gruber, A., and C.D. Watkins, 1982. Mon. Wea. Rev., 110, 867-876.

Hillger, D.W., and T.H. Vonder Haar, 1981. Mon. Wea. Rev., 109, 1788-1806.

McMillin, L.M., and C. Dean, 1982. J. Appl. Meteor., 12, 1005-1014.

Scott, N.A., and A. Chedin, 1981. J. Appl. Meteor. 20, 802-812.

Scott, N.A., A. Chedin, E. Devedeux, C. Wahiche, N. Husson, P. Moulinier and I. Cohen-Hallaleh, 1984. 1984 : Validation of a fast line-by-line transmittance and radiance algorithm against observations from the satellites of the TIROS-N series. In preparation.

Smith, W.L., 1968. Mon. Wea. Rev., 96, 387-396.

Susskind, J., and R. Rosenberg, 1980 : Remote Sensing of Atmospheres and Oceans, Academic Press. pp. 45-64.

Wahiche, C., 1983 : Internal Report LMD n° 122.

B.3

IMPROVED VERTICAL SOUNDINGS FROM AN AMALGAMATION OF POLAR AND GEOSTATIONARY RADIANCE OBSERVATIONS

William L. Smith and Harold M. Woolf
NOAA/NESDIS Development Laboratory
1225 West Dayton Street, 2nd Floor
Madison, Wisconsin 53706

1. INTRODUCTION

The VISSR Atmospheric Sounder (VAS) on the current operational geostationary satellites is capable of sounding the atmosphere's temperature and water vapor distribution with either 14 km or 7 km horizontal resolution. However, the instrument operates in the infrared (Table 1) and therefore soundings to the ground cannot be achieved in cloud overcast situations. On the other hand, the TIROS Operational Vertical Sounder (TOVS) on the current polar orbiting satellites operates in the microwave as well as in the infrared (Table 1) and is therefore capable of sounding through most cloud overcasts.

TABLE 1

CHARACTERISTICS OF VAS AND TOVS (HIRS AND MSU) SOUNDING CHANNELS

VAS channel number	Channel central wavenumber	Principal absorbing constituents	Level of peak energy contribution
1	679	CO_2	60
2	691	CO_2	100
3	702	CO_2	400
4	714	CO_2	600
5	751	CO_2	950
6	2214	CO_2	900
7	789	H_2O	surface
8	889	window	surface
9	1379	H_2O	600
10	1486	H_2O	400
11	2254	CO_2	500
12	2538	window	surface
HIRS channel number	**Channel central wavenumber**	**Principal absorbing constituents**	**Level of peak energy contribution**
1	668	CO_2	30 mb
2	679	CO_2	60 mb
3	691	CO_2	100 mb
4	704	CO_2	400 mb
5	716	CO_2	600 mb
6	732	CO_2/H_2O	800 mb
7	748	CO_2/H_2O	900 mb
8	898	window	surface
9	1028	O_2	25 mb
10	1217	H_2O	900 mb
11	1364	H_2O	700 mb
12	1484	H_2O	500 mb
13	2190	N_2O	1000 mb
14	2213	N_2O	950 mb
15	2240	CO_2/N_2O	700 mb
16	2276	CO_2/N_2O	400 mb
17	2361	CO_2	5 mb
18	2512	window	surface
19	2671	window	surface
20	14367	window	cloud
MSU channel number	**Frequency (GHz)**	**Principal absorbing constituents**	**Level of peak energy contribution**
1	50.31	window	surface
2	53.73	O_2	700 mb
3	54.96	O_2	300 mb
4	57.95	O_2	90 mb

For synoptic scale analysis/forecast applications, TOVS alone provides the necessary initial data. However, for subsynoptic scale applications, the six or twelve hour sampling interval of one or two polar orbiting satellites is too long; the higher frequency soundings (e.g., one to two hour) over certain geographical regions (e.g., North America) achievable from the geostationary satellites are required. Because of gaps in geostationary sounding coverage produced by extended cloud, it is desirable to utilize the less frequently sampled TOVS information, particularly the microwave radiances, together with the VAS sounding radiances for deducing atmospheric profiles down to the earth's surface across extended cloud areas. The importance of microwave sounding data in cloudy regions is exemplified in Figure 1 which shows the locations of reliable soundings to the ground achieved from VAS and TOVS radiance observations at 1600 GMT on 26 April 1982 over the southeastern United States. The locations are superimposed on a visible cloud image obtained within the hour of the sounding observations.

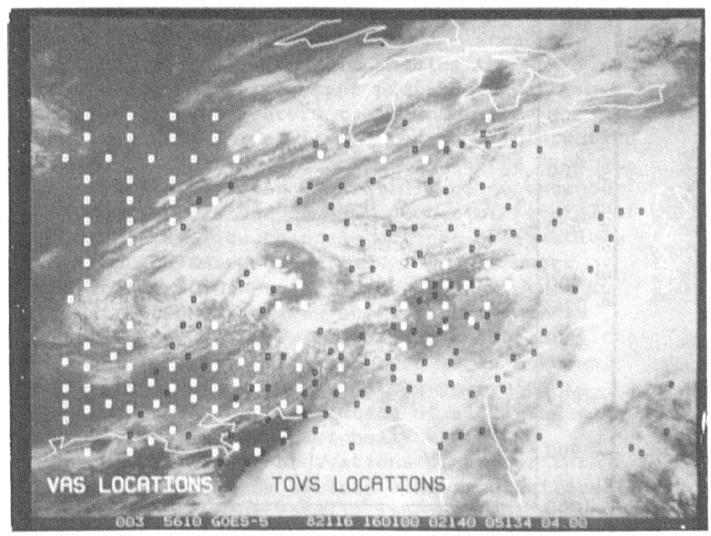

Figure 1: Locations of reliable 75 km resolution soundings from VAS and TOVS at 1600 GMT on 26 April 1982. White circles indicate VAS sounding locations and black circles indicate the TOVS sounding locations.

Finally, since the combination of VAS and TOVS provides many more radiances for the retrieval of atmospheric profiles than is provided by either system alone, improved sounding performance is expected.

In this paper the expected accuracy of sounding retrievals achieved from combined VAS

and TOVS radiance observations is compared to that achieved by each system alone. A new physical matrix inverse retrieval algorithm is formulated for retrieving simultaneously the temperature and water vapor profile from VAS and/or TOVS sounding radiances. The case study results achieved from the application of the new retrieval algorithm to actual radiance observations from VAS and TOVS are to be presented at the conference.

2. EXPECTED PERFORMANCE

The performance expected from a combined VAS-TOVS sounding system was estimated using multiple linear regression analysis of radiances simulated from a large statistical sample of radiosondes. Three latitude zones were considered (polar, mid-latitude, and tropical) with 300 soundings being used to formulate the dependent set from which regression equations are derived and 100 soundings being used as the independent set for testing the regression relations. For this performance analysis clear sky conditions and nominal instrument noise were assumed for simulating the VAS and TOVS sounding radiances. Furthermore, a spatial resolution of 75 km was assumed so that a spatial sample of 25 VAS, 9 HIRS, and 1 MSU fields of view were assumed to be associated with each sounding, thereby reducing the nominal instrument noise by the square-root of the number of fields of view available.

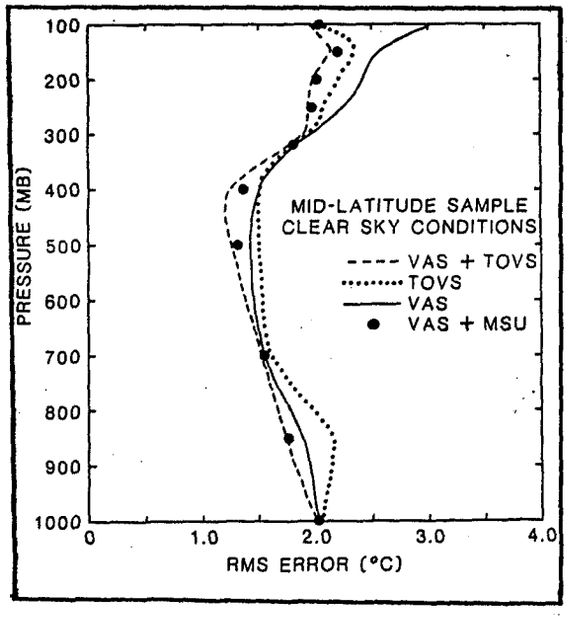

Figure 2: Accuracy of statistical regression retrievals of atmospheric temperature for various instrument configurations. The results shown are for the mandatory pressure levels only.

Figure 2 shows the performance at mandatory pressure levels for mid-latitude conditions. (The polar and tropical zone results are similar.) The combined set of VAS and TOVS radiances provides greater accuracy than either system alone, particularly in the lower troposphere (e.g., near 850 mb) and in the upper troposphere (300-100 mb). It is interesting to note that for these clear sky conditions VAS contributes more than TOVS to the accuracy of the lower tropospheric temperatures (1000-700 mb layer) because of the higher signal-to-noise ratio of average radiances achieved for a 75 km sounding area. In the mid-troposphere (700-300 mb), VAS and TOVS performance is similar while in the upper troposphere (300-100 mb) TOVS is superior to VAS because of the sharper vertical resolution in this region provided by the monochromatic microwave observations. Thus the VAS and the Microwave Sounding Unit (MSU) portion of the TOVS provide highly complementary observations. As can be seen from Figure 2, VAS and MSU provide a system that yields a performance almost equal to that of the entire VAS-TOVS combination. This result was expected because of the similarity between VAS and TOVS infrared channels (Table 1). It should be remembered that the major enhancement of sounding retrieval accuracy by MSU observations is expected to be in cloud covered regions where VAS sounding information is restricted to the atmosphere above the cloud.

3. RETRIEVAL PROCEDURES

A recently developed (by the authors) "one step" simultaneous temperature/water vapor profile retrieval method will be used to calculate soundings from the VAS and/or TOVS radiances used for this study. As can be easily shown, the radiative transfer equation is expressible in the perturbation form:

$$\delta T^* = \int_0^{P_S} \delta U \left[\frac{\partial T}{\partial p}\frac{\partial \tau}{\partial U}\frac{(\partial B/\partial T)}{(\partial B/\partial T^*)}\right] dp - \int_0^{P_S} \delta T \left[\frac{\partial \tau}{\partial p}\frac{(\partial B/\partial T)}{(\partial B/\partial T^*)}\right] dp + \delta T_S \left[\frac{(\partial B/\partial T_S)}{(\partial B/\partial T^*)}\right] \tau_s \qquad (1)$$

where T^* is brightness temperature, U is precipitable water vapor, B is Planck radiance, T is temperature, T_S is surface-skin temperature, τ is transmittance, and p is pressure. The perturbation, δ, is with respect to an <u>a priori</u> estimated or mean condition. The pressure dependence of all integrand variables is to be understood. In order to solve (1) for δU, δT, and δT_S from a set of spectrally independent radiance observations, we make the following profile representations in terms of arbitrary pressure functions, $\phi(p)$:

$$\delta q(p) = g \sum_{i=1}^{N} \alpha_i q_0(p) \phi_i(p) \qquad (2a)$$

$$\delta T(p) = - \sum_{i=N+1}^{N} \alpha_i \phi_i(p) \qquad (2b)$$

where q(p) is the water vapor mixing ratio and g is gravity. The zero subscript indicates the <u>a priori</u> condition. Equation 2a implies from the gas law and hydrostatic equation that

$$\delta U(p) = \sum_{i=1}^{N} \alpha_i \int_0^{P} q_0(p) \phi_i(p) dp \ . \qquad (2c)$$

Substituting representations (2b) and (2c) into (2) and letting $\alpha_0=\delta T_S$ yields for each spectral radiance observation, δT_j^*, for a set of K spectral channels:

$$\delta T_j^* = \sum_{i=0}^{M} \alpha_i \Phi_{ij} \qquad j=1,2,\ldots,K \tag{3}$$

where

$$\Phi_{0,j} = \frac{\partial B_j/\partial T_S}{\partial B_j/\partial T_j^*}\,\tau_{S,j}$$

$$\Phi_{i,j} = \int_0^{P_S}\left[\int_0^{P} q_0\phi_i dp\right]\left[\frac{\partial T}{\partial p}\frac{\partial \tau_j}{\partial U}\frac{\partial B_j/\partial T}{\partial B_j/\partial T_j^*}\right]dp \quad i\leq N \tag{4}$$

$$\Phi_{i,j} = \int_0^{P_S}\phi_i\left[\frac{\partial \tau_j}{\partial p}\frac{\partial B_j/\partial T}{\partial B_j/\partial T_j^*}\right]dp \qquad N<i\leq M\ .$$

The $\Phi_{i,j}$ quantities are calculated from the a priori estimated or mean profile conditions. Written in matrix form

$$t^* = \Phi\alpha \tag{5}$$

where t^* is a row vector of K radiance observations, α is a row vector of M+1 coefficients, and Φ is a matrix having dimensions (K×M+1). Assuming that K>M+1, then the least squares solution of (5) is employed to give stability to the solution, so that

$$\alpha = (\Phi^T\Phi)^{-1}\,\Phi^T t^* \tag{6}$$

where $(\ )^T$ indicates matrix transposition and $(\ )^{-1}$ indicates matrix inverse. Once the α_i's are determined, δT_S, δq, and δT are specified from (2) and added to the a priori estimates to yield the final solutions for surface-skin temperature and the water vapor mixing ratio and temperature profiles.

3.1. Choice of Basis Functions

The choice of pressure functions $\phi(p)$ is arbitrary, although the accuracy of the solution will ultimate depend upon them. For example, empirical orthogonal functions (i.e., eigenvectors of the water vapor and temperature profile covariance matrices) can be used. In this study natural functions, the profile weighting functions ($d\tau/d\ln p$) of the radiative transfer equation, are to be used. One of the temperature and water vapor functions is for $\phi_i(p)=1$ in order to account for any vertically constant displacement between the true and a priori profiles.

3.2. Incorporating Ancillary Data

Ancillary information such as surface observations can be easily incorporated into the profile solutions. For example for surface observations it follows from (2) that

$$q(p_S) - q_0(p_S) = g\sum_{i=1}^{N}\alpha_i q_0(p_S)\phi_i(p_S)$$

and

$$T(p_S) - T_0(p_S) = -\sum_{i=N+1}^{M}\alpha_i\phi_i(p_s)$$

have the same form as (3) and therefore can be added to the set to yield K+2 equations to solve for M+1 unknowns (α).

3.3. Accounting for Observational Errors

Observational errors are accounted for in the solution by dividing both t^* and Φ by the expected errors for each radiance (or surface) observation. The result is an inverse error weighted least squares solution for α where the more accurate observations receive the greater weights in the determinations.

Furthermore, the matrix inverse is stabilized by adding a small diagonal element to $\Phi^T\Phi$ prior to inversion. That is, the matrix to be inverted in (6) is

$$\Phi^T\Phi + \gamma I$$

where γ is a scalar (nominally 0.1) and I is the identity matrix.

3.4. Handling the Influences of Clouds

To be discussed at the conference.

3.5. Advantages of "One Step" Procedure

The main advantage of the "one step" retrieval method is that it enables the temperature and water vapor profiles and the surface skin temperature to be determined simultaneously using all the radiance information available. This solution alleviates the problem associated with water vapor radiance dependence upon temperature and the dependence of several of the carbon dioxide channel radiance observations used for temperature profiling, on the water vapor concentration. The dependence of the radiance observations on surface emissions is accounted for in the simultaneous solution by the inclusion of surface temperature as an unknown. Also, since only a single matrix inversion is required for the specification of all parameters, the solution is computationally efficient. Finally, ancillary observations of temperature and/or moisture from surface sensors or aircraft, for example, can be readily incorporated in the solution.

3.6 Simulation Test of "One Step" Method

The "one step" retrieval method was applied to the VAS data synthesized for the independent sample of radiosonde/radiance sets described in section 2. The temperature and water vapor profile basis functions were taken as the weighting functions for carbon dioxide channels 2 through 5 and water vapor channels 7, 9, and 10, respectively. All spectral VAS radiances with the exception of channels 11 and 12 together with surface temperature and mixing ratio were used for the retrieval thus providing a system of twelve equations and ten unknowns. The errors of surface air temperature and mixing ratio were assumed to be 1°C and 10%, respectively, for

these simulations. The statistical regression solution was used as the a priori estimate for the "one step" retrieval. Figure 3 shows that the "one step" retrieval provides a significant improvement of the profile accuracy achieved by multiple linear regression, particularly for the lower troposphere and for water vapor mixing ratio. These improvements are due to the interdependencies of the water vapor retrieval upon temperature and the influence of water vapor on temperature (carbon dioxide) sounding radiance observations which are accounted for in the "one step" method. (Low latitude results are not shown because of their similarity to those for mid-latitudes.)

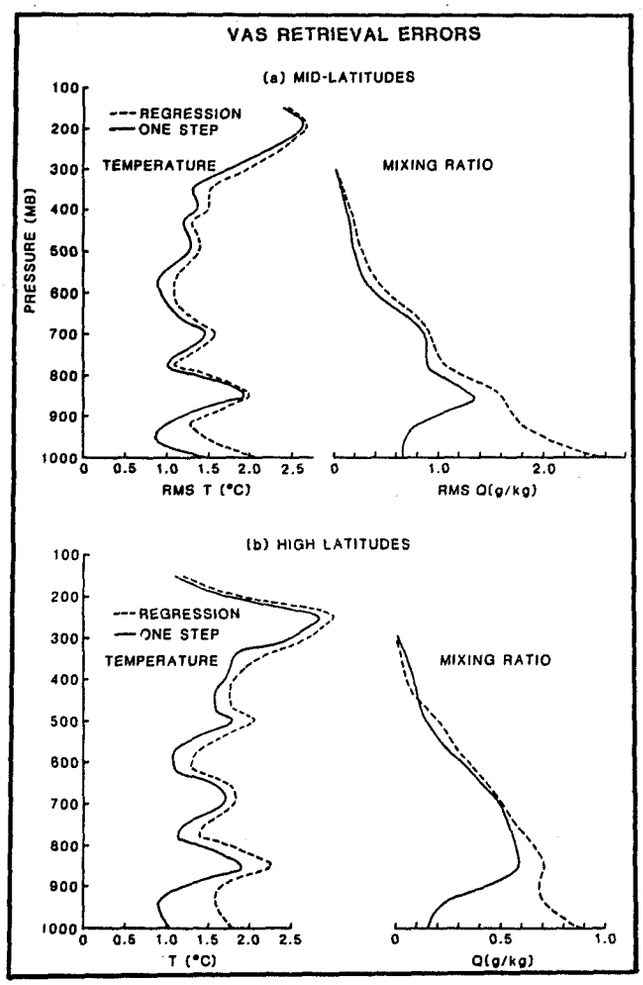

Figure 3: Comparison of retrieval accuracy using multiple linear regression and the "one step" matrix inverse methods. Results are presented for 20 levels between 100 and 1000 mb.

4. VAS/TOVS STUDIES

The "one step" retrieval algorithm is just now being tested as part of the National Environmental Satellite, Data, and Information Service/University of Wisconsin-Madison (UW-Madison) VAS and TOVS sounding retrieval systems. A special retrieval module has been constructed to enable soundings to be performed from the combination of coincident VAS and MSU radiance observations under all cloud conditions. This new retrieval system is to be used with daily VAS and TOVS observations obtained in real time at the UW-Madison. Performance evaluations will be made from the daily sounding products produced at the UW-Madison for (a) VAS-only and (b) VAS + MSU. Particular emphasis will be placed on those products which are being evaluated for their operational forecast utility as part of the NOAA Operational VAS Assessment (NOVA) program. Also, the influence of the retrievals on the analyses used to initialize mesoscale forecast models is being evaluated. A comparison between mesoscale numerical weather forecasts generated from (a) VAS alone and (b) VAS + MSU produced soundings will be presented at the conference.

THE CLOUDS AND VAS

Christopher M. Hayden
NOAA/NESDIS Development Laboratory
1225 West Dayton Street, 2nd Floor
Madison, Wisconsin 53706

W. Paul Menzel
NOAA/NESDIS Satellite Applications Laboratory
1225 West Dayton Street, 2nd Floor
Madison, Wisconsin 53706

Anthony J. Schreiner
Space Science and Engineering Center
University of Wisconsin
1225 West Dayton Street, 2nd Floor
Madison, Wisconsin 53706

1. INTRODUCTION

The VISSR Atmospheric Sounder (VAS) has been operating on the geostationary satellites, GOES 4-6 since September 1980. This instrument has the capability of measuring radiance in 12 infrared spectral channels which permits vertical temperature and moisture profile definition. Since the infrared measurements are highly susceptible to cloud attenuation, special care must be taken to avoid or correct for cloud interference. Techniques used in this process are essentially an extension of methods used with the polar orbiter instruments except that the absence of microwave measurements place a higher premium on a predetermined surface skin temperature. Partially offsetting this deficiency is the improved horizontal resolution of the VAS, which permits a greater probability of finding holes in the clouds.

Whereas the clouds are an impediment to the depiction of the atmosphere's temperature structure they are of benefit in determining the motion field. Cloud motion vectors have been determined from the geostationary satellites since the earliest ATS series (Hubert and Whitney, 1971) and are reputed to be very useful to numerical forecasting. Height assignment for these vectors has always been a problem (Bengtsson et al., 1982), but the multispectral capability of the VAS can reduce the uncertainty (Menzel et al., 1983).

In the following we shall describe the current techniques and results for both avoiding the cloud for temperature sounding and measuring the cloud height for wind derivation. A case study taken from a recent episode in the north Pacific is used to demonstrate and discuss method sensitivity and error sources.

2. CLEAR COLUMN RADIANCE DETERMINATION

It has been the policy of National Environmental Satellite, Data, and Information Service (NESDIS) operations and the Cooperative Institute for Meteorological Satellite Studies (CIMSS) to separate the task of determining clear column radiance values from the temperature retrieval problem. Our motivation is largely one of computer limitations; but there are also advantages in the production of clear radiance fields for editing and even for possible use in defining cloud heights as will be discussed in the next section. In obtaining clear column radiances there are two options: avoid the clouds or correct for them. Our approach has been to emphasize the former, and to employ the adjacent field of view (McMillin, 1978) technique for the latter. In all cases the problem is approached with a sample of measurements coming from 3 x 3 up to 11 x 11 fields of views (25 up to 90 km on a side) according to the desired final resolution of the temperature retrievals.

It should be emphasized that both our approaches are extremely dependent on ancillary knowledge of the surface skin temperature, since comparison of the window channel with this "a priori" information ultimately determines the cloud contamination. In the following we shall briefly discuss the methods and examine the effectiveness of the second option in enhancing the representation of the meteorology.

For an estimate of the surface skin temperature we rely on an objective analysis of the surface air temperature. This is not an ideal technique since the data coverage is frequently inadequate (especially over the ocean) and since the surface air is frequently not representative of the surface skin. It would be considerably better for an operator to make a subjective determination of "clear," using images of high resolution visible and infrared with a capability of looping several images in time. However, such a manpower intensive operation is not practical. The basic criterion used in comparing the VAS measurement with the surface analysis is:

- Reject any sample whose warmest 11 micrometer value is more than 10°C colder than the surface air temperature.

If the sample passes the initial test it will follow a "probably clear" filter path unless either of two additional tests send it to the adjacent field of view filter. These tests are:

- The variance of the 11 micrometer sample must be less than 9°C.

- The warmest value must be accompanied by measurements in all the channels.

2.1 Probably Clear Filter

The philosophy behind this filter is to collect the largest sample for each measurement accepting that the warmest measurement is indeed clear. Since the assumptions is certainly incorrect under some circumstances, it remains for the retrieval program or the post retrieval editing programs to catch the error. Their success in this area will be treated later. However, accepting that the warmest is "clear," samples are collected for cloud sensitive channels as shown in Table I. A minimum sample of five is required for retention, otherwise the program reroutes to the partly cloudy, adjacent field of view option.

TABLE I

"CLEAR" TOLERANCES FOR VAS CHANNELS MEASURED AGAINST THE WARMEST SAMPLE OF THE POPULATION. ANY VALUE COLDER THAN TOLERANCE ELIMINATES ALL CHANNELS LISTED. LEVEL 2 IS TESTED ONLY IF LEVEL 1 FAILS.

Channel Level 1	Channel Level 2	Frequency cm^{-1}	Tolerance K	Channels Eliminated
6		2214	1.0	6,12
	9	1380	(Temp. Chan 6-20.0)	9,10
8		890	2.0	5,6,7,8,12
	5	751	1.5	4,9
	4	715	1.0	3,10

2.2 Partly Cloudy Filter

The adjacent field of view technique for correcting for broken cloud is an extrapolation method as shown in Figure 1 where the line joining two cloud contaminated radiances is

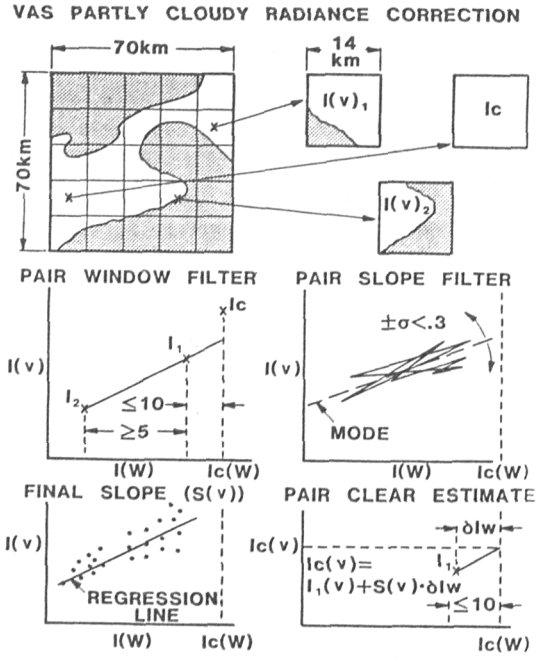

Figure 1: The adjacent field of view (NSTAR) filter. See text for details.

extended to give an estimate of the clear value. The degree of extrapolation is controlled by the value assigned to the clear window. This is a critical choice. One can use any "a priori" estimate of the surface skin temperature to assign it. In our applications, in order to be consistent with the "probably clear" filter, we have chosen to use the warmest measurement, rather than a manipulation of the surface air temperature analysis. The surface air temperature analysis is used as a filter, and the NSTAR correction is not attempted unless the clearest 11 micrometer measurement is within 3 degrees of the value expected from the surface temperature analysis.

The partly cloudy algorithm is not as complicated as a quick glance at Figure 1 would suggest. Note first that all fields of view are compared to each other (not just adjacent pairs) yielding a sample of Nx(N-1)/2 partly cloudy pairs where N is the number of observations. The suitability of each pair is tested in a number of ways:

- The warmest 11 micrometer value of a pair must be within 10 degrees of the warmest sample (to limit extrapolation).
- The colder of the pair must be at least 5 degrees colder than the warmer (to achieve a reasonable "slope" estimate).
- The slope formed by a pair must be within 0.3 of the modal slope (checked for two of the more transparent 15 micrometer channels). For all pairs that meet these restrictions a single slope is calculated by least squares, and a final clear sample is derived by extrapolating all the warmest values.

2.3 Example of Filters

Figure 3 gives an example of a) the radiances obtained from the "mostly clear" path, b) the "partly cloudy" path, and c) the residual

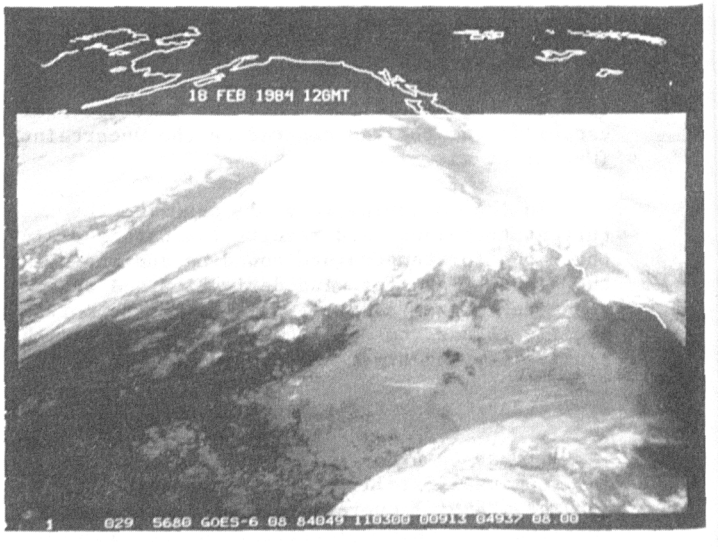

Figure 2: 11 micrometer window image of eastern Pacific, 18 February 1984.

remaining after retrieval and editing. In terms of quantity, the "partly cloudy" typically adds about 20% to the total radiance sample, but these

are somewhat noisier and more susceptible to later elimination. A net increase of 10% in the number of final retrievals is a rough average. Comparison with the 11 micrometer picture of the clouds (Figure 2) shows that the sample increase does indeed occur in the partly cloudy areas. Generally, however, the additional soundings occur around the edges of the large cloud systems.

Figure 3 shows that the rather forgiving "probably clear" criterion let through a considerable number of radiances which are later rejected during the temperature retrieval (based on channel to channel consistency). For this example about 17% of the mostly clear were subsequently filtered. Of the partly cloudy selections, almost 45% were eliminated.

The most important consideration in evaluating the cloud filters is whether the results capture the meteorology of the situation. There is no question that large cloud masses continue to be a problem. The partly cloudy filtering helps, but not dramatically. The greatest improvement we have observed with the VAS has come from processing with the small (8 km) as opposed to large (16 km) field of view, simply because of the increased probability of finding cloud free fields of view. Even with this "small detector," however, occasions of obtaining soundings within large cloud masses are infrequent, and the case shown in Figure 2 is typical.

3. MULTISPECTRAL CLOUD HEIGHT ASSIGNMENT

The assessment of cloud height and amount by infrared sounder retrieval methods has been considered by Chahine (1975), Smith and Platt (1978), Weilicki and Coakley (1981), and Menzel et al., (1983). There are two basic techniques, a "direct" method and a "ratio" method. In the "direct" method a candidate group of assumed effective cloud amounts and cloud pressures is used to calculate outgoing radiances in two or more channels from a presumed temperature moisture structure. These radiances are compared to observations in the same channels and by some minimization criteria the most probable cloud pressure and amount are selected. The "ratio" method is a form of the direct method for 2 channels. Its advantage is that by ratioing the channels the effective cloud amount can be separated from the solution for cloud pressure. Thus the cloud pressure can be found efficiently. For application in determining wind tracer pressure altitude, the ratio method is an obvious choice since cloud amount is of no significance.

The mathematical expression for the ratio technique is given by

$$\frac{I(\upsilon_1) - I_{CL}(\upsilon_1)}{I(\upsilon_2) - I_{CL}(\upsilon_2)} = \frac{E_1 \int_{P_s}^{P_c} \tau(\upsilon_1,p) \frac{dB(\upsilon_1,T(p))}{dp} dp}{E_2 \int_{P_s}^{P_c} \tau(\upsilon_2,p) \frac{dB(\upsilon_2,T(p))}{p} dp}$$

where υ_1 and υ_2 are spectral frequencies, τ the respective transmittance functions, and E the effective cloud amounts (assumed equal when the frequencies are chosen close together). I

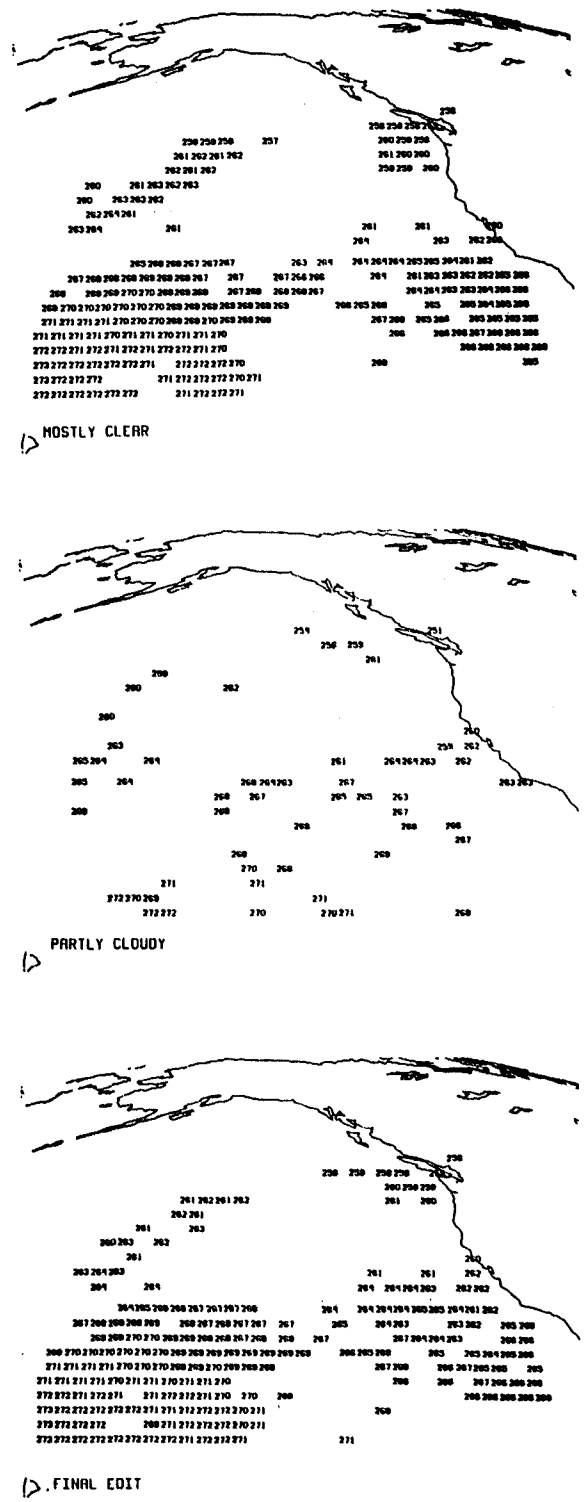

Figure 3: Top--radiance observations obtained as "mostly clear."
Middle--radiance observations obtained as "partly cloudy."
Bottom--final sample of clear column radiances.

represents the measured radiance whereas I_{CL} is the radiance which would be observed in the absence of cloud. In other words, both numerator

and denominator equate the observed cloud attenuation (on the left) with candidate calculated cloud attenuations obtained by varying the cloud pressure P_c in the integral limits (on the right). The lower limit, P_s is the pressure at the surface. As described by Weilicki and Coakley (loc. cit.) the ratio method is somewhat limited by the inherent lack of vertical resolution in the measurements. An example is shown in Figure 4 where the equation is recast in the form

$$R = \frac{A}{B},$$

or

$$RB = A$$

and each side is calculated for a single (midlatitude) atmosphere for the cloud pressures shown on the ordinate. The observed radiance is in this case simulated for a cloud at 320 mb, and the two channels correspond to an 11 micrometer window (RB) and a semitransparent 15 micrometer channel (A). As the cloud is (erroneously) assumed at higher or lower pressures, the two functions spread, but at a rather gentle rate. The shaded area is an approximation of the uncertainty associated with actual measurement and it is of the order of 30-40 mb.

With the VAS, 3 CO_2 channels are used to attempt 2 ratio estimates of cloud pressure. For both, the residuals ($I-I_{CL}$) must exceed instrumental noise or the ratio is rejected. If both are rejected, the cloud height determination reverts to the "direct" method where an overcast is assumed and the 11.2 micrometer window is matched with the guess brightness temperature profile (Menzel et al., loc. cit.).

Since proof of concept has been established, recent application of the cloud height algorithm has been concerned with integrating the scheme

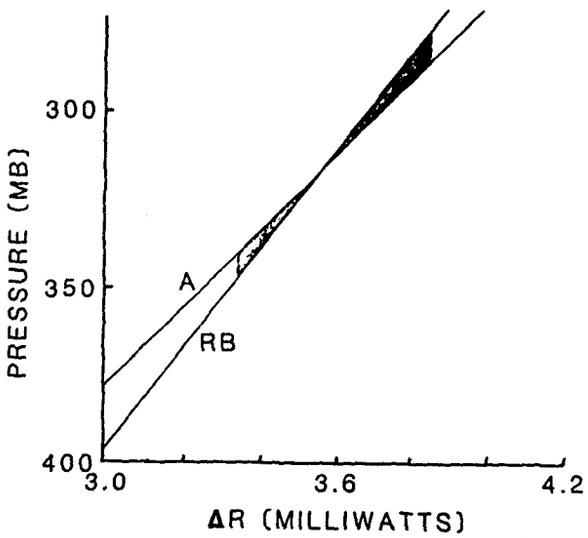

Figure 4: Sensitivity of the ratio method for determining cloud pressure. This example involves measurements at 750 and 890 wavenumber.

into routine VAS processing. To do this within the limitations of the Man-computer Interactive Data Access System (McIDAS), it has been necessary to dissociate the cloud height algorithm from the wind derivation procedure. This is accomplished by preparing a data set of cloud heights which can be plotted over the infrared (visible) images used to derive wind vectors. An example is shown as Figure 5. The operator assigns the pressure altitude of the wind vector from his interpretation of the plotted values. The figure separates the cloud assignments according to the choice made by the algorithm. The top shows results defaulting to the direct method. It is apparent that the ratio method is more successful in thicker, higher cloud where the attenuation is well in excess of probable measurement noise. Note further, however, that there is reasonably good correspondence between cloud pressures achieved by the different methods where both occur. There does appear to be a slight bias in that the direct estimates are systematically lower (higher pressure) than the ratio estimates. A true cloud emissivity of less than one would lead to this result.

Apart from the fundamental uncertainty of measurement accuracy as shown in Figure 4, there are other sources of error in practical

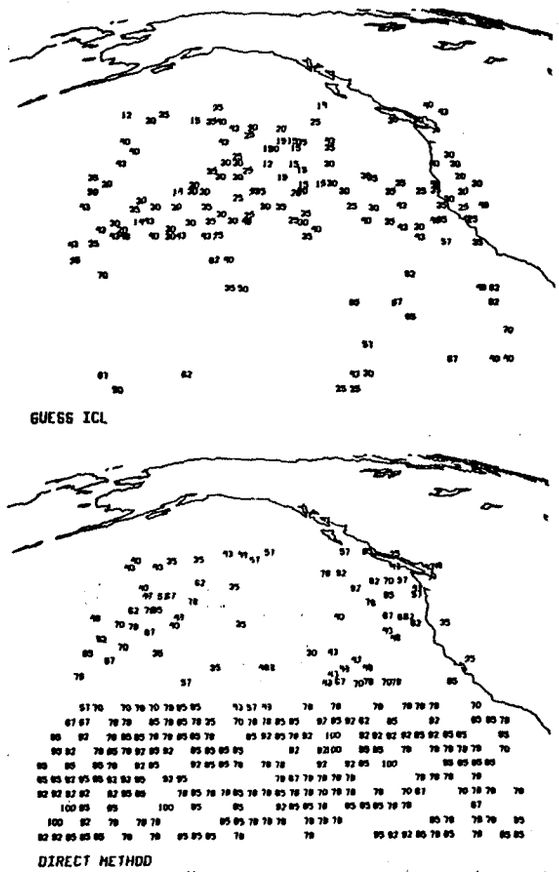

Figure 5: Cloud pressures derived for 18 February 1984. Top: cloud pressures achieved by the ratio technique. Bottom: cloud pressures defaulting to the "direct" method. NMC global temperature forecast used for calculating radiances.

application of the cloud height ratio algorithm. A major one is the determination of clear column radiance (I_{CL}). We have investigated two options for the estimation of this quantity: calculate the value by the radiative transfer equation from a temperature/moisture profile estimate; select the value from a gridpoint analysis of observed clear values. The error associated with the first choice is the accuracy of the temperature estimate at high levels, and the accuracy of the transmittance properties for each channel. The errors in the transmittance are potentially more serious, but in practice one maintains a running account of the bias error associated with each measurement and minimizes its effect. The accuracy of the temperature profile will vary with location and synoptic situation, but its effect is smoothed by the averaging properties of the radiative transfer integral. Also, since I_{CL} appears in both numerator and denominator of the ratio there is a tendency for the temperature profile error to compensate. The error involved in the second option of choosing I_{CL} is directly related to the accuracy of cloud filtering as discussed in the previous section. The major source of uncertainty is in large regions of dense cloud where sampling is difficult. Figure 6 is an example of the clear brightness temperatures obtained from the NMC global forecast valid at 1200 GMT for 18 February 1984 and from VAS observations made at approximately the same time. Note that there is a considerable discrepancy in the amount of detail portrayed. Some of the finer scale given by the measurements seems reasonable where there are supporting observations, but the trough ridge pattern in the heavy cloud is an invention of the analysis algorithm. The discrepancies in the analyses are carried over to the determination of cloud pressures as shown by comparing Figures 5 and 6, and a comparison of analyzed fields of cloud pressures from the two sources shows an rms difference of approximately 100 mb. The statistic is somewhat misleading inasmuch as the operator using the plotted values will subjectively smooth the discontinuities. However, the choice of a source for I_{CL} remains a significant source of uncertainty. It is perhaps worth noting that use of clear radiance fields approximately doubles the CPU effort to produce the cloud heights.

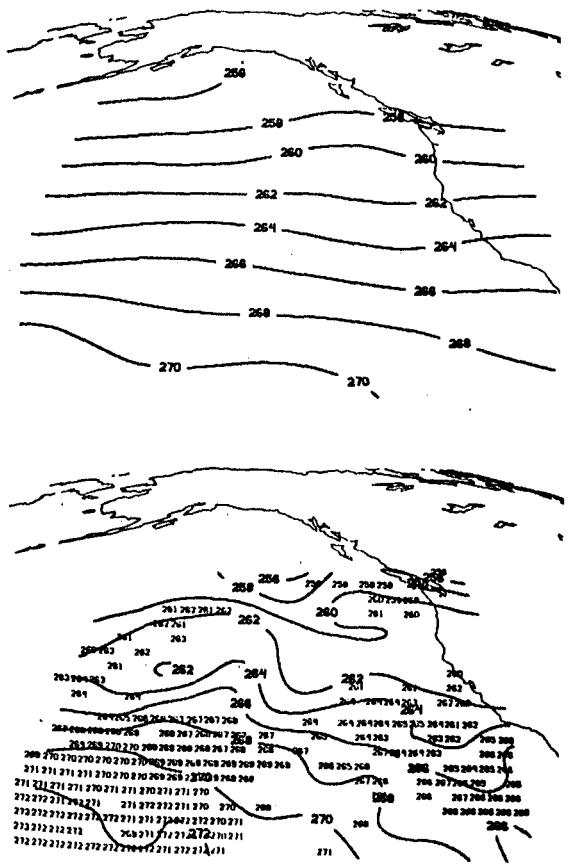

Figure 6: Clear T_b estimates for the VAS 750 wavenumber channel as obtained from an integration of the NMC global forecast (top) and from cloud filtering of observations.

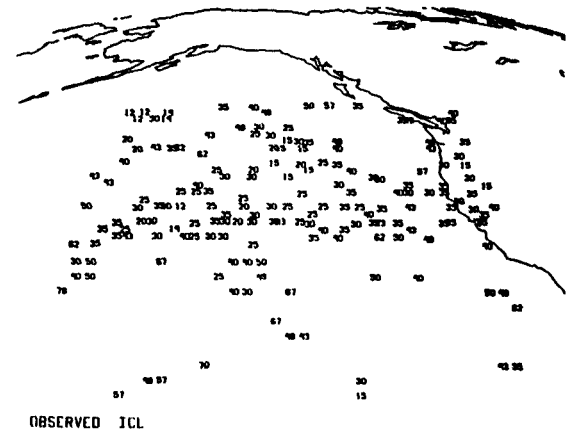

Figure 7: Cloud pressures derived from the ratio technique using analyses of observed clear column brightness temperatures.

4. SUMMARY

The foregoing has described the current status in dealing with the clouds seen by the VAS. We are reasonably satisfied with the methods for avoiding cloud contamination in the radiances used temperature retrieval. The higher horizontal resolution of the small detector array is especially valuable. We are somewhat less satisfied with the method of cloud pressure assignment, but the technique is limited by the vertical resolution of a radiometric measurement. It does not appear that much more can be done to avoid the cloud. One suggestion has been to sample frequently over a short interval so that the clouds will "move out of the way." However, for large cloud masses which cause most of the problem, the cloud stays in about the same place relative to the meteorological situation. Future work will concentrate on better amalgamation of the wind and temperature derivations since they are truly complementary, and there seems little further progress to be made in avoiding or correcting for the clouds.

5. REFERENCES

Bengtsson, L., M. Kanamitsu, P. Kallberg, and S. Uppala, 1982: FGGE 4-dimensional data assimilation at ECMWF. Bull. Amer. Meteor. Soc., 69, 29-43.

Chahine, M. T., 1975: An analytical transformation for remote sensing of clear column atmospheric temperature profiles. J. Atmos. Sci., 32, 1946-1952.

Hubert, L. F., and L. F. Whitney, Jr., 1971: Wind estimates from geostationary satellite pictures. Mon. Wea. Rev., 99, 665-672.

McMillin, L. M., 1978: An improved technique for obtaining clear radiances from cloud contaminated radiances. Mon. Wea. Rev., 11, 1590-1597.

Menzel, W. P., W. L. Smith, and T. R. Stewart, 1983: Improved cloud motion wind vector and altitude assignment using VAS. J. Clim. and Applied Meteor., 22, 377-384.

Smith, W. L., and C. M. R. Platt, 1978: Comparison of satellite-deduced cloud heights with indications from radiosonde and ground based laser measurements. J. Applied Meteor., 17, 1796-1802.

Weilicki, B. A., and J. A. Coakley, Jr., 1981: Cloud retrieval using infrared sounder data: error analysis. J. Applied Meteor., 20, 157-169.

PHYSICAL RETRIEVAL OF PRECIPITABLE WATER USING THE SPLIT WINDOW TECHNIQUE

Thomas J. Kleespies
Naval Environmental Prediction Research Facility
Monterey, California

Larry M. McMillin
National Environmental Satellite, Data, and Information Service
Washington, D. C.

1. INTRODUCTION

The split window technique (see McMillin, 1975) has been used to determine the radiance adjustment necessary to correct satellite measurements in atmospheric "windows" for atmospheric attenuation. Since the correction can be obtained and most of the absorption in the "windows" is due to moisture, it is natural to conclude that the procedure can be used to provide an estimate of total moisture. In fact, Chesters et al. (1983) have proposed one method for doing this by calculating the average air temperature from radiosondes and assuming the value is conserved between successive radiosonde launches. For channels dominated by gases with constant mixing ratios, this assumption becomes equivalent to assuming the air temperature above the surface changes slowly with time, which is not unreasonable. However, Chesters et al. apply the assumption to moisture channels and the average atmospheric temperature is a function of the moisture profile as well as the temperature profile. If this assumption is used in a technique to monitor a changing moisture pattern, there must be some concern about the effect of changing moisture on the value of average temperature which was used in its derivation. Although Chesters et al. had no alternative to this assumption, we present a method which avoids it.

Our method takes advantage of the fact that there are situations where over short distances or over short time intervals, different surface temperatures can be observed through effectively the the same atmosphere. For example, Figure 1 is a trace of the variation of 11 μm brightness temperature as observed by GOES West. In this case surface temperature increased by about 5 deg celsius/hour beginning shortly after sunrise at 6:15 local time. In situations such as these, the atmospheric transmittance can be determined and used to estimate moisture. The method also has application to retrievals of atmospheric temperature since an accurate determination of the atmospheric transmittance can be used to eliminate surface effects on radiance measurements (Hayden et al., 1981).

2. MATHEMATICAL FORMULATION

The radiance measured from a satellite can be written as

$$I = B_s\tau_s + \int_{\tau_s}^{1} B d\tau \qquad (1)$$

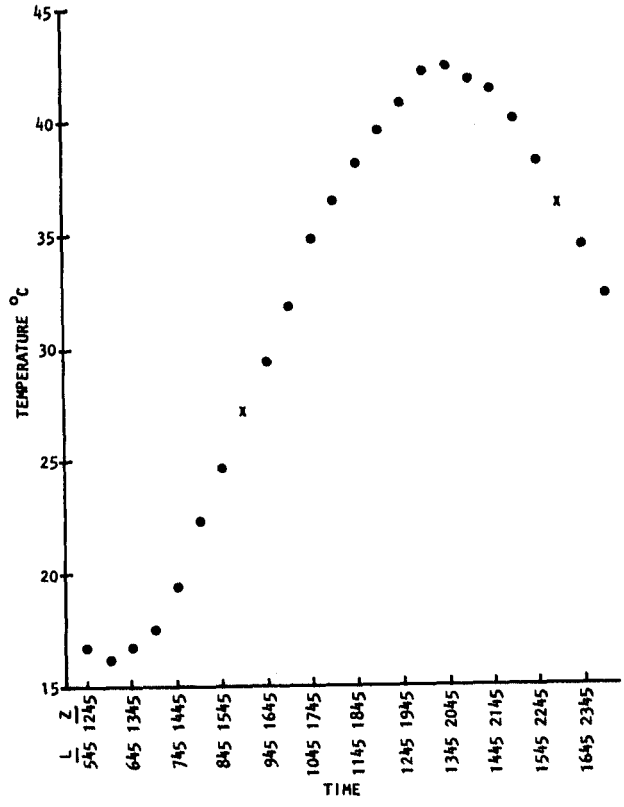

Fig. 1. Goes West 11 micrometer brightness temperature as a function of time on 17 Sep 1983. Average of 3x3 array of 7 km resolution elements, upper left corner at 36N, 120W, about 110 km NW of Bakersfield, CA.

where I is the radiance measured at the satellite, B_s is the Planck radiance at the surface, τ_s is the surface transmittance, and the integral is the radiance originating in the atmosphere. Using the mean value theorem, it is possible to write Eq. (1) as

$$I = B_s\tau_s + \bar{B}_a(1-\tau_s) \qquad (2)$$

where $\bar{B}_a$ is a weighted average given by

$$\bar{B}_a = \int_{\tau_s}^{1} B d\tau \Big/ \int_{\tau_s}^{1} d\tau \qquad (3)$$

To illustrate the effect, it is helpful to write Eq. (2) as

$$B_s - I = (B_s-\bar{B}_a)(1-\tau_s) \qquad (4)$$

In this form it is clear that the atmospheric attenuation is the product of a term related to temperature, $(B_s-\bar{B}_a)$, and a term related to moisture, $(1-\tau_s)$.

To develop the split window relation, Eq. (4) is converted to brightness temperature to eliminate the wavelength dependence, then written for two channels to give

$$T_s-T_1 = (T_s-\bar{T}_a)(1-\tau_1) \qquad (5)$$

$$T_s-T_2 = (T_s-\bar{T}_a)(1-\tau_2) \qquad (6)$$

where the T's are brightness temperatures and where the subscripts denote the channel. For appropriately selected window channels, the values of T_a are equal and Eqs. (5) and (6) can be solved for T_s to give

$$T_s = T_1 + (T_1-T_2)(1-\tau_1)/(\tau_1-\tau_2) \qquad (7)$$

For channels with similar absorbers and a relatively small total absorption, the quantity $(1-\tau_1)$ is proportional to the quantity $(1-\tau_2)$ and the ratio $(1-\tau_1)/(\tau_1-\tau_2)$ becomes a constant that is independent of the particular atmosphere. When these conditions hold, Eq. (7) can be written as

$$T_s = T_1 + (T_1 + T_2)\gamma \qquad (8)$$

where γ is a constant.

Given Eq. (8), it is possible to determine T_s and thus B_s in Eq. (2). If measurements are obtained over two different values of B_s with the air temperature being invariant, Eq. (2) can be used to give

$$\Delta I = \Delta B_s \tau_s \qquad (9)$$

where the Δ's denote the differences due to the different B_s. Eq. (9) is easily solved for τ_s to give

$$\tau_s = \Delta I/\Delta B_s \qquad (10)$$

Now if the two different surface temperatures are viewed by the two different channels, it is possible to arrive at estimates of τ for each of these channels given by

$$\tau_1 = \Delta I_1/\Delta B_{s1} \qquad \tau_2 = \Delta I_2/\ B_{s2} \qquad (11)$$

which after combining by division yields

$$\frac{\tau_1}{\tau_2} = \frac{\Delta I_1}{\Delta I_2}\ \frac{\Delta B_{s2}}{\Delta B_{s1}} \qquad (12)$$

If this equation is converted to brightness temperatures to eliminate temperature dependence, the B_s's become T_s's and cancel, and we are left with

$$\frac{\tau_1}{\tau_2} = \frac{\Delta T_1}{\Delta T_2} \qquad (13)$$

This expression states that the ratio of the transmittances of the two channels can be estimated by the ratio of the differences of observed brightness temperatures in those two channels, where the difference in brightness temperatures is due only to different surface temperatures. This ratio can be related to precipitable water (see Chesters et al., 1983).

3. SIMULATION OF TECHNIQUE

This technique was tested using simulated radiances for the Visible Infrared Spin Scan Radiometer (VISSR) Atmospheric Sounder (VAS). Radiosonde reports were collected over North America for 12Z 12 November 1981. The radiosondes were divided quasi-randomly into two sets, the dependent set having 55 observations and the independent set having 27 observations. Radiances were computed from each of the dependent radiosondes for the VAS channels 7 (12 μm) and 8 (11 μm). Transmittances were computed using algorithms described in Weinreb et. al. (1981). Total ozone was taken to be 357 D.U. The surface temperature was taken to be first the reported air temperature, then the reported air temperature plus 10 deg celsius. The ratio of the estimated transmittances for channels 7 and 8 was computed from Eq. (13) and compared with the actual ratio of transmittances for those channels. The comparison is given in Figure 2. The results were sufficiently

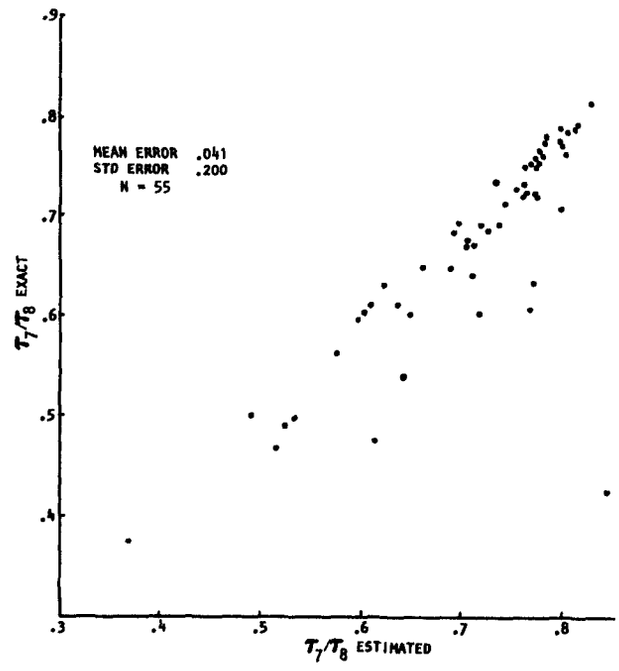

Fig. 2. Estimated ratios of transmittance versus observed for VAS radiances simulated from dependent radiosonde set.

consistent to encourage us to attempt to predict precipitable water from the ratio τ_7/τ_8 using simple linear regression. The regression equation was conditioned using the dependent set and tested on the independent set. The results are given in Figure 3. As can be seen the correspondence between estimated and observed precipitable water is quite good. However, the range of precipitable water in this sample is not large enough to perform a rigorous test. Such testing is intended in further work.

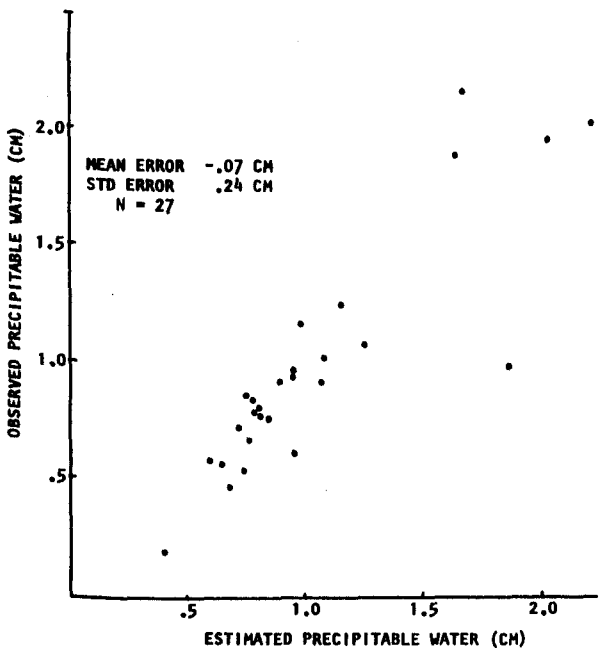

Fig. 3. Estimated precipitable water versus observed for independent radiosonde set.

4. CONCLUSIONS

A technique has been presented to estimate atmospheric transmittance from observations of split window radiances under conditions when the surface temperature changes substantially, but the atmospheric conditions are invariant. For the 11-12 μm region, atmospheric attenuation is caused primarily by precipitable water. Thus it is possible to estimate precipitable water from split window observations under conditions of varying surface temperature. Simulation of radiances for the VAS instrument indicate that this technique holds great promise for physical retrieval of precipitable water.

5. REFERENCES

Chesters, Dennis, Louis W. Uccellini and Wayne D. Robinson, 1983: Low-Level Water Vapor Fields from the VISSR Atmospheric Sounder (VAS) "Split Window" Channels. J. Clim. Appl. Met., Vol. 22, No. 5. pp 725-743.

Hayden, C.M., W.L. Smith and H.M. Woolf, 1981: Determination of Moisture from NOAA Polar Orbiting Satellite Sounding Radiances. J Appl. Met., Vol. 20, No. 4, pp 450-466.

McMillin, L.M., 1975: Estimation of Sea Surface Temperatures from Two Infrared Window Measurements with Different Absorption. J. Geo. Rsch., 79, pp 5039-5044.

Weinreb, M.P., H.E. Fleming, L.M. McMillin and A.C. Neuendorffer, 1981: Transmittances for the TIROS Operational Vertical Sounder, NOAA Technical Report NESS 85, 60pp.

B.6

A New Technique to Infer Convective Rainfall from Satellite Infrared Cloud Observations

Andrew J. Negri
and
Robert F. Adler

Goddard Laboratory for Atmospheric Sciences
NASA/Goddard Space Flight Center
Greenbelt, MD 20771

1. INTRODUCTION

There is presently a keen interest in rain estimation from satellites, as well as a need for high time resolution in the estimates. This time resolution implies the use of geosynchronous satellites, which contain only visible and infrared (IR) channels. As such, we must attempt to infer rainfall from cloud observations, and usually limit our inference to convective clouds. Previous work in objective rain estimation involved empiricism, such as the Griffith-Woodley technique (GWT),[Griffith et al., 1976, 1978, 1981, Woodley et al., 1980], or the GOES Precipitation Index (GPI) [Arkin, 1984].

This paper describes a new method of estimating convective precipitation from satellite infrared (IR) data, henceforth known as the GLAS-2 technique. The method locates (in an array of GOES digital IR data) all local minima in blackbody temperature (T_{bb}) lower than 253 K and assumes these are rain centers (similar to radar echoes). Rainrate and rain area are assigned to the minimum point as a function of minimum blackbody temperature (T_{min}). These T_{min}-rain relationships are derived using the approach of Adler and Mack (1984), which entails using a one-dimensional cloud model to account for ambient temperature, moisture, and shear conditions. This approach hopefully provides a stronger physical (and less empirical) basis for the applied cloud-rain relations, and allows for the transportability of the technique to various climatological regimes or synoptic situations.

The technique is first tested for south Florida cases during the Florida Area Cumulus Experiment (FACE) and verified against raingage and radar data. We hope to understand the limitations of the technique at the smallest time and space scales. This will in turn enable us to understand errors and biases in longer and larger scale estimates. We also compare the results of GLAS-2 to the GWT, to a modified (non-life history) simulation of the GWT denoted GLAS-1 (Negri, et al., 1984) and to a modified Arkin method. In this way we hope to quantify obvious limitations of the technique and establish a baseline against which to test future, more sophisticated approaches to rain estimation.

In section 2 we briefly describe the estimation techniques, presenting examples of rain images produced by each. We subsequently present statistical results for three days (section 3). Section 4 summarizes the limitations of satellite IR rain estimation in general and GLAS-2 in particular and outlines future versions of the GLAS scheme.

2. DESCRIPTION OF TECHNIQUES

2.1 Griffith-Woodley Technique

The GWT is a life-history dependent method that requires a sequence of IR imagery. Clouds are defined by outline of the 253 K isotherm. (See Griffith et al., 1976, 1978, 1980, 1981). A concise summary may be found in Negri et al. (1984). Half-hourly and daily totals for the FACE target region were taken from Meitin et al. (1981).

2.2 GLAS-1

GLAS-1 is a simplification to the GWT described by Negri et al. (1984). The analysis area of GLAS-1 is the same as that used in the GWT: an 8° by 12° region centered on 27^oN, 81^oW. Clouds are defined in the IR data by the 253 K isotherm and for each cloud two temperature thresholds are calculated. These are $T_{10\%}$ and $T_{50\%}$, the temperatures that define the coldest 10% and coldest 50% cloud area respectively. Integer rainrates are then assigned to the pixels of each cloud according to pixel temperature T:

8 mm h^{-1}	$(T < T_{10\%})$
2 mm h^{-1}	$(T_{10\%} < T < T_{50\%})$
0	$(T > T_{50\%})$

A minimum cloud area of 2000 km^2 is proscribed, below which no rain estimates are made for that cloud. The non-life history GLAS-1 simulated to first order the GWT rainmaps on three test days (Negri et al., 1984.) An example of a rainrate estimate for 1930 GMT 29 July 1978 is shown in Fig. 1a.

2.3 Modified Arkin scheme

Arkin (1979) and Richards and Arkin (1981) have examined the relationship between 6 h rain accumulation and the fractional coverage of 2.5^o by 2.5^o squares by clouds of varying temperature for the GATE region. This has led to the creation of a GOES Precipitation Index (GPI) [Arkin, 1984]. In this study, a modification is made such that the Arkin rainrate (3 mm h^{-1}) is applied to any IR pixel (4 km by 8 km) colder that the Arkin threshold (235K). An example is shown in Fig. 1b.

2.4 GLAS-2

The location of convective "cells" is done objectively in GLAS-2 by isolating pixels (or clusters of pixels) in the IR data colder than all

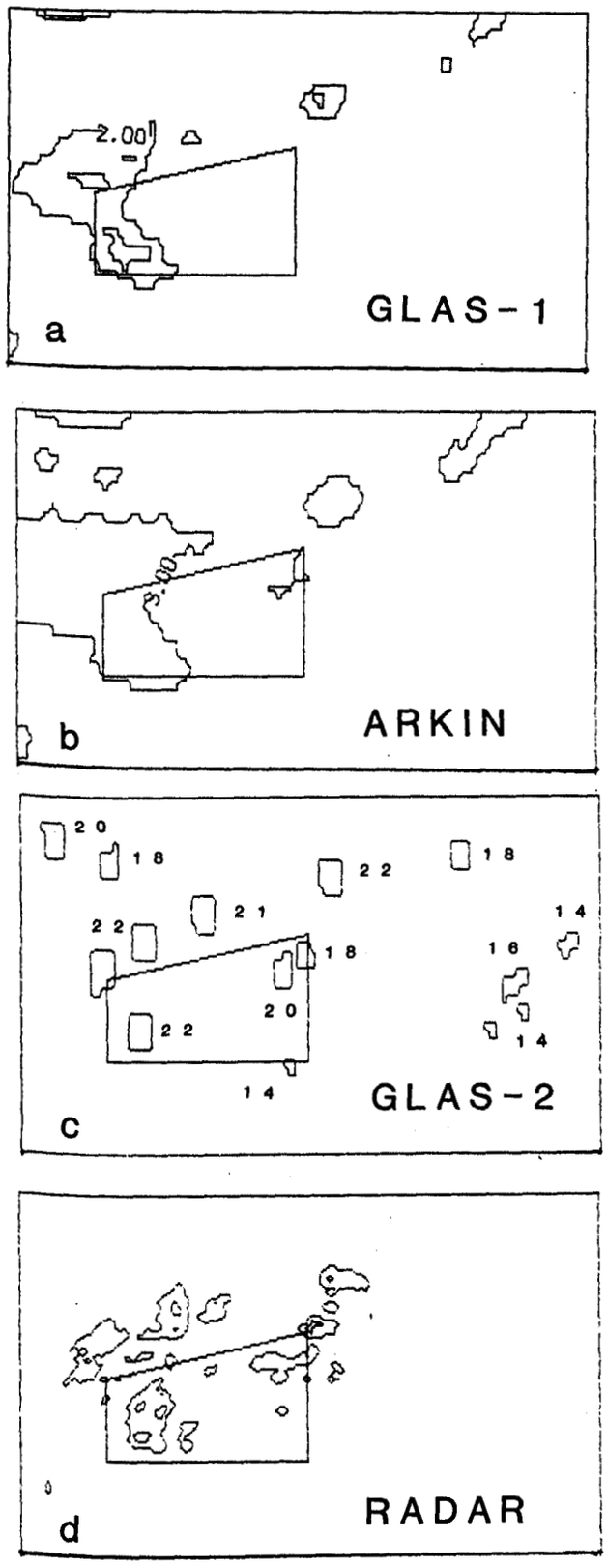

Figure 1. Estimates of rainrate at 1930 GMT 29 July 1978 in the vicinity of the FACE target region. a) GLAS-1 technique. Contours are 2 and 8 mm h^{-1}. b) Modified Arkin technique. Contours are 3 mm h^{-1}. c) GLAS-2 technique. Contours are labelled. d) Radar (WSR-57) at Miami using $Z=300R^{1.4}$. contours are 1 and 20 mm h^{-1}.

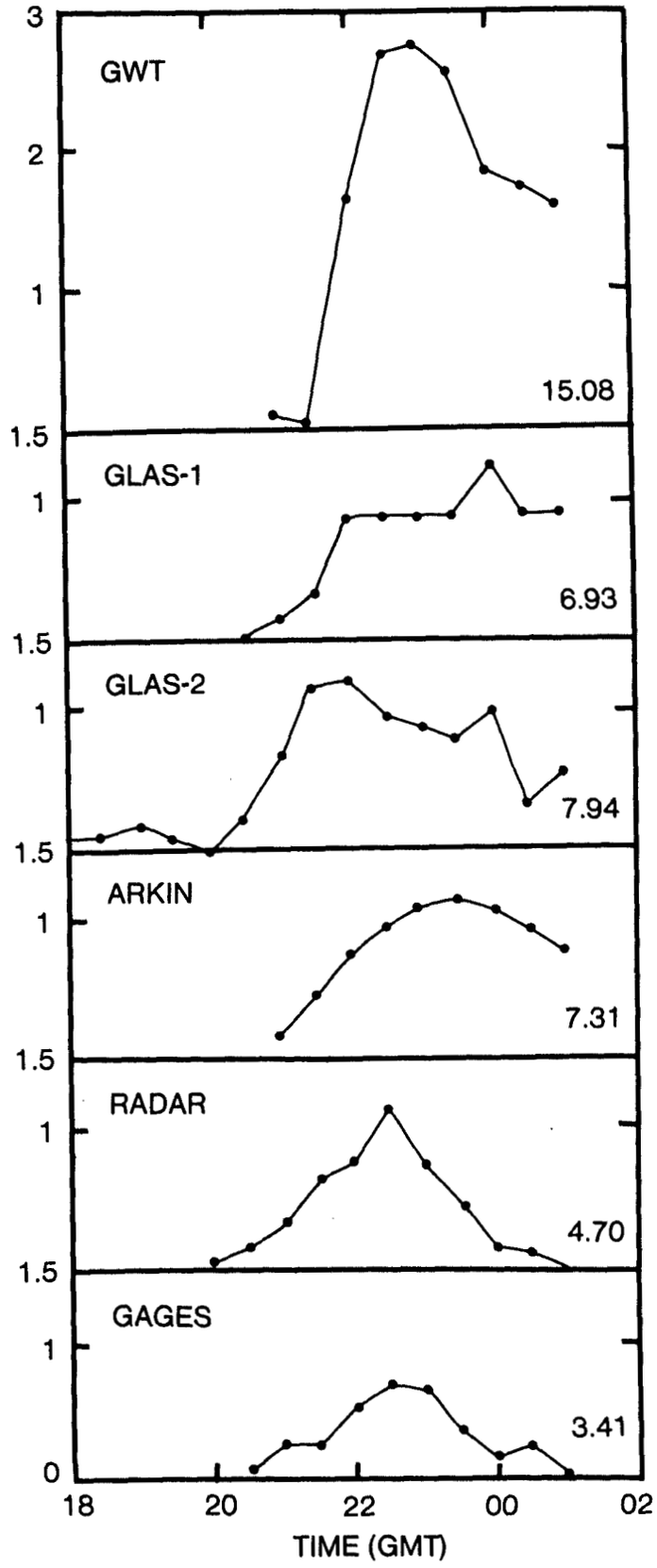

Figure 2. Target area average rain depth (mm) as a function of time on 3 Aug 1979. Total rain depth (1600-0100 GMT) shown in lower right corner.

neighboring pixels (local minima in the temperature field are defined). When a minimum consists of several pixels at that temperature, the centroid location is used. Again, the threshold temperature used is 253 K.

Once the locations of rain cells have been determined, the rain parameters to be assigned to that feature are defined based on the one-dimensional cloud model results of Adler and Mack (1984). In that study maximum rainrate and maximum volume rainrate were calculated from a sequence of cloud model runs as a function of maximum cloud height (or minimum model cloud temperature T_c). The model results simulated fairly well the observed profiles in Florida (summer) and Oklahoma (spring). For this study the model results of Adler and Mack (1984) for the Florida (summer) case are converted for use in the GLAS-2 technique in the following way: A rain-no rain threshold was arbitrarily set at 253 K, corresponding to a volume rainrate of 50 $m^3 s^{-1}$ for the Florida model runs. The magnitude of the rain area (A_R) is assummed to be five times the model updraft area (see Adler and Mack, 1984 for comparisons with observations). Therefore,

$$A_R = 5 \pi r^2 \qquad (1)$$

where r is the model updraft radius. The average rainrate over the raining area of the cell is

$$\overline{R} = VRR / A_R \qquad (2)$$

where VRR is the volume rainrate. With T_c being the model calculated cloud top temperature, a subjective fit of $\overline{R}$ and T_c from the model results yield

$$\overline{R} = 77.65 - 0.28\, T_c \qquad (3)$$

while a subjective log-linear fit of rain area and T_c yields

$$\ln A_R = 15.95 - .049\, T_c \qquad (4)$$

Because of the coarse (8 km) field of view of the GOES IR data the satellite T_{min} must be adjusted toward lower values to compare with the model temperature. This is done crudely, based on Adler et al. (1982) observational results, as given by

$$T_c = 0.65\, T_{min} + 66.5 \qquad (5)$$

An example of GLAS-2 rainrates is shown in Fig. 1c.

2.4 Radar and gages

Data from the WSR-57 10 cm radar at Miami, FL were used. Digital data were remapped to satellite coordinates using RADPAK (Heymsfield et al., 1983) and the relationship $Z = 300R^{1.4}$. Tabular values of half-hourly and daily totals of FACE target area average rain depth were taken from Barnston et al. (1981) and Meitin et al. (1981) [for radar and gage estimates, respectively]. An example of the radar rainrates is shown in Fig. 1d.

3. STATISTICAL RESULTS

The GLAS-1, GLAS-2 and modified Arkin schemes were run each half hour from 1600 to 0100 GMT on each of three days, selected by the local availability of satellite and radar data. Full resolution IR data (4 km E-W and 8 km N-S) were used. Figure 2 shows a comparison of five rainfall estimates to ground truth (raingages) on 3 Aug 1979. The estimates are of the average rain depth in the FACE target area (1.3×10^4 km^2) every 30 min. Daily (1600-0100 GMT) totals are displayed in the lower right corner of each panel of Fig. 2. The GWT, which has a pronounced tendency to underestimate the rain early, and overestimate later (Negri et al., 1984), on this day overestimated consistently, resulting in a 440% overestimate of the "daily" total. (In fairness to the GWT, this was the second worst overestimate in 53 FACE-2 days). The three other satellite techniques also overestimated the total rain by about a factor of two on this lightly raining day in the FACE region. No satellite technique clearly detected the maximum at 2230 GMT.

The day with the heaviest rain in FACE-2 (1978-80) was 29 July 1978, when 19.31 mm were recorded by the gages between 1900 and 0100 GMT. Clearly, in this extreme situation, the Arkin scheme (designed for monthly averages and using essentially a climatological rainrate) produced the lowest estimate. It quickly reached its saturation value of 1.5 mm per 30 min as the target region became completely covered by cloud colder than 235 K. Both the GWT and GLAS-1 tended to lag the gages and radar, producing maxima 1.5 and 1.0 h later respectively. While numerically closest to the gage total GLAS-2 is poorly correlated to the gages on the 30 min scale. Extensive coverage of the Florida peninsula by cold cloud, as opposed to coverage by isolated thunderstorms, perhaps hindered GLAS-2 identification of convective cells on this day.

A third day examined was 31 July 1980 (Fig. 4), when extremely light rainfall fell over the target region (1.84 mm total). The GWT, GLAS-1 and ARKIN schemes display three pronounced maxima, as do the gages, however the correlation is poor. Total estimates are all comparable with the exception of GLAS-2, due to overestimates of all three maxima, particularly the one at 2100 GMT. Examination of the IR imagery revealed that there was much thin cirrus debris in the target region which GLAS-2 incorrectly identified as rain cloud. It is apparent that visible data and/or some parameter based on the pattern or gradient in the IR data may be useful in discriminating cirrus from active convection in future versions of the GLAS technique.

The availability of digital radar data on 29 July 1978 enabled us to expand the region of comparison to an annular region extending from 25 n.m. to 90 n.m. (40-145 km) around Miami. (No analysis was done in the ground clutter region). Remapped radar data were compared pixel by pixel to the three satellite estimates. Results are presented in Tables 1 ,2 and 3. The probability of detection (POD) is defined as the

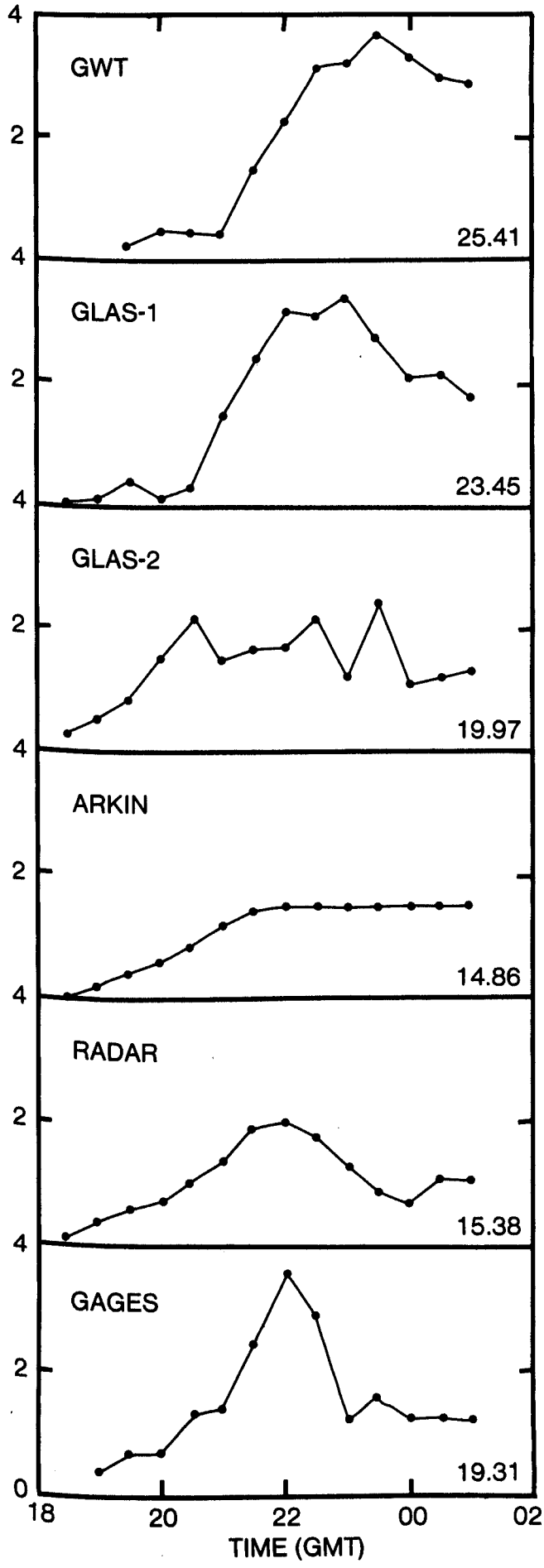

Figure 3. Same as Fig. 2 except 29 July 1978.

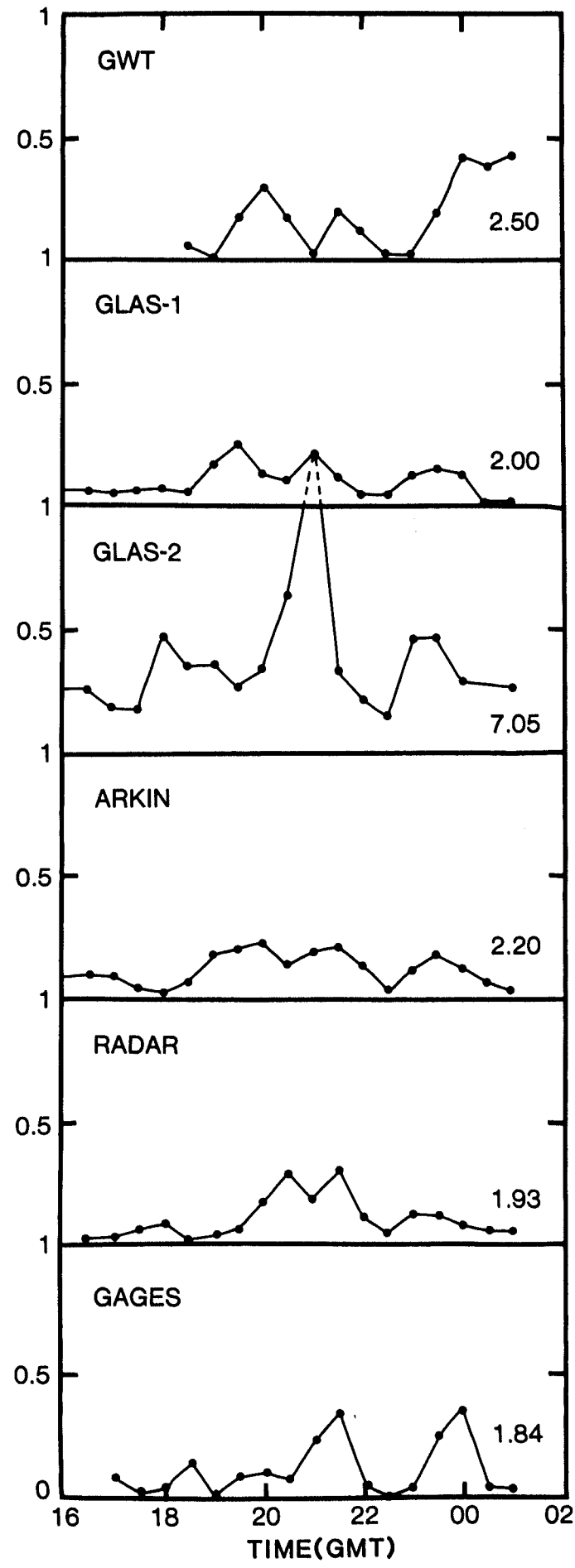

Figure 4. Same as Fig. 2 except 31 July 1980.

ratio of the number of satellite rain estimates > 0 coincident with radar points > N, to the total number of radar points > N. N is a radar threshold rainrate equal to 1, 12 or 25 mm h^{-1}. The false alarm ratio (FAR) is defined as the ratio of the number of satellite rain estimates > 0 coincident with a zero radar point, to the total number of satellite rain estimates > 0. The critical success index (CSI) is defined as:

$$CSI(N) = ([POD(N)]^{-1} + [1 - FAR]^{-1} - 1)^{-1} \quad (6)$$

As defined these parameters are representative of the statistics of areal coverage rather than of the statistics of rainrate.

Tables 1-3 reveal a high FAR for all techniques early in the day (1600-1800), prior to intense convection. These decrease during the day. GLAS-2, being the most restrictive in areal rain apportionment, has the lowest aggregate FAR, though improvements could be made. In contrast, the POD's for the GLAS-1 and Arkin schemes tend to increase during the day, as the areal extent of rainfall increases. GLAS-2 POD's are poor and variable, as is the period aggregate of 47% (168/355). This indicates that further study needs to be done on the relationship between local minima in temperature (as observed in half-hourly GOES data) and convective cells as defined by the radar.

While POD's approaching 1.0 appear desirable, <u>any</u> scheme with a high temperature threshold will detect 100% of the precipitation. CSI's, particularly for the 25 mm h^{-1} threshold were similar (0.36, 0.36 and 0.30). POD's remained constant with threshold for GLAS-1 and Arkin, but increased rapidly in GLAS-2 for higher thresholds. This indicates that GLAS-2 rain areas may be too small, or that the technique is concentrating on strong convective entities and missing "anvil" or non-convective rain.

4. CONCLUSIONS AND FUTURE WORK

This paper has described a first attempt at estimating rainfall from a physically based satellite IR method (GLAS-2). Attempts have been made to quantify how well the technique does by comparisons with digital radar data and with area averaged raingage data. The relative merits of using GLAS-2 are examined by comparison to simpler, empirical schemes (Arkin, GLAS-1) and to a previously existing, but complicated scheme (the GWT).

On 3 Aug 1980, a day of light to moderate rain in the FACE target region, all satellite schemes overestimated the gage determined rainfall. The estimates ranged from a factor of two (GLAS-1) to a factor of 4.5 (GWT). On a lightly raining day (31 July 1980) all techniques except GLAS-2 came within 18% of the gages.

Table 1. Statistics for GLAS-1 on 29 July 1978.

TIME	POD 25	POD 12	POD 1	FAR	CSI 25	CSI 12	CSI 1
1600			0.21	0.94			0.04
1630			0.23	0.92			0.06
1700			0.31	0.86			0.10
1730		0.50	0.14	0.94		0.05	0.04
1800	0.66	0.46	0.26	0.88	0.10	0.09	0.08
1830	0.66	0.51	0.49	0.77	0.20	0.18	0.18
1900	0.33	0.38	0.43	0.75	0.16	0.17	0.18
1930	0.35	0.22	0.50	0.64	0.21	0.16	0.26
2000	0.32	0.40	0.61	0.53	0.23	0.27	0.36
2030	0.50	0.55	0.65	0.56	0.30	0.32	0.35
2100	0.89	0.89	0.88	0.60	0.37	0.37	0.37
2130	0.95	0.94	0.94	0.56	0.43	0.42	0.42
2200	1.00	1.00	0.99	0.58	0.41	0.41	0.41
2230	1.00	0.99	0.98	0.53	0.46	0.46	0.45
2300	1.00	1.00	0.99	0.49	0.50	0.50	0.50
2330		1.00	0.98	0.55		0.47	0.45
2400	1.00	1.00	0.99	0.60	0.39	0.39	0.39
2430	1.00	1.00	0.99	0.59	0.40	0.40	0.40
2500	1.00	1.00	0.99	0.64	0.35	0.35	0.35
TOTAL	0.80	0.78	0.89	0.60	0.36	0.36	0.38

Table 2. Statistics for Arkin on 29 July 1978.

TIME	POD 25	POD 12	POD 1	FAR	CSI 25	CSI 12	CSI 1
1600			0.25	0.91			0.06
1630			0.29	0.90			0.07
1700			0.30	0.85			0.11
1730		0.50	0.15	0.92		0.07	0.05
1800	0.66	0.66	0.32	0.80	0.17	0.17	0.13
1830	0.66	0.51	0.51	0.67	0.28	0.25	0.25
1900	0.33	0.56	0.55	0.68	0.19	0.25	0.25
1930	0.76	0.58	0.70	0.66	0.30	0.27	0.29
2000	0.61	0.62	0.78	0.60	0.31	0.32	0.36
2030	0.91	0.85	0.87	0.62	0.36	0.35	0.35
2100	0.93	0.92	0.94	0.62	0.36	0.36	0.36
2130	0.98	0.96	0.98	0.59	0.40	0.40	0.40
2200	1.00	1.00	0.99	0.61	0.38	0.38	0.38
2230	1.00	1.00	1.00	0.60	0.39	0.39	0.39
2300	1.00	1.00	1.00	0.53	0.46	0.46	0.46
2330		1.00	1.00	0.62		0.38	0.38
2400	1.00	1.00	1.00	0.64	0.35	0.35	0.35
2430	1.00	1.00	1.00	0.62	0.37	0.37	0.37
2500	1.00	1.00	0.99	0.65	0.34	0.34	0.34
TOTAL	0.91	0.87	0.93	0.62	0.36	0.35	0.36

Table 3. Statistics for GLAS-2 on 29 July 1978.

TIME	POD 25	POD 12	POD 1	FAR	CSI 25	CSI 12	CSI 1
1600			0.01	0.99			0.00
1630			0.00	0.99			0.00
1700			0.00	1.00			0.00
1730		0.50	0.06	0.93		0.05	0.03
1800	1.00	0.53	0.22	0.82	0.18	0.15	0.11
1830	0.50	0.40	0.19	0.72	0.21	0.19	0.12
1900	0.33	0.38	0.33	0.71	0.18	0.19	0.18
1930	0.35	0.25	0.24	0.61	0.22	0.18	0.17
2000	0.35	0.35	0.21	0.40	0.28	0.28	0.18
2030	0.58	0.45	0.33	0.49	0.37	0.31	0.25
2100	0.62	0.39	0.21	0.45	0.41	0.30	0.18
2130	0.58	0.42	0.18	0.45	0.39	0.31	0.15
2200	0.34	0.29	0.14	0.59	0.23	0.20	0.11
2230	0.43	0.38	0.21	0.22	0.38	0.34	0.19
2300	0.00	0.23	0.07	0.25	0.00	0.22	0.07
2330		0.47	0.18	0.29		0.40	0.17
2400	0.00	0.00	0.11	0.56	0.00	0.00	0.09
2430	0.40	0.54	0.11	0.53	0.27	0.33	0.10
2500	0.00	0.22	0.11	0.66	0.00	0.15	0.09
TOTAL	0.47	0.36	0.15	0.54	0.30	0.25	0.13

Contamination by cirrus debris caused a gross overestimate in GLAS-2. On 29 July 1978, when nearly 20 mm of rain fell across the target area, daily estimates ranged from a 30% overestimate (GWT) to a 20% underestimate (Arkin). In no satellite estimation scheme could the correlations of half-hour estimates to gages be considered anything but poor.

The utility of a GLAS-2 type scheme may arise when shorter time scales are required, for example estimates for flash floods or for 1-3 h precipitation and when applied under different climatological conditions. GLAS-2 has its basis in the work of Negri and Adler (1981), who used 5 min interval IR data and showed a good correlation between T_{min} and VRR.

The 0.54 FAR of GLAS-2 is easy to conceptualize: there are many T_{min} in the IR data that don't represent active convection. There are several ways in which the FAR could be improved:

1. decrease the threshold temperature

2. examine the size (number of pixels) of the defined T_{min}. Large areas of constant (however cold) temperature may be the remnants of convection. Such an areal cutoff would be hard to determine.

3. examine the two-dimensional gradient about T_{min}. Cirrus debris would tend to have smoother gradients than active convection, particularly in the direction of the upper level wind.

4. set a proximity criteria such that two T_{min} would be associated with only one "cell" if they were located within some predetermined distance of each other.

5. quantitatively use the visible channel data.

We plan to examine many more FACE days with digital radar data to quantify the relationship between satellite determined T_{min} (and second order temperature variables) to radar determined convective cells. It is only with these statistics in hand can one realistically formulate or evaluate an estimation scheme. On several days, 15 min interval satellite data is available. This will prove invaluable in examining the effect of higher temporal resolution data on the estimation scheme.

ACKNOWLEDGEMENTS

We would like to thank Andrew I. Watson of NOAA/ERL for supplying the digital radar data, and John Taylor and Harold Pierce for the preparation of radar and satellite data sets.

REFERENCES

Adler,R.F., and R.A.Mack, 1984: Thunderstorm height/rainfall rate relations for use with satellite rainfall estimation techniques. J. Clim. Appl. Meteor. 23, (in press).

____, M.J.Markus, A.J.Negri, G.P.Byrd, 1982: Estimating the temperature and height of overshooting thunderstorm tops from geostationary satellite infrared data. Conf. on Cloud Physics, (Chicago, IL), AMS, Boston, MA, 500-503.

Arkin,P.A., 1979: The relationship between fractional coverage of high cloud and rainfall accumulations during GATE over the B-scale array. Mon. Wea. Rev., 107, 1382-1387.

____, 1983: A diagnostic precipitation index from IR satellite imagery. Tropical Ocean-Atmosphere Newsletter, No. 17, 5-7. (Available from JSIAO, U. of Washington, AK-40, Seattle, WA 98105).

Barnston,A.G., W.L.Woodley, and M.Brown, 1981: FACE-2 data reductions and analyses. Part II: The FACE-2 confirmatory radar rainfall and covariate data sets. NOAA Tech. Memo. ERL OWRM-8. Boulder, CO., 380pp.

Griffith,C.G., J.A.Augustine, and W.L.Woodley, 1981: Satellite rain estimation in the U.S. High Plains. J. Appl. Meteor., 20, 53-66.

____, W.L.Woodley, and J.A.Augustine, 1980: Final report to the Water and Power Resources Service on the estimation of convective, summertime rainfall in the U.S. High Plains from thermal infrared geostationary satellite data, Vol. 1. NOAA/ERL, Boulder, CO., 157pp.

____,____, S.Browner, J.Teijeiro, M.Maier, D.W.Martin, J.Stout and D.N.Sikdar, 1976: Rainfall estimation from geosynchronous satellite imagery during daylight hours. NOAA Tech. Rep. ERL 356-WMPO 7, Boulder, CO, 106pp.

____,____, P.G. Grube, D.W. Martin, J. Stout and D.N. Sikdar, 1978: Rain estimation from geosynchronous satellite imagery: Visible and infrared studies. Mon. Wea. Rev., 106, 1153-1171.

Heymsfield,G.M., K.K.Ghosh, and L.C.Chen, 1983: An interactive system for compositing digital radar and satellite data. J. Clim. Appl. Meteor. 22, 705-713.

Meitin,J.G., W.L.Woodley and C.G.Griffith, 1981: FACE-2 data reductions and analyses: Part V. Satellite estimated rainfall from a geostationary platform in FACE-2. NOAA Tech. Memo. ERL OWRM-11, Boulder, CO, 141pp.

Negri,A.J. and R.F.Adler, 1981: Relation of satellite-based thunderstorm intensity to radar-estimated rainfall. J. Appl. Meteor.,20, 288-300.

____,____, and P.J.Wetzel, 1984: Satellite rain estimation: An Analysis of the Griffith-Woodley technique. J. Clim. Appl. Meteor. 23, January, (in press).

Richards,F. and P.Arkin, 1981: On the relationship between satellite observed cloud cover and precipitation. Mon. Wea. Rev., 104, 1081-1093.

Woodley,W.L., C.G.Griffith, J.S.Griffin and S.C.Stromatt, 1980: The inference of GATE convective rainfall from SMS-1 imagery. J. Appl. Meteor., 19, 388-408.

PASSIVE MICROWAVE RAIN ESTIMATION OVER LAND AND OCEAN AT 37 GHz

Roy W. Spencer

Space Science and Engineering Center
1225 W. Dayton St.
University of Wisconsin-Madison
Madison, Wisconsin 53706

1. INTRODUCTION

The remote sensing of rainfall and severe storms from satellites has most commonly been attempted with visible and infrared (IR) observations (Barrett and Martin, 1981). These techniques rely on the existence of some relationship between the occurrence or intensity of rainfall and the temperature, appearance, or behavior of the cloud top as observed by the satellite. Microwave radiation at frequencies below about 40 GHz easily penetrates clouds but not precipitation. To estimate rain rates at these frequencies, the rain must have a significantly different electromagnetic signature than its surroundings, whether land or ocean. This condition is easily met over the ocean because of the ocean's relatively low and uniform brightness temperature ($T_B = \varepsilon T$) due to its low emmissivity ($\varepsilon \sim 0.5$), while the rain has a uniform and high emissivity ($\varepsilon \sim 0.95$) and thus, a high brightness temperature. Therefore, theoretical and empirical treatments of the problem have, with some differences, indicated that rain rates over the ocean are retrievable (Wilheit et al., 1977; Huang and Liou, 1983; Spencer et al., 1983a). Land has an emissivity that is much closer to that of rain and is more variable, due primarily to variations in soil moisture. This can result in some ambiguity between wet land surfaces and rain (e.g. Rodgers and Siddalingaiah, 1983). Even if the land background were uniform, previous theoretical results suggested that only light rain rates would be detectable (Savage and Weinman, 1975; Weinman and Guetter, 1977).

However, the observations from the Nimbus-7 SMMR (Scanning Multichannel Microwave Radiometer), a ten channel, five frequency instrument (Table 1), have revealed brightness temperatures as low as 163 K in conjunction with heavy thunderstorm rainfall (Spencer, et al., 1983b). The low brightness temperatures were attributed to the presence of precipitation-sized ice particles in the upper portions of the storms. This work led to the development of a multifrequency rain rate measurement algorithm based upon comparisons between rain rates from operational WSR-57 radars and SMMR brightness temperatures over the United States (U.S.) during the summer (Spencer et al., 1983c).

	frequency (GHz)				
	37	21	18	10.7	6.6
polarization	V,H	V,H	V,H	V,H	V,H
wavelength (cm)	0.81	1.36	1.66	2.80	4.54
footprint size(km)	22	37	43	74	120

Table 1 SMMR frequencies, wavelengths, and field of view sizes at the earth's surface. Horizontal (H) and vertical (V) polarizations are sampled at each frequency. This is accomplished with two radiometers at 37 GHz and one radiometer at each of the lower frequencies, which is shared between H and V on alternating scans of the instrument.

The purpose here is to review the meteorological versatility of passive microwave measurements through descriptions of multi-frequency spring, summer, and fall rain rate algorithms for use over land, a single frequency algorithm for use over the warm oceans, and preliminary results on the utility of 37 GHz observations for detection of severe thunderstorms.

2. RAIN OVER LAND

Comparisons between rain rates from 234 radars and brightness temperatures from 25 SMMR passes over the U.S. have been utilized to derive rain estimation algorithms for the spring, summer, and fall seasons. These data sets resulted in over 12000 records of 40 x 40 km averaged rain rates and brightness temperatures. Fig. 1 shows the average brightness temperatures for different rain rate intervals and different seasons. It is clear that the summer rain classes are the most separable in brightness temperature. It can also be seen that there are large differences in average brightness temperature between seasons for the same rain classes. This difference is due to the variations in land background T_B resulting from seasonal variations in the thermometric temperatures,

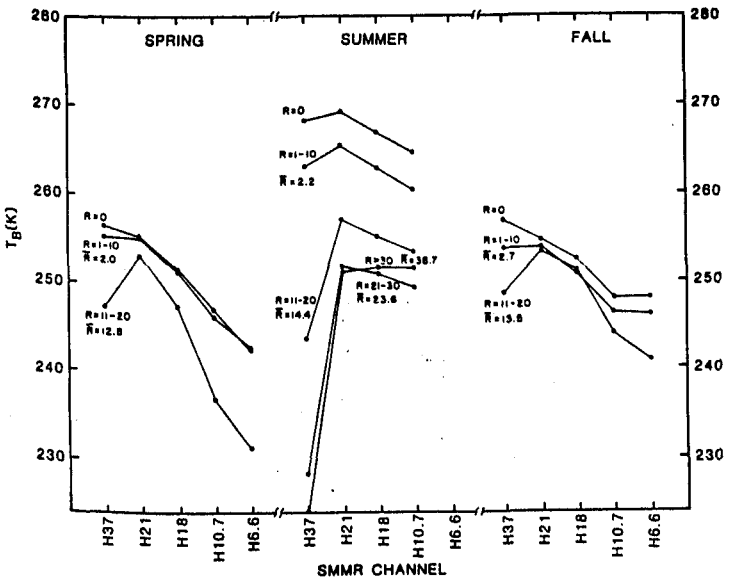

Fig. 1 Average SMMR horizontally polarized brightness temperatures for different rain rate intervals during the spring, summer, and fall. Each rain rate class is represented by a series of connected dots and labeled with the rain rate interval and the average rain rate within that interval.
Data are from 25 SMMR passes and 234 WSR-57 radars, resulting in a total of over 12,000 records of 40x40 km average SMMR T_B's and rain rates (mm/h).

and to a lesser extent, emissivity. These variations can be accounted for by seasonal equations. But what about the synoptic variations in the land temperature? Table 2 shows the equations for the spring, summer and fall seasons, derived from a multiple linear least-squares regression procedure with radar rain rate as the dependent variable. It can be seen that the rain rate is roughly proportional to the T_B contrast between the 37 GHz channels and the 18 and 21 GHz channels. This contrast provides a measure of the extent to which the land-emitted radiation is attenuated by the precipitation, since the 18 and 21 GHz channels are more sensitive to the land radiation than is the 37 GHz channel, due to the longer wavelengths and the larger footprints. This contrast is needed to account for the synoptic variations in land temperature which might be mistaken for variations due to rain activity. Fig. 2 shows the order in which the variables were chosen and the increase in explained variance of the radar rain rates at each regression step. Note that the 37 GHz channels are always chosen first because of their highest individual correlation with rain rate. Also note that the 37, 21 and 18 GHz channels contain most of the information on rain rate, with the 10.7 and 6.6 GHz channels providing little improvement.

The best performance of the algorithms is during the summer and fall, when vegetation covers the ground. During the spring, the skill is reduced because of variations in the land T_B which are due to emissivity variations of partly exposed soils, thus making multi-spectral T_B contrast measurements somewhat ambiguous at times. The 37 GHz polarization ($T_B^V - T_B^H$) was almost always found to be less than 16°C for rain systems, so this criterion was used to screen out cases of wet soil, whose values of polarization always exceed this amount.

The heavy rain cases involved in the summer algorithm (>20 mm/h) constitute less than 4% of all non-zero rain cases, and yet add 11% to the total explained variance of the summer equation. Therefore, heavy rains are the most easily detected over land (which is verified by Fig. 1), and are a significant part of the algorithms success. Their detection is attributable to precipitation-sized ice particles in the upper portions of storms which produce heavy rain. All relatively unpolarized 37 GHz T_B's less than 220 K have been found to be associated with heavy rainfall as depicted by radar.

3. RAIN OVER OCEAN

Comparisons of radar rain rates and SMMR T_B's over the Gulf of Mexico have revealed that the T_B's can explain 72% of the variance of radar rain rates (Fig. 3). The form of this relationship is quite different from plane-parallel theory (also shown in Fig. 3). Most of this difference can be attributed to footprint filling effects. It was found that most of the rain systems in this randomly chosen six day sample had rain rates at which they were essentially opaque to 37 GHz radiation. The variations in brightness temperature were found to be primarily due to variations in the amount of the footprint filled by these relatively opaque rain cells. Also, the size of the rain cell is correlated with the storm-scale rain rate, leading to a natural correlation between rain rate and T_B. This analysis is only applicable to warm season or warm ocean showery rain systems. In higher latitudes where more stratiform rains fall, plane-parallel theory should provide much improved measurements. Therefore, over tropical oceans, footprint filling should not necessarily be considered a problem, unless rain information is sought on a scale smaller than what the satellite observes.

4. SEVERE STORMS OVER LAND

Quite low 37 GHz T_B's (less than 220 K) have been found to be associated with heavy thunderstorm rainfall. Extremely low T_B's (less than 200 K) have been found in association with storms that produce severe weather. Table 3 summarizes 13 storms that the SMMR observed over the U.S. between February and July, 1979. Note that a large percentage of these storms were reported in Storm Data (1979) even though many severe weather events never make it into this publication. In addition, many storms observable by the SMMR

	SMMR CHANNEL												
	const.	H37	V37	H21	V21	H18	V18	H10.7	V10.7	H6.6	V6.6	r	r^2
spring	38.3	-.107	-.442	.279	.119	.107	.105	-.109	-.121	X	.034	.625	.391
summer	32.6	-.408	-.378	.215	.137	.406	.090	-.242	.062	*	*	.795	.631
fall	49.9	-.157	-.789	.437	.261	.055	.258	-.136	-.102	X	X	.752	.565

* -- not included in the analysis X -- not chosen by regression procedure

Table 2. SMMR rain rate regression equations and their performance for spring, summer, and fall seasons. For the summer the T_B's must have satisfied the following screening conditions: $(V37 - H37) \leq 16^oC$ and $H37 < 280K$ and $H10.7 > 225K$. For the spring and fall, the data must satisfy: $(V37 - H37) \leq 16^oC$ and $H18 < 230K$. The total number of records utilized in the analysis after screening/before screening were : spring (3031/4753); summer (3782/4663); fall (2288/2615).

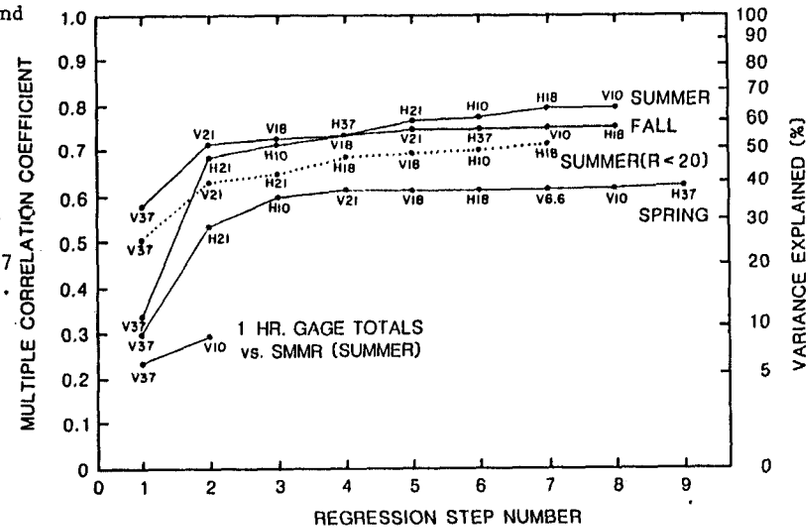

Fig. 2. The multiple correlation and explained variance achieved at each regression step in the derivation of the spring, summer, and fall equations, and the channels chosen at those steps. The dotted line represents the summer equation if the analysis is restricted to R<20 mm/h. The short line at the bottom shows the correlations achieved if the summer T_B's are compared to 1307 U.S. cooperative network rain gages.

occur in desolate areas where severe weather may occur without being reported. Heavy storms have also been found in the SMMR data in other parts of the world: e.g. west Africa, India, South America, Mexico, Canada, Russia, and China. Currently, a much more ambitious summary of the severe weather characteristics of these low brightness temperature events is being performed, utilizing newspaper reports from around the U.S.

5. CONCLUSIONS AND RECOMMENDATIONS

A large amount of information on rain rate over land and ocean is contained in the observations of the Nimbus-7 SMMR. It also appears that severe thunderstorms are detectable with 37 GHz observations. The many uses of this kind of observation, especially in those countries with little or no ability to monitor rainfall or storms, suggests that more satellite microwave radiometers are needed. The most useful system would be an instrument in geostationary orbit. This would allow the timely monitoring of rain and storms over land and sea.

6. ACKNOWLEDGEMENTS

Portions of this research have benefitted from discussions with Drs. Barry B. Hinton, David W. Martin, and James A. Weinman. This research was supported by NOAA contract NA-80-SAC-00742 and NASA contract NAG 5-391.

7. REFERENCES

Barrett, E. C., and D. W. Martin, 1981: The Use of Satellite Data in Rainfall Monitoring. Academic Press, London, 340 pp.

Huang, R., and K.-N. Liou, 1983: Polarized microwave radiation transfer in precipitating cloudy atmospheres: Applications to window frequencies. J. Geophys. Res., 88, 3885-3893.

NOAA, 1979: Storm Data, 21, U.S. Department of Commerce, 25 pp.

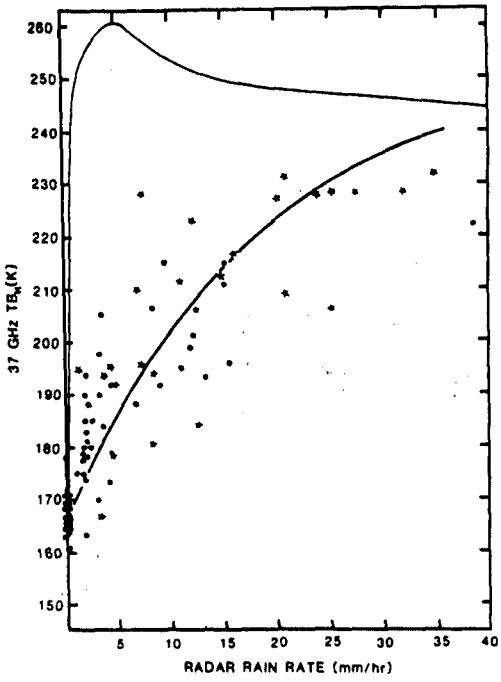

Fig. 3 Observed 37 GHz horizontally polarized brightness temperatures vs. radar rain rates from the Galveston radar at 1801 GMT 16 April, 1755 GMT 27 June, 1735 GMT 7 July, 0638 GMT 9 July, and 1744 GMT 13 July, 1979 (dots); and from the Apalachicola radar at 0530 GMT 17 July 1979 (stars), manually digitized and assigned to 20x20 km bins. The line through the data points is a least squares best fit of a function proportional to the sixth power of the brightness temperatures. The upper curve depicts the theoretical results of Olson (1983) for rain-filled fields of view, and is representative of the results of several other investigators. The rain rates are expected to be accurate to ±60%.

Date	Time(GMT)	Minimum H37 T_B	State	Weather
23 February	1743	185K	TX	tornado
4 May	0648	195K	TX	funnel
"	"	191K	TX	?
"	"	194K	TX	funnel
"	"	189K	TX	?
"	"	185K	TX	?
"	"	180K	TX	**
20 May	0633	195K	KS-OK	windstorm
19 June	0713	192K	NE-SD	**
9 July	0635	163K	MO	windstorm,hail
15 July	0643	183K	IA	windstorm
"	"	188K	MO	windstorm
"	"	187K	MO	windstorm

Table 3. Severe weather characteristics of the storms observed by the Nimbus-7 SMMR to have horizontally polarized 37 GHz T_B's less than or equal to 195K, during the first half of 1979.

Rodgers, E., and H. Siddalingaiah, 1983: The utilization of Nimbus-7 SMMR measurements to delineate rainfall over land. J. Climate Appl. Meteor., 22, 1753-1763.

Savage, R. C., and J. A. Weinman, 1975: Preliminary calculations of the upwelling radiance from rainclouds at 37.0 and 19.35 GHz. Bull. Amer. Meteor. Soc., 56, 1272-1274.

Spencer, R. W., B. B. Hinton, and W. S. Olson, 1983a: Nimbus-7 37 GHz radiances correlated with radar rain rates over the Gulf of Mexico. J. Climate Appl. Meteor., 22, 2095-2099.

_____, W. S. Olson, Wu Rongzhang, D. W. Martin, J. A. Weinman and D. A. Santek, 1983b: Heavy thunderstorms observed over land by the Nimbus-7 Scanning Multichannel Microwave Radiometer. J. Climat. Appl. Meteor., 22, 1041-1046.

_____, D. W. Martin, B. B. Hinton and J. A. Weinman, 1983c: Satellite microwave radiances correlated with radar rain rates over land. Nature, 304, 141-143.

Weinman, J. A. and P. J. Guetter, 1977: Determination of rainfall distributions from microwave radiation measured by the Nimbus-6 ESMR. J. Appl. Meteor., 16, 437-442.

Wilheit, T. T., A. T. C. Chang, M. S. V. Rao, E. B. Rodgers, and J. S. Theon, 1977: A satellite technique for quantitatively mapping rainfall rates over the oceans. J. Appl. Meteor., 16, 551-560.

EFFECTS OF INSTRUMENT PARAMETERS ON SATELLITE RETRIEVAL ACCURACY

Larry M. McMillin

National Oceanic and Atmospheric Administration
National Environmental Satellite, Data, and Information Service
Washington, D.C.

1. INTRODUCTION

Accuracies of temperature profiles retrieved from measurements of satellite radiances are determined by several factors. Among the more important are the width of the atmospheric weighting functions, the noise in the measurements, and the number and location of the channels. Although the width of the channels is an important factor, there is a theoretical result which states that, given an infinite number of channels with zero noise, the true profile can be recovered regardless of the width. Previous studies have examined the effect of changing two or more of the various parameters. However, a comparison of two parameters when three have an effect reaches a point where the third parameter is the limiting one. If this factor is not considered in the evaluation, very misleading conclusions can be drawn. The potential for misleading conclusions is particularly great when instruments are compared which differ in all of the factors. If the effects on accuracy are not attributed to the appropriate causes, serious design errors can result.

2. REVIEW

It is interesting to note that, at first glance, the studies which have been done seem to contradict the fact that width is not important if an infinite number of perfect observations is available. For example, Weinreb and Crosby (1972) examined the effect of channel number on retrieval accuracy. They found that the effect of an additional channel decreased as the number of channels increased, suggesting that, beyond some number of channels, an additional channel makes no difference. However, since the study was done for a single instrument and thus a single noise level, it did not illustrate that, as the noise level decreased, the number of channels determined to be useful would have increased. Although their study was useful for the noise levels they considered, it did not provide insight into possible accuracy gains if the noise level could have been changed.

Chahine (1979) examined the effect of instrument noise on retrieval accuracy for two instruments which differed in number of channels as well as weighting function width. Both instruments showed an increase in retrieval accuracy with decreasing noise. A point was reached where additional decreases in noise had little effect. This is partly because the other factors were fixed, as illustrated by the fact that the curve for the instrument with more channels and narrower weighting functions flattened out at a lower noise level. Chahine attributed the increase in accuracy to the narrow width. Since the two instruments differed in number of channels as well as the weighting function width, there is some uncertainty in the assumption that the increase in accuracy is due to weighting function width and not the other differences. It was this uncertainty which prompted the current study.

3. SIMULATION

The intent of the current study was to isolate the effects of the various factors on retrieval accuracy. This was done by changing one factor at a time while keeping the others fixed. To start, seven 15 μm HIRS sounding channels (channels 1 - 7) were selected as a base. The properties of these channels are summarized in Smith et al. (1979) and have weighting functions which peak at 30, 60, 100, 400, 600, 800, and 900 mb. A set of narrow weighting functions was generated by keeping the peak pressure fixed while narrowing the weighting function to one-half its original value. A third set of 14 weighting functions was generated by adding one channel halfway between any two adjacent ones, with a 14th channel being placed halfway between the peak of channel seven and the ground. To complete the combinations, a fourth set of 14 narrow weighting functions was generated. This resulted in four sets of channels: one set of seven at normal width; one set of seven narrow channels; one set of 14 at normal width; and one set of 14 at narrow width.

Another set of four groups was created to evaluate the effect of channel characteristics. The basic set consisted of the same seven 15 μm CO_2 channels plus the four lowest (channels 13 - 16) 4.3 μm HIRS channels. These four additional channels peak at 1000, 950, 700, and 400 mb. Combinations identical to the previous four were generated, resulting in a set of 11 normal channels, a set of 11 narrow channels, a set of 22 normal channels, and a set of 22 narrow channels.

One factor remaining is noise. To evaluate this effect, values were varied about the nominal values given for the TIROS-N satellite (see Schwalb, 1978). Noise was varied by

multiplying the nominal values by factors of 0, 0.25, 0.50, 1.00, 2.00, 3.00, and 4.00 to vary the effects. A second noise component was added to those channels which sense the ground to simulate errors in the boundary term.

4. SAMPLE DESCRIPTION

The evaluations are based on a set of rocketsonde profiles screened by Uddstrom and Wark (1984). For each month and latitude zone, a separate covariance matrix was produced. Four of these were used in this study. The four used were January midlatitude, January polar, August midlatitude, and August polar. Each of the four covariance matrices was based on a sample of 100 to 200 profiles.

5. RETRIEVAL METHOD

Although it would be desirable to find that the results are independent of retrieval method, examination of studies contained in the literature hint that there might be differences, particularly in the ability of physical and more statistical approaches to benefit from reduced noise. An evaluation of such a possible effect is beyond the scope of this paper. However, the hint of a connection requires that this paper, as well as others dealing with the same subject, fully describe the retrieval approach used. In fact, a full description of the retrieval method would be in order even if the hint of a dependence on the method turns out to be false.

Comparisons used in this study are based on the well-known minimum variance retrieval algorithm (see Westwater and Strand (1968)) which is given by

$$b - \bar{b} = S_b A^T \{AS_b A^T + S_e\}^{-1} (r - \bar{r}) \qquad (1)$$

where b is the profile of atmospheric radiances at the reference wavelength, $\bar{b}$ is the mean atmospheric profile of the sample, S_b is the covariance matrix of the sample, A^T is the matrix of weighting functions, S_e is the error covariance matrix, r is the vector of radiance measurements, $\bar{r}$ is the vector of radiances calculated for the sample mean, and the superscript T denotes a matrix transposed.

To calculate retrieval errors, it is necessary to calculate the radiances used in Eq. (1). These are generated from the relation

$$r = A\, b_t \qquad (2)$$

where the values of b_t are the true profiles rather than the retrieved values which are designed by "b" in Eq. (1).

To calculate rms retrieval errors, it is necessary to use a sample of profiles. To expand Eqs. (1 and 2) to a sample, it is convenient to note that A has only a slight dependence on temperature which can be ignored by using a value of A generated from the mean profile. In addition, if $\bar{b}$ and $\bar{r}$ are generated from the same sample used to generate the other parameters, then

$$\bar{b} = \bar{b}_t$$

With these simplifications plus a substitution of Eq. (2) for r, Eq. (1) can be written for the entire sample as

$$B = S_b A^T \{AS_b A^T + S_e\}^{-1} AB_t \qquad (3)$$

where B denotes the matrix resulting from the individual b's. Since the desire of this study is to compare various alternatives, the rms error is required. If the squared retrieval errors are denoted by the diagonal elements of S_E, then

$$S_E = BB^T - BB_t^T = S_b - BB_t^T \qquad (4)$$

Substituting Eq. (3) into Eq. (4) gives

$$S_E = S_b - S_b A^T \{AS_b A^T + S_e\}^{-1} AS_b \qquad (5)$$

which is the desired result. With Eq. (5), errors can be calculated from values of the three matrices without going through the actual retrieval. This is a significant advantage for a comparative study where many variations must be run. Another advantage is that S_e enters directly rather than as the result of a random number generator. In a comparative study with even moderately-sized samples, differences due to the sequence of random numbers frequently mask real differences. Finally, the major disadvantage of Eq. (5) (that it has small errors due to approximations such as the single value of "A") does not affect a comparative study because all alternatives are affected equally.

6. RESULTS

Table 1 gives values derived from the diagonal elements of S_E. Elements of S_E were generated for each of the 40 TOVS pressure levels (see Weinreb et al., 1981) and these were used to produce rms errors in terms of thickness temperatures for each of the nine 100 mb layers between 1000 and 100 mb. The rms values for the 100 mb layers were then averaged to obtain a single value for each of the various combinations of channels and noise that were tried. Table 1 confirms expectations in that it shows that reducing the instrument noise, narrowing the weighting functions, and increasing the number of channels, all increase the retrieval accuracy. In addition, Table 1 provides information about the relative effects of the various parameters. For example, it shows that a seven channel instrument with narrow weighting functions produces results similar to those obtained from a 22 channel instrument with normal weighting functions.

Although Table 1 provides basic information, it is difficult to detect patterns. Tables 2 - 4 help to illustrate some of the relationships present in Table (1). Table 2 was constructed by selecting a noise level such as 0.25. For this level of instrument noise, the retrieval error for the normal weighting function width was determined to be 1.9. Then a retrieval error of 1.9 was found in the column of errors for the narrow weighting function. For this retrieval error, the instrument noise was determined to be 2.5 Finally, the second noise level of 2.5 was

divided by the first noise level of 0.25 to obtain the ratio of 10. Thus, narrowing the weighting function width by a half has the same effect as reducing the noise by a factor of 10 at that combination. As Table 2 shows, the improvement is a strong function of the noise level.

Two other tables were constructed in a similar manner. In Table 3, the number of channels was doubled and the weighting function width was kept constant. Thus, it gives the change in noise that has the same effect as doubling the number of channels. In Table 4, the change from the seven to the 11 channel instrument, rather than doubling the channels, is evaluated.

The advantage of Table 2 is that the ratios turn out to be relatively independent of the latitude, season, and number of channels. At the same time, Table 2 shows that the ratio is a strong function of the noise. At the low noise level of 0.25, the ratio averages about nine but at higher noise levels the ratio drops. For example, at a noise level of 1.0, the ratio drops to 4.5. This behavior is consistent with expectations since, at high noise levels, noise is the major limitation to accuracy and the other effects can be expected to be small. At the same time, when noise is low, the other factors limit accuracy and changes in noise have a relatively small effect.

Table 3 shows that doubling the number of channels is roughly as effective as halving the noise in increasing retrieval accuracy. This table also shows that, as noise increases, noise becomes more important in determining the final accuracy, but the effect is not as great as it is in Table 2.

Table 4 is similar to Table 3. The major difference is that it shows that channel number is not as important as the channel characteristics. The addition of the four 4.3 μm channels produced more improvement than did the addition of the seven 15 μm channels.

When all the factors are considered, the results show that, at present values of the various parameters, weighting function width has the largest effect on noise, probably because the other parameters are more easily changed and have been more nearly optimized. The number and type of channel is the next most important parameter and noise, at present noise levels, is the least important. While the channel width is the largest single effect, the other factors are significant.

While these results provide useful guidelines, they should not be used in place of trade off analysis for specific instruments. One example of the danger in applying generalizations is shown in Table 1. Generally, the combination of 11 channels produced more accurate results than did the 14 channel combination. It is, however, important to note that this trend vanished when the instrument noise went to zero.

7. SUMMARY AND CONCLUSIONS

When different satellite instruments are considered, they seldom differ in only one of the several factors which affect retrieval accuracy. This study provides some general guidelines for evaluating the various effects when several factors are involved. The study also demonstrates the need for evaluations of specific instruments if accurate results are desired. This is because some of the effects on accuracy are the result of the specific channel combinations used in this study. Finally, a comparison of a subset of several factors involved in a specific case may result in misleading conclusions and even the selection and building of an instrument that provides less than optimal performance. While narrowing weighting functions had the largest single effect on accuracy, it is clear that noise levels, and the number and location of sounding channels have effects on retrieval accuracy which can't be ignored.

REFERENCES

Chahine, M. T., 1979: Derivation of clear-column temperature profiles with high vertical resolution and accuracy. (COSPAR) Remote sensing of the atmosphere from space, Pergamon Press, Oxford and New York, 129-135.

Smith, W. L., H. M. Woolf, C. M. Hayden, D. Q. Wark, and L. M. McMillin, 1979: The TIROS-N operational vertical sounder. Bull. Am. Meteorol. Soc. 60, 1177-1187.

Uddstrom, M. J., and D. Q. Wark, 1984: private communication.

Weinreb, M. P., and D. S. Crosby, 1982: Optimization of spectral intervals for remote sensing of atmospheric temperature profiles. Remote Sens. Environ., 2, 193-201.

Weinreb, M. P., H. E. Fleming, L. M. McMillin, and A. C. Neuendorffer, 1981: Transmittances for the TIROS operational vertical sounder. NOAA Technical Report NESS 85, Environmental Science Information Center (D822) Environmental Data and Information Service, National Oceanic and Atmospheric Administration, U. S. Department of Commerce, 6009 Executive Boulevard, Rockville, MD 20852, 60 pp.

Westwater, E. R., and O. N. Strand, 1968: Statistical information content of radiation measurements used in indirect sensing. J. Atmos. Sci., 25, 750-758.

Table 1.

	Noise Factor	Error (°K) 7 ch Normal	7 ch Narrow	14 ch Normal	14 ch Narrow	11 ch Normal	11 ch Narrow	22 ch Normal	22 ch Narrow
Jan. Polar	0	1.8	1.1	1.2	0.7	1.2	0.8	0.9	0.3
	0.25	1.9	1.2	1.7	1.0	1.6	1.0	1.4	0.9
	0.50	2.0	1.3	1.9	1.1	1.8	1.1	1.6	1.0
	1.00	2.2	1.5	2.1	1.3	2.0	1.3	1.9	1.2
	2.00	2.5	1.8	2.3	1.6	2.3	1.6	2.1	1.4
	3.00	2.7	2.0	2.5	1.8	2.5	1.8	2.3	1.6
	4.00	3.0	2.2	2.7	2.0	2.6	2.0	2.4	1.8
Jan. Midlatitude	0	1.8	1.2	1.3	0.7	1.6	0.8	1.2	0.4
	0.25	1.9	1.3	1.8	1.1	1.7	1.1	1.5	0.9
	0.50	2.1	1.4	1.9	1.2	1.8	1.2	1.7	1.1
	1.00	2.3	1.5	2.2	1.4	2.0	1.3	1.8	1.2
	2.00	2.5	1.8	2.4	1.6	2.3	1.6	2.1	1.4
	3.00	2.7	2.0	2.6	1.8	2.5	1.7	2.3	1.6
	4.00	2.9	2.2	2.7	2.0	2.6	1.9	2.4	1.7
Aug. Polar	0	1.3	1.0	1.1	0.6	1.2	0.7	0.9	0.4
	0.25	1.5	1.0	1.4	0.9	1.3	0.8	1.2	0.7
	0.50	1.6	1.1	1.5	1.0	1.5	0.9	1.3	0.8
	1.00	1.8	1.3	1.7	1.1	1.6	1.1	1.5	1.0
	2.00	2.1	1.5	1.9	1.4	1.9	1.3	1.7	1.2
	3.00	2.3	1.7	2.1	1.5	2.0	1.5	1.9	1.3
	4.00	2.5	1.9	2.3	1.7	2.2	1.6	2.0	1.4
Aug. Midlatitude	0	1.4	0.9	1.0	0.6	1.2	0.6	0.9	0.3
	0.25	1.5	0.9	1.4	0.8	1.3	0.8	1.2	0.7
	0.50	1.6	1.1	1.5	0.9	1.4	0.9	1.3	0.8
	1.00	1.8	1.2	1.7	1.1	1.5	1.0	1.4	0.9
	2.00	2.0	1.5	1.9	1.3	1.7	1.2	1.6	1.1
	3.00	2.1	1.6	2.0	1.5	1.9	1.4	1.7	1.2
	4.00	2.2	1.8	2.1	1.6	2.0	1.5	1.8	1.3

Table 2. Noise ratios for equivalent performance (one-half filter width)

Noise factor = 0.25

	7	14	11	22
Jan. Polar	10	10	8	8
Jan. Midlatitude	8	12	12	10
Aug. Polar	8	8	8	8
Aug. Midlatitude	8	10	10	12

Noise factor = 0.5

	7	14	11	22
Jan. Polar	6	7	6	6
Jan. Midlatitude	7	7	7	8
Aug. Polar	5	6	6	6
Aug. Midlatitude	6	6	6	8

Noise factor = 1.0

	7	14	11	22
Jan. Polar	4	4.5	4	4.5
Jan. Midlatitude	4.5	5.0	4.5	4.5
Aug. Polar	3.5	4.0	4.0	4.5
Aug. Midlatitude	4.0	4.5	4.0	4.5

Table 3. Noise ratios for equivalent performance (double the channel number)

Noise factor = 0.25

	7-14 Normal	7-14 Narrow	11-22 Normal	11-22 Narrow
Jan. Polar	2	3	2	2
Jan. Midlatitude	2	3	2	2
Aug. Polar	2	2	2	2
Aug. Midlatitude	2	2	2	2

Noise factor = 0.5

	7-14 Normal	7-14 Narrow	11-22 Normal	11-22 Narrow
Jan. Polar	1.5	2	1.7	1.5
Jan. Midlatitude	1.7	2	2	2
Aug. Polar	1.5	2	2	1.5
Aug. Midlatitude	1.5	2	2	2

Noise factor = 1.0

	7-14 Normal	7-14 Narrow	11-22 Normal	11-22 Narrow
Jan. Polar	1.5	1.7	1.5	1.5
Jan. Midlatitude	1.5	1.5	1.7	1.5
Aug. Polar	1.5	1.7	1.5	1.5
Aug. Midlatitude	1.5	1.5	1.5	1.5

Table 4. Noise ratios for equivalent performance (add the four 4.3 μm channels)

Noise factor = 0.25

	7-11 Normal	7-11 Narrow	14-22 Normal	14-22 Narrow
Jan. Polar	3	3	2.7	2
Jan. Midlatitude	1.5	2	4	2
Aug. Polar	2	3	3	3
Aug. Midlatitude	4	2	4	3

Noise factor = 0.5

	7-11 Normal	7-11 Narrow	14-22 Normal	14-22 Narrow
Jan. Polar	2	2	2	1.5
Jan. Midlatitude	2.7	2.7	2.7	2.0
Aug. Polar	2.0	2.0	2.0	2.0
Aug. Midlatitude	1.5	3.0	3.0	2.0

Noise factor = 1.0

	7-11 Normal	7-11 Narrow	14-22 Normal	14-22 Narrow
Jan. Polar	1.7	1.7	2.0	1.5
Jan. Midlatitude	2.0	1.7	2.5	2.0
Aug. Polar	1.7	2.0	2.0	1.5
Aug. Midlatitude	2.5	2.0	3.0	2.0

SURFACE ALBEDO OVER THE SAHEL FROM METEOSAT RADIANCES

Bernard Pinty(*), Gérard Szejwach(**) and Jacques Stum(*)

(*) L.A.M.P., University of Clermont II, Aubière, France
(**) L.M.D., Ecole Polytechnique, Palaiseau, France

1. INTRODUCTION

Knowledge of surface albedo is of fundamental importance in climatic studies and modeling. In a recent paper, Henderson-Sellers and Wilson (1983) have indicated that the required accuracy in surface albedo data must be 0.05 for all land surfaces over usual GCM grid mesh (General Circulation Climate Models).

In this paper, we are following a quasi-experimental type approach which includes surface measurements in addition to satellite data and model. Our method is used to discuss the possibility of deriving sahelian surface albedoes from Meteosat radiances. The additional measurements are surface global radiation measurements routinely provided by the AGRHYMET network (WMO Bulletin, 1980)

2. METHOD DESCRIPTION

The proposed method is based on simultaneous measurements of satellite radiance (L_S) and surface global radiation (E_G). Over a flat homogeneous terrain with Lambertian albedo α, these two parameters can be related by the following equation :

$$L_S = E_S/\pi \left(\alpha_a + \alpha T(\theta_0)\ T(\theta_V)/(1 - \alpha\ \alpha_S)\right) \qquad (1)$$

where E_S is the solar irradiance, α_S and α_a the spherical albedo and intrinsic reflectance of the atmosphere respectively, $T(\theta_0)$ and $T(\theta_V)$ the total transmission factor for the solar zenith angle θ_0 and the zenithal viewing angle θ_V, respectively.

With these definitions, the surface global radiation E_G is given by Equation (2) :

$$E_G = E_S\ T(\theta_0)/(1 - \alpha\ \alpha_S) \qquad (2)$$

In the following we are dealing with geographical areas where θ_0 and θ_V are close to each other, therefore Eq.(1) can be parameterized as follows :

$$\pi\ L_S \simeq C + A\ \alpha + B\ \alpha^2 \qquad (3)$$

where $A = E_G{}^2/E_S$, $B = -\ \alpha_S\ A$, $C = \alpha_a\ E_S$.

In our application, A is derived from surface measurements provided by the AGRHYMET Office, B and C are computed from a parameterized formulation of a standard model as suggested by Tanré et al. (1979).

3. TEST OF THE METHOD

To test the method, observations done on 2 July 1979 over the sites of Dori (14.05°N, 0°), Ouagadougou (12.42°N, 1.5°W) and Fada-Ngourma (12.06°N, 0.4°E) in Upper Volta have been used. In each case, surface albedo was computed for various solar angles, experimental and computed values of E_G, α_a and α_S.

Site	Time (GMT)	θ_0°	θ_V°	ψ°	E_S (W m^{-2})	E_G (W m^{-2})	α_a	α_S	$\bar{\alpha}$
Dori	1100	14	16	49	1287	866	0.053	0.122	0.354 ± 0.005
	1130	10	—	24	1309	880	0.054	—	
	1200	9	—	17	1311	882	0.054	—	
	1230	13	—	46	1292	869	0.053	—	
Ouagadougou	1100	14	14	49	1287	877	0.053	0.122	0.265 ± 0.002
	1130	11	—	21	1304	895	0.055	—	
	1200	11	—	14	1301	899	0.056	—	
	1230	16	—	37	1278	890	0.054	—	
Fada-Ngourma	1100	15	14	46	1281	835	0.053	0.122	0.257 ± 0.008
	1130	11	—	21	1301	849	0.055	—	
	1200	11	—	13	1302	850	0.056	—	
	1230	15	—	39	1282	838	0.054	—	

Table 1. *Mean surface albedoes estimated from Eq.(3) over three different sites. Data are for 2 July 1979.*

Definitions : θ_0 = *solar zenith angle,* θ_V = *satellite viewing angle,* ψ = *relatif azimuthal angle,* E_S = *solar irradiance at the top of the atmosphere,* E_G = *surface global radiation,* α_a = *intrinsic atmospheric reflectance,* α_S = *spherical albedo,* $\bar{\alpha}$ = *mean surface albedo.*

A time of our investigation, the AGRHYMET Office only delivers in routine the mean daily value of E_G. In this application, the diurnal cycle of E_G is assumed to be represented by a cosinus law, in order to estimate E_G at local times corresponding to Meteosat observations.

The results are summarized in Table 1 for the three considered sites. In this application, satellite radiances have been spatially averaged over an area of size ≃ 25 10^8 m^2. Note that Meteosat digital counts within the visible channel (0.4 - 1.1 µm) have been converted into radiances over the whole spectrum with an appropriate conversion factor of 1.71 (W m^{-2} str. per count 8-bits).

The absolute value shown in Table 1 has not been compared since no other independent data set exists corresponding to this time and spatial scale. However, we can notice that the north-south albedo gradient varies in the expected fashion. Because of the scale representativity of E_G which is about (1 - 2) 10^5 m in clear sky conditions, only one measurement of surface global radiation allows the estimation of albedoes over this given area. It is important to note that the spatial scale of the derived albedo is compatible with climatic requirements.

4. SENSITIVITY STUDY

The variability of the derived albedo has been investigated as a function of E_G, α_S and α_a. *Results of this sensitivity study are shown in* Fig. 1.

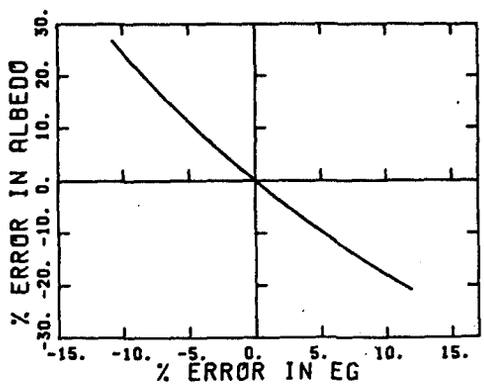

Fig.1a. *Relative error in surface albedo versus the relative error in surface global radiation. The curve is computed using values at the site of Dori on 2 July 1979.*

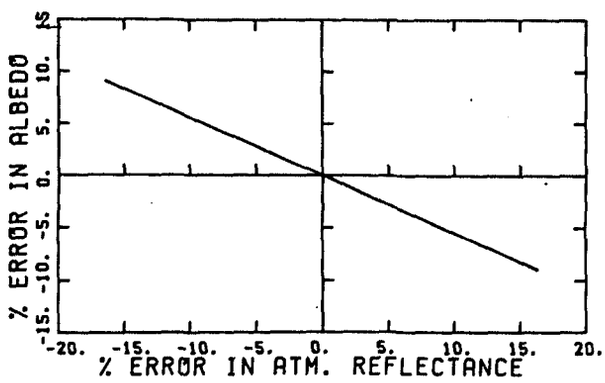

Fig.1b. *As in Fig.1a except for intrinsic atmospheric reflectance* α_a.

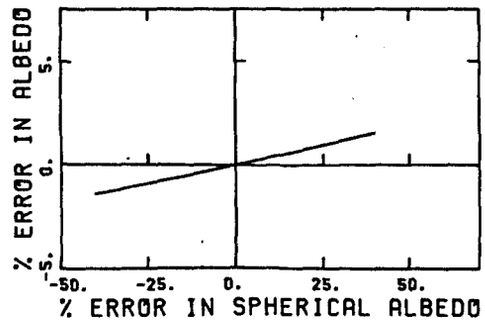

Fig.1c. *As in Fig.1a except for spherical albedo* α_S.

It appears, for instance, that an uncertainty of 5 % in the derived albedo can be induced by either an error of 3 % in E_G, or 10 % in α_a, or 100 % in α_S. These results show that the quality of the surface albedo is mainly dependent upon the uncertainty in surface global radiation. This indicates that accurate measurements of E_G are desirable.

5. ALBEDO ESTIMATE AT A GCM GRID SCALE

The spatial scale involved in the present method is compatible with general circulation model grid scale. Use of an average value of radiance ($\langle L_S \rangle$) and its variability (σ_{L_S}) within a given region can be made to infer the expected attainable accuracy (σ_α) on the average derived albedo ($\langle \alpha \rangle$) at a GCM grid scale.

Under the required conditions for the application of the method, the following approximated relationship is obtained :

$$\sigma_\alpha / \langle \alpha \rangle = \sigma_{L_S} / \langle L_S \rangle \; \pi / A \; \langle L_S \rangle / \langle \alpha \rangle \; (1 - 4 \, \alpha_S \, \langle \alpha \rangle)^{-1/2} \qquad (4)$$

Eq.(4) relates the surface albedo standard deviation to that of the radiance. The error in satellite inferred albedo involved by the use of satellite radiance is illustrated in Fig. 2.

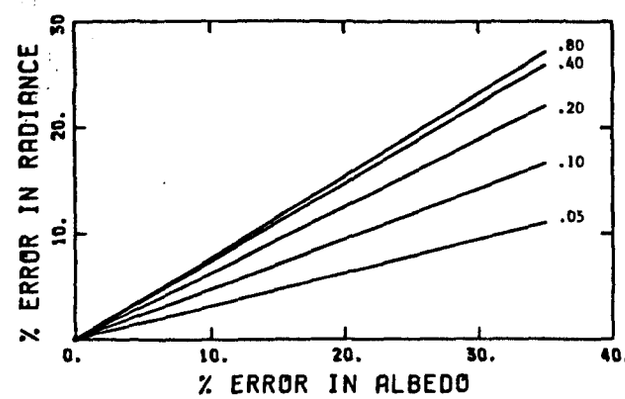

Fig.2. *Relative error in surface albedo versus relative error in radiance for different albedo values.*

Fig.2 indicates, for instance, that if we want to estimate a surface albedo within 20 % for $\langle \alpha \rangle$ equals 0.2, the required accuracy on the radiance has to be 12 %. According to Koepke (1982) the actual conversion factor used to get unfiltered Meteosat radiances is known with an uncertainty of about 6 % and this leads to uncertainties of

10 % to 20 % for typical land and ocean albedo respectively.

6. SUMMARY AND CONCLUSION

A method has been developed to infer surface albedo from measurements of surface global radiation and satellite radiances.

A sensitivity study of the method shows that an error of 5 % in surface albedo is attainable either with an error of 100 % in spherical albedo, or 10 % in intrinsic atmospheric reflectance, or 3 % in surface global radiation, or 3 % - 4 % in radiance.

The main interest of this method is to permit an estimate of albedoes over an area corresponding to the grid mesh of GCM (1 - 4) 10^{10} m^2. In the studied case, the method has been applied with Meteosat data and routine measurements of the mean daily surface global radiation. The only knowledge of the mean daily value has limited the application of the method to a clear sky day (optical depth about 0.3), since the surface global radiation as function of local time must be deduced from the daily mean. However, as long as instantaneous surface global radiation is available, the method is applicable under cloudless conditions with optical depth less than 0.75.

ACKNOWLEDGMENTS

The authors would like to express their appreciation to the Directors and personnel at L.M.D. and L.A.M.P. laboratories. We are indebted to AGRHYMET Office which supplied surface data. Also, we are grateful to Drs D.Ramond, C. Boutin and H. Isaka for their supports and encouragements. Special thanks are due to Dr. Y. Pointin for helpful discussions.

We thank C. Baraduc for typing the manuscript and J. Squarise for editing aid.

REFERENCES

Henderson-Sellers, A. and M.F. Wilson, 1983 : Surface albedo data for climatic modeling. Rev. Geoph. and Space Phys., 21, 1743-1778.

Koepke, P., 1982 : Vicarious calibration in the solar spectral range by means of calculated radiances and its application to Meteosat. Appl. Opt., 21, 2845-2854.

Tanré, D., M. Herman, P.Y. Deschamps and A.de Leffe, 1979 : Atmospheric modeling for space measurements of ground reflectances, including bidirectional properties. Appl. Opt., 18, 3587-3594.

W.M.O. Bulletin, 1980 : Vol. XXIX, n°2, 117-119.

INVESTIGATION OF SURFACE ALBEDO VARIATIONS OVER WEST AFRICA FROM METEOSAT

Bernard Pinty(*); Gérard Szejwach and Michel Desbois(**)

(*) L.A.M.P., University of Clermont II, Aubière, France
(**) L.M.D., Ecole Polytechnique, Palaiseau, France

1. INTRODUCTION

Climatic studies, Charney (1975) for instance, have stressed the necessity of a good knowledge of surface albedo in the understanding of the Sahelian drought. Rockwood and Cox (1978) or Norton et al.(1979) have published surface albedo maps for this region, using SMS and ATS 3 satellite data.

We present here a new technique developed in order to determine surface albedo values at a climatic scale over Western Africa using METEOSAT measurements.

The method is tested using test-sites values obtained from simultaneous satellite and ground data. Surface albedo maps are then derived and discussed.

2. ALBEDO ESTIMATE

2.1 Technique description

The proposed technique is based on the estimate of the reflectance ratios between several pairs of neighbouring areas.

For an area (i), the effective spectral radiance is given by the following equation (Slater, 1980) :

$$L_{\lambda s,i} = 1/\pi \; E_{\lambda,i} \; \rho_i(\lambda) \; \tau_i(\lambda) + L_{\lambda d,i} \qquad (1)$$

where $L_{\lambda s,i}$ is the spectral radiance measured by the sensor, $E_{\lambda,i}$ is the surface spectral irradiance, $\tau_i(\lambda)$ the spectral atmospheric transmittance, $\rho_i(\lambda)$ the surface spectral reflectance and $L_{\lambda d,i}$ the spectral atmospheric path radiance.

For two neighbouring areas (i) and (j) observed during a whole day under similar atmospheric conditions, we can assume that $\tau_j(\lambda) = \tau_i(\lambda) + \varepsilon_{i,j}(\lambda)$.

Therefore $L_{\lambda s,j}$ and $L_{\lambda s,i}$ are related by Eq. 2

$$L_{\lambda s,j} = \frac{E_{\lambda,j}}{E_{\lambda,i}} \frac{\rho_j(\lambda)}{\rho_i(\lambda)} L_{\lambda s,i} + L_{\lambda d,j} \; F(\lambda) - \frac{E_{\lambda,j}}{E_{\lambda,i}} \frac{\rho_j(\lambda)}{\rho_i(\lambda)} L_{\lambda d,i} \; F(\lambda) + 1/\pi \; E_{\lambda,j} \; \rho_j(\lambda) \; \varepsilon_{i,j}(\lambda) \; F(\lambda) \qquad (2)$$

where $F(\lambda)$ is the sensor spectral response.

With the following hypothesis : 1) $E_{\lambda,i} = E_{\lambda,j}$ (the surface global radiation is identical for the two areas at the considered scale $\lesssim$ 150-200 km) 2) the spectral reflectance variation with respect to λ satisfies Eq. 3,

$$\frac{\partial(\rho_j(\lambda)/\rho_i(\lambda))}{\partial \lambda} = 0 \qquad (3)$$

We can derive Eq.(4) :

$$L_{s,j} = \frac{\rho_j}{\rho_i} L_{s,i} + \int_{\lambda_1}^{\lambda_2} L_{\lambda d,j} \; F(\lambda) \; d\lambda - \frac{\rho_j}{\rho_i} \int_{\lambda_1}^{\lambda_2} L_{\lambda d,i} \; F(\lambda) \; d\lambda + 1/\pi \int_{\lambda_1}^{\lambda_2} E_{\lambda,j} \; \rho_j(\lambda) \; \varepsilon_{i,j}(\lambda) \; F(\lambda) \; d\lambda \qquad (4)$$

where λ_2 and λ_1 are the upper and lower wavelength limits of the sensor response, respectively.

In Equation 4, the contribution of the fourth term and its diurnal variation is negligible. Since we can assume that ρ_j/ρ_i and the spatial difference of sky effects (second + third terms) are constant during the day, then the reflectance ratio ρ_j/ρ_i can be derived from a linear regression between the respective radiances $L_{s,j}$ and $L_{s,i}$ measured during a diurnal cycle. Similarly, reflectance ratios ρ_i/ρ_k, ρ_k/ρ_l ..., can be obtained by considering other pairs of adjacent areas until coverage of the considered climatic region is completed. The absolute reflectance values of each area can then be obtained from the knowledge of one only of the reflectances considered in the series of reflectance ratios.

Since very little data is available concerning the bidirectional properties of the region investigated in this study, we will assume that the surface is a Lambertian reflector and from now on we will consider that the derived reflectance values are representative of the surface albedoes.

2.2 Technique validation

The proposed technique has been applied to METEOSAT data for February 18 to July 2, 1979. We first independently derived the (50 km x 50 km) surface albedo around three test-sites : Dori (14.05° N, 0°), Ouagadougou (12.42° N, 1.5° W) and Fada-Ngourma (12.06° N, 0.4° E) in Upper Volta following the method described by Pinty et al. (1984). These values (Table 1) will be now referred as reference albedoes.

To test the proposed method, we computed the surface albedoes of the test-sites using the ratio technique. The three reference values are used successively to initiate the process. Results are presented in Table 2.

Test-sites	February albedo	July albedo
Dori (1)	0.380	0.354
Ouagadougou (2)	0.307	0.265
Fada-Ngourma (3)	0.226	0.257

Table 1. *Reference surface albedoes.*

	Dori		Ouagadougou		Fada-Ngourma	
	Feb.	Jul.	Feb.	Jul.	Feb.	Jul.
Dori	0.380	0.354	0.271	0.274	0.220	0.261
Starting position	*	*				
Ouagadougou	0.430	0.342	0.307	0.265	0.249	0.252
Starting position			*	*		
Fada-Ngourma	0.390	0.349	0.279	0.270	0.226	0.257
Starting position					*	*
$\bar{\alpha}$	0.402 ± 0.020	0.348 ± 0.005	0.283 ± 0.017	0.269 ± 0.004	0.233 ± 0.014	0.257 ± 0.004

Table 2. *Test-results of the ratio technique. (symbols * indicates the considered reference in each case).*

Results indicate that the ratio technique gives a consistent albedo estimate for each location. On February 18, a discrepancy is observed between the sites of Ouagadougou and the two other sites. However, the observed discrepancy between results derived from the ratio technique and the reference value remains within the uncertainty involved in the estimate of the reference value.

Figure 1 represents the albedo map for February 18, of the northern Upper Volta obtained using the ratio technique with Fada-Ngourma as a reference value. White squares correspond to regions where the technique is not applicable due to cloud contamination for instance. It can be noted that results are consistent despite the large spatial variability of derived albedoes between the test-sites.

3. RESULTS

3.1 Surface albedo maps

Surface albedo maps were derived using the ratio technique for February 18 and July 2, 1979 over the Northwestern part of Africa (Fig. 2a and 2b). Each square represents an average albedo value over 20 x 20 pixels (approximately 100 km x 100 km). "Albedo" refers to reflectances integrated over the Meteosat sensor response (0.4 - 1.1 μm). Values range from 0.18 to 0.6, the highest value being located over Central and Northeastern part of the maps. A latitudinal gradient can be observed south of 20°N while a well marked west-east gradient is also observed north of 18°N.

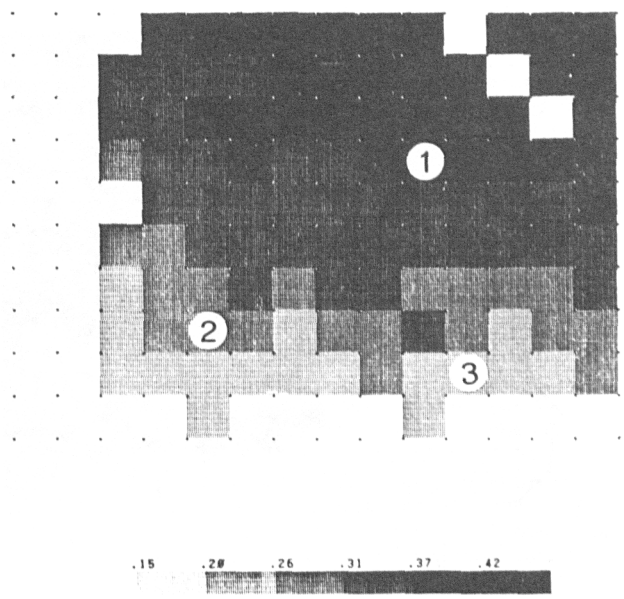

Fig.1. *Albedo maps for February 18, 1979 of the northern Upper-Volta. Sites identification: 1 - Dori ; 2 - Ouagadougou ; 3 - Fada-Ngourma.*

The general pattern of the July surface albedo map agrees reasonably well with the map derived by Rockwood and Cox (1978) and Norton et al.(1979). The major difference occurs over Sahara where our values are somewhat higher than the ones previously derived. This difference can be explained by the difference between the various sensors involved in these studies.

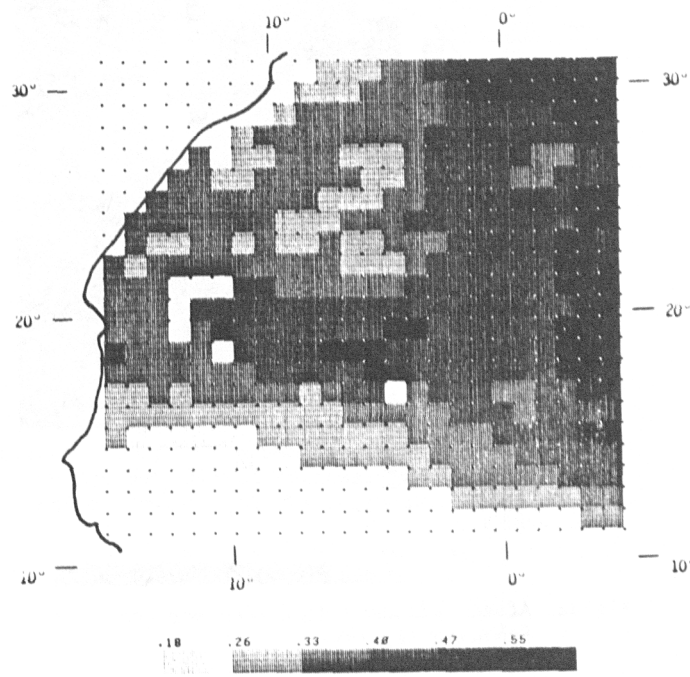

Fig.2a. *Surface albedo map for February 18, 1979.*

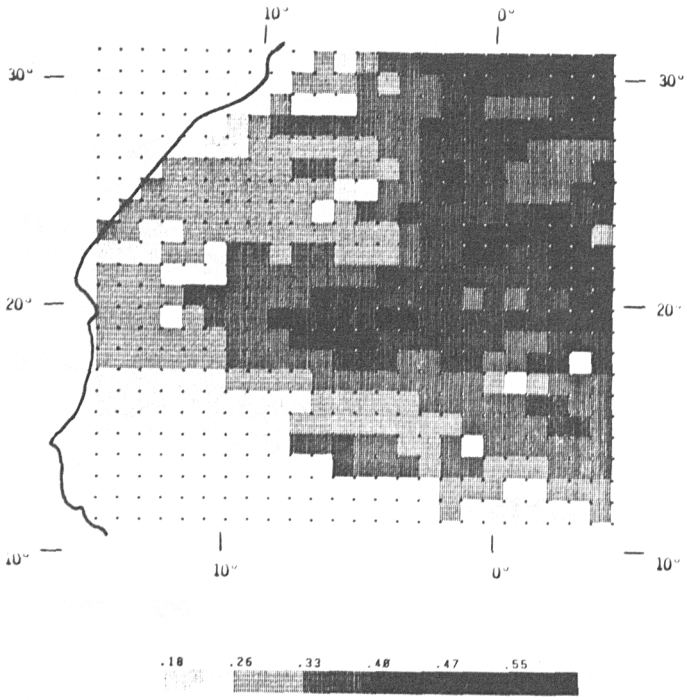

Fig.2b. *Surface albedo map for July 2, 1979.*

Figures 3a and 3b present the albedo standard deviation σ_ρ computed for each 20 x 20 pixels area as described by Pinty et al. (1984).

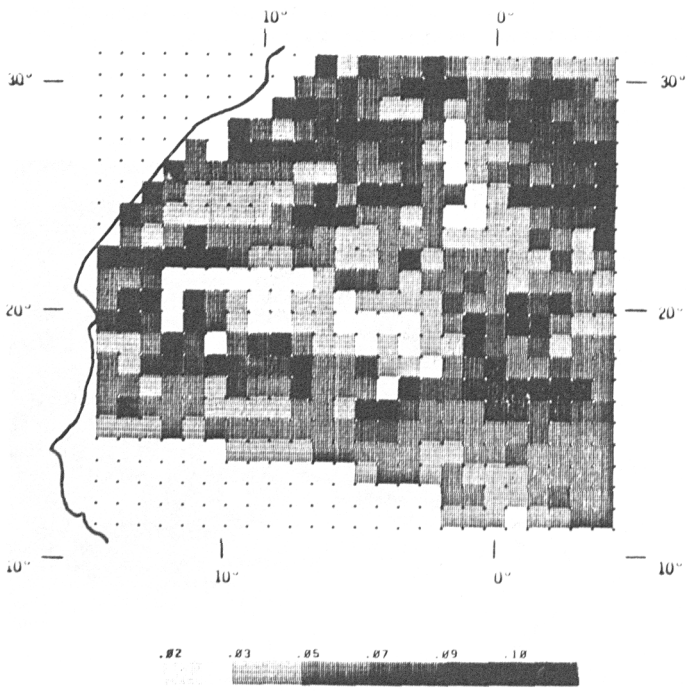

Fig.3a. *Albedo standard deviation map for February 18, 1979.*

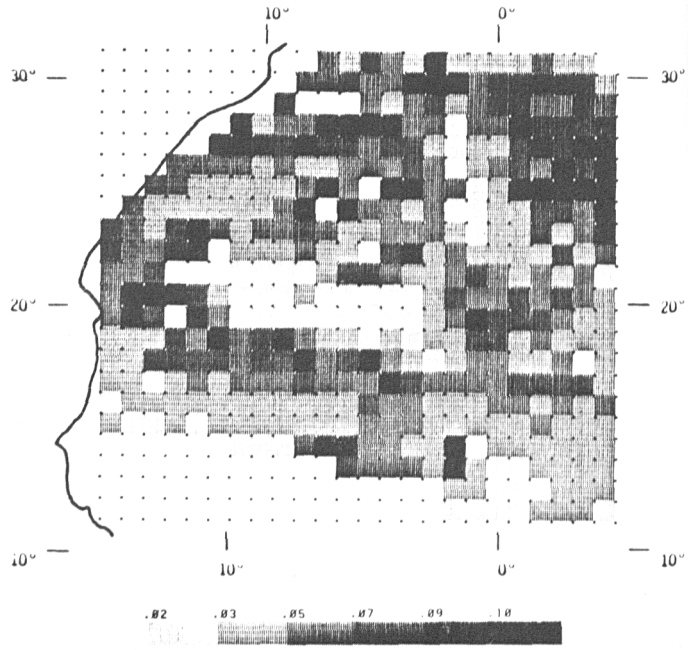

Fig.3b. *Albedo standard deviation map for July 2,1979.*

These maps for February and July show similar patterns particularly in regions of high desert albedo ($\rho \gtrsim 0.35$). Values obtained for σ_ρ range from 0.02 to 0.15. In most cases, high albedo values are associated to low standard deviations. The fact that we observe a good correlation between both maps indicates that for the considered scale (100 km x 100 km) the natural heterogeneity of the surface albedo does not vary significantly.

These maps represent also a good quantitative estimate of the expected accuracy attainable for the albedo at the climatic scale with Meteosat sensor.

3.2 Seasonal albedo change

Figures 4a and 4b present the albedo variation in per cent between February 18 and July 2, 1979.

$$SV(\%) = (\rho_{Jul.} - \rho_{Feb.})/\rho_{Feb.} 100 \qquad (5)$$

Fig. 4a corresponds to positive values of SV with two distinct regions of albedo increase between July and February. The first one is located in the Sahel ($\sim$ 15°N, 5°W) where this significant increase reaches 40 % over swamps and lakes regions. The second increase, in the Sahara desert, is much weeker (less than 10 %) and since no appreciable seasonal change can be expected in this region, this increase is certainly related to the uncertainties associated to our technique.

The well-known general decrease in albedo over the Sahel between the dry season (February) and the wet season (July) is clearly depicted in Fig. 4b. The largest values (over 25 %) are found near the western regions ($\phi \gtrsim 10°W$) associated to a large east-west gradient. Over the central eastern part of the Sahel region, the mean seasonal change remains smaller than 20 %.

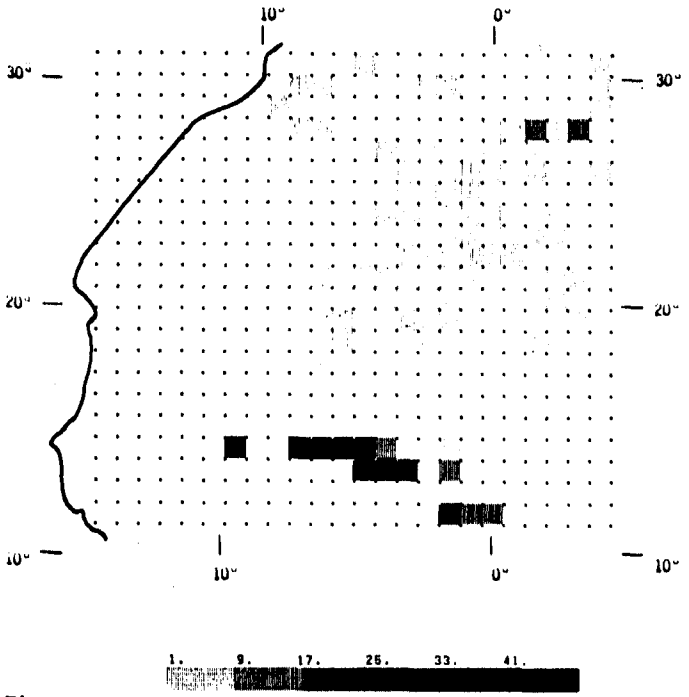

Fig.4a. *Positive change (percent) in surface albedo between July 2 and February 18, 1979.*

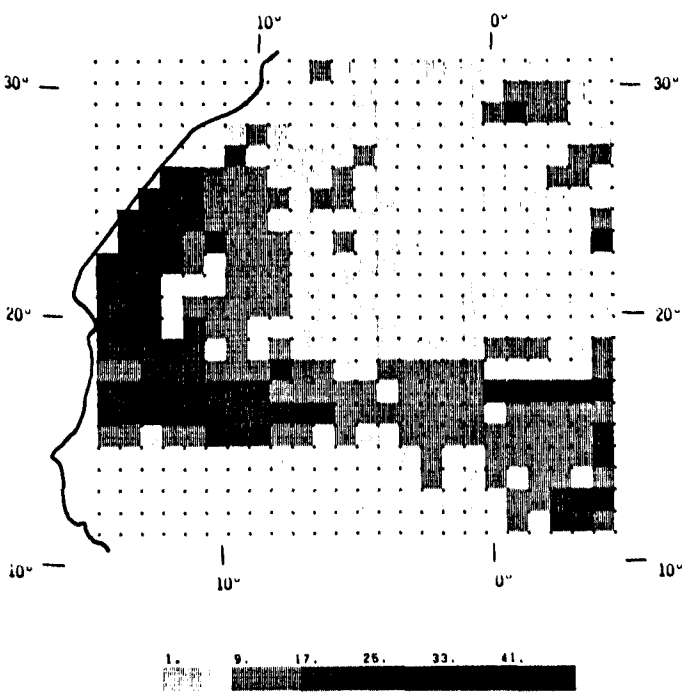

Fig.4b. *Negative change (percent) in surface albedo between July 2 and February 18, 1979.*

4. CONCLUSION

A technique has been developed and tested to infer surface albedo values for 100 km x 100 km areas (corresponding to the climatic scale) from Meteosat data.

The technique requires several measurements over the same region during one day. Its application is limited to clear sky conditions and necessitates the knowledge of at least one surface reference point. The method has been tested for several reference test-sites and albedo maps were derived for two days during the dry and wet seasons respectively, over the Northwestern part of Africa.

The general seasonal change related to the growth of vegetation with the onset of the wet season has been quantitatively estimated. A significant decrease of albedo between February and July has been observed west of 9°W and south of 18°N. The largest changes (over 25 %) occur along 14°W over Senegal and Western Mauritania.

5. ACKNOWLEDGMENTS

The authors would like to express their appreciation to the Directors and personnel at L.M.D. and L.A.M.P. laboratories. We are indebted to AGRHYMET Office which supplied surface data. Also, we are grateful to Drs D. Ramond, C. Boutin, I. Rasool and H. Isaka for their supports and encouragements. Special thanks are due to R. Pejoux for his assistance in programing.

We thank O. Guillot and C. Baraduc for typing the manuscript and J. Squarise for editing aid.

6. REFERENCES

Charney, J.G., 1975 : Dynamics of deserts and drought in the Sahel. Quart. J. Roy. Met. Soc., 101, 193-202.

Norton, C.C., F.R. Mosher and B. Hinton, 1979 : An investigation of surface albedo variations during the recent Sahel drought. J. Appl. Met., 18, 1252-1262.

Pinty, B., G. Szejwach and J. Stum, 1984 : Surface albedo from Meteosat and global radiation measurements. Proc. Amer. Soc. Atm. Rad., (in press).

Rockwood, A.A. and S.K. Cox, 1978 : Satellite inferred surface albedo over northwestern Africa, J. Atmos. Sci., 35, 513-522.

Slater, P.N., 1980 : Remote sensing. Optics and optical systems. SIMONETT, Adison Wesley Publishing Company, 575 p.

C.4

A CASE STUDY ON THE APPLICATION OF GEOSYNCHRONOUS SATELLITE INFRARED DATA TO ESTIMATE SOIL MOISTURE

Robert H. Woodward[1], Peter J. Wetzel, and David Atlas

Goddard Laboratory for Atmospheric Sciences
NASA/Goddard Space Flight Center, Greenbelt, MD 20771

[1]and General Software Corporation, Landover, MD 20785

1.0 INTRODUCTION

Recently, researchers have demonstrated the capabilities of GOES imagery to infer surface properties including soil moisture. Vieillefosse and Favard (1978) utilized infrared and visible geosynchronous imagery to identify the influence of sensible heat, wind, surface roughness, and topography on the thermal inertia of bare soil. Polansky (1982) employed a boundary layer model in conjunction with surface temperature difference images obtained from GOES-IR data to infer moisture availability, thermal inertia, atmospheric heat flux, and total evaporation in areas small enough to be meteorologically homogeneous. Using a similar technique, Carlson et al. (1984) found significant correlations between moisture availability inferred from GOES-IR imagery and antecedent precipitation index (API). Wetzel et al. (1984; hereafter referred to as WAW) proposed an approach to develop a technique that infers root zone soil moisture on regional or continental scales from GOES-derived surface temperatures. Their approach requires an archive of GOES surface temperature data at known soil moisture and wind speed which is used to account for horizontal variations in vegetation and soil characteristics. Each of these approaches make use of the fact that the amount of soil moisture has a strong influence on the temperature of the earth's surface, and that other interfering effects on surface temperature such as wind speed, surface cover variations, season, etc. must be removed or accounted for.

The work reported here is a follow-up of the study by WAW. However because no GOES surface temperature archive is available at present, it is necessary to draw upon alternative data sources to provide the information needed to separate the soil moisture signal from interfering effects on surface temperature. In this study, independent data on relative vegetation biomass, geostrophic wind speed and surface dewpoint are incorporated into a statistical relationship between observed surface temperature and antecedent precipitation index (API) for a six day case in July 1978 over Kansas and Nebraska. The following section discusses the method of analysis which was chosen. Section 3 describes data sources and methods of processing. Finally, results of the analysis are presented and discussed.

2.0 BACKGROUND

Soil moisture plays an important role in influencing the diurnal march of surface temperature. Liquid water filling soil pores increases the soil's thermal conductivity and heat capacity. More importantly, evapotranspiration of water from the soil controls the partitioning of available surface energy between latent and sensible heat. Enhanced soil moisture results in greater evaporative cooling of the surface and a subsequent decrease in the sensible heat available for distribution to the atmosphere. One should expect the effect of soil moisture to be most apparent in the morning when surface temperatures are changing most rapidly in concert with the rapid warming of a still shallow boundary layer. In the afternoon the boundary layer is deeper, the sensible heat is distributed through a greater depth and the surface temperature changes only slowly. At night, surface evaporation usually becomes negligible or surface condensation may occur and the effect of soil moisture on the surface temperature becomes negligible.

The strong relationship between soil moisture and the surface temperature progression during the morning was confirmed by Carlson and Boland (1978) and WAW. In the latter study, it was concluded that the mid-morning temperature slope, dT_s/dS where T_s is surface temperature and S is the absorbed solar radiation, is especially sensitive to soil moisture. However they found that this parameter is also strongly affected by wind speed, vegetation biomass, and roughness length, and to a lesser extent by a number of other surface and atmospheric parameters which were subsequently neglected in their analysis. To isolate the soil moisture information in the surface temperature signal, one must obtain an independent measurement for each parameter which affects surface temperature. As mentioned, the GOES parameter dT_s/dS was found to be optimally sensitive to soil moisture. A similar parameter, the slope change at sunrise, d^2T_s/dt^2, was shown to respond most strongly to wind speed. To remove the interference from vegetation biomass and roughness as well as variations in near-surface soil characteristics, a procedure was proposed in which the GOES measurements are normalized by reference values obtained at known wind speed and soil moisture, yielding:

$$A = (d^2T_s/dt^2)/(d^2T_s/dt^2)_{ref}$$

$$B = (dT_s/dS) \ / \ (dT_s/dS)_{ref}$$

Least squares fit techniques were employed on a model generated data set to characterize both A and B as functions of soil moisture and geostrophic wind speed. Thus, one can eliminate geostrophic wind speed from the ensuing set of two equations and solve for soil moisture. This approach was found to be subject to the least error for relatively dry soil conditions with sparce vegetation.

To become operational the technique proposed by WAW requires an extensive library of reference values to normalize the GOES observations. Apart from the difficulty in producing such a reference library, one must also consider the loss of accuracy introduced into the procedure by

measurement errors in the reference values. In place of the above normalizing procedure, this paper explores the application of multiple linear regression to deduce relationships between the GOES temperature slope (dT_s/dS) and other independent measurements not obtained from GOES. For wind, an in situ computation of the surface geostrophic wind speed is used. Vegetation cover is measured using a satellite derived green leaf biomass index obtained from two channels on TIROS-N. Both of these derived parameters have the advantage of continuous coverage over the surface, but suffer the disadvantage of an uncertain physical relationship with the surface temperature. This necessitates for a statistical, rather than a more physical algorithm to infer soil moisture. Procedures for obtaining these data are described in the next section. When GOES-IR imagery is used to derive dT_s/dS one must also consider absorption of solar and terrestrial radiation by the atmosphere. Therefore, to extract soil moisture information from the GOES imagery, dT_s/dS must be adjusted to account for interference from atmospheric moisture as well as wind speed and biomass.

Given an adequate set of measurements of the desired variables, and assuming all the parameters affecting the surface temperature slope act independently of each other, a two step regression scheme can be implemented to estimate soil moisture. The two step procedure is indicated since the goal is to estimate soil moisture, while the physical cause-and-effect relationship is between the morning slope parameter and all other variables including soil moisture:

1. Generate a regression equation to diagnose the surface temperature slope parameter which accounts for the effects of all the pertinent variables except soil moisture. This produces an equation of the form:

$$(dT_s/dS)' = b_o + \Sigma\, b_i\, K_i \qquad (1)$$

The observed scatter about this regression line is then ideally only a function of soil moisture. Coefficients K_i represent functions of geostrophic wind speed, biomass, and atmospheric moisture and b_i are regression coefficients.

2. Regress the residuals of the temperature slope (the difference between the observed temperature slope and that computed by eq. (1)) against soil moisture yielding:

$$m = c_o + c_1\, \{dT_s/dS - (dT_s/dS)'\} \qquad (2)$$

where m is a function of soil moisture which is linearly related to temperature slope, and c_0 and c_1 are regression coefficients.

Assuming the regression coefficients are stable, soil moisture can be determined at any location by observing K_i, and dT_s/dS and solving eqs. (1) and (2) in succession.

3.0 DATA ACQUISITION AND PROCESSING

Observations of relevant parameters from Southeastern Nebraska and Eastern Kansas spanning a six day period (July 24 to July 29, 1978) were incorporated into a case study data base. This case provided several advantages for extracting statistical relationships with general applicability. The period was precipitation-free and largely cloud-free, and the study area contained a wide range of soil moisture and vegetation cover. On the other hand, there is an inherent disadvantage when extracting statistical relationships from observations collected over consecutive days. Statistical theory requires successive observations to be independent. Since meteorological parameters typically occur in temporal regimes, it is difficult to satisfy the independent sampling requisite when collecting data at fixed locations over successive days.

The synoptic meteorology of this case was dominated by a progression of dry frontal zones traversing the region on July 26 and July 29. Data from July 26 were not included in the regression analyses since low-level advection of relatively cool and dry air associated with the frontal passage had a substantial impact on dT_s/dS. The temperature slope was derived from differences in images several hours apart and the effects of rapidly changing meteorological conditions on dT_s/dS are difficult to assess. Also, WAW showed that cold advection significantly affected the morning surface temperature changes.

The data base consisted of variables representing temperature differential (dT_s), soil moisture, water vapor, wind speed, and biomass. To permit regression analyses, all observations were interpolated and analyzed at approximately 250 NOAA climatological network raingauge stations in southeastern Nebraska and the eastern two-thirds of Kansas. The processing to produce each of these variables is described below.

Infrared and visible GOES data were processed on the Atmospheric and Oceanographic Information Processing System (AOIPS) at the Goddard Space Flight Center. Full resolution digital data were obtained for the study area on each day. These images were earth located using a sophisticated navigation package. The resulting data are located to within 10 km everywhere on the image. Among the utilities available on AOIPS is a subtraction routine which was used to compute the surface temperature differential for cloud-free areas. Clouds were identified on the IR images by overlaying concurrent visible images and by "slicing off" the coldest temperatures on the infra-red image. Wetzel and Atlas (1983) reported that surface temperature remains nearly a linear function of time for much of the morning. This allowed some freedom in selecting image pairs for subtraction. AOIPS was utilized to create several subtracted images for each day of the case study. The work below used the average of brightness temperatures from two two-hour differences (1000-0800 and 1030-0830 local time). Maps of the 1000-0800 differences for this case are presented in Wetzel and Atlas (1983).

Since the atmospheric water vapor distribution, surface albedo and the sun-surface geometry were all relatively constant during the study period, the solar insolation differential (dS) was assumed to be constant. Thus the surface temperature differential was used without further processing to infer soil moisture.

A measure of soil moisture "ground truth" was required to assess the diagnostic usefulness of the temperature slope. The Antecedent Precipitation Index is perhaps the best estimate of area average soil moisture available on a regional scale (Blanchard et. al. 1981; Choudhury and Blanchard, 1983). API may be defined as:

$$(API)_i = P_i + k(API)_{i-1} \quad (3)$$

where k is a seasonally dependent depletion coefficient and P is the precipitation on day i. Daily precipitation totals for the case study were obtained from the NOAA climatological network raingauge stations. The API was computed beginning on June 1 with an initial value assumed to be zero everywhere. The recession coefficient k was set at 0.939 in June and 0.92 in July Although the soil was considered saturated at an API value of 10 cm, API was allowed to accrue to 12.5 cm. If additional precipitation resulted in API exceeding 12.5 cm, it was assumed to run off, and the API retained a value of 12.5.

To account for the effects of atmospheric moisture on infrared brightness temperatures, the surface dewpoint temperature was incorporated as a variable in the regression. Surface dewpoint has been shown to be related to vertically integrated water vapor (Smith, 1966). This approximation is in lieu of a direct surface temperature correction, currently under development, which uses sounding data to adjust long-wave transmittances. Dewpoints were interpolated to rainguage locations using a subjective analysis of the surface charts.

The regression analyses required averaged or smoothed measurements of wind speed to interface with the resolution of temperature slope measurements. Standard observations of surface wind speeds are difficult to average spatially and are often subject to localized measurement errors from obstacles or terrain. Hence, surface geostrophic wind speeds (V_g) were computed from subjectively analyzed surface pressure fields. This method produced smoothed estimates of a wind speed parameter from routinely analyzed data. For operational determination of soil moisture, Vg can also be estimated from model output in data sparce regions.

Finally, vegetaion biomass (Bm) was estimated from Tiros-N AVHRR data taken in July 1982 over the study area. The procedure, developed by Tucker (1979), combines visible and near-infrared channel radiances to produce a "greenness index" which is qualitatively related to green leaf biomass or leaf area index. Values of this index were smoothed using a one degree latitude and longitude bivariate normal smoothing function, and were then manually entered into the data set at each raingauge site.

4.0 STATISTICAL ANALYSES

Statistics were generated from the previously described data set consisting of 820 observations of soil moisture, temperature slope, geostrophic wind speed, dewpoint and vegetation biomass. The parameters were analyzed at the coordinates of the rain gauge sites for each day of the case study period. Soil moisture was represented by the square of the soil moisture deficit which is described below. Temperature slopes were calculated by averaging brightness temperatures from two two-hour difference images. This averaged temperature slope exhibited less scatter and somewhat stronger correlation with API than either of the individual two-hour differences taken separately. All statistics discussed below were generated using the Statistics Analysis System (SAS) on an IBM 370/3081 at the Goddard Space Flight Center.

The regression scheme represented by eqs. (1) and (2) requires all variables to be linearly related to temperature slope. WAW show that temperature slope is a linear function of the square of the moisture deficit:

$$m = (1 - W/W_s)^2$$

where W is the bulk root zone soil moisture content and W_s is saturation value of W (specified to be 10 cm). Values of m were computed at raingauge sites by assuming API to be related to soil moisture as follows:

$$API = 0.94W + 0.06W_s$$

This representation accounts for the moisture retained by the soil at the wilting point (i.e. that which is unavailable for evaportranspiration). The result is an expression for m in terms of API:

$$m = [1 - \{(API - 0.06W_s)/0.94W_s\}]^2 \quad (4)$$

To remove gross irregularities, m was mapped and subjectively smoothed for each day of the case study.

Fig. 1 is a scatter diagram of m as a function of temperature slope alone, with an acompanying regression line. Although the apparent scatter is large, the general trend of the relationship appears linear and is in agreement with modelling results. A significant part of the scatter in this plot is caused by variations in wind, atmospheric moisture, and vegetation biomass

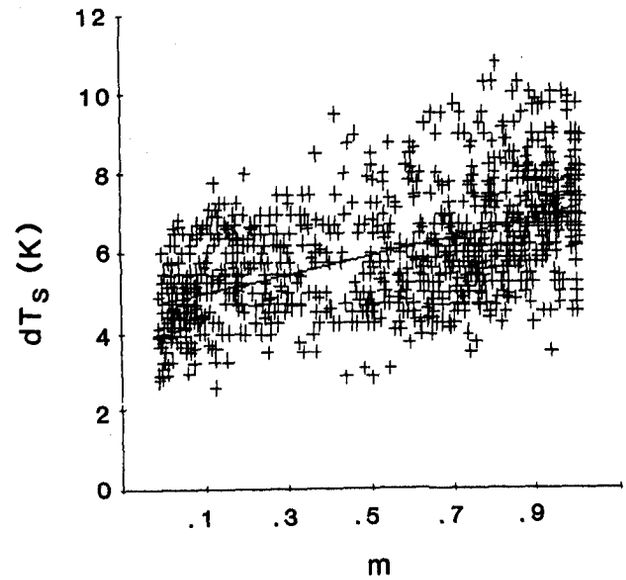

Fig. 1. Scatter diagram from complete case study showing the linear trend in the relationship of temperature slope to m (Regression line: dT_s = 4.76 + 0.24m).

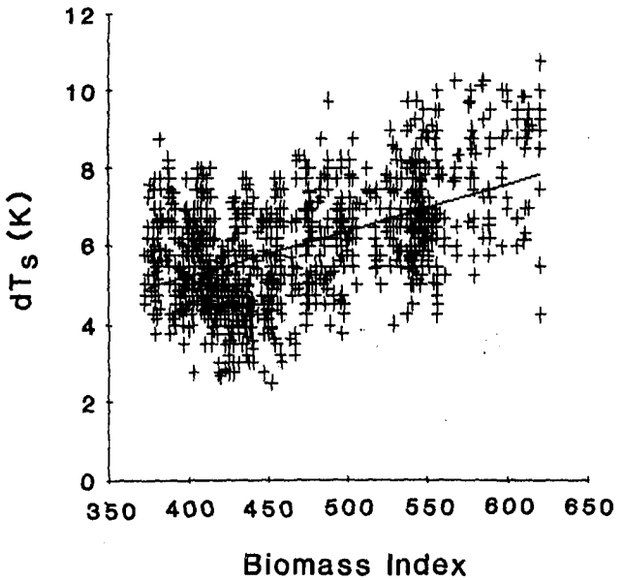

Fig. 2. Scatter diagram from complete case study showing the linear trend in the relationship of temperature slope to Bm. (Regression line: $dT_s = 0.49 + 0.012Bm$)

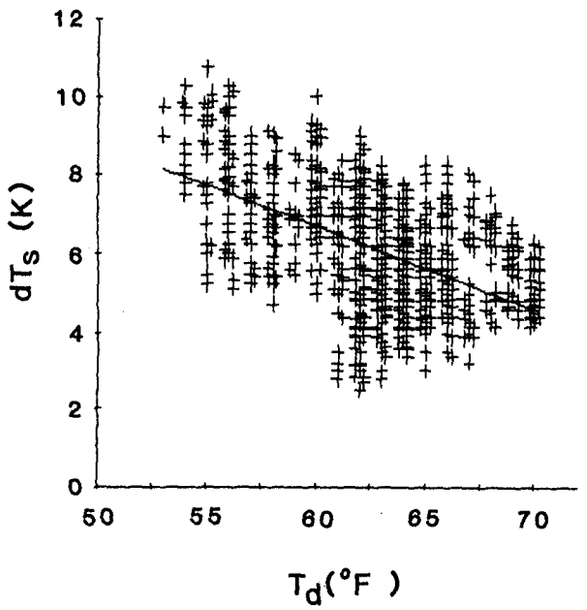

Fig. 3. Scatter diagram from complete case study showing rhe linear trend in the relationship of temperature slope to T_d. (Regression line: $dT_s = 19.02 - 0.21T_d$)

Table 1. Correlations of individual observed parameters to temperature slope derived from the entire case study (N=820).

Variable	Correlation Coefficient
V_g	0.09
ln V_g	0.10
T_d	-0.51
m	0.51
Bm	0.52
smoothed m	0.59

which also influence temperature slope. In spite of the large scatter, an analysis of variance test verifies that the regression line is significant at the 99% confidence level.

Figs. 2 and 3 show temperature slope plotted as functions of vegetation biomass index and surface dewpoint, respectively. The biomass index has an inverse relationship to vegetation biomass measured in mass per unit area. As in Fig. 1, the regression lines are statistically significant at the 99% confidence level. The general trend in these relationships are once again linear and the scatter in both plots are to some degree a result of variations in other parameters. The slopes of the regression lines are also physically realistic and in agreement with modelling tests.

Table 1 lists correlation coefficients of temperature slope to each of the parameters obtained from the entire case study period. The correlation of logarithm of geostrophic wind speed to temperature slope is also presented in this table since modelling tests suggest such a relationship (see WAW). However, correlations involving geostrophic wind speed are not significant and have a positive correlation whereas the modelling studies and physical reasoning indicate a negative correlation. Table 1 also shows the improvement in the correlation of m to temperature slope after m is smoothed.

Table 2 presents results of the multiple linear regression analysis using eq. (1) compiled from all the case study observations. Note that there is little change in regression coefficients and total correlation when geostrophic wind speed is omitted from the analysis. Partial correlations which preclude interference from other variables also show the relative unimportance of geostrophic wind speed as a predictor of temperature slope for this case. However, modelling tests suggest a strong relation between these two parameters. This inconsistancy may be a result of the coarseness of the geostrophic wind speed analysis or the lack of adequate variablity in wind speed through the case study period.

Regression analyses of eq. (2) with and without geostrophic wind speed are presented in Table 3. Inclusion of geostrophic wind speed changes the regression coefficients slightly and

Table 2. Multiple linear regression of eq. (1) with ln V_g (a) and without ln V_g (b) included as an independent variable (N=820).

	(a)	(b)
Bm slope	0.0079	0.0083
partial r	0.35	0.37
T_d slope	-0.144	-0.139
partial r	-0.36	-0.36
ln V_g slope	0.25	----
partial r	0.09	----
Intercept	10.85	10.89
total R^2	0.36	0.36

Table 3. Multiple linear regression of eq. (2) with ln V_g (a) and without ln V_g (b) included in determination of dT_s'.

	(a)	(b)
$(dT_s - dT_s')$ slope	0.1913	0.1886
Intercept	0.5399	0.5403
Total R^2	0.50	0.49
N	820	820

only marginally improves the regression fit. In spite of this, one should expect wind speeds to increase vertical mixing and to damp the temperature fluctuations at the surface. It is suspected that a broader data set would support this hypothesis. Therefore in all the following analyses the geostrophic wind speed is retained as a variable.

Fig. 4 shows m plotted as a function of the residual of the temperature slope. This plot illustrates the improvement in fit that is obtained by using the residual of the temperature slope rather than simply the temperature slope (cf. Fig. 1).

Observations from an independent data period were not available for testing the regression scheme. Therefore, independent testing of the scheme was accomplished by sequentially excluding one day at a time from the five day case study period. The regression coefficients were determined from the remaining four days and tested against data from the excluded day. This effectively produces five independent tests of the regression scheme.

The coefficients for the five periods are presented in Tables 4 and 5. Table 4 shows multiple linear regression of eq. (1) for the five periods each with one day of the case study excluded. The most notable aspect of this analysis is the lack of stability in the slope associated with the logarithm of geostrophic wind speed. Table 5 presents analysis of eq. (2) for the same periods. The regression coefficients are relatively stable with both the intercepts and the slopes varying within a narrow range.

Table 6 tabulates the results of a test in which m (observed) was regressed against m′ (predicted) for each individual day of the case study. Values of m′ were obtained from the regressions listed in Tables 4 and 5. The correlations between m and m′ are significant at the 99% confidence level for each day. July 28 has the highest R^2 (0.65) and the best one-to-one correspondence between m and m′ as evidenced by the slope (1.070) and intercept (0.05779). This day also had the least amount of cloud cover. July 29 had the worst fit between m and m′ and also the most cloud cover. On this day clouds obscured much of the area with the wettest soil thus preventing an adequate range of values. In general, the results presented in Table 6 indicate that soil moisture can be extracted with some degree of precision. However, the data may not be totally independent since the observations were collected over successive days.

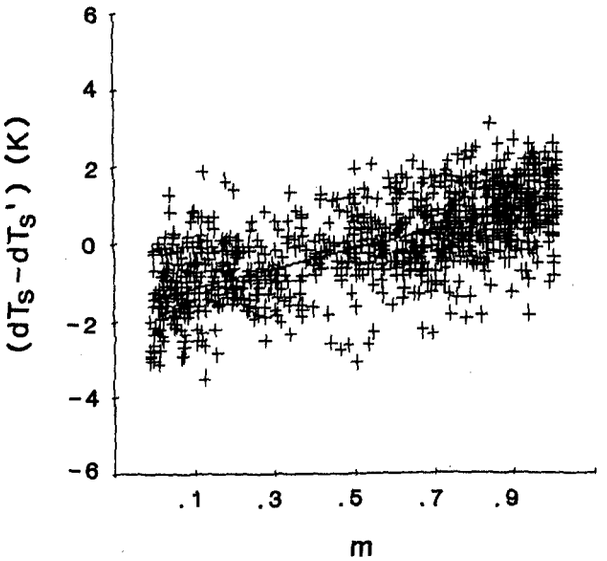

Fig. 4. Scatter diagram of residual of temperature slope as a function of m. (Regression line: $(dT_s - dT_s')' = -1.39 + 2.5m$)

Table 4. Multiple linear regression of eq. (1) after excluding observations from one day of the case study.

Excluded date	24	25	27	28	29
Bm slope	0.0078	0.0060	0.0068	0.0083	0.0091
T_d slope	-0.154	-0.226	-0.090	-0.160	-0.132
ln V_g slope	0.241	0.127	0.506	0.571	-0.0786
Intercept	11.72	17.00	7.334	11.01	10.05
Total R^2	0.45	0.38	0.25	0.39	0.40
N	694	637	621	618	710

Table 5. Linear regression of eq. (2) after excluding observations from one day of the case study.

Excluded date	24	25	27	28	29
$(dT_s - dT_s')$ slope	0.199	0.187	0.196	0.186	0.192
Intercept	0.572	0.551	0.547	0.540	0.498
Total R^2	0.47	0.53	0.56	0.46	0.46
N	694	637	621	618	710

Table 6. Linear regression comparing m′ (predicted) and m (observed) for each day of case study.

Tested date	24	25	27	28	29
m′ slope	1.063	1.406	0.8588	1.070	0.3609
Intercept	0.0666	-0.482	-0.0166	0.00578	0.554
Total R^2	0.54	0.56	0.37	0.65	0.26
N	126	183	199	202	110

Figs. 5 and 6 are subjectively analyzed maps from July 28 of observed and predicted API, respectively. Predicted values of API were calculated from regressions that excluded July 28 (Tables 4 and 5). The figures exhibit good agreement of features larger than one degree of latitude and longitude; relative maxima and minima of API are located in the same general regions. However small scale features show much less agreement. Carlson et al. (1984) found a similar pattern of agreement between predicted moisture availability and API. The lack of agreement for small scale features is expected since the observed API map represents point measurements during the convective rainfall season when precipitation can be highly variable over short distances. On the other hand, predicted API were derived from variables of lower horizontal resolution.

5.0 SUMMARY AND CONCLUSIONS

Data from Kansas and Nebraska collected during a five day case study in July 1978 are assimilated into a case study data set to extract statistical relationships that infer soil moisture. The data set includes the morning temperature change, dT_s, derived from GOES infrared images, a soil moisture variable derived from raingauge data, a satellite derived vegetation biomass index, and the observed surface dewpoint and geostrophic wind speed. All data were analyzed at the coordinates of raingauge sites. These data are selected on the basis of the modelling studies of WAW. Surface dewpoints are included to correct for the interference of atmospheric moisture to terrestrial radiation.

A two-step regression procedure is devised which first adjusts dT_s for interference from all parameters except soil moisture. The residuals obtained from this regression are then regressed against soil moisture. The variables chosen are shown to have a linear relationship to dT_s. However, V_g and dT_s are found to be poorly related. Several reasons can be forwarded for this lack of agreement. The data are not truly independent since they were obtained over successive days. Also the coarseness of the V_g analysis and the lack of variability in V_g may have obscured the relationship.

The regression procedure is tested by excluding one day of data, developing the regressions from the remaining four days, and testing the regressions on the excluded day. With the exception of the slopes associated with V_g, the regression coefficients exhibit some stability. The tests indicate that the regressions diagnose soil moisture with statistically significant precision. Maps of predicted API for July 28 show that large scale patterns of soil moisture are represented well by the regression procedure.

Further testing of the regression procedure on independent data periods are required to insure general application of the technique and refine the regression coefficients. This is especially true for geostrophic wind. It is also expected that a technique to explicitly correct infrared surface emissions for vertically integrated atmospheric moisture will improve the result.

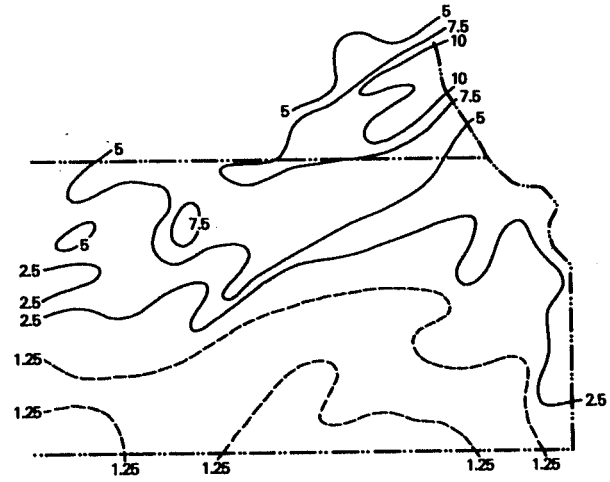

Fig. 5. Subjective analysis of observed API for the case study area on July 28, 1978.

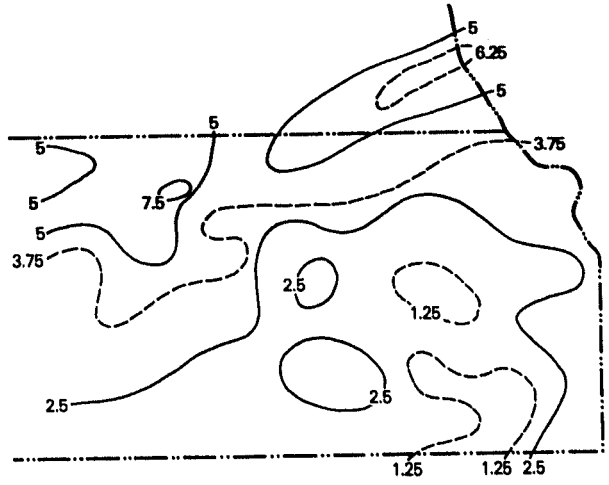

Fig. 6. Subjective analysis of predicted API for the case study area on July 28, 1978.

REFERENCES

Blanchard, B. J., M. J. McFarland, T. J. Schmugge and E. Rhoades, 1983: Estimation of soil moisture with API algorithm and microwave emission. Water Resour. Bull., 19, 767-774.

Carlson, T. N. and F. E. Boland, 1978: Analysis of urban-rural canopy using a surface heat flux/temperature model. J. Appl. Meteor., 17, 998-1013.

Carlson, T. N., F. G. Rose and E. M. Perry, 1984: Regional scale estimates of surface moisture availability from GOES satellite. Submitted to Agron. J.

Choudhury, B. and B. J. Blanchard, 1983: Simulating soil water recession coefficients for agricultural watersheds. Water Resour. Bull., 19, 241-247.

Polansky, A. C., 1982: A method for diagnosing surface parameters using geostationary satellite imagery and a boundary-layer model. Unpublished Master's Thesis, Department of Meteorology, The Pennsylvania State University.

Smith, W. L., 1966: Note on the relationship between total precipitable water and surface dewpoint. J. Appl. Meteor. 5, 726-727.

Tucker, C. J., 1979: Red and photographic infrared linear combinations for monitoring vegetation. Remote Sens. Environ., 8, 125-150.

Vieillefosse, M. and J. C. Favard, 1978: "CITHARE" thermal inertia and humidity cartography over Africa by geostationary satellite. Preprint from 29th Congress, International Astronautical Federation, Oct 1-8, Dubrovnik, Yugoslavia.

Wetzel, P. J. and D. Atlas, 1983: Inference of soil moisture from geosynchronous satellite infrared observations. Preprints, 16th AMS Conference on Agricultural and Forest Meteorology, Fort Collins, Co., 178-181.

Wetzel, P. J., D. Atlas and R. M. Woodward, 1984: Extracting soil moisture information from geosynchronous infrared surface temperature temperature data. some numerical experiments. J. Climate Appl. Meteor., (In press).

VERTICAL DISPLACEMENTS OF THE MID-TROPOSPHERIC WATER VAPOR BOUNDARY IN THE TROPICS DERIVED FROM THE VISSR ATMOSPHERIC SOUNDER (VAS) 6.7 μm CHANNEL

John Stout and Joseph Steranka
General Software Corporation
Landover, Maryland 20785

Ralph A. Petersen
NASA/Goddard Space Flight Center
Greenbelt, Maryland 20771

1. INTRODUCTION

Vertical motions in the atmosphere are difficult to measure directly. Consequently the most commonly used methods, the omega equation and the kinematic and adiabatic methods, are indirect. Over the tropical oceans, however, even these techniques are hampered by insufficient measurements of pressure, wind or temperature.

Vertical motion patterns over tropical oceans have been inferred using a variety of techniques. Downward motions have been implied from the suppression of low-level clouds observed by satellite (Shenk and Rodgers, 1978). Schoeberl and Krueger (1983) estimated vertical motion near the tropopause from the change in satellite-measured depth of the ozone layer. Patterns of 6 μm infrared water vapor absorption channels have also been associated with presumed vertical motion fields (e.g. Ramond, et.al. (1981) and Weldon (personal communication)). Rodgers, et. al. (1976) found sinking computed by the omega equation to correspond to high brightness temperature in the 6.7 μm channel of the polar-orbiting NIMBUS 5 Temperature Humidity Infrared Radiometer (THIR). Petersen, et. al. (1983) using VISSR Atmospheric Sounder (VAS) data found high brightness temperatures in regions where sinking would be expected from dynamical reasoning: in areas associated with propagating jet streaks and other locations where the upper level wind fields are convergent.

The present paper studies displacements of the top part of the atmosphere's water vapor envelope in a manner analogous to the way Schoeberl and Krueger (1983) traced movement of the bottom of the ozone layer. First we determine that measurements of the VAS 6.7 μm channel can represent the altitude of the upper boundary of the water vapor. Second we use the temporal changes of this altitude to infer patterns of rising and sinking.

2. METHOD

2.1 Concept

A strong relationship can be noted between the 6.7 μm radiance and the level of the water vapor upper boundary. The 6.7 μm channel receives all of its radiation from the layer containing the upper few millimeters of precipitable water vapor (Chesters and Uccellini, 1982). Since this layer is an order of magnitude less than the total atmospheric water content, it can be called the water vapor upper boundary. The intensity of the 6.7 μm radiation is determined to a large degree by a weighted mean of the temperature of the air in the water vapor upper boundary. In turn, in the tropics the weighted-mean temperature can be assigned a unique pressure from the mean tropical sounding. Since the actual sounding only deviates slightly from the mean, we will call this level the pressure of the water vapor upper boundary. Since radiosondes measure low amounts of moisture poorly, the actual thickness of the layer represented by the radiance is not known. Nevertheless, Chesters and Uccellini (1982) calculate that 80% of the weighting of the 6.7 μm channel is in a layer 200-300 mb thick.

In section 2.2 the relationships between the 6.7 μm channel radiance and pressure of the water vapor upper boundary are defined and their correlations are quantified. This allows the construction of topographical maps of the pressure of the water vapor upper boundary. Changes of the height of the water vapor upper boundary are then monitored over a fixed geographical area by noting observed satellite temperature and radiance decreases or increases.

2.2 Relationship of the brightness temperature to the altitude of the water vapor upper boundary.

In order to define the relationship which exists between the radiance of the 6.7 μm channel and the pressure of the water vapor upper boundary, we define a pressure P and precipitable water depth d as: d is the amount of precipitable water above P. A depth d, of 1.0 mm, for example will have a high pressure when the water vapor upper boundary is at a low altitude and vice-versa. Each depth d will have a distribution of pressure levels P. Calculations of P as a function of d are shown in Fig. 1 for the saturated and the dry mean tropical atmosphere (Jordan, 1958) and the mean of 100 clear air soundings in the Gulf of Mexico and the Caribbean during September, 1982. The moister the atmosphere, the higher the water vapor is found.

Correlations between P and the brightness temperature T^* (measured within 100 km of the sounding site) were determined for the full range of possible water vapor boundary depths at the 100 observation sites (Fig. 2). Since the correlation (0.70) is highest at d = 1.0 mm, T^* can be considered as a measure of the pressure of the first 1.0 mm of precipitable water. However, since the maximum is broad, any d between 0.5 mm and 1.5 mm may be acceptable. The broad maximum and the strength (0.70) of the correlation support the finding of Ramond, et. al. (1981) that 730 European moisture soundings in the water vapor upper boundary were well approximated as vertical translations of a standard water vapor boundary profile. Fig. 3 shows the scatter and the linear regression line relating T^* and P at d = 1.0 mm precipitable water as

$$(P - 471 \text{ mb}) = 11.17 \text{ mb K}^{-1} (T - 244.6 \text{ K}) \quad (1)$$

Since radiosondes do not measure these low amounts of moisture well, more accurate moisture measurements might yield stronger relationships.

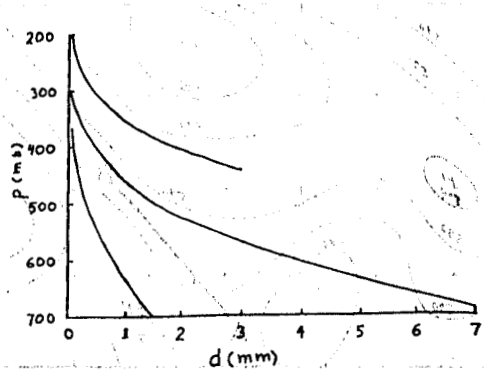

Figure 1. Precipitable water depth d accumulated above P vs pressure P. The top curve is the saturated mean tropical sounding (Jordan, 1958); the middle curve is the average for the 100 soundings used in this study; the bottom curve is the mean tropical sounding with a dewpoint depression of 30 K.

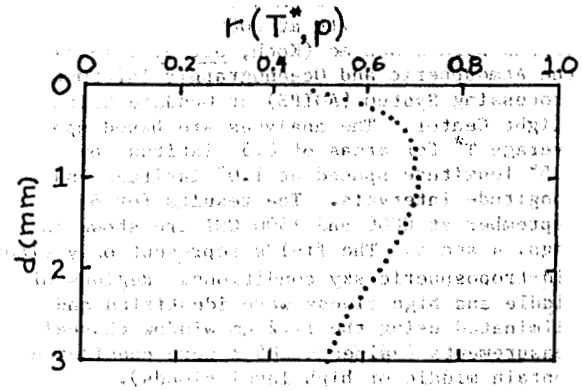

Figure 2. Precipitable water depth d accumulated above P vs r, the correlation coefficient between the 6.7 μm radiance and the pressure P, for 100 Caribbean soundings.

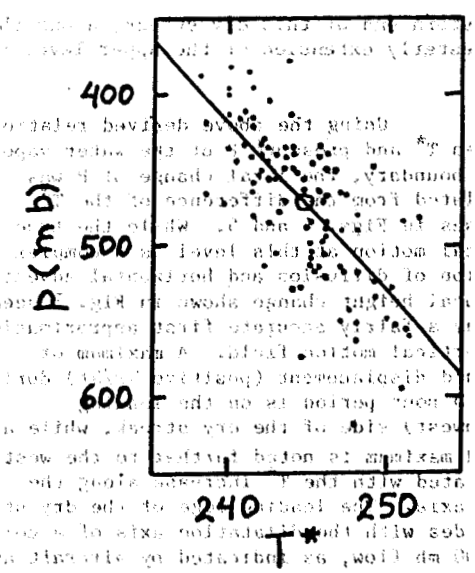

Figure 3. Scatter diagram and regression line between 6.7 μm brightness temperature T^* and pressure P above which 1.0 mm precipitable water has accumulated. Correlation coefficient is 0.70. The mean is shown by a circle.

In the following section, a sequence of 6.7 μm water vapor data are discussed. Changes of T^* are noted and related to the local change of the water vapor upper boundary height.

3. APPLICATION TO 5-7 SEPTEMBER 1982

The horizontal T^* fields of the 6.7 μm channel were analyzed for a region over the North Atlantic Ocean between 20°-40°N latitude and 35°-75°W longitude during September

1982, the 5th at 1500 GMT, the 6th at 0000 and 1500 GMT, and the 7th at 0000 GMT, using the GEMPAK Barnes scheme (Koch, et. al., 1983) on the Atmospheric and Oceanographic Information Processing System (AOIPS) at Goddard Space Flight Center. The analyses are based upon average T^* for areas of 0.5° latitude by 0.5° longitude spaced at 1.0° latitude and longitude intervals. The results for 6 September at 0000 and 1500 GMT are shown in Figs. 4 and 5. The fields represent only clear mid-tropospheric sky conditions. Regions of middle and high clouds were identified and eliminated using the 11.2 μm window channel measurements (values < 285 K were considered to contain middle or high level clouds).

The correlations shown above suggest that the T^* field can provide an adequate representation of the topography of the water vapor upper boundary. For example, the boundary is depressed (high T^*) in an elongated region on Fig. 4 found on the southern side of the major ridge on the 500 mb chart shown in Fig. 6. This dry streak moves to the southwest between the two times, and rises (cools) slightly. Large falls (T^* increases) are also observed at the western end of this dry streak, along the southwesterly extension of the upper level ridge.

Using the above derived relationship between T^* and pressure P of the water vapor upper boundary, the local change of P was calculated from the difference of the T^* analyses in Figs. 4 and 5. While the true vertical motion at this level is a complex function of diffusion and horizontal advection, the local height change shown in Fig. 7 seems to portray a fairly accurate first approximation of the vertical motion field. A maximum of downward displacement (positive $\partial P/\partial t$) during this 15 hour period is on the leading (southwest) side of the dry streak, while a second maximum is noted farther to the west, associated with the T^* increase along the ridge axis. The leading edge of the dry streak coincides with the dilatation axis of a col in the 200 mb flow, as indicated by aircraft and satellite winds. Shenk and Rodgers (1978) similarly found a dilatation axis of the 200 mb wind field near where T^* was warm (dry). The maximum of downward displacement is 1.5 μb s^{-1} (3 cm s^{-1}); the maximum of upward displacement is 1 μb s^{-1} (2 cm s^{-1}). These values are within the range of previous maximum estimates of synoptic scale vertical motion in the tropics: Yanai and Nitta (1967) have 3 μb s^{-1} for upward and downward motion, Reed and Recker (1971) have 1 μb s^{-1} for upward motion, and Holton (1979) has 0.3 μb s^{-1} for downward motion in dry systems.

Fig. 8 shows the section AB in Figs. 4, 5, and 7 throughout the period of study. Both the dry streak in T^* and the downward displacement (positive $\partial P/\partial t$) on the leading side of the dry streak appear as a consistent feature moving southwestward along the section at 3-4 m s^{-1} throughout the 45 hour period.

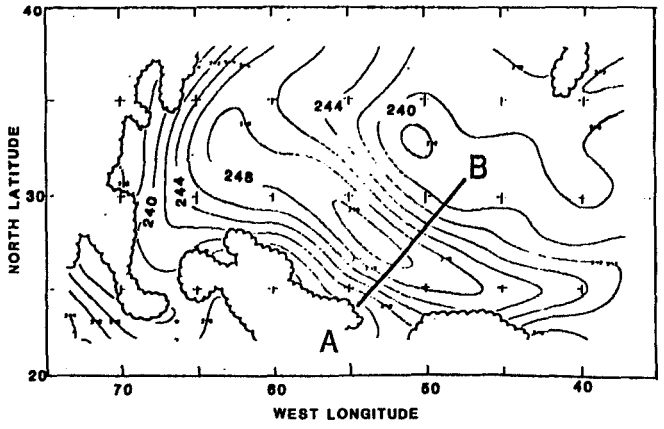

Figure 4. Brightness temperature of the 6.7 μm channel for 6 September 1982 at 0000 GMT. AB is the cross section in Fig. 8. Scalloped areas are missing data due to cloudiness. Contour intervals are 2 K.

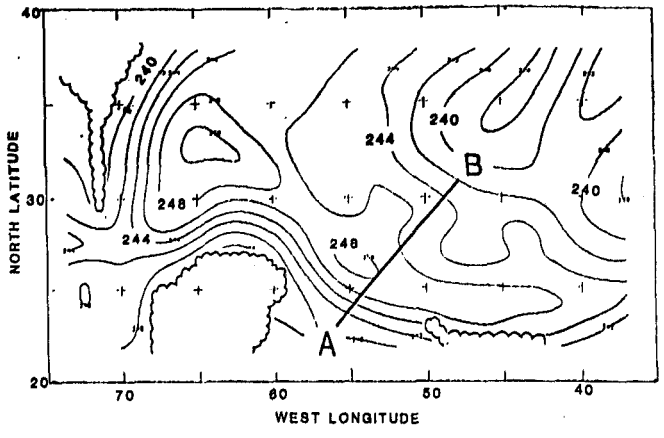

Figure 5. Brightness temperature of the 6.7 μm channel for 6 September 1982 at 1500 GMT. AB is the cross section in Fig. 8. Scalloped areas are missing data due to cloudiness. Contour intervals are 2 K.

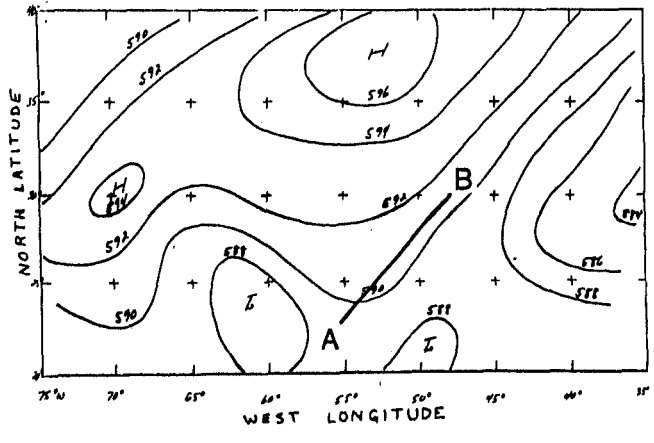

Figure 6. Analysis in 20 m intervals of the NMC 500 mb height field for 6 September 1982 at 0000 GMT. AB is the cross section in Fig. 8.

4. CONCLUSIONS.

The 6.7 μm T^* has been shown to represent the level of the upper boundary of the water vapor in the tropics. A strong (0.70) correlation was found between T^* and the level of the 1.0 mm depth of precipitable water. Topographical maps of the water vapor upper boundary derived from the 6.7 μm T^* showed physical consistency. While the topographical interpretation of the 6.7 μm T^* presented here depends on the small variability of temperature found in the tropics, the procedure might be adapted to the mid-latitudes by including temperature soundings in the method.

An approximation of the mid-tropospheric vertical motion was also obtained from the local change of the water vapor boundary. These results were consistent with the available nearby conventional upper-air data. For a more accurate vertical motion estimate, horizontal advection and diffusion should be taken into account. The vertical displacement rates found by this method, however, fall within the range of other estimates of vertical motion.

REFERENCES

Chesters, D., L.W. Uccellini and A. Mostek, 1982: VISSR Atmospheric Sounder (VAS) simulation experiment for a severe storm environment. Mon. Wea. Rev., 110, 198-216.

Holton, J.R., 1979: An Introduction to Dynamic Meteorology, 2nd Ed., New York, Academic Press, 391pp.

Jordan, C.L., 1958: Mean sounding for the West Indies area. J. Appl. Meteor., 15, 91-97.

Koch, S.E., M. desJardins and P.J. Kocin, 1983: An interactive Barnes objective map analysis scheme for use with satellite or conventional data. J. Clim. Appl. Meteor., 22, 1487-1503.

Petersen, P.A., D.A. Keyser, A. Mostek, and L.W. Uccellini, 1983: Techniques for diagnosing mesoscale phenomena affecting aviation using VAS satellite data. Preprints Ninth Conf. on Aero. and Aeron. Meteor., Omaha, Amer. Meteor. Soc., 12-17.

Ramond, D., H. Corbin, M. Desbois, G. Szejwach and P. Waldteufel, 1981: The dynamics of polar jet streams as depicted by the METEOSAT water vapor channel radiance field Mon. Wea. Rev., 109, 2164-2176.

Reed, R.J. and E.E. Recker, 1971: Structure and properties of synoptic-scale wave disturbances in the Equatorial Western Pacific. J. Atmos. Sci., 28, 1117-1133.

Rodgers, E.B., V.V. Salmonson, and H.L. Kyle, 1976: Upper tropospheric dynamics as reflected in Nimbus 4 THIR 6.7 μm data. J. Geophys. Res., 81, 5749-5758.

Schoeberl, M.R. and A.J. Krueger, 1983: Medium scale disturbances in total ozone during southern hemisphere summer. Bull. Amer. Meteor. Soc., 64, 1358-1365.

Shenk, W.E. and E.B. Rodgers, 1978: Nimbus 3/ATS 3 observations of the evolution of hurricane Camille. J. of Appl. Meteor., 17, 458-476.

Yanai, M. and T. Nitta, 1967: Computation of vertical motion and vorticity budget in a Caribbean easterly wave. J. Meteor. Soc. Japan, 45, 444-465.

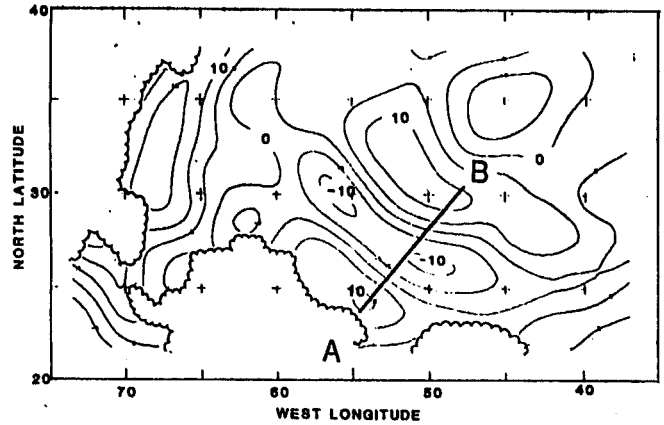

Figure 7. Analysis of the local change of the pressure of the water vapor upper boundary field for the 15 hour period 6 September 1982 from 0000 GMT to 1500 GMT calculated from the analyses in Figs. 4 and 5 using the method of this paper. AB is the cross section in Fig. 8. Scalloped areas are missing data due to cloudiness. Contour intervals are 0.5 μb s^{-1}.

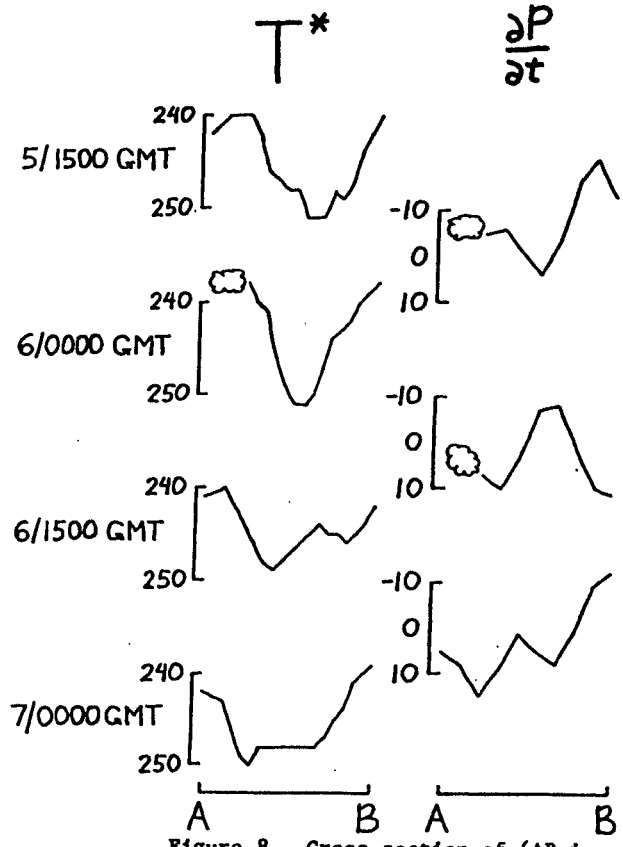

Figure 8. Cross section of (AB in Figs. 4 to 7) of T^* and $\partial P/\partial t$, the local change of the pressure of the water vapor upper boundary, across the dry streak from 5 September 1982 to 1500 GMT to 7 September 1982 at 0000 GMT. A represents 22°N, 56°W; B represents 31°N, 47°W. T^* and $\partial P/\partial t$ sections, the vertical coordinate increases downward. Scalloped areas are missing data due to cloudiness.

ON A SIMPLE METHOD FOR DETERMINING THE RELATIVE SHIFT BETWEEN THE VISIBLE AND INFRARED GOES IMAGES

by

A. A. TSONIS

Atmospheric Environment Service
4905 Dufferin Street
Downsview, Ontario M3H 5T4
Canada

1. INTRODUCTION

There have been many indications that, in general, a relative displacement between the visible and infrared GOES images exists in some data sets. This problem is probably caused by misalignments of the visible and infrared sensors of the satellite and it is usually corrected by trying to identify, be eye, some strong gradient caused by coastline features, small cumulus clouds etc. (Bellon et al., 1982). The purpose of this paper is to present preliminary results of a method which corrects this relative shift automatically.

2. DATA

The data used in this work consists of GOES visible (0.7 μm wavelength) and infrared (11.5 μm wavelength) images. After the processing, the data are presented in cartesian coordinates with a spatial resolution of 4 x 4 km. It should be noted at this point that the true spatial resolution of the sensed infrared images is 8 x 8 km. From these images 4 x 4 km resolution images have been constructed for a better resolution equivalence between the visible and infrared data. More details on this can be found in Bellon (1979). The temporal resolution of the GOES data is 30 minutes. The intensity range of the visible image is 0-63 and that of the infrared is 0-255.

3. METHOD

The employed method can be presented in two steps. In the first step the variance operator is used and in the second step the cross-correlation between two patterns is used.

Over the neighbourhood of each point (i, j) of the image, the variance operator, $\sigma^2(i, j)$, is defined as (manual of remote sensing, 1975):

$$\sigma^2(i,j) = \frac{1}{9}\sum_{k=i-1}^{i+1}\sum_{l=j-1}^{j+1}\left[f(k,l) - \bar{f}(i,j)\right]^2$$

where:

$$\bar{f} = \frac{1}{9}\sum_{k=i-1}^{i+1}\sum_{l=j-1}^{j+1} f(k,l)$$

For any point (k, l), f(k, l) is the infrared count, when the infrared image is considered, or the visible count when the visible image is considered. In other words the variance operator at each point will involve the 8 immediate neighbours.

The variance operator works on the principle that at the boundary of two different classes there is a large mix of pixel values, and so the variance is high. After the reception of the first results from the use of the variance operator, it became apparent that the main features of the image in both the visible and infrared channels give rise to high variance operator value in the boundaries of the main features. It was also observed that the position of these boundaries did not coincide in the visible and infrared images. This gave the idea that a shift between the two variance operator fields, in such a way so that the best matching is achieved, will indicate to a fair degree the actual shift between the visible and infrared images. Figures 1 and 2 are examples of variance operator fields for the visible and infrared image, respectively, over the Toronto, Ontario area on December 4, 1980 at 1600 Z. It should be mentioned that on this date and over this area the skies are mainly clear. Some clouds are also present. The geographical boundaries around the Toronto area are also indicated. The hatched areas indicate values of the variance operator greater than 8. This is an arbitrary consideration based on visual inspection of the images and their variance operator fields. It was observed that within regions that represent smooth fields (e.g. lakes, overcast, smooth land etc.) the variance operator hardly exceeds the value of eight. On the other hand, in the boundary of two different classes, this value is usually higher than eight. In any case, this value can be regarded as a limit which will separate higher from lower values and it is used for illustration purposes

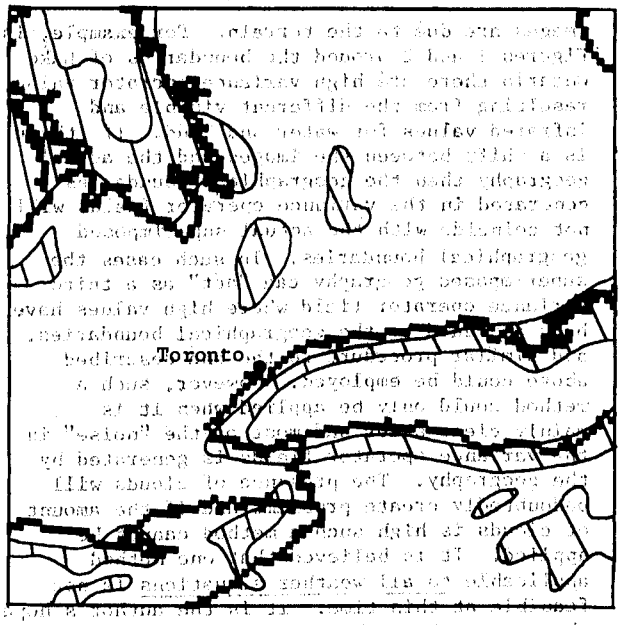

Figure 1: Variance operator field of the visible image over the Toronto area, at 16:00 Z, December 4, 1980. Hatched areas represent regions with variance operator values greater than 8. The actual geographical boundaries are also indicated.

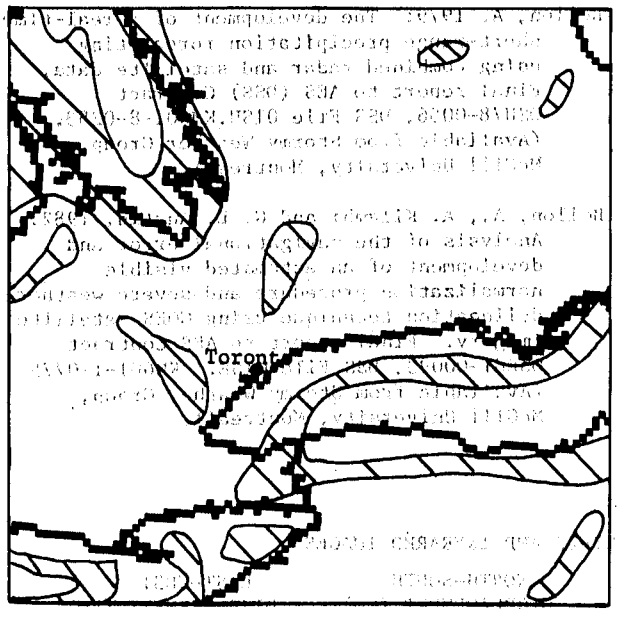

Figure 2: Variance operator field of the infrared image over the Toronto area, at 16:00 Z, December 4, 1980. Hatched areas represent regions with variance operator values greater than 8. The actual geographical boundaries are also indicated.

only. As can be observed from figures 1 and 2 the position of the boundaries is not the same on both maps. It can also be observed that there is a shift between each image and the actual geography. This problem is discussed later.

After the variance operator has been applied to both images a cross-correlation between the two variance operator fields is performed. The cross-correlation is expressed mathematically as below and indicates the degree of matching which exists between two patterns as their relative position in space is varied.

$$\gamma(x_0, y_0) = \frac{1}{N S_V S_I} \iint \left[V(x,y) - \bar{V} \right] * \left[I(x+x_0, y+y_0) - \bar{I} \right] dx\,dy$$

where:

a) $\gamma(x_0, y_0)$ is the cross-correlation coefficient between the two patterns at a spatial lag (x_0, y_0).

b) $V(x, y)$ and $I(x, y)$ are the spatial distributions of the variance operator values for the visible and infrared images.

c) $N = \iint dx\,dy$ is the area of integration

d) $\bar{V}$, $\bar{I}$ are the average values of the fields $V(x, y)$ and $I(x, y)$ over the area N.

e) S_V, S_I are the standard deviations of $V(x, y)$ and $I(x, y)$ over N i.e.:

$$S_V = \left(\iint \left[V(x,y) - \bar{V} \right]^2 dx\,dy / N \right)^{1/2}$$

The spatial lag at which the cross-correlation coefficient is maximized will indicate the displacement in the west-east (x) and north-south (y) direction. For more information on the computation of $\gamma(x_0, y_0)$ see Tsonis & Austin (1981).

4. RESULTS

Table 1 gives some preliminary results obtained according to the above procedure, over the area of Figure 1. The sky conditions are also given for each day. The north-south and west-east displacement is given in km. Positive displacements mean that the infrared image is displaced south-eastwards with respect to the visible image. The number in the parenthesis is a comparison with results obtained by Bellon (1982), who tried to navigate the visible and infrared by examining, visually, sharp coastline features etc. An apparent agreement between the two methods is rather clear. The method seems to work satisfactorily for different weather situations such as partly cloudy, cloudy or mainly clear skies. This was expected because in any case different "classes" will exist and therefore boundaries between those "classes" will be defined by the variance operator. The advantage of a method like the above presented is that visual inspection is not necessary and the navigation between visible and infrared image can be done fast and previous to any analysis of the data which will involve both

images. Since, some times, the relative shift varies even from one time step to the other (i.e. every 30 minutes), it is obvious that the use of the above method shows some advantages.

5. CONCLUSIONS

A simple method was presented for the correction of the relative shift between the visible and infrared GOES images. The method employs the variance operator and the cross-correlation between two patterns. The use of the variance operator results in a variance operator field with higher values in the boundaries of the various classes that exist in a satellite image. After that, the cross-correlation between the variance operator fields of the visible and infrared images can be used effectively to determine the spatial lag at which the best matching between the two fields is achieved. This spatial lag indicates the relative shift between the two variance operator fields and consequently between the visible and infrared images. Comparison of the results with those taken by visual inspection of the images indicates that the method appears to be very promising. It should be mentioned that the use of the variance operator is necessary because a direct cross-correlation between the visible and infrared images is not very effective. The cross-correlation is very effective when strong gradient is present and this is better achieved by using the variance operator. Finally, even though a correction of the relative shift between the two images is very important for point to point comparisons, for classification purposes etc., a correction between the shift of the images and the actual geography is always desirable. Such shifts are also present and are usually caused by satellite manouvres. Research is ongoing on this problem and some methods have been proposed. Bellon et al., 1982, for example used rain areas as determined from radar and satellite to correct for the shift, assuming the radar as "ground truth". However, if there is no rain such a method cannot be applied.

One idea which is under study is the following: Geographical boundaries could be superimposed in the satellite images. If the weather situation is mainly clear skies then most of the high values in the variance operator fields of the visible and infrared images are due to the terrain. For example, in Figures 1 and 2 around the boundaries of Lake Ontario there are high variance operator values resulting from the different visible and infrared values for water and land. If there is a shift between the images and the actual geography then the geographical boundaries generated in the variance operator fields will not coincide with the actual superimposed geographical boundaries. In such cases the superimposed geography can "act" as a third variance operator field where high values have been assigned to the geographical boundaries, and similar procedure to the one described above could be employed. However, such a method could only be applied when it is mainly clear skies and most of the "noise" in the variance operator fields is generated by the geography. The presence of clouds will undoubtedly create problems and if the amount of clouds is high such a method cannot be applied. It is believed that one method applicable to all weather situations is not feasible at this time. It is the author's hope that research on this subject will be forthcoming.

6. ACKNOWLEDGEMENTS

Many thanks are extended to Dr. G. A. Isaac for his useful comments. This research was supported by the Atmospheric Environment Service. Typing by C.M. Sguigna.

REFERENCES

Bellon, A. 1979: The development of a real-time short-range precipitation forecasting using combined radar and satellite data. Final report to AES (DSS) Contract OSU78-0056, DSS File 01SU.KM601-8-0253. (Available from Stormy Weather Group, McGill University, Montreal).

Bellon, A., A. Kilambi and G. L. Austin, 1982: Analysis of the navigational error and development of an automated visible normalization procedure and severe weather delineation technique using GOES satellite imagery. Final report to AES Contract OSE81-00093, DSS File 01SE. KM601-1-0775 (Available from Stormy Weather Group, McGill University, Montreal).

TABLE 1

RELATIVE SHIFT BETWEEN THE VISIBLE AND INFRARED IMAGES

DATE	TIME	SKY CONDITIONS	NORTH-SOUTH DISPLACEMENT (km)		EAST-WEST DISPLACEMENT (km)	
December 4, 1980	1600 Z	Mainly Clear	16	(12)	8	(10)
April 1, 1981	1800 Z	Cloudy	12	(12)	12	(10)
June 6, 1980	1730 Z	Partly Cloudy	8	(9)	12	(10)
July 23, 1980	1800 Z	Cloudy	6	(6)	8	(10)
October 13, 1981	1900 Z	Mainly Clear	6	(6)	4	(3)

Manual of Remote Sensing, 1975: Published by the American Society of Photogrammetry. 105 N. Virginia Ave., Falls Church, VA, 22046.

Tsonis, A. A. and G. L. Austin, 1981: An evaluation of extrapolation techniques for the short-term prediction of rain amounts. Atmos-Ocean, 19, 54-65.

MESOSCALE APPLICATIONS OF VAS IMAGERY

Raymond M. Zehr and Robert N. Green
Regional and Mesoscale Meteorology Branch
NOAA/NESDIS
Cooperative Institute for Research in the Atmosphere
Colorado State University
Fort Collins, Colorado

1. INTRODUCTION

The VAS (VISSR Atmospheric Sounder) instrument on the GOES satellite transmits data from twelve different channels in addition to the visible imagery. Each channel measures outgoing radiation from the earth-atmosphere system for a particular wavelength. Specific information about each channel is included in Table 1. Initial research with VAS concentrated on deriving vertical profiles of temperature and water vapor based on the observed radiances. These profiles, often referred to as retrievals, are generated routinely for real-time applications by the Cooperative Institute for Meteorological Satellite Studies (CIMSS) at the University of Wisconsin (Smith, 1983). Retrievals have been used to refine data initialization for operational numerical models (Tracton, et al, 1980). Smith, et al, (1982), demonstrated the capablility of VAS generated parameters in detecting temperature, moisture, and jet streak conditions, important to severe thunderstorm development. Dynamically consistent synoptic-scale geopotential analyses have been generated from VAS data (Lewis, et al, 1983).

Several examples of short-range forecast problems and mesoscale applications of geostationary satellite images, were presented by Purdom (1982). The more difficult problems involve thunderstorms and the analysis of the subsynoptic forcing mechanisms which control the evolution of deep convective cloud systems. The new observational data from VAS in combination with other data sources should lead to a better understanding of a variety of mesoscale phenomena.

Table 1

VAS Instrument Characteristics

Spectral Channel	Central Wavelength ($\mu m = 10^{-6} m$)	Absorbing Constituent	Weighting Function: Peak Level (mb)	Weighting Function: Representative Thickness (mb)	Weighting Function: Surface or Cloud Emission Effect
1	14.7	CO_2	40	150-10	usually none
2	14.5	CO_2	70	200-30	nothing below 500 mb
3	14.2	CO_2	300	500-10	nothing below 800 mb
4	14.0	CO_2	450	800-300	weak
5	13.3	CO_2	950	SFC-500	moderate
6	4.5	CO_2	850	SFC-500	moderate
7	12.7	H_2O	surface	SFC-700	strong
8	11.2	window	surface	----	strong
9	7.2	H_2O	600	800-400	weak at sfc
10	6.7	H_2O	450	700-250	nothing at sfc
11	4.4	CO_2	500	800-100	weak
12	3.9	window	surface	----	strong

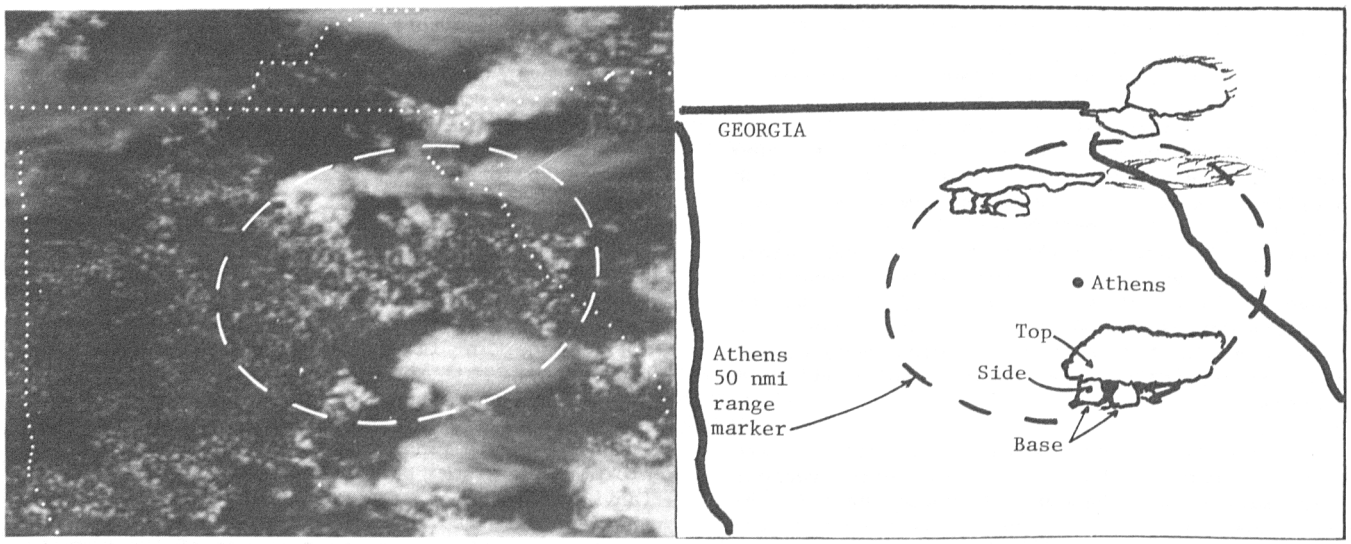

Figure 1 - GOES-East image and analysis of that image for 31 July 1977 at 2023 GMT. The thunderstorm activity may be thought of as being observed in a 3-dimensional presentation--showing their bases, sides and tops.

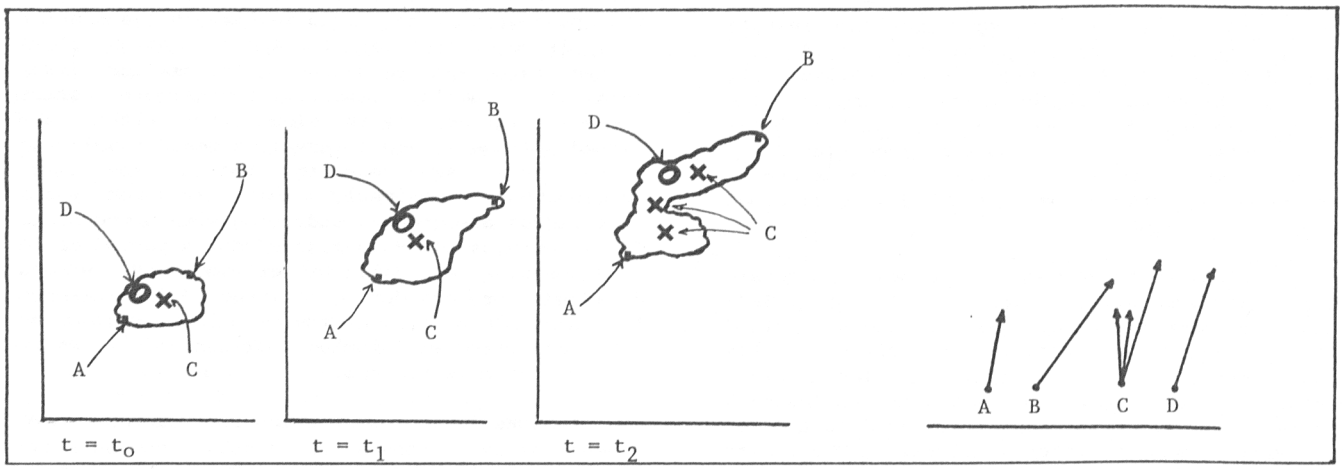

Figure 2 - Illustrative example of a cloud that grows from t_o to t_1 and then begins to decay by t_2. The possible vectors represent cloud motions determined by tracking various parts of the cloud: A (base), B (top), C (centroid), D (brightest spot).

strong low level flow, cumulus clouds move rapidly as they evolve over short time periods. Under such conditions, the top portion of a cumulus may be vertically growing while also moving in a direction that is different from its lower portion. The rapid movement and growth of the cumulus in a sheared environment can produce a confusing picture to the cloud trackers and make the determination of accurate cloud motions very difficult. With these thoughts in mind, as well as those discussed in the previous section, a new and simple method for mesoscale cloud tracking was developed for the CSU IRIS system.*

In the new method, a sequence of up to seven images are precisely land mark registered, and the area for cloud tracking is expanded to cover the entire 512 x 512 CRT picture element array. The cloud field of interest is observed in animation in an earth relative frame, and a cloud whose motion is representative of the cloud field of interest is identified. That cloud is then tracked, and its motion is used to renavigate the original sequence of images over the area of interest. All images are now re-registered and displayed in a cloud relative framework. When this re-registered image sequence is viewed in animation, the "representative cloud" (or the proper part of it) is stationary as are other clouds like it. With the mean motion having been extracted from the cloud field, variations in motion between similar clouds as well as growth, decay and shear are readily detectable. Clouds of interest are now tracked keeping in mind the points brought out in the previous section, with height determinations being made stereographically using data from both GOES spacecraft. The advantages of using stereographic means for height determination versus infrared height assignments has been discussed previously by Hasler (1981).

While the tracking of clouds in a cloud relative mode may seem the same in principal to that in an earth relative framework, it is not.

*Information on the CSU Intensive Research and Imaging System, IRIS, may be found in Green and Kruidenier (1982).

There is a very basic and fundamental difference. For now instead of following a cloud from one point to another, the function of the cloud tracker has changed. The analyst is now monitoring cloud growth and changes over a finite amount of time and assigning displacements to appropriate portions of that cloud - this is easy to do since the cloud is basically standing still and we are observing its evolution. This same function is extremely difficult to do in earth relative coordinates where a cloud is seen to rapidly translate as it changes character.

4. EXAMPLE OF RELATIVE FLOW FIELDS

While the methodology addressed thus far has focused on quantitative determinations of cumulus motions and shears in a developing severe storm environment, its application does not stop there. In cases where intense thunderstorms are developing, the renavigation may be done relative to a thunderstorm. In such cases, the flows at different levels with respect to the storm may be inspected with the hope of improving our insight into the nature of the storm's evolution. Such a study is underway for the storm which produced the Wichita Falls tornado on April 10, 1979. A GOES-East view of that storm at 6:15 pm CST is shown in figure 3a. Note the arc cloud line extending west from the storm and the flanking lines whose bases are at the level of the arc cloud line while at upper levels they extend vertically into the overshooting top area. Figure 3b shows the relative flow derived from 3 minute interval GOES-East data at low, middle and high levels with respect to the Wichita Falls storm. It is interesting to note how closely that relative flow compares to that proposed by Browning (1964) for severe storms which travel to the right of the wind, figure 4a, and storm relative proximity soundings from Maddox (1976), figure 4b.

5. TWO APPLICATIONS FOR SEVERE STORM INVESTIGATIONS

As mentioned in section 2, it is well known that vertical wind shear plays an important role in determining the character of storms that evolve in a mesoscale environment. Furthermore, recent numerical cloud modeling studies have shown the importance of vertical wind shear in the formation of rotation in growing thunderstorms (Klemp and Wilhelmson, 1978, Bleckman, 1981). However, a severe storm environment is one in which both the dynamic and thermodynamic characteristics of the atmosphere are changing on mesoscale space and time domains. This has been shown repeatedly in data from NASA's Atmospheric Variability Experiment, A.V.E. (Hill, et al, 1979). Determination of vertical wind shear in regions of growing cumulus using rapid scan satellite imagery appears to be a feasible method of studying submesoscale variations in that parameter over large areas that may encompass several states. Work is currently underway at CIRA to study variations in vertical wind shear and storm intensity using the cloud tracking methodology described in section 3.

GOES VAS (VISSR Atmospheric Sounder) has the unique ability to frequently observe atmospheric structure (sounding) and its cloud cover (visible and infrared) from the synoptic scale down to the cloud scale. Satellite sounding data's applicability for studying the severe storm environment is currently a subject of intense investigation. With VAS data, cloud cover will often make it so that no retrievals are possible. However, the clouds and cloud patterns in a satellite image or animated series of images represent the integrated effect of ongoing dynamic and thermodynamic processes in the atmosphere. Knowledge of the horizontal variation in the vertical wind shear should be able to be combined with knowledge of the thermal field from VAS in clear regions to provide very high resolution three dimensional analyses of the atmosphere. Work is also currently underway at CIRA in this area.

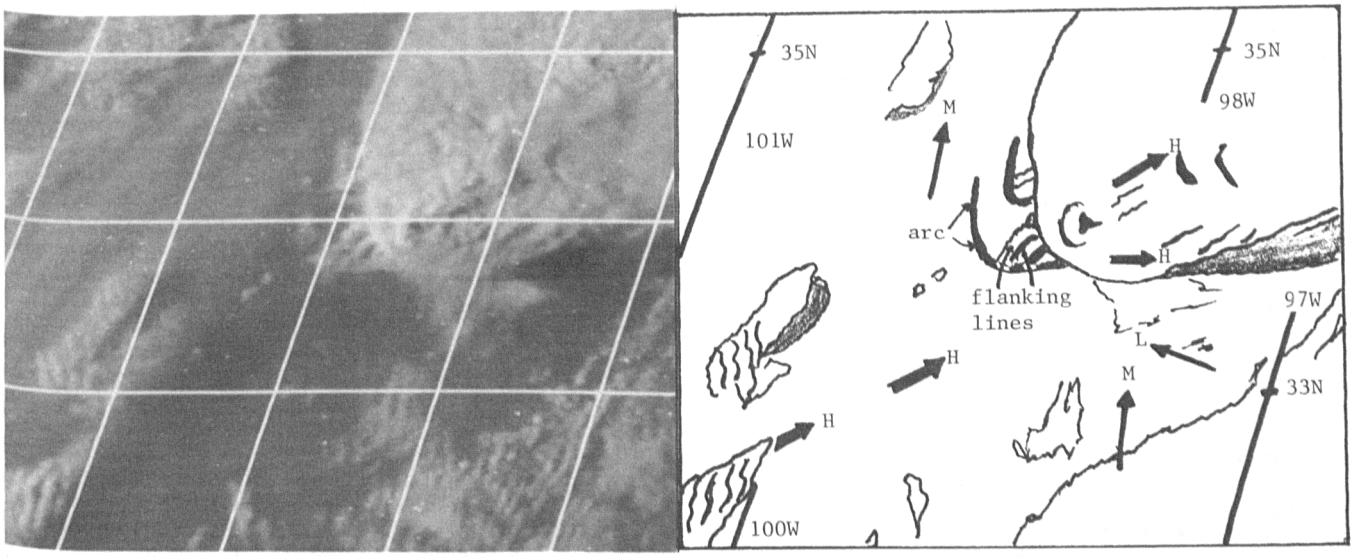

Figure 3 - GOES-East image and analysis of that image for 10 April 1979 at 6:15 pm CST. Cloud flow relative to the storm shows how cloud motions veer from low levels (≈ 105°) through middle levels (≈ 170°) to high levels (≈ 250°).

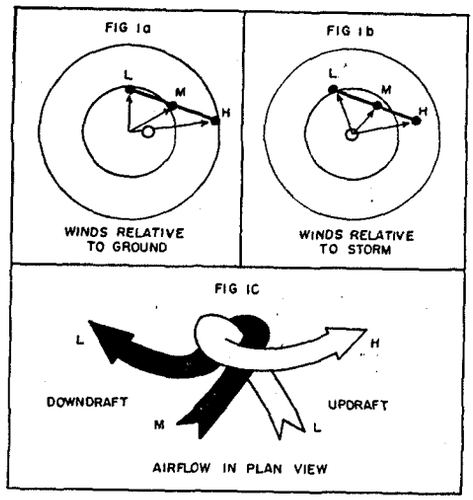

Figure 4a - (From Browning, 1964) Diagrams illustrating how the airflow within an SR storm is governed by the environmental wind field and its own direction of travel. Wind directions in the hodographs are represented as directions toward which the winds are blowing. In each case the velocity of the storm is denoted by an open circle.

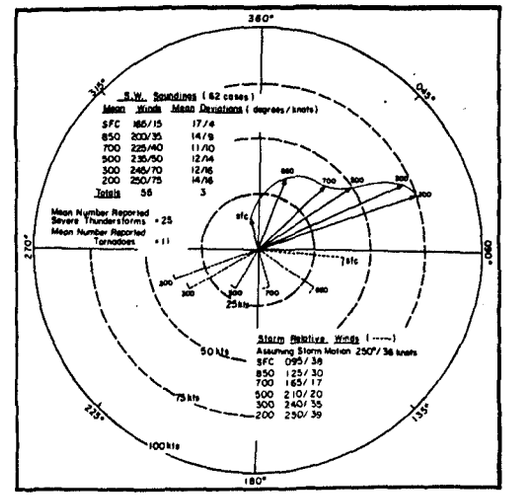

Figure 4b - (From Maddox, 1976) SW type tornado sounding mean hodograph. SW type has mean direction 210° to 235° and a mean speed > 30 kt. Also included are the computed storm relative winds, mean numbers of reported severe events, Totals Index, and mean deviation.

6. CONCLUSION

A new method in cloud tracking and observing storm development using satellite imagery in a cloud relative mode has been presented. Using this method, the function of the analyst has changed. The analyst's main function is now to monitor cloud growth and changes over a finite time period and identify portions of the cloud that are suitable for use as tracers. As we extend cloud motion studies into more complex (mesoscale) applications the analyst must be more discriminating than was previously required for estimates of large-scale flow fields.

If cloud targets are sought out in areas of cumulus shear, then through proper height identification the vertical wind shear in the vicinity of stronger storms may be defined. This has important implications for defining mesoscale regions that are favorable for the production of rotating storms. The information should also be useful in combination with GOES-VAS sounder data in constructing detailed three dimensional mesoscale analyses.

7. ACKNOWLEDGEMENTS

Main support for this work has been under NASA Grant NAGW-504. Partial support was provided by NOAA Grant NA82AA-H-00026.

8. REFERENCES

Bengtsson, L., and P. Morel, 1974: The performance of space observing systems of the First Global Experiment. The GARP Working Group on Numerical Experimentation, Rep. No. 6 (July 1974), WMO, Geneva.

Bierly, E.W., 1982: Key scientific questions and the role of satellites. The Conception, Growth, Accomplishments, and Future of Meteorological Satellites. NASA Conf. Pub. 2257, NASA. Scientific and Technical Information Branch, Washington, DC, 101 pp.

Bleckman, J.B., 1981: Vortex generation in a numerical thunderstorm model. Mon. Wea. Rev., 109, 1061-1071.

Browning, K.A., 1964: Airflow and precipitation trajectories within severe local storms which travel to the right of the winds. J. Atmos. Sci., 21, 634-639.

Green, R.N., and M.. Kruidenier, 1982: Interactive data processing for mesoscale forecasting applications. Preprints 9th Conf. on Weather Forecasting and Analysis, Amer. Meteor. Soc., 190-193.

Hasler, A.F., 1981: Stereographic observations from geosynchronous satellites: An important new tool for the atmospheric sciences. Bull. Amer. Meteor. Soc., 62, 194-212.

Hasler, A.F., W. Shenk, and W. Skillman, 1976: Wind estimates from cloud motions: Phase 1 of an in situ verification experiment. J. Atmos. Sci., 15, 10-15.

Hasler, A.F., W. Shenk, and W. Skillman, 1977: Wind estimates from cloud motions: Results from Phases I, II, III of an in situ aircraft verification experiment. J. Atmos. Sci, 16, 812-815.

Hill. K., G.S. Wilson, and R.E. Turner, 1979: NASA's participation in the AVE SESAME '79 program. Bull. Amer. Meteor. Soc., 60, 1323-1328.

Houghton, D., and D.K. Lee, 1977: Mesoscale wind fields for the May 6, 1975 Omaha tornado situation derived from SMS cloud observations. Preprints 10th Conf. Severe Local Storms, Omaha, Amer. Meteor. Soc., 16-21.

Hubert, L.F., 1979: Wind derivation from geostationary satellites. Quantitative Meteorological Data from Satellites, WMO Technical Note 166, (J.S. Winston, ed.), WMO, Geneva, 33-59.

Hubert, L.F., and A. Timchalk, 1972: Convective clouds as tracers of air motion. NOAA Technical Memorandum, NESS 40, NOAA/NESS, Washington, DC, 12 pp.

Hubert, L.F., and L.F. Whitney, Jr., 1971: Wind estimations from geostationary satellite pictures. Mon. Wea. Rev., 99, 665-672.

Hubert, L.F.. and L.F. Whitney, Jr., 1974: Compatibility of low cloud vectors and rawins for synoptic scale analysis. NOAA Tech. Report NESS 70, Washington, DC, 26 pp.

Johnson, G.L., and D. Suchman, 1980: Intercomparisons of SMS wind sets: A study using rapid-scan imagery. Mon. Wea. Rev., 108, 1672-1688.

Klemp, J.B., and R.B. Wilhelmson, 1978: The simulation of three-dimensional convective storm dynamics. J. Atmos. Sci., 35, 1070-1096.

Maddox, R.A., 1976: An evaluation of tornado proximity wind and stability data. Mon. Wea. Rev., 104, 133-142.

Maddox, R.A.. A.J. Negri, and T.H. Vonder Haar, 1977· Analysis of satellite derived winds for April 24, 1975. Preprints 10th Conf. on Severe Local Storms, Omaha, Amer. Meteor. Soc., 54-60.

Maddox, R.A.. and T.H. Vonder Haar, 1979:Covariance analyses of satellite derived mesoscale wind fields. J. Appl. Meteor., 18, 1327-1334.

Negri, A.J., and T.H. Vonder Haar, 1980: Moisture convergence using satellite-derived wind fields: A severe local storm case study. Mon. Wea. Rev., 108, 1170-1182.

Newton, C.W., 1963: Dynamics of severe convective storms. Meteor. Monogr., 5, No. 27, 33-58.

Peslin, C.A., 1977: A satellite interpretation of the dynamics of a severe local storm area using 5 minute interval SMS data. Preprints 10th Conf. on Severe Local Storms, Omaha, Amer. Meteor. Soc., 1-7.

Rodgers, E., R.D. Gentry, W. Shenk, and V. Oliver, 1979: The benefits of using short-interval satellite images to derive winds for tropical cyclones. Mon. Wea. Rev., 107, 575-584.

Soumi, V.E. and R.J. Parent, 1968: A color view of the planet Earth. Bull. Amer. Meteor. Soc., 49, 74-75.

Suchman, D. and D. Martin, 1976: Wind sets from SMS images: An assessment of quality for GATE. J. Appl. Meteor., 15. 1265-1278.

Tecson, J.A., T.A. Umenhofer and T.T. Fujita, 1977: Thunderstorm-associated cloud motions as computed from 5-minute SMS pictures. Preprints 10th Conf. Severe Local Storms, Ohama, Amer. Meteor. Soc., 22-29.

Young, M.T., 1975: The GOES wind operation. NOAA Technical Memorandum, NESS 64, NOAA/NESS, Washington, DC, 111-121.

D.3

Using Satellite Imagery to Understand Mesoscale Weather Development

James F.W. Purdom

Regional and Mesoscale Meteorological Branch
Development Laboratory
NOAA/NESDIS

and

Cooperative Institute for Research in the Atmosphere
Colorado State University
Fort Collins, Colorado

1. INTRODUCTION

The importance of clouds in defining the state of the atmosphere has long been recognized. As was pointed out by Schereschewsky (1945), "Every feature of the air masses ... is reflected by the shape, amount, and structure of the clouds. Thus close scrutiny of clouds will assist an analyst in identifying and analysing air masses." At the time, Schereschewsky was speaking about using surface based observations for large scale air mass analysis. Today, such a statement might read: "Features that are important in the development of weather, from the synoptic scale to the mesoscale, are reflected in the evolution of the clouds and cloud patterns observed in GOES imagery. Thus, close scrutiny of the evolving clouds and cloud patterns shown by GOES will assist the analyst in identifying and analysing important features that effect mesoscale weather development."

The importance of cloud imagery to the meteorological satellite program has been recognized since it inception. According to Kellog (1982):

> The idea that satellites could be used as weather reconnaissance vehicles seemed fairly obvious... What we needed was evidence that observations from a satellite would be useful in meteorology.
>
> In January, 1949, Delbert Crowson (Crowson, 1949)... published a short paper in the Bulletin of the AMS... In it he showed for the first time a photograph taken looking down on clouds from a rocket, and he included a short analysis.
>
> Joc Bjerknes had great enthusiasm for the idea of doing a detailed analysis of rocket pictures... Bjerknes wrote "...rocket pictures add a considerable amount of interesting information to the ordinary weather map analysis and, in addition, that the accumulated knowledge from the maps help us in the new problem of interpreting what we see from high-level rocket pictures. It may be added that...accumulated experience from several analyses from joint rocket and conventional methods would make it possible to arrive at the right analysis by rocket pictures only."

It was not until after the launch of TIROS-I on April 1, 1960 that cloud imagery from space became available. In the decades that have elapsed since the flight of TIROS-I, tremendous advances in the science and technology of meteorological satellites have been made. These advances include an improvement in imaging capability from the infrequent views of the early TIROS to the high resolution visible and infrared imagery available at frequent intervals from GOES.

Along with advances in technology have come advances in our ability to interpret and analyze meteorological satellite imagery. This paper will address some of the mesoscale applications of GOES satellite imagery.

2. MESOSCALE ANALYSIS FOR DEEP CONVECTIVE DEVELOPMENT

A lack of information on the mesoscale evolution of deep convective clouds and their local environment existed, in large part due to a gap in meteorological observing capability, prior to the high resolution geostationary satellite. The geostationary satellite has the unique ability to frequently observe atmospheric structure (sounders) and its cloud cover (visible and infrared) from the synoptic scale down to the cumulus scale. The clouds and cloud patterns in a satellite image or animated series of images represent the integrated effect of ongoing dynamic and thermodynamic processes in the atmosphere. When that information is combined with radar, surface and upper air observations, then many of the important processes in storm development may be better analyzed and understood. It is with that philosophy that satellite data should be used to help understand mesoscale weather development.

With GOES cloud imagery, we have an observation of the atmosphere in the form of its clouds and cloud cover every 1 km (visible) to 8 km (11u infrared). Many of the mesoscale to cloud scale features important in the development and evolution of convection are only detected in the imagery. Phenomena important in the initiation and maintenance of strong convection, such as dry lines (Rhea, 1966; Purdom, 1971), areas of pre-squall line development (Miller, 1972), areas of convective cloud merger (Woodley and Sax, 1976), and mesoscale high pressure systems (Fujita, 1963), which meteorologists previously tried to infer from macroscale patterns, are readily detectable in GOES imagery. For severe weather

applications, satellite data can be combined with conventional observations to construct an accurate and timely mesoscale analysis and isolate areas with a high potential for severe weather. For example, arc cloud lines (Purdom, 1973) and other shallow baroclinic zones detected using satellite imagery have been shown to be important initiators of severe convection and tornadic thunderstorms (Purdom, 1976; Parker and Hickey, 1980; Maddox, et al, 1980). It is interesting to note that our understanding of such observations has been improved using insight gained from high resolution numerical simulations of the tornadic region within mature thunderstorms (Klemp and Rotunno, 1983).

Prior to satellites, meteorologists were forced to make inferences about the mesoscale from macroscale patterns. Many of the mesoscale phenomena important in the initiation and maintenance of convection are readily detectable in geostationary satellite imagery. The sections that follow will refer to previous work at CIRA as well as new information concerning uses of satellite imagery for analysing and understanding mesoscale weather development.

3. MESOSCALE ANALYSIS AND UNDERSTANDING

An accurate mesoscale analysis is one of the most important tools available for detecting phenomena that lead to convective development and intensification. GOES imagery is an unparalleled tool for use in improving mesoscale analysis and providing a basis for the mesoscale reasoning that must accompany it. With GOES data, a "reporting station" exists every 1 km using the information in visible data, and every 8 km with infrared data. The clouds and cloud patterns in a satellite image may be thought of as a visualization of mesoscale meteorological processes. When that imagery is viewed in animation, the movement, orientation and development of important mesoscale features can be observed, adding a new dimension to mesoscale analysis. Furthermore, animation provides observations of convective behavior at temporal and spatial resolutions compatible with the scale of the physical mechanisms responsible for triggering deep and intense convective storms.

An interesting observation concerning local trigger mechanisms for convective development is the strong influence exerted by differential heating, as well as the many "masks" it wears. A well understood differential heating mechanism whose convective development is routinely observed in satellite imagery is the land sea breeze (Purdom, 1976). Another, that surely would have gone unnoticed without geostationary satellite imagery is the effect of early morning cloud cover on afternoon thunderstorm development (Purdom, 1982): see figure 1. Arc cloud lines (section 4), the driving force for deep convection over the southeast United States, represent another trigger mechanism that is due to differential heating - produced very quickly due to rain cooled air.

When using satellite imagery and working with concepts such as those mentioned above, one must realize what they represent. That is, the setting up of local convergence zones that are generated

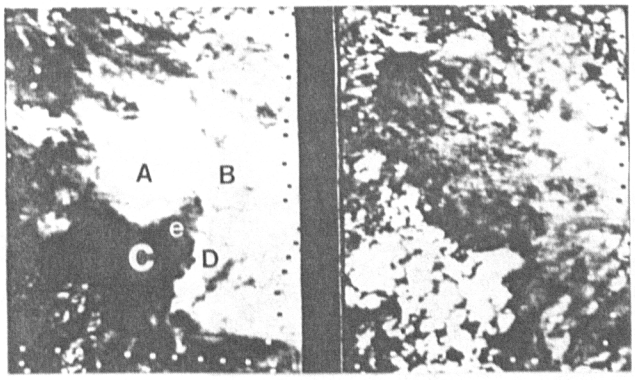

Figure 1 - May 27, 1977 GOES-East visible imagery over Alabama at 1030 EST (left panel) and 1330 EST (right panel). Note that the early clear region in SW Alabama (C) is becoming filled with convection during the day as the early cloudy region (A,B,D) is evolving toward mostly clear skies. Stronger activity develops in the "notch" of the clear region (E) due to merging cloud breeze fronts.

due to differential heating. Other properties of the atmosphere help determine the effectiveness of those local mechanisms in their ability to generate new deep convection. They include instability, large scale dynamics, and the trajectory of the low level air with respect to the convergence zone (amount of time an air parcel will experience vertical motion in the local forcing region). For example, an entirely different effect from that mentioned above may be realized due to early morning cloud cover under conditions of strong dynamic forcing (Purdom and Weaver, 1983).

4. ARC CLOUD LINES

Movie film strip analyses using geostationary satellite imagery have shown convective scale interaction is of primary importance in determining the evolution of deep convection (Bohan, 1981). This interaction manifests itself as the merger and intersection of thunderstorm-produced outflow boundaries (arc cloud lines (Purdom, 1973)) with other convective lines, areas and boundaries (Purdom, 1979). Arc cloud lines and their attendant convective scale interactions are fundamental to the evolution and maintenance of deep convective activity. In fact, thunderstorm evolution that appears as a random process on radar is often observed to be well ordered when viewed in time lapse using satellite imagery.

Figure 2 shows the characteristic appearance of arc cloud lines in satellite imagery. In this case interaction of an arc cloud and sea breeze front in Texas produced a large thunderstorm complex that continuously regenerated along the intersection (Zehr, 1982).

Using GOES satellite imagery, Purdom and Marcus (1982) classified convective development over the southeast United States. Their results, figure 3, show that when the most intense convection has developed, the dominant generation mechanism is convective scale interaction. The

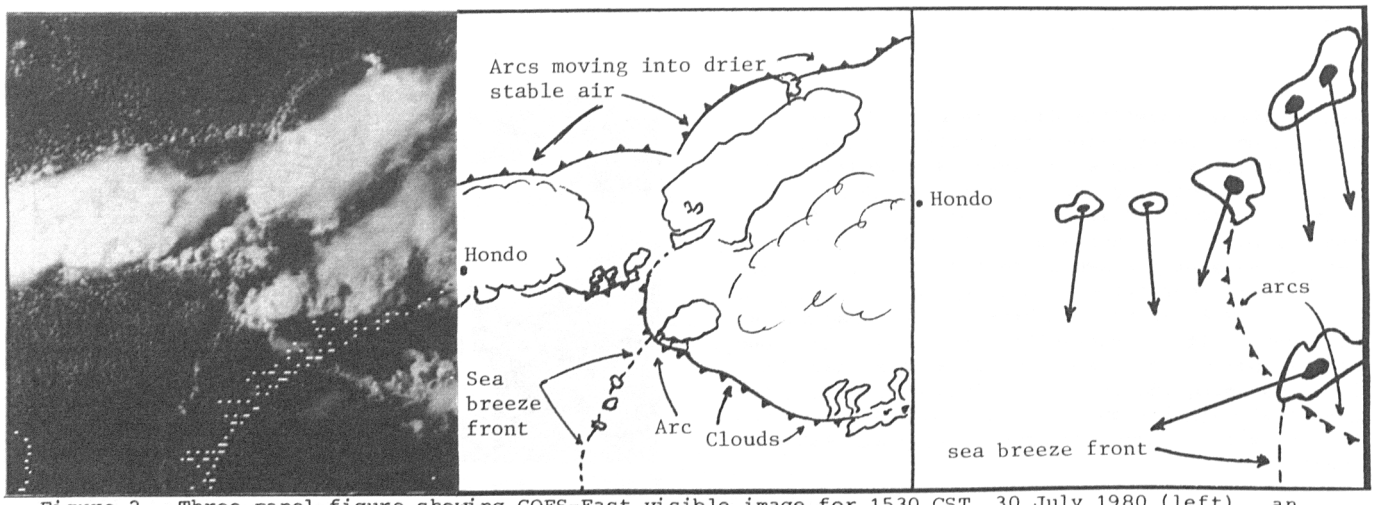

Figure 2 - Three panel figure showing GOES-East visible image for 1530 CST, 30 July 1980 (left), an analysis of the image (middle) and radar echo movements centered on 1600 CST (right). The large thunderstorm generated at the sea breeze and arc cloud line merger propagated (continuously regenerated) along the moving intersection of those two boundaries.

results of Purdom and Marcus have been extended to include rainfall over the southeast during the study period. Figure 4 shows the cumulative amount of rainfall (normalized) by hour for all hourly rainfall recording stations in the study area: notice the dominance of arc generated rainfall. During the study period no mesoscale convective complexes (Maddox, 1980) moved through the study area.

The character of arc cloud lines has been the subject of direct aircraft measurements (Sinclair and Purdom, 1982,1983,1984). The purpose of those flights was to improve our understanding of arc cloud lines as they relate to future convective development. Their most recent results concerning the structure and organization of arc cloud lines are contained elsewhere in this preprint volume (ibid, 1984).

5. ISOLATION OF SEVERE STORMS

Arc clouds and their convective scale interactions are a natural part of the convective cloud genesis and evolution process. They occur anywhere in the United States and are often the cause of severe thunderstorm development (Purdom, 1976). An extreme example was the severe storm associated with the most destructive tornado in Wyoming history (Parker and Hickey, 1980). Figure 5 shows the mesoscale convective environment prior to the Chicago tornadoes of June 13, 1976. The tornadic activity began shortly after the west to east oriented arc cloud line south of Chicago moved north and interacted with the storm over that area. The aircraft observations of Sinclair and Purdom (ibid) point to the importance of arc cloud lines in the production of both vorticity and convergence. Additionally, recent modeling efforts by Klemp and Rotunno (1983) support these observations from satellite imagery on the importance of arc cloud lines (outflow) in producing tornadoes. As stated on page 365 of their paper (ibid):

> We emphasize that within the simulation, large positive vorticity does not first develop at midlevels and then descend within the storm to the ground; rather, strong vertical vorticity is generated at low levels in response to the increased convergence.

Often organized convergence lines that trigger strong convection (dry lines, fronts, etc) are detectable in GOES imagery prior to deep convection forming on them (Purdom, 1976). Under proper dynamic forcing when the thunderstorms that form along such lines interact with other boundaries severe storms develop (Miller, 1972). In many instances satellite imagery is extremely useful in detecting such boundaries and isolating regions favorable for tornadic storm development. For example, on May 6, 1975, strong tornado activity that began in northeast Nebraska developed southeastward into the Omaha area along a squall line and warm frontal intersection. Figure 6 shows how these features as identified in satellite imagery could be tracked during the outbreak. The developing squall line appeared as an organized line of convective clouds along a surface windshift line separating moist and dry air. The warm frontal boundary appeared as another organized line of convection separating warm moist air embedded in southerly flow from slightly cooler and drier air in southeasterly to easterly flow. Other clues helpful in the precise location of the warm frontal boundary may be found by inspecting the change in cloud type across it (cumulus versus stratus), as well as through cloud track winds.

6. CONCLUSIONS

Satellite imagery is an unparalleled tool that can be used to improve our mesoscale reasoning--thus providing a means for better understanding of mesoscale meteorological processes. Many of the mesoscale cloud features important in the development and evolution of deep convection are only detectable in the imagery. When satellite imagery is viewed in animation, the movement, orientation and development of important mesoscale features can be observed, adding a new dimension to mesoscale analysis and short range forecasting.

The basic premise of this paper is that the clouds and cloud patterns in a satellite image or animated series of images represent the ongoing effect of dynamic and thermodynamic processes in the atmosphere. While it is possible to misinterpret the imagery, the imagery will not misrepresent the atmosphere.

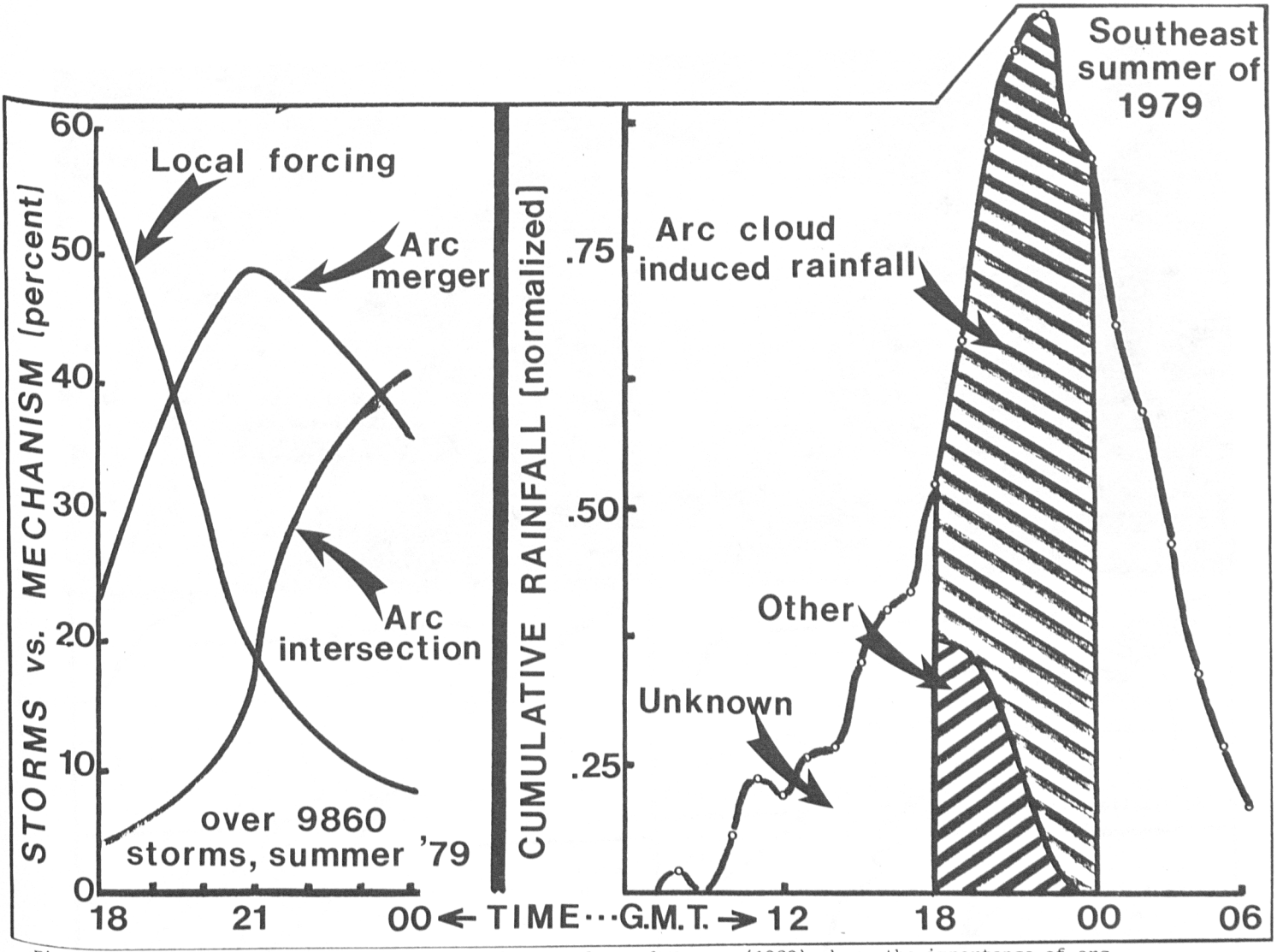

Figures 3 and 4 - Figure 3 (left) adapted from Purdom and Marcus (1982) shows the importance of arc cloud lines in the generation of deep convection (colder than -20 C) over the southeast United States. Figure 4 (right) extends the results from figure 3 into rainfall during the classification period.

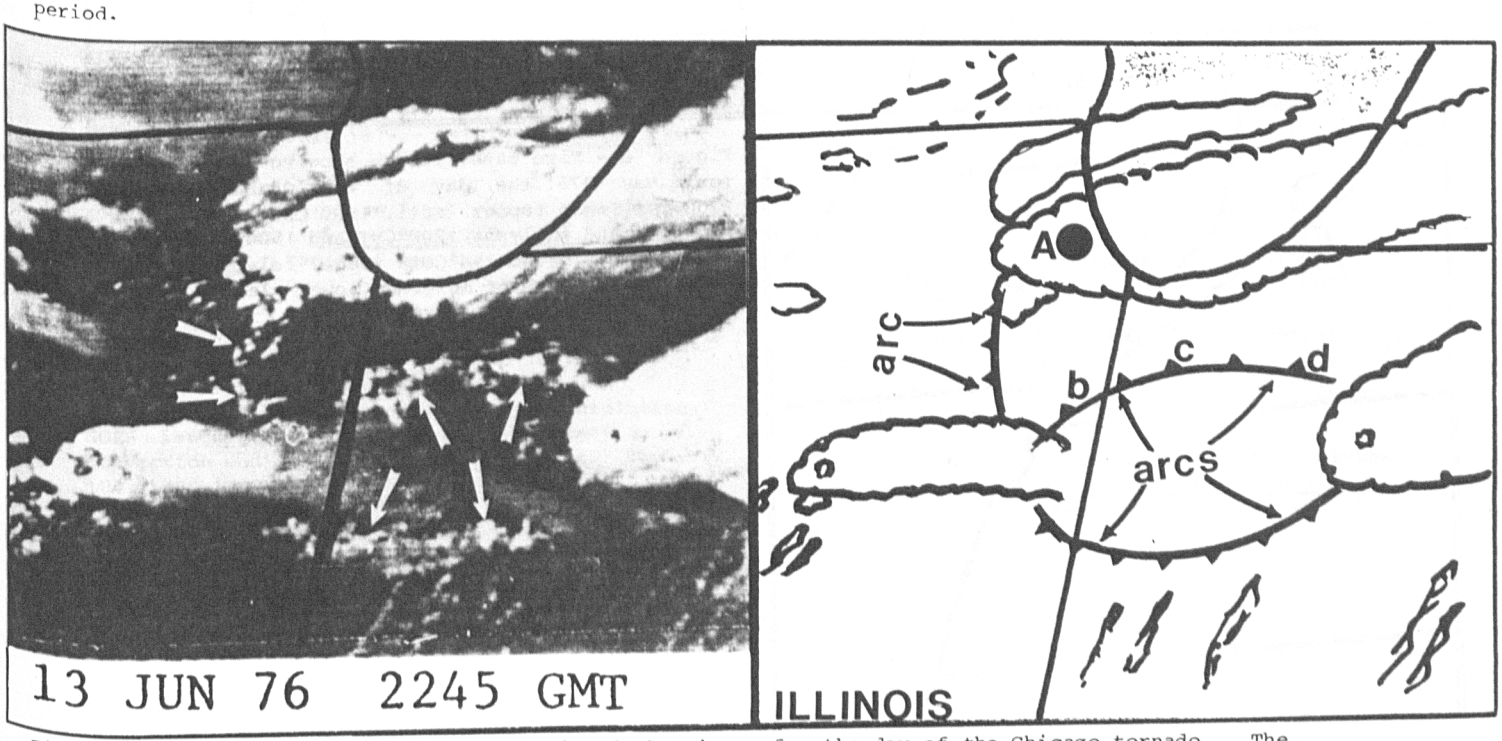

Figure 5 - GOES-East image and hand analysis of that image for the day of the Chicago tornado. The tornado hit Chicago (a) when the east-west oriented arc cloud (b,c,d) moved northward and interacted with the storm complex over the Chicago area.

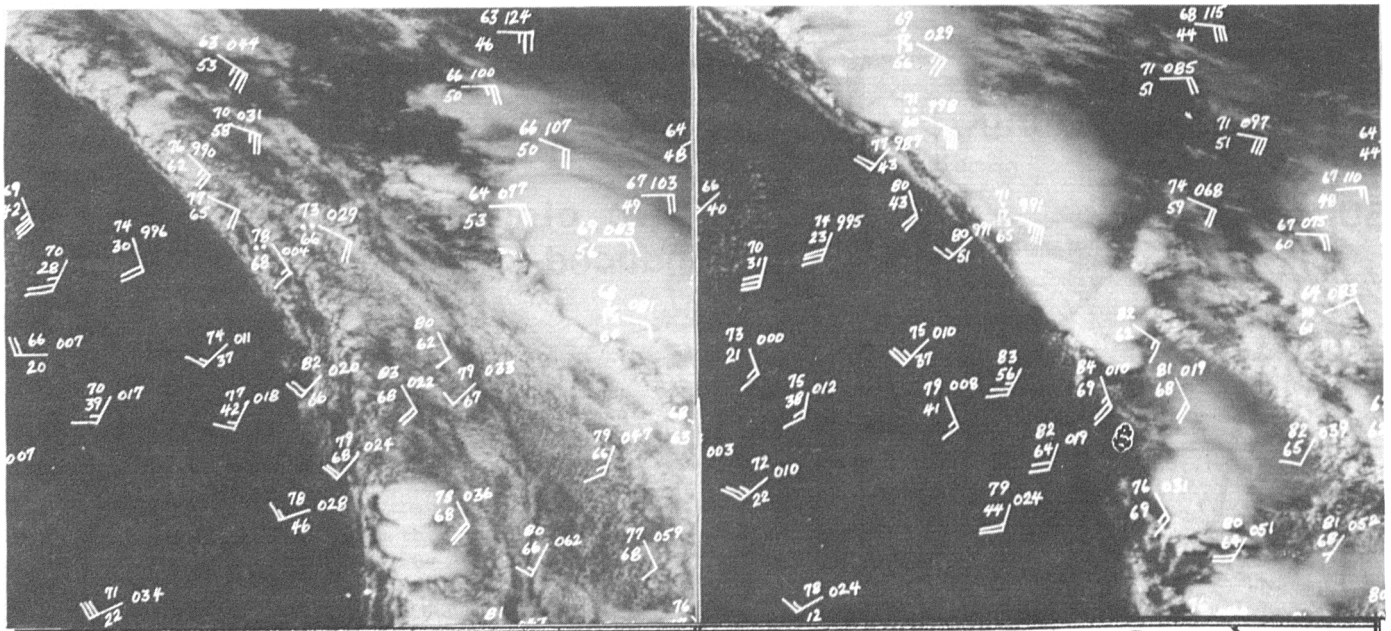

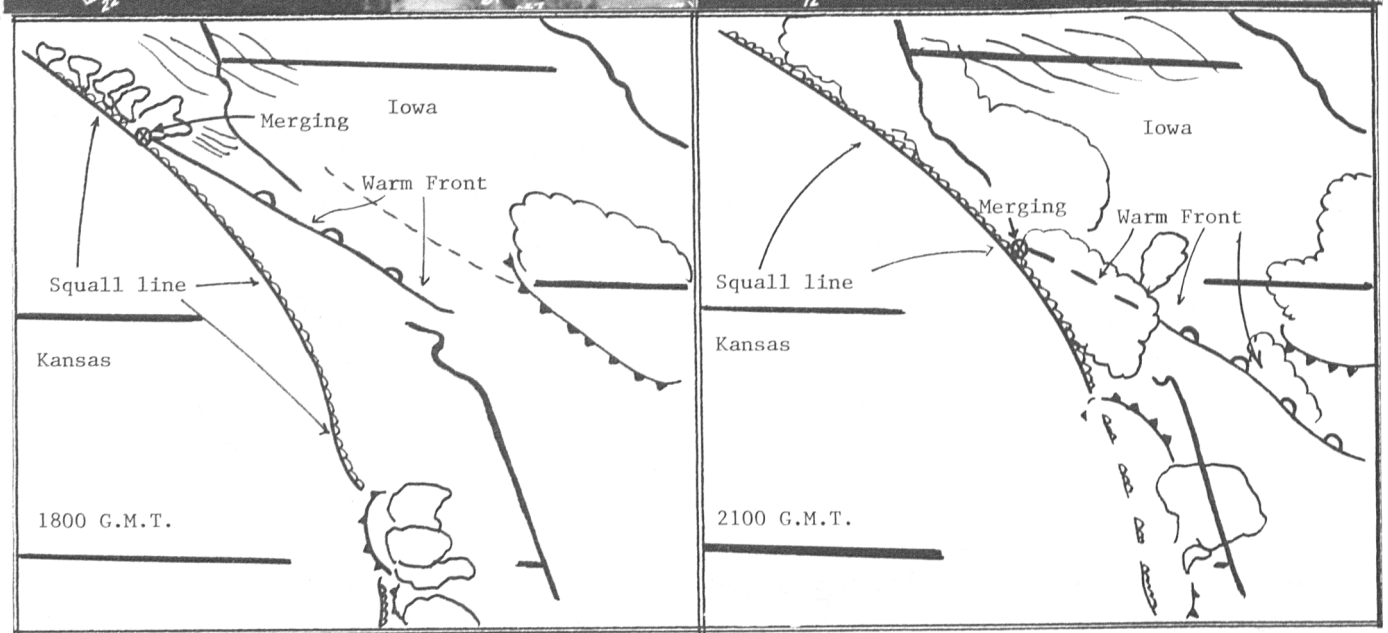

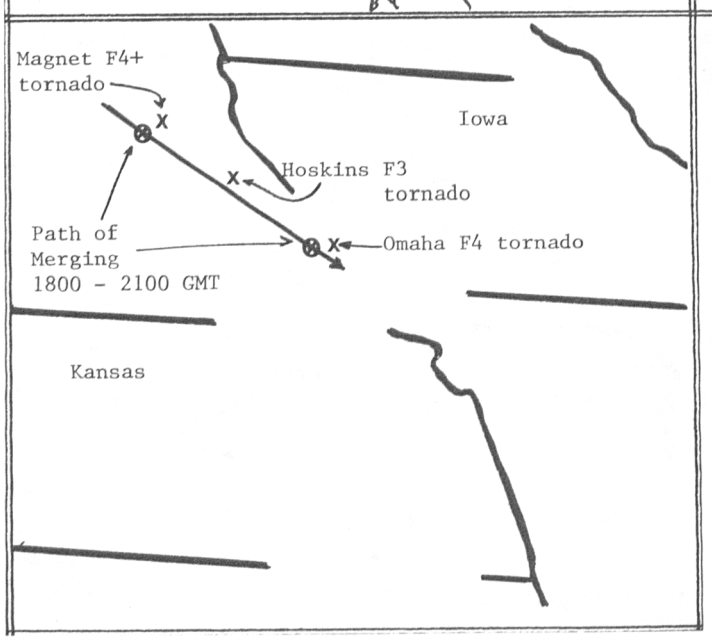

Figure 6 - Five panel figure showing GOES imagery for 6 May 1975. the day of the Omaha tornado. 1200 CST image (upper left), 1500 CST image (upper right), hand analysis 1200 CST and 1500 CST images immediately below the GOES image, relationship of tornadoes to path of merging (lower left). For other information see text.

7. ACKNOWLEDGEMENTS

Portions of this work were supported by NOAA under NA84AA-D-00017.

8. REFERENCES

Bohan, W.A., 1981: The importance of thunderstorm outflow boundaries in the development of deep convection. WAB 456, 16mm Color Sound Movie, The Walter A. Bohan Co., 2026 Oakton Street, Park Ridge, IL, 29 minutes.

Crowson, D.L., 1949: Cloud observations from rockets. Bull. Amer. Meteor. Soc., 30, 17-22.

Fujita, T.T., 1963: Analytical mesometeorology: A review. Meteor. Monogr., 27, 77-128.

Kelloq, W.W., 1982: Early satellite program developments. The Conception, Growth, Accomplishments and Future of Meteorological Satellites. NASA Conf. Pub. 2257, NASA, Scientific and Technical Information Branch, Washington, DC, 101 pp.

Klemp, J.B., and R. Rotunno, 1983: A study of the tornadic reqion within a supercell thunderstorm. J. Atmos. Sci., 40, 359-377.

Maddox, R.A., 1980: Mesoscale convective complexes. Bull. Amer. Meteor. Soc., 61, 1374-1387.

Maddox, R.A., L.R. Hoxit, C.F. Chappell. and F. Carcena, 1980: A study of tornadic thunderstorm interactions with thermal boundaries. Mon. Wea. Rev., 108, 322-336.

Miller, R.C., 1972: Notes on anlysis and severe-storm forecastinq procedures of the Air Force Global Weather Central. AWS Technical Report 200 (rev), Air Weather Service (MAC), U.S. Air Force, 190 pp.

Parker, W.T., and R.D. Hickey, 1980: The Cheyene tornado of 16 July 1979. Nat. Wea. Digest, 5, 45-62.

Purdom, J.F.W., 1971: Satellite imagery and severe weather warnings. Preprints 7th Conf. Severe Local Storms, Kansas City, Amer. Meteor. Soc., 120-127.

Purdom, J.F.W.. 1973: Meso-highs and satellite imagery. Mon. Wea. Rev., 101, 180-181.

Purdom. J.F.W., 1976: Some uses of high-resolution GOES imagery in the mesoscale forecasting of convection and its behavior. Mon. Wea. Rev., 104, 1474-1483.

Purdom, J.F.W., 1979: The development and evolution of deep convection. Preprints 11th Conf. Severe Local Storms, Kansas City, Amer. Meteor. Soc., 143-150.

Purdom, J.F.W., 1982: Integration of research aircraft data and 3 minute interval GOES data to study the genesis and development of ddep convective stomrs. Preprint Volume: 12th Conf. Severe Local Storms, San Antonio, Amer. Meteor. Soc.

Purdom, J.F.W, and K. Marcus, 1982: Thunderstorm trigger mechanisms over the southeast United States. Preprints 12th Conf. Severe Local Storms, San Antonio, Amer. Meteor. Soc., 487-488.

Purdom, J.F.W., and J.F. Weaver, 1982: Nowcasting during the 10 April 1979 tornado outbreak: A satellite perspective. Preprints 12th Conf. Severe Local Storms, San Antonio, Amer. Meteor. Soc., 467-470.

Rhea, J.O., 1966: A study of thunderstorm formation alonq dry lines. J. Appl. Meteor., 5, 58-63.

Schereschewsky, P., 1945: Clouds and states of the sky. Handbook of Meteorology, (ed. by Berry, Bollay. and Beers), McGraw-Hill, New York, 1068 pp.

Sinclair, P.C., and J.F.W. Purdom, 1982: Integration of research aircraft data and 3 minute interval GOES data to study the genesis and development of deep convective storms. Preprints 12th Conf. Severe Local Storms, San Antonio, Amer. Meteor. Soc., 269-271.

Sinclair, P.C., and J.F.W. Purdom, 1983: Shuttle recovery requirements and the development of arc cloud lines from thunderstorm outflows. Preprints 9th Conf. on Aerospace and Aeronautical Meterorology, Omaha, Amer. Meteor. Soc.

Sinclair, P.C., and J.F.W. Purdom, 1984: Aircraft penetrations of arc cloud lines. Preprints Satellite Meteorology/Remote Sensing and Applications, Clearwater, Amer. Meteor. Soc.

Woodley, W.L., and R.I. Sax, 1976: The florida area cumulus experiment: Rationale, design, procedures, results, and future course. NOAA Tech. Rep. ERL 345-WMP06, 204 pp.

Zehr, R.M.. 1982: Thunderstorm motion analyses. Preprints 9th Conf. on Weather Forecasting and Analysis. Seattle, Amer. Meteor. Soc., 455-458.

APPLICATIONS OF CUMULUS CLOUD FIELD STATISTICS FROM GOES DATA

Jan L. Behunek
Thomas H. Vonder Haar

Department of Atmospheric Science
Colorado State University
Fort Collins, Colorado 80523

1.0 INTRODUCTION

Clouds form as a result of atmospheric processes that often are complex. Their behavior contains information about the relevant processes, and knowledge of the atmosphere may be increased by studying them individually or in groups. Satellites furnish data that are unsurpassed for examining certain aspects of cloud behavior. This paper describes methods employed at Colorado State University to diagnose the statistical behavior of clouds from Geostationary Operational Environmental Satellite (GOES) digital data, and some applications of the results to the study of the atmosphere.

The Sierra Cooperative Pilot Project (SCPP) is a weather modification experiment which seeks to manage and enhance snowpack in the Sierra Nevada Range of California. An important part of SCPP examines precipitation from small orographic convective cells during the winter. The successful conduct of that experiment requires knowledge of how often convective clouds suitable for modification are available, where they form, the optimum cloud seeding location, and the natural effect of topography on cloud properties for evaluation purposes. The satellite helps answer those questions by supplying information about distributions as a function of location of areal cloud coverage and cloud top temperature.

Another application of satellite-derived cloud field statistics is as input to a numerical air pollution model at the Environmental Protection Agency (EPA)[Lamb (1983)]. That model simulates the formation and transport of photochemical oxidants. Satellite data provide model input for the cloud amount and location, which are used to parameterize the photochemical formation of pollutants. In addition, cumulus cloud top temperatures derived from the GOES data are converted to cloud top heights. Those cloud top heights are used to estimate the vertical mixing of pollutants, which is believed to occur mostly in convective cells during summertime. Horizontal pollutant transport then is accomplished by the vertically sheared wind.

2.0 METHOD

The data utilized in these studies were obtained at CSU's Direct Readout Satellite Earth Station from the Visible and Infrared Spin Scan Radiometer (VISSR) aboard GOES. Data from both the visible (0.55 μm to 0.75 μm) and infrared window (10.0 μm to 12.6 μm) spectral channels were employed. The horizontal resolution of the visible data at nadir was .9 km, whereas the infrared data had a 6.9 km nadir resolution. The resolution of those data was slightly degraded at the latitudes and longitudes studied, which encompassed the eastern U.S. for the EPA research and central California for the SCPP work. It is worth noting that the apparent resolution of the infrared data received at CSU was doubled (to 3.5 km) in the x-direction due to oversampling performed by the National Environmental Satellite, Data, and Information Service within the signal processing chain.

The satellite data analyses were accomplished with the aid of CSU's Interactive Research Imaging System (IRIS), which is a computerized display system. Specially designed interactive software within the IRIS simplified routine data manipulations and made possible the more complex process of computing the cloud field statistics. Some effort was devoted to the careful navigation of the satellite data before the statistical calculations were begun. The accuracy of the mapping of satellite coordinates into earth (latitude-longitude) coordinates was important for the subsequent interpretation of results.

The first task in the actual computation of statistics was to separate cumulus clouds from clouds of other types. That was accomplished by simultaneous analysis of coincident visible and infrared data on the IRIS. The physical basis for this method is illustrated in Figure 1. It is founded on the observational evidence that different cloud types usually fall on different parts of a two-dimensional histogram of visible brightness versus infrared brightness [Desbois, et al. (1982)]. The analyst interactively selected brightness thresholds for the visible and infrared channels that allowed the computer to distinguish cumuli from the surface and from other clouds. The computer then calculated the fractional coverage of all clouds and cumulus clouds within each cell of a latitude-longitude grid.

The computation of cumulus cloud temperatures also was based on both the infrared and visible data. Brightness temperatures ordinarily are derived from infrared data alone by application of the Planck function to the raw infrared radiance values. However, that technique could cause serious errors where small cumulus clouds were present because those clouds only partly filled the field of view of the infrared sensor. The top temperatures of small cumulus clouds would have been overestimated because of contami-

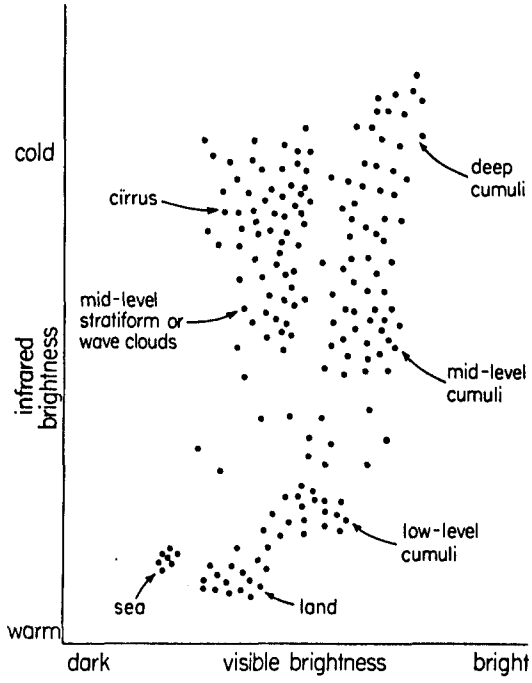

Fig. 1. Sample histogram of infrared versus visible brightness.

nation by the surface temperature. This effect was corrected by computing the cloud top temperature as a function of the observed brightness temperature, the background surface temperature, and the percent cloud cover within the infrared pixel obtained from the higher resolution visible data. The weighted brightness temperature from a single observed infrared pixel is given by

$$T_O = N\,T_{CT} + (1-N)T_B \qquad (1)$$

where T_O is the temperature from the observed pixel, T_{CT} is the cloud top temperature, T_B is the background surface temperature, and N is the fractional cloud amount within the infrared pixel. Equation (1) was inverted to give the cloud top temperature:

$$T_{CT} = \frac{T_O - (1-N)T_B}{N} \qquad (2)$$

In applying Equation (2), T_B was estimated from the maximum T_O within the grid cell being processed. This method of computing cloud top temperatures is analogous to Reynolds and Vonder Haar (1977) in several respects.

3.0 RESULTS

A sample of the output cloud field statistics for the SCPP region from March 2, 1982 are shown in Figures 2 and 3. Figure 2 depicts a latitudinal cross section across the barrier of the Sierra Nevada of fractional cumulus cloud coverage within each grid cell, and Figure 3 shows a similar cross section of cumulus cloud top temperatures. The four curves in each figure correspond to cross sections at slightly different latitudes. Each grid cell had dimen-

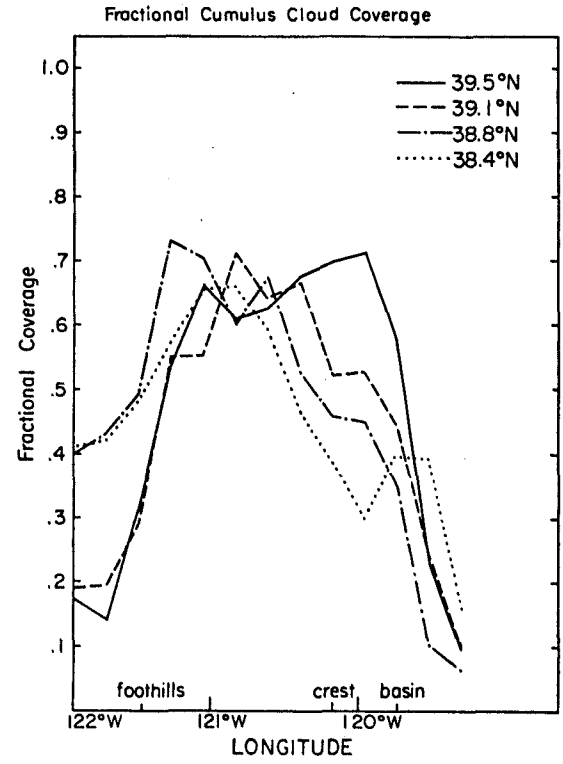

Fig. 2. Latitudinal cross sections of fractional cumulus cloud coverage. Each curve corresponds to a different latitude.

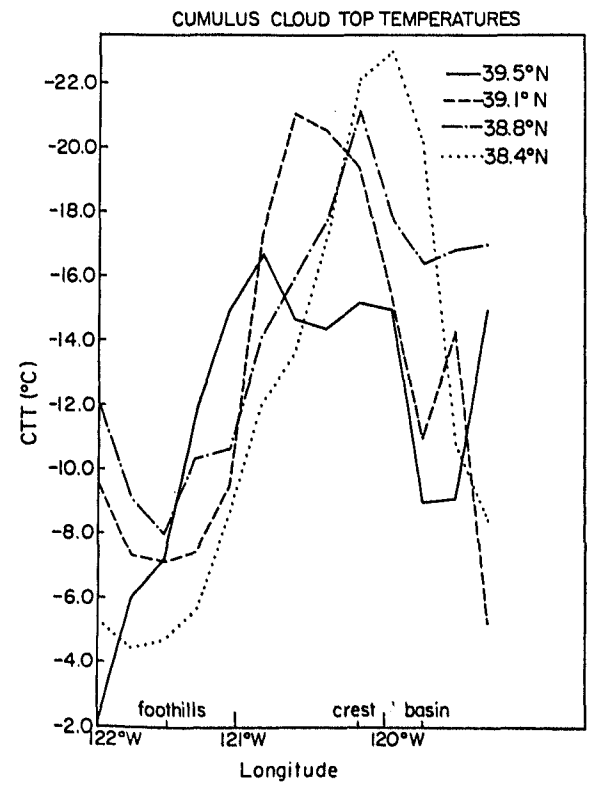

Fig. 3. Latitudinal cross sections of cloud top temperature. Each curve corresponds to a different latitude.

sions of 20 km per side. The approximate locations of the foothills, crest, and downwind basins of the Sierra Nevada are indicated in Figures 2 and 3 in order to help interpret orographic influences on the results. Awareness of the northwest to southeast orientation of the mountain barrier at the latitudes studied is useful for a precise interpretation of results, however.

Both Figure 2 and Figure 3 clearly show the topographic effect. Figure 2 indicates significant increases in fractional cumulus cloud coverage from a point west of the foothills to approximately midway up the barrier. The presence of a mean cloud formation zone is implied by Figure 2 in the northern half of the region studied, whereas the southern portion experienced more gradual increases in coverage. The association of a formation zone with the initial region of forced ascent at the foothills suggests that the orographic release of convective instability dominated purely atmospheric triggering mechanisms in the northern portion. Coverage maxima downwind of the crest were caused by high peaks or small mountain ranges in those areas. It is interesting to note the decrease in cumulus cloud coverage to the west of the crest at most latitudes. The cloud cover generally became stratiform in nature in that area on March 2, which was consistent with the observation of a temperature inversion near 3 km on that day. The cloud top temperature cross sections in Figure 3 also show the topographic effect. Decreases in cloud top temperature began at the foothills at all but one of the latitudes studied. Those decreases began to the east of the starting point for increases in areal coverage, however. Temperature minima were found to be somewhat west of the barrier crest in the northern part of the study area, and at the crest further south. The application of cloud top temperature criteria established for SCPP ($-20^{\circ}C \leq T \leq 10^{\circ}C$) indicate that the optimum seeding location on March 2 was 20 to 40 km downwind of the western edge of the foothills.

The results of the effort that provided cloud field statistics to the EPA for pollution model input will not be discussed here because they were not designed for separate interpretation. The usefulness of the cloud statistics supplied to the EPA must be judged by the improvement caused in the air pollution model, which is unprecedented in its attempt to simulate all of the processes relevant to the formation and transport of pollutants.

4.0 CONCLUSION

This study has demonstrated several applications of satellite data to the phenomenology of cloud fields. The data and methods employed generated observational analyses which would have been very difficult or impossible to obtain without satellite data. Improvements made over straightforward analysis of the data were the use of interactively selected bispectral thresholds that allowed the IRIS to distinguish cloud types and the infrared brightness temperature correction for partially filled sensor fields of view. Further applications of cloud field statistics may be envisioned anytime that detailed cloud observations are needed. They could be drawn from endeavors such as mesoscale diagnostic studies and mesoscale and cloud scale model input and validation.

5.0 ACKNOWLEDGMENTS

The authors would like to thank Mr. Pat Labye, who assisted with the data analysis, and Ms. Kris Randolph, who performed the computer programming. Ms. Judy Sorbie drafted the figures and Ms. Loretta Stevens typed the manuscript. This research was supported by the Bureau of Reclamation under contract number 9-07-85-V0025 and the Environmental Protection Agency under contract number 68-02-3731.

6.0 REFERENCES

Desbois, M., G. Seze, and G. Szejwach, 1982: Automatic classification of clouds on METEOSAT imagery: Application to high-level clouds. J. Appl. Meteor., 21, 401-412.

Lamb, R.G., 1983: A regional scale (1000 km) model of photochemical air pollution. Part I: Theoretical formulation. EPA, Environmental Sciences Research Lab., Research Triangle Park, NC.

Reynolds, D.W., and T.H. Vonder Haar, 1977: A bispectral method for cloud parameter determination. Mon. Wea. Rev., 105(4), 466-457.

D.5

THUNDERSTORM CLOUD TOP DYNAMICS AS INFERRED FROM SATELLITE OBSERVATIONS AND MODELS

Robert F. Adler

Goddard Laboratory for Atmospheric Sciences
NASA/Goddard Space Flight Center
Greenbelt, MD 20771

Robert A. Mack

General Software Corporation
Landover, MD 20785

1. INTRODUCTION

Satellite observations of convective towers penetrating the tropopause have revealed a number of characteristics that need to be explained in order to enhance our understanding of cloud top processes and also in order to infer cloud top height from satellite infrared (IR) data and storm intensity from the same observations. In this paper, satellite observations are summarized and three classes of storm tops are described and the causes of their unique temperature/height structures are explored with a one-dimensional cloud parcel model applied in the overshooting region.

2. SATELLITE-OBSERVED THUNDERSTORM TOP STRUCTURE

Thunderstorm tops typically appear in 11 micron infrared (IR) satellite images as points of relative minimum in IR brightness temperature, T_B. The point of T_B minimum (T_{min}), or cold point, is usually co-located with the point of maximum height. The T_{min} observed by GOES (with a 10 km Instantaneous Field of View (IFOV) at mid-latitudes) can be as much as 10-12 K lower than tropopause (or neutral point) temperature (Adler and Markus, 1983). AVHRR observations (1 km IR) indicate that the GOES IFOV accounts for 3-10 K warm bias in mature overshooting thunderstorms (Adler et al., 1982), so that actual (high resolution) T_{min}'s may be up to 15-20 K colder than the tropopause and/or ambient temperatures at cloud top level.

In these "typical" overshooting tops, there is evidence that the effect of mixing is relatively weak and temperature-height relations are much closer to adiabatic than ambient (Adler et al., 1983; Negri, 1982). For example, Negri (1982) has shown an 8 K km^{-1} temperature-height relation among a collection of penetrating storms using AVHRR (1 km) T_{min}'s and maximum height deduced from stereo calculations from GOES-East and GOES-West. These typical penetrating thunderstorm tops will be termed Class 1 thunderstorm tops in this paper. A majority of storm tops fall into this category.

In a second class of penetrating storms, a cold V-shaped feature in the IR is produced with the apex of the V (with the IR cold point) pointed upwind and a relative maximum in T_B inside the V shape (Heymsfield et al., 1983a, b; Fujita, 1982). This produces a cold-warm couplet in the IR image, as shown in Fig. 1b in the southwest portion of the anvil. These close-in, cold-warm couplets have a dimension of ∿40 km, are situated over the convective tops, and should not be confused with the larger anvil-scale feature of the same pattern (see Heymsfield, 1983a, b for a more complete description). The general V-shaped cold feature and cold-warm couplet have been shown by McCann (1983) and Adler and Markus (1983) to be correlated with the occurrence of severe weather. Satellite stereo height patterns do not show a V-shaped or high/low couplet, but indicate instead a typical pattern of concentric height contours (see Fig. 1). In this class (Class 2), the storm tops have a co-located cold and high point with the warm point located in an area of downward sloping convective clouds downwind of the summit.

The Class 3 storm is a variation on Class 2, when, in addition to cold-warm couplet, the cold point is offset upwind from the high point, with the cold-warm couplet straddling the convective cloud top (as determined from stereo). An example of a Class 3 thunderstorm top is shown in Fig. 2. The relation of T_{min} to

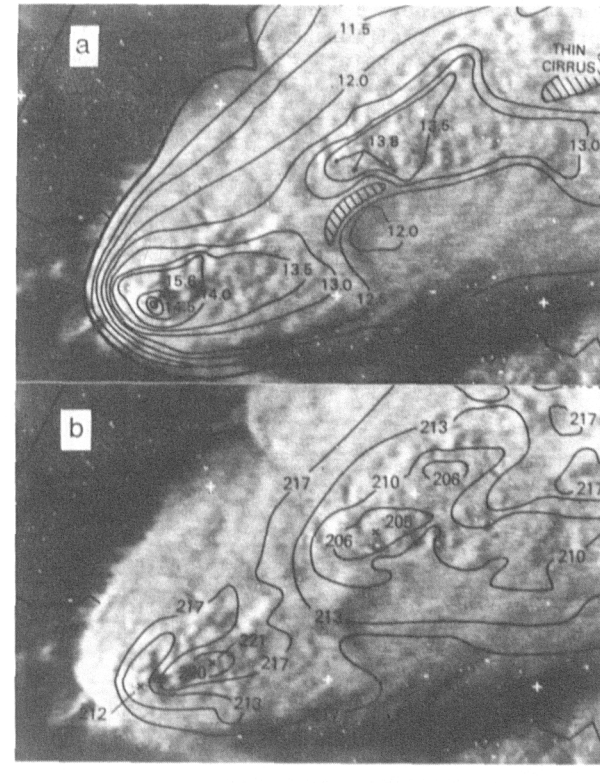

Fig. 1. GOES-East visible image of Wichita Falls, TX, April 10, 1979 storm (southwest end of anvil). a. Stereoscopic cloud height contours. b. GOES-East IR T_B contours.

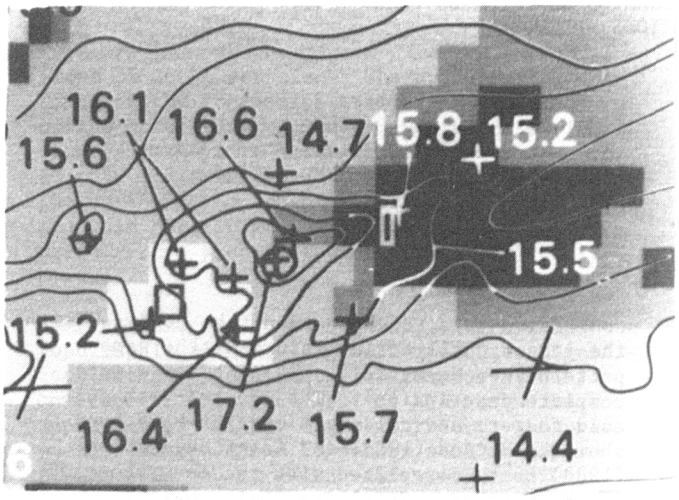

Fig. 2. *An IR image of a thunderstorm top overlain with stereo height contours on May 2, 1979. The white area has low T_B's with the boxed point having a T_{min} of 199 K, while the boxed point in the black area is at 215 K. The distance between cold and warm point is ~40 km. Adapted from Mack et al. (1983).*

Z_{max} for a collection of storms in this situation is also quite different, as seen in Fig. 3 for the storm complex on May 2, 1979, of which the thunderstorm top in Fig. 2 was a part. The data points in Fig. 3 connected by horizontal lines are storm tops with cold-high offsets. The point on the right end of the line is the T_B at the point of Z_{max}. The left hand point is the coldest T_B in the area, thus the ΔT represents the T_B difference between the cold point and the high point. The observed "lapse rate" of the collection of thunderstorm tops is near isothermal, closer to the ambient than adiabatic, indicating a larger effect of mixing than the storms in Class 1.

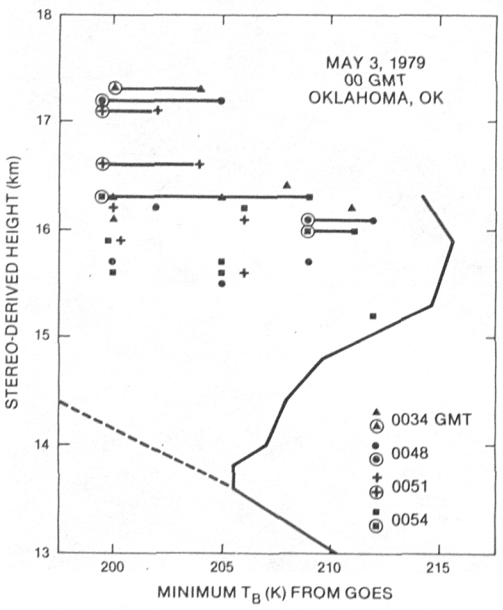

Fig. 3. *Observed GOES T_{min}-stereo Z_{max} for a collection of storm tops on May 2, 1979. This figure is similar to those of Hasler (1981) and Fujita (1982).*

The causes for the IR V-shaped cold feature and imbedded warm point of classes 1 and 2 have been discussed by Heymsfield et al. (1983a, b) and Fujita (1982). Heymsfield pointed out that the warm point sometimes is located close-in to the cold point or apex of the cold V with a cold-warm separation of ~40 km, as mentioned in the Class 2 description before. Additionally, another point can occur much farther downwind, about 100 km from the cold point. These two points may exist at the same time (as in Heymsfield's case study) and probably have different causes. The large-scale (anvil-scale), V-shaped cold area with the downwind (100 km) warm point is probably related to the distribution of Ice Water Content (IWC) in the anvil and its effects on the upwelling radiance (Heymsfield et al., 1983b). An alternate hypothesis for the warm point is the presence of above-anvil cirrus in the stratosphere radiating at temperatures warmer than the anvil background and producing the interior warm point (Fujita, 1982).

The close-in warm point (40 km) may be related to the dynamics of the overshooting top itself and its interaction with the lower stratosphere (Heymsfield et al., 1983a), where the warm point is related to subsidence in the convection region and mixing with the stratospheric environment. Schlesinger (1982) has used a three-dimensional cloud model to simulate the temperature and height pattern at cloud top in an intense storm in a high-shear environment and the resulting patterns are shown in Fig. 4. The model produces the cold-warm couplet (only 12 km apart) with the high point just slightly upwind of the cold point and the warm point on the sloping cloud surface downwind of the cold-high point. These model results support the dynamic cause for the close-in feature. An alternate hypothesis is that of the above-anvil cirrus (Fujita, 1982). This current

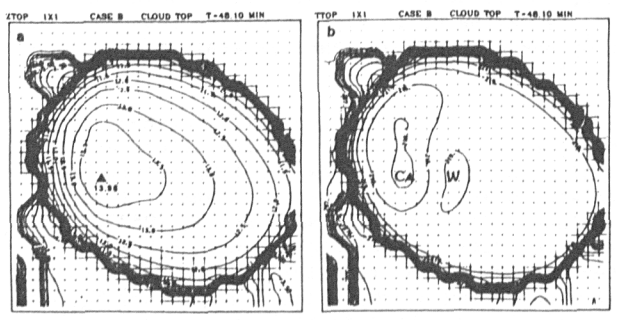

Fig. 4. *Three-dimensional cloud model results, showing temperature and height patterns at a top of a model mature, overshooting thunderstorm. Adapted from Schlesinger (1982).*

paper centers on exploring the dynamic explanation for the close-in, cold-warm couplet, and for convective top structure and T_B-Z relations for all three classes of storms.

3. PARCEL MODEL DESCRIPTION

The vertical equation of motion appropriate for cloud-scale dynamics given by Schlesinger (1980, 1983) is

$$\frac{dw}{dt} = -\frac{1}{\rho_o}\frac{\partial p'}{\partial z} + g\left(\frac{\theta'}{\theta_o} + aq_v'\right) - g\frac{Cv}{Cp}\frac{p'}{p_o} - g\,q_\ell + F_z \ , \qquad (1)$$

where w = vertical velocity, ρ = air density, p = pressure, z = height, g = gravity, θ = potential temperature, $a = R_v/R_d - 1$ (.606), R_d = gas constant for dry air, R_v = gas constant for water vapor, q_v = water vapor mixing ratio, Cp = specific heat of dry air at constant pressure, Cv = specific heat of dry air at constant volume, and q_ℓ = liquid water mixing ratio. The individual terms on the right-hand side are, from left to right: the perturbed vertical pressure gradient force which nearly always opposes the thermal buoyancy; the moist thermal buoyancy which accelerates an air parcel upward if it is warmer or more moist than its surroundings; the pressure buoyancy which will accelerate an air parcel upward if it is at lower pressure than its surroundings; the liquid water drag and, finally, the vertical friction.

In our one-dimensional parcel (or Lagrangian) model, the pressure perturbation terms cannot be calculated directly, but are parameterized as usually done in one-dimensional Lagrangian models (e.g., Simpson and Wiggert, 1969). This formulation is given by

$$\frac{dw}{dt} = g\frac{(T-T_e)}{(1+\gamma)T_e} - gq_\ell - \mu_w|w|w \ , \qquad (2)$$

where T = cloud parcel temperature, T_e = environmental temperature, γ = apparent mass coefficient, and μ_w = vertical momentum mixing coefficient.

The first term on the right-hand side of Eq. (2) is a combination of the thermal buoyancy force and the effect of the pressure perturbation terms. The apparent mass coefficient, γ, (Simpson and Wiggert, 1969) is used in Eq. (2) to parameterize the pressure gradient and pressure buoyancy terms in Eq. (1), i.e.,

$$g\frac{(T-T_e)}{(1+\gamma)T_e} = g\left(\frac{\theta'}{\theta_o}\right) - \frac{1}{\rho_o}\frac{\partial p'}{\partial z} - g\frac{Cv}{Cp}\left(\frac{p'}{p_o}\right) \ . \qquad (3)$$

The magnitude of γ near the cloud top was selected based on an analysis of three-dimensional cloud model parcel trajectories from Schlesinger (1983). The magnitudes of the terms on the right-hand side of Eq. (3) were determined at various heights above the tropopause from parcels (KM1, LM2) in the Schlesinger study. The sum of these three terms at various heights along the parcels' path near the cloud top were plotted versus the thermal buoyancy. A regression line was fit to the points and a correlation coefficient of 0.87 was found. The regression line has a slope of 0.22 and an intercept near zero. This indicates that the pressure gradient and pressure buoyancy forces at cloud top act to reduce the thermal buoyancy to about one-fourth its value. Therefore, a γ = 3.0 was used to parameterize the effect of these two terms on the parcels' vertical motion.

To solve for the parcel temperature (T) in Eq. (2), the following relation is used:

$$\frac{dT}{dt} = -w(g/C_p) - w\ \mu_T(T-T_e) \ , \qquad (4)$$

where μ_T is the thermal mixing coefficient and is set equal to 3 μ_w, similar to three-dimensional model work.

A fourth-order Runge-Kutta numerical scheme with a 5 sec time step was used to solve simultaneously Eqs. (2) and (4), thus calculating a parcel trajectory in T and Z space. The one-dimensional parcel model is initiated by starting a parcel at the neutral point with w set equal to some initial value, w_o, and parcel temperature (T) set equal to the environmental temperature (T_e).

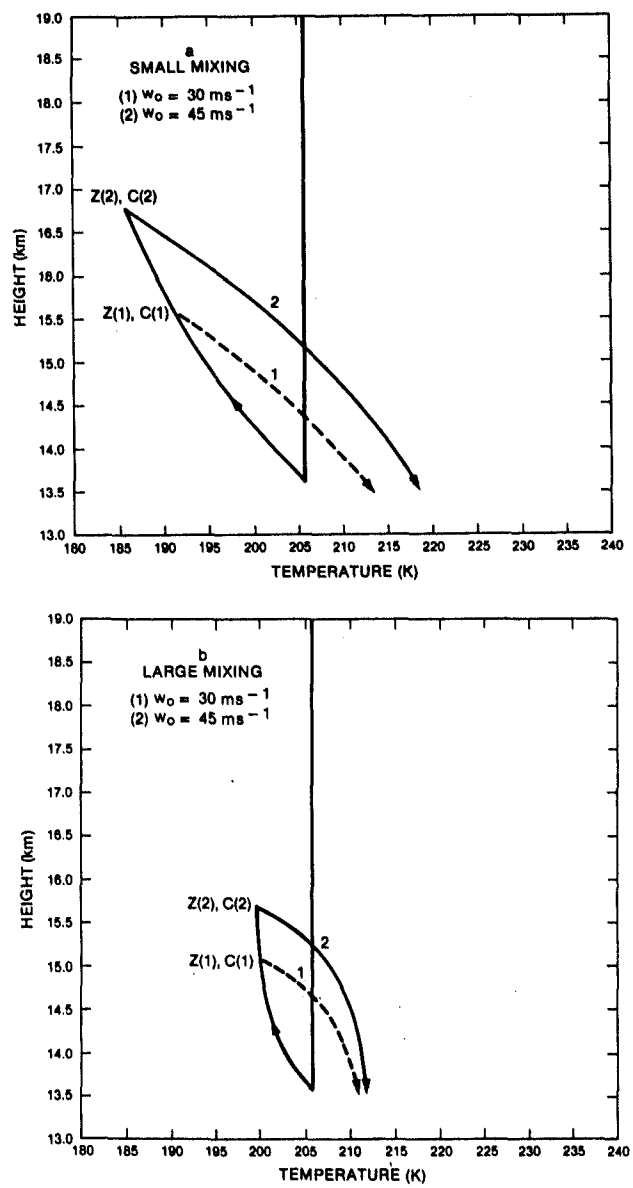

Fig. 5. *Parcel model trajectory results for an isothermal stratosphere and (a) small mixing, μ_T = .3 km^{-1}; (b) large mixing, μ_T = 1.5 km^{-1}. In both cases, γ = 3.0 and drag = .08 m s^{-2}.*

4. RESULTS

The simple model attempts to reproduce the parcel path in temperature-height space for a parcel ascending through the updraft core to the top of the overshooting dome and then descending down the downwind side of the dome. Fig. 5 gives a synopsis of parcel runs with an isothermal stratosphere, with Fig. 5a having $\mu_T = 0.3\ km^{-1}$ and Fig. 5b having $\mu_T = 1.5\ km^{-1}$. The variation in mixing as parameterized by variations in μ_T and μ_w represents differences in cloud top-environment interactions, which may be a direct function of the magnitude of the cloud top air flow relative to storm motion.

In Fig. 5a, two model runs are shown. Both start at the same neutral point (as all runs do) at 13.6 km and 206 K (an arbitrary point). Because every variable is identical except the w_o in the two runs, both runs initially have the same parcel path, up to 15.6 km where run (1), with $w_o = 30\ m\ s^{-1}$, reaches its maximum height and begins to descend as shown. Run (2) with $w_o = 45\ m\ s^{-1}$ ascends farther to 16.8 km and to a lower T_{min} (by ~5 K). In Fig. 5b, the same runs are shown for large mixing ($\mu_T = 1.5\ km^{-1}$). The larger mixing obviously tends to pull the parcel trace toward the ambient lapse rate and produces lower maximum heights and higher T_{min}'s for the same w_o's as in Fig. 5a.

In all parcel runs displayed in Fig. 5, the cold point (C) is co-located with the high point (Z) and there is no point along the trace where a point of relative maximum of temperature (W) is produced. An examination of the model equations indicates that in our simple system the parcel trajectories can only be between adiabatic and environmental lapse rates (on the way up), so that for an isothermal stratosphere or a lapse of temperature with height no cold-high offset can occur and no downside, or downwind warm point, can occur. The model runs in Fig. 5a represent the Class 1 storm observations.

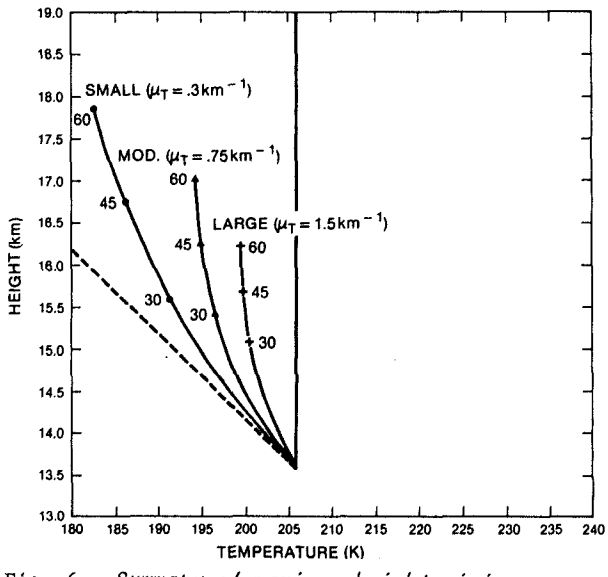

Fig. 6. *Summary of maximum height-minimum temperature model results for isothermal stratosphere for various mixing coefficients.*

Fig. 6 shows a summary of the temperature and height at the parcel peak height for the isothermal runs. The distribution for the small mixing has a temperature height relation of $7\ K\ km^{-1}$ in the first 2 km above the neutral point, similar to observations of Negri (1982).

Fig. 7 gives the model results for a $3\ K\ km^{-1}$ inversion, similar to that observed with the May 2, 1979, case discussed in the observations. The starting neutral point is realistic for that case also. The first parcel (Fig. 7a), for small mixing, is similar to the results for the isothermal situation, except the parcel paths on the upward path are farther from adiabatic because of the greater distance of the environmental lapse rate from adiabatic.

For the moderate ($\mu_T = 0.75\ km^{-1}$) and large mixing, the stratospheric inversion begins to produce cold-high offsets and downwind warm points. For the moderate mixing (Fig. 7b), the run with $30\ m\ s^{-1}$ has a co-located cold and high point. For the $45\ m\ s^{-1}$ and $60\ m\ s^{-1}$ runs in Fig. 7b, the coldest point (C) of the run is achieved before the maximum height. The occurrence of the cold-high offset in the model is due to the strong inversion, relatively large mixing, and strong updraft. Run (3) in Fig. 7b also produces a warm point (W), but at a low point, not on a downward slope as observed (see Section 2).

With still larger mixing (Fig. 7c), the relative warm point on the downward path appears. The cold point-warm point temperature difference of 10-15 K is approximately in agreement with observations. The appearance of the warm point on the descent leg is critically dependent on a large drag in the model. The value of $.08\ m\ s^{-2}$ used here corresponds to a value of $1.5\ gm^{-3}$ in Ice Water Content (IWC). This is a large value, but perhaps not out of the question for very strong updrafts. The cold-high-warm points of run (3) in Fig. 7c represent the Class 3 storm of the observations. Fig. 8 summarizes the minimum temperature-maximum heights of the model runs for the small, moderate, and large mixing, with the points connected by curves being the temperatures at the maximum height and the circled points offset toward lower temperature being the T_{min}, where there is a cold-high offset. The general isothermal distribution for the moderate and large mixing, the occurrence of cold-high offsets for storms at higher heights, and the increase of the temperature offset as a function of height agree, at least qualitatively, with the plotted observations of Fig. 3.

The observations of Class 2 storms, which have co-located cold-high points and a warm point on the downward-sloping cloud surface, are not reproduced in Fig. 7. The April 10, 1979 case that is the example Class 2 storm (Fig. 1) occurred with an apparent near isothermal above-cloud lapse rate and although our simple model will not produce a warm point for an isothermal lapse rate, a small inversion ($1\ K\ km^{-1}$) produces a parcel trajectory (Fig. 9) with a relatively small cold-high offset and

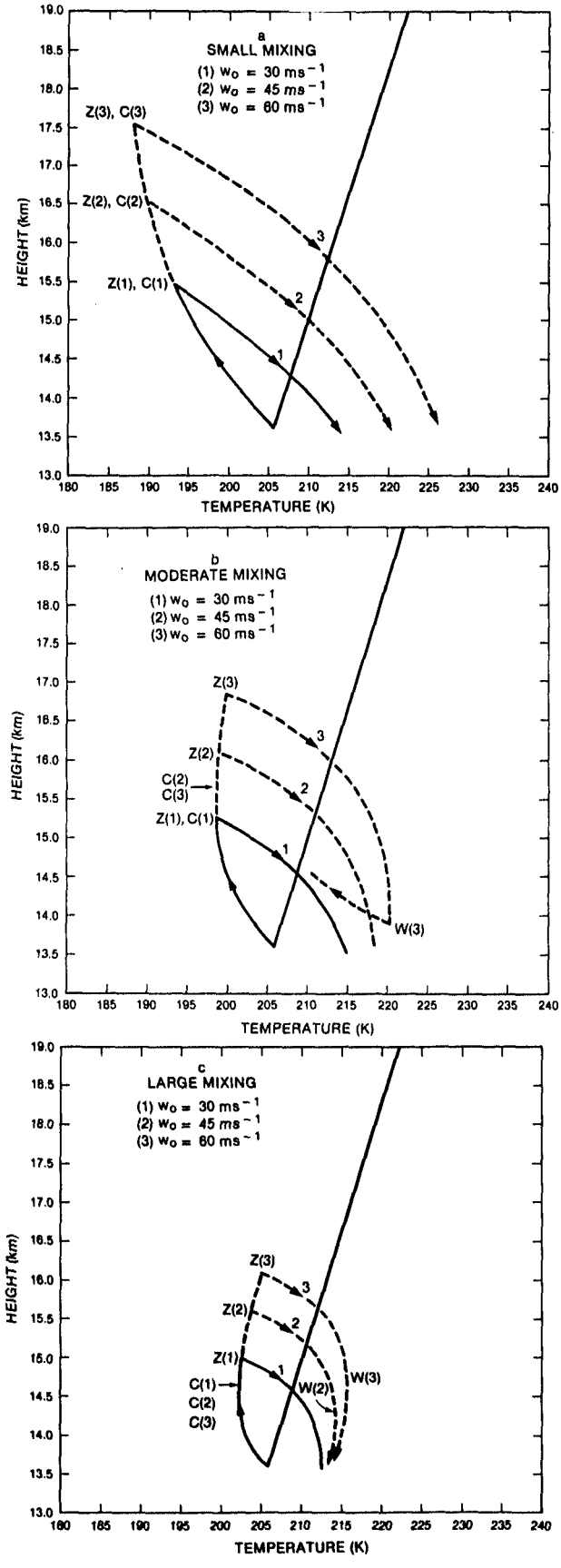

Fig. 7. *Parcel model trajectory results for a 3 K km^{-1} inversion and (a) small mixing, μ_T = .3 km^{-1}; (b) moderate mixing, μ_T = .75 km^{-1}; (c) large mixing, μ_T = 1.5 km^{-1}. In all cases, γ = 3.0 and drag = .08 m s^{-2}.*

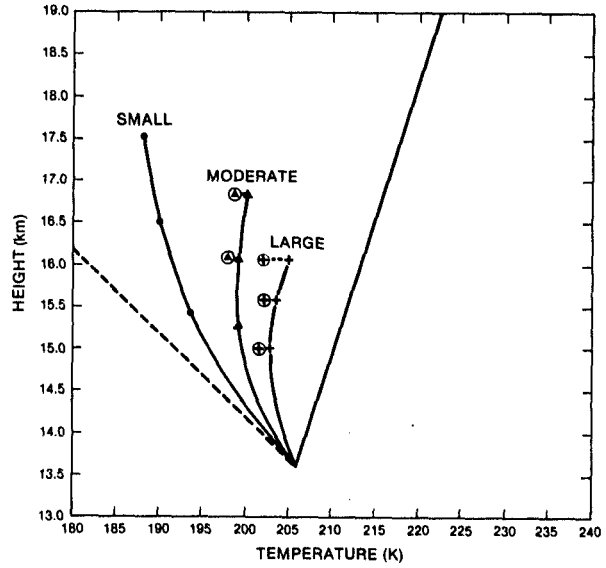

Fig. 8. *Summary maximum height-minimum temperature model results for 3 K km^{-1} inversion for various mixing coefficients.*

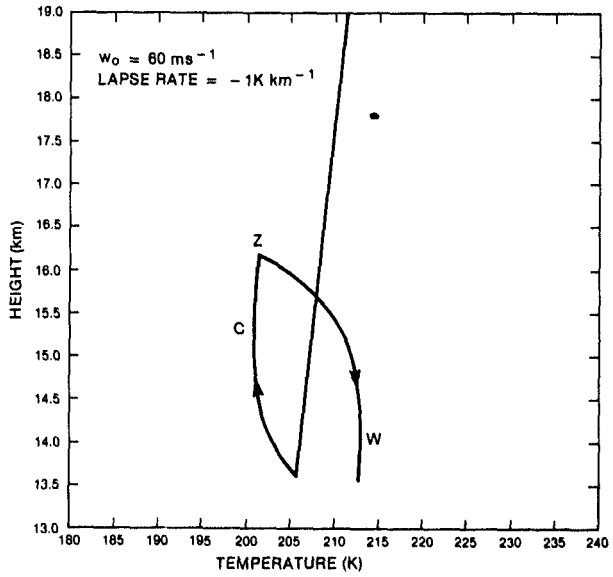

Fig. 9. *Parcel model trajectory results for 1 K km^{-1} inversion. All other variables the same as run (c) in Fig. 7.*

with the cold point significantly higher than the warm point. This is in contrast to run (3) in Fig. 7c, which is identical except for the environmental lapse rate. Thus, Class 2 storms probably have a small, but difficult to observe, cold-high offset and occur when the environmental lapse rate has only a weak inversion.

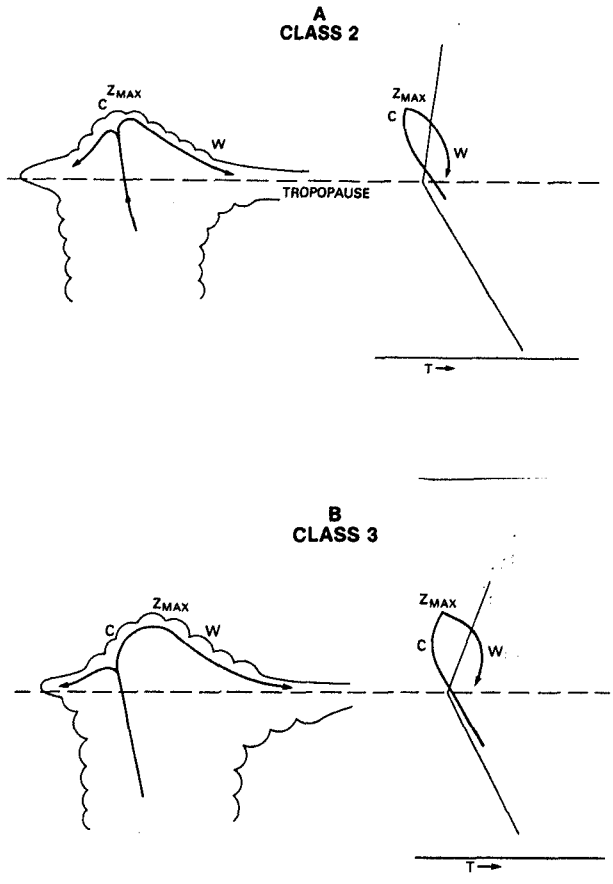

Fig. 10. *Schematics of overshooting thunderstorm top and associated parcel trajectory for: (a) Class 2 storm; (b) Class 3 storm.*

Interpreting the parcel results in terms of the instantaneous image or contour fields of the satellite data is not always obvious. First of all, one has to assume steady state so that the Lagrangian model results can be thought of in the space domain. Second, for those storms with a cold-high offset, the cold point location has been interpreted as on the cloud surface, whereas it could be buried from satellite "view" in the interior of the tower, below the high point. We have assumed that the cold point location on the satellite image is the updraft location at cloud top.

5. SUMMARY

Typical thunderstorm tops have a monotonic temperature-height pattern with the highest point being the coldest and a collection of storm tops with different maximum heights (above the tropopause) having a maximum height/minimum T_B relation closer to adiabatic than ambient (Class 1). This temperature-height relation is reproduced by the model for low values of mixing, presumed to relate to small relative ambient winds at tropopause level.

Two classes of storms with an observed cold-warm IR T_B couplet (∿40 km dimension) have been identified and simulated with the simple model. In the Class 2 storm, the cold point is co-located (or nearly co-located) with the highest point and the warm point is on the downward slope to the rear (downwind) of the highest point (Fig. 10a). The occurrence of the warm point is due to a combination of intense mixing, a strong updraft, large drag, and the presence of a weak inversion. This explanation is applicable to the example shown in Fig. 1.

As the inversion steepens, the cold-high offset grows until the cold and warm points are at about the same altitude (Fig. 10b). This is a Class 3 storm and is represented by the example in Fig. 2. Minimum temperature-maximum height plots from the model also indicate that, in these situations, the larger mixing will produce temperature-height relations closer to ambient, in agreement with observations.

The success of this simple model and the results of Schlesinger (1982) indicate that a dynamical explanation for the close-in cold-warm couplet is very plausible.

6. REFERENCES

Adler, R. F., D. D. Fenn, and D. Moore, 1981: Spiral feature observed at top or rotating thunderstorm. Mon. Wea. Rev., 109, 1124-1129.

_____, M. J. Markus, A. J. Negri, and G. P. Byrd, 1982: Estimating the temperature and height of overshooting thunderstorm tops from geostationary satellite infrared data. Conference on Cloud Physics, Amer. Meteor. Soc., 500-503.

_____, M. J. Markus, D. D. Fenn, G. Szejwach, and W. E. Shenk, 1983: Thunderstorm top structure observed by aircraft overflights with an infrared radiometer. J. Clim. Appl. Meteor., 22, 579-593.

_____, and M. J. Markus, 1983: Satellite severe thunderstorm detection: Potential and limitations. Preprints, Thirteenth Conf. Severe Local Storms, Amer. Meteor. Soc., 333-336.

Fujita, T. T., 1982: Principle of stereoscopic height computations and their application to stratospheric cirrus over severe thunderstorms. J. Meteor. Soc. Japan, 60, 355-368.

Hasler, A. F., 1981: Stereographic observations from geosynchronous satellites: An important new tool for the atmospheric sciences. Bull. Amer. Meteor. Soc., 62, 194-212.

Heymsfield, G. M., R. H. Blackmer, Jr., and S. Schotz, 1983a: Upper-level structure of Oklahoma tornadic storms on 2 May 1979. I: Radar and satellite observations. J. Atmos. Sci., 22, 1740-1755.

_____, G. Szejwach, S. Schotz, and R. H. Blackmer, Jr., 1983b: Upper-level structure of Oklahoma tornadic storms on 2 May 1979. II: Proposed explanation of V pattern and internal warm region in infrared observations. J. Atmos. Sci., 22, 1756-1767.

Mack, R. A., A. F. Hasler, and R. F. Adler, 1983: Thunderstorm cloud top observations using satellite stereoscopy. Mon. Wea. Rev., 111, 1949-1964.

McCann, D. W., 1983: The enhanced-V, a satellite observable severe storm signature. Mon. Wea. Rev., 111, 887-894.

Negri, A. J., 1982: Cloud-top structure of tornadic storms on 10 April 1979 from rapid scan and stereo satellite observations. Bull. Amer. Meteor. Soc., 63, 1151-1159.

Schlesinger, R. E., 1980: A three-dimensional numerical model of an isolated thunderstorm. Part II: Dynamics of updraft splitting and mesovortex couplet evolution. J. Atmos. Sci., 37, 396-420.

_____, 1982: Mature thunderstorm cloud top structure: Three-dimensional numerical simulation versus satellite observations. Conf. on Cloud Physics, Amer. Meteor. Soc., 512-515.

Simpson, J., and V. Wiggert, 1969: Model of precipitating cumulus towers. Mon. Wea. Rev., 97, 497-498.

D.6

ESTIMATING PRECIPITATION AREAS OVER THE EASTERN PACIFIC USING GOES SATELLITE IMAGERY

Laurie K. Neil

Atmospheric Environment Service
Pacific Weather Centre
Vancouver, British Columbia, Canada

1. THE CHALLENGE

Knowledge concerning areas of precipitation at analysis time is a necessary requirement for the preparation of accurate forecasts. However, delineating precipitation areas over the data sparse Pacific Ocean provides a difficult challenge to operational meteorologists. In many instances ship reports are very scarce, and the removal of the weather ship at Ocean Station PAPA further deteriorated the situation. As a result the forecaster must rely quite heavily upon satellite imagery. Although this imagery is received in a timely manner, and adequately covers the eastern Pacific, discriminating between precipitating cloud areas and non-precipitating cloud areas based on the satellite data has proven to be difficult.

This paper describes a procedure for determining areas of precipitation which is based on elementary atmospheric dynamics theory. The procedure utilizes the unique satellite data processing system available at the Pacific Weather Centre. In the future the technique which is employed will be partially automated, and utilized on an operational basis in the Weather Centre.

2. THE CONCEPT

Within a developing synoptic scale cloud system, the mean vertical motion is upward. This is true notwithstanding the mesoscale downward motions which take place. In order to be able to estimate precipitation amounts falling under the cloud (or for that matter to determine whether or not a cloud area is precipitating at all), some knowledge of the mean vertical velocity of air within the cloud is required. From the continuity equation it follows that for upward vertical velocity to occur, convergence must be present at low levels and divergence at high levels. Low level convergence is a very difficult quantity to measure, as is vertical velocity. In many cases, however, divergence at high levels can be estimated by examining the amount of expansion in the cloud tops over some time interval.

Several researchers have previously utilized the idea that expanding cloud tops imply upward vertical velocity and hence suggest a likelihood of precipitation falling beneath them. However their work, for the most part, dealt with mesoscale cloud systems. In particular, Stout et al (1979) produced estimates of precipitation amounts from cumulonimbus clouds over the tropical Atlantic. Wylie (1979) presented evidence to suggest that the same technique, with some modifications, would work at higher latitudes. Griffith et al (1981) developed a scheme to provide estimates of convective rainfall in the tropics beyond the range of calibrated radars. Their technique involved the change with time in the size of echo areas. Scofield and Oliver (1982) designed a technique utilizing both infrared and visible imagery. This procedure was implemented in the form of a decision tree, and was especially designed for use in predicting flash floods. Fenner (1982) applied similar concepts in his research on extratropical cyclones over Europe.

Despite the considerable amount of work which was being carried out on mesoscale precipitation areas, it was not until Ingraham and Russel (1979) explored this concept in terms of synoptic scale precipitation that its full potential began to be realized. More recently, Spagnol (1980) and Siermacheski (1983) have continued to refine the basic concepts described by Ingraham. It is from this basis that the technique described in this paper is derived.

3. THEORY

Assuming that all condensate is immediately precipitated, the maximum possible rate of precipitation at the bottom of an atmospheric column is given by the vapour flux through the column. Therefore, $R_{max} = \rho_w W$ where ρ_w is the density of water vapour and $W = dz/dt$ is the vertical velocity (see Figure 1). Futhermore, since $\rho_w = dm/dz$ where m is the precipitable water, we have:

$$R_{max} = \frac{dm}{dz} W . \qquad (1)$$

Assume that the real rate of precipitation at the surface is directly proportional to the maximum rate of precipitation through the bottom of the cloud layer, i.e.

$$R_{max} \propto R_{real} = R. \tag{2}$$

From the continuity equation...

$$\frac{dW}{dz} = -\frac{1}{A}\frac{dA}{dt} = -\frac{d(\ln A)}{dt}. \tag{3}$$

Let the area enclosed by a certain contour of radiance on the infrared imagery (or a certain contour of reflectivity on visible imagery) at some time t be represented by "A". Then from the continuity equation, the rate of change in the cloud top area A is related to the change in vertical velocity through a layer dz. Extending this to the deep layer based at the level of non-divergence (LND) and topped at the cloud top level, it can be seen that the change in cloud top area should be related to the vertical velocity at the LND. It is the premise of this paper that this is generally true even though the air diverges throughout the atmospheric column above the LND, and not solely at the cloud top level. Then...

$$W \approx \frac{-d(\ln A_{top})}{dt}\Delta z, \tag{4}$$

where $\approx$ indicates "is approximately proportional to".

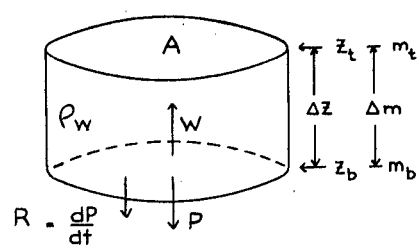

Figure 1
Schematic model of a cloud cell.
See text for annotation.

To further simplify the equations, assume that the vertical distribution of precipitable water through a cloud varies linearly through its cross section, i.e.

$$\frac{dm}{dz} \approx \frac{m_{top} - m_{bot}}{z_{top} - z_{bot}} = \frac{\Delta m}{\Delta z}. \tag{5}$$

Combining equations (1) to (5)...

$$R \approx \frac{\Delta m}{\Delta z} \cdot -\frac{d(\ln A_{top})}{dt}\Delta z,$$

or letting P = precipitation amount...

$$R = \frac{dP}{dt} \approx (m_{bot} - m_{top}) \cdot \frac{d(\ln A_{top})}{dt}. \tag{6}$$

If the moisture content is assumed to decrease to zero at the top of the column, then:

$$P_2 - P_1 \approx m\Delta \ln A_{top}, \tag{7}$$

where m is the precipitable water content through a vertical cross section of the cloud, and $P_2 - P_1$ is the precipitation amount that falls during some time interval Δt. Then $P_2 - P_1$ can be written as a function of the product of precipitable water content and change in cloud area...

$$P_2 - P_1 = \Delta P = f[m\Delta \ln A]. \tag{8}$$

Now if a function f(x) is differentiable and continuous over an interval in question, an approximating polynomial function g(x) of degree n can be found such that:

$$f(x) \approx g(x) = \sum_{i=0}^{n} a_i x^i.$$

Then the function for ΔP can be approximated by a polynomial of degree n...

$$\Delta P \approx \sum_{i=0}^{n} a_i (m\Delta \ln A)^i, \tag{9}$$

where a_i are empirically derived coefficients. In other words, ΔP can be represented by the series...

$$\Delta P \approx a_0 + a_1 m\Delta \ln A + a_2 (m\Delta \ln A)^2 + \ldots + a_n (m\Delta \ln A)^n. \tag{10}$$

The true area of a pixel on a satellite image is given by $A = r^2 A_s$, where A_s is the area of the pixel (picture element) at the satellite's subpoint and r is a resolution factor defined by the geographic position of the pixel, and by the satellite's position. Also, A_s is directly proportional to N, the number of pixels on the imagery contained in the cloud top. So equation (9) becomes...

$$\Delta P = P_2 - P_1 \approx \sum_{i=0}^{n} a_i [m\Delta \ln(r^2 N)]^i, \tag{11}$$

where a_i are empirical constants.

4. THE APPROACH

From a large number of cases of cloud systems moving over coastal British Columbia, a subset consisting of those cases where the cloud area was expanding or remaining constant was chosen for analysis. Seven such test cases were studied in detail and these constituted a dependent sample. Precipitation amounts are available for a number of ground stations along the British Columbia coast. Precipitable water content is available from TOVS (Tiros Operational Vertical Sounder) data. The resolution factor r is easily calculated, and the number of pixels contained in a cloud area can be measured at the Pacific Weather Centre using the METDAS (Meteorological Data Analysis System) statistics program. Two GOES images were used, taken one hour apart, to measure the change in cloud top area in each case. Hence all of the required information was available for the compilation of a dependent sample.

Cases in which the cloud area was decreasing were also inspected though in a more superficial manner to ensure that the precipitation from such systems was only light. This was generally true for the cases studied thus far.

The degree of the polynomial which best fit the observed data was then determined, and the empirical constants obtained by application of the principle of least squares. Once the empirical constants were determined, precipitation amounts could theoretically be predicted for any cloud area where GOES imagery and TOVS data are available. However, as a first step we only wish to find whether a determination of "widespread rain" versus "little or no rain" can be made using this technique, and not actually to quantify precipitation amounts. As a second step, the results of this technique will be used in a procedure for determining more specifically the location of precipitation within a cloud system.

5. COMPLICATIONS

This approach can only work for cloud areas in which the term $\Delta \ln(r^2N)$ in equation (11), the governing equation, is positive or zero. A discontinuity exists where this term becomes negative, and the relationship is no longer valid. However spotty precipitation may still occur even in weakening systems where the cloud area is decreasing, due mainly to airmass instability. The question of whether or not a direct measure of stability should be included in this rain estimation technique is something which will have to be determined on the basis of observation and experimentation. It is probable that a subjective determination of stability by the meteorologist will be the best method of approaching this problem.

Orographic effects obviously have a strong influence on cloud systems. The necessity of collecting data for the development sample over an area for which precipitation values are available meant that the coastal mountains influenced the results. In general, precipitation values along the coast can be assumed to be higher than they would have been over the ocean (Spagnol, 1982). The fact that many of the coastal stations are located in "rainshadows" compensates for the topographical enhancement of precipitation.

A third complication arises due to the fact that the particular threshold radiance value that is selected to delineate a meaningful cloud top on the imagery may influence the results when using this technique. In general it was found that no single threshold value could be used in all cases. This agrees with the findings of Blackmer (1975) in his studies of convective clouds. Rather, the threshold value giving the best results was one near the middle of the strongest gradient in pixel values (Figure 2). In particular it was found that a threshold value near the coldest tops should not be chosen, as these areas were not always representative of cloud systems as a whole. In one case, the area of coldest tops was definitely seen to be decreasing, while the cloud system as a whole was expanding. Another guideline which can be followed in choosing the threshold contours is to include cloud areas below which precipitation is being reported by surface based stations.

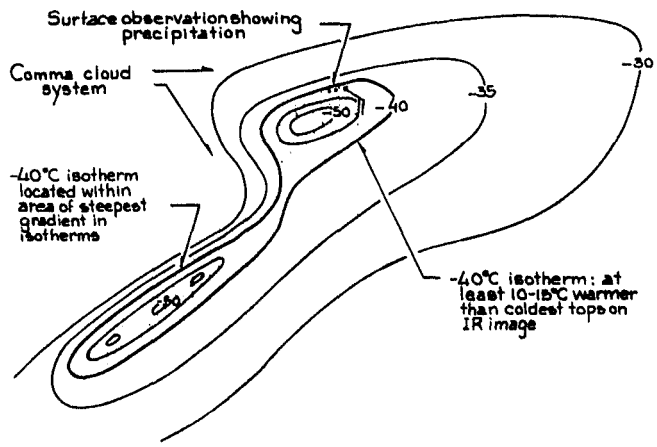

Figure 2
An example showing a method of choosing a threshold temperature for measuring the change in area of clouds on GOES infrared imagery. In this case the -40°C isotherm was chosen as most suitable.

6. DATA ANALYSIS AND RESULTS: THE DEPENDENT SAMPLE

Data was collected for a number of cases over a seven week period during the late autumn of 1983. Changes in area of well-defined cloud systems were measured from GOES-West images over a one hour time interval as they moved over the British Columbia coast. Only infrared images were used for this purpose, since software to enable normalization of visible imagery to noon local time was not yet operational at the Pacific Weather Centre.

As a rule, entire synoptic scale cloud systems were analyzed for changes in size. However subsets of the system cloud, where they were well defined and significant, were used at times. In particular, in areas of widespread baroclinic cloudiness it was sometimes useful to analyze changes in more localized areas of enhanced cloud associated with shortwave features. A note of caution is in order here. This technique is for use with large cloud systems; if smaller cloud elements are measured (approaching the mesoscale), different constants are needed for the equation. This is because such mesoscale cloud systems change their relative size much more quickly than synoptic scale systems, since different processes are involved.

Hourly precipitation amounts over British Columbia's coastal weather stations for the hour spanned by two GOES-West images was estimated using six hour synoptic reports and

hourly aviation reports. The time lag between precipitation events and cloud top expansion that has been noted by researchers dealing with mesoscale cloud systems (Stout et al, 1979) was not noticed in this study. Rather, if there was a time lag involved it appeared to be in the opposite direction. Especially in the case of rapid development, heavy precipitation continued for some time after the strongest growth in the cloud system had been evident. This is presumably due to the large amounts of moisture which saturate the atmospheric column during such development. Considerable time is required for this moisture to precipitate out of the system.

TOVS data appeared to give consistent and reliable values of precipitable water content over the area. Although accurate precipitable water values cannot be obtained in areas of thick (i.e. precipitating) cloud, values immediately on the warm side of the cloud band can be considered to be representative. Isolines of precipitable water were drawn around the cloud area facilitating the analysis.

The degree of the polynomial which best fit theoretical expectations as well as the observational data turned out to be of order 2. Therefore truncating the series at n=2, equation (11) becomes:

$$\Delta P = a_0 + a_1 m \Delta \ln(r^2 N) + a_2 [m \Delta \ln(r^2 N)]^2. \quad (12)$$

Theoretically, one would expect a limit to the amount of precipitation that would fall in some finite time interval given an arbitrary value of m, the precipitable water content. Equation (12) yields just such a result in explaining the variation in precipitation rates within the range covered by the dependent sample.

Table 1 shows a summary of the results of the seven case studies which have been analyzed to date. The results are depicted graphically in Figure 3. The curve best fitting the data was found to be...

$$\Delta P = -.12 + .78\, m \Delta \ln(r^2 N) - .05 [m \Delta \ln(r^2 N)]^2.$$

CASE #	AVG. PRECIP. RATE AT SFC. STATIONS UNDER THRESHOLD AREA (mm)	TTL. PRECIP. WATER (m) (mm)	THRESHOLD TEMP. °C	PRODUCT OF m & CHANGE IN CLD. AREA OVER 1 HR. $m\Delta \ln(r^2 N)$
1	.37	11	-35	1.254
2	.84	12	-20	2.004
3	.13	10	-20	.150
4	2.48	15	-45	9.915
5	1.67	12	-20	2.172
6	1.67	12	-40	2.448
7	.88	15	-50	1.125

Table 1
Table summarizing results of the test cases which constituted the dependent sample.

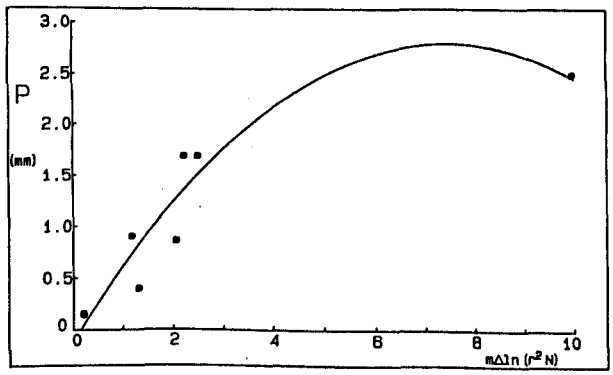

Figure 3
Graph showing the relationship between precipitation versus the product of precipitable water content and change in the logarithmic value of cloud area over a one hour period. The seven data points are seen plotted along with the curve of best fit.

It can be seen from the graph that the curve fits the data reasonably well, with a coefficient of determination of .87 and standard error of the estimate of .36 mm. This implies that 87% of the variation in precipitation amount that was observed in the dependent sample was explained by the change in cloud area together with precipitable water values. Although the sample size was too small to yield a statistically significant value for standard error, the value of .36 does suggest that the equation could predict hourly precipitation amounts to within approximately 15% of their actual value, 68% of the time.

The decrease in expected precipitation amounts predicted for very rapid cloud expansion rates is not reasonable in a physical sense, though a limit is likely approached in this region for maximum precipitation amounts. This situation is explained by the fact that only small cloud systems could realistically be expected to expand by more than 60% over a one hour period (an expansion corresponding to a $\Delta \ln(r^2 N)$ value of 0.5). This was in fact the situation in one of the cases constituting the dependent sample (case 4). The reason why this case was not rejected from the development (dependent) sample was that it shows the effective limiting of precipitation amounts for rapid increases in cloud. This technique should be used with great caution, however, for values of $\Delta \ln(r^2 N) > .5$ if actual precipitation values are desired.

7. POSSIBLE OPERATIONAL USE

In the initial stages of development at the Pacific Weather Centre, all that will be required of this technique is that it classify cloud systems into one of three categories, as shown in Figure 4. Typical precipitation patterns under clouds in each category and for three different types of synoptic situations are shown. These patterns are based on cloud models illustrated by Weldon (1979) and also from patterns observed during the case studies, and in day-to-day forecast operations. Using these models, together with any information supplied by surface observations and other sources, the meteorologist should be able to make a much improved estimate of where precipitation is falling under a given cloud system.

Much of the data required in utilizing this technique is available to the Pacific Weather Centre's METDAS computer system. Only the precipitable water content, because it is not derived through GOES, needs to be input into the system by the meteorologist. Consequently, this procedure lends itself very handily to partial automation.

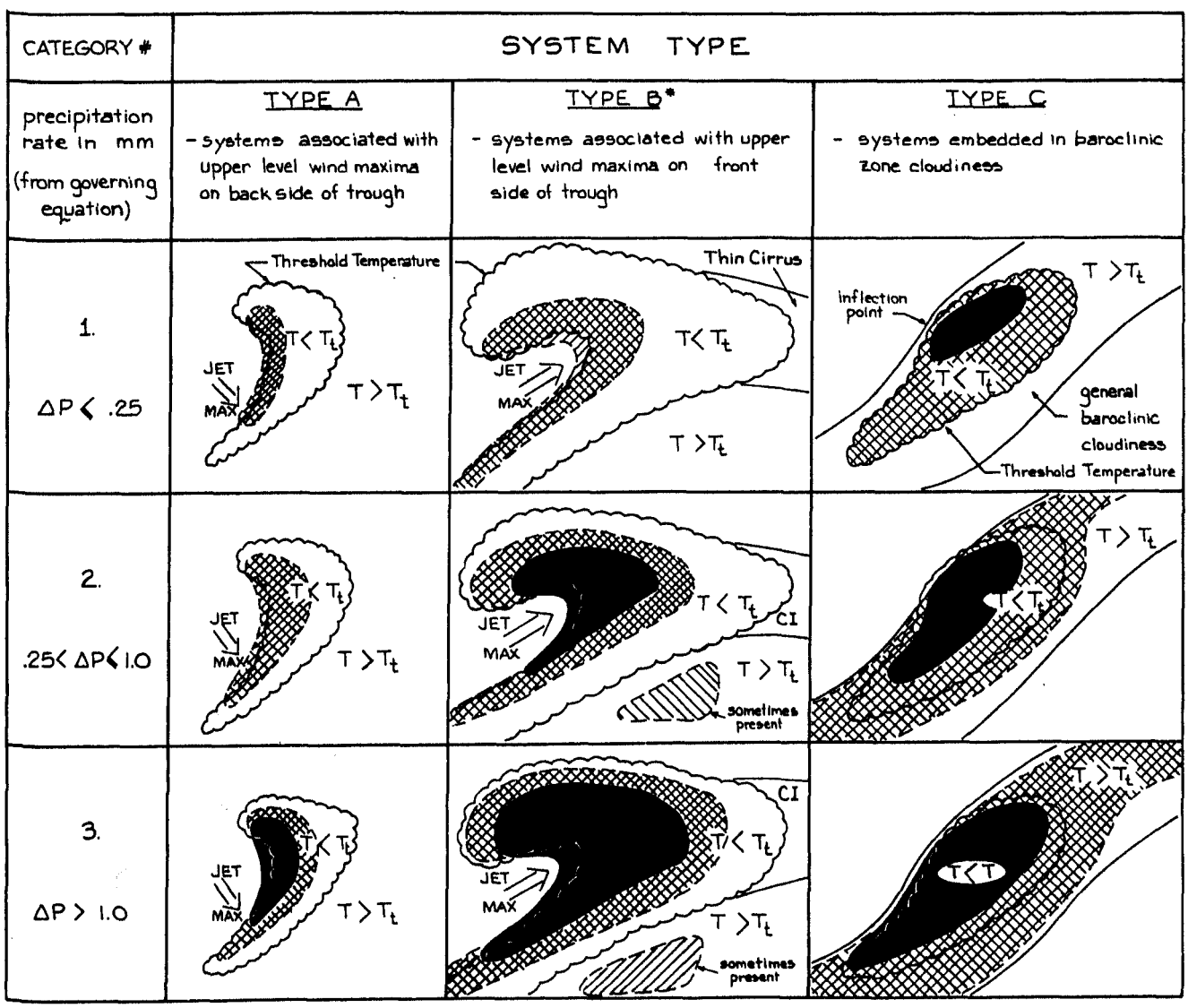

Figure 4

Typical precipitation patterns for each of the three cloud expansion categories, and for three different types of synoptic situations. Areas of occasional or patchy convective precipitation are enclosed by dashed lines and stippled, while probable areas of widespread continuous precipitation are enclosed within solid lines and shaded. Scalloped lines represent selected threshold temperatures (i.e. relatively cold cloud tops).

*NOTE: For type B systems, if strong development has occurred during the preceeding six hours, add one to the category number, e.g. category "1" becomes category "2".

8. SUMMARY

The technique described in this paper for defining precipitation areas from satellite imagery utilizes a man/machine mix which can be expected to be quite efficient in an operational setting. The scheme will be tested over the next year at the Pacific Weather Centre. The same procedures will be applied to normalized visible data. Also, combinations of visible and infrared thresholds will be used to determine whether more accurate results can be obtained. If the technique performs as expected, it will be implemented operationally at the Weather Centre.

9. ACKNOWLEDGEMENTS

The author wishes to thank Mr. John Spagnol who initiated this project and also supplied technical support and advice throughout. The assistance of Mr. Bob Loveless in preparing the graphics was greatly appreciated, as was the help rendered by Ane Street in typing the manuscript.

10. REFERENCES

Blackmer, R.H., Jr., 1975: Correlation of Cloud Brightness and Radiance with Precipitation Intensity. Final Report on Contract N66314-74-C-2350, Stanford Research Institute, Menlo Park, Cal., 121 pp.

Fenner, J.H., 1982: Using Satellite Imagery to Estimate Winter Season Rainfall in Europe. Ninth Conference, Weather Forecasting and Analysis, Seattle, Washington, 245-249.

Griffith, C.G., J.A. Augustine, and W.L. Woodley, 1981: Satellite Rain Estimation in the U.S. High Plains. Journal of Applied Meteorology, Volume 20, 53-56.

Ingraham, Diane V., and S.O. Russel, 1979: Estimating Precipitation from Satellite Photographs. Department of Civil Engineering, University of British Columbia.

Scofield, R.A. and V.J. Oliver, 1982: Preliminary Efforts in Developing a Technique that uses Satellite Data for Analyzing Precipitation from Extratropical Cyclones. Ninth Conference, Weather Forecasting and Analysis, Seattle, Washington, 235-244.

Siermacheski, P., 1983: Rain Estimates from Satellite Imagery for the Northeast Pacific Region. Pacific Weather Centre Internal Report 83-039.

Spagnol, J., 1980: Combining Radar and Satellite Data to Estimate Precipitation Rates over the Pacific. Pacific Region Technical Note 80-002.

Spagnol, J., 1982: The Upslope Effect? Ninth Conference, Weather Forecasting and Analysis, Seattle, Washington, 258-262.

Stout, John E., D.W. Martin, and D.N. Sikdar, 1979: Estimating GATE Rainfall with GOES Images. Monthly Weather Review, 107, 585-598.

Weldon, R., 1979: Part IV Cloud Patterns and the Upper Air Wind Field. In-house publication of the Applications Laboratory, NESS/NOAA, 42-45.

Wylie, D.P., 1979: An Application of a Geostationary Satellite Rain Estimating Technique to an Extratropical Area. Journal of Applied Meteorology, Volume 18, 1640-1648.

NIMBUS 7 SMMR DERIVED SEASONAL VARIATIONS IN THE WATER VAPOR, LIQUID WATER, AND SURFACE WINDS OVER THE GLOBAL OCEANS

C. PRABHAKARA
DAVID A. SHORT
Goddard Laboratory for Atmosphere Sciences
NASA/Goddard Space Flight Center
Greenbelt, Maryland 20771

1. INTRODUCTION

The Scanning Multichannel Microwave Radiometer (SMMR) flown on the Nimbus 7 satellite measured the brightness temperature of the earth-atmosphere system at five frequencies (6.6, 10.7, 18, 21 and 37 GHz) in dual polarization. This instrument is designed with the objective of mapping over the open ocean sea surface temperature (SST), surface wind speed, atmospheric integrated water vapor content, integrated liquid water content and rain fall and to determine sea-ice type and extent (Gloerson and Barath, 1977). In this study we are limiting the scope to the examination of atmospheric water vapor and liquid water, and surface wind speed. The SMMR derived SST information is not included here as the antenna side lobe contamination introduces significant errors in the vicinity of land masses (Njoku, 1980). A brief discussion of the retrieval technique used to derive these parameters is presented.

The atmospheric and surface parameters sensed by SMMR over oceans strongly reflects the state of the atmospheric boundary layer. The ocean-atmosphere interactions that take place through this boundary layer can thus be inferred from an examination of the SMMR observations.

This study is based on monthly mean maps of water vapor, liquid water and surface winds over the oceans generated from 13 months of SMMR data. These maps are presented with detailed discussion in a study by Prabhakara and Short (1984). The December 78 and June 79 maps of these parameters are shown here to reveal the seasonal changes. Zonal averages for December and June of these parameters are compared with information derived from conventional measurements.

2. RETRIEVAL TECHNIQUE

The SMMR brightness temperature measurements in the 18 and 21 GHz channels strongly reflect the atmospheric water vapor information. The difference, $T_{21} - T_{18}$, between the two brightness temperatures is mainly dependent on the water vapor content in the atmosphere. This difference is nearly independent of SST and is only weakly affected by surface winds and liquid water in the atmosphere. Utilizing this signal we have derived atmospheric water vapor over the oceans with an accuracy of about 0.25 g/cm^2.

The 6.6 GHz channel of SMMR is least affected by the atmospheric absorption due to water vapor and liquid water. The sea surface emissivity at this frequency is nearly independent of SST (Wilheit and Chang, 1980). Applying a small correction (0.3K per 1g/cm^2 of water vapor in the atmosphere) to the brightness temperature at 6.6 GHz in the vertical polarization we have estimated the SST. Measurements affected by liquid water in the atmosphere and winds are objectively eliminated in the SST retrievals.

Moderate winds (< 10m/s) produce a relatively weak effect on the SMMR brightness temperatures when compared to that of the liquid water in the atmosphere. Furthermore, the combined effect of the liquid water and surface wind in the SMMR brightness temperatures is non-linear. For this reason the surface winds and liquid water are estimated, respectively, under divergent and convergent circulation regimes in the boundary layer. The technique used to identify the divergent and convergent wind regimes as well as the methods to estimate the liquid water and surface winds are described in a study of Prabhakara, et. al (1983).

3. SEASONAL VARIATIONS

Monthly mean maps of water vapor and liquid water, and the surface wind derived from SMMR over the oceans for Dec. 78 and June 79 are presented in Figures 1 and 2 respectively. In order to appreciate the information contained in the satellite measurements monthly mean maps of 1000mb wind vectors derived from FGGE data are shown in these figures.

The intertropical convergence zone (ITCZ), about 5° north of the equator, and the south Pacific convergence zone are characterized by maxima in the liquid water content and water vapor. On the east side of the subtropical oceans where subsidence generally prevails there is a minimum in the water vapor and liquid water. In the regions where there are warm ocean currents such as the Gulf Stream, Kuroshio, Brazil and Agulhas currents there is above average liquid water content in the atmosphere. The surface wind speed maps show weak winds of about 5 m/s in the low latitudes and stronger winds in excess of 10 m/s in the middle and high latitudes particularly over the regions of warm ocean currents. The seasonal changes in the strength and position of several of these water vapor, liquid water, and surface wind features may be noticed by comparing December and June maps. The wind vector maps deduced from FGGE data, when compared with the SMMR water vapor maps, show that the water vapor in the atmosphere is a good tracer of the large scale atmospheric motions.

In Figure 3 zonal averages (over the ocean) of the water vapor, liquid water, and surface wind speed derived from SMMR observations for December and June are shown. The zonal average of water vapor (Fig. 3a) is compared with that of the climatology of air temperature over the oceans (Fig. 3b). Notice the water vapor in Fig. 3a is displayed on a non-linear scale that reflects the vapor pressure dependence on the temperature. The seasonal change of air temperature over the oceans is somewhat larger than that of the SST and the atmospheric water vapor seems to follow this surface air temperature.

Zonal averages of atmospheric liquid water (Fig. 3c) clearly show the maximum associated with the ITCZ. This maximum is shown to move from about 7°N in June to about 4°N in December. The liquid water content in the middle and higher latitudes particularly in the northern hemisphere is significantly larger in winter compared to summer suggesting the importance of the mid latitude baroclinic activity in winter. In the southern hemisphere the seasonal changes are considerably smaller. Zonal average precipitation estimates (See for eg. Dorman and Bourke, 1979) deduced from conventional observations show several features that resemble the zonal average liquid water measurements made by SMMR.

Zonal average wind speed derived from SMMR over the oceans (Fig. 3d) is compared with that of the FGGE wind speed (Fig. 3e). Although a close quantitative agreement is not obtained, the SMMR wind estimates show the minimum near the equator and a seasonal variation somewhat similar to FGGE data.

4. CONCLUSIONS

The SMMR measurements of surface and atmospheric parameters over the oceans describe the state of the atmospheric boundary layer. The water vapor distribution on the oceans not only follows the surface-air temperature but is strongly influenced by the advective, subsidence and rising motions in the atmosphere. The seasonal and spatial distributions of liquid water content in the atmosphere derived from SMMR over the oceans resemble the climatological precipitation patterns. The spatial and temporal variations in all the parameters sensed by SMMR suggest potential application of these data to air-sea interaction studies.

5. REFERENCES

Dorman, C. E. and R. H. Bourke, 1979: Precipitation over the Pacific Ocean, 30°S to 60°N. Monthly Weather Review, 107, 896-910.

Gloersen, P., and F. T. Barath, 1977: A scanning multichannel microwave radiometer for Nimbus-G and Seasat-A. IEEE Jour. Ocean Eng., OE 2., 172-178

Njoku, E. G., 1980: Antenna pattern correction procedure for the scanning multichannel microwave radiometer (SMMR). Boundary Layer Met., 18, 79-98

Prabhakara, C. and D. A. Short, 1984: Nimbus 7 SMMR derived seasonal variations in the water vapor, liquid water and surface winds over the global oceans. NASA/ Goddard Technical Memorandum.

Prabhakara, C., I. Wang, A.T.C. Chang and P. Gloersen, 1983: A statistical examination of Nimbus 7 SMMR data and remote sensing of sea surface temperature, liquid water content in the atmosphere, and surface wind speed. Jour. of Clim. and App. Met., 22 (December 1983).

Wilheit, T. T., and A. T. C. Chang, 1980: An algorithm for retrieval of ocean surface and atmospheric parameters from observations of the Scanning Multichannel Microwave Radiometer. Radio Science, 15, 525-544.

a.

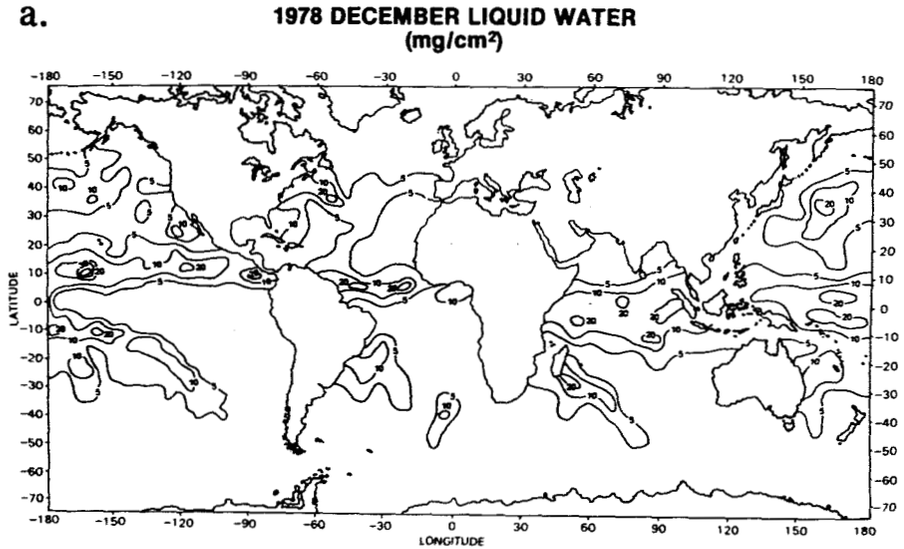

c.

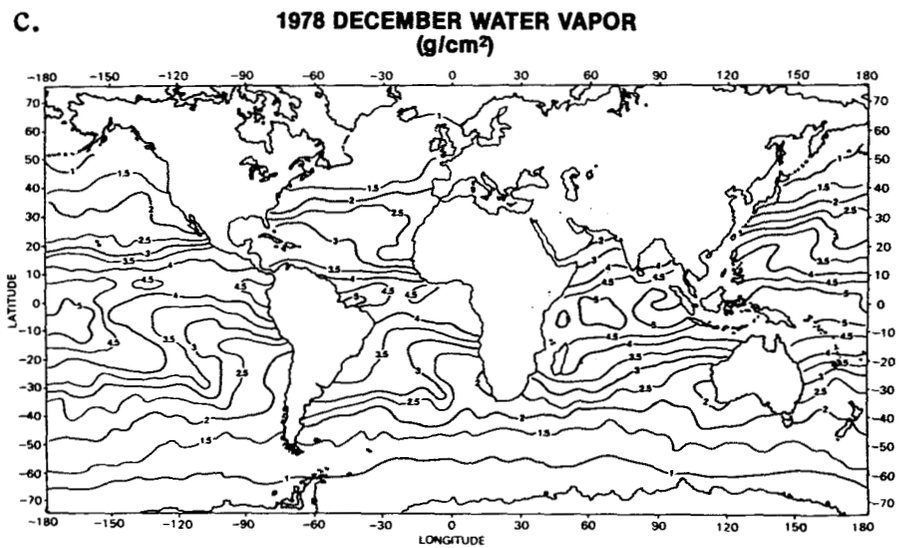

b.

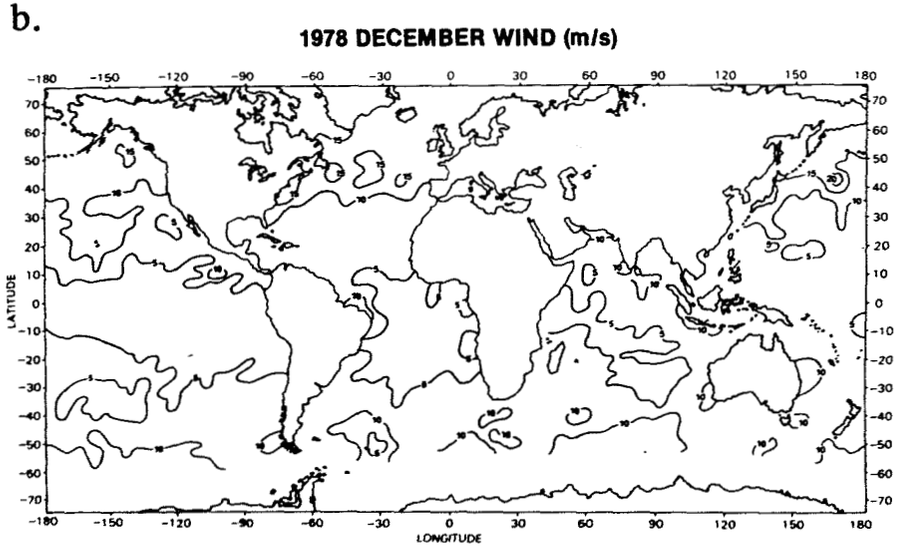

d.

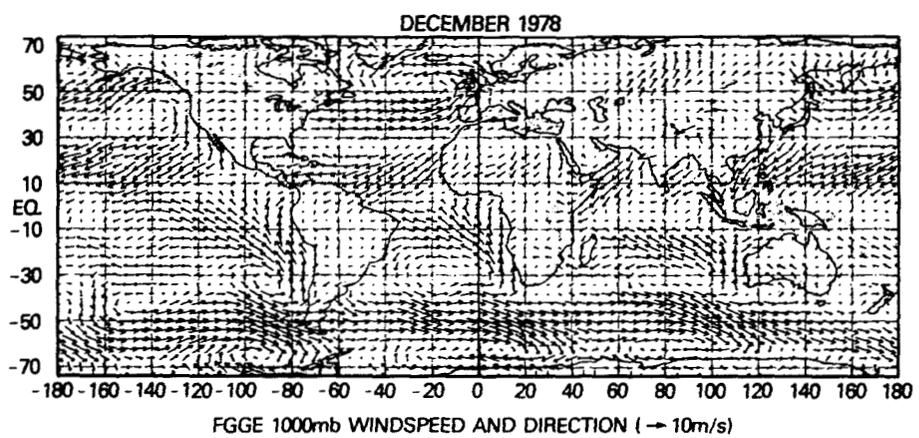

Fig. 1. Distribution of a. liquid water in clouds and rain, b. wind speed at sea surface, and c. water vapor in the atmosphere, derived from SMMR for December 78 over global oceans. d. Global distribution of wind velocity at 1000 mb. level based on FGGE data for December 78.

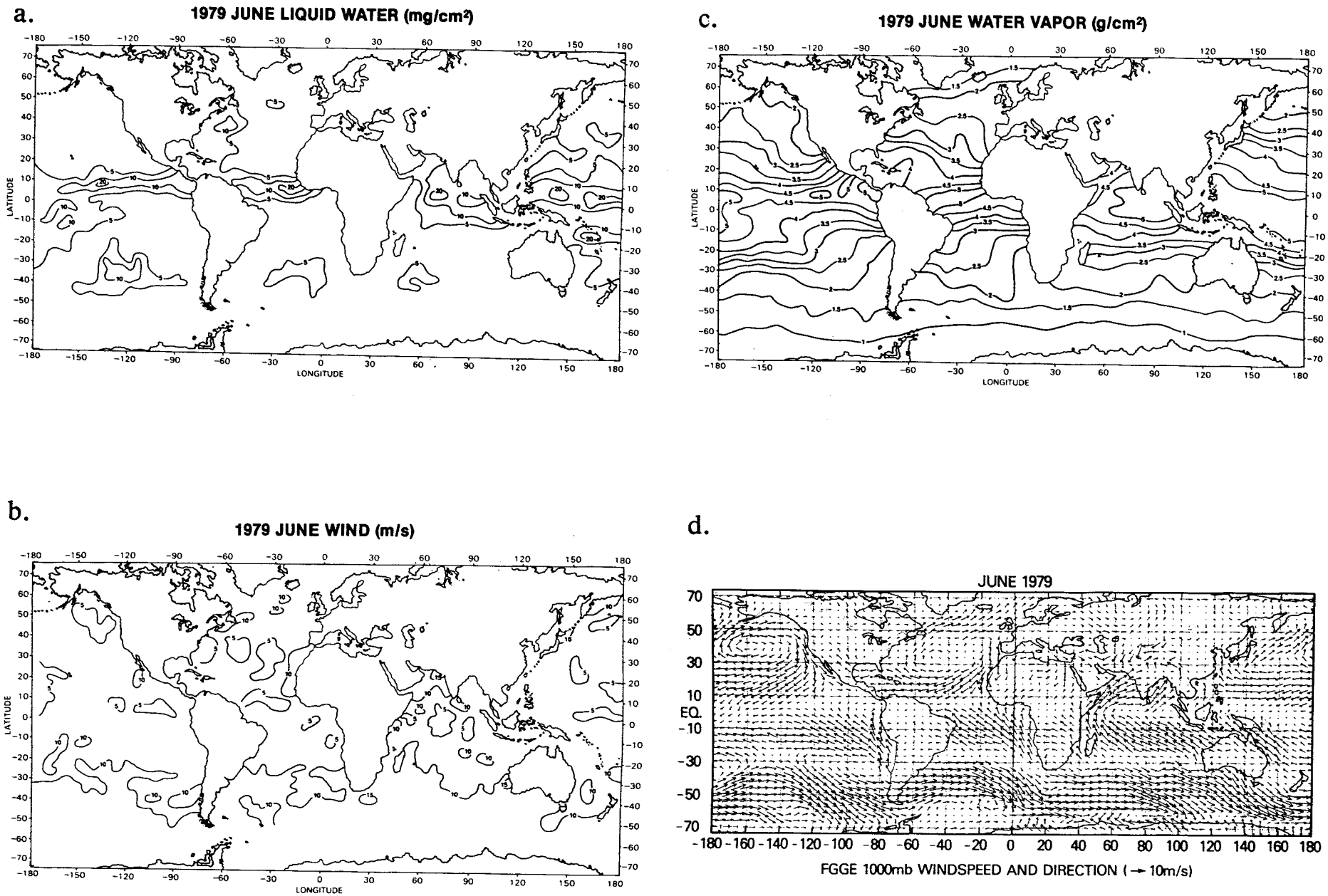

Fig. 2. Distribution of a. liquid water in clouds and rain, b. wind speed at sea surface, and c. water vapor in the atmosphere, derived from SMMR for June 79 over the global oceans. d. Global distribution of wind velocity at 1000 mb. level based on FGGE data for June 79.

a.

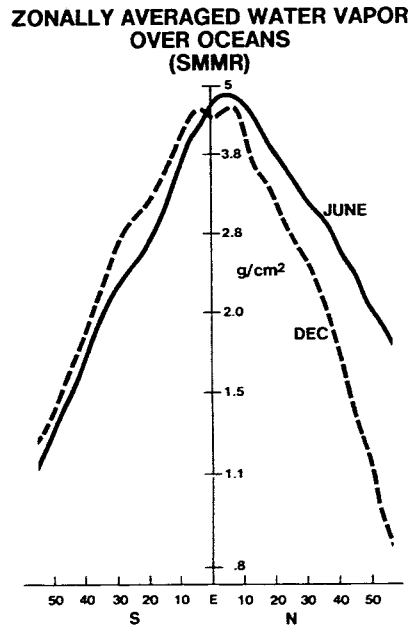

b.

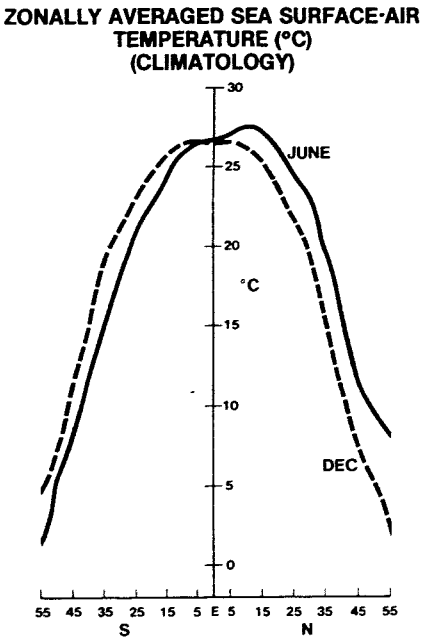

c.

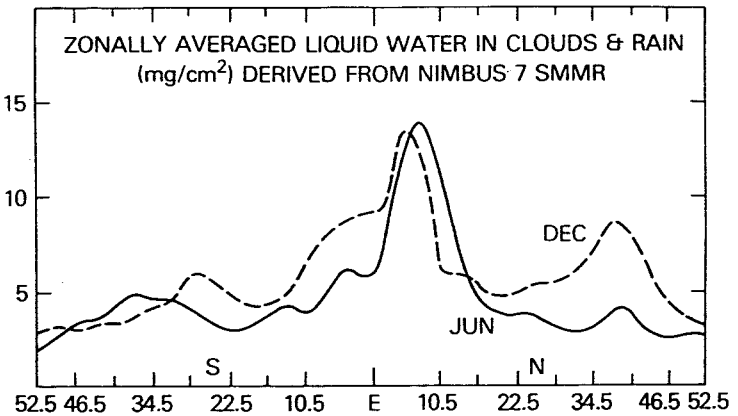

d.

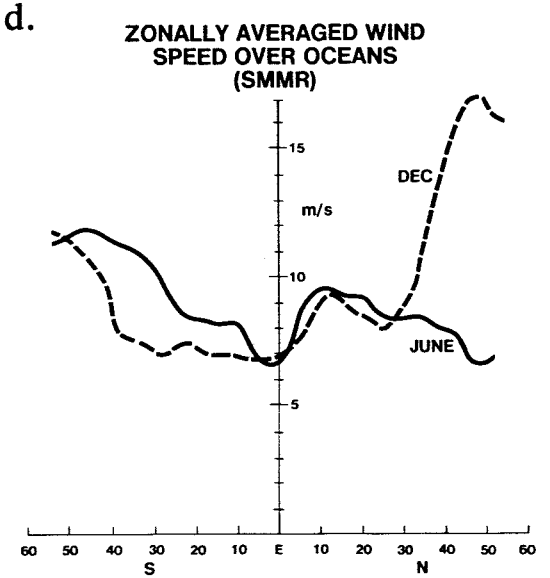

e.

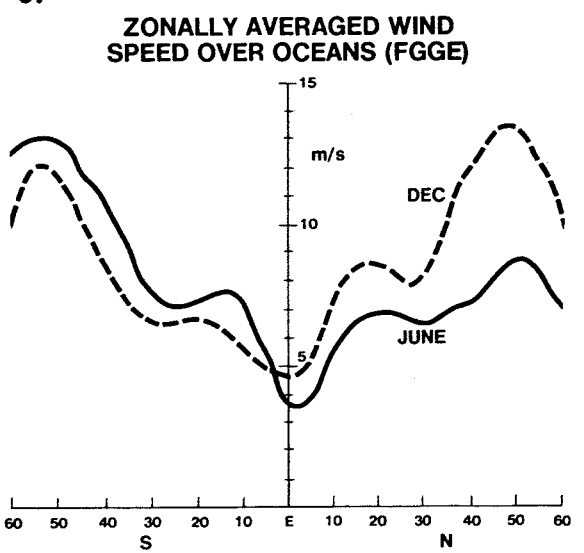

Fig. 3. a. Zonally averaged water vapor over oceans derived from SMMR for December 78 and June 79. The scale for the water vapor is based on the temperature dependence of vapor pressure.

b. Zonally averaged sea surface - air temperature over oceans for December and June derived from climatology.

c. Zonally averaged liquid water in clouds and rain over oceans derived from SMMR for December 78 and June 79.

d. Zonally averaged wind speed over oceans derived from SMMR for December 78 and June 79.

e. Zonally averaged wind speed at 1000 mb. level over oceans derived from FGGE data for December 78 and June 79.

ARCTIC ATMOSPHERE - ICE INTERACTION STUDIES USING NIMBUS-7 SMMR

Mark R. Anderson and Robert G. Crane

Cooperative Institute for Research in Environmental Sciences
University of Colorado
Boulder, Colorado

1. INTRODUCTION

The interaction between sea ice and atmospheric dynamics and thermodynamics has been the subject of numerous recent empirical and modeling studies (cf. reviews by the Polar Group, 1980; Crane, 1981). Most analyses, however, have been on seasonal, interannual, or longer time scales. Short term variations in ice extent have been noted and synoptic scale ice-atmosphere interactions have been examined, for example, by Ackley and Keliher (1976), Carleton (1981) and Overland and Pease (1982).

The influence of the atmosphere on the ice is seen primarily in the heat exchange at the surface, and also in the effect of surface winds on ice drift. Very rapid changes in sea ice distribution are possible in the marginal ice zone due to ablation and to ice advection as a response to changes in atmospheric circulation. The present paper describes two such events, one in the Greenland Sea and one in the Sea of Okhotsk, both for April/May 1979.

Analysis of such rapid events have been hampered, in the past, by the lack of accurate data on a suitable time and space scale. Research in this direction has been improved following the availability of satellite borne microwave radiometers. The major advantage of passive microwave sensors is the ability to "see" through cloud and the polar night. Data from the single channel Nimbus-5 Electrically Scanning Microwave Radiometer (ESMR) have been analysed in the context of ice-atmosphere interactions by Cavalieri and Parkinson (1981) for the Southern Ocean and by Crane et al. (1982) and Crane (1983) for regions of the Arctic.

The ESMR data provide a valuable resource for sea ice research. In the absence of supplementary data on ice temperatures and ice type or concentration, however, studies based on the single channel ESMR data are limited by their inability to resolve quantitatively these separate surface parameters. An attempt to alleviate this problem has been made with the launch of the Scanning Multichannel Microwave Radiometer (SMMR) on board Nimbus-7. Using SMMR data, ice concentration, the multi-year ice fraction, and the physical ice temperature have been derived sequentially from the multiple channel and dual polarization information. These parameters are produced by NASA Goddard Space Flight Center and are currently available for the first year of SMMR operation (November 1978 - October 1979). The derived sea ice concentration data for April and May 1979 are used here in the analysis of ice edge movement and ice concentration changes for the two study periods mentioned above.

2. NIMBUS-7 SMMR SEA ICE PARAMETERS

The Nimbus-7 SMMR records passive microwave radiation, at both horizontal and vertical polarizations, for each of five wavelengths: 6.6GHz (4.6cm); 10.7GHz (2.8cm); 18 GHz(1.7cm); 21GHz (1.4cm); and 37GHz (0.81cm). A method for retrieving ice concentration, multi-year ice fraction and the physical ice temperature has been described by Cavalieri et al. (in press). The procedure defines a polarization ratio, given by:

$$R = (TB_v - TB_h) / (TB_v + TB_h)$$

where TB_v and TB_h are the vertical and horizontal brightness temperatures recorded in a given channel. Use is made of the large polarization difference between open water and sea ice to estimate ice concentration at the 18GHz wavelength (water vapor has little effect on atmospheric attenuation at this wavelength). The use of the polarization ratio enables the derivation of the parameters to be virtually independent of the physical temperature of the surface. An initial value of 50% multi-year ice fraction is used to obtain an approximate sea ice concentration, and an iterative procedure is then used to arrive at final values of ice concentration and multi-year ice fraction. The physical ice temperature is inferred from the ice concentration and the 6.6GHz vertical brightness temperature, and the multi-year ice fraction is used to obtain the ice concentration at 37GHz.

The ice concentration retrievals at 18GHz correspond to a spatial resolution of approximately 60km, while those at 37GHz correspond to a 30km resolution. The multi-year ice fraction has a 60km resolution and the multi-year ice fraction, since it makes use of the 6.6GHz channel, has a resolution of 150km.

3. THE GREENLAND SEA

Ice extent in the Greenland Sea is largely determined by ice export from the Arctic Basin via the East Greenland Current (EGC), and by the formation of new ice within the current. This ice forms a continuous flow from north to south along the east Greenland coast. The distribution of the ice, however, is also influenced by an oceanic gyre (the Jan Mayen Gyre) north of Iceland. In winter this frequently causes an extension eastwards of a lobe of ice, referred to as "Odden", (Vinje, 1980) in the southern limb of the gyre.

An examination of the U.S. Navy-NOAA Joint Ice Center (JIC) sea ice analyses shows this feature to be particularly well developed in March/April 1979. The JIC analyses routinely use SMMR in the determination of the ice edge location. Ice concentration within the pack is based primarily on visual analysis of higher resolution visible and infrared imagery from the NOAA and Defense Meteorological Satellite Program (DMSP) series of satellites. Ice analyses from these sensors, however, are restricted by cloud conditions.

During April, under conditions of weak surface winds, Odden was separated from the main

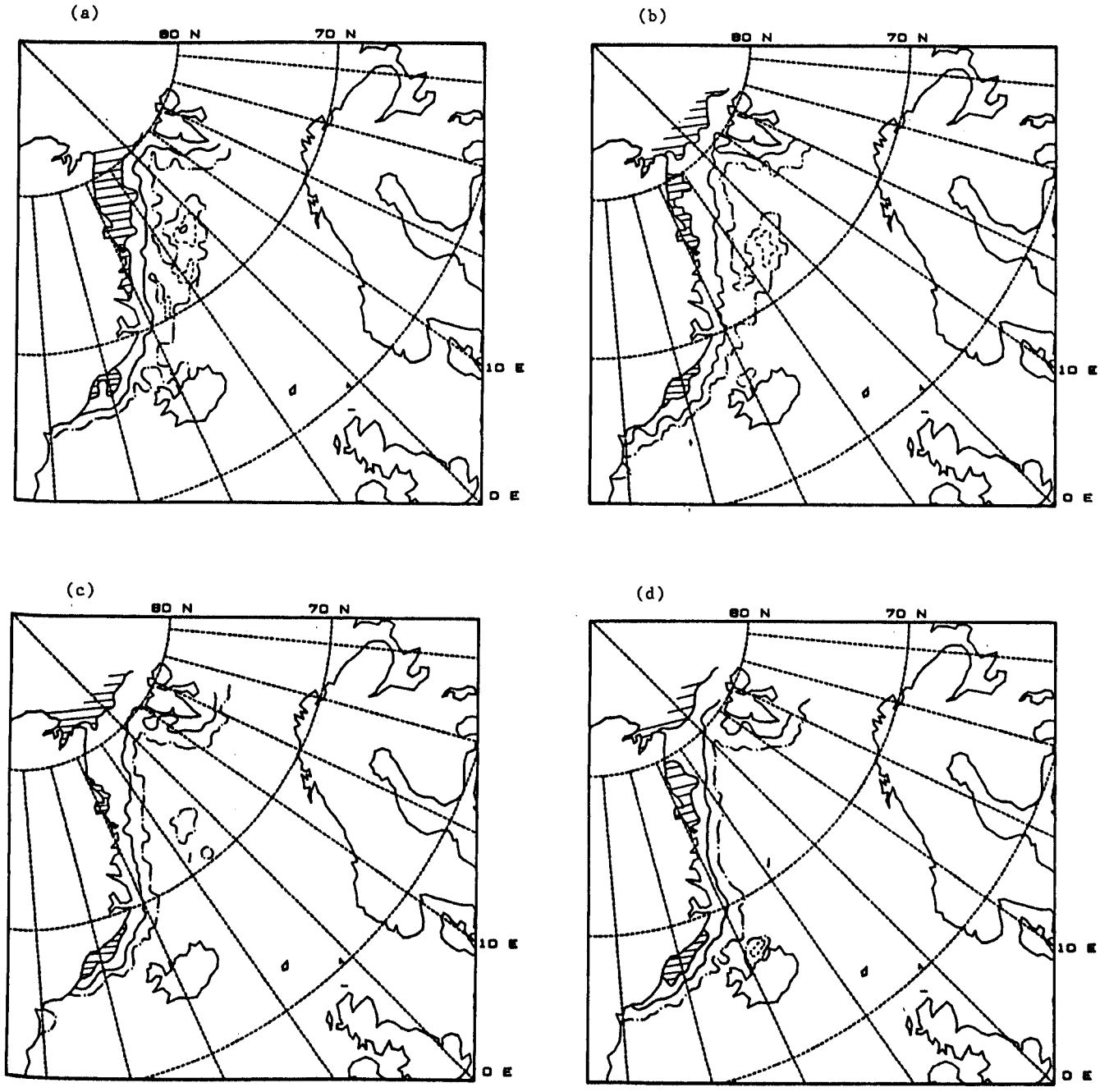

Figure 1. Nimbus-7 SMMR sea ice concentrations in the Greenland Sea for: a) 28 April; b) 30 April; c) 2 May; d) 4 May 1979. —·— = ice edge; ---- = 30%; and ——— = 50% ice concentration. The hatched areas are greater than 90% concentration.

coastal flow by a strip of open water 80-150km wide. The weekly JIC ice charts show that the lobe disappears sometime between the 29 April and 8 May. The daily DMSP visual and IR imagery shows extensive cloud cover over the region for much of the period, limiting its usefulness for ice analysis. A detailed analysis of the SMMR data, however, indicates that the change took place between the first and the fourth of May (Figure 1).

The ice band is present in the SMMR data through the end of April (Figure 1a;b). The next data day on the 2 May (SMMR operates only on alternate days due to power limitations), showed a rapid decrease in ice extent and concentration (Figure 1c). On 4 May (Figure 1d) the ice had completely disappeared from the region northeast of Iceland. Figure 1d also shows that the ice extent in the EGC decreases between about 71N and 74N, and that there is a slight increase in the Denmark Strait between Greenland and Iceland.

An analysis of the surface pressure charts shows weak high pressure in the region in late April; a representative surface pressure map is shown in Figure 2a. During this period the ice distribution is determined by the oceanic gyre (Vinje, 1980), with the weak atmospheric circulation having very little influence.

A low pressure system develops in the region towards the end of April. The system intensifies and moves southeast during the first four days of May (eg. Figure 2b). The change in wind speed results in the rapid break-up of Odden. The strong cyclonic flow may also account for the apparent ice convergence in the Denmark Strait (cf. Aagaard, 1972).

(a)

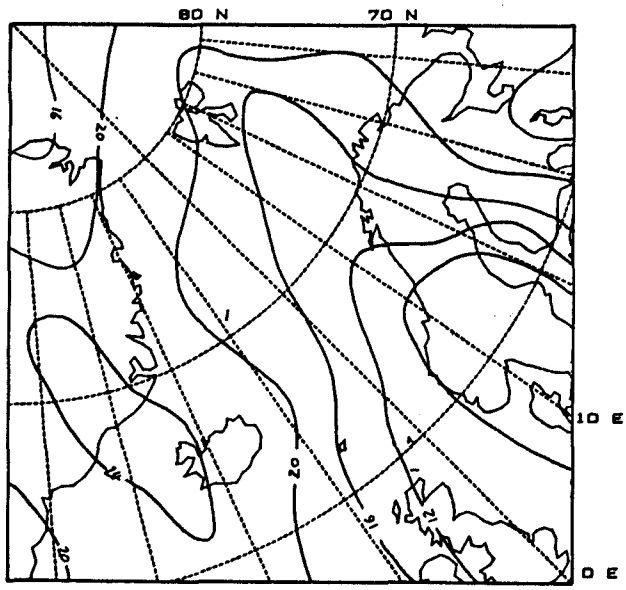

(b)

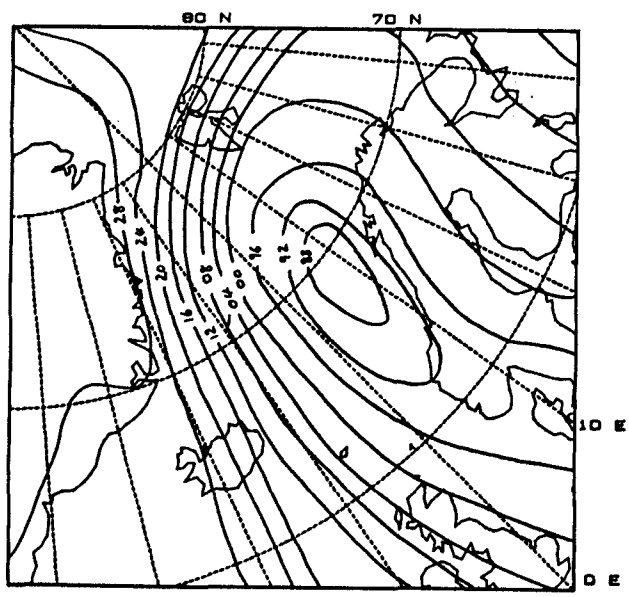

Figure 2. Sea level pressure patterns for: a) 26 April and b) 2 May 1979.

4. SEA OF OKHOTSK

The seasonal sea ice distribution in the Sea of Okhotsk has been described by Parkinson and Gratz (1983), using Nimbus-5 ESMR data. Their results suggest that there is a rapid retreat of ice from the Kamchatka coast in mid-March, with the ice remaining along the northern and western coasts through April/May.

A similar situation to the Greenland case can be seen in early May in the Sea of Okhotsk. The JIC ice analyses show a change occurring from one weekly analysis to the next. Again, analysis of the sea ice extent is hindered by cloud cover in the visual and IR DMSP imagery, while variations in ice cover can be clearly seen in the SMMR data.

From late April to early May, ice extent and concentration remains fairly stable (ice extent between 4-7 May is given in Figure 3a). SMMR data for 8-10 May shows little change in ice extent, but a substantial decrease in ice concentration in the northern part of the region (Figure 3b). Figure 3c for 12-14 May shows a rapid break-up of the ice pack with large changes in both ice concentration and areal extent. The atmospheric circulation again changes from one of weak anticyclonic flow (Figure 4a) to a more intense cyclonic flow (Figure 4b)

Parkinson and Gratz (1983) found that the typical ablation pattern in April/May consisted of ice lingering along the western coasts with in situ break-up as a result of polynya formation. A similar situation is observed in the SMMR data, except that in this case, the change in atmospheric circulation results in the rapid disintegration of the ice cover. It would appear that the break-up is accelerated by warm air advection. The resulting ice distribution (Figure 3c) is probably related to the Okhotsk gyre north east of Sakhalin Island.

5. DISCUSSION

The temporal and spatial resolution available with the satellite - borne microwave radiometers provide a valuable source of information for sea ice analysis and monitoring in the marginal ice

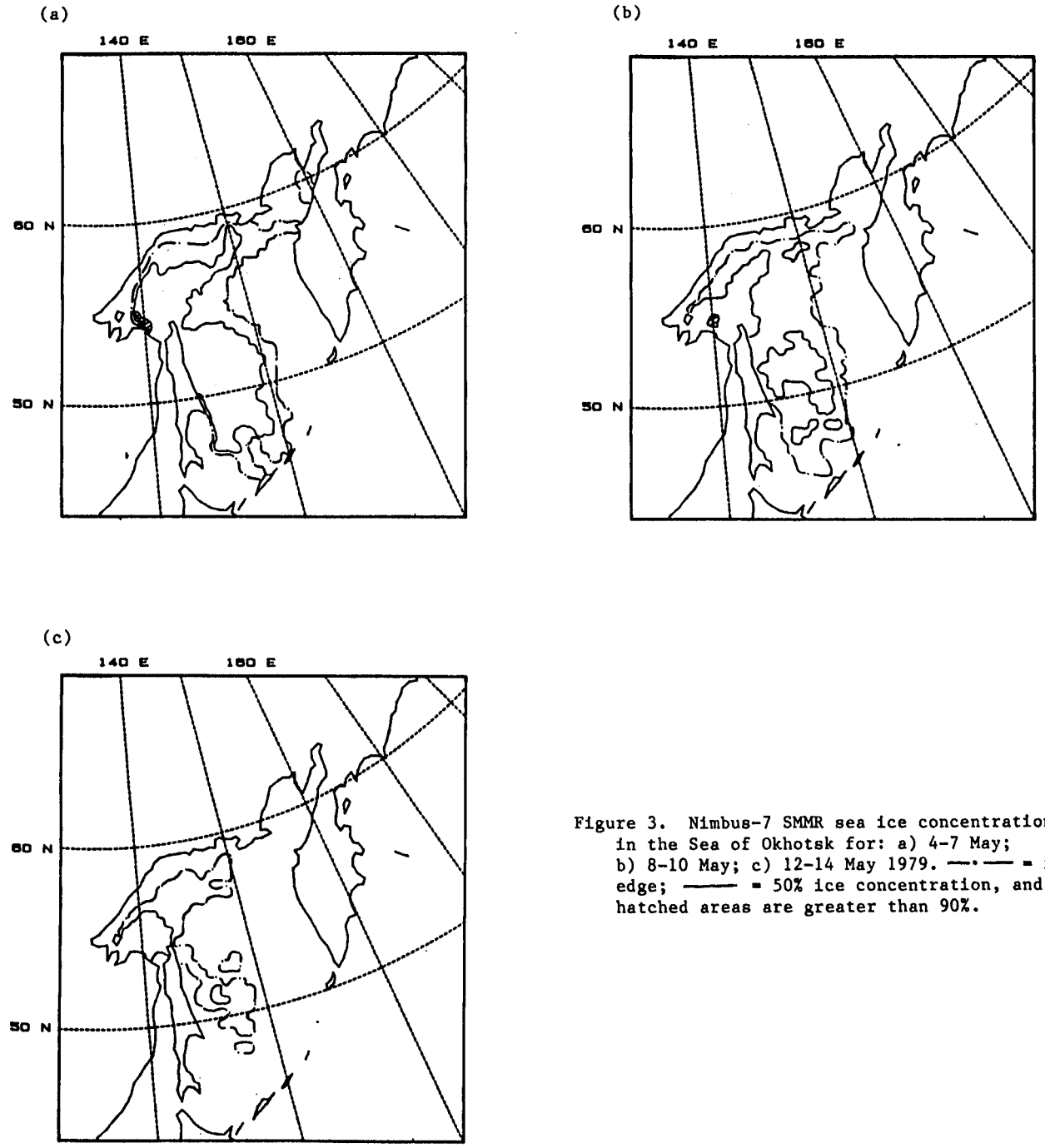

Figure 3. Nimbus-7 SMMR sea ice concentrations in the Sea of Okhotsk for: a) 4-7 May; b) 8-10 May; c) 12-14 May 1979. —·— = ice edge; ——— = 50% ice concentration, and the hatched areas are greater than 90%.

zone. Using the SMMR data, rapid changes in ice extent and concentration have been observed in association with changes in synoptic atmospheric circulation.

Case studies and analyses of sample data indicate that ice concentration estimates may be accurate to within 10% (Cavalieri et al., in press). Limitations in ice concentration retrievals exist in the marginal ice zone due to ocean surface roughness and precipitation, both of which tend to return erroneous ice concentration values over areas of open water. Work is still in progress to improve the sea ice algorithms.

In the case studies described above, orbital characteristics provide sufficient overlap to permit data every two days in the Greenland Sea. Three-day averages are used for the Sea of Okhotsk due to the limited orbital coverage at this latitude. In 1985/6 a multi-channel microwave radiometer will be included on a DMSP platform. The sensor will operate at four frequencies: 19.3, 22.2, 37.0 and 85.5 GHz. Vertical and horizontal polarizations will be provided for all frequencies except the 22.2 GHz, which will only have vertical polarization. The lower frequency channels will have a scene station resolution of

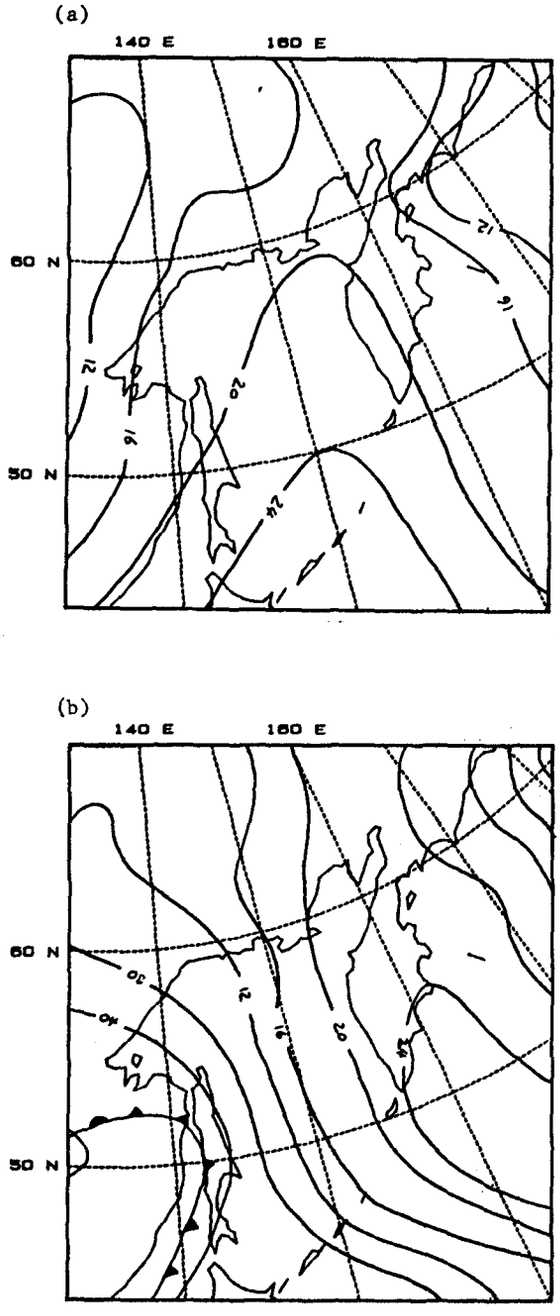

Figure 4. Sea level pressure patterns for: a) 4 May and b) 9 May 1979.

25km, and the 85.5 GHz channel will have a resolution of 12.5km.

The satellite orbital characteristics will permit improved temporal coverage compared to SMMR, with repeat global coverage every 24 hours. In the polar regions, complete coverage will be possible every 12 hours due to orbital overlap. The first launch is scheduled for late 1985, with subsequent launches in 1986 and 1987. This sensor will, therefore, provide the primary sea ice data source for the remainder of the decade and permit more extensive studies of the type reported here.

ACKNOWLEDGEMENTS

Data for this study were made available under NASA grant (NAGW-363) and the analysis was performed under NSF grant (DPP-817265) to the University of Colorado, Dr. Roger G. Barry, Principal Investigator. The authors would like to thank Vince Troisi for programing support and Roger Barry for his comments on the manuscript.

REFERENCES

Aagaard, K., 1972: On the drift of the Greenland pack ice. In Karlsson (ed), Sea Ice: Proceedings of an International Conference, Nat. Res. Council, Reykjavik, Iceland, 17-21.

Ackley, S. F. and T. E. Keliher, 1976: Antarctic sea ice dynamics and its possible climatic effects. AIDJEX Bulletin 33, 53-76.

Carleton, A. M., 1981: Monthly variability of satellite-derived cyclonic activity for the Southern Hemisphere winter. J. Climatol., 1, 21-38.

Cavalieri, D. J., P. Gloersen and W. J. Campbell, in press: Delimitation of sea ice parameters with the Nimbus-7 SMMR. J. Geophys. Res.

Cavalieri, D. J. and C. L. Parkinson, 1981: Large scale variations in observed Antarctic sea ice extent and associated atmospheric circulation. Mon. Wea. Rev., 109(11), 2323-2336.

Crane, R. G., 1981: Surface-atmosphere interactions over the polar oceans. Prog. Phys. Geog., 5(2), 186-216.

Crane, R. G., 1983: Atmosphere-sea ice interactions in the Beaufort/Chukchi Sea and in the European sector of the Arctic. J. Geophys. Res., 88(7), 4505-4523.

Crane, R. G., R. G. Barry and H. J. Zwally, 1982: Analysis of atmosphere-sea ice interactions in the Arctic Basin using ESMR microwave data. Int. J. Rem. Sensing, 3(3), 259-276.

Overland, J. E. and C. H. Pease, 1982: Cyclone climatology of the Bering Sea and its relationship to sea ice extent. Mon. Wea. Rev., 110(1), 5-13.

Parkinson, C. L. and A. J. Gratz, 1983: On the seasonal sea ice cover of the Sea of Okhotsk. J. Geophys. Res., 88(C5), 2793-2802.

Polar Group, 1980: Polar atmosphere-ice-ocean processes: A review of polar problems in climate research. Rev. Geophys. Space Phys., 18(2), 525-543.

Vinje, T. E., 1980: On extreme sea ice conditions observed in the Greenland and Barents Seas in 1979. Norsk Polarinstitutt Arbok 1977, 59-65.

E.1

ANALYSIS OF TROPICAL SYNOPTIC DISTURBANCES USING SATELLITE-DERIVED SOUNDINGS AND RADIANCE DATA FROM SELECTED CHANNELS

A.H. Thompson, J.P. McGuirk, L.L. Anderson, Jr., and N.R. Smith

Texas A&M University
College Station, Texas 77843-3146

1. INTRODUCTION

Recent interest in the Southern Oscillation, the Walker circulation, and El Niño has led to increased demand for reliable analyses of the structure of the atmosphere of the eastern portion of the tropical and subtropical Pacific Ocean. Our own interest in these analyses is related to the phenomena listed above, but also is because of concern with plumes, or bursts, of middle and high clouds which originate in or near the intertropical convergence zone (ITCZ) of the eastern Pacific Ocean. These bursts move northeastward into middle latitudes, as either a jet-stream or merging there with the jet stream; they are often associated with cyclogenesis and precipitation events over the southern tier of states. We require analyses of the area mentioned above to examine the origin and subsequent behavior of the moisture plumes or "moisture bursts" as we have chosen to call them. The most satisfactory procedure in attaining analyses for such data-poor regions as the eastern Pacific is to combine conventional meteorological data with data retrieved from satellite radiance measurements. This paper presents some of the results of comparing and combining information from the two sources (satellite and conventional) in determining the atmospheric structure associated with a portion of the life cycle of an eastern Pacific moisture burst.

The cloud bands we refer to as moisture bursts have been observed by others, for example, Morel et al. (1978), Davis (1981), and Thepenier and Cruette (1981). McGuirk and Thompson (1984) describe the bursts in some detail and suggest that they may be related to the behavior of the Hadley circulation. Figure 1 shows a schematic depiction of the moisture burst of the period described in the paper. Thepenier and Cruette suggest that if the bursts are associated with (subtropical) jet formation and/or with subsequent cyclogenesis and precipitation events, then it seems essential to understand more of the triggering and development processes. McGuirk and Thompson also note that clouds in the vicinity of the burst genesis region sometimes move into the region from the southern hemisphere. Further, the clouds sometimes exhibit winds with the meridional component exhibiting "jet stream" speeds near, or south of, the ITCZ. Neither observation is consistent with conventional understanding of the subtropical circulation or of the Hadley cell. Such concepts require further evaluation.

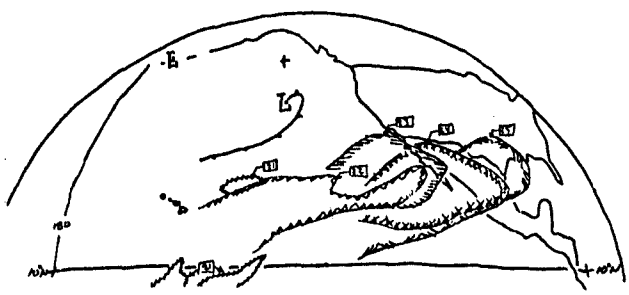

Fig. 1. *Schematic depiction of the time evolution of the high cloud boundary of a moisture burst occurring between 21 and 25 January 1979. Flagged numbers give the date of the associated cloud leading edge. (From McGuirk and Thompson, 1984.)*

2. DATA AND ANALYSES

The current investigation uses data from the First GARP Global Experiment (FGGE) Special Observing Period (SOP). The tropical eastern Pacific Ocean is characteristically a data-sparse region. The supplementary radiosondes, dropsondes and pibals, together with an expansion of the operationally available aircraft, surface and ship reports aid in making the FGGE SOP more amenable to study. Even these special data, however, leave the coverage far from ideal.

The satellite coverage also was increased during the SOP. Enhanced coverage of satellite-derived winds and temperatures and radiance data for several wavelength channels were available for melding with the conventional data.

Data from two satellite systems were used. These systems were the Geostationary Operational Environmental Satellite (GOES) system (especially GOES-West) and the sun-synchronous TIROS-N satellite. Data from the NOAA-5 system, in polar orbit, have been prepared but are not included in this paper. Infrared radiances mapped out as pictures of the cloud cover were obtained from the GOES system. Information from the TIROS-N Operational Vertical Sounder (TOVS) was also used. The TOVS was described by Smith et al., (1979). We are using mapped data from several of the individual channels of TOVS radiance measurements, and also retrieved atmospheric temperature soundings. In this paper we have used information

from only four of the channels. The channels used include Channels 10 and 12 of the High resolution Infrared Radiation Sounder (HIRS-2) and Channels 1 and 2 of the Microwave Sounding Unit (MSU). For convenience, we have chosen in our diagrams to refer to the two MSU channels as Ch. 21 and Ch. 22, respectively.

Another form of information retrieved from the satellite data is the wind obtained by tracking identifiable portions of the cloud patterns, or the "cloud-tracked winds". The upper cloud-tracked winds are based on cloud elements estimated to be at or above the 30 kPa pressure level. The lower cloud-tracked winds are presumed to represent flow below the 70 kPa pressure level. These data are available from the FGGE Level II archive. We have superimposed the upper-level cloud-tracked winds on the brightness temperature analysis of the Ch. 12 data, while the lower-level winds are on the corresponding chart of the Ch. 10 information.

Extensive use was made of the Level IIb and Level IIIb data as prepared by the European Center for Medium Range Weather Forecasts (ECMWF). Gridded data from the ECMWF set were extracted for an area bounded by latitudes 20°S and 30°N and by longitudes 180° and 90°W on a 3.75° x 3.75° lat/lon grid. Analyses of the satellite-derived data cover the same area when possible, and are our own objective analysis based on the Level IIb data.

The period examined in detail extended from 21 January 1979 to 28 January 1979. The examples presented in this paper were selected from mappings for the 24th and 25th.

3. SYNOPTIC PATTERNS DETECTED BY TOVS MICROWAVE AND WATER VAPOR CHANNELS

The four TOVS channels are selected to depict synoptic scale systems over the Pacific Ocean. The two microwave channels discussed herein represent, approximately, brightness temperatures in the vicinity of 70 kPa (Ch. 22) and the surface (Ch. 21). The infrared channels measure, approximately, moisture (expressed as brightness temperature) at the 50 kPa (Ch. 12) and 90 kPa (Ch. 10) levels. Additionally, 20 kPa temperature and 85 kPa geopotential height and relative humidity fields from the ECMWF Level IIIb analyses are used. Comparisons are made between the synoptic patterns for 00 GMT on 24 January and those for 00 GMT on 25 January.

The microwave channels are used because of their ability to probe through clouds where IR channel data are not available. The water vapor channels are used to delineate moisture-rich areas and also to track wind maxima (Martin and Salomonson, 1970). The cloud-tracked winds are unreliable in the presence of an overcast cloud cover.

3.1 Case 1: 00 GMT on 24 January 1979

3.1a Upper Troposphere (70 kPa and above)

There are two upper tropospheric microwave channels available from the TOVS MSU. The uppermost channel has a peak energy contribution from near the 30 kPa level. The features in this channel are not shown because they are very broad and lack detail. The MSU Channel 2, [here referred to as TOVS Channel 22] is discussed instead. North of 20°N (see Fig. 2) the temperature field is predominantly zonal with small-amplitude short waves embedded. The striking feature is the deep cold axis near 145°W extending from 20°N to a position south of the equator. In addition, there is a southern hemisphere cold axis near 140°W which also extends across the equator into the northern hemisphere. These two cold axes could be interpreted readily as a single cold axis extending across the equator between 140°W and 150°W. The eastern and western equatorial regions are dominated by broad zonally-oriented warmer regions.

The HIRS Water Vapor Channel 12 (50 kPa) and the cloud-tracked winds above 30 kPa are illustrated in Fig. 3. As can be seen, there is good synoptic-scale detail in the satellite-derived pattern, with extensive troughs and ridges. There also appear to be large embedded mesoscale (500-1,000 km) features.

A warm (or dry) axis extends from 10°N, 170°W to 25°N, 140°W to 25°N, 120°W, where the data become sparse; it appears again at 30°N, 95°W. According to Martin and Salomonson (1970), certain water vapor channel radiances have a strong relationship to the southwesterly subtropical jet stream (STJ) maxima over the United States. The suggestion is that the STJ parallels the high (dry) temperature axis which extends deep into the tropics. Other high temperature axes exist in the eastern Pacific Ocean, and also one is centered at 10°S, 135°W to 2°N, 142 °W. The cloud-tracked winds, denoted in the figures by arrows, appear to lie in the areas of tight gradient except at 15°N between 125°W and 105°W, where they are transverse to the low temperature (wet) axis.

Low temperature axes in this channel should delineate moisture-rich areas. Since this is an IR channel peaking at approximately 50 kPa, it is not a mapping of cloud tops, but primarily of water vapor. An extensive cold (wet) axis (Fig. 3) extends from 5°S, 165°W to the equator at 150°W where it splits into northern and southern branches. The northern branch runs from 2°N, 147°W to 20°N, 115°W while the southern branch curves from 2°N, 147°W to 2°N, 131°W then southeastward. The two branches suggest a moisture "canal" extending from the southern hemisphere tropics into the mid-latitudes and also a branch circulating near the equator in the southern hemisphere. These two features are well depicted in the Level IIIb relative humidity analysis for 70 kPa (not shown).

The Level IIIb 200-mb temperature analysis for 20 kPa (Fig. 4) shows an extensive cold axis from 10°N, 145°W northeastward and a cold core near 15°S, 140°W. By comparing Figs. 2, 3 and 4, we can see that the cloud-tracked winds are closely associated with both microwave and 20 kPa temperature patterns. Also, the moisture "canal" present in the water vapor channel lies just east of the microwave cold axis and generally parallels the cold axis at 20 kPa. The southern hemisphere moisture "canal" is easily associated

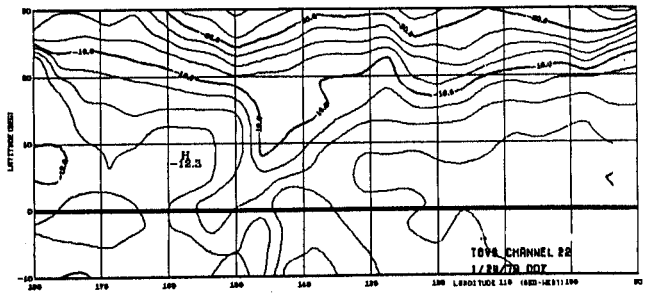

Fig. 2. *Mapping of grid-point values of brightness temperature (Celsius) of Ch. 22 (Ch. 2, 0.558 cm, of the MSU, with peak energy contribution from near 70 kPa) radiances. Approximately 00 GMT 24 January 1979.*

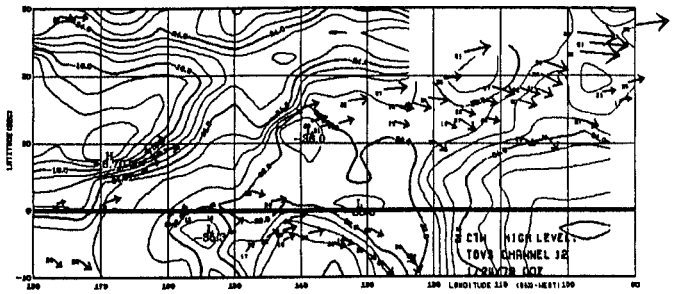

Fig. 3. *Mapping of grid-point values of brightness temperature (Celsius) of HIRS Ch. 12 (6.70 μm, a water vapor channel with peak energy contribution from near 50 kPa) radiances. The upper cloud-track winds are superimposed (speeds in m/sec). Approximately 00 GMT 24 January 1979.*

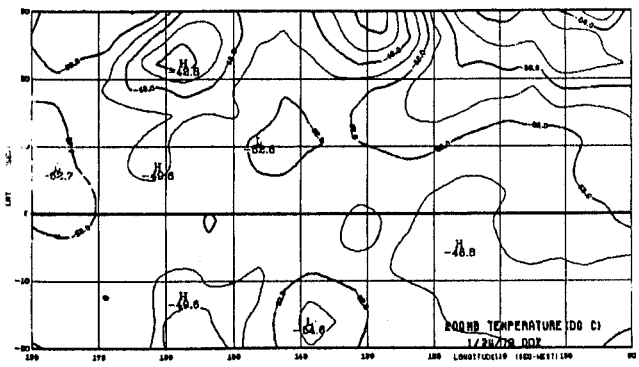

Fig. 4. *Temperature (Celsius) at the 20 kPa surface from the ECMWF Level IIIb analysis. For 0000 GMT 24 January 1979.*

with the microwave channel and the 20 kPa analysis patterns.

Appropriate TOVS channels and Level IIIb analyses in the lower troposphere are now discussed.

3.1b Lower Troposphere (below 70 kPa)

The lower tropospheric microwave channel [MSU Channel 1, here referred to as TOVS Channel 21] is a "window" channel with peak energy contribution from the surface. Figure 5 shows that considerable detail is available in this channel, with a major warm axis along the equator from 180° to 155°W then northeastward to 30°N, 105°W.

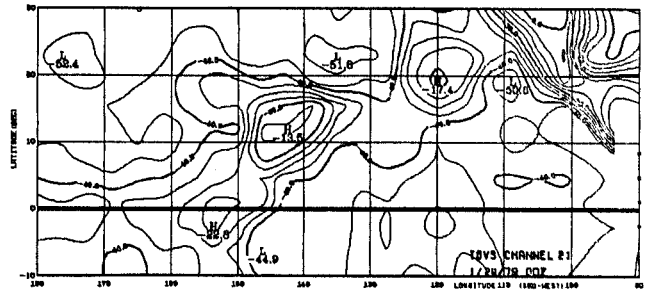

Fig. 5. *Mapping of grid-point values of brightness temperature (Celsius) of Ch. 21 (Ch. 1, 0.596 cm, of the MSU, with peak energy contribution from the surface) radiances. Approximately 00 GMT 24 January 1979.*

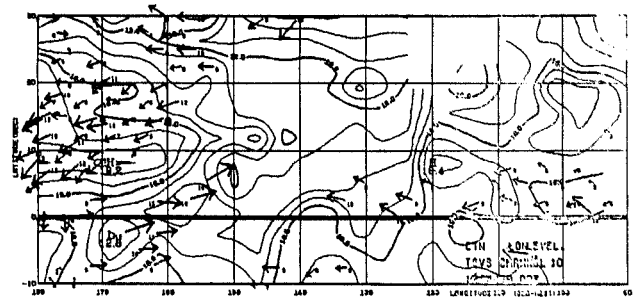

Fig. 6. *Mapping of grid-point values of brightness temperature (Celsius) of HIRS Ch. 10 (8.30 μm, a water vapor channel with peak energy contribution from near 90 kPa) radiances. The lower cloud-track winds are superimposed (speeds in m/sec). Approximately 00 GMT 24 January 1979.*

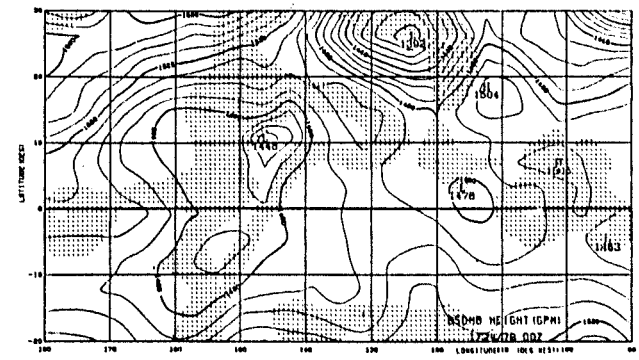

Fig. 7. *Height (gpm) of the 85 kPa (850 mb) surface from the ECMWF Level IIIb analysis. The stippled areas have relative humidities at 85 kPa between 70 % and 90 %. For 00 GMT 24 January 1979.*

This warm axis coincides very closely with the upper tropospheric moisture "canal" (see Fig. 3) and the upper microwave cold axis (Fig. 2). The Channel 21 cold axis from 10°S, 115°W to 25°N, 135°W does not relate as well to the upper tropospheric warm axis. Thus, the moisture burst shows its signal throughout the depth of the troposphere.

TOVS Channel 10 is a water vapor channel, peaking at 90 kPa. As with the upper tropospheric water vapor channel, cold axes should delineate moisture-rich areas ("canals"). The lower tropospheric cold (wet) axes (Fig. 6) reflect the upper tropospheric patterns (Fig. 3) but with

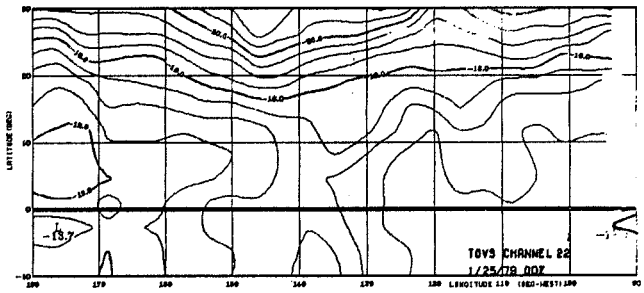

Fig. 8. *Same as Fig. 2 except for 00 GMT 25 January 1979.*

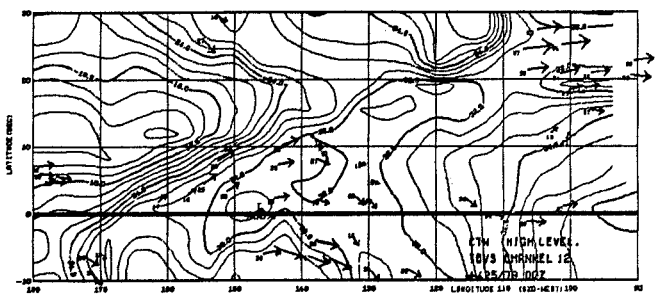

Fig. 9. *Same as Fig. 3 except for 00 GMT 25 January 1979.*

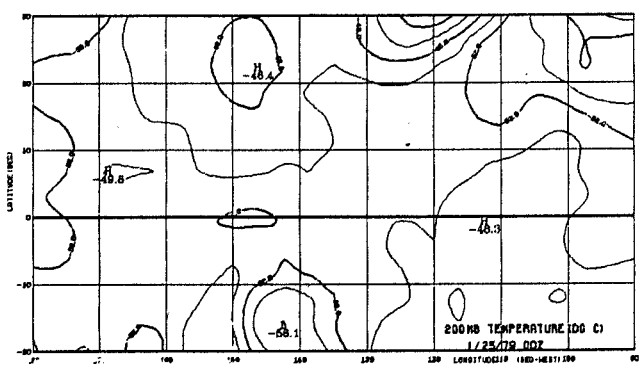

Fig. 10. *Same as Fig. 4 except for 00 GMT 25 January 1979.*

much less detail. There are broad warm (dry) areas in the eastern and western parts of the region which are similar to upper tropospheric patterns, but the upper warm (dry) axis paralleling the STJ is not reflected near the surface. The cloud-tracked winds (Fig. 6) indicate the expected easterly (trade) winds in the east and relatively strong easterlies a short distance east of the dateline. The interesting feature is the belt of strong westerlies, up to 16 m/s, along the equator near 175°W and along the moisture "canal" to 10°N. Although the South Pacific Convergence Zone was located 30° to 40° east of its normal position, these westerlies do not seem to be a northward extension of that complex. The lower water vapor channel does not appear to be as useful a signal of the wind pattern as the upper water vapor channel, with the possible exception of the unusually strong westerlies feeding the moisture "canal". Notice also the cross-equatorial flow in the moisture "canal" denoting the southern hemisphere's contribution to northern mid-latitude moisture.

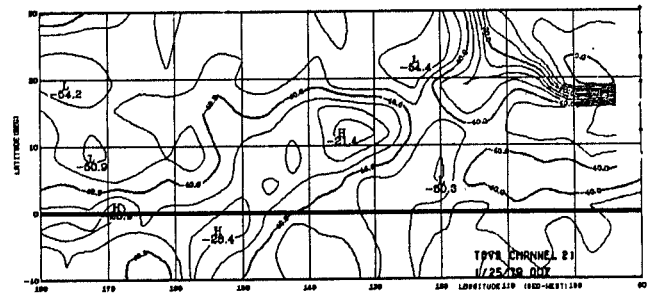

Fig. 11. *Same as Fig. 5 except for 00 GMT 25 January 1979.*

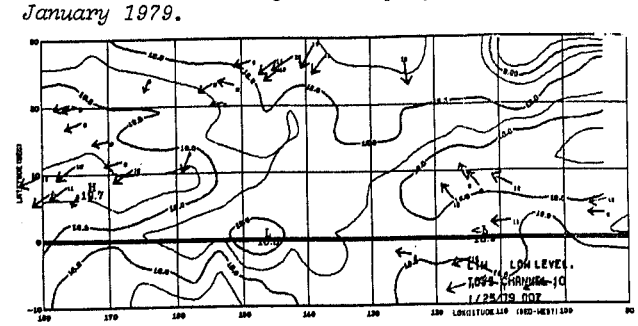

Fig. 12. *Same as Fig. 6 except for 00 GMT 25 January 1979.*

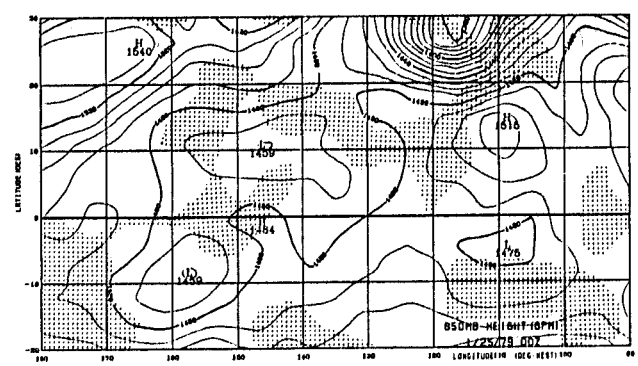

Fig. 13. *Same as Fig. 7 except for 00 GMT 25 January 1979.*

The Level IIIb height and relative humidity fields for 85 kPa are shown in Fig. 7. The height field shows an extensive trough throughout the tropics from 20°S, 160°W to 25°N, 125°W. This trough coincides with the microwave warm axis and the water vapor channel cold (wet) axis (moisture "canal"). The cloud-tracked winds correspond quite well to the height field: parallel to the contours at locations away from the equator and blowing from high to low along the equator. The 85 kPa relative humidity field is captured well by the moisture "canals" with the exception of the eastern equatorial region in which the Level IIIb analysis denotes high relative humidity and the satellite data indicate dryness; which is representative in this case is uncertain.

3.2 Case 2: 00 GMT on 25 January 1979

We discuss the same TOVS Channels and Level IIIb analyses as are presented for Case 1.

3.2a Upper troposphere (70 kPa and above)

The synoptic-scale patterns detected in the microwave temperature (Channel 22) data (Fig. 8) are similar to those 24 h earlier, but moved 10° to 15° of longitude to the east. Zonal patterns still are predominant north of 20°N with broad warm regions over most of the equatorial region. The cross-equatorial cold axis is now located near 140°W and is less distinct than before. The cloud-tracked winds (Fig. 9) indicate that the southern hemispheric circulation has extended northward across the equator to nearly 10°N.

The cloud-tracked winds (Fig. 9) also indicate some upper-level troughing near the equator in the eastern part of the region. This is supported by a cold axis in the microwave channel and a warm dry axis in the water vapor Channel 12. The cloud-tracked winds, as earlier, appear parallel to the warm dry axes in the Channel 12 high gradient areas. Also, the Channel 12 cold wet axes, or moisture "canals", coincide with the circulation inferred from the cloud-tracked winds with the exception of the troughing near the equator in the east. The moisture "canal" once again extends from the southern hemisphere near 155°W northeastward into the mid-latitudes. The southern hemisphere branch is still evident, now near 130°W. The moisture "canal" branches for the most part parallel the microwave cold axes.

The Level IIIb 20 kPa temperature analysis (Fig. 10) shows a strengthened cold cell in the southern hemisphere which is stationary. The northern hemisphere cold axis has greatly diminished while moving northeastward. The cloud-tracked wind trough near the equator at 105°W is not discernable in the 20 kPa temperature analysis.

The features are consistent during the 24 hour period up to 00 GMT on the 25th except for the appearance of a cold axis in the microwave pattern from 15°N, 115°W to the equator at 105°W. The new cold axis is reflected in the troughing in the cloud-tracked winds. It also appears that the southern hemisphere circulation pattern is nearly stationary near 140°W while the northern hemisphere cold axis moves eastward.

3.2b Lower Troposphere (below 70 kPa)

The microwave channel (21) shows that the warm axis has moved east approximately 5° of longitude to 10°S, 155°W northeastward to 25°N, 100°W (Fig. 11). This warm axis is the only clear synoptic scale feature as there are no continuous cold axes present.

As before, the microwave warm axis is approximately colocated with the lower water vapor channel (10) cold (wet) axis. This cold axis (Fig. 12) extends from the equator near 160°W to 30°N, 105°W approximately 5° longitude east of its previous position. Extension of the cold axis, or moisture "canal", into the southern hemisphere is not apparent at this time. Zonal warm regions flank the moisture "canal" near 10°N. The cloud-tracked winds (Fig. 12) indicate easterly (trade) winds persisting in the east and northwest while the previous strong westerlies feeding the moisture "canal" in the west are not detected. However, higher level cloud-tracked winds are now indicated (Fig. 9) over the low-level moisture "canal", suggesting changes in cloud height and/or depth. Thus, the low-level cloud motions which would reveal the westerlies (if present) have been masked by higher clouds. Comparison of the two 85 kPa analyses (Figs. 7 and 13; see also the next paragraph) suggests that the low-level westerlies may still be present, though perhaps shifted eastward a few degrees.

The 85 kPa Level IIIb height analysis bears little resemblance to the microwave temperature field. The 85 kPa trough (Fig. 13) extending from 10°S, 160°W to 30°N,115°W, broadly bounds the water vapor cold axis, or moisture "canal". The trough in the height field has moved little in the equatorial region and weakened somewhat. Figure 13 also shows that the 85 kPa humidity field has become less distinct and the cross-equatorial continuity, observed 24 hours earlier, is no longer present.

3.3 Atmospheric cross sections

Vertical sections along the west coast of North America and along zonal transects at 8°N and 3°N were constructed using radiosondes and dropsondes. Temperature retrievals from the TOVS were utilized to prepare satellite-derived cross sections for approximately the same times and locations. Although these data are not described herein, we expect to show and discuss results in the verbal Conference presentation.

4. SUMMARY AND REMARKS

The satellite-derived data, consisting of microwave and water vapor channel brightness temperature fields and cloud-tracked winds, detect synoptic scale patterns of temperature, moisture and winds. The water vapor channel data are not available in overcast cloud areas; the cloud-tracked winds are limited to cloudy areas and are normally mutually exclusive high cloud winds or low cloud winds. The microwave channel temperatures provide "all weather" coverage but require special interpretation in rain areas. The satellite data do capture time variation in synoptic scale features, as illustrated by the changes over the 24-h period between 00 GMT 24 January and 00 GMT 25 January 1979, even in the equatorial tropics where horizontal contrasts are thought to be weak.

Promising results include the ability of the upper tropospheric microwave channel to detect temperature variations in the tropical region and the presence of a moisture "canal" in the water vapor channels. The moisture "canal" extends from the southern hemisphere or near the equator northward toward mid-latitudes in both time periods.

Microwave temperatures, the water vapor channel moisture "canals" and the cloud-tracked winds all suggest a quasi-stationary southern hemisphere circulation "coupled" with a transient

northern hemisphere system.

Strong equatorial westerlies are initially present at low levels, apparently feeding the moisture "canal," but are not detected 24 h later. Also, the lower tropospheric microwave warm axis lying in the moisture "canal" is a persistent feature. These two observations are among features requiring further investigation. Parallelism between satellite-derived analyses and more conventional analyses is not perfect, even though the satellite data are incorporated into the FGGE Level IIIb analyses. Continued evaluation and experience should allow us to improve our abilities to infer structure from the satellite-derived information. Further investigation will include analysis of satellite channel brightness temperature fields using an empirical orthogonal function (EOF) synoptic mapping technique. Emphasis will be placed on using the microwave channels because of their "all weather" capability.

5. ACKNOWLEDGEMENTS

Our efforts are receiving financial and technical support from the George C. Marshall Space Flight Center, National Aeronautical and Space Administration, Huntsville, AL, through Contract No. NAS8-35182. We also acknowledge the assistance of our colleagues P. E. Riba and Shellie L. Craig.

6. REFERENCES

Davis, N. E., 1981: METEOSAT looks at the general circulation: III. Tropical-extratropical interaction, Weather, 36, 168-173.

Martin, R., and V. Salomonsom, 1970: Statistical characteristics of subtropical jet-stream features in terms of MRIR observations from Nimbus 2, J. Appl. Meteor., 9, 508-520.

McGuirk, J.P., and A.H. Thompson, 1984: Transient tropical disturbances within the Pacific Hadley cell. Proceedings, 15th Tech. Conf. on Hurricanes and Tropical Meteorology. Amer. Meteor. Soc., Miami, FL, pages unk.

McGuirk, J.P., A.H. Thompson, L.L. Anderson, and N.R. Smith, 1984: Reliability of circulation statistics over the tropical Pacific Ocean based on FGGE data, Proceedings, 8th Climate Diagnostics Workshop, Toronto, October 12-16, 1983.

Morel, P., M. Desbois, and G. Szejwach, 1978: A new insight into the troposphere with the water vapor channel of Meteosat, Bull. Amer. Meteor. Soc., 59, 711-714.

Smith, W., H. Woolf, C. Hayden, D. Wark and L. McMillin, 1979: The TIROS-N operational vertical sounder, Bull. Amer. Meteor. Soc., 60, 1177-1186.

Thepenier, R., and D. Cruette, 1981: Formation of cloud bands associated with the American subtropical jet stream and their interaction with midlatitude synoptic disturbances reaching Europe, Mon. Wea. Rev., 109, 2209-2220.

SATELLITE DERIVED ATMOSPHERE WATER VAPOR AS A TRACER OF LARGE SCALE INTERACTIONS BETWEEN THE ATMOSPHERE AND OCEAN

DAVID A. SHORT
C. PRABHAKARA
Goddard Laboratory for Atmospheric Sciences
Goddard Space Flight Center
Greenbelt, Maryland 20771

INTRODUCTION

Observations from the Scanning Multichannel Microwave Radiometer (SMMR), flown aboard the Nimbus 7 satellite, have been utilized to remotely sense the vertically integrated atmospheric water vapor and liquid water, and surface wind speed over the global oceans (Prabhakara, et al., 1982, 1983). Maps of monthly averages of these quantities for the period December 1978-November 1979 are presented in Prabhakara and Short (1984). The vertically integrated atmospheric water vapor is strongly coupled to the sea surface temperature and further modified by the vertical motion field in the atmosphere. Convergent low level winds over a warm sea surface and rising motion through a deep layer of atmosphere (as in the intertropical convergence zone) results in water vapor amounts in the range of 4 to 6 g/cm^2. Conversely, over the eastern subtropical coastal upwelling regimen, low level divergence, sinking motion and cool surface temperatures result in water vapor amounts as low as 1.5g/cm^2. Liquid water amounts are highest in the presence of precipitating clouds; the liquid water distribution detected by SMMR closely resembles the climatological precipitation distribution (Prabhakara and Short, 1984) and thereby the latent heat released to the atmosphere. Wind stress on the ocean surface, the mixed layer depth and latent heat and sensible heat fluxes to the atmosphere are all dependent on the surface windspeed. Satellite observations of the water vapor, liquid water and surface windspeed provide important information on the state of the atmosphere over the ocean and the ocean-atmosphere interaction.

The purpose of this report is to describe two anomalous water vapor distributions and accompanying circulation patterns which occurred over the North and South Atlantic Ocean during February 1979. FGGE data (as analyzed by the ECMWF) are used to provide corroborative evidence of the events revealed in the satellite observations.

NORTH ATLANTIC

Fig. 1a shows the monthly averaged water vapor for February 1979 over the Atlantic Ocean. Notice the tongue of higher values projecting northeastward towards Europe from the central Atlantic and the minimum near the African coast. The 1000mb wind field shows an area of strong southwesterly flow associated with the water vapor maximum, an anticyclonic gyre centered at 30°N, 20°W and northeasterly winds along the African coast. This trough/ridge configuration persisted throughout most of the month, but was not evident in January and March (Dickson, 1980). The circulation anomaly is consistent with atmospheric subsidence and oceanic upwelling near west Africa; both mechanisms tending to decrease the atmospheric water vapor. In the central Atlantic over the area of low pressure and storminess SMMR observations (figs. 1c and 1d) show surface wind speeds in the range of 10 to 15 m/s liquid water content 10mg/cm^2 and water vapor enhanced by a factor of one third as compared to adjacent months. The water vapor increase could be due to advection of warm moist air from the southwest, an increase in sea surface temperature, an increase in the depth of the moist layer because of low level convergence or all of the above. TIROS-N AVHRR observations show a similar pattern of enhanced cloudiness (W. K. M. Lau, personal communication).

SOUTH ATLANTIC

From figs. 1a and 1b we can see in the South Atlantic, a basin wide atmospheric gyre with southerly winds and low atmospheric water vapor along the south western coast of Africa. This is a region of persistent atmospheric subsidence and oceanic upwelling; desert conditions exist along the coast as far north as 14°S (see, for example, Matthews, 1983). The annual average precipitation at Mocamedes (15°12's,12°9'E) is a scant 50mm (the February average is 10mm).

In fig. 2a the atmospheric water vapor for the last week of January shows an equatorial ITCZ maximum, a minimum along the African coast and a maximum projecting southeastwards from the South American coast. This latter feature is consistent with the stationary atmospheric wave pattern observed by Kalnay and Paegle (1982) which persisted during January but not February 1979. For the first week of February fig. 2b shows a more zonal orientation of the South American maximum and surprisingly, a maximum of 5 g/cm^2 at 20°S on the eastern side of the basin. Values as high as 5 g/cm^2 are usually seen only in conjunction with the ITCZ and its deep layer of moist air. By the second week of February (fig. 2c) the pattern has returned to a more climatological configuration (it remains this way for the rest of the month). The remainder of this study presents evidence of the atmospheric events which accompanied the early February episode and speculations on mechanisms of atmosphere-ocean interaction which may have taken place.

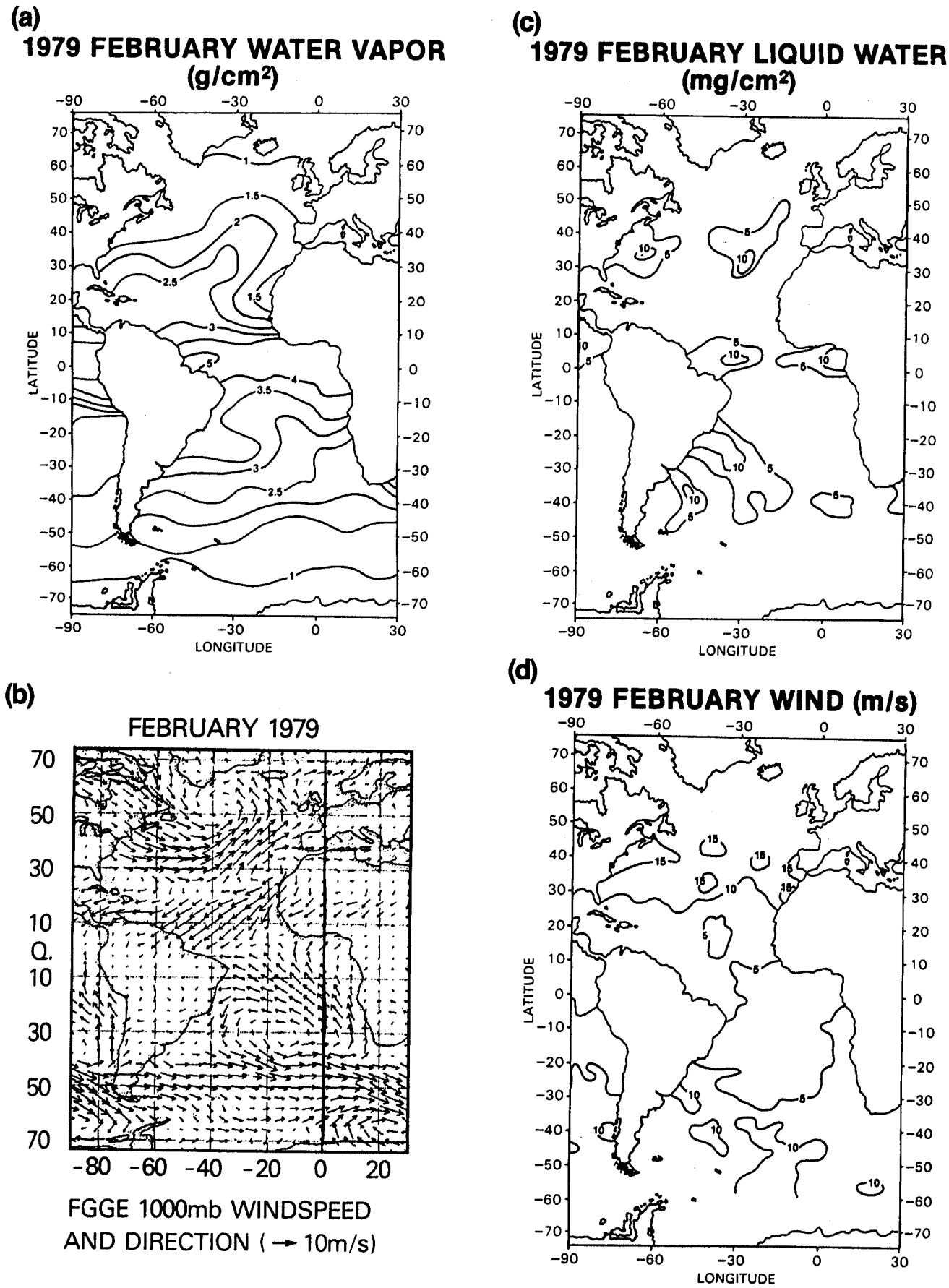

Fig. 1. a) Vertically integrated atmospheric water vapor from SMMR. b) 1000mb wind vectors. c) liquid water in clouds and rain from SMMR. d) surface windspeed from SMMR.

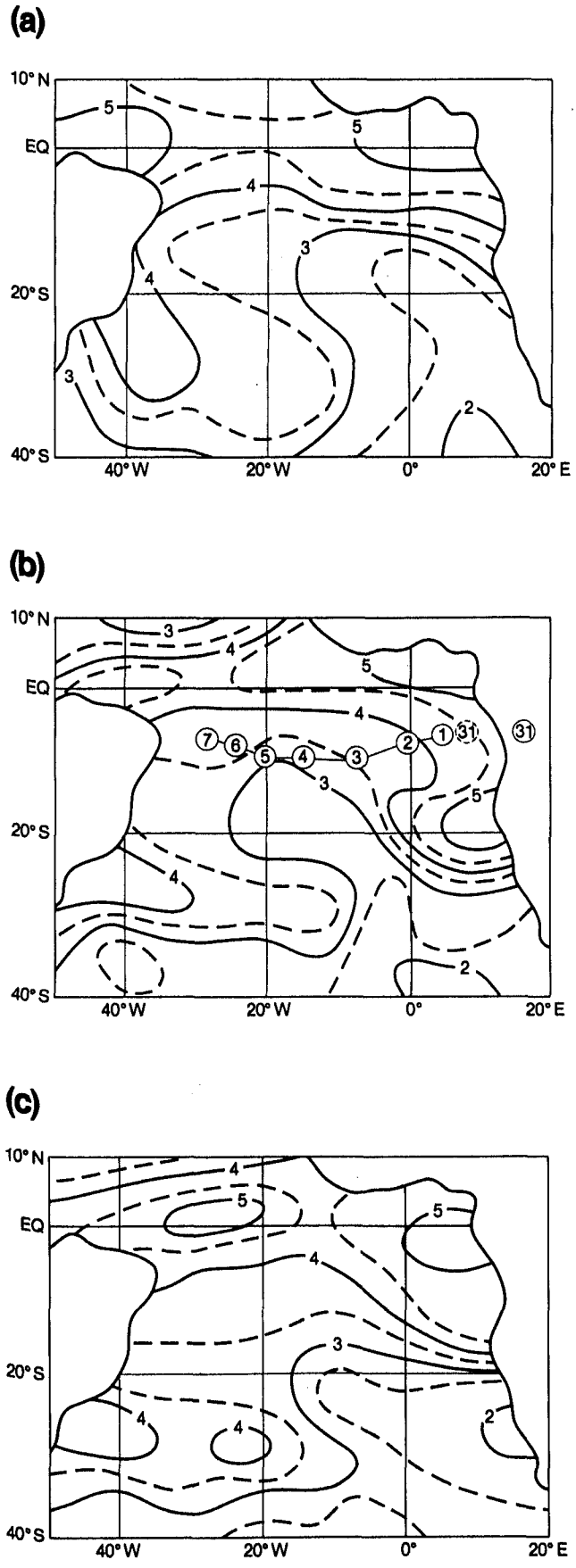

Fig. 2. Vertically integrated atmospheric water vapor from SMMR a) last week in Jan. 1979. b) first week in Feb. 1979. c) second week in Feb. 79.

A time series of the meridional winds (fig. 3a) near the surface at 18°S, 10°E shows a consistent component from the south throughout January and February 1979. It is not unreasonable to expect that the water vapor increase seen in fig. 2b may have been due in part to a local relaxation of the wind stress, a cessation of the oceanic upwelling and an increase in the SST (Philander and Pacanowski, 1981). However, we see that the winds during the first week of February do not appear to be uniquely different from the rest of the time period.

At 700mb the meridional winds are more variable (fig. 3b). Major fluctuations with strong flow from the north take place in early February. These variations were associated with a disturbance which was centered between 5-10°S and propagated westward across the basin. The disturbance seems to have originated over the continent in late January during a strong surge of southeasterly winds along the east coast of Africa following the passage of a major trough in the midlatitude westerlies. The locations of the tropical low pressure center is indicated by the circled numbers in fig. 2b.

Regional weather forecasters have long been aware of westward moving disturbances and their effects on the coastal weather. The circulation pattern with this particular episode is similar to those which have been described as producing "El Niño-like" conditions along the Angolan coast (see pages 31-36 in the GARP WMO WAMEX publication No. 21, 1978). Other sources consider a comparison with the South American El Niño events as dubious (see Trewartha, 1981 and references therein). At the present time, however, detailed studies of westward moving disturbances are lacking in tropical Africa, except for the easterly waves of west Africa in northern summer (Asnani, 1982). This is due in part to a lack of comprehensive observations over the oceans. During the FGGE year we have found even surface observations in the Angolan sector fragmentary. Satellite observations are able to fill in many observational gaps and promise to contribute more information in the future.

The upper level winds are generally easterly from East Africa across to South America from about 10°S to 20°S during the southern summer. The time series of V(700mb) at 10°S, 10°E (fig. 3c) suggests that disturbances in the easterlies are not uncommon. Minima in the V component are separated by 5-10 days. The average speed of the Feb. 1-7 disturbance was approximately 6 m/s and its scale was consistent with that observed for "easterly waves." The 1000mb winds at 10°S, 10°E (fig. 3d) are not as variable as the upper level winds but they do show a significant relaxation during the first week of February. Observations of SST from TIROS-N AVHRR measurements in this area indicate an increase of 1-3°C from late January to early February. (W. Pichel, personal communication). Thus, a local cessation of upwelling may have increased SST in the region providing a richer source region of water vapor to be advected to the south by winds in the lower troposphere. We also see that the water vapor enhancement observed by SMMR took place as the wave trough passed through the area (fig. 3f). Cloudiness, precipitation and a deep moist planetary boundary layer after trough passage are commonly observed characteristics of disturbances in the easterlies. The horizontal divergence field at 850mb (fig. 3g) shows an area of significant convergence along the Angolan coast. The convergence at 1000mb is considerably weaker. This may be due to the strong low level trade wind inversion. Apparently the low level wind field remains somewhat isolated from the free atmosphere above (compare figs. 3e and 3f). The vertical stratification of the atmosphere can have a significant effect on the structure of

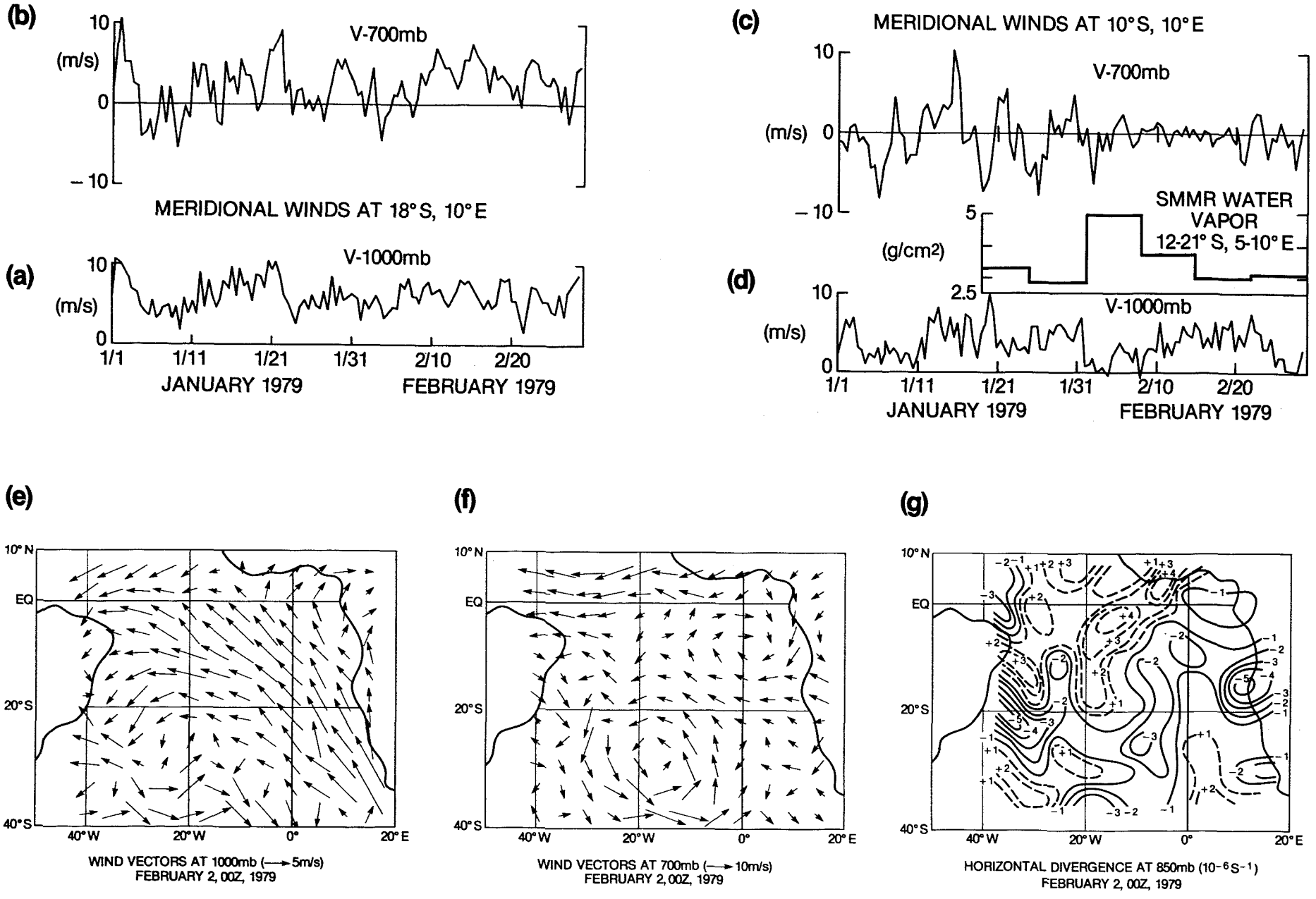

Fig. 3. a) 1000mb meridional winds at 18°S, 10°E. b) 700mb meridional winds at 18°S, 10°E. c) 700mb meridional winds at 10°S, 10°E. d) 1000mb meridional winds at 10°S, 10°E. e) 1000mb wind vectors 02/02/00Z, 1979. f) 700mb wind vectors 02/02/00Z, 1979. g) 850mb divergence 02/02/00Z, 1979.

tropical disturbances and their associated cloud fields (Thompson, et al., 1979).

The maximum water vapor event along the Angolan coast appears to have peaked on Feb. 4, 1979. Fig. 4 shows a METEOSAT infrared image for 1155 GMT on the 4th. The trailing edge of a frontal cloud band is visible across the southern tip of Africa. High cold cloud tops off the Angolan coast are suggestive of convective cloud elements. The surface observation for Mocamedes on this date indicates surface winds from the west, thunderstorms in the area and recent precipitation. During the proceeding days the arid coastal region again becomes clearly visible from space as strong southerly flow becomes re-established along the coast and conditions return to normal.

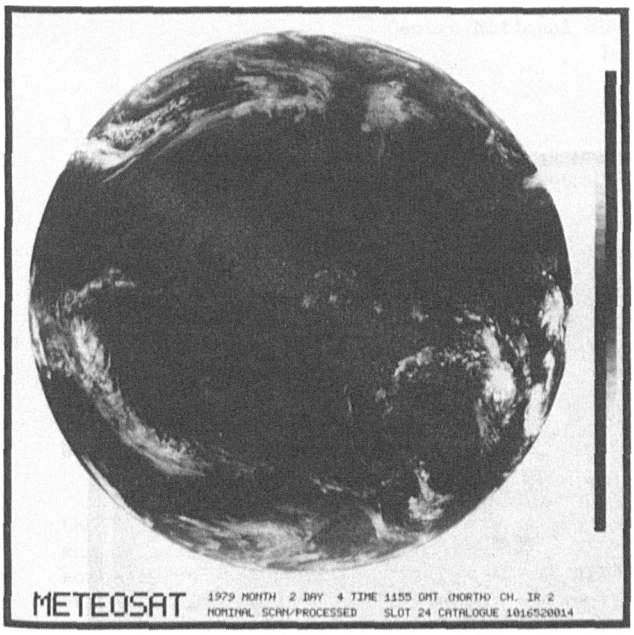

Fig. 4. METEOSAT infrared image 02/04/1155Z, 1979.

(Repeated on following page.)

There are interesting questions which can be raised in re-examining fig. 3c-d. Why is it that each major thrust of winds from the north at 700mb is not accompanied by a complete relaxation of the southerly winds near the surface, and an increase in atmospheric water vapor? Does a strong response at the surface occur only when the environment has been preconditioned by an oceanic event? Does remote forcing of the ocean play an important role in these short time scale phenomena? Are these short time scale events related to the monthly and seasonal anomalies examined in previous investigations (Hirst and Hastenrath, 1983; Servain and Picaut, 1982)?

Time series of SST at several stations along the Guinea Gulf show a rapid increase of several degrees centigrade in early February 1979 (see Picaut, 1983, fig. 7). Although the coastal ocean responds to a variety of forcing mechanisms (Philander, 1977) this early February response may be related to the SST increase observed farther south, in the satellite observations mentioned previously. The SST increase may represent a response to local forcing or it may have been remotely forced.

The east-west component of the 1000mb winds averaged over the western equatorial Atlantic (4°N-4°S, 40°W-10°W) is toward the west throughout December 1978-February 1979. A crude estimate of the variations in westerly wind stress is shown in fig. 5 when the daily and areally averaged $(\overline{U})^2$ is plotted. Notice that the most precipitous decrease occurs in early January 1979, about one month before the February event described above. This is approximately the time scale for propagation of large scale oceanic waves across the basin. Monthly averaged rainfall and SST anomalies along the eastern side of the basin frequently occur one to two months after major relaxations of the wind stress on the western equatorial side (Hirst and Hastermath, 1983, Servain and Picaut, 1982). As a matter of interest we also show SMMR-derived monthly and areally averaged scalar wind speed squared for the same region.

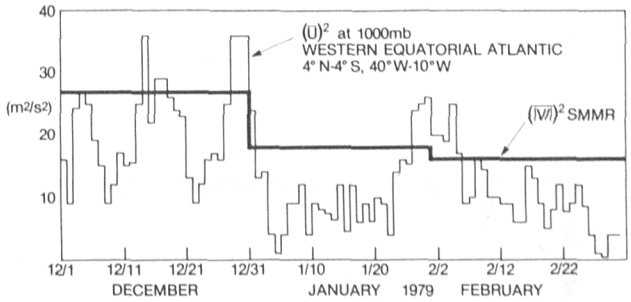

Fig. 5. Westward windspeed squared (at 1000mb) in western equatorial Atlantic.

Time and space have allowed only a cursory presentation of the dynamical aspects of this particular atmospheric-oceanic disturbance. Nevertheless we feel that the information and ideas discussed thusfar may be useful in further studies of such phenomena. SMMR observations for the four year period 1979 through 1982 will soon be available for more extensive investigations.

ACKNOWLEDGEMENTS

The authors are grateful to P. S. Schopf and A. J. Busalacchi for informative discussions, to W. K. M. Lau and W. Pichel for access to unpublished data analyses and to G. Szejwach of the Laboratorie de Météorologie Dynamique for supplying the Meteosat images.

REFERENCES

Philander, S. G. H., 1977: The effects of coastal geometry on equatorial waves (Forced waves in the Gulf of Guinea), J. Mar. Res., 35, 3, 509-523.

Hirst, A. C., and S. Hastenrath, 1983: Atmosphere-Ocean Mechanisms of Climate Anomalies in the Angola-Tropical Atlantic Sector. J. Phys. Oceanogr., 13, 1146-1157.

Servain, J., and J. Picaut, 1982: Evidence of Remote Forcing in the Equatorial Atlantic Ocean, J. Phys., Oceanogr., 12, 457-463.

Thompson, R. M. Jr., S. W. Payne, E. E. Recker and R. J. Reed, 1979: Structure and properties of synoptic-scale wave disturbances in the intertropical convergence zone of the eastern Atlantic. J. Atmos. Sci , 36, 53-72.

Kalnay, E., and J. Paegle, 1982: Large amplitude stationary Rossby waves in the Southern Hemisphere. Proceedings of the 14th Tech. Conf. on Hurricanes and Tropical Meteorology, June 7-12, San Diego, Ca.

Picaut, J., 1983: Propagation of the seasonal upwelling in the eastern equatorial Atlantic. J. Phys. Oceanogr., 13, 18-37.

Philander, S. G. H., and R. C. Pacanowski, 1981: The oceanic response to cross-equatorial wind (with application to coastal upwelling in low latitudes) Tellus, 33, 204-210.

Asnani, G. C., 1982: In-World Climate Programme-Proceedings of the Technical Conference on Climate-Africa-. Arusha, United Republic of Tanzania, 25-30 January, 1982, WMO Publication No. 596, pages 107-129.

Matthews, E., 1983: Global vegetation and land use: New high resolution data bases for climate studies. J. Climate. Appl. Meteor., 22, 474-487.

Prabhakara, C., I. Wang, A. T. C. Chang and P. Gloersen, 1983: A statistical examination of Nimbus 7 SMMR data and remote sensing of sea surface temperature, liquid water content in the atmosphere and surface wind speed. J. Clim. Appl. Meteor., 22, 2023-2037.

Prabhakara, C., H. D. Chang, and A. T. C. Chang, 1982: Remote sensing of precipitable water over the oceans from Nimbus 7 microwave measurements. J. Appl. Meteor., 21, 59-68.

Dickson, R. R., 1980: Weather and circulation of February 1979: Near-record cold over the northeast quarter of the country. Mon. Wea. Rev., 107, 624-630.

Prabhakara, C., and D. A. Short, 1984: Nimbus 7 SMMR derived seasonal variations in the water vapor, liquid water and surface winds over the global oceans. NASA Technical Memorandum, atlas in preparation.

Trewartha, G. T., 1981: The Earth's Problem Climates. University of Wisconsin Press, Madison, Wisconsin, 371pp.

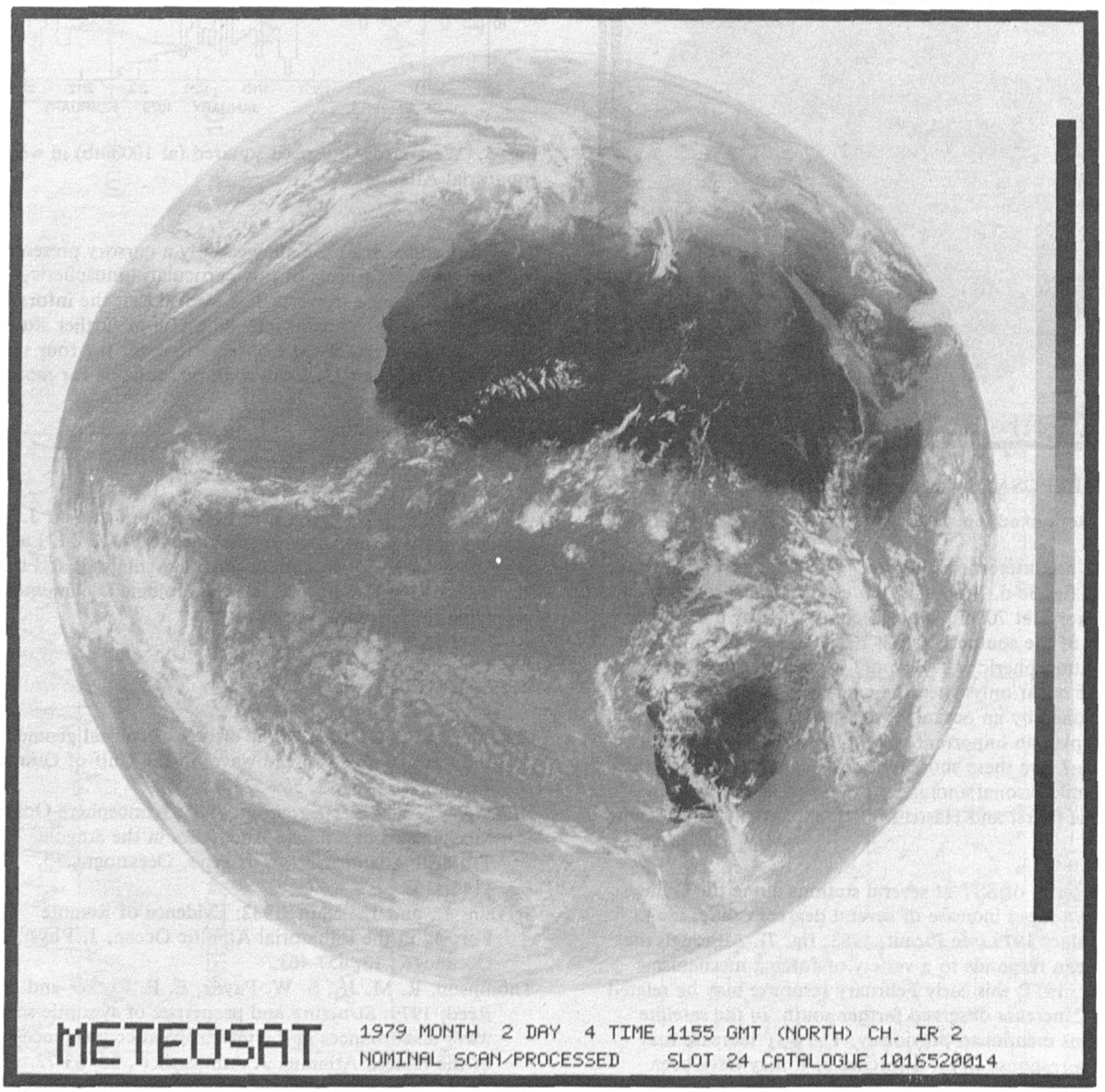

Repeat Fig. 4. METEOSAT infrared image 02/04/1155Z, 1979.

DETECTION OF TROPOPAUSE FOLDS USING BOTH WATER VAPOR AND OZONE SATELLITE DATA

J. TOURNADRE*, D. RAMOND*, S. MULLER**

* Institut et Observatoire de Physique du Globe du Puy de Dôme
Clermont-Ferrand, France

** Centre National de Recherches Météorologiques (CNRM/EERM)
Toulouse, France

1. INTRODUCTION

The concept of tropopause fold has been studied by Reed (1955), Staley (1960), Danielsen (1968, 1977), Danielsen et al. (1980), Shapiro (1978, 1980) and Shapiro et al. (1980). Using the potential vorticity as a criterion to define the tropopause, they showed that in the vicinity of an upper jet stream, the tropopause can fold delineating the upper frontal zone. With the World Meteorological Organization's thermal definition of the tropopause only a tropopause break could be observed.

With measurements from research aircraft , they showed that both potential vorticity and ozone within lower stratosphere are horizontally and vertically displaced by actions of three-dimensional motions near the tropopause and that air from lower stratosphere descends within the frontal zone.

Shapiro (1980) and Gidel et al. (1979) suggested that the turbulent mixing within tropopause folds is of importance as a mechanism for stratospheric-tropospheric exchanges in the vicinity of upper jet-stream frontal systems. The evaluation of this kind of exchange mechanism has yet only been conducted for few cases ; the determination of its importance in comparison with other mechanisms of stratospheric tropospheric exchanges already known requires a climatological study of tropopause folds for the determination of the frequency of events and of the involved volumes.

The detection of tropopause folds by the means of radiosonde data requires a relatively dense network and a consequential work of data analysis that kind of means seems thus more appropriate to cases studies than to a climatological study. Satellite data appear more promissing for that kind of climatological study in regards to their large spatial coverage. We present in this paper a study of feasibility of tropopause fold detection using satellite data.

In the frontal zone delineated by the folded tropopause, the subsiding air of stratospheric origin, presents a higher ozone concentration and a lower water vapor concentration as compared to the surrounding tropospheric air. It could therefore be expected that tropopause folds may have a significant signature in satellite data representative of ozone and water vapor. For the present study, we use data from channel 12 (6.3 µm water vapor vibration-rotation band) of the High Resolution Infrared Spectrometer 2 (HIRS2), flown on the TIROSN satellite series, and total ozone data from the Total Ozone Mapping Spectrometer (TOMS), flown on the NIMBUS 7 satellite.

Ramond et al. (1981) (RA) have studied the signature of tropopause folds in the Meteosat water vapor (WV) channel radiance fields ; they showed that maximum radiance bands are associated with upper jet-streams and accurately delineate the tropopause breaks. In the present paper, we show that the results they presented can be extended to the HIRS 2 channel 12 Radiance field.

Then, we present a study of the tropopause folds signature in the total ozone fields, and a case study which compares TOMS observations and HIRS 2 Channel 12 Radiance fields with the results of a three-dimensional isentropic analysis of the radiosonde network data.

2. SIGNATURE OF TROPOPAUSE BREAKS IN HIRS 2 CHANNEL 12 RADIANCE FIELDS

TIROSN/HIRS 2 Channel 12 (C 12) has a response function similar to Meteosat WV Channel. Bériot et al. (1982) have shown that in spite of their difference in the spectral range, strong correlations exist between synthetic radiances computed for the both channels, and for scenes observed under the same zenith angle they proposed an empirical linear relation between the two radiances. We must thus examine the influence of the zenith angle on the radiance in order extend the results of the Meteosat WV channel to C 12.

Indeed along a slant path of the HIRS 2 sensor the zenith angle varies from 0° up to 58° while the viewing (or nadir) angle varies from 0° to 45°. Using LOWTRAN 4 Transmittance/Radiance code (Selby et al. 1978), we have

computed synthetic radiances for 5 standard atmospheres as function of the zenith angle for this range of values ; the results show that the relative variation of radiance is less than 2 %. Thus the influence of the zenith angle in a first order approximation can be neglected, as far as we are particulary interested in local relative variations of radiance to detect tropopause breaks, and the results given by (RA) for the Meteosat WV channel radiance fields can be extended to the HIRS 2 C 12 radiance fields.

3. TROPOPAUSE FOLDS AND TOTAL OZONE FIELDS.

A vertical ozone distribution in a cross section of an upper jet-stream, obtained from measurements from research aircraft by Shapiro (1980) is shown on Figure 1 ; it presents the same characteristics as those presented by other authors (Danielsen et al., 1977, 1980 ; Shapiro 1979). On Figure 2, the wind speed, potential temperature analysis from the same author in the same cross section as Figure 1 is presented. The tropopause is defined as a threshold of potential vorticity (10^{-5} K/(mb s)). The analysis of ozone is divided into two parts corresponding to two flight paths : because of temporal changes in O_3 concentration between the two flights, the author was not able to mesh the two distributions.

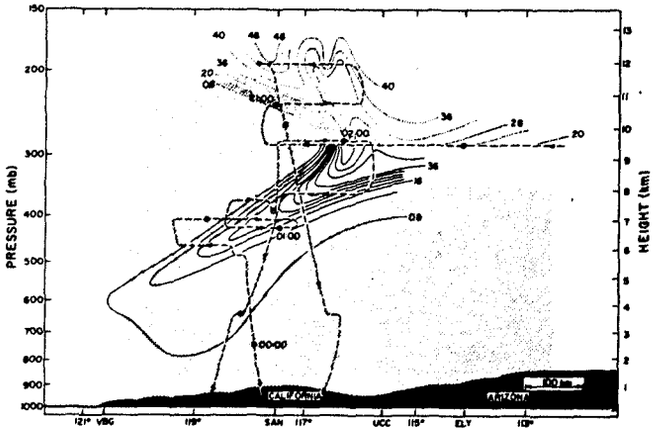

Fig. 1. *Ozone concentration analysis (parts per 100 millions by volume (pphm/vol)). Analysis for upper flight track data, doted lines ; lower flight track, solid lines ; troposphere, stippled aera. After Shapiro (1980).*

The O_3distribution presents the characteristic intrusion of ozone-rich air within the frontal zone delineated by the folded tropopause. As it can be seen from Figure 1 above the polar tropopause level large horizontal gradients of O_3 concentration are found across the jet-stream. The columnar amount of O_3 computed between this level and the 150 mb-pressure level, must thus also present a large horizontal gradient across the jet-stream. Between the level of polar tropopause and the ground, the horizontal variation of the columnar amount of ozone depends on one hand on the difference of tropospheric ozone distri-

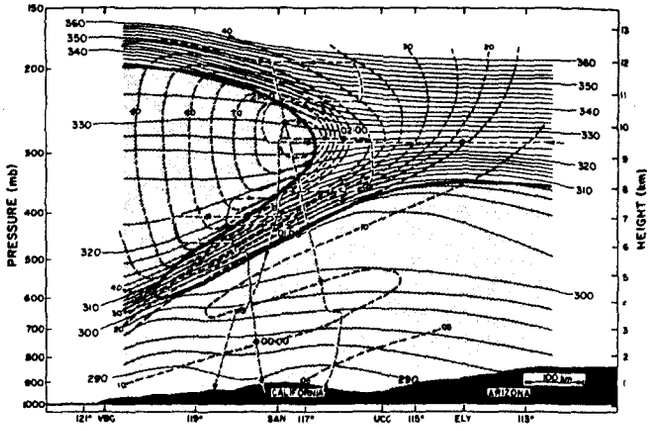

Fig. 2. *Cross section through a tropopause folding event. Potential temperature (K) their solid lines ; wind speed (ms^{-1}) heavy dashed lines ; aircraft flight track, thin dashed lines ; tropopause, heavy solid line ; troposphere, stipped area. After Shapiro (1980).*

bution between cold polar air and warm subtropical air and on the other hand on the contribution on the intrusion of ozone-rich air within the tropopause fold. However because of the limited altitude range of research aircraft, it has not been yet possible to investigate the mesoscale distribution of ozone above the 150 mb-pressure level and so to ascertain the extent to which the variation of columnar amount of ozone below this level would modulate the total columnar amount of ozone, and thus give a significant signature in total ozone fields.

If we assume that middle and high stratosphere are not sensitive to fast (< 24 h) variations of the dynamics of upper jet-streams at mesoscale (< 1 000 km), i. e. that the maximum concentration layer of ozone is not disturbed. The signature of tropopause fold could be point out from the variations of columnar ozone amount below the 150 mb pressure level.

The O_3 distribution from research aircraft are too scare in troposphere and lower stratosphere, and the ozone radiosonde network is not dense enough to authorize an accurate estimation of the variation of the columnar amount of ozone below 150 mb pressure level. However, Muramatsu (1979) and Piaget (1971) showed that the thin layers of high O_3 concentration observed on ozonograms below the conventionnal tropopause level are associated with the intrusion of stratospheric air within the tropopause folds. Using their data and ozonograms of the West European ozonesonde network, we have computed the increase of columnar O_3 amount brought by these thin layers. The values we found, are highly variable as function of the position of the sounding with regard to the jet-stream, and can reach 20 DU (matm - cm) with a mean value around 15 DU.

In regard to these values, the tropopause folds might be detectable in total ozone fields,

if the method of ozone restitution from TOMS in sensitive enough.

As compared with ground truth stations the total ozone can be determined from TOMS with a precision less than 2 % (Klenk et al. 1982). For an amount of 400 DU which is the spring average amount of ozone over Europe (Handbook of Geophysics and Space Environment) the error in TOMS total ozone is less than 8 DU.

4. CASE STUDY

A case has been studied, which illustrates the detection of a tropopause fold event using TOMS total ozone fields and C 12 Radiance fields. This example is taken from two consecutives days during which a folding of tropopause occured and was detected over Central Europe through a three-dimensional isentropic analysis of the radiosonde network data.

Figures 3 and 4 present the 300 mb wind analysis for the 0000 GMT 19 march 1980 (T_1) and the 1200 GMT 20 march 1980 (T_2) using radiosondes data. On march 19 , the analysis shows that the polar jet-stream is divided into two branches referenced as JS_1 and JS_2. On Figure 3. JS_1 flows from Norway to Scotland with a maximum wind speed exceeding 50 m s^{-1}. JS_2 flows over Sweden, then incurvates over Denmark towards Central Europe with a maximum wind speed of 51 ms^{-1}. Between march 19 and march 20, a cut off low process occures over Great Britain and results in the disappearance of the JS_1 branch on march 20.

In the northern part of JS_2, the wind speed decreases to values less than 30 m s^{-1}. Over Central Europe, the jet streak moves southeastwards, with an increase of the maximum wind speed (55 m s^{-1}). The wind analysis shows a new branch of the polar jet-stream referenced as JS_3 on Fig. 4, which flows over North Atlantic. Our study focuses on the JS_2 branch which flows over a region of high density radiosonde network and is associated to a surface front.

In order to have a better three-dimensional knowledge of the frontal zone associated to JS_2 a set of 25 vertical sections roughly perpendicular to the jet axis was analysed (wind, potential temperature) every 12 hours between T_1 and T_2.

This analysis shows the development of a strong upper and mid tropospheric front over Central Europe. Figures 5 and 6 illustrate its spreading out : they present the wind speed, potential temperature and frontal analysis in the cross section along the line AA' of Fig. 3 and 4 at T_1 and T_2 respectively. As it can be seen, the jet core is relatively stable in position and wind speed. At T_1 the frontal zone is confined within the upper troposphere, then spreads out during the following 36 hours, and descends towards the ground. At T_2 it extends horizontally over more than 600 km.

The origin of the air constituting the newly formed frontal zone has been investigated through a set of isentropic trajectories constructed

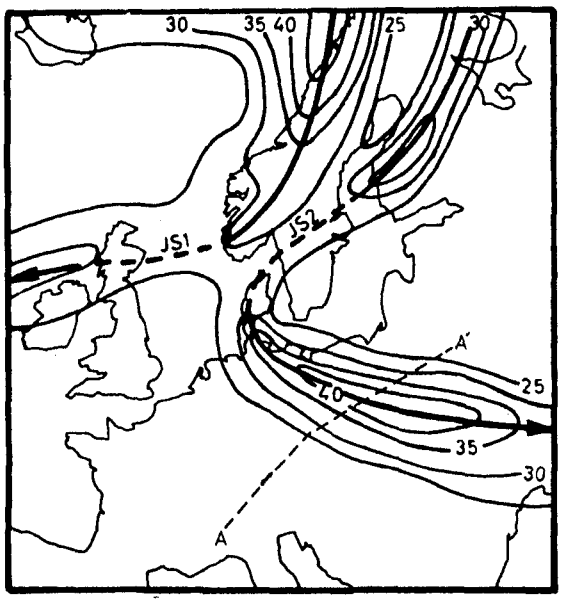

Fig. 3. *300 mb level wind analysis at 0000 GMT 19 March 1980. Isotachs (ms^{-1}) over 25 ms^{-1}, solid lines ; jet axis heavy solid lines when wind speed exceeds 30 ms^{-1}, dashed heavy lines for wind speed less than 30 ms^{-1}.*

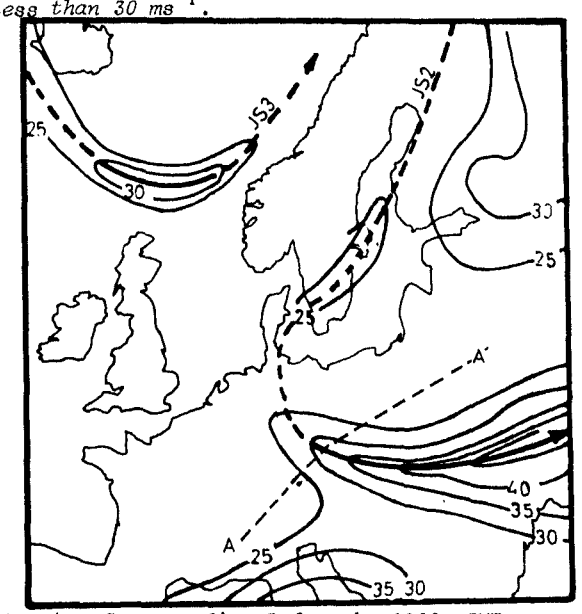

Fig. 4. *Same as fig. 3 for the 1200 GMT, 20 March 1980.*

according to the method proposed by Danielsen (1961) Figure 7 presents the trajectories constructed along the 22°, 24°, and 26 °C isentropic surfaces. These surfaces intersect the frontal zone over Central Europe at T_2. On them, the air parcels which are on the cyclonic side of the jet at T_1 arrive on the anticyclonic side of the jet at T_2. The trajectories present an appreciable sinking and penetrate deeply in the troposphere while remaining within the frontal zone. At T_1, the air parcels were stratospheric or within the upper part of the frontal zone associated to JS_2 over Scandinavia at T_1, which shows that the frontal zone is mostly constitued by air from stratospheric origin.

The TOMS total observations corresponding to the synoptic situations of Figs. 3 and 4 are shown

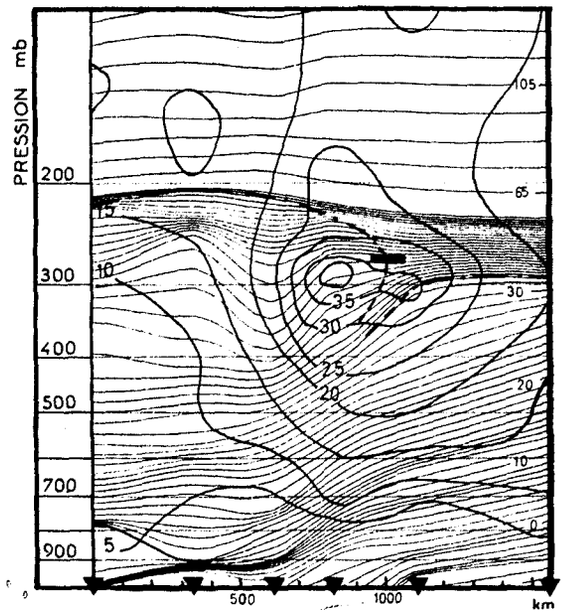

Fig. 5. *Cross section analysis along line AA' of fig. 3 at 0000 GMT 19 March 1980. Isotachs (ms^{-1}) solid lines ; isolines of potential temperature (°C) every 1 °C below the highest tropopause level and every 10 °C above, thin solid lines ; tropopause, dashed dotted lines ; frontal boundaries dashed lines ; radiosonding stations , black triangles. The location of tropopause break is indicated by a black rectangle allowing for a ± 50 km error in position.*

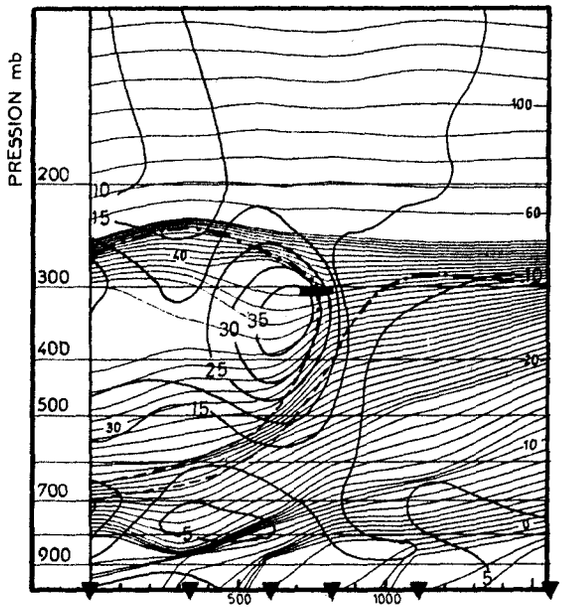

Fig. 6. *Same as Fig. 5 at 1200 GMT 20 March 1980*

on figures 8 and 9 respectively. Each ozone map incorporates two consecutive orbits : 0759 GMT and 0947 GMT for T_1 and 0741 GMT and 0929 GMT for T_2 . On these figures, the maximum radiance bands, as detected by the TIROSN/HIRS2 channel 12 sensor, along the JS_2 branch are also drawn. Two orbits were used to locate them on March 19 (0651 and 0831 GMT) and two more on March 20 (0629 and 0810 GMT). These maximum radiance bands give the location of the tropopause break associated with JS_2 , as it has been verified by

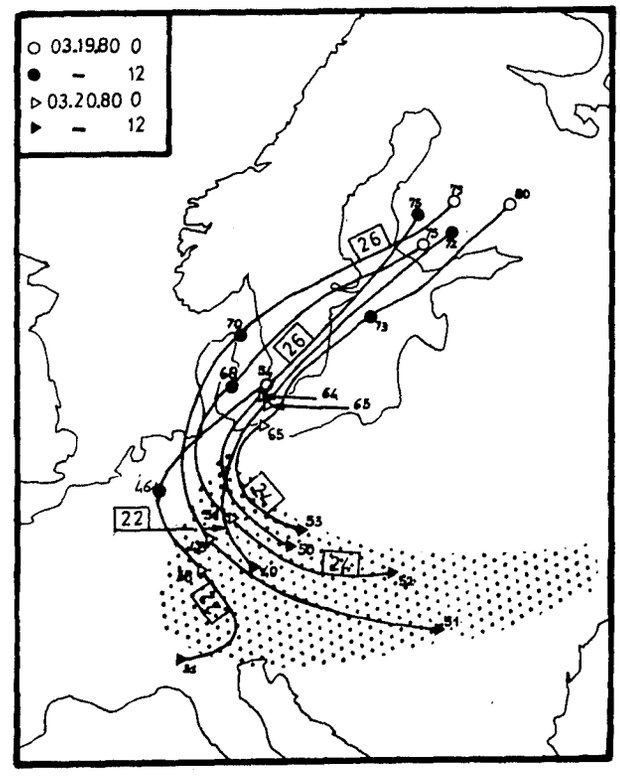

Fig. 7. *Isentropic trajectories along the 22, 24, 26 °C surfaces between 0000 GMT or 1200 GMT 19 March 1980. Altitude of air parcels every 12 hours in km. Frontal zone projection at 1200 GMT 20 March 1980 stippled area.*

isentropic analysis. The ozone analysis at T_1 (Fig. 8) reveals that the ozone isopleths are nearly parallel to the wind direction in the vicinity of the jet core of JS_2, the area of maximum gradient of total ozone content being close to the jet axis. The large scale features of the total ozone distribution show that high values are associated with the through over North East Europe and that the lower values are found within the anticyclonic flow over North Atlantic. These features are related to the mean altitude of the tropopause within these respective geographic regions. At T_2 the ozone isopleths no more follow the wind direction in the vicinity of JS_2 over Central Europe. The total ozone horizontal gradient found at T_1 in the vicinity of the jet axis dilutes while the area of high total ozone extends across the jet axis. This extension coincide well with the spreading within the tropopause fold of the subsiding air of stratospheric origin, as it can be seen on Fig. 9.

Coming back to the assumption that this local variation in the total ozone, which seems to be closely related to the jet-stream dynamics, does not result from ozone content fluctuations in the middle and high stratosphere, it remains possible that it may result from advection in the lower stratosphere. In order to investigate such an eventuality, trajectories were constructed on the stratospheric isentropic surfaces 50° and 120° C (about 10 and 15 km in altitude respectively). They are presented on fig. 10. If advection in the lower stratosphere was to be the major factor of the increase of the total ozone in the area of the spreading frontal zone, then the trajectories reaching this area should have origins in region having at least an equal amount of total ozone. Now it can be

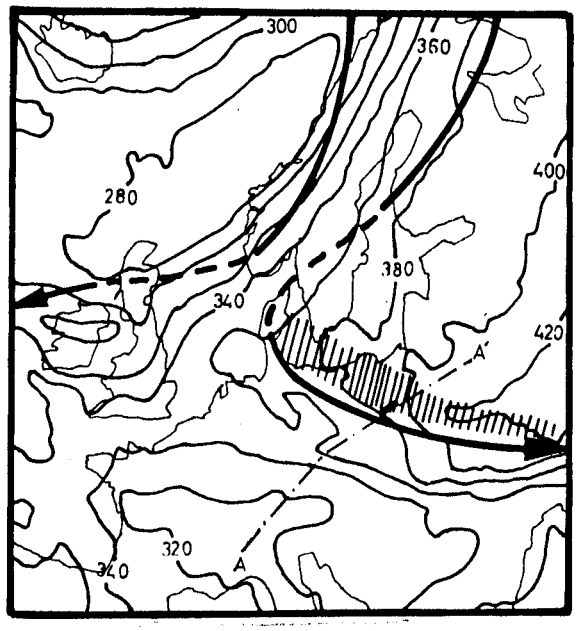

Fig. 8. *Total ozone isopleths from TOMS in D.U. (matm. - cm) for two consecutive Nimbus 7 orbits 0759 GMT and 0947 GMT 19 March 1980. 300 mb jet axis at 0000 GMT 19 March 1980 heavy solid lines (or dashed lines when wind speed less than 30 ms^{-1}). The maximum radiance band associated to JS_2 as deducted by the analysis of the HIRS2 channel 12 radiance field is schematically represented by a dashed area.*

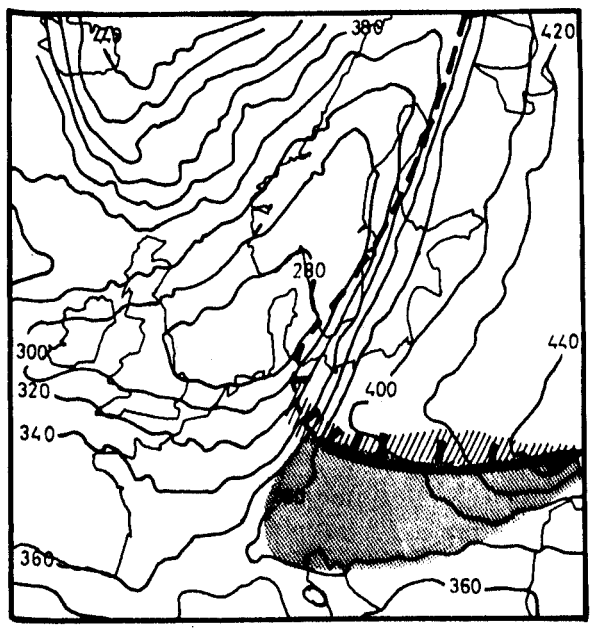

Fig. 9. *Same as fig. 12 for two consecutive orbits at 0741 GMT and 0929 GMT 20 March 1980. Frontal zone projection as deducted from the cross sections analysis, stippled area. Location of tropopause breaks along analyzed vertical cross sections are indicated by black rectangles allowing for a ± 50 km error in position.*

seen on Fig. 10 that the total ozone at the origin of these trajectories is at least 50 DU below the value encountered in the frontal zone area. Thus, the increase of total ozone is likely to come mostly from the intrusion of stratospheric air

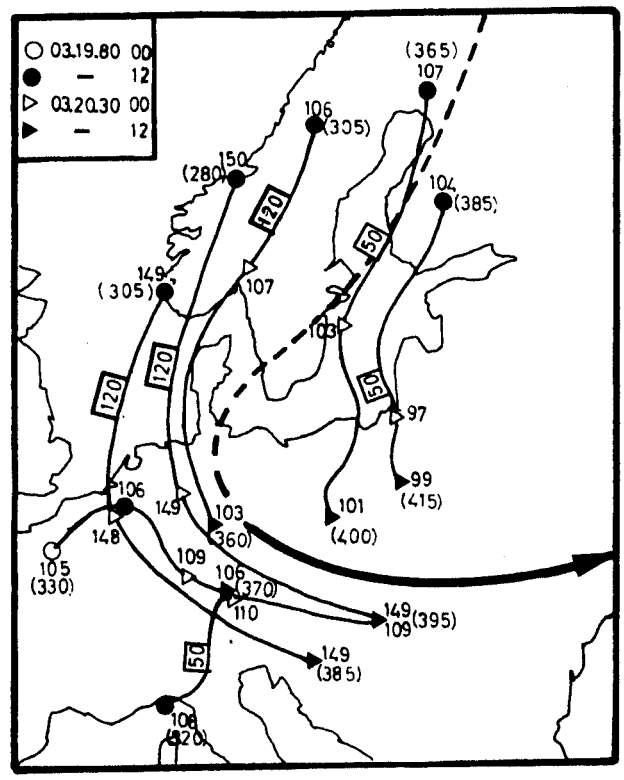

Fig. 10. *Isentropic trajectories along the 50° and 120 °C surfaces between the 0000 GMT or 1200 GMT 19 March 1980 and 1200 GMT 1980. Altitude of air parcels every 12 hours in hm. Total ozone content at the beginning and the end of each trajectory in DU (matm - cm in brackets. 300 mb jet axis same as fig. 4.*

within the fold. The observed value of the temporal change in the region of the fold is about 40 DU : it is in excess of the increase of total ozone which can be expected from the estimate we have given for the mean contribution (15 - 20 DU) of the thin layers of high ozone concentration associated with the tropopause folds. However, Figs. 8 and 9 show a bulk increase of the total ozone about 20 DU over the whole eastern half of the map. The origin of this bulk increase is difficult to determine accurately : it would require the knowledge of the threedimensionnal ozone distribution and of the motion of air parcels within the whole stratosphere.

However, if we take this phenomenon in account and substract the general trend from the local change in the region of the tropopause fold, the resulting value is very close to the expected one (15 - 20 DU).

What has been said above emphasizes the importance of the horizontal gradient of total ozone to interpretate the ozone fields in terms of jet-stream dynamics. On figure 11, we present the isocontours of the horizontal gradient of total ozone ($grad_h$ (O_3)) computed from TOMS observations at T_2. The analysis reveals that the areas of maximum values follow the jet axis in the region where the upper frontal zone is of small extent and follow the edge of the fold in the region of the tropopause fold. The values observed at the edge of the fold (about 20 DU/100 km) are high enough to come out of the noise in the TOMS

Fig. 11. *Isopleths of horizontal gradient of total ozone (10^{-1} DU/km) from TOMS observations presented in Fig. 9. Frontal zone projection as deducted from cross sections analysis, stippled area, band of maximum radiance of HIRS2 channel 12 associated to the jet, dashed area, 300 mb JS_2 jet axis same as Fig. 4.*

observations, which allows to consider the feasibility of an operational mapping of the edge of the fold. As the localization of the tropopause break can be done through the use of satellite data in WV channel, it is the whole tropopause fold that can be mapped by satellite.

5. CONCLUSION

From vertical distributions of ozone in sections across jet-stream-frontal systems from research aircraft and from ozonagrams, it has been pointed out that the intrusion of stratospheric air within the tropopause folds may have a non neglectable response in total ozone fields, which is confirmed by a case study of a tropopause fold event using both the TOMS total ozone fields and a threedimensional isentropic analysis.

It has been shown that the mapping of the folds is likely to be done by the mean of satellite data. A band of maximum horizontal gradient of total ozone delineate the edge of the fold, while a maximum radiance band of HIRS2 channel 12 radiance fields delineate the beginning of the fold (i.e. the tropopause break). However it is clear that more studies are to be performed in order to ascertain the detection criteria before establishing operational detection algorithms. A first step would be to incorporate the results obtained by Muller and Cayla (1982) on the retrieval of total ozone from HIRS2 data, which should enable the whole tropopause fold mapping from a single satellite.

Acknowledgments. We are deeply indebted to the NASA Goddard Space Flight Center, who provided us with a copy of total ozone measurements from TOMS needed for this study, and to Jacqueline Duron for her most useful support in data processing.

Part of this work was supported by CNES (ATP "Atmosphere moyenne"), one of us acknowledges personnal support (doctoratefellowship) by CNES.

REFERENCES

Beriot, N., N.A. Scott, A. Chedin, O. Sitbon, 1982: Calibration of Geostationary-Satellite Infrared radiometer Using the TIROSN Vertical Sounder : Application to Meteosat 1. *J. Appl. Met.*, 201, 84-89.

Danielsen, E.F., 1961: Trajectories : isobaric, isentropic and actual. *J. Met.*, 18, 479-486.

——, 1968: Stratospheric-tropospheric exchange based on radioactivity, ozone and potential vorticity. *J. Atmos. Sci.*, 25, 502-518.

——, V.A. Mohnen, 1977: Project Dustorm Report : Ozone Transport, in Situ Measurements, and Meteorological Analysis of Tropopause folding. *J. Geo. Res.*, 82, 58675877.

——, R.S. Hipskind, 1980: Strastospheric-tropospheric exchange at polar latitudes in summer. *J. Geo. Res.*, 85, 393-400.

Gidel, L.T., M.A. Shapiro, 1979: The role of clear air turbulence in the production of potential vorticity in the vicinity of jet-stream-frontal systems. *J. Atmos. Sci.*, 36, 2125-2138.

Klenk, K.F., P.K. Bhartia, A.J. Fleig, V.G. Kaweshwar, R.C. McPeters, 1982: Total Ozone Determination from the Backscattered Ultraviolet (BUV) Experiment. *J. Appl. Met.*, 21, 1672-1684.

Muller, S., F.R. Cayla, 1982: Total Ozone Measurements derived from TOVS radiance. *Planet. Spa. Sci.*, 317, 779-785.

Muramatsu, H., 1980: A Case Study of the transport of the Stratospheric Ozone into the Troposphere. *Pap. Met. Geoph.*, 31, 97-106.

Piaget, A., 1971: Utilisation de l'ozone atmosphérique comme traceur des échanges entre la troposphère et la stratosphère. *Publication de l'Institut Suisse de Météorologie*, Zürich.

Ramond, D., H. Corbin, M. Desbois, G. Szejwach, P. Waldteufel, 1981: The dynamics of Polar jet-stream as depicted by the Meteoast WV Channel Radiance Fields. *Mon. Wea. Rev.*, 109, 2164-2176.

Reed, R.J., 1955: A study of a characteristic type of upper-level Fontogenesis. *J. Met.*, 12, 226-237

Selby, J.F., F.X. Kneizys, J.H. Chetwynd, R.C. Mc Clatchey, 1978: Atmospheric Transmittance/Radiance Computer Code LOWTRAN IV. A.F.G.L. TR 78.0053.

Shapiro, M.A., 1974: A multiple Structure Frontal Zone Jet-stream System as revealed by a Meteorologically Instrument Aircraft. *Mon. Wea. Rev.*, 102, 244-253.

——, 1980: Turbulent mixing within tropopause folds as a mechanism for the exchange of constituents between the Stratosphere and the Troposphere. *J. Atmos. Sci.*, 37, 994-1004.

——, 1978: Further evidence of the mesoscale and turbulent structure of Upper level jet-stream-frontal zone systems. *Mon. Wea. Rev.*, 106, 1100-1111.

Staley, D.O., 1960: Evaluation of potential vorticity changes near the tropopause and related vertical motions, vertical advection of vorticity and transfert of radioactivity debris from strastosphere to troposphere. *J. Met.*, 17, 591-620.

E.5

Satellite Cloud and Precipitation Analysis Using Interactive Computer System

C. Wash, L. Chou, C. Nelson, C. Moren and L. Spray

Department of Meteorology
Naval Postgraduate School, Monterey, CA 93943

1. INTRODUCTION

Satellite imagery has become an important tool for today's meteorologist. Significant mesoscale and subsynoptic scale (10-1000 km) meteorological phenomena, not readily discernible through either synoptic or airway surface observations or 12-hourly upper-air reports, often can be determined from an interpretation of satellite imagery. Interpretation of satellite imagery, however important, is often neglected because of the excessive time required and the subjective nature of the analysis. Because of these constraints, operational meteorologists often rely on the imagery as a source of information for determining only the gross synoptic scale features, such as frontal placement, ridge axes and surface pressure centers. This does not adequately utilize the potential information available.

This paper describes a detailed automated cloud and precipitation intensity analysis for the Navy's interactive Satellite Data Processing and Display System (SPADS). Specifically, this program was designed to produce in real-time (10 minutes) analyses of particular important cloud and weather features, namely; cloud types, cloud amounts, cloud-top heights, cloud-top temperatures and precipitation intensity. This system collects and analyzes digital satellite data from the visual and infrared channels which have a one-half hour temporal and 0.5 to 4.0 n mi spatial resolution respectively, from the Geostationary Operational Environmental Satellite (GOES) Visual-Infrared Spin Scanner Radiometer (VISSR).

The objective of this paper is to describe and evaluate the automated cloud and precipitation intensity analysis program utilizing the SPADS at the Naval Environmental Prediction Research Facility (NEPRF) in Monterey, California. Systematic evaluation of significant meteorological features are conducted with available imagery, particularly GOES EAST, for regions in the southeastern United States. Verification data will consist of a subjective, manual analysis of the imagery with a correlation of surface observations, upper-air observations, pilot reports and the automated radar summary.

2. CLOUD AND PRECIPITATION INTENSITY ANALYSIS

The SPADS automated cloud and precipitation intensity analysis model and program is a composite of previous work, namely, Liljas' (1982) cloud threshold and qualitative precipitation model, Reynolds and Vonder Haar's (1977) bispectral cloud-top temperature calculation, and Harris and Barrett's (1978) cloud amount estimate techniques. Additionally, a texture test for determining particular cloud types is included. Each previous model input to the SPADS model is briefly described in the following sections.

Cloud Type. The Liljas model (1982) utilizes the visual and infrared thresholds in three sensor channels from the TIROS-N Advanced Very High Resolution Radiometer (AVHRR) to type clouds and discriminate between water and land. These thresholds were converted for the GOES VISSR data. Only visual and thermal infrared aspects of the method are used due to the non-availability of the near-infrared channel in the GOES VISSR data. The

procedure for calculating cloud type consists of calculating pixel array values for the average visual brightness, infrared brightness counts and the standard deviation of the cloudy visual counts. The standard deviation values representing texture discriminates between stratiform and cumulus humilis, small and large cumulus congestus, and altostratus and cirrostratus. The initial standard deviation values were approximated from the Harris and Barrett (1978) and Fye (1978) studies.

Cloud-Top Temperature/Height and Cloud Amount. The method for determining cloud-top temperature requires the calculation of the average cloud amount from the number of cloud decisions in the grid space (based on comparing the visual digital count of each pixel in the grid to a no-cloud threshold value) divided by the total number of pixels per grid space [Harris and Barrett, 1978]. Cloud-top radiance is given by combining cloud and ground portions using appropriate emissivities. The values for emissivity used are 0.55 for cirrus, 1.0 for nimbostratus and cumulonimbus and 0.9 for all other cloud types. Using Planck's function a cloud-top temperature appropriate for scattered, broken and overcast situations is produced. These temperatures are subsequently compared to the representative upper-air soundings to yield cloud-top heights in millibars.

Precipitation Intensity. Liljas model (1982) adopted his precipitation thresholds from the results of Muench and Keegan (1979). When cumulonimbus or nimbostratus clouds are identified from the cloud type method, the precipitation intensity subroutine is called and produces an intensity profile of the precipitation. The precipitation intensity categories are broken down according to the summation of the infrared radiance and the visual brightness. Liljas' model utilizes six categories. The SPADS model utilizes three categories to specify light, moderate and heavy rainfall. The SPADS precipitation intensity categories are given as rainfall rates similar to the rainfall rates established by the surface observation rain/rainshower intensities, as inferred from Muench and Keegan (1979).

The upper-air and surface temperatures are obtained from the grid point upper-air profiles from Fleet Numerical Oceanography Center (FNOC) in Monterey, California.

After obtaining the GOES and FNOC data, the SPADS program is implemented and initially calculates the average visual and IR brightness, standard deviation and cloud amount. From these values, the cloud types can be produced through the use of two tests, a comparison of the infrared and average visual counts and a texture test (standard deviation) as a supplement. If nimbostratus or cumulonimbus are identified in the cloud type section, the precipitation intensity portion of the program is initiated in order to determine a qualitative estimate of the intensity.

The cloud-top temperature and height portion of the program is initiated for all cloud cases and utilizes the FNOC upper-air soundings for temperature and height distributions.

Each portion of the program produces output for verification; cloud amount, cloud type, precipitation intensity, cloud-top temperature and cloud-top height. These are available for display, contouring or permanent file. The average visual brightness, standard deviation and the amount of cloud corresponding to each infrared pixel can be printed for validation, reference or further testing.

3. EVALUATION

The geographical location of this research is centered over the eastern United States with the center-point of the 512x512 satellite array located at 35°N 80°W. The digitized satellite data were acquired from the Geostationary Operational Environmental Satellite EAST (GOES EAST) by the NEPRF SPADS system. The geographic location was selected in order to:

- Maximize the coverage of significant meteorological phenomena;
- Maximize the surface and upper-air station verification data network and the meteorological observational pilot reports;
- Facilitate the satellite retrieval by NEPRF (GOES EAST); and
- Facilitate the utilization of the automated satellite cloud analysis program on the recently operational SPADS unit at the Naval Eastern Oceanography Center (NEOC) at Norfolk, Virginia.

GOES visual and infrared data were extracted from the 1530 GMT image for local input to the SPADS. The data received were modified to provide a center point at 35°N 80°W on a 512x512 grid at 2x2 n mi visual resolution (infrared resolution 2x4 n mi) for an approximate 1024 x 1024 n mi area coverage.

Concurrently FNOC data fields were obtained for the model from the 1200 GMT analysis. Sixteen grid points, each centered on the sixteen 64x64 IR grids (128x128 VIS grids) were established. Surface and upper-level temperature profiles were extracted for each center point.

At the same time, the verification data are acquired through an automated retrieval system. The surface observation verification data are acquired from the hourly airway observations. The 1200 GMT upper-air observations are utilized for the verification. As each satellite case study was selected, a surface, upper-air and pilot report network of verification data are selectively polled from the Automated Weather Network (AWN) and received via the Continental U.S. Meteorological Data System (COMEDS) to coincide with the satellite image time. The surface and upper-air station verification data network consists of approximately 62 surface stations and 22 upper-air stations scattered throughout the geographic study region. The Automated Radar Summary (ARS) Chart is received hourly on the half-hour from the National Meteorological Center (NMC) via landline facsimile. The 1535 GMT ARS chart is utilized.

Five case studies will evaluate the accuracy, utility and timeliness of the SPADS cloud analysis. Data collection consists of capturing coincident infrared and visual data along with the verification data for 1530 GMT on 02 Aug 83, 11 Aug 83, 23 Aug 83, 31 Aug 83 and 02 Sep 83.

As an example of the program output, data for 11 Aug case are presented. Fig. 1 A and B shows the GOES visible and IR sectors for the east coast region. Objective analyses of cloud type and precipitation (Fig. 2 A and B) from the program can be compared with a composite of radar and surface verification data on Fig. 3.

This case presented a large variety of cloud and precipitation features to analyze including low stratus to the west of a major cyclone, embedded frontal convection, large warm frontal cloud band, oceanic thunderstorms, fair weather cumulus and thin cirrus. Details of the evaluation are found in Moren (1983). Key results are:

- successful mapping of stratus, cumulus and cumulonimbus areas.
- good precipitation area determination but less successful at precipitation intensity.
- accurate cloud top temperature and pressure analyses.

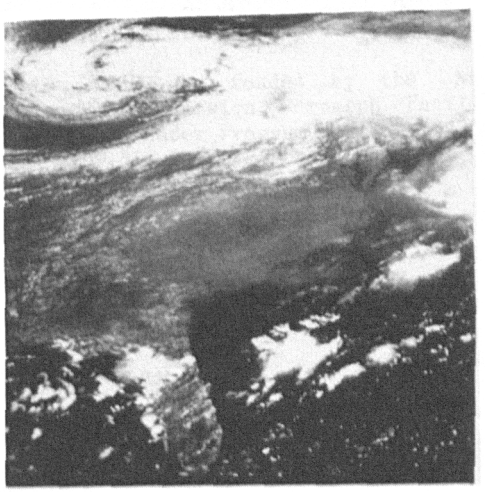

Figure 1A. GOES Visual Imagery for 11 August 1983.

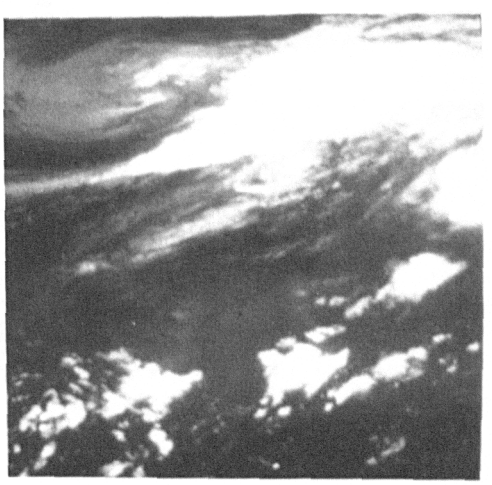

Figure 1B. GOES Infrared Imagery for 11 August 1983.

A

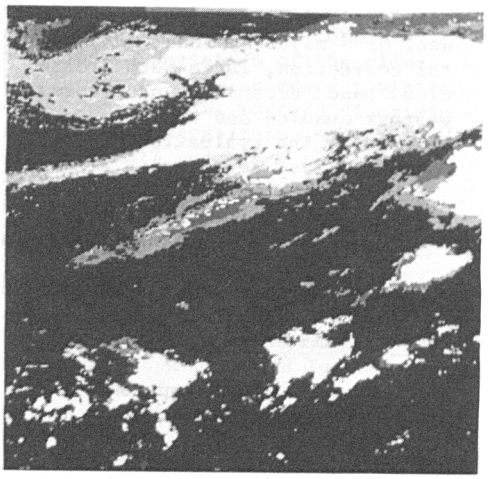

B

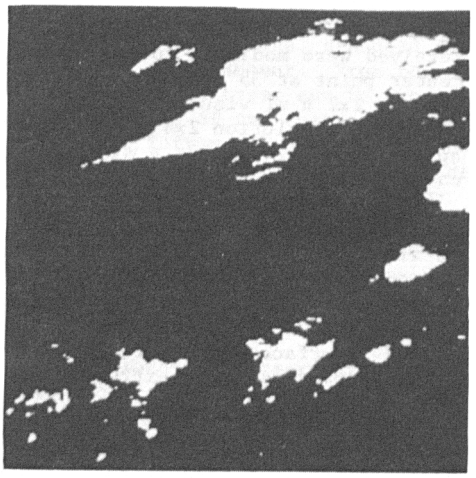

Figure 2A. SPADS Analysis of Cloud Type (A) and Precipitation (B) for 11 August 1983.

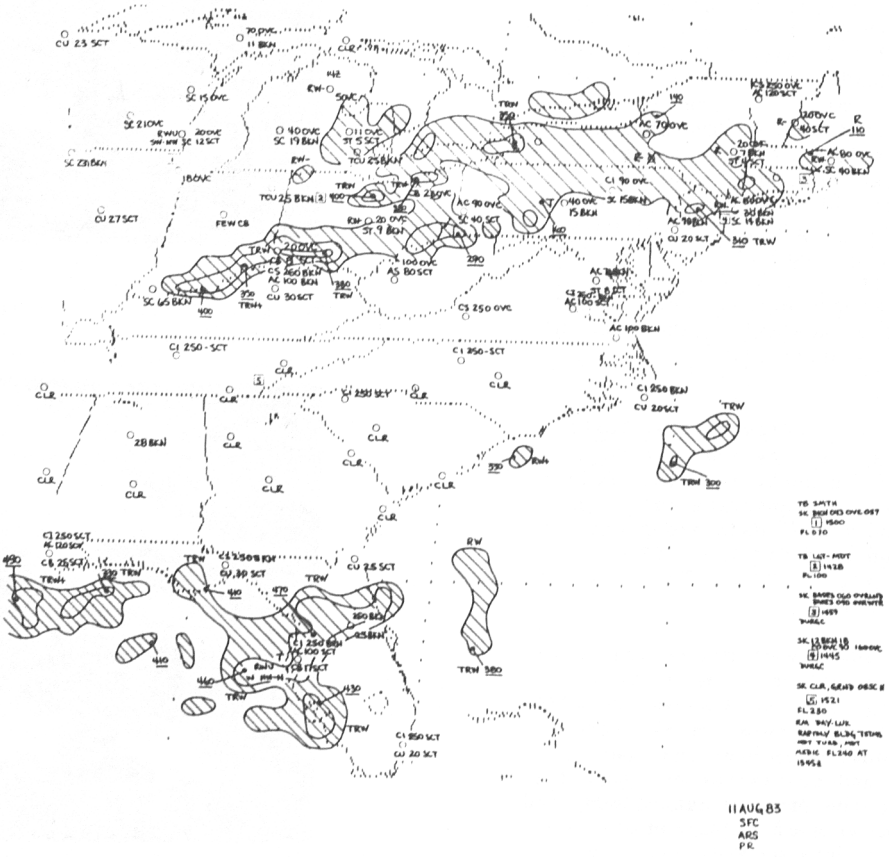

Figure 3. Surface Observation and ARS Verification Chart for 11 August 1983.

4. RESULTS

The SPADS automated cloud and precipitation intensity analysis program produced information on cloud amount, cloud type, cloud-top temperature/height and precipitation intensity rapidly after data receipt. Five case studies were successfully analyzed utilizing as many current specific verification tools as were available. The following SPADS program output successes were observed:

- The cloud amount analysis is skillful. Alignment and orientation are excellent.
- The cloud type analysis is skillful but can be improved. Classification of cumuliform cloud types is successful, particularly for cumulonimbus. Cirrus typing was the least successful.
- The cloud-top temperature/height analysis is excellent. Realistic temperatures and heights were established in most instances and were consistent with other SPADS generated output.
- The precipitation intensity analysis is fair. Differentiation of intensity levels was difficult to establish. The precipitation intensity analysis does provide evidence of potential precipitaton areas.

5. REFERENCES

Fye, F.K., 1978: The AFGWC Automated Cloud Analysis Model. AFGWC Technical Memorandum 78-102, H.Q. Air Force Global Weather Central, Offutt AFB, Nebraska, 97 pp.

Harris, R. and E. C. Barrett, 1978: Toward an Objective Nephanalysis. J. Appl. Meteorol., 17, 1258-1266.

Liljas, E., 1982: Automated Techniques for the Analysis of Satellite Cloud Imagery. Nowcasting, ed. K. Browning, Academic Press, 177-190.

Moren, C., 1984: Evaluation of the SPADS Automated Cloud Analysis Model. M.S. Thesis, Naval Postgraduate School, 139 pp.

Muench, H. S. and T. J. Keegan, 1979: Development of Techniques to Specify Cloudiness and Rainfall Rate Using GOES Imagery Data. AFGL-TR-79-0255, AD A084, 757 pp.

Nelson, C. A., 1982: Estimation and Mapping of Cloud and Rainfall Areas with an Interactive Computer. M.S. Thesis, Naval Postgraduate School, 134 pp.

Reynolds, D. W. and T. H. Vonder Haar, 1977: A Bispectral Method for Cloud Parameter Determination. Mon. Wea. Rev., 105, 446-457.

6. ACKNOWLEDGEMENT

This work was funded by the Naval Environmental Prediction Research Facility, Monterey, CA under Program Element 62759N, Project WF59-553, "GOES Data Analysis for Weather Analysis and Forecasting."

"AIRCRAFT PENETRATIONS OF ARC CLOUD LINES"

Peter C. Sinclair

Department of Atmospheric Science
Colorado State University
Fort Collins, Colorado

and

James F.W. Purdom

Regional and Mesoscale Meteorology Branch
Development Laboratory
NOAA/NESDIS

Cooperative Institute for Research in the Atmosphere
Colorado State University
Fort Collins, Colorado

1. INTRODUCTION

Nowcasting and the very-short-range forecasting of mesoscale weather events are critically dependent on our perception and understanding of the phenomena causing those events. Arc cloud lines, as detected in satellite imagery, have been shown to be important initiators of new strong convection (Purdom and Marcus, 1982). In fact, Purdom (1984) has shown most of the rainfall occurring over the southeastern United States during summertime can be attributed to storms generated by arc cloud lines. Furthermore, under proper conditions thunderstorm outflow boundaries (arc cloud lines) can provide the organized flow field required for the development of severe and tornadic storms. This has been shown both in case study analyses (Purdom, 1976, Maddox et al., 1980, Parker and Hickey 1980), and recently with advanced numerical cloud modeling (Klemp and Rotunno, 1983). Understanding the arc cloud line's dynamic and thermodynamic characteristics is imperative if we are to understand the development and evolution of deep convection.

During the summer's of 1982 and 1983, NOAA and NASA co-sponsored a research field program in the Colorado high plains* (1982) and in Florida** (1983) that combined research aircraft flights with rapid scan (3 minutes interval) GOES imagery. The purpose of the program was to improve our understanding of the dynamic and thermodynamic characteristics of arc cloud lines as they relate to future convective development as well as determine how their flow fields might impact aircraft and space shuttle operations. Penetrations were made of arc cloud lines on several flight days in both 1982 and 1983. In contrast to our previous aircraft measurements (Sinclair and Purdom, 1982, 1983) which were confined to the subcloud layer above the density surge line, see figure 3, a portion of the 1982 flights and all of the 1983 flights were made at lower levels through the density surge line.

*NOAA NA82RA-C-00103
**NOAA NA82RA-C-00103 and NASA & NOAA NA82AA-H-00026

2. THE EXPERIMENT

2.1 General

2.1.a. Colorado - The arc cloud line investigations in the Colorado high plains were carried out in late July and early August of 1982. The main purpose of those investigations was to establish similarities and differences between arc cloud lines in the more moist southeast United States (ibid) and those that are generated over the more arid high plains. Arc cloud lines were investigated, with penetrations being made through the density surge line (DSL) region as well as in the subcloud layer above the DSL.

For a variety of reasons, including logistics, fuel availability and access to weather information operations were based out of Christman Field at Colorado State University. General areas for penetrations were chosen using near real time GOES satellite data from the CSU IRIS system (Green and Kruidenier, 1982). Once the aircraft reached an area for investigation, decisions concerning penetrations points were made visually. Aircraft position was determined from VOR-DME and Doppler navigation systems, and could be cross referenced using visual landmarks such as towns, roads and other ground features. This is important because LORAN-C is not always usable in the N.E. Colorado area, and low level penetrations might at times be too low to acquire the VORTAC signal.

2.1b Florida - The arc cloud line investigations in Florida were carried out during the last two weeks of August, 1983. The main purpose of those investigations was to determine the dynamic and thermodynamic characteristics of the density surge line region. This was our most successful series of flights (7) to date, with arc cloud lines of varying intensity being investigated on each of five flight days. Penetrations were made in the clear air, well below cloud base and in the DSL. Generally, multiple traverses were made through the DSL at altitudes ranging from 120 m to 650 m. One reason for our high success rate during this series of experiments was the fine support provided us, in terms of both logistics and weather support, by the USAF at Patrick AFB and Cape Canaveral AFS (see acknowledgments). General

areas of penetration were chosen using near real time GOES satellite data that were transmitted over closed circuit TV from Cape Canaveral AFS to Patrick AFB Operations. Once the aircraft reached an area where arc activity had been detected, decisions concerning penetration points were made visually. Aircraft position was determined from VOR-DME, LORAN-C, and Doppler navigation systems. At all times aircraft location accuracy was well within the resolution of one GOES visible pixel (1 km).

2.2 Aircraft Observational System

The CSU Atmospheric Research Flight Facility (ARFF) has developed a number of Airborne Atmospheric Data Systems (AADS-1A to 5A) from direct measurement of the three-dimensional velocity field, temperature, dew point, pressure, atmospheric gases and particulates, etc. These instrumentation systems have been specially designed for various aircraft (McDonnell F-101B, North America T-6 and T-28, Beech Queen Air, Cessna T207, Shinn 215A, and Laister Kaufmann sailplane) for measurements in atmospheric systems ranging from mesoscale systems and thunderstorm complexes to waterspouts and dust devils (Sinclair 1969, 1973, 1974, 1977). A miniaturized version (AADS-5A) of these previous systems has been designed and constructed by ARFF for a Cessna T207 aircraft. This is the first installations of this type on a light, single-engine aircraft. The gust velocity measurement system is designed so as to be independent of the aircraft sensitivity to atmospheric motion and/or pilot induced motions. The measurement technique (Sinclair, 1969, 1973) requires knowledge of the motion of the air relative to the airplane ($V_{a,p}$) and the motion of the airplane relative to the ground ($V_{p,g}$) in order to calculate the atmospheric motion with respect to the ground ($V_{a,g}$) thus

$$V_{a,g} = V_{a,p} + V_{p,g}$$

which for the vertical component ($w_{a,g}$) can be expressed as

$$w_{a,g} = V_T\alpha + V_T\beta\phi - V_T\Theta + \int_0^t a_z dt + w_{p,g}(0) + L\dot{\Theta}$$

where V_T is the true airspeed; α the angle of attack; Θ, β, and ϕ the pitch, yaw and roll angles, respectively; a_z the vertical acceleration of the aircraft; $w_{p,g}(0)$ the vertical motion of the aircraft at time $t = 0$; $\dot{\Theta}$ the pitch rate; and L the accelerometer displacement from the angle of attack measurement point. The measurement of a α and β are made with lightweight, but durable, flow vanes (response <0.05 sec). The aircraft, pitch and roll angles and the pitch rate ($\dot{\Theta}$) are measured with high precision vertical and rate gyros. Accelerations are measured by a three-axis accelerometer system at the aircraft center of gravity. True airspeed and static temperature are determined from the compressible, subsonic flow equations using measurements of total and static pressures and total temperature. Relatively fine structure of the turbulent velocity spectrum (0.04-10 Hz) can be obtained from the data which are recorded on a 1000 character per second, digital, incremental magnetic tape recorder. The entire gust probe system is mounted below the left wing of the aircraft in a modified drone tip tank. The α - β vane system and pilot tube are located at the front of the instrumentation boom which extends from the nose of the tip tank to a point ahead of the wing and the plane of the propellor. All of the gust vane electronics as well as the pressure transducers and gyros are rigidly fastened to the boom structure inside the drone tip tank.

In addition to the gust velocity (u', v', w') measurement system, an on-board doppler wind system (APN-153V) provides accurate ($\pm$ 0.5 - 1.0 m sec) measurements of ground speed and drift angle which coupled with aircraft heading and true airspeed provide mean (25 sec. avg.) horizontal wind components ($\bar{u}$, $\bar{v}$). Precise flight tracks over the ground can be programmed into the doppler computer to satisfy a wide variety of sampling requirements. The dew point and the total temperature are also continuously recorded with the other parameter at a sampling rate of 0.04 sec (the gust vanes are fast sampled at 0.02 sec). The measurement locations are obtained continuously from LORAN-C ($\pm$ 70 km), VOR-DME (< $\pm$ 10 m), and/or doppler navigation coordinates (< $\pm$ 500 m relative).

2.3 GOES Data

For all but one of the case study days, nominal 3 minute interval GOES imagery were taken during the flight periods: the scheduling was the same as was used in SESAME Operations (Barnes, 1981). The three minute images covered the study area very well, and in all cases sufficient landmarks were available to insure aircraft and satellite cloud locations to within the resolution of the GOES image. Inspection of the satellite data versus aircraft locations leave no doubt that the aircraft measurements represent continuous data sets through the arc cloud lines in the sub-cloud region.

3. OBSERVATIONS

In Florida, seven research flights were made on five flight days, with arc cloud line DSL's of varying intensity being encountered on each day. Among the more interesting of the research days was the last flight in August when an arc cloud line region was studied near the northwest coast of Florida, figure 1. We feel that the

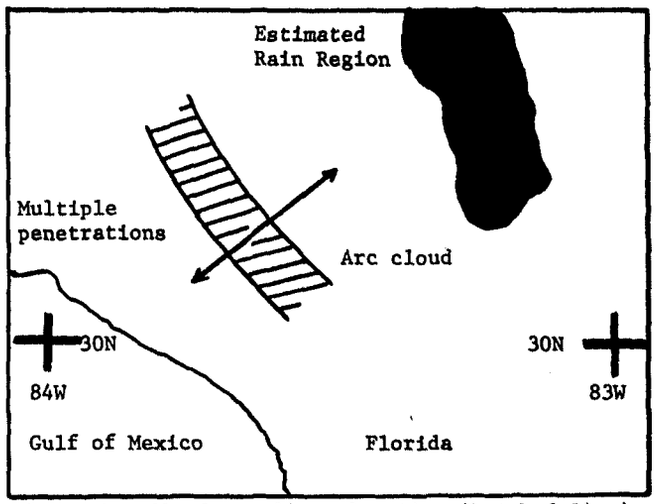

Figure 1 - Cloud arc lines location (hatched-line) for penetrations in N.W. Florida. Aircraft penetration directions are shown by the arrow through the hatched area.

circulations encountered on this day are representative of those found with the active arcs penetrated; consequently only this case will be discussed in detail. Penetrations within the DSL were made between approximately 620 meters and 180 meters (AGL). The drawing shown in Figure 2 summarize the results of the penetrations, all in a coordinate system relative to the DSL boundary. At different levels, the wind shift between the DSL and the warm unstable airmass into which it was moving was between 9 and 15 m/s. Ahead of the DSL vertical motion which was unorganized, became organized into an upward moving current of warm moist air as it moved into the region of the DSL. At the DSL interface vertical motions increased sharpely and the air was very turbulent in nature. Solid upward motion, with peaks as high as 10 m/s were found in this interface region. In the outflow air, between 2 and 7 km behind the DSL interface a sharp transition zone was found between upward moving air and sharply descending air. Vertical motions in the sinking air ranged from -3 to -5 m/s. This downward motion gradually diminished with deeper penetration into the cool air (note however, we never encountered the thunderstorm rain shaft). The entire flight within the DSL and rain-cooled air was turbulent. When flying in the rain-cooled air toward the DSL interface an effective tail wind of 12 to 18 m/s was realized. During the entire time of the penetrations there was no nearby precipitation or virga. In fact, estimates placed all visible precipitation shafts in excess of 20 km from the flights. It should be noted that these latter facts concerning precipitation were not true of the other arc's we investigated.

Several important differences exist between the air and flow fields in the DSL and in the subcloud layer above the DSL. Figure 3 is from our earlier work (Sinclair and Purdom, 1983), and is a composite from our flights in the sub cloud layer above the DSL. Comparison of Figure 3 with Figure 2 shows that strong differences in dynamic characteristics of air within and above the DSL. Air motions within the DSL were much more turbulent, and both stronger upward and downward motions were encountered within the DSL than in the subcloud layer above the DSL. The strong turbulence and shear in the vertical wind across the DSL interface supports our hypothesis that mixing of air from the DSL with the warm unstable air ahead of it provides a modified updraft structure that feeds the cumulus clouds of the arc cloud line (Sinclair & Purdom, 1983). Additionally, the strong tailwind within the cold outflow air was only experienced within the vertical extent of the DSL and not above it.

Similar results to those discussed above were found in our penetrations of colorado high plains arc cloud lines. The major difference found between the Colorado arcs and those in Florida was the strength of all fields were stronger in the high plains cases.

4. CONCLUSIONS

1. The lateral extent of the vertical motion field compared to the cloud scale (Figures 2 and 3) indicates that the main driving force for the initial cloud development along the arc-line is controlled by the thunderstorm outflow (s) interacting with the convectively unstable air of the environment. The individual

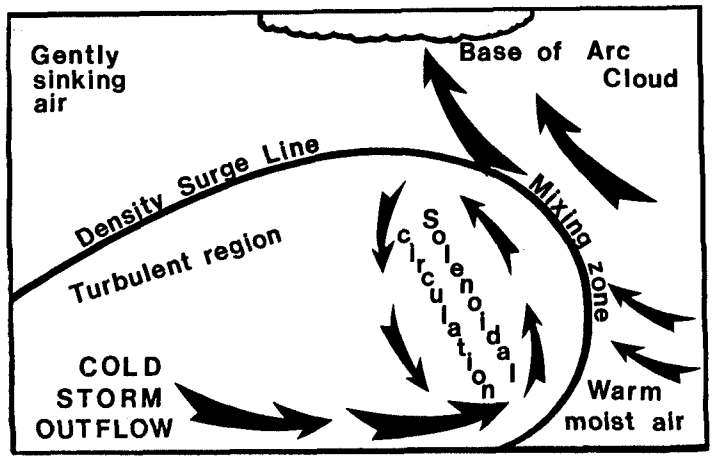

Figure 2 - Schematic illustration of the Arc Cloud Line features in the DSL. For a description of the vertical motions and outflow speeds, see the text to the left. The thunderstorm that produced the arc cloud was over 20 km from the mixing zone region (see figure 1).

cumulus cloud scale motions along the arc line can then be visualized as being superimposed on this somewhat larger-scale, initiating process.

2. Arc cloud lines and their associated DSL region can pose extreme hazards to aircraft operations. One of several critical situations might involve an arc cloud line approaching the end of an airport runway with its parent thunderstorm 15 to 20 km away. An aircraft in a landing pattern might circumnavigate the thunderstorm and then descend through the top of the DSL, at perhaps an altitude of 500 meters. If the outflow is strong, a tailwind of 15 to 20 m/s might suddenly be encountered upon descent into the DSL. Depending on aircraft speed prior to its descent into the DSL, the loss of relative flow across the wing in the DSL can cause critical sink rates which may lead to an aircraft accident.

3. An arc cloud line's major threat to space shuttle operations lie in its ability to generate new thunderstorm activity along the shuttle glide path in time frames that occur after the decision for reentry has been made. In this case requirements for cloud cover, precipitation and weather type could all be seriously violated. Additionally, lateral wind shears across the runway could exceed shuttle landing requirements in either an arc cloud DSL environment or the environment of the thunderstorm it might have triggered.

5. ACKNOWLEDGMENTS

For their excellent support, we express our sincere thanks to Col. Billy Washam and the 6550th Air Base Group and Lt. Col. John Oliver and Det. 11, 2nd Wq Sq, both located at Patrick AFB, Florida. Additional thanks is due Det. 11's Cape Canaveral Forecast Facility for their support with real time satellite data. This excellent USAF cooperation played a major role in the success of these flights. The research reported in this paper was supported by NOAA under NOAA NA82RA-C-00103 and NASA and NOAA under NOAA NA82AA-H-00026.

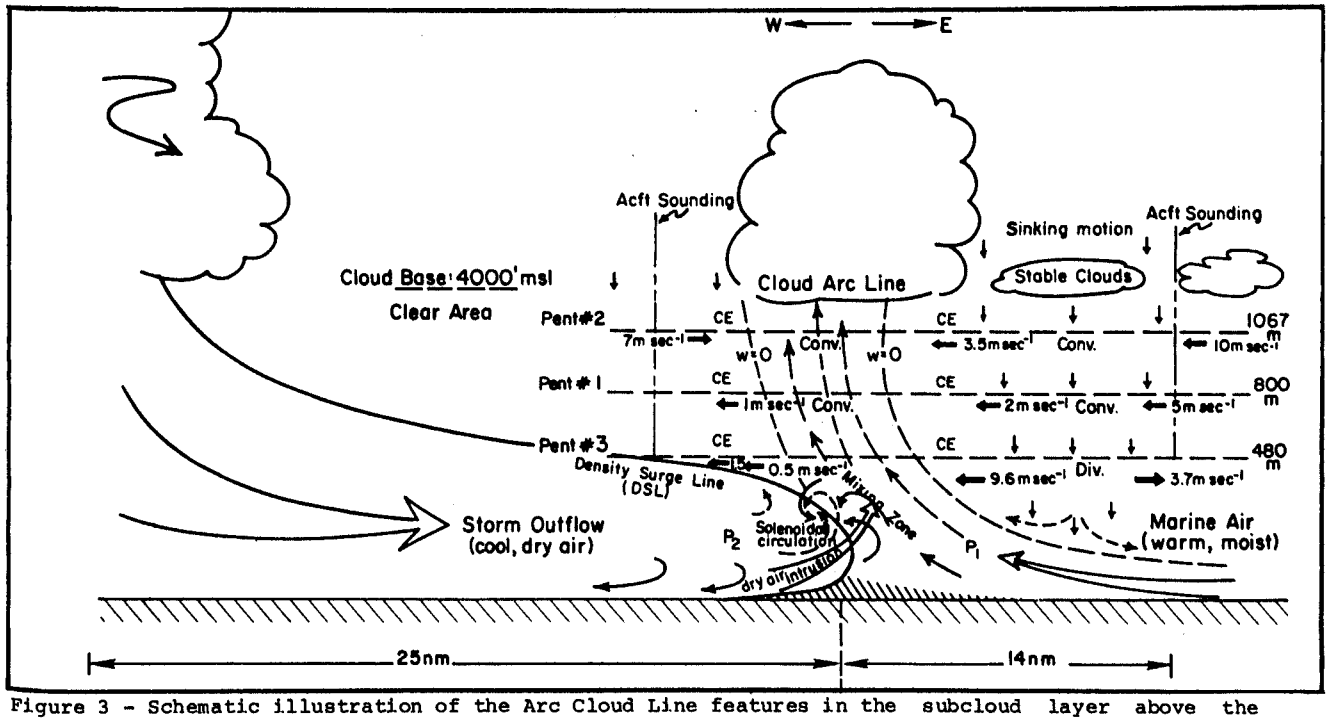

Figure 3 - Schematic illustration of the Arc Cloud Line features in the subcloud layer above the DSL, from Sinclair and Purdom (1983).

6. REFERENCES

Barnes, S.L. (Ed.), SESAME 1979 Data User's Guide. NOAA/ERL, U.S. Department of Commerce, Boulder, CO, 236 pp.

Green, R.N., and M. Kridenier, 1982: Interactive data processing for mesoscale forecasting applications. Preprints 13th Conf. on Severe Local Storms, Tulsa, Amer. Meteor. Soc., 190-193.

Klemp, J.B., and R. Rotunno, 1983: A study of the tornadic region within a supercell thunderstorm. J. Atmos. Sci., 40, 359-377.

Leverson, V.H., P.C Sinclair, J.H. Golden, 1977 Waterspout wind temperature and pressure structure deduced from aircraft measurements. Mon. Wea. Rev., 105, (6), June, 725-732.

Maddox, R.A., L.R. Hoxit. C.F. Chappell and F.Carcena, 1980: A study of tornadic thunderstorm interactions with thermal boundaries. Mon. Wea. Rev., 108, 322-336.

Parker, W.T., and R.D. Hickey, 1980: The Cheyenne tornado of 16 July 1979. Nat. Wea. Digest, 5, 45-62.

Purdom, J.F.W., 1976: Some uses of high-resolution GOES imagery in the mesoscale forecasting of convection and its behavior. Mon. Wea. Rev., 104, 1474-1483.

Purdom, J.F.W. 1979. The development and evolution of deep convection. Preprints 11th Conf. Severe Local Storms, Kansas City, Amer. Meteor. Soc., 143-150.

Purdom, J.F.W., 1984: Using satellite imagery to understand mesoscale weather development. Preprint Satellite Meteorology/Remote Sensing and Applications, Clearwater, Amer. Meteor. Soc.

Purdom, J.F.W., and K. Marcus, 1982: Thunderstorm trigger mechanisms over the southeast United States. Preprints 12th Conf. Severe Local Storms, San Antonio, Amer. Meteor. Soc., 467-470.

Sinclair, P.C., 1969: Vertical motion and temperature structure of severe convective storms, Preprints Sixth Conf. Thunderstorm Phenomena, Severe Local Storms, Chicago, AMS, Apr. 8-10, 346-350.

Sinclair, P.C., 1973: Severe storm air velocity and temperature structure deduced from penetrating aircraft. Preprints 8th Conf. on Severe Local Storms, Denver, Amer. Meteor. Soc., Oct. 15-17. 25-32.

Sinclair, P.C., 1974: Severe storm turbulent energy structure, Preprints Sixth Conf. Aerospace and Aeronautical Meteorology, El Paso. Amer. Meteor. Soc., Nov. 12-14, 13 pp.

Sinclair, P.C., and J.F.W. Purdom, 1982: Integration of research aircraft data and 3 minute interval GOES data to study the genesis and development of deep convective storms. Preprints 12th Conf. Severe Local Storms, San Antonio, Amer. Meteor. Soc., 269-271.

Sinclair, P.C., and J.F.W. Purdom, 1983: Shuttle recovery requirements and the development of arc cloud lines from thunderstorm outflows. Preprints 9th Conf. on Aerospace and Aeronautical Meteorology, Omaha, Amer. Meteor. Soc

AUTOMATED MESOSCALE WIND FIELDS DERIVED FROM GOES SATELLITE IMAGERY

Gregory S. Wilson

Atmospheric Sciences Division
Systems Dynamics Laboratory
NASA/Marshall Space Flight Center
Huntsville, Alabama

1. INTRODUCTION

Wind estimates in the earth's troposphere have been derived from cloud motions seen in satellite imagery dating back to the use of ATS picture sequences in the late 1960's. Global and synoptic use of cloud-drift winds quickly became an operational reality in the early 1970's even though many problems and limitations still remained. Hubert (1979) gives an excellent review of all aspects of the satellite cloud-drift wind problem describing the many research accomplishments and operational systems for synoptic-scale wind estimation as they evolved during the 1970's.

By the mid 1970's, the SMS/GOES spacecraft was providing unique 1 km resolution visible imagery of cloud fields over limited regions at time intervals of a few minutes during special research rapid-scan periods. The ability to manually extract unique and meaningful mesoscale wind fields from these data sets was demonstrated by several investigators (Negri and Vonder Haar, 1980, Maddox and Vonder Haar, 1979, Wilson and Houghton, 1979, Rodgers et al., 1979, Peslen, 1980, and others). However, these data sets are difficult and very time-consuming to produce so that mesoscale cloud winds are not currently available in real-time or for many research applications.

The purpose of this paper is to describe a new multispectral image-processing system for extracting mesoscale wind fields automatically from sequences of GOES imagery. This system is unique for many reasons including 1) no limitations on the computational power required for system execution was used as a constraint on system design, 2) a new pattern-recognition technique was used, 3) the system is multispectral in design so that both visible and infrared data are required and new VAS water vapor tracking and CO_2-slicing cloud height assignments will be an integral part of the final system, 4) wind vectors are generated at mesoscale resolution in space ($\sim$10 km spacing), 5) quality control is done objectively based upon image processing parameters requiring much less than 1% of the computed winds to be edited by objective or subjective meteorological procedures and 6) quasi-real-time (within 1 hour) mesoscale wind fields can be generated for research or operational evaluations over a 512 X 512 image using super minicomputers with array processors (< 1 minute of class 6 computer time is required for real-time purposes since the computer code is vectorized.)

This system was applied in this paper to SMS II five-minute imagery on April 24, 1975 in which several investigators have manually computed and extensively analyzed the extracted cloud wind estimates. Structural and kinematic analyses of the automated vs manual winds are performed to demonstrate that the automated wind estimates have an overall statistical error smaller than the manual winds and produce spatially and temporally consistent results down to the small meso-β scale in numerous pre-thunderstorm areas.

2. THE AUTOMATED MESOSCALE CLOUD-WIND SYSTEM

2.1 Preprocessing GOES Visible/Infrared Digital Imagery

After extracting image sector pairs (either 512 X 512 or 1024 X 1024 pixel matrices) at full resolution from the GOES full disc or limited-scan scenes, the following image-processing functions are required before wind estimates are begun:

1) Image clean-up to reduce random missing elements and lines using nearest-neighbor averaging.

2) Contrast-stretch to expand the image count-value range over the sectors to the full 0-255 dynamic pixel resolution.

3) Alignment of the visible/infrared scenes to account for element-shift offset.

4) Resample the infrared imagery to an equivalent resolution of the visible scene using an approximation of the ideal sin X/X interpolation function (Moik, 1980 and Bernstein, 1976)

5) Edge-preserving filtering of the visible data (Yoo et al., 1979) to de-stripe and remove random noise as well as to enhance cloud-edge boundaries.

2.2 Cloud subscene tracking and height assignment

Figure 1 shows the basic concept of cloud-subscene templates defined in the reference image that are compared with all equivalent subscene candidates in their respective search areas of the search image to define the (j*, k*) position of "best match." The displacement vector for a given cloud subscene motion is directed from the center of the search area to point (j*, k*). For mesoscale wind calculations, the optimal size of the template matrix (MXN) was found to vary from about 25 X 25 to 50 X 50 visible pixels depending

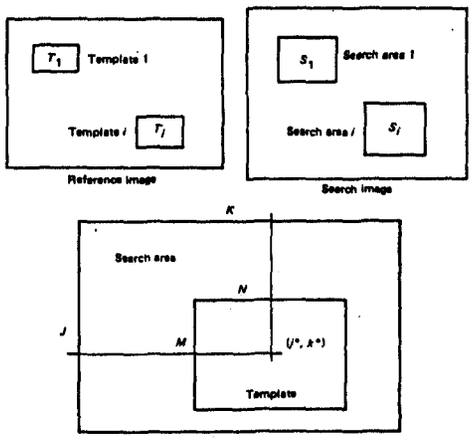

Fig. 1. Concept depiction of reference image, search image, subscene templates and search areas (from Moik, 1980)

upon the cloud subscene structure and resultant pattern matching success. In addition, candidate cloud templates were examined every tenth pixel location along the element direction and every tenth row was used so that a maximum mesoscale wind vector spacing of about 10 km results. Calculations of template displacement were performed at each candidate location for template pixel sizes of 25 X 25, 37 X 37, 49 X 49 only if both of the following criteria were met:

1) the visible variance over the template was $\geq$ 100, (i.e., reasonable image structure for tracking exists).

2) the infrared variance over the template was $\leq$ 100, (i.e., black-body scene temperature variations are usually < 10°C).

The black-body temperature of the cloud template was computed as the average of the infrared pixel temperatures except when that average was less than 5°C and the coldest pixel was used to compensate for cirrus emissivities much less than 1.0 in portions of the template.

The simplest form of height assignment for cloud winds involves positioning the wind estimate in the vertical at the location where the ambient air temperature equals the template temperature. However, this and other methods have various shortcomings as discussed in detail by Lee (1979), particularly when mesoscale wind estimates are made in strong vertical shear conditions (Peslen et al., 1984). Mengel et al., (1983) has shown that the use of additional GOES/VAS infrared imagery in the 15 micron region can be used to compute cloud heights with accuracies equal to or greater than that obtained by other complicated methods such as bi-spectral and stereo techniques. However, the current system uses only the infrared cloud temperature method since the original system design employed the use of VAS radiances as a natural improvement to this technique.

Since the template search area size in Fig. 1 (JXK) is a function of both wind speed and image-pair separation time, a "first guess" of the actual wind speed is made based upon a "guess" vertical wind profile and the height assignment just discussed interpolated into that vertical profile. A wind speed deviation $\pm$ the first guess actually leads to search areas that are elliptical in shape and are contained within the search area matrices.

The automatic determination of local similarity between cloud templates and all search locations in the search area has traditionally been done using either cross-correlation methods (Leese et al., 1971, Green et al., 1975, Novak and Young, 1977) or pattern recognition (Endlich et al., 1971, Wolf et al., Wolf and Endlich, 1980). However, Barnea and Silverman (1972) describe a different class of digital image registration known as the sequential similarity detection algorithm (SSDA). SSDA involves the simple calculation of a field of "template matching" numbers at every location in the search area, each of which is the sum of the absolute value difference between every pixel in the template minus the corresponding pixel in the search area for a given tested template displacement. This method is unique in that it is computationally fast, requires no normalization of the correlation surface, and, therefore, yields an exact "0" minimum value template match in the ideal nonnormalized registration case. Therefore, SSDA involves the search for a minimum "template matching" number and position over the search area where inter-pixel displacements are estimated by quadratic interpolation in two-dimensions. SSDA is applied here only to the visible imagery in determining mesoscale wind estimates.

2.3 Earth navigation and vector quality control

Earth navigation of the image pixels in both the reference and search images is performed with the same navigation package currently used by McIDAS (Suomi et al., 1983) and NOAA. Navigation errors of $\pm$1 pixel or more are frequently found in operational imagery but must be eliminated before unbiased wind estimates can be made. Furthermore, three objective image-processing quality control parameters were developed for use with the SSDA method with the goal of eliminating almost all subjective meteorological editing.

The first involves SSDA minima that fall on the borders of the search area. These vectors are eliminated. The second and third involve wind vector template match quality. Define

$$TMQ_1 = \frac{\text{SSDA mean}}{\text{SSDA minimum}} \quad \text{(over the entire search area)}$$

and the SSDA secondary minimum parameter as

$$SSM = \frac{TMQ_2}{TMQ_1} \cdot 100.$$

where $TMQ_2 = \frac{\text{SSDA mean}}{\text{SSDA secondary min.}}$ (over the search area minus the 3X3 array surrounding first minimum)

Successful quality control has consistently been achieved with

$$TMQ_1 \geq 1.6$$

and 88.>SSM> 0.,

so that much less than 1% of the wind estimates require meteorological editing.

3. STRUCTURAL AND KINEMATIC ANALYSIS OF AUTOMATED SATELLITE MESOSCALE WIND ESTIMATES

3.1 The 24 April 1975 (AVE IV) case study

During NASA's Atmospheric Variability Experiment IV (Hill and Turner, 1977) in which special 3-h rawinsonde data were taken at NWS sites and 5-min limited-scan VISSR data were recorded from SMS II, extensive low-level (∿850 mb) cumulus and upper-level cirrus cloud fields evolved over the Central Plains during the pre-thunderstorm period between 1200 and 2100 GMT on 24 April (see Figs. 2a and 2b) supported by a strong upper-level short-wave trough moving eastward across Texas, Oklahoma, and Kansas. Severe thunderstorms began developing within the cumulus cloud fields primarily in Central and Eastern Oklahoma after 2100 GMT that eventually evolved into two historically significant storms; the Neosho, MO tornadic storm and the Wewoka, OK hail storm (see Negri and Vonder Haar, 1980 for more details). Five-minute SMS-II imagery around 2105 and 2130 GMT have previously been used to estimate low-level pre-storm mesoscale moisture convergence and kinematic structure from manually extracted satellite winds computed on NASA's AOIPS computer (Maddox and Vonder Haar, 1979, and Negri and Vonder Haar, 1980). Automated cloud winds were also produced by the new system described herein to allow for both objective and subjective evaluations of the systems performance. Figures 3a and 3b show the surface analysis and 850/300 mb composite rawinsonde winds, respectively, for 2100 GMT 24 April for comparison with the satellite imagery in Figs. 2a and 2b onto which are superimposed a small percentage of the low-level (∿850 mb) and upper-level (∿300 mb) automated winds.

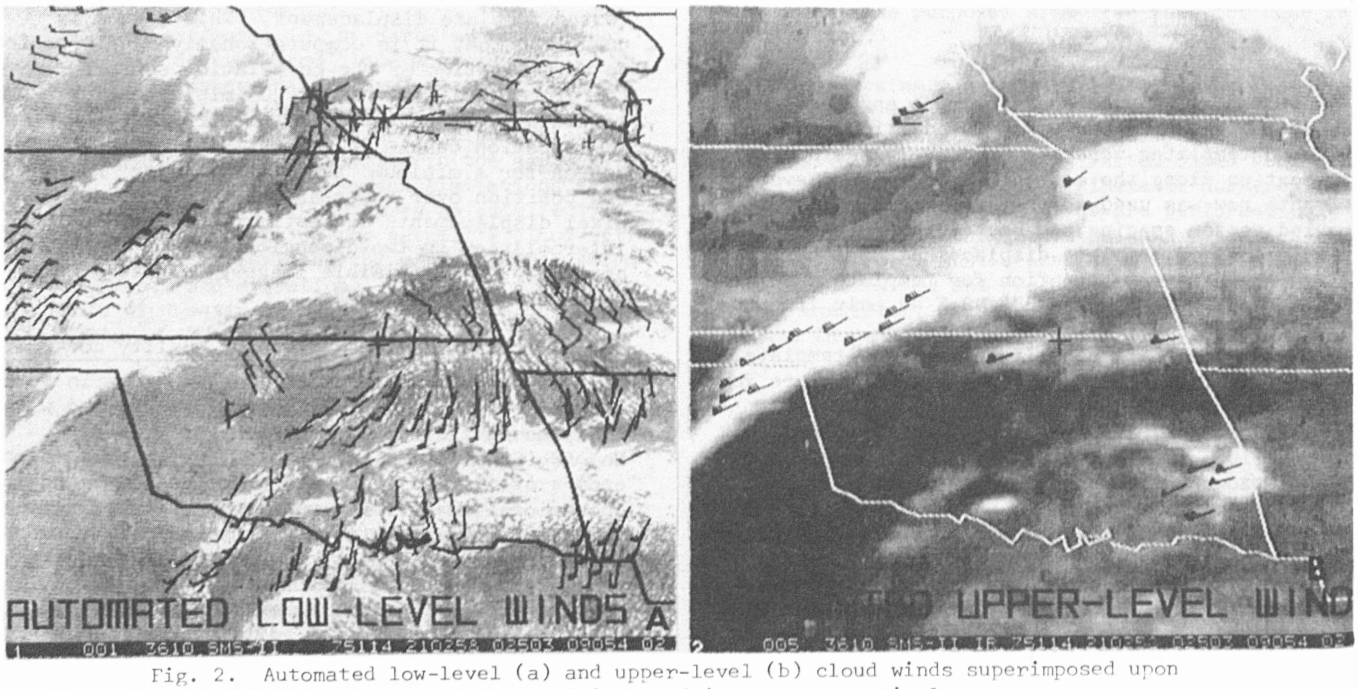

Fig. 2. Automated low-level (a) and upper-level (b) cloud winds superimposed upon the 2105 GMT SMS-II visible and infrared images, respectively.

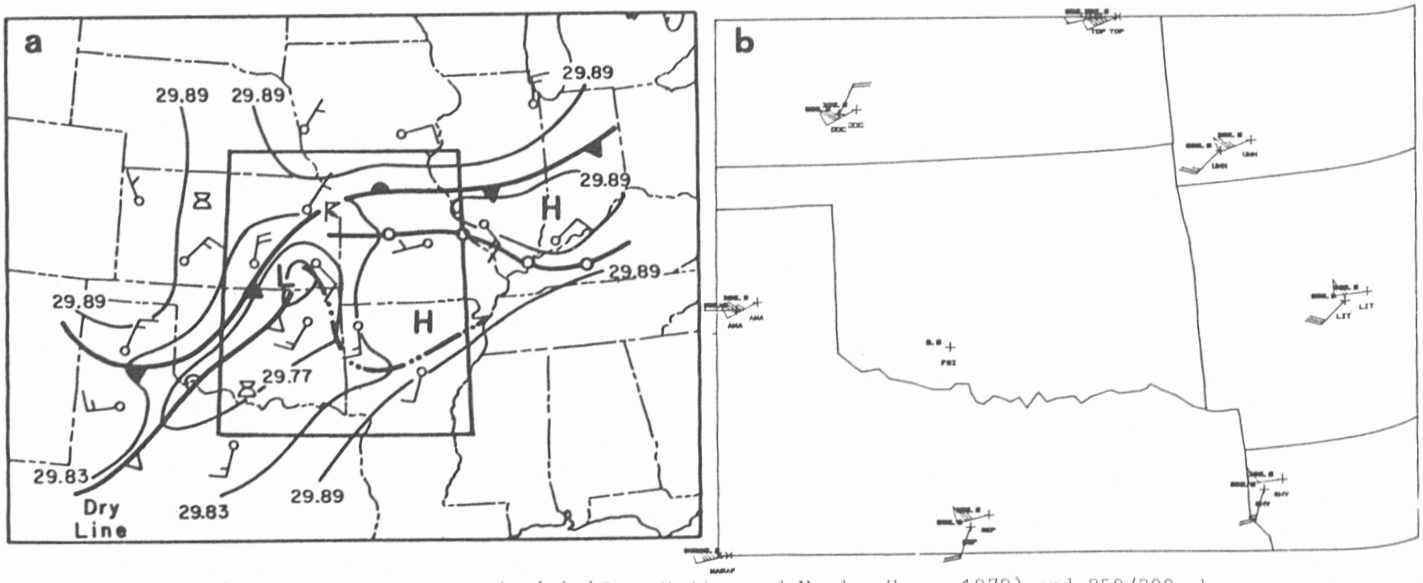

Fig. 3. Surface analysis (a) (from Maddox and Vonder Haar, 1979) and 850/300 mb composite rawinsonde winds (b) for 2100 GMT 24 April 1975.

3.2 Meso-α analysis

Figures 4 and 5 are shown to provide a qualitative comparison between all of the low-level automated cloud winds and the AOIPS manually derived winds plotted over a regional-scale area for both the 2105 (Figs 4a and 5a) and 2130 (Figs. 4b and 5b) GMT data sets. Both techniques provide similar flow structure but the automated vector fields contain nearly six times the number of vectors and somewhat better coverage in areas like northern Missouri.

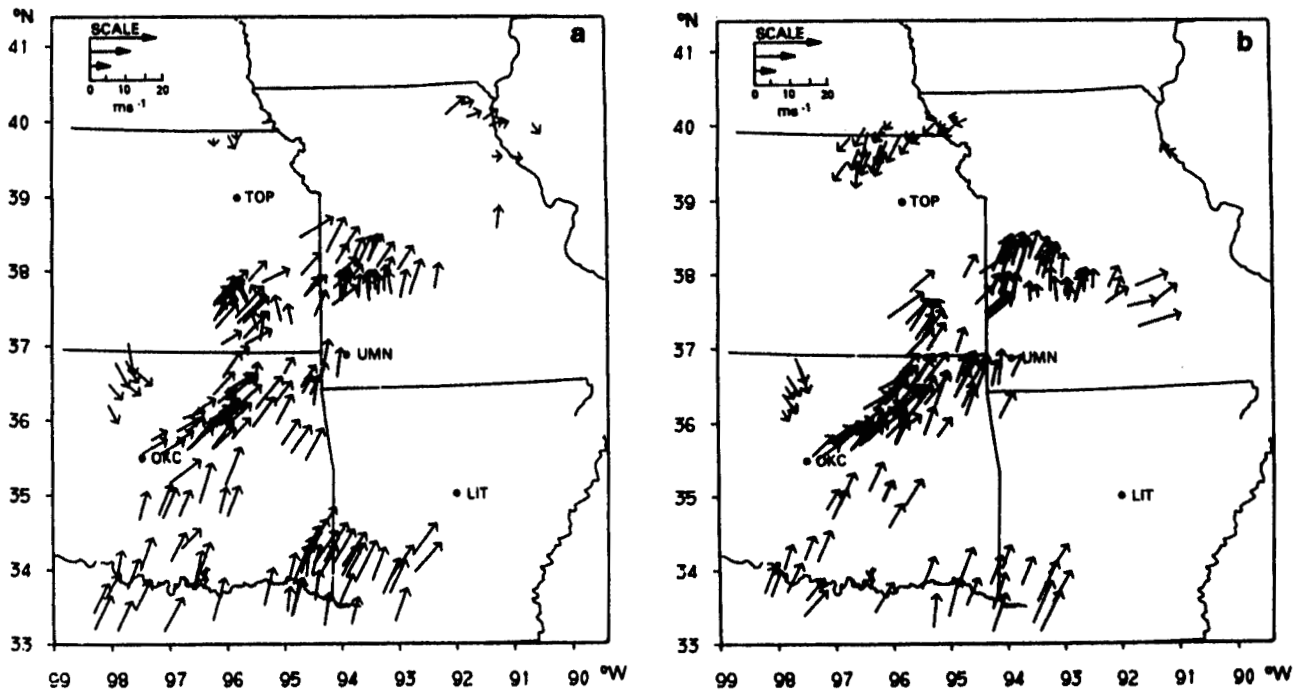

Fig. 4. Manually derived low-level cloud-drift winds (from Negri and Vonder Haar, 1980) for a) 2105 GMT and b) 2130 GMT 24 April 1975.

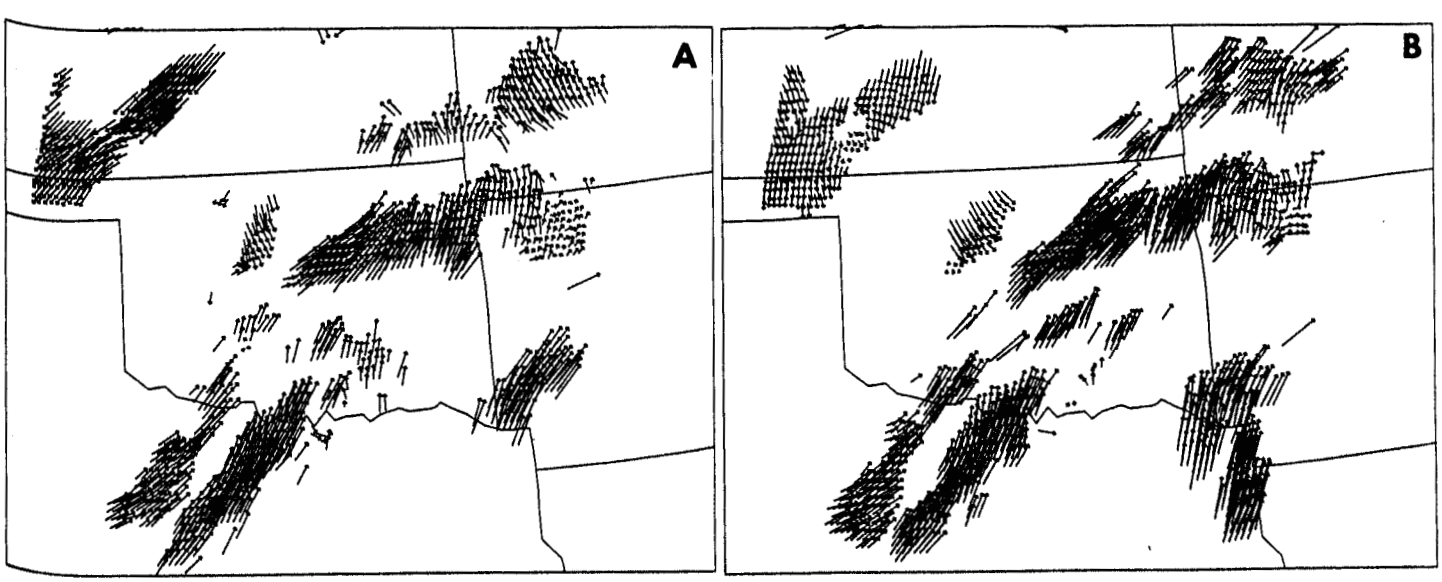

Fig. 5. Automated low-level cloud-drift winds for a) 2105 GMT and b) 2130 GMT 24 April 1975.

Following the approach of Maddox and Vonder Haar (1979) statistical structure functions were computed for the automated cloud winds in Fig. 4a as a quantitative means of comparing both spatial structure and random error estimates of manual vs automated winds. Plots of the wind-component structure functions for the two data sets over separation distances extending past 600 km are shown in Figure 6. The manual vs automated component flow structures are similar in shape but the automated plots are smoother, contain about 30% more spatial variance, and were calculated with many more data pairs.

If the smoother component structure function plots for the automated winds are examined near zero separation distance (values in the 0-20 km separation bin were actually used), a random error estimate of the cloud winds can be made since the structure function will approach twice the inherent variance of the measuring system (assuming isotrophy, homogeneity, and spatially uncorrelated errors). A surprisingly small random error of approximately .90 m/s was computed for the 2105 GMT data set, almost 50% smaller than the 1.75 m/s value computed by Maddox and Vonder Haar (1980) using a composite of nine manually-produced cloud-wind data sets used for research purposes.

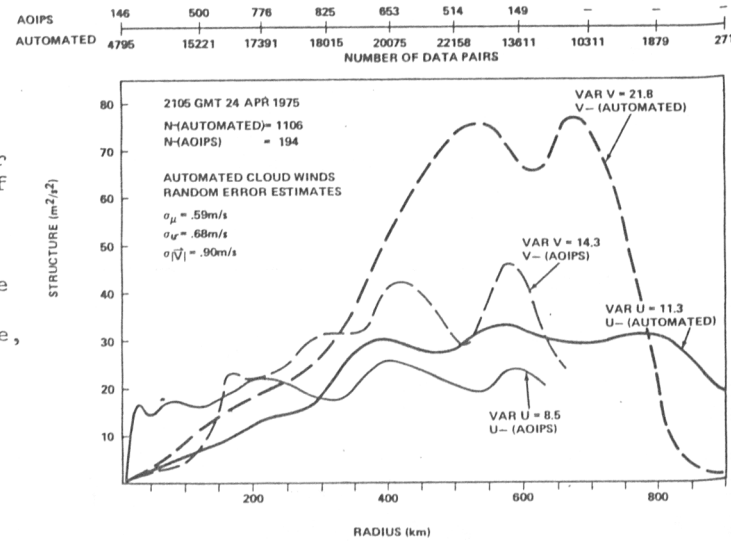

Fig. 6. Structure function plots of the u and v low-level cloud-wind components as a function of separation distance for the manually derived AOIPS winds (from Maddox and Vonder Haar, 1979) and the automated winds for the 2105 GMT data set. Random error estimates (σ) are also shown.

Automated low-level wind estimates over the region shown in Fig. 4 were objectively analyzed onto a 30 km grid using a Barnes objective analysis procedure. Figures 7 and 8 show plots of (a) raw automated winds and (b) the resultant low-level divergence, both superimposed in the visible satellite image for the 2105 and 2130 GMT data-sets, respectively. Of particular interest is the temporal consistency of the divergence patterns in relation to the cloud-field structure and subsequent thunderstorm development. The strong convergence patterns seen in southwest Oklahoma, northeastern Oklahoma, and Missouri each are associated with severe thunderstorm development during the next three hours as discussed in the next section.

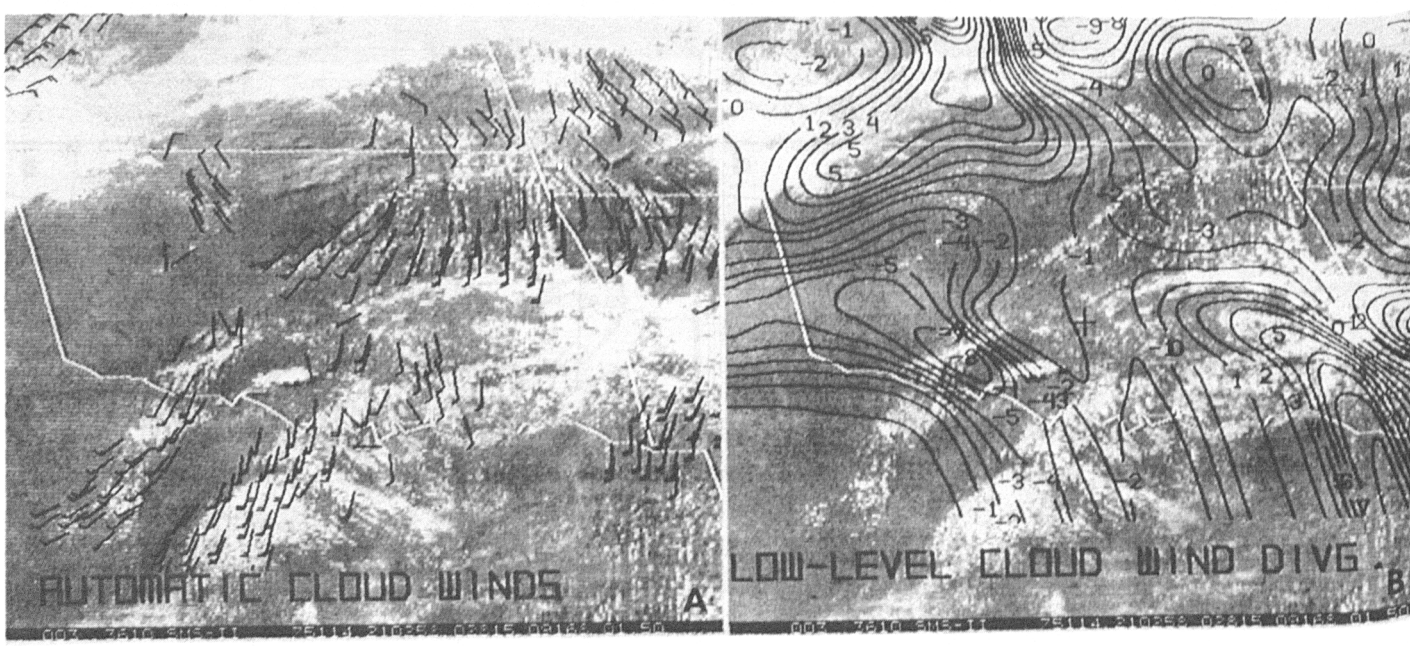

Fig. 7. Low-level automated cloud wind vectors (a) and cloud-wind divergence (b) (in units of 10^{-5} s^{-1}) superimposed in the visible satellite image for 2105 GMT 24 April 1975.

Fig. 8. Same as Fig. 7. except for 2130 GMT 24 April 1975.

3.3 Meso-β analysis

A meso-β size subset of the analysis area in Section 3.2 covering most of Oklahoma was chosen to provide a finer-scale look at relationships between mesoscale cloud wind fields and subsequent severe thunderstorm development. Automated low-level cloud winds were objectively analyzed this time onto a 20 km grid again using a Barnes technique. The resultant mesoscale divergence fields (a), gridded wind vectors (b), and raw wind-vector plots surrounding a growing thunderstorm in southwestern Oklahoma (c), are shown in Figures 9 a-c and 10 a-c for the 2105 and 2130 GMT data sets, respectively. As before, the temporal consistency of mesoscale divergence and vector wind fields is excellent over the 25-minute period, supported primarily by the high density of automated cloud wind vectors as shown surrounding the thunderstorm complex in Figs. 9c and 10c. Strong centers of meso-β wind convergence associated with 1) a meso-β scale wind-field perturbation in southwestern Oklahoma and 2) flow-field confluence in northeastern Oklahoma within cumulus cloud-field lines, relate well to the subsequent severe thunderstorm development in these regions discussed earlier and shown in the visible imagery of Figure 11. The 2145, 2240, 2330 GMT image sequence shown in Figs. 11a - 11c clearly illustrates the rather slow development of the Wewoka hail-producing thunderstorm complex in southwestern Oklahoma as well as the rapid growth of the Neosho tornadic thunderstorm in northeastern Oklahoma from within the cumulus clouds shown with an arrow in Fig. 11a.

4. CONCLUSIONS

A new automated technique for extracting mesoscale wind fields from GOES visible/infrared satellite imagery has been developed that can produce equivalent or superior cloud-wind estimates as compared to the time-consuming manual methods used on various interactive meteorological processing systems. Analysis of automated mesoscale cloud winds yield an estimated random error value < 1 m/s and produce both regional and mesoscale vector wind-field structure and divergence patterns that are consistent in time and highly correlated with subsequent severe thunderstorm development.

The final automated system will incorporate the use of VAS infrared water vapor and CO_2 imagery to yield wind estimates outside of cloudy regions and provide much improved cloud height assignments. Acquisition of a special limited-scan multispectral dwell-imaging data set from the GOES-E VAS is scheduled for Spring 1984 and will allow testing of the final system.

5. ACKNOWLEDGEMENTS

Special thanks go to Dr. Bob Atkinson and Dr. Bob Jayroe for suggesting and developing some of the image-processing concepts and computer codes used in this system. Dr. Fred Mosher, Dr. Don Wylie, Mr. Bill Shenk, and Mr. J. T. Young provided helpful suggestions and information regarding existing manual cloud-winds systems and image navigation.

6. REFERENCES

Barnea, D. I., and H. F. Silverman, 1972: A Class of algorithms for fast digital image registration. IEEE Transactions on Computers, C-21, 179-186.

Bernstein, R., 1976: Digital image processing of earth observation sensor data. IBM J. Res. Develop., 20, 40-57.

Endlich, R. M., D. E. Wolf, D. J. Hall, and A. E. Bran, 1971: Use of a pattern recognition technique for determining cloud motions from sequences of satellite photographs. J. Appl. Meteor., 10, 105-117.

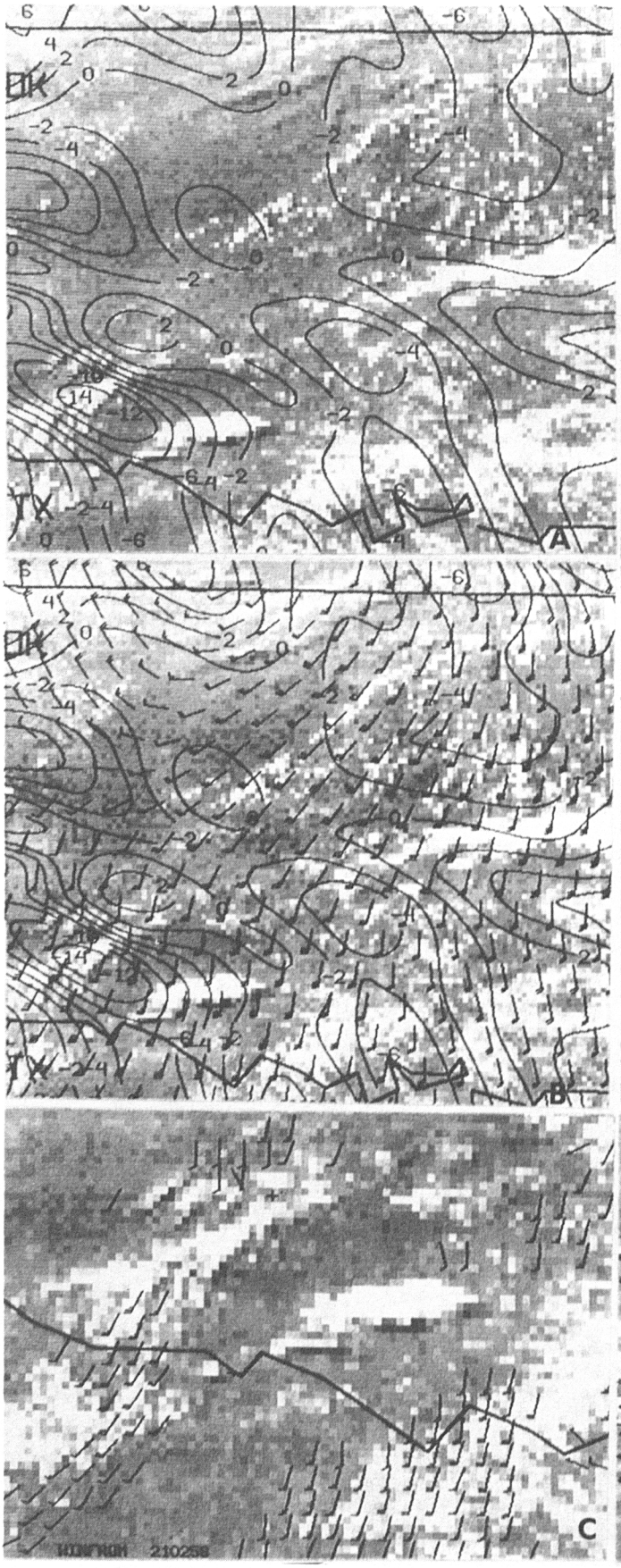

Fig. 9. Low-level automated cloud-wind divergence (a) (in units of 10^{-5} s^{-1}), gridded vector winds (in ms^{-1} times 4) (b), and raw cloud-wind vectors plotted around a growing thunderstorm (c) for 2105 GMT 24 April 1975.

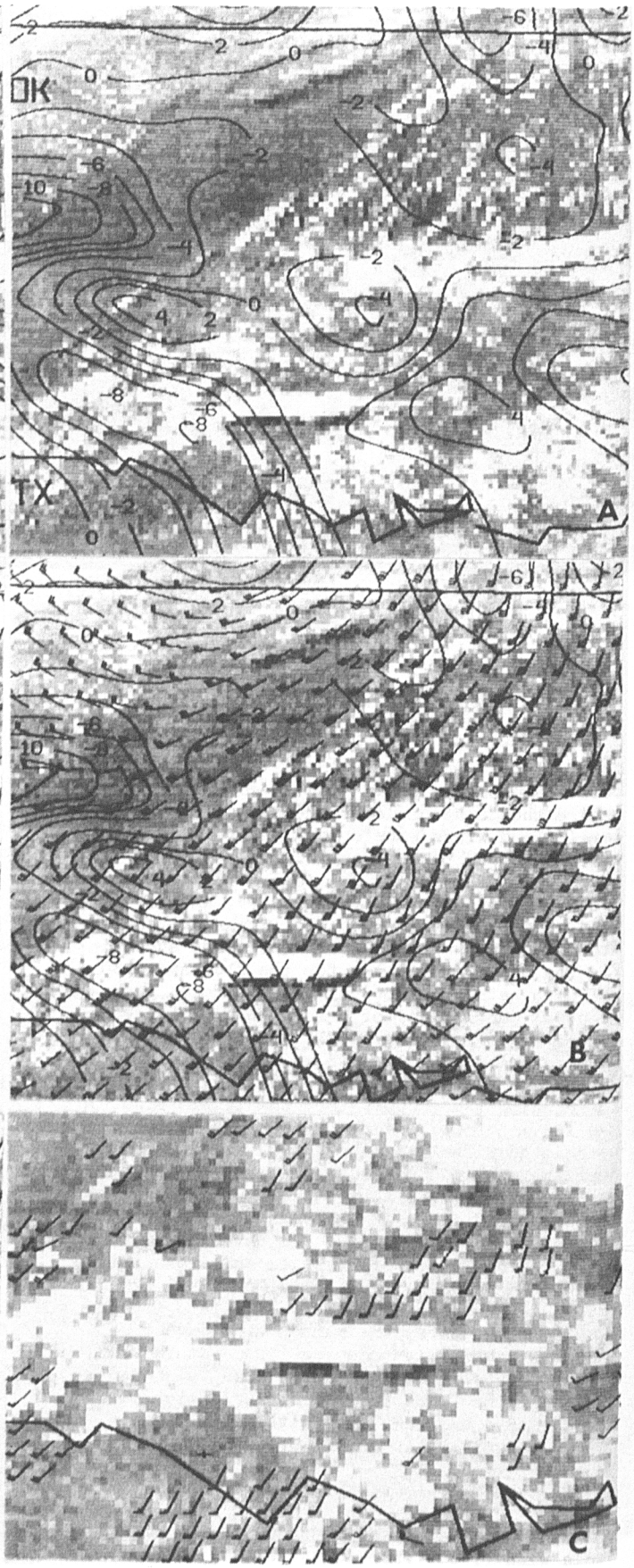

Fig. 10. Same as Fig. 9 except for 2130 GMT 24 April 1975.

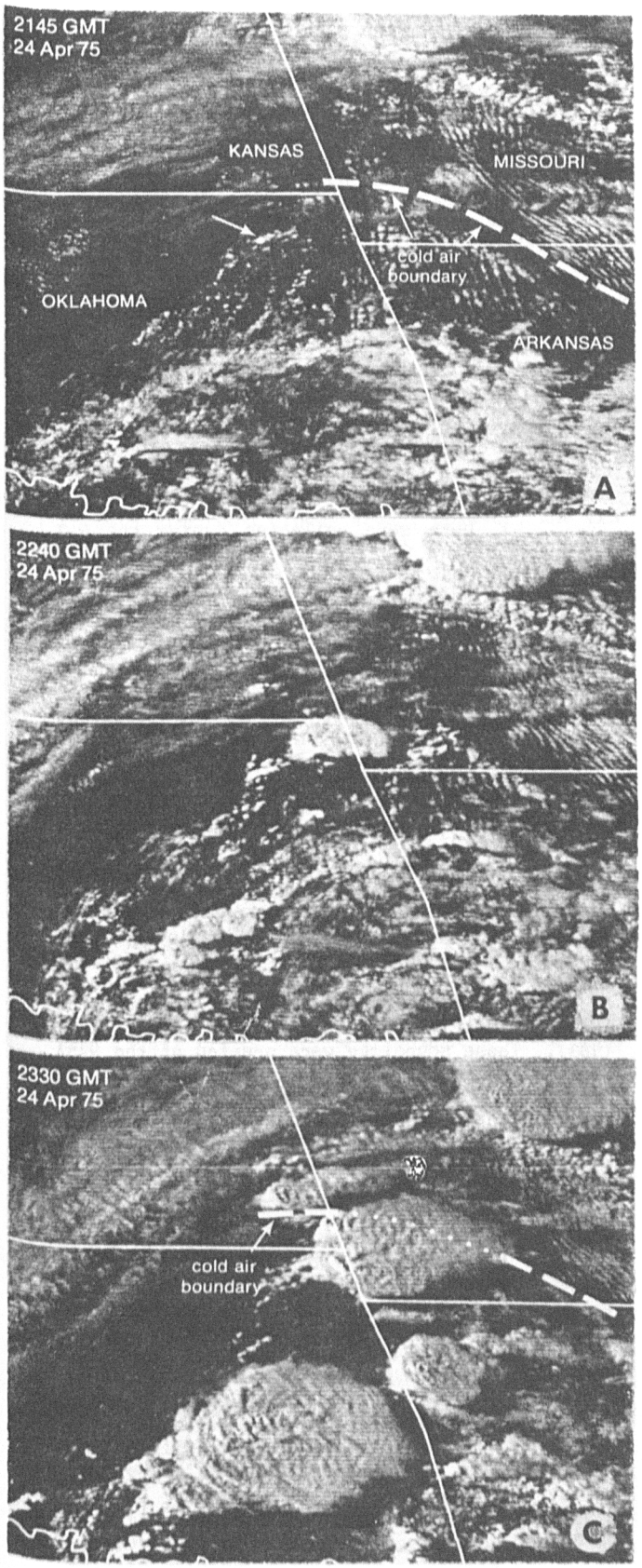

Fig. 11. SMS-II 1 km visible image for a) 2145, b) 2240, and c) 2330 GMT 24 April 1975.

Green, R., G. Hughes, C. Novak, and R. Schertz, 1975: The automatic extraction of wind estimates from VISSR data. Central Processing and Analysis of Geostationary Satellite Data, NOAA Technical Memorandum NESS-64, 94-110.

Hill, K., and R. E. Turner, 1977: NASA's Atmospheric Variability Experiments (AVE). Bull. Amer. Meteor. Soc., 58, 170-172.

Hubert, Lester, F., 1979: Wind derivation from geostationary satellites. In Quantitative Meteorological Data from Satellites, World Meteorological Organization Technical Note No. 66, edited by Jay S. Winston, 33-59.

Lee, David H., 1979: Level assignment in the assimilation of cloud motion vectors. Mon. Wea. Rev., 107, 1055-1074.

Leese, John A., Charles S. Novak, and Bruce B. Clark, 1971: An automated technique for obtaining cloud motion from geosynchronous satellite data using cross correlation, J. Appl. Meteor., 10, 118-132.

Maddox, R. A., and T. H. Vonder Haar, 1979: Covariance analysis of satellite derived mesoscale wind fields. J. Appl. Meteor., 18, 1327-1334.

Menzel, W. P., W. L. Smith, and T. R. Stewart, 1983: Improved cloud motion wind vector and altitude assignment using VAS. J. Appl. Meteor., 22, 377-384.

Moik, J. G., 1980: Digital processing of remotely sensed images. NASA Special Publication 431, Scientific and Technical Information Branch, Washington, D.C., 112-113.

Negri, A. J. and T. H. Vonder Haar, 1980: Moisture convergence using satellite-derived wind fields: a severe local storm case study. Mon. Wea. Rev., 108, 1170-1182.

Novak, C., and M. Young, 1977: The operational processing of wind estimates from cloud motions: Past, present and future. Proceedings of Eleventh International Symposium on Remote Sensing of the Environment, Ann Arbor, Michigan, 1589-1598.

Peslen, C. A., 1980: Short interval SMS wind vector determination for a severe local storms area. Mon. Wea. Rev., 108, 1407-1418.

Peslen, C. A., S. E. Koch and L. W. Uccellini, 1984: Effect of wind and moisture gradients on the arbitrary assignment of cloud motion to a vertical coordinate system in two Sesame cases. Preprints, Conf. on Satellite Meteorology/Remote Sensing and Applications, AMS, (this issue).

Rodgers, Edward R., Cecil Gentry, William Shenk, and Vincent Oliver, 1979: The benefits of using short-interval satellite images to derive winds for tropical cyclones. Mon. Wea. Rev. 107, 575-584.

Suomi, V. E., R. Fox, S. S. Limaye and W. L. Smith, 1983: McIDAS III: a modern interactive data access and analysis system. J. Appl. Meteor., 22, 766-778.

Wilson, T. A., and D. D. Houghton, 1979: Mesoscale Wind fields for a severe storm situation determined from SMS cloud observations, Mon. Wea. Rev., 1198-1209.

Wolf, D. E., and R. M. Endlich, 1980: Application of the SRI cloud tracking technique to rapid-scan GOES observations. Final Report, Contract NAS 5-25027, SRI International, Menlo Park, California, 26 pp.

Wolf, D. E., D. J. Hall, and R. M. Endlich, 1977: Experiments in automatic cloud tracking using SMS-GOES data. J. Appl. Meteor., 16, 1219-1230.

Yoo, J. K., J. J. Hogan, P. H. McIngvale, and W. W. Malcolm, 1979: Image preprocessing for ATHOC imaging sensors. Proceedings of the Workshop on Image Trackers and Autonomous Acquisition Applications for Missile Guidance. U. S. Army Missile Command, Redstone Arsenal, Alabama, 252-271.

STRUCTURE FUNCTION ANALYSES OF MESOSCALE VAS RETRIEVALS

Paul J. Meyer and Henry E. Fuelberg

Saint Louis University
St. Louis, MO 63103

1. INTRODUCTION

The recently launched series of GOES satellites is equipped with an advanced Visible-Infrared Spin-Scan Radiometer (VISSR). This new instrument, called the VISSR Atmospheric Sounder (VAS), has imaging capabilities in numerous spectral channels, thereby permitting atmospheric sounding from geostationary orbit for the first time. Major efforts are underway to utilize the new sounding data in various mesoscale analysis and forecasting techniques. Therefore, it is important to document its various strengths and weaknesses.

Structure functions quantify the nature of patterns seen in a field of data but about which the analyst has only qualitative feelings. The statistical tool has been used to investigate mesoscale rawinsonde data (Barnes and Lilly, 1975; Fuelberg and Meyer, 1984), satellite-derived, cloud tracked winds (Maddox and Vonder Haar, 1979), as well as radiances and retrieved soundings from the NOAA 4 satellite (Hillger and Vonder Haar, 1979).

Using structure function analyses, this paper will compare VAS retrievals obtained using a physical algorithm with those from a regression technique. Results from both procedures are evaluated against those from a special mesoscale network of radiosonde stations that was operated as part of the 1982 AVE-VAS Field Experiment.

2. METHODOLOGY

The use of structure functions in objective analysis procedures has been described by Gandin (1963). In the current study, calculations were performed in a manner similar to that of Hillger and Vonder Haar (1979) and Maddox and Vonder Haar (1979). The structure function of quantity f is defined as

$$STR(R) = \frac{1}{N} \Sigma\{f'(\vec{r}_1) - f'(\vec{r}_2)\}^2 ,$$

where $\vec{r}_1$ and $\vec{r}_2$ are observing sites, N is the number of data pairs whose separation $|\vec{r}_1 - \vec{r}_2|$ is within the interval R, and $f'(\vec{r}_i) = f(\vec{r}_i) - \bar{f}$ where $\bar{f}$ is the spatial mean of the particular data. A separation interval (R) of 100 km is used in this study; thus, categories are 0-100 km, 100-200 km, etc. The homogeneous and isotropic assumptions are made; therefore, the value for a particular station pair depends only on their scalar separation and not on their position or orientation in the field.

Data were collected during the 6-7 March day of the 1982 AVE/VAS Ground Truth Field Experiment. Rawinsonde data were obtained at 3 h intervals from 13 special sites and 24 regular stations operated by the National Weather Service (NWS). The special sites have an average spacing of 125 km whereas the NWS network has a separation of approximately 400 km. Since the goal of this study is to investigate mesoscale properties of the data, only the special sites and eleven nearby NWS stations were utilized (Fig. 1). Data from five times were included in our investigation, i.e., 1200, 1500, 1800, and 2100 6 March 1982 and 0000 GMT 7 March 1982.

Two retrieval procedures were used to prepare soundings from the VAS imagery. In the first, a physical inversion technique (Smith, 1983) was utilized. These data were prepared by the National Environmental Satellite Service Development Laboratory at the University of Wisconsin-Madison. The second set was made using a linear regression technique (Lee et al., 1983). These soundings were created at the NASA Goddard Space Flight Center. Both sets of VAS data were provided to us by the NASA Marshall Space Flight Center. In each case, the sounding

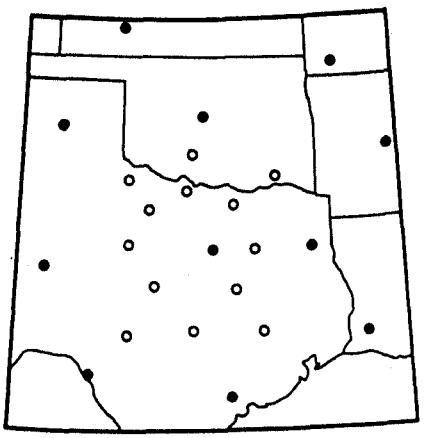

Fig. 1. The area of interest (box) together with National Weather Service (dark circles) and special site (open circles) rawinsonde stations.

spacing was between 75-100 km over the cloud free regions of the area. The five observation times, corresponding to the beginning of the satellite scan, were 1100, 1435, 1735, 2035, and 2335 GMT 6 March 1982.

Several data handling procedures were performed at NASA Marshall (Jedlovec, 1984). First, to account for non-simultaneous sonde releases and variable ascent rates, the rawinsonde data were adjusted to a common time of release by using a linear time interpolation scheme (Fuelberg and Jedlovec, 1982). The selected times correspond to when VAS was scanning the mesonetwork area, i.e., 1100, 1445, 1745, 2045, and 2345 GMT. A second task was to compute mixing ratios from the originally reported dew point temperatures. Finally, since geopotential heights were not provided as part of the regression soundings, these values were calculated using standard techniques. The final data set is identical to that created and employed by Jedlovec (1984).

Radiosonde soundings were available in both clear and cloudy areas; however, the VAS retrievals were made only in relatively clear areas. Therefore, to provide a better comparison between the two types of data, radiosonde soundings in cloudy areas were excluded. The selection procedure was subjective, although, in general, RAOBs farther than 150 km from the nearest VAS sounding were deleted. This task was relatively simple since a single, well defined line of clearing moved eastward through the area. Table 1 gives the number of VAS and rawinsonde soundings that were contained within the region of interest (Fig. 1) and utilized in the current investigation. At 1100 GMT 6 March, only thirteen RAOB sites could be used since the cloud line was along a north-south axis, approximately midway through the region. However, all but three of the NWS sites were in the clear region by 2345 GMT, the last observation time that was used.

It should be noted that the structure function is a random function. Thus, Gandin (1963) urged that many synoptic situations be included in statistical analyses. Since the current case is a single event, the stationarity assumption must be invoked in the calculation of all mean quantities. Similar assumptions were needed in previous single event studies (e.g., Maddox and Vonder Haar, 1979).

3. RESULTS

Structure functions were computed for the basic variables of temperature, geopotential height, and mixing ratio at five levels: 850, 700, 500, 300, and 200 mb. The composite 12 h period was evaluated, i.e., the combination of the five 3 h observation times. To account for the downwind drift of the radiosonde instruments, all computations utilized sonde positions at the individual levels instead of the surface station locations. In the diagrams that follow, results were plotted midway between separation intervals of 100 km. The maximum number of satellite pairings within the intervals was 2,444, and no plots were made for fewer than ten pairings. Sensitivity analyses (Fuelberg and Meyer, 1984) show that the current number of pairings is sufficient for the interpretations that follow.

Table 1. Number of soundings at each observation time.

Time (GMT)	RAOB	VAS-Physical	VAS-Regression
1100	13	36	37
1445	17	48	69
1745	18	57	67
2045	20	84	87
2345	21	99	113

Figure 2 contains structure functions of temperature at 700 and 300 mb. Hillger and Vonder Haar (1979) noted that the slope of the structure profile is a measure of mean non-directional gradients. That is, rapid changes in structure with increasing station separation are indicative of large horizontal gradients. Thus, in the current case, it is clear that both types of VAS retrievals underestimate magnitudes of mean non-directional gradients that are detected by the mesoscale radiosonde network. Similar findings were seen at all levels investigated. At 700 mb, for example, the difference in structure between the physical retrievals and the conventional soundings is 6.0 $^{o}C^{2}$ at 500 km. This corresponds to a systematic gradient difference of approximately 2.5 ^{o}C over 500 km. Since the VAS instrument and the retrieval algorithms produce volumetric averages, whereas the radiosonde is approximately a point source sensor, the weaker VAS-derived gradients are to be expected. Similar findings were made for the NOAA 4 satellite (Hillger and Vonder Haar, 1979) and for TIROS-N (Schlatter, 1981).

Figure 3 presents structure functions for geopotential height at the same two levels. At 700 mb, slopes from the three data sources are similar; thus, strengths of the mean non-directional gradients are comparable. The vertical displacement of the curve representing the regression retrieval is due to a greater component of random error and will be described later. At 300 mb, the two forms of VAS retrievals yield similarly shaped structure curves, but as observed with temperature (Fig. 2), both slopes are less than produced by the rawinsonde data. The structure difference between the VAS data and conventional soundings at 500 km separation is approximately 7,500 m^2 which corresponds to a mean gradient difference of approximately 87 m over 500 km.

Results for mixing ratio at 850 mb (Fig. 4) are somewhat different from those of the previous two parameters. The physical retrievals produce considerably stronger gradients than provided by the radiosonde data or the regression soundings. Horizontal analyses of mixing ratio (not shown) verify the stronger gradients as well as a greater amount of detail. Statistical parameters (Table 2) show that horizontal means of the three data sources are similar, approximately 2.0 g/kg; however, standard deviations for the physical retrievals are more than twice those obtained from the other two sources (0.8 versus 0.3 g/kg). Thus, it ap-

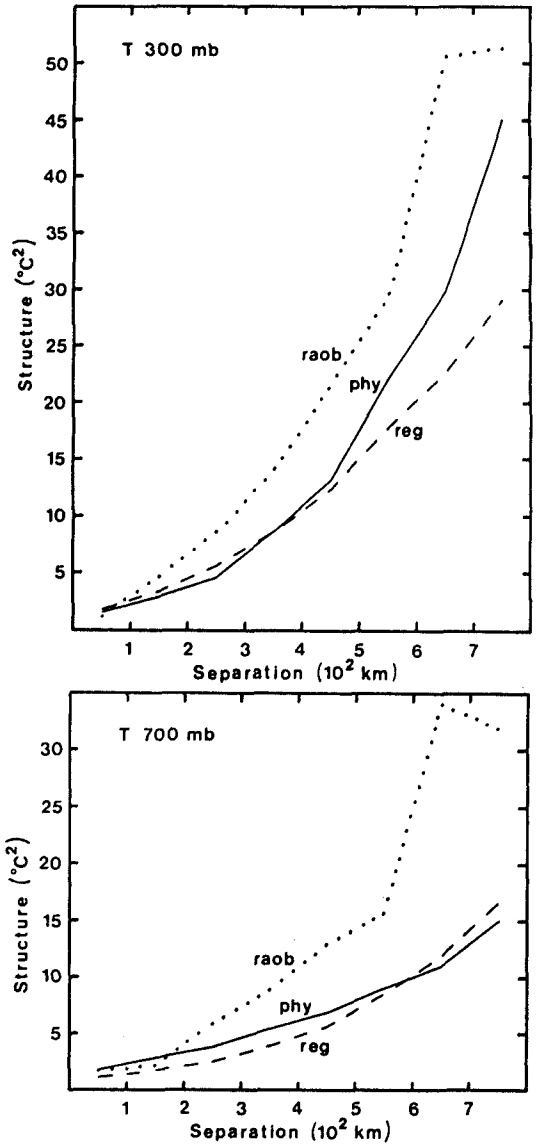

Fig. 2. Structure functions of temperature for the three data sources: regression (reg), physical (phy), rawinsonde (raob).

pears that at 850 mb, the physical retrievals provide humidity information that was not available from the radiosonde or regression soundings.

Results of the satellite-derived mixing ratio at 700 mb (Fig. 4) are less encouraging. Mean non-directional gradients from the physical retrievals are somewhat weaker than observed by the radiosondes; whereas, for the regression soundings, the gradients are much weaker. Table 2 shows that the physical retrievals produced a greater mean horizontal mixing ratio than the RAOBs (1.4 versus 1.0 g/kg) although standard deviations were slightly less (0.6 versus 0.8 g/kg). On the other hand, horizontal means of the regression data were similar to those from the sondes (0.9 and 1.0 g/kg) although there was much less horizontal variation in the spatial patterns (0.2 versus 0.8 g/kg). Thus, as noted by Jedlovec (1984), the regression-derived analysis merely seems to

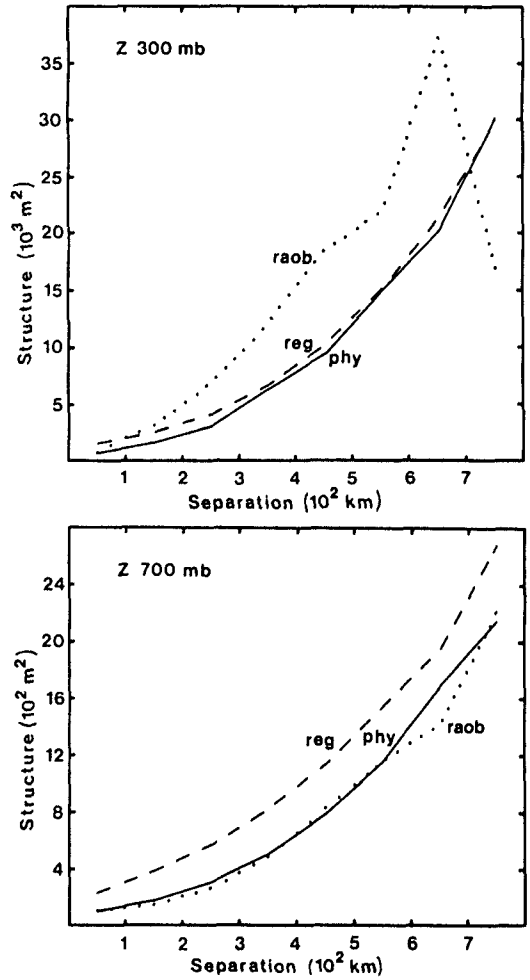

Fig. 3. Structure functions of geopotential height for the three data sources.

represent the mean of the rawinsonde-derived field.

To investigate the isotropic assumption, additional calculations categorized the structure results according to directions of separation vectors between station pairs. Intervals of 30° were used. Figure 5 shows that 300 mb heights are highly anisotropic during the period. Gradients are maximized along a northeast-southwest direction, approximately perpendicular to the area-averaged flow. Results from the three data sets are similar; thus, each portrays mean directional gradients in a similar manner. Although horizontal analyses reveal that orientations at specific locations and times exhibit more pronounced differences, it is nonetheless important that overall patterns are comparable. The anisotropy and degree of agreement in Fig. 5 are comparable to that seen at other levels and for temperatures (not shown). Results for mixing ratio (not shown) indicate somewhat greater disagreement.

An important attribute of structure functions is their measure of random error within a data set (Hillger and Vonder Haar, 1979). Structure-derived values do not include bias or systematic errors, and a major advantage of the procedure is that results are not based on comparisons with other types of data. Thus, satellite data are not directly evaluated

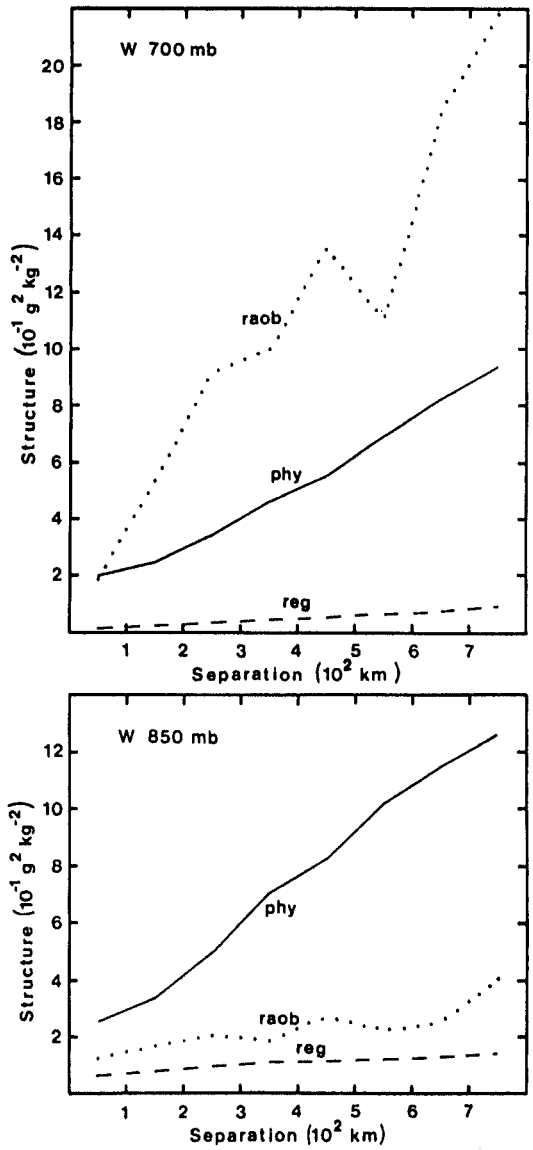

Fig. 4. Structure functions of mixing ratio for the three data sources.

against their rawinsonde-derived counterparts, and this avoids the problems associated with rawinsonde data errors and with soundings not being co-located in time and/or space. The procedure is to estimate the random errors by extrapolating structure curves to zero separation distance, i.e.,

$$STR(0) = 2\sigma^2$$

Based on Fuelberg and Meyer (1984), the least-squares technique is used to fit the function

$$STR(X) = B \exp(aX)$$

to structure values of the first six separation categories. In the above equation, "X" is separation distance, "a" is the coefficient of curvature and "B" is the intercept value at X = 0.

Random error (σ) estimates for temperature are given in Table 3. Results show a vertically averaged random error of 0.75 °C for the physical retrievals and 0.95 °C for the regression soundings. Using similar techniques, Hillger and Vonder Haar (1979) obtained 0.5 °C

Table 2. Means and standard deviations (parentheses) of mixing ratio (g/kg) from the three data sources.

Level (mb)	Physical	Regression	RAOB
700	1.4 (0.6)	0.9 (0.2)	1.0 (0.8)
850	2.2 (0.8)	1.8 (0.3)	2.1 (0.3)

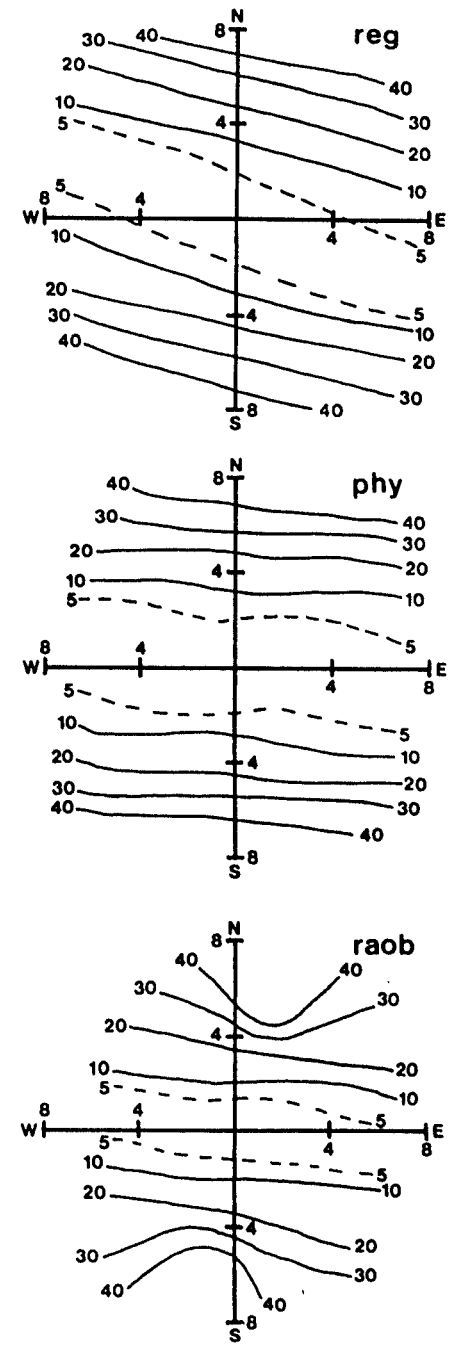

Fig. 5. Anisotropic structure functions for geopotential height at 300 mb. Structure units are 10^3 m^2 while separations are 10^2 km.

Table 3. RMS errors for temperature (°C). Standard deviations of the RAOBs are given in parentheses.

Level (mb)	Physical	Regression	RAOB
200	0.5	0.9	0.7 (2.0)
300	0.8	0.9	0.8 (3.0)
500	0.7	1.0	1.4 (3.7)
700	0.9	0.7	0.8 (2.5)
850	0.9	1.2	0.7 (2.6)

for soundings from NOAA 4. These values compare to 0.88 °C for the radiosonde data. An important point is that all of the error values are much smaller than standard deviations of the rawinsonde-derived patterns which are similar to those of the VAS retrievals (not shown). Thus, the signal to noise ratios of the VAS temperature data are favorable. Based on paired, simultaneous radiosonde ascents, Hoehne (1980) obtained an uncertainty of 0.6 °C whereas Lenhard (1970) noted the value 0.35 °C. Thus, it appears that VAS's temperature uncertainty is somewhat greater than that of radiosondes; however, the differences do not appear excessive. Results from additional periods may slightly modify the findings of this single case, but the effects would be expected to be slight since the structure curves already appear quite smooth and "well behaved".

Random errors in geopotential height (Table 4) show the expected increase with altitude that is attributable to integration of virtual temperature over progressively deeper layers. Errors from the regression procedure are somewhat greater than those of the physical retrievals. Although the results are certainly not conclusive, it appears that the VAS soundings contain comparable height uncertainties to those of rawinsondes. As observed with the temperature data, uncertainties in geopotential height are much smaller than the observed variability that is described by the standard deviations.

Finally, error estimates for mixing ratio are given in Table 5. The two VAS retrieval sets exhibit similar random errors to those of the radiosondes. Even though the regression algorithm produces the smallest uncertainties, one should recall that it also yielded very weak horizontal gradients (Fig. 4, Table 2). Therefore, as noted earlier, its information content is less than that of the other data sources.

4. CONCLUSIONS

VAS soundings during the 6-7 March 1982 period produced mean non-directional gradients that were weaker than those of the special mesoscale rawinsonde network. This is expected since the VAS provides a volumetric sample of the atmosphere. Depending on the level and parameter, random errors within the VAS retrievals are comparable or only slightly greater than those from the radiosondes. These estimates do not include systematic errors, and uncertainties in the rawinsonde data do not influence the satellite statistics. Thus, current values are smaller than would be expected from a direct comparison of satellite and rawinsonde data -- the more widely used procedure.

Table 4. RMS errors for geopotential height (m). Standard deviations of the RAOBs are given in parentheses.

Level (mb)	Phys.	Reg.	RAOB	Hoehne (1980)	Lenhard (1970)
200	20.0	25.4	19.0 (81)	30	44
300	18.4	26.2	21.6 (83)	27	31
500	12.3	15.0	13.1 (38)	19	26
700	6.6	10.4	6.3 (19)	11	8
850	3.1	8.4	6.1 (16)	6	-

Table 5. RMS errors for mixing ratio (g/kg). Standard deviations of the RAOBs are given in parentheses.

Level (mb)	Physical	Regression	RAOB
700	0.3	0.2	0.4 (0.8)
850	0.3	0.1	0.3 (0.3)

An important consideration in the use of any type of data is the signal to noise ratio. With radiosondes, for example, uncertainty that can easily be tolerated at the synoptic scale, may render the data useless for some mesoscale applications. The same concept applies to VAS data. The current tentative results suggest that VAS retrievals will provide valuable data at the synoptic and meso α-scales. However, its utility as a meso β-scale data source is more uncertain at this time because the atmospheric signal may approach the noise level within the soundings.

Additional verification studies will specify the characteristics of VAS retrievals in greater detail. We are currently using structure function analyses to investigate VAS- and rawinsonde-derived fields of thickness and precipitable water. A better understanding of VAS data hopefully will lead to improved data handling techniques that will enable us to take maximum advantage of VAS's strengths as well as to correct or cope with its limitations.

ACKNOWLEDGEMENTS

This research was sponsored by the National Aeronautics and Space Administration under Training Grant NGT 26-006-800. Additional support was provided by NASA under Contracts NAS8-33370 and NAS8-35330 which are under the auspices of the Atmospheric Sciences Division, Systems Dynamics Laboratory, Marshall Space Flight Center, AL. We sincerely appreciate the efforts of Gary Jedlovec of NASA/Marshall in providing the data for this study. Paul Meyer thanks the personnel of the Atmospheric Sciences Division for their assistance during his summer

residency at NASA/Marshall where much of this research was performed.

REFERENCES

Barnes, S. L., and D. K. Lilly, 1975: Covariance analysis of severe storm environments, Preprints Ninth Conf. Severe Local Storms, Norman, Amer. Meteor. Soc., 301-306.

Fuelberg, H. E., and G. J. Jedlovec, 1982: A subsynoptic-scale kinetic energy analysis of the Red River Valley tornado outbreak (AVE-SESAME I). Mon. Wea. Rev., 110, 2005-2024.

_____, and P. J. Meyer, 1984: An analysis of the AVE-SESAME I period using statistical structure and correlation functions. Mon. Wea. Rev., Conditionally accepted for publication.

Gandin, L. S., 1963: Objective analysis of meteorological fields. Translated from Russian, Israel Program for Scientific Translations, Jerusalem, 242 pp. [NTIS TT-65-50007].

Hillger, D. W., and T. H. Vonder Haar, 1979: An analysis of satellite infrared soundings at the mesoscale using statistical structure and correlation functions. J. Atmos. Sci., 36, 287-305.

Hoehne, W. E., 1980: Precision of National Weather Service upper air measurements, NOAA Tech. Memo. NWS T&ED-16, Sterling, Va, 23 pp. [NTIS 81N17683].

Jedlovec, G. J., 1984: MSFC special network statistical evaluation. VAS Demonstration Final Report, NASA Ref. Pub., in press, NASA Goddard Space Flight Center, Greenbelt, Md.

Lee, T. -H., D. Chesters, and A. Mostek, 1983: The impact of conventional surface data upon VAS regression retrievals in the lower troposphere. J. Climate Appl. Meteor., 22, 1853-1874.

Lenhard, R. W., 1970: Accuracy of radiosonde temperature and pressure-height determination. Bull. Amer. Meteor. Soc., 51, 842-846.

Maddox, R. A., and T. H. Vonder Haar, 1979: Covariance analysis of satellite-derived mesoscale wind fields. J. Appl. Meteor., 18, 1327-1334.

Schlatter, T. W., 1981: An assessment of operational TIROS-N temperature retrievals over the United States. Mon. Wea. Rev., 109, 110-119.

Smith, W. L., 1983: The retrieval of atmospheric profiles from VAS geostationary radiance observations. J. Atmos. Sci., 40, 2025-2035.

F.3 APPLICATIONS OF AUTOMATIC CLOUD DETECTORS TO INTERACTIVE METEOROLOGICAL OPERATIONS

John F. Moses

Satellite Applications Laboratory
National Environmental Satellite, Data and Information Service
Washington, D.C. 20233

1. INTRODUCTION

Meteorologist have observed many obvious and sometimes subtle events or features in the structure, organization and evolution of clouds through the use of sequences of enhanced IR and visible GOES imagery. Experience shows that some of these features are manifestations of a physical or dynamic process which has occurred, is occurring or will occur in the near future. Features such as very cold expanding convective cloud tops are so well known and occur so frequently that meteorologists have developed specific discriptions of behavior and evolution which relate to heavy rainfall and severe convective storms.

In heavy rainfall and severe weather situations meteorologist must quickly recognize only the important mesoscale features in obscure cloud patterns covering large geographic regions. The value of a particular feature must be based on success and false alarm radios determined through analysis of past events. Many hours of image interpretation and classification by a skilled meteorologist are required before enough cases can be compiled to provide a fair correlation with historical ground observed events. The most desirable alternative to this time consuming effort requires an automatic procedure which detects the features as effectively as the meteorologist.

The next best alternative is to employ a stochastic modeling approach and examine cloud features which can be automatically detected. The most noted feature is the short lived appearance of small areas of cloud minimum temperature. This paper describes a simple method for examining the features and structure of the top of clouds observed in GOES digital imagery. The heavy precipitation event in Mississippi and Louisiana on April 6, 1983, was selected to illustrate some initial applications of the cloud top detector.

2. A CLOUD DOME DETECTOR

Experience with the interpretation of convective rain clouds observed in GOES infrared and visible imagery provided the impetus for development of an automatic procedure specifically designed to detect the location of the coldest cloud tops in GOES imagery. Attention was given to producing a list of minimum values, their contours, and location of their centroids from a large array of GOES temperatures. The temperature contours identified as unique isolated minimums are treated as individual cloud domes which rize above the general cloud top. All clouds observed in a GOES image can be uniquely referenced in this manner.

One degree cloud temperature contours below the coldest cloud dome contours are also automatically traced and their edge locations retained with the detected cloud dome contours. For practical purposes, the cloud contours with areas larger than 22,000 sq. Km (an arbitary maximum of 350 GOES 8 Km pixels) are discarded. The cloud contours associated with the fifty coldest cloud domes are saved for further analysis. Identification numbers are assigned to each cloud dome and they are ranked according to temperature.

The shapes of the closed temperature contours are quantified by examining the first and second derivative at each point along the contour. In this process, the edge pixel locations are first transformed into polar coordinates with the origin at the centroid of the dome. The maximum and minimum distances found along the closed contour are the lowest and highest gradients associated with the cloud dome. For convenience, these are referred to as moments and nodes of the contour. Moments and nodes of a particular dome and contour are uniquely defined by their distance and direction (heading) from the dome's centroid. They provide the essential information about the cloud top shape. Table #1 summarizes the detector parameters.

TABLE 1

GOES IR CLOUD DETECTOR PARAMETERS

- o Dome Identification Number (1-50)
- o Contour Temperature (°K)
- o Contour Area (GOES 8 km pixels)
- o Contour Centroid Position (latitude, longitude)
- o Nodes (minimums) Heading and Distances (degrees, GOES 8 km pixels)
- o Moments (maximum) Heading and Distances (degrees, GOES 8 km pixels)

3. LIFE HISTORY OF CLOUD TOPS

Animation of the GOES 30 minute interval images has given meteorologists the opportunity to observe the propagation of cloud anvils and embedded convective cloud tops. Individual convective domes appear to rise and fall rapidly in the imagery, and often they appear only once in a particular area of a half-hour image. The anvil moves as new clouds grow along the upwind side or leading edge and old clouds dissipate along the downwind side or trailing edge.

The importance of measuring anvil growth and separating new cloud top growth from old dissipating cloud tops is recognized through observations of intense convective storms in the GOES half-hour imagery (Scofield/Oliver, 1977), and GOES rapid scan imagery (Adler and Fenn, 1979) Comparison with radar observations (Griffith et al., 1978) and high density raingauge networks (Moses, 1980) show that the most intense rainfall is found in the early part of the convective storm life cycle. Comparisons with severe storm sightings indicate that growth is a key feature of the Enhanced V severe storm signature (McCann, 1983).

Griffith first employed a radar echo tracking technique for measuring cloud growth automatically. Similarly, the technique used here was developed by Oslund (1974). In principle, if a cloud centroid position cannot be found within a characteristic search area in the previous GOES image then the cloud area in the current image is considered to have grown completely within the picture interval (normally one half-hour). The search radius is defined from the size and centroid of the detected cloud contour. A minimum search radius has been defined at 18 km for the standard GOES resolution and 30 minute picture interval. The minimum search radius can be adjusted up or down depending on the actual picture interval, resolution or speed of the particular meteorological system.

The tracking technique provides a method for detecting cloud contour areas which have merged into one or split into two or more entities. In the present application an independent search is made for each temperature contour below the current cloud dome. In addition, for each cloud dome, a search is made through all the previous cloud dome locations regardless of their temperature. Results from cloud contour tracking provide vectors which belong to one of three groups: (1) Vectors which are a composite of the ambient wind and storm propagation, (2) Vectors which represent thunderstorm propagation and (3) Vectors which represent thunderstorm direction of motion. (Moses 1981)

4. SATELLITE MEASUREMENTS OF CLOUD DOMES

The cloud dome detector has been tested using GOES infrared digital imagery of the heavy precipitation event in Mississippi and Louisianna on April 6, 1983. An enhanced IR image of the target area at 2000 GMT (Figure 1) contains several convective cloud tops embedded in a large cloud anvil spreading northeast over the Gulf States. Torrential rains began in the early afternoon across southern Mississippi in the area between A and B. The heaviest reported rains were in the vicinity and northwest of Purvis, Mississippi, (PVS). For the half-hour period ending at 2100 GMT, 1.6 inches was reported at Purvis. One inch or more per half-hour continued to fall for the next 2 hours.

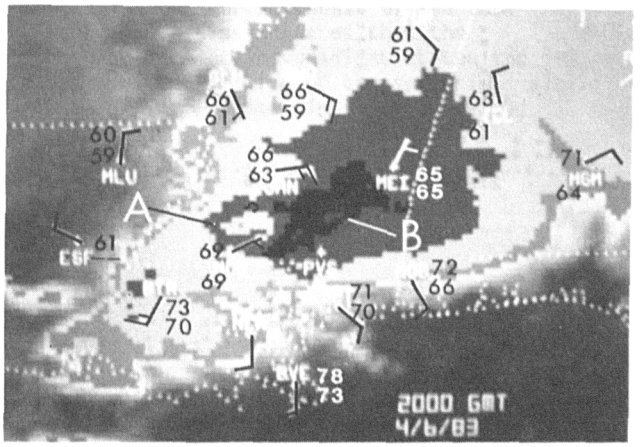

Figure 1. *The GOES enhanced infrared image of the southern part of the target area at 2000 GMT (2 p.m. CDT) April 6, 1983. Surface reports at 2000 GMT are shown with the temperature (°F) plotted above the dew point (°F). Surface winds indicate strong convergence into the southern edge of the anvil.*

The number of cloud domes detected in the sequence of images taken during the morning, afternoon and evening of April 6th is given in figure 2. A graphical represen-

```
   205         215         225         235         243         248
    +....+....+....+....+....+....+....+....+....+....+....+....+.
1500        2 31 22 64    6424 5   11 232
1530      3 2  4 41 1  2  6764 223  2 1
1600      1 1 22 23 25 11 3524 321    1121122
1630
1700
1730
1800     12 1  2 13 1  44 1442 43  2  2 221 2 1
1830
1900  1       25 3  B6 2  4343 6                        A=10
1930                                                    B=11
2000  2 11    14 36 35 36 2331 231     -                C=12
2030  1 12 1  31 73 33 29 4331 2 1
2100    32 2 1A 51 12 55 B2          <-
2130  1 1     46 11 26 63 1512 342 1
2200  2 1  1   1  1 63 51 4214 13      1212112 2 2
2230
2300
2330     6  1 11 13 23 11 3423 432311 1  3
   0  1  4 2 4    2 14 2  2312 32526    211
  30     11 1 44 32 22 32 1 11 211548 1
 100      1 1 55 41 23 31 523     3235 1
 130  1       1  42 22 14 2221 31 312 542221
 200      1 1  4  5 23 7  3341 12 131 215
 230      2 4 1    1 42 33 2324 3323 2 1 32
    +....+....+....+....+....+....+....+....+....+....+....+....+.
   205         215         225         235         243         248
```

Figure 2. *The frequency of cloud domes occurring on April 6, 1983. Each value represents the number of domes detected at the time (GMT) given on the ordinate and temperature (°K) given on the abscissa.*

tation of the distribution of cloud dome temperatures is shown in figure 3. Each asterisk represents a cloud dome detected at the temperature given on the abscissa. The distribution begins with the coldest dome detected and ends at the limit of 50 domes. The limit is reached at one of the warmest cloud domes indicated for each image. More cloud domes were detected 225°K (-47°C) or colder at 2100 GMT than for any other image time during the period.

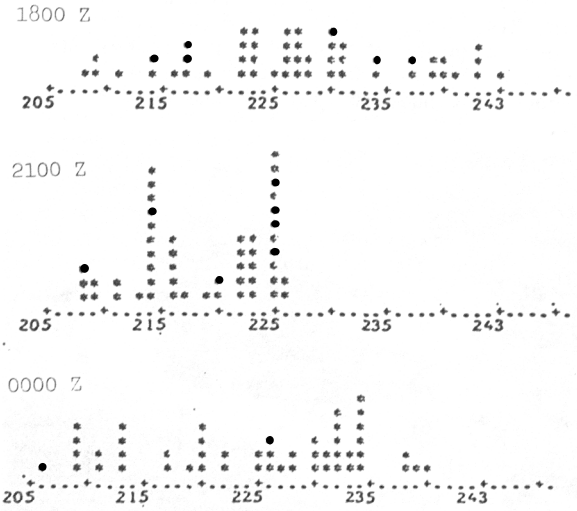

Figure 3. *Same as figure 2 except for selected image times. Each asterisk represents a detected cloud dome.*

The distribution of cloud dome area for the sequence of images on April 6th is shown in figure 4. In situations where many convective storms are occurring such as on April 6th, most of the domes are smaller than the GOES field-of-view and are only one pixels at the top (1 pixel - 56 km ^{2}). The large areas of 36 pixels at 1800 GMT, 38 pixels at 1900 GMT, and 23 and 27 pixels at 2330 GMT are very cold, flat areas in the downwind side of the anvil. Areas greater than 20-25 pixels are usually not associated with deep convection.

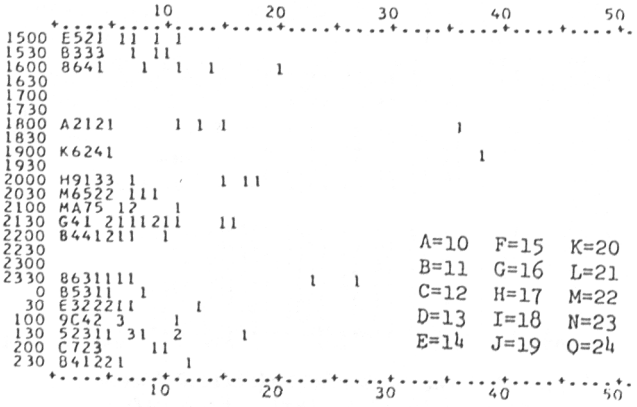

Figure 4. *The distribution of cloud dome area for the sequence of images on April 6th. Area is given on the abscissa in units of GOES IR pixels (8 km resolution).*

The cloud domes detected in the target area on April 6th fall into three general categories. The coldest domes represent the strongest upward motion, reach well above the anvil level, and are usually two degrees or more colder than the anvil. The locations of the coldest cloud domes at 2100 GMT (#1 through #8) are shown in figure 5 for an enlarged area around the most intense convection.

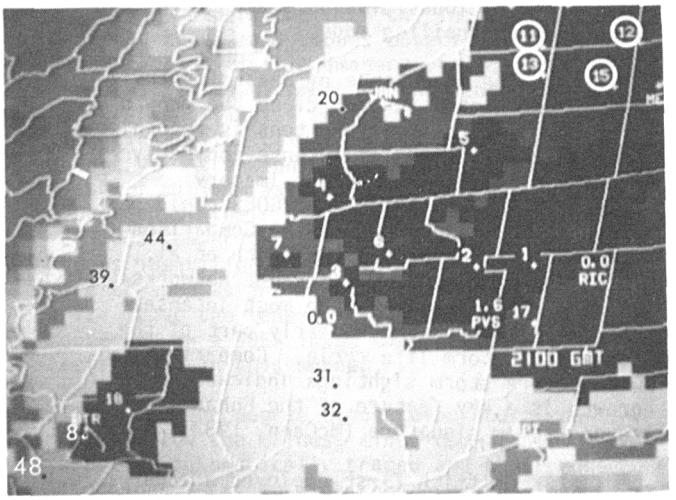

Figure 5. *Enlarged area of the enhanced IR image at 2100 GMT showing the coldest cloud dome locations (#1 through #8) associated with the most intense convection.*

A second category of domes which are close in temperature to the anvil itself, can be found downwind of the coldest tops. They are sometimes associated with active convection, but often they represent debris which has drifted downwind from earlier storms. At 2100 GMT about 12 of these cloud domes were located downwind of the coldest tops in the anvil. Some of them are indicated in figure 5 by the white circles. These domes were all 214° near the anvil temperature and correspond to the peak at 214°K in the cloud dome frequency distribution for 2100 GMT (figure 3). The peak at 219°K in the cloud dome frequency distribution for 1900 GMT is caused by the same category of domes found in the anvil near the anvil temperature.

The third category of domes have the warmer tops and are found toward the upwind side of the anvil. These represent active new convective storms since they occur with a strong gradient about the dome. Without a special enhancement of the infrared imagery, the gradients about cloud domes #39 and #44 (figure 5) are difficult for the meteorologist to identify. The detector shows that both of these domes are at least two degrees colder than the anvil and and have a strong gradient associated with them.

The cloud top structure of cloud dome #1 and #2 is depicted in figure 6. These cloud domes display the important features associated with thunderstorms possessing strong updrafts coupled with strong downdrafts and heavy rain. The first is a small cold peak towards the upwind (southwest) side of the anvil. The anvil is elongated in the direction of the upper level wind. Second is a strong temperature gradient out from the cold peak usually corresponding to the direction of strongest surface inflow. The third is the appearance of a cold axis extending eastward in the direction of individual cell propagation when the winds veer with height (Moses, 1981).

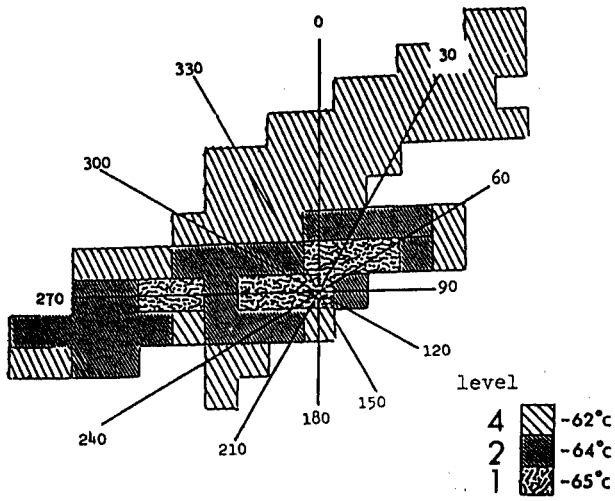

Figure 6. *Cloud top structure of cloud domes #1 and #2 at 2100 GMT.*

In this example the computer reveals these features by detecting the moments (maximums) and nodes (minimums) along the temperature contour associated with each dome. Figure 7 shows the direction and distance of the moments and nodes associated with cloud dome #1 2100 GMT. At level 4 below the top (-62°C contour) the moments have headings of 45° (Northeast) and 265° (west). The northeast maximum corresponds to the downwind direction of the anvil. The western maximum is caused by the merging of clouds associated with the contours of domes #3 and #6. The minimum node at all detected levels is south or southeast of the dome (Figure 7b). This indicates that the strongest temperature gradient at the top is aligned with direction of the synoptic scale low level inflow (see winds in Figure 1).

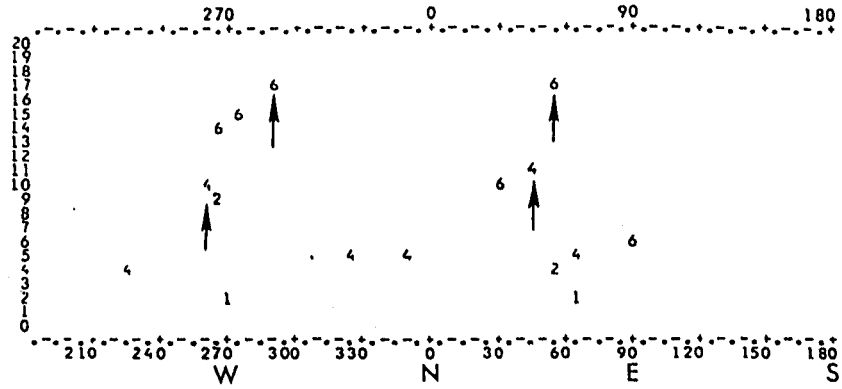

Figure 7a. *Moments (Maximums) detected along the temperature contours of cloud top #1 at 2100 GMT. Each value corresponds to a level given in figure 6 at the distance on the ordinate (GOES pixels) and heading on the abscissa.*

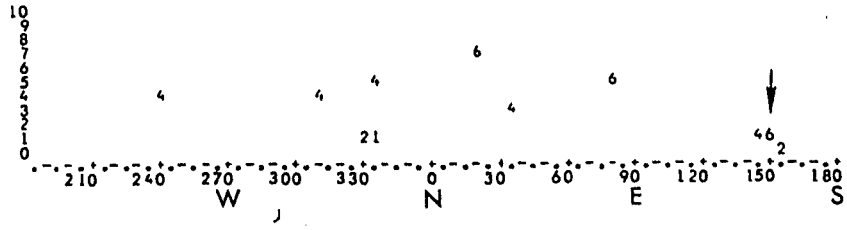

Figure 7b. *Nodes (Minimums) detected along the temperature contours of cloud top #1 at 2100 GMT. The heading of the tightest IR gradient is given by the lowest level at the smallest distance.*

The influence of synoptic scale low level and upper level winds on the shape of the cloud tops can be seen by looking at the maximum mode and minumim mode of the fourth temperature contour below cloud domes during the day (figure 8). The most frequently observed direction of the maximum is aligned with the upper level wind. A slow synoptic scale veering can be seen from the Northeast (60°) at 1500-1600Z to an eastward direction at 0100-0200Z on April 7, 1983. This corresponds to a shift in the upper level winds from the southwest to more westerly.

Few maximums occur to the north and northwest through the period, however a fair number of maximums are found in a west-southwest direction. These maximum moments are attributed to anvils of new storms forming to the west of existing storms and merging with the existing anvil. In figure 5 cloud domes #4 and #5 show the location a line of convection which formed behind the convection associated with domes #1 and #2.

As expected, the most frequently observed direction of the highest gradient, or minimum nodes are opposite of the maximum moments (figure 8b). Through most of the day the synoptic scale inflow slowly shifted from the southeast to more southerly. There were more nodes found in the south and southwest for the period of heaviest rain between 2000 and 2200 GMT. The increase of nodes to the north for the period late in the day represents a noticable change in the distribution of the alignment of upper level gradients.

5. CLOUD TOP TRACKING OBSERVATIONS

As expected, the majority of cloud domes detected are not associated with any previously detected dome in the half-hour GOES imagery. About 15% of the domes were normally tracked and the number of tracked domes increase up to a maximum of 22% as the density of the detected domes increased in the target area during the period of heaviest rainfall. Less than 2% of the domes were considered possible mergers or splits where two or more domes were detected in the search area.

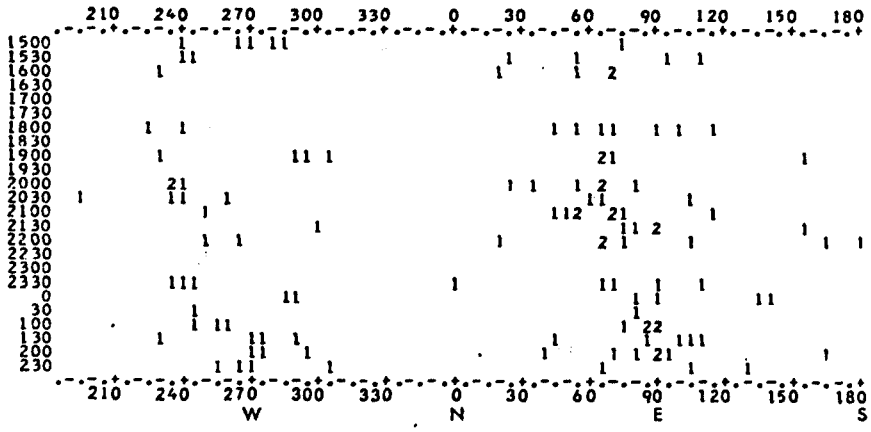

Figure 8a. *Frequency of moments detected during the morning, afternoon and evening of April 6, 1983. Each value represents the number of moments detected at the heading on the abscissa and the time (GMT) on the ordinate.*

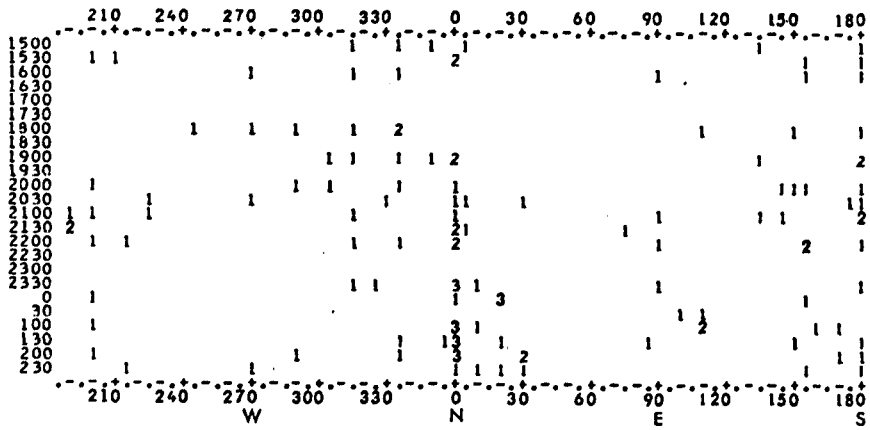

Figure 8b. *Same as 8a except for nodes.*

The heading between the previous cloud domes and current dome locations are shown in figure 9. Cloud domes are found in every sector except northwest where new growth is not favored and debris does not blow. An increase of domes are found in the southwest during the heavy rainfall period between 2000-2200 GMT. Domes tracked in this sector are indicative of new thunderstorms initiated by propagation to the southwest.

Centroids of the contours several degrees warmer than the dome were routinely tracked in the general direction of propagation of the thunderstorm complex. The majority of tracks oscillated between upwind propagation and downwind drifting of the cloud debris. For example, the centroid of the -62 contour around cloud top #1 and #2 at 2100 GMT (figures 5 and 6) was tracked from the 1800 GMT image. The heading at 2100 GMT was southeast, the heading at 2030 GMT was northeast, the heading at 2000 GMT was again southeast.

The change in direction is attributed to growth of new convective cells at 2000 GMT and 2100 GMT and the tracking of debris at 2030 GMT. Growth of the lower contours is as erratic as their track. For the above mentioned sequence, the greatest growth in contour area occurred between 2000 GMT and 2030 GMT, when the apparent motion was downwind.

6. SUMMARY AND FUTURE WORK

Numerical techniques for detecting clouds, their structure and evolution provides the essential information from GOES images for developing stochastic models of cloud patterns associated with heavy precipitation and severe weather. A simple model of linear convective systems like the example on April 6th is being developed to monitor intense convection and estimate heavy rainfall. This model uses maximum and minimum distances and directions between the cloud dome and associated temperature contours to find the orientation of the cloud system with respect to synoptic scale surface and upper level winds. The parameters of this model will be tested for their effectiveness through automatic comparisons with special and operational networks of raingauge reports.

More complex stochastic models are required to recognize the Enhanced V severe storm signature, coma shaped systems or hurricanes. For example, to detect the Enhanced V, headings of adjacent contour moments must be differenced and compared to the node postioned between them. The moment parameter must be modified to include piece wise continuous line segments which represent the shape of comas.

Operational meteorologists can immediately use graphical displays of their most important parameters or cloud signatures in preparation of site specific warnings. Interactive techniques would permit the timely incorporation of the meteorologist's experience and intuitive observations into a cloud pattern classifier.

7. ACKNOWLEDGEMENTS

The author would like to thank Russel L Pfost, WSFO, Jackson, Mississippi, for providing the half-hour observations in Mississippi. Sincere appreciation is expressed to Ralph K. Anderson and Roderick A. Scofield for reviewing the manuscript. The author is also grateful to Ms. Laura Wydick for typing this manuscript and to John Shadid for drafting some of the figures.

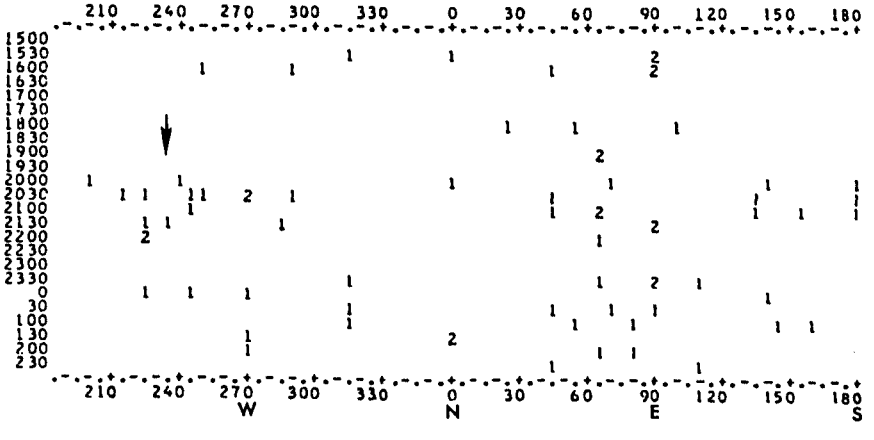

Figure 9. *Frequency of tracked cloud domes during the morning, afternoon and evening of April 6, 1983. Each value represents the number of tracked domes with the heading on the abscissa and the time on the ordinate. Note the increase of tracked domes in the southwest between 2000 and 2200 GMT.*

8. REFERENCES

Adler, R. F., and D. D. Fenn, 1979: Detection of sereve thunderstorms using short interval geosynchronous satellite data. Preprints 11th Conference Severe Local Storms, Kansas City, AMS, 166-171.

Griffith, C. G., Woodley, W. L. Grube P. G., Martin, D. W., Stout J., and Sikdar, D. N. Rain Estimation from Geosynchronous Satellite Imagery-Visible and Infrared Studies. Monthly Weather Review, 106, August 1978, AMS, 1153-1171.

McCann, D. W., 1983: The Enhanced-V: A Satellite Observable Severe Storm Signature. Monthly Weather Review, 3, April 1983, AMS, 887-894.

Moses, J. F., 1980: Numberical methods for the analysis of satellite rainfall estimates. Preprint Volume, Eighth Conference on Weather Forecasting and Analysis, Denver, CO, AMS, 101-107.

Moses, J. F., 1981: Convective cloud-tracking techniques for estimating precipitation from geostationary imagery. Proceedings of the Fourth Conference on Hydrometeorology, October 7-9, 1981, Reno, NV, AMS, 151-158.

Oslund, S. S., 1974: Computer software for rainfall analyses and echo tracking of digitized radar data. NOAA Technical Memorandum ERL WMPO-15, U.S. Department of Commerce, NOAA, Washington, D.C., 82 pp.

Scofield, Roderick A. and V. J. Oliver, 1977: A scheme for estimating convective rainfall from satellite imagery. NOAA/NESS Technical Memorandum 86, U.S. Dept. of Commerce, NOAA, Washington, D.C., 47 pp.

MESOSCALE ANALYSIS OF 6.7μm IMAGE DATA FROM THE VISSR ATMOSPHERIC SOUNDER (VAS) FOR SEVERAL CASE STUDIES

Gary J. Jedlovec

Universities Space Research Association
Marshall Space Flight Center
Huntsville, Alabama

1. INTRODUCTION

Moisture imagery from the 6.7μm water vapor channel on the VISSR Atmospheric Sounder (VAS) has been available to scientists in the last few years in the research and operational communities on a somewhat regular basis. This imagery has also been substituted for the conventional infrared full disk image from the GOES West satellite every six hours making limited water vapor imagery available to those who regularly receive GOES data. This type of imagery is not new, however, and similar moisture data has been available from the Nimbus, TIROS, and NOAA series polar orbiting satellites and the European geostationary satellite (METEOSAT). Normally this information is just one channel used to produce temperature and moisture soundings via various inversion techniques. In the last few years, however, studies have been performed using this moisture measurement for other purposes. Smith and Zhou (1982), Erye (1981), and Poc et al. (1980) have demonstrated ways in which this radiance data can be used to produce mean relative humidity and precipitable water values corresponding to the layer in which the radiation is emitted. More recent work (Petersen et al., 1982,1983) has used this imagery for diagnosing areas of potential instability by using this imagery to infer upper level dry regions which propogate over relatively moist low layers of the atmosphere.

Anyone who has seen a few of these images realizes that there can often be much variability in brightness temperatures over a particular region. This variability often occurs at scales of motion much smaller than our current upper air observation network can detect. It is the purpose of this paper to present several case studies where interesting features appear in the 6.7μm water vapor data and try to relate the mesoscale variability seen in the images with special rawinsonde measurements.

2. VAS AND RAWINSONDE MOISTURE DATA

The VISSR Atmospheric Sounder (VAS) is a passive radiometer on the current operational geostationary satellites. VAS has 12 channels which detect radiation emitted by the atmosphere in the infrared portion of the spectrum from 3.7 to 15.0 μm (see Chesters et al., 1982; Smith et al., 1981; or Menzel et al., 1981 for instrument description and operating modes). The radiance measurements in these channels typically have a horizontal resolution of 14km (nadir) providing detailed horizontal structure with vertical resolution over rather deep layers. Three channels detect radiation emitted from atmospheric water vapor at various levels of the atmosphere. Figure 1 shows the weighting functions depicting layers of the atmosphere in which moisture is detected by VAS for a standard atmospheric temperature and moisture profile. VAS channel 10 (6.7μm) is the one often used to infer middle and upper tropospheric moisture. The structure of the atmosphere can then be deduced from the horizontal distribution of moisture inferred from the images, its movement with time, and the dynamical relationships between jet streaks, subsidence, and the middle and upper level moisture distributions associated with atmospheric features (Ramond et al., 1981). As seen in Fig. 1, most of the radiation emitted by water vapor from the standard atmospheric conditions comes from the 600 - 300mb layer with the peak contribution coming from about 450mb. For atmospheric profiles of temperature and moisture which depart significantly from the standard, the weighting function for channel 10 can take on many different forms. For a very dry middle troposphere, contributions in this channel can occur from moisture down to 800mb. Thin layers of upper level moisture, on the other hand, can dominate the channel radiances and mask the middle level moist or dry regions.

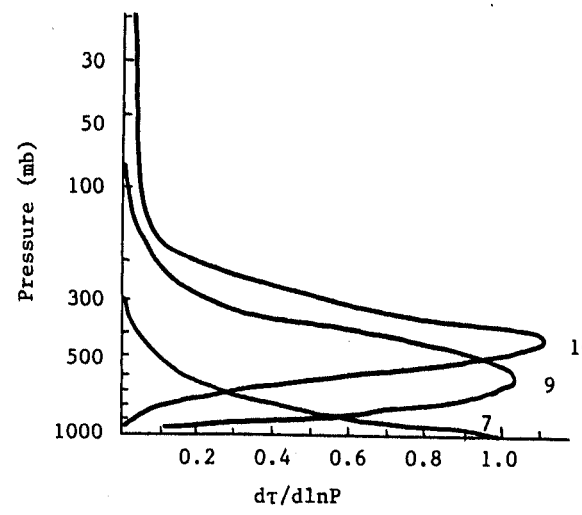

Figure 1. VAS water vapor channel weighting functions for the 6.7μm band (10), the 7.3μm band (9), and the 12.7μm band (7) for standard atmospheric conditions (from Chesters et al., 1982).

The broadness of the weighting functions and the dependence of the radiation received by VAS on both the temperature and moisture, often make it difficult to determine what radiance variations in this channel actually represent. Attempts to evaluate this variability with conventional observations can be frustrating because of the courseness of synoptic scale moisture observations aloft. Upper level moisture measurements from conventional rawinsonde observations are nearly point measurements having typical spacing of 400km which is at least an order of magnitude greater than VAS provides. A single radiance measurement from VAS (single field of view) in the 6.7μm channel represents some type of volumetric average over a couple hundred square kilometers in the horizontal and several kilometers in the vertical. Thus, what is measured by the synoptic scale rawinsonde network may not be representitive of the actual moisture distribution nor that measured by VAS.

The two case studies presented in this paper correspond to periods when mesoscale rawinsonde observations were made over a special network in central Texas and Oklahoma (Fig. 2) as part of the AVE/VAS experiment. Details of this experiment and the data collected can be found in Greaves et al. (1982), Jedlovec (1982), and Hill and Turner (1983). Rawinsonde observations were made at three-hourly intervals from this special network and 24 surrounding National Weather Service (NWS) rawinsonde sites. Relative humidity measurements from these observations will be presented in order to describe the three dimensional moisture distribution on the synoptic- and meso-scale in relation to the structure of the VAS 6.7μm imagery.

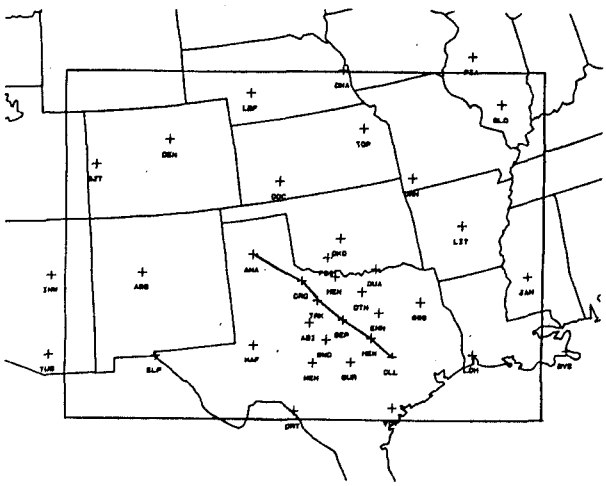

Figure 2. National Weather Service (NWS) and special site locations participating in the AVE/VAS experiment. Solid diagonal line in central Texas indicates the location of the cross sections referred to in the text.

3. CASE STUDY: 6 - 7 MARCH 1982

Figure 3 presents atmospheric conditions at 1100 GMT 6 March 1982 over the central part of the United States. At the surface, a low pressure center was present off the Gulf Coast with a stationary front extending southwestward into Mexico. Behind this front, a shallow high pressure area was positioned over the Texas-Oklahoma panhandle. To the north, a cold front extending from a low up in Canada was pushing south through the upper

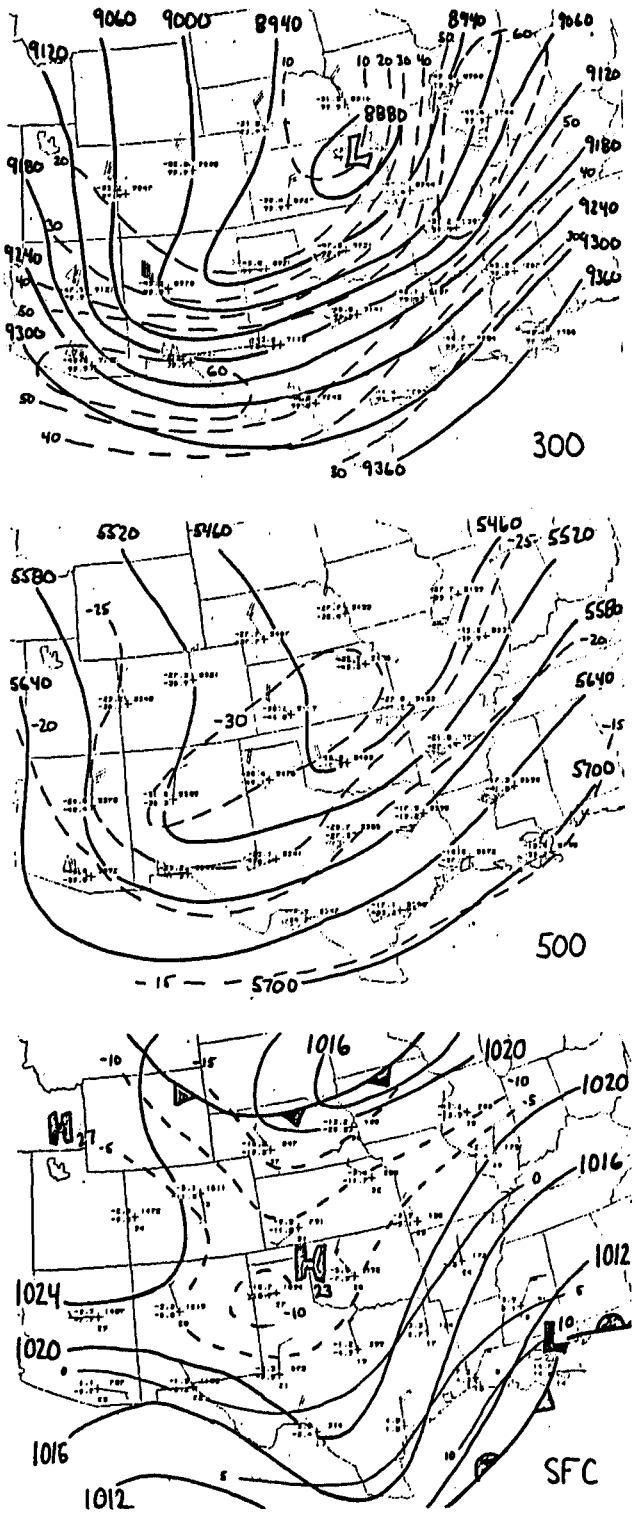

Figure 3. Surface and upper air charts for 1100 GMT 6 March 1982. At the surface pressure contours are in millibars and temperatures in degrees Celsius. For the upper air analyses, geopotential heights are in meters, 500mb temperatures are in degrees Celsius, and 300mb isotachs are in meters per second.

Great Plains states. The thermal gradient over the central portion of the region was quite strong with a 15°C gradient over Texas and an equally strong gradient over Kansas and Nebraska. The regional

network was predominantly cloud-free except for low, scattered middle and high clouds in east Texas and convective clouds with thunderstrom activity over Louisiana and Arkansas. Several inches of snow were present on the ground in portions of Oklahoma and west Texas but melted during the sunlight hours.

At 500mb a large amplitude trough was positioned over the regional network with a northeast-southwest orientation. A very strong temperature gradient was present on the leading edge of the trough line with a magnitude close to 3°C/100km. This strong baroclinic zone provided support for an upper level jet streak as it moved through the region. Maximum winds of $60ms^{-1}$ occurred at 300mb at the base of the trough and propogated through Texas during the next 24h.

Figure 4 presents the 6.7μm water vapor image from VAS at 1735 GMT 6 March 1982. This image was taken roughly 6h after the conditions described above and shown in Fig. 3. Several major areas of interest need to be pointed out. First, a rather narrow dark band is present over the region with a trough-like shape and extends from the Great Lakes region down through west Texas where it begins to broaden and swings back into Arizona and Nevada. The darkest region exists over Arizona and a dual banded structure is present over Oklahoma and Missouri. Presumably these dark regions correspond to dry middle and upper tropospheric air supported by dynamic interactions of the propogating jet streak. Away from this dark band, increasingly lighter gray-shades (colder temperatures) are present indicating increasing moisture content in this layer. Bright areas in this image represent clouds which contaminate the water vapor signal received by VAS.

Conventional moisture analyses at the middle and upper levels (not shown) poorly define the moisture variability seen in the VAS image. This could occur for several reasons. First, the sampling constraints discussed in the previous section could make the moisture patterns delineated by the rawinsonde data misleading. Second, radiation measured by VAS in this channel depends on both the temperature and moisture of the atmosphere and does not directly relate to an absolute moisture quantity (Poc and Roulleau, 1983). In an attempt to relate a rawinsonde derived moisture parameter to the 6.7μm image, relative humidity values from the rawinsonde network were objectively analyzed to a grid, weighted in the vertical based on the standard atmosphere weighting function (Fig. 1), and then averaged in the vertical to produce a weighted mean layer relative humidity value. These values

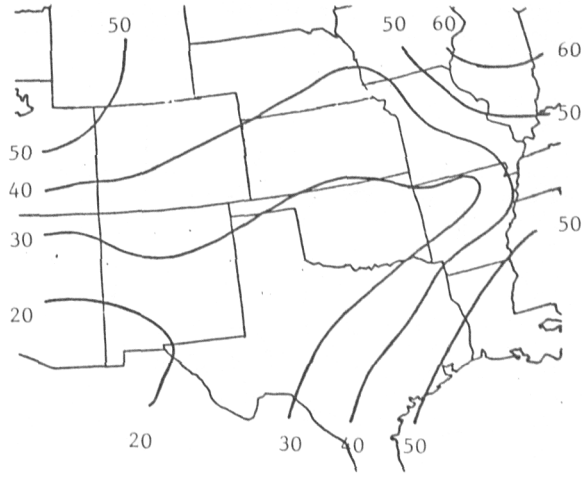

Figure 5. Weighted mean layer relative humidity over the regional area at 1745 GMT 6 March 1982. Units are in percent.

are presented for 1745 GMT in Fig. 5 for the regional network. This analysis bears a good likeness to the water vapor image for the same time

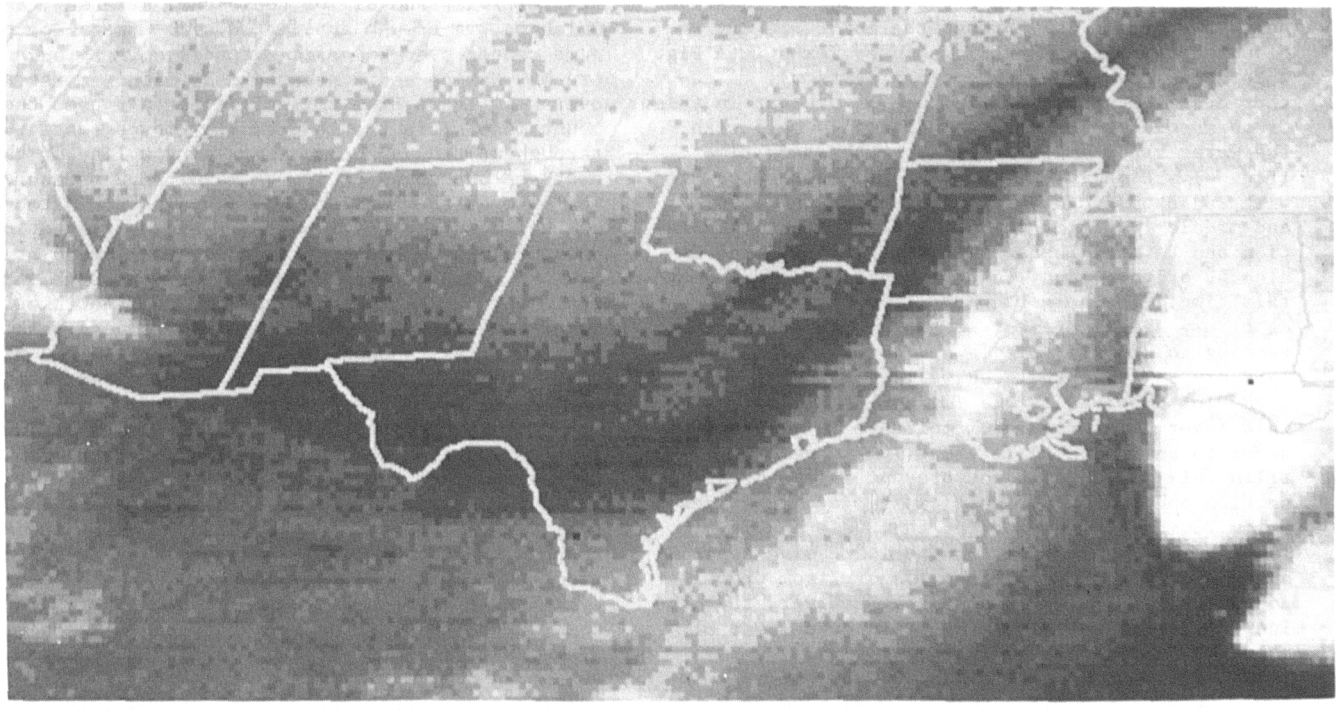

Figure 4. VAS 6.7μm water vapor image at 1735 GMT 6 March 1982. Gray-shade values ranging from black to white correspond to warm and cold blackbody temperatures, respectively.

(Fig. 4) except for over Illinois and Missouri where high moisture content from a cloudy sounding at Peoria affects the analysis in this region. This field lacks detailed mesoscale structure (as expected) since only large scale rawinsonde observations were utilized. Figure 6 presents the same weighted relative humidity parameter but calculated over central Texas and Oklahoma using the special network rawinsonde sites having a spacing of about 125km. Relating this analysis to the corresponding region of the VAS water vapor image provides only a slightly better verification of the satellite image but still lacks detail. This is probably due to the intricate emission of energy from the atmospheric water vapor and the crudeness of the scheme used to produce the weighted mean relative humidity values.

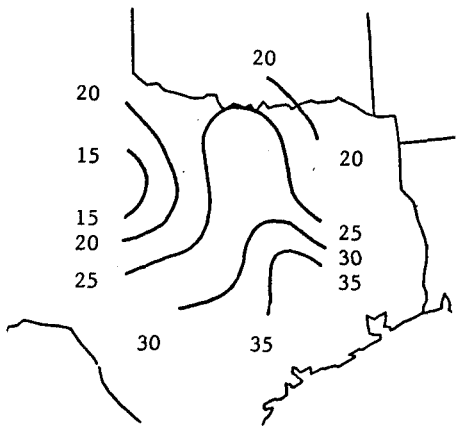

Figure 6. Weighted mean layer relative humidity over the mesoscale rawinsonde network in central Texas and Oklahoma at 1745 GMT 6 March 1982. Units are in percent.

Figure 7 presents a cross section of relative humidity at 1745 GMT through the moist and dry regions as they appear in Fig. 4 over Texas (see Fig. 2 for stations used in the cross section). A rather detailed moisture structure is present in this cross section which corresponds fairly well with the water vapor image from VAS at the same time (Fig. 4). High relative humidity values associated with and around clouds are present in the lower and middle layers of the atmosphere at College Station and Hewitt, Texas. The water vapor image indicates bright cloudy features over these areas at this time. To the northwest of Hewitt, a deep layer of dry air is present in the cross section extending to Crowell (single and double hashed areas). This dry region correlates well with the narrow dark slot observed in the image. At Crowell, a thin layer of middle level moisture is present and seems to be indicated in the 6.7μm image. At Amarillo this moisture is not present in the cross section and the only significant moisture resides below 700mb. It is doubtful that this low level moisture is responsible for the increasing grayshade values observed in the imagery from Crowell to Amarillo. It may be possible, however, that the increasing grayshades are due to a deep layer of cold air behind the upper level trough. Ramond et al. (1981), investigating METEOSAT moisture imagery on a case similar to this one, have shown that the radiance field can reflect the temperature along an isosteric surface on the cyclonic side of a propogating polar jet streak. This theory is the focus of ongoing research.

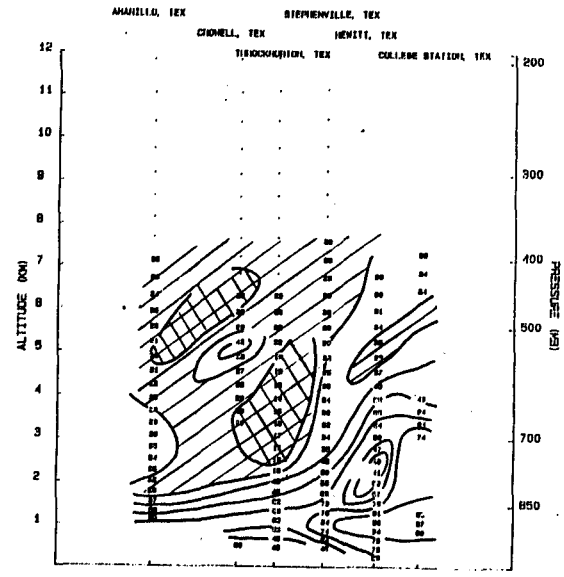

Figure 7. Cross sectional analysis of relative humidity from rawinsonde data at 1745 GMT 6 March 1982. The station locations used are indicated in Fig. 2. Units of relative humidity are in percent.

4. CASE STUDY: 24 - 25 APRIL 1982

Figure 8 presents the atmospheric conditions at 1100 GMT 24 April 1982 over the central part of the United States. At the surface, a weak warm front was located off the Gulf Coast. Over-running moisture produced stratus clouds and light precipitation ahead of this front and covered the eastern half of Texas and all of Louisiana, Arkansas, and Oklahoma. A trough associated with a weak low pressure center over Colorado extended down through eastern New Mexico and separated only mildly moist air over west Texas from slightly drier air over the mountains. This trough gradually moved eastward throughout the day producing a narrow line of thunderstorms out ahead of it. A major high pressure region over the Appalachian mountains dominated the weather over the east coast. Aloft, a closed low pressure system was positioned over Colorado at both 500 and 300mb. An isotherm analysis at 500mb indicated a weak temperature gradient over northwest Texas extending from the cold core low. A weak jet core existed at 300mb over southern Texas and Mexico which propogated eastward with the slow movement of the entire weather system.

Figure 9 presents the 6.7μm water vapor image from VAS at 1745 GMT 24 April 1982 over the south-central part of the United States. The very bright areas in this image over east Texas, Arkansas, Louisiana, Missouri, and in the Gulf of Mexico correspond to cloudy regions in the middle and upper troposphere which contaminate the radiation received by VAS from atmospheric water vapor. There are also some scattered cloud contaminated areas associated with convective activity around the low pressure system in Colorado. Away from these bright features, varying gray-shades can be seen around this low. In a time lapse sequence of water vapor images (not presented) these bands move in a circular pattern around the low . A rather dark area in the image

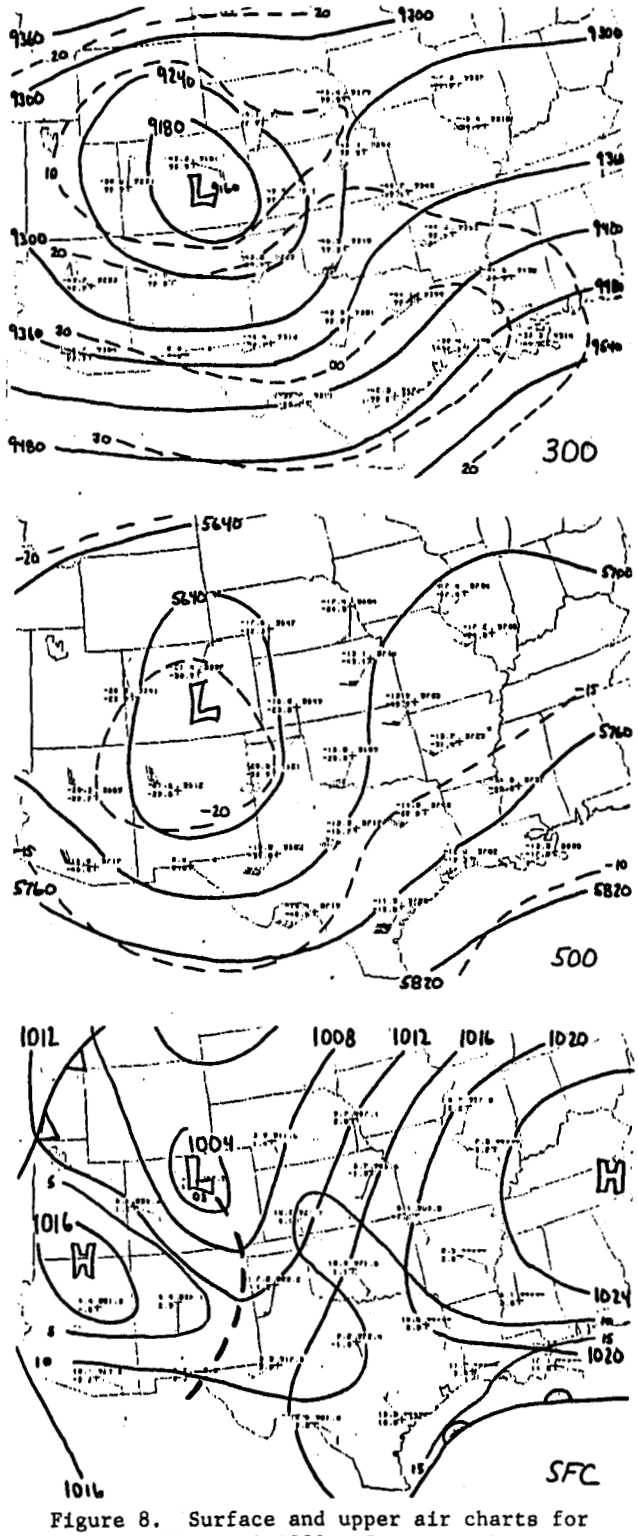

Figure 8. Surface and upper air charts for 1100 GMT 24 April 1982. Contours shown are labeled as in Fig. 3.

is present over Texas and extends back into south-New Mexico, Arizona, and northern Mexico. As in the March case study, this feature seems to correspond to the upper level jet (Fig. 8) although both the dark region and the upper level jet streak are less well defined in this case.

Figure 10 presents the weighted mean layer relative humidity over the regional area at 1745 GMT 24 April 1982. This parameter was calculated as before and described in Section 3 above. High values of this parameter appear over cloudy regions previously denoted. Lower values of layer relative humidity are present over northern Colorado and western Kansas where the VAS water vapor image indicates small areas of dark gray-shades (warmer blackbody temperatures). The misalignment of the relative humidity patterns in this region and in east Texas appear to be due to the coarse resolution of upper air moisture measurements. A large region containing low values of layer relative humidity is present in the southwestern portion of the analysis region (Fig. 10) and correlates well with the dark region in the water vapor image.

Figure 11 presents a cross sectional analysis of relative humidity at 1745 GMT from the rawinsonde observations which run diagonally through Texas (Fig. 2). Note that the water vapor image for this time (Fig. 9) indicates a variety of gray-shades from Amarillo down through College Station with the darkest values occurring near Crowell. The cross section of relative humidity indicates a major area of high relative humidity associated with clouds over Stephenville, Hewitt, and College Station. These clouds extend up to the 500mb level and are detected in the water vapor imagery as rather bright areas. Relative humidity values at Crowell show a very dry profile above 700mb with only a moderate increase in moisture below this level. Crowell's location and dry profile corresponds to the darkest region in the cross section plane. This dry region gives way to significant moisture near Amarillo as shown in the cross section and depicted by the VAS image.

5. CONCLUSIONS

The VAS 6.7μm water vapor images presented in this paper indicated much gray-shade (blackbody temperature) variability associated with several different synoptic conditions. It is not as easy as one might expect to relate these variations to the atmospheric water vapor distribution. Sampling characteristics of the two measurements are contrastingly different and often prevent direct comparison. Mesoscale moisture observations help in determinating small scale variability, however, variations in the imagery can occur at wavelengths down to about 15 - 30km. A simple weighted layer relative humidity parameter was produced from the rawinsonde measurements and served to verify the larger scale features in the water vapor imagery but failed, even with mesoscale observations, to account for smaller scale variations. Cross sections through various features provided a better representation of the moisture structure depicted by the VAS imagery but also hinted that other parameters might be related. The variation of temperature in deep layers of the atmosphere might significantly affect the radiation received by the satellite in this channel despite negligible variations in water vapor.

Acknowledgements. This work was performed under the Universities Space Reseach Association's Visiting Scientist Program at Marshall Space Flight Center under contract NAS8-34767. NASA's support of this program is appreciated.

REFERENCES

Chesters, D., L. W. Uccellini, and A. Mostek, 1982: VISSR Atmospheric Sounder (VAS) simulation experiment for a severe storm environment. Mon. Wea. Rev., 110, 198-216.

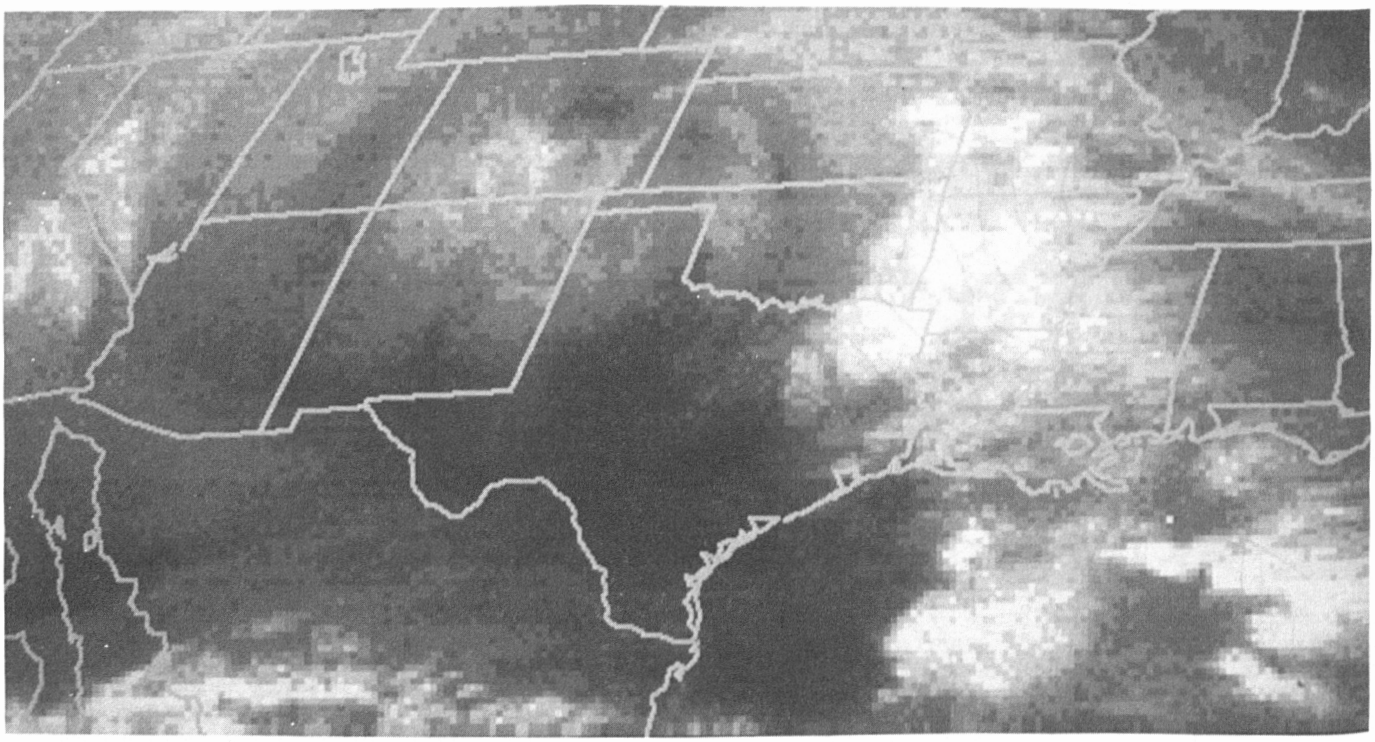

Figure 9. VAS 6.7μm water vapor image at 1735 GMT 24 April 1982. Gray-shade values rangeing from black to white correspond to warm and cold blackbody temperatures, respectively.

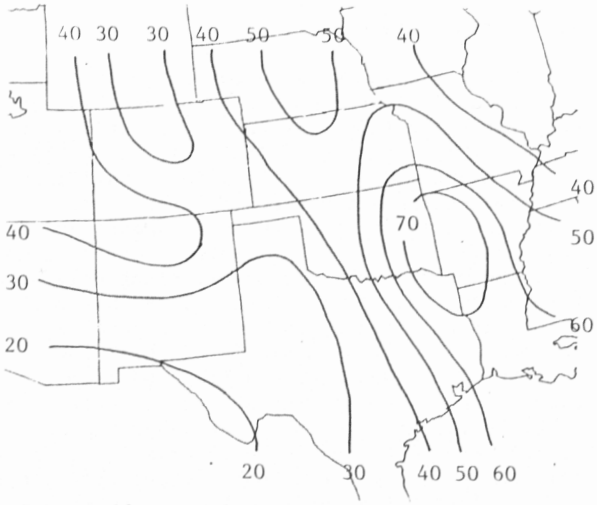

Figure 10. Weighted mean layer relative humidity for the region network at 1745 GMT 24 April 1982. Units are in percent.

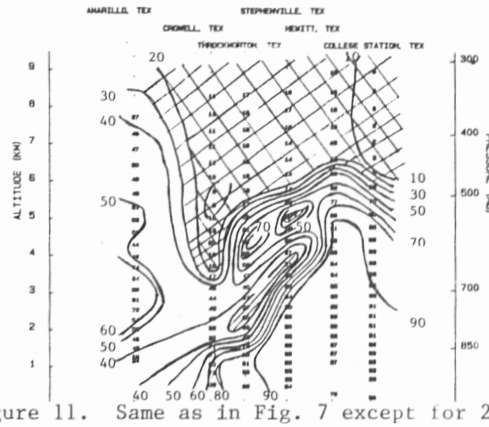

Figure 11. Same as in Fig. 7 except for 24 April 1982.

Erye, J. R., 1981: Improvement of humidity analyses by direct use of METEOSAT water vapor channel radiances. Proc. IAMAPS Symposium, Hamburg, 63-66.

Greaves, J. R., H. E. Montgomery, L. W. Uccellini, and D. L. Endres, 1982: 1982 AVE/VAS ground truth field experiment: Satellite data acquisition summary and preliminary meteorological review. NASA Report X-903-82-17, 27pp.

Hill, C. K., and R. E. Turner, 1983: NASA's AVE/VAS Program. Bull. Amer. Meteor. Soc., 64, 796-797.

Jedlovec, G. J., 1982: AVE/VAS experiment: Synoptic summary and preliminary results. VAS Research Review, NASA CP 2253, Greenbelt, Md., 39-42.

Menzel, W. P., W. L. Smith, and D. L. Herman, 1981: VISSR Atmospheric Sounder radiometric calibration: An inflight evaluation from intercomparisons with HIRS and radiosonde measurements. Appl. Opt., 20, 3641-3644.

Petersen, R. A., L. W. Uccellini, D. Chesters, A. Mostek, and D. Keyser, 1982: The use of VAS satellite data in weather analysis, prediction, and diagnosis. Preprints 9th Conf. Wea. Forecasting and Analysis, Boston, 219-226.

Petersen, R. A., D. A. Keyser, A. Mostek, and L. W. Uccellini, 1983: Techniques for diagnosing mesoscale phenomena affecting aviation using VAS satellite data. Preprints 9th Conf. on Aerospace and Aeronautical Meteorology, AMS, Boston, 12-17.

Poc, M. M., M. Roulleau, N. A. Scott, and A. Chedin, 1980: Quantitative studies of METEOSAT water-vapor channel data. J. Appl. Meteor., 19, 868-876.

Poc, M. M., and M. Roulleau, 1983: Water vapor fields deduced from METEOSAT-1 water vapor channel data. J. Clim. Appl. Meteor., 22, 1628-1636.

Ramond, D., H. Corbin, M. Desbois, G. Szejwach, and P. Waldteufel, 1981: The dynamics of polar jet streaks as depicted by the METEOSAT WV channel radiance field. Mon. Wea. Rev., 109, 2164-2176.

Smith, W. L., V. E. Suomi, W. P. Menzel, H. M. Woolf, L. A. Sromovsky, H. E. Revecomb, C. M. Hayden, D. N. Erickson, and F. R. Mosher, 1981: First sounding results from VAS-D. Bull. Amer. Meteor. Soc., 62, 232-236.

Smith, W. L., and F. X. Zhou, 1982: Rapid extraction of layer relative humidity, geopotential thickness, and atmospheric stability from satellite sounding radiometer data. Appl. Opt., 21, 924-928.

F.5

REMOTE SENSING OF TEMPERATURE PROFILES BY A COMBINATION OF GROUND-BASED PROFILER AND SATELLITE-BASED MSU RADIOMETRIC OBSERVATIONS

Ed R. Westwater and Wang Zhenhui*
NOAA/ERL/Wave Propagation Laboratory
Boulder, CO 80303

and

Norman C. Grody and Larry M. McMillin
NOAA/NESDIS
Washington, D.C. 20233

1. INTRODUCTION

Remote sensing of temperature profiles using a combination of passive microwave radiometric observations from surface- and satellite-based platforms was suggested by Westwater and Grody (1980). Their computer simulations showed that over the pressure interval 1000-300 mb, rms retrieval accuracies of 1 to 2°C were achievable with current radiometric technology. In addition, if supplementary measurements of tropopause height were available (e.g., from a VHF radar), similar accuracies could be achieved up to 100 mb.

Data are now available to verify these original theoretical predictions. A ground-based remote sensing system, called the Profiler, has been operating at Denver, Colorado, for about 3 years. The Profiler (Hogg et al., 1983) is an instrument that combines both microwave radiometers and VHF and UHF radars to derive several quantities of meteorological interest. Satellite microwave radiometric observations have, of course, been available for several years. For the present study, we collected Microwave Sounding Unit (MSU) data that were taken over Denver, Colorado during the period December 1981 to December 1982. National Weather Service (NWS) radiosonde observations (RAOB's) were also collected to serve as our standard of comparison.

In addition, we obtained VHF radar soundings of tropopause height that were taken during a short period in March 1981. This active (radar) information, when combined with passive (radiometric) measurements, is shown to improve substantially temperature retrieval accuracy in the vicinity of the tropopause.

* On leave from Nanjing Institute of Meteorology, Nanjing, People's Republic of China.

2. DESCRIPTION OF INSTRUMENTS

The Profiler is a ground-based remote sensing system designed to measure profiles of wind and temperature as well as integrated water vapor and cloud liquid. Instrumental details of this system and its initial remote sounding results are extensively described by Hogg et al. (1983). Below, we describe briefly the portion of the instrumentation that we use in this paper.

The Profiler is less than 100 m from the NWS radiosonde launch site. The Profiler's six-channel radiometer has one channel operating at 20.6 GHz, one at 31.65 GHz, and four channels between 50 and 60 GHz. The two lower channels are used to derive precipitable water and cloud liquid and also provide corrections for these variables to the 50-60 GHz temperature channels. Data from the six channels, supplemented with surface measurements of pressure, temperature, and relative humidity, are converted to profiles of temperature and humidity by linear statistical inversion.

Although 2-min samples of profile retrievals are derived and archived, we used 20-min averages for combination with the satellite data and for comparison with radiosonde data. For the RAOB comparison, the time average started at the time of radiosonde release.

The data processing for the Profiler eliminates strong cloud and rain effects by rejecting data for which the 31 GHz brightness temperature exceeds 100 K. This threshold was exceeded for 3 of the 460 cases we analyzed. In these three cases, we replaced the deleted data with those from another 20-min period within ±1 h of radiosonde launch time. For all other data, no additional processing was necessary.

The MSU is a component of an operational sounding system and was designed 1) to produce global temperature soundings under nearly all weather conditions, and 2) to complement an infrared sounder that contains more channels but is limited to clearer atmospheres. The MSU is

aboard the polar-orbiting NOAA 6/7/8 satellites and contains four channels in the oxygen band, at 50.30, 53.74, 54.96, and 57.95 GHz, to provide temperature profile information from the lower troposphere to the lower stratosphere. Further details of this instrument, including its scan pattern, are given by Grody (1983).

Both the Profiler and the MSU observe the brightness temperature $T_b(\nu)$ emitted by the atmosphere at frequency ν. This quantity is related to the vertical temperature profile T(h), where h = height, by an equation of the form

$$T_b(\nu) = \int_0^\infty T(h)\, W(\nu,h)\, dh + T_{BACK}(\nu)\, e^{-\tau(\nu)} \quad , \quad (1)$$

where $W(\nu,h)$ is the so-called temperature weighting function, $T_{BACK}(\nu)$ is a background brightness temperature, and $\tau(\nu)$ is the opacity from Earth to space. For upward-viewing observations, $T_{BACK}(\nu)$ describes the "big bang" cosmic background of 2.9 K, as well as emission from discrete sources. For downward-looking observations, $T_{BACK}(\nu)$ describes reflected and emitted radiation from the Earth's surface. Profiler and MSU temperature weighting functions are shown in Fig. 1. Note how the Profiler capabilities, which are exponentially reduced above 500 mb, are complemented by the MSU; conversely, note how the relatively high vertical resolution at lower altitudes of the Profiler complements the MSU below 500 mb.

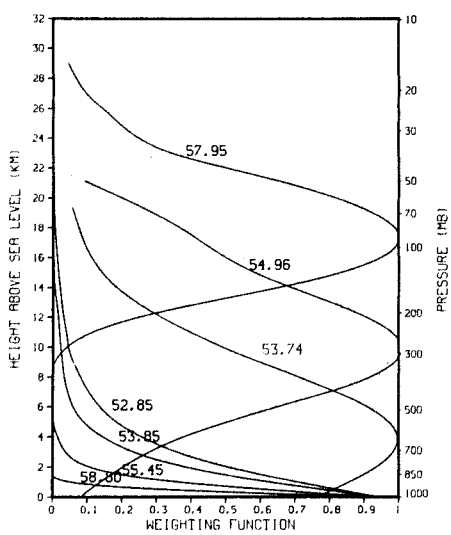

Fig. 1. Temperature weighting function, in relative units, for various channels of the radiometric Profiler and the MSU. The upper three curves are for the MSU; the lower four curves are for the Profiler.

3. RETRIEVAL METHOD

Our method of deriving temperature and humidity profiles from observed brightness temperatures was a straightforward application of linear a priori statistical inversion (Strand and Westwater, 1968). With this method, a profile vector $\underset{\sim}{p}$ is estimated from a data vector $\underset{\sim}{d}_e$ by

$$\underset{\sim}{p} = \langle \underset{\sim}{p} \rangle + \langle \underset{\sim}{p}'\, \underset{\sim}{d}_e'^T \rangle \langle \underset{\sim}{d}_e' \underset{\sim}{d}_e'^T \rangle^{-1} (\underset{\sim}{d}_e - \langle \underset{\sim}{d}_e \rangle) \quad (2)$$

where $\langle \cdot \rangle$ represents ensemble averaging over a joint distribution of profiles and experimental noise, $\underset{\sim}{v}^T$ is the matrix transpose of the column vector $\underset{\sim}{v}$, and the primes refer to departures from ensemble average; e.g., $\underset{\sim}{v}' = \underset{\sim}{v} - \langle \underset{\sim}{v} \rangle$. The data vector $\underset{\sim}{d}_e$ consists of a "true" component $\underset{\sim}{d}$ and an experimental error $\underset{\sim}{\varepsilon}$

$$\underset{\sim}{d}_e = \underset{\sim}{d} + \underset{\sim}{\varepsilon} \quad . \quad (3)$$

We generated the retrieval coefficients entering into (2) by computer simulations using a priori NWS RAOB data taken at Denver, Colorado during 1972-1977. The details of our method are discussed by Westwater et al. (1984). In particular, we used an experimentally determined covariance matrix to model the MSU noise characteristics.

In Section 4, we compare with RAOB's the separate Profiler and MSU retrievals as well as those from the combined Profiler + MSU system. In addition, we evaluate the effect of constraining the MSU data with surface meteorological observations. The various choices of data vectors from thich we generated retrievals are shown in Table 1.

4. RESULTS OF TEMPERATURE RETRIEVAL BY COMBINING MSU AND PROFILER DATA

The data base used to compare and combine Profiler and MSU retrievals consisted of NWS RAOB's, 20-min averages of Profiler data, starting at RAOB release time, and NOAA 6/7 measurements over the Denver, Colorado area. The satellite data were restricted to be within ±3 h from 0000 or 1200 GMT and to fall within an area -0.5 to +1.0°N and 0.0 to +2.0°E of the joint NWS-Profiler site at 39°46N latitude and 104°53W longitude. The area included the plains east and north of Denver and excluded all of the Rocky Mountains. For the time period December 1981 through December 1982, we obtained 460 RAOB-Profiler-MSU data cases.

As discussed in Section 3, we derived temperature profile retrieval coefficients from various choices of data vectors. Thus, we retrieved profiles using data from the 1) Profiler; 2) MSU; 3) MSU + surface meteorological measurements; and 4) Profiler + MSU. The total rms difference statistics relative to RAOB's, for each of the four temperature retrievals, are shown in Fig. 2. As a baseline value, we also show the rms variation using surface meteorological measurements as predictors. We note that the MSU + Profiler results are everywhere more accurate than any of the separate subsystems. This result was both expected and desired, but if we had incorrectly modeled relative covariances, for example, combined retrievals might be poorer than the separate ones. A curious feature is revealed

Table 1. Components of data vectors used in temperature and water vapor profile retrieval. T_S = surface temperature (°C), P_S = surface pressure (mb), RH_S = surface relative humidity, $T_{b,P}$ = Profiler brightness temperature (K), T_{bMSU} = MSU brightness temperature (K), T_p = optical depth (nepers), frequencies in parentheses (GHz).

Component Number	Profiler	MSU	MSU + Surface Meteor.	Profiler + MSU
1	T_S	$T_{b,MSU}$ (53.74)	$T_{b,MSU}$ (53.74)	T_S
2	P_S	$T_{b,MSU}$ (54.96)	$T_{b,MSU}$ (54.96)	P_S
3	RH_S	$T_{b,MSU}$ (57.95)	$T_{b,MSU}$ (57.95)	RH_S
4	$T_{b,P}$ (53.85)		T_S	$T_{b,P}$ (53.85)
5	$T_{b,P}$ (55.45)		P_S	$T_{b,P}$ (55.45)
6	$T_{b,P}$ (58.80)		RH_S	$T_{b,P}$ (58.80)
7	T_P (20.6)			T_P (20.6)
8	T_P (31.65)			T_P (31.65)
9	$T_{b,P}$ (52.80)			$T_{b,P}$ (52.80)
10				$T_{b,MSU}$ (53.74)
11				$T_{b,MSU}$ (54.96)
12				$T_{b,MSU}$ (57.95)

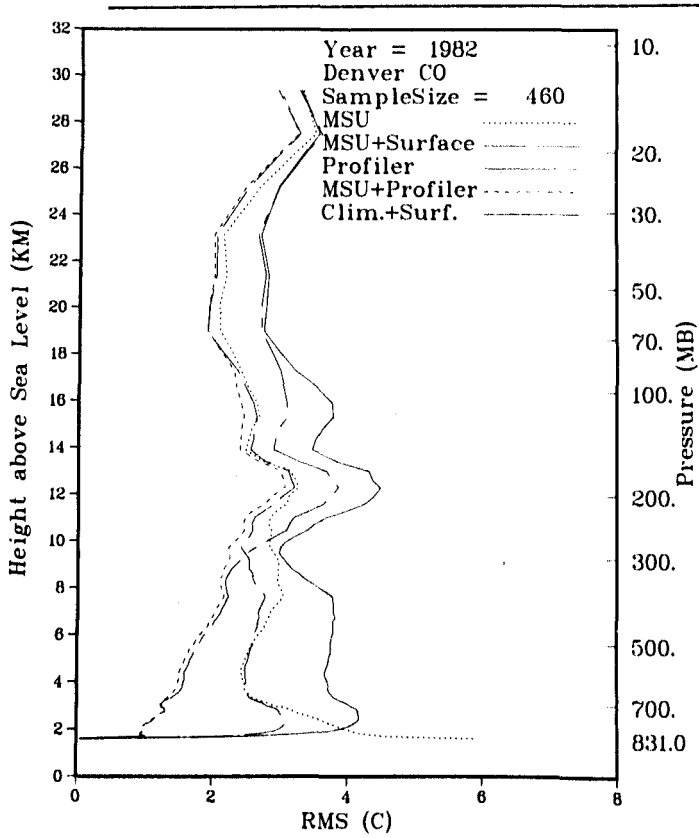

Fig. 2. The rms statistics of differences in temperature profiles between RAOB's and retrievals.

in the results of the combination of MSU and surface data. As expected, surface predictors (namely surface temperature) improved retrieval accuracy in the first ≈ 100 mb above the surface. However, in the 400-200 mb region, as much as 0.5 K improvement was achieved using surface data. As suggested by Westwater and Grody (1980), this improvement resulted from a correlation of surface pressure with the temperature aloft. We also observe that the retrieval results of all the systems improved substantially over predictions based on surface climatology, except for the MSU in the first 50 mb above the surface.

In addition to temperature retrievals, we derived geopotential heights and thicknesses for the various systems. These quantities also depend on water vapor, a quantity derived by the Profiler but not by the MSU. To derive pressure heights from the MSU data, we used monthly mean water vapor profiles with the MSU-derived temperature profiles and vapor profiles estimated from surface data with the (MSU + surface)-derived temperature. Retrievals of all systems used RAOB surface pressure as a reference. These results of the geopotential height and the thickness determinations are given in Tables 2 and 3. In Table 2 we also present the estimated functional precision of radiosondes, as given by Hoehne (1980). Hoehne's original values were taken at sea level and required an adjustment (about 6 m) to Denver's surface pressure. From these tables, we observe that the Profiler + MSU

Table 2. Rms differences in determination of geopotential height (m) for various combinations of remote sensing systems. N = sample size.

	Climatology (monthly means)	Surface Meteor.	MSU	MSU + surface	Profiler	MSU + Profiler	Functional precision of radiosondes (Hoehne, 1980)
700 mb (N = 458)	32.2	18.7	17.2	13.5	3.8	3.8	5.1
500 mb (N = 458)	71.3	49.6	32.2	31.2	13.1	12.4	12.7
300 mb (N = 456)	117.9	89.5	57.3	56.9	33.0	31.1	20.3
100 mb (N = 446)	93.1	74.3	60.6	51.7	67.6	46.0	27.9

Table 3. Rms differences in determination of geopotential thickness (m) for various combinations of remote sensing systems. N = sample size.

	Climatology (monthly means)	Surface meteor.	MSU	MSU + surface	Profiler	MSU + Profiler
700-500 mb (N = 458)	42.0	33.3	21.0	21.4	12.3	11.5
500-300 mb (N = 456)	53.7	45.3	37.8	33.6	26.4	25.6
300-100 mb (N = 446)	85.7	82.2	47.5	47.9	65.8	41.9

results were a significant improvement over the Profiler's, primarily in the 300-100 mb range.

5. COMBINED RADAR-RADIOMETRIC TEMPERATURE RETRIEVALS

Studies have shown that VHF radars can measure the height of the tropopause (Gage and Green, 1979). As predicted theoretically by Westwater and Grody (1980) and verified experimentally (Westwater et al., 1983), the tropopause height information can be used to improve temperature retrieval accuracy of radiometric sensors. In this section, we will show examples of the combined passive-active (radiometric-VHF radar) techniques for a small data set taken during March 1981.

The VHF radar is located at the Platteville (Colorado) Radar Facility, about 50 km north of Denver, and is operated jointly by the NOAA/Aeronomy Laboratory and the NOAA/Wave Propagation Laboratory. Although the primary purpose of the radar is to measure horizontal winds, during the month of March 1981 the radar was operated in the vertical sounding mode. Tropopause heights were derived from the vertical sounding data using the algorithms given by Westwater et al. (1983). In particular the so-called RC (reflectivity correlation) method that we used is described there.

Power spectra were averaged for 1 min before further processing. The noise level was then estimated and subtracted, following the method of Hildebrand and Sekhon (1974). The power density of the adjusted spectra was then integrated for a return power value. The range-gate spacing was set at 1.2 km, i.e., at one-half the pulse width.

For the three systems--Profiler, MSU, Profiler + MSU--we were able to compare both passive and passive + active temperature re-retrievals. Our retrieval algorithms for combining active and passive measurements is a straightforward generalization of the method given in Section 2 and is described by Westwater et al. (1983). However, the retrieval coefficients used for the March 1981 retrievals were calculated for an assumed satellite noise level of 0.5 K, and thus were not based on an experimentally determined covariance matrix.

Sample profiles derived from various combinations of sounding systems are shown in Fig. 3. Note that in Fig. 3A the ground-based radiometer's retrieval closely matches the RAOB up to about 10 km, but then departs by several degrees from the sonde. Also note the improvement added when the tropopause information was introduced. In Fig. 3B, the MSU retrievals are much closer to the radiosonde in the tropopause

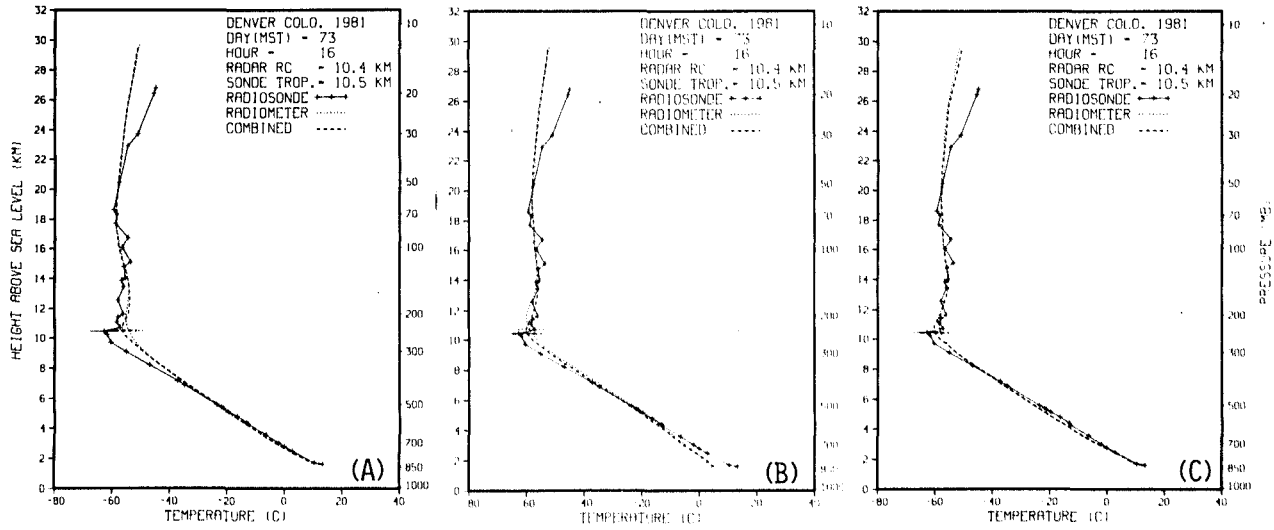

Fig. 3. Temperature profile retrievals from VHF radar, radiometric Profiler, and MSU data. Curves labeled "combined" refer to radiometer + radar: (A) radiometric Profiler + VHF radar; (B) MSU + VHF radar; (C) radiometric Profiler + MSU + VHF radar.

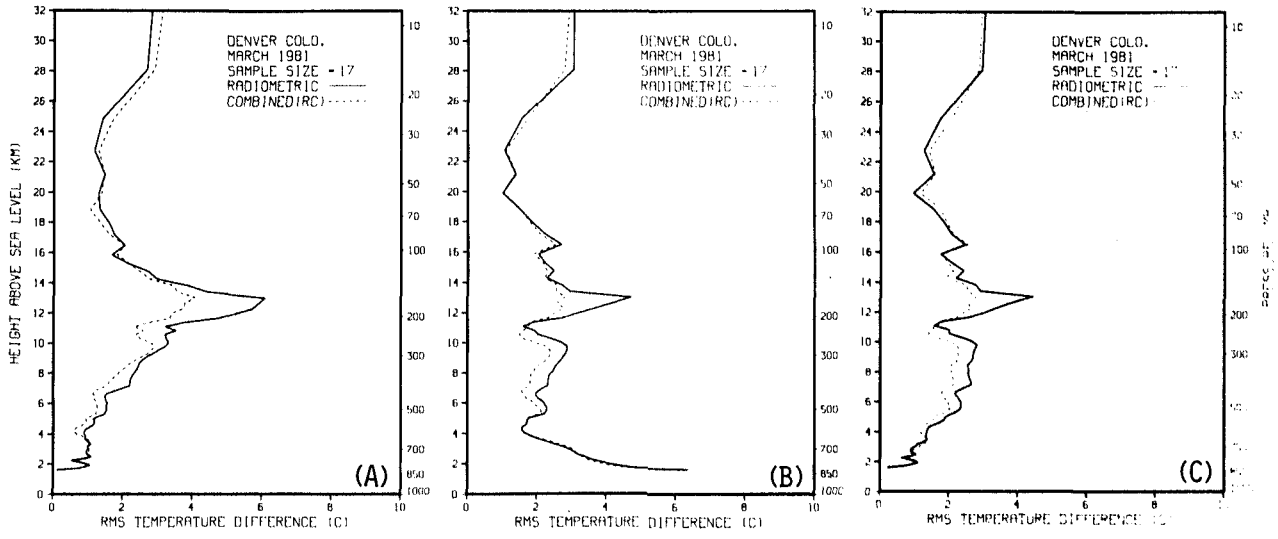

Fig. 4. The rms differences between temperature retrievals and NWS RAOB's. Curves labeled "combined" refer to radiometer + radar. (A) radiometric Profiler + VHF radar; (B) MSU + VHF radar; (C) radiometric Profiler + MSU + VHF radar.

region, but are seriously in error below about 600 mb. Again, as for the ground-based radiometer, the tropopause height measurements add structure in the 100-200 mb region. Finally, Fig. 3C shows combined retrievals (ground- and satellite-based) that are superior in accuracy to either of the separate retrievals.

The rms errors for the three combinations are shown in Fig. 4A-C:

A. Ground-based radiometer and VHF radar. Note the large improvement in retrieval accuracy, ~2 K rms, near tropopause pressures (~300 to 100 mb), when tropopause height measurements are added. However, retrieval accuracy above 300 mb is poor.

B. MSU + VHF radar. Again, note the ~2 K rms improvement of MSU results when the tropopause height measurements are inserted. Here, retrieval accuracy below about 700 mb ranges from almost 3 to 6 K rms.

C. Ground-based radiometer + VHF radar + MSU. The solid curve, representing the combined radiometric systems, is improvement over either of the pure radiometric results of Fig. 4A or B, except in the vicinity of the tropopause. A further improvement is achieved by adding the radar's measurement of tropopause height, as shown by the dashed curve in this figure. Except for a narrow pressure region near 200 mb, the rms differences are less than 2 K from the surface to

30 mb. It should be noticed that below 500 mb, retrieval accuracy of the combined system is slightly degraded relative to that of the Profiler. We suspect this anomaly occurs because the degraded "effective noise level" of the MSU channels are larger than the value assumed in calculating retrieval coefficients (0.5 K). When we used an empirically determined noise covariance matrix in the December 1981 through December 1982 results, this degradation did not occur (see Fig. 2).

6. CONCLUSIONS

Computer simulations of Westwater and Grody (1980) showed that a combination of ground-based and satellite microwave radiometers could lead to an effective temperature sensing system by overcoming some of the separate weaknesses of each system. These predictions showed the accuracy of the ground-based system degrades rapidly above 500 mb, a region where the MSU retrieval accuracy is good; conversely, the MSU accuracy is poor below 500 mb, a region of good coverage by the Profiler. Our experimentally achieved rms temperature retrieval errors, based on 460 cases, are close to the earlier theoretical predictions.

Passive temperature retrievals from the combined ground-based radiometers and MSU demonstrated accuracy that is approaching operational requirements for synoptic scale numerical forecasting. Retrievals of geopotential heights, in the lowest 500 mb, are competitive with radiosondes. However, as with most passive retrievals, the vertical resolution of recovered profiles is poor. We have shown here that tropopause height information obtained from an active sensor (VHF radar) improved the resolution of profiles derived from each of three separate sensors. An analysis of this technique, using a much larger data set than that of March 1981, is now under way.

In addition to improving profiles by using tropopause height measurements, Gage and Green (1982) suggested a technique from which stratospheric temperature gradients could be obtained directly from the power returns of a calibrated VHF radar. Such a technique could lead to a highly effective combination of active and passive sensors.

REFERENCES

Gage, K. S., and J. L. Green, 1979: Tropopause detection by partial specular reflection with very-high-frequency radar. Science, 203, 1238-1239.

_____, and _____, 1982: A technique for determining the temperature profile from VHF radar aobservations. J. Appl. Meteor., 21, 1146-1149.

Grody, N. C., 1983: Severe storm observation using the Microwave Sounding Unit. J. Climate Appl. Meteor., 22, 609-625.

Hildebrand, P. H., and R. S. Sekhon, 1974: Objective determination of the noise level in Doppler spectra. J. Appl. Meteor., 13, 808-811.

Hoehne, W. E., 1980: Precision of National Weather Service upper air measurements. NOAA Tech. Memo. NWS T&ED-16. [NTIS No. PB81-108136.]

Hogg, D. C., M. T. Decker, F. O. Guiraud, K. B. Earnshaw, D. A. Merritt, K. P. Moran, W. B. Sweezy, R. G. Strauch, E. R. Westwater, and C. G. Little, 1983: An automatic profiler of the temperature, wind, and humidity in the troposphere. J. Climate Appl. Meteor., 22, 807-831.

Strand, O. N., and E. R. Westwater, 1968: Minimum rms estimation of the numerical solution of a Fredholm integral equation of the first kind. SIAM J. Numer. Analy., 5, 287-295.

Westwater, E. R., and N. C. Grody, 1980: Combined surface- and satellite-based microwave temperature profile retrieval. J. Appl. Meteor., 19, 1438-1444.

_____, M. T. Decker, A. Zachs, and K. S. Gage, 1983: Ground-based remote sensing of temperature profiles by a combination of microwave radiometry and radar. J. Climate Appl. Meteor., 22, 126-133.

_____, Wang Zhenhui, N. C. Grody, and L. M. McMillin, 1984: Remote sensing of temperature profiles from a combination of satellite-based Microwave Sounding Unit and ground-based Profiler observations. Submitted to J. Climate Appl. Meteor.

ATMOSPHERIC AND SURFACE SHORT-WAVE ENERGY BALANCE FROM COMBINED SATELLITE AND GROUND-BASED DATA

C. G. Justus

School of Geophysical Sciences
Georgia Institute of Technology
Atlanta, Georgia 30332-0340

1. INTRODUCTION

After an early introduction by Fritz et al. (1964), the use of coordinated satellite and ground-based observations for atmospheric absorption and transmission studies has seen only relatively limited use. Hanson et al. (1967), Hanson (1971), Major (1976), and Raschke and Preuss (1979) all have used long-period (e.g. monthly averaged) ground-based data with similarly long-period-averaged satellite-measured reflected energy to derive absorption within the entire atmospheric column. These investigators made no attempt to examine seasonal, synoptic or diurnal variations, or to separate clear-sky from cloud absorption processes. Platt et al. (1980) used hourly time scale data from GOES satellite and surface radiometers and lidar to study absorption and reflection processes in cirrus clouds. Other studies (e.g. Cox and Griffith, 1979 a,b) have been intense, but fairly brief, specialized studies conducted in connection with major field programs such as GATE. The work reported here is a preliminary study of coordinated data from the GOES-East satellite and surface pyranometers at 11 sites throughout the eastern portion of the United States, for a period of five months.

1.1 Satellite Data Base

Since May 1980, for a set of up to 99 locations, within the coverage of GOES-East, the NOAA Satellite Applications Lab has collected hourly sets of VISSR Data Base (VDB) data, consisting of mean brightness, standard deviation in brightness, and center-pixel brightness for both VIS and IR, averaged over a 5x5 array of 8-km resolution pixels at each target site. Column precipitable water values, from the NMC upper air data, are also merged with this data set.

Data from 11 VDB target sites, coincident with the location of pyranometers in the NOAA insolation monitoring network, were selected for use in this study. These sites are: Montgomery, AL; Tallahassee, FL; Dodge City, KS; Lake Charles, LA; Columbia, MO; Raleigh, NC; Bismark, ND; Omaha, NB; Brownsville, TX; Midland, TX; and Madison, WI. From data of Kung et al. (1964), the surface albedo at these sites varies from 0.12 to 0.19, with an average value of 0.15. Data for the period August-December 1980 have been examined here. Study of later periods is partially hampered by the lack of continued data from the surface pyranometer network.

1.2 Ground Based Data

Coincident data from the same 11 sites and same time period have been combined with the GOES VDB data and used in this preliminary study. The ground-based observations consist of hourly total global radiation (on a horizontal surface) and observer-determined amounts of total cloud and total opaque cloud. From the use of GOES imagery to estimate surface insolation (Tarpley, 1979; Justus and Tarpley, 1983), it has been determined that the 5x5 pixel average brightness from the satellite image, measured over a short time period, compares reasonably well with hourly total radiation measured at the site in the center of the target array (better than the correspondence with the satellite-measured brightness at the single 8-km pixel centered on the surface site).

2. ANALYSIS PROCEDURES

2.1 GOES Sensor Calibration

The nominal (pre-launch) calibration of the visible sensor on the GOES VISSR system can be expressed as

$$I/I_o = k\,C^2 \quad , \qquad (1)$$

where I/I_o is the radiance received relative to that which would be received from a 100% reflective Lambertian surface, under full (directly overhead) solar illumination. For 8-bit resolution counts C, the value of k is nominally $k = 1/63^2$. Norton et al. (1980) have used observations of the dark side of the earth and from an on-board calibration mirror to determine a calibration of the form

$$I/I_o = k\,(C^2 - a) \qquad (2)$$

where a is a "dark counts" offset in the actual sensor measurements. From coincident observations with GOES and Nimbus 7 ERB broad-band data, Minnis and Harrison (1984) have determined an equivalent broad-band calibration for the VISSR sensor, which can be represented by

$$I/I_o = a + bC + cC^2 \quad , \qquad (3)$$

with values, determined by least-squares fit to their reported data, determined to be a = -64.6, b = 16.6, c = 0.704 (for C in 8-bit counts). This calibration curve keeps the "dark-counts" and upper calibration point from the on-board mirror consistent with the results of Norton et al. and yields an average value for inferred surface albedo at the study sites of 0.15, consistent with the Kung et al. (1964) estimates. Use of this calibration also results in inferred cloud reflectances which are consistent with those determined from the Nimbus 7 ERB by Taylor and Stowe (1984).

2.2 Analysis of the Coordinated Data

Conceptually, the analysis method is quite simple: (1) Use the surface pyranometer data at a given site and time to measure the transmitted flux to the surface, F_t. (2) Use the simultaneous GOES reflectance measurement for the same site and time to measure the reflected flux, F_r, out the top of the atmosphere. (3) Combine these measurements with the known incoming flux, F_i, at the top of the atmosphere to calculate the corresponding absorbed flux, F_a, by the relation

$$F_a = F_i - F_r - F_t\ (1 - r_g) \quad , \qquad (4)$$

where r_g is the surface reflectivity (albedo). In terms of planetary reflectivity, $r_p = F_r/F_i$, and atmospheric transmissivity to the surface, $T = F_t/F_i$, equation (4) can be written as

$$A = (1 - r_p) - T(1 - r_g) \quad , \qquad (5)$$

where A is the total atmospheric column absorptivity ($A = F_a/F_i$).

If the data are sorted into clear cases and cloudy cases, based on the ground-observer reported cloud amounts, separate transmissivities and absorptivities in clear and cloudy cases (T_{clr}, A_{clr}, T_{cld}, A_{cld}) may be evaluated.

In practice, the analysis according to equation (5) is complicated by the fact that the GOES sensor measures directional radiance $r(Z_o, Z, \phi) = r_p\ f(Z_o, Z, \phi)$, where f is the bi-directional reflectance factor, and by the fact that narrow-band to broad-band corrections must be taken into account. For both of these problems, some analysis with an appropriate radiative transfer model is necessary for the proper interpretation of the data. Some results with such a model are presented in the following section.

2.3 Radiative Transfer Model Analysis

The spectral radiative transfer model used here has been described by Justus and Paris (1984). The model includes spectral absorption by gaseous constituents, molecular (Rayleigh) scattering, and both scattering and absorption by aerosols. The spectral values of aerosol single-scattering albedo and asymmetry factor can be selected from parameterizations of the values of Shettle and Fenn (1979), for either urban or rural aerosols, and as a function of relative humidity. Aerosol optical depth can be specified at 500 nm, with spectral variation according to a selected value of Angstrom wavelength exponent. Figure 1 shows a comparison between the spectral-modeled planetary reflectance, in the GOES VISSR wavelength band, with that from the Dave (1978) model (Dave results supplied by Paul Davis, Research and Data Systems, Inc.). Figure 2 shows a comparison between broad-band and VISSR-band planetary reflectance, calculated with this spectral model, for various uniform surface reflectances, and at various solar zenith angles. Measured GOES reflectances at a given site and time, together with the corresponding precipitable water values, are used in the model to infer the surface reflectivity for the site. Further study will be required to best determine the diurnal and seasonal variations of surface reflectance, and their impact on analyses such as the preliminary results reported here.

Figure 1 results were computed for conditions used by Dave: 0.318 cm of ozone, 2.295 cm of precipitable water, and the Dave model C1 aerosol properties (optical depth = 0.1 at 500 nm). Figure 2 results are for 0.34 cm of ozone, 1.42 cm of precipitable water, aerosol optical depth 0.1 (rural model aerosol at 50% relative humidity). Additional comparisons with the model are given in Justus and Paris (1984). Some model refinements not reported there are the addition of a routine to model directional reflectances in clear-sky conditions, and a routine to model spectral fluxes with a simulated cloud layer (treated as a scattering and absorbing layer in the middle of the model atmosphere and computed with a delta-Eddington flux calculation routine).

2.4 Bi-Directional Reflectances

By sorting the GOES reflectance measurements by solar zenith angle Z_o, satellite zenith angle Z, and relative satellite-solar azimuth angle ϕ, directional reflectances, $r_p\ f(Z_o, Z, \phi)$, may be determined. Figures 3-5 compare these results with those from Taylor and Stowe (1984) from the NIMBUS 7 ERB system for clear and cloudy cases. Figure 6 presents values computed with the spectral model for the clear case. Further analysis is obviously required, since comparison of Figures 3, 4, and 6 show the model values agree better with the Nimbus 7 results at low solar zenith angles and with the GOES results at high solar zenith angles.

3. RESULTS

Figures 7-10 show the results of this preliminary analysis of transmissivity and absorptivity in clear and overcast-cloud cases. Solid lines in these figures are empirical regression curves fit to the collection of 11 sites of data results as functions of solar zenith angle and precipitable water amount. The satellite-measured reflectances have been converted to planetary reflectances, r_p, by the use of the empirical bi-directional reflectance factors, $f(Z_o, Z, \phi)$. Satellite-measured reflectances under clear-sky conditions have been used to estimate surface albedoes, r_g, through interpretation with the spectral model, discussed above. The data points in Figures 7-10 were computed with the spectral model for either clear-sky or overcast-cloud conditions, as noted.

Figure 7 compares the clear-sky transmissivity to the surface, T_{clr}, as measured by the pyranometers, with values from the spectral model. Data for low (0-1 cm), medium (1-3 cm), and high (3-5 cm) precipitable water ranges are shown.

For the model results, the aerosol optical depths at 500 nm were taken to be 0.1, 0.25, and 0.4 for the low, medium and high precipitable water cases, respectively. This accounts for hygroscopic effects which cause the aerosol optical depth to increase with humidity, and is consistent with the magnitude of such increases observed from surface measurements made at Georgia Tech. Actual aerosol optical depths for the measured data have not yet been determined. Although the observed variation in T_{clr} agrees generally well with the model variations with solar zenith angle, observed variations with precipitable water are smaller than those for the model results in Figure 7. However, if the hygroscopic effect is not included, and a constant aerosol optical depth of 0.2 is assumed, the model variations with precipitable water are not as large as those observed (as indicated by the arrows in Figure 7).

In Figure 8, the pyranometer-measured transmissivities under overcast-cloud conditions, T_{cld}, are plotted versus $\cos(Z_o)$, for various values of satellite-measured planetary reflectance (an approximate measure of cloud albedo). As expected, T_{cld} decreases rapidly with increasing cloud albedo, but the current model results tend to overestimate the measured T_{cld} values for the low cloud albedo cases.

Measured and modeled column atmospheric absorptivities under clear-sky conditions, A_{clr}, are shown in Figure 9. The form of the observed variation with solar zenith angle is generally as expected from the model results, although the measured values of A_{clr} are somewhat higher than expected, and the variation with precipitable water is not as pronounced as expected from the hygroscopic aerosol (PW-dependent optical depth) model results. However, model values computed by assuming a fixed optical depth of 0.2, indicated by the arrows in Figure 9, show less variation of A_{clr} with precipitable water than the observations.

Figure 10 shows total atmospheric column absorptivity, A_{cld}, for the overcast-cloud cases. As in the clear-sky case, the observed values of A_{cld} are somewhat higher than expected from the model results, averaging about 30%, compared to model values of about 20%. The form of the variation with solar zenith angle and the amount of variation with precipitable water, are approximately as expected from the model, however.

ACKNOWLEDGEMENTS

Much of the work reported here was done while the author was on an Intergovernmental Personnel Act (IPA) assignment with the NOAA Satellite Applications Lab of the National Environmental Satellite Data and Information Service. Special thanks go to Dr. J. D. Tarpley, NOAA Project Director of the AgRISTARS program, and Dr. Earl Droessler, former Director of the NOAA Office of University Affairs for their support for this IPA assignment.

REFERENCES

Cox, S. K., and K. T. Griffith (1979a): J. Atmos. Sci, 36, 576-585.

Cox, S. K., and K. T. Griffith (1979b): J. Atmos. Sci., 36, 586-601.

Dave, J.V. (1978): Solar Energy, 21, 361-369.

Fritz, S. et al. (1964): J. Atmos. Sci., 21, 141-151.

Hanson, K.S. (1971): "Studies of cloud and satellite parameterization of solar irradiance at the earth's surface", NOAA Miami Workshop on Remote Sensing, May 29-31.

Hanson, K.S. et al. (1967): Monthly Wea. Rev., 95, 354-362.

Justus, C.G. and M. V. Paris (1984): "A model for solar spectral irradiance at the top and bottom of a cloudless atmosphere", submitted to J. Clim. Appl. Meteorol.

Justus, C. G. and J. D. Tarpley (1983): "Accuracy and availability of solar radiation data from satellites and from forecast estimates" Fifth AMS Conf. on Atmos. Radiation, Oct. 31-Nov. 4, Baltimore.

Kung, E. C. et al. (1964): Month. Wea. Rev., 92, 543-546.

Major, G. (1976): Beitr. Phys. Atmos., 49, 212-215.

Minnis, P. and E. G. Harrison (1984): "Diurnal variability of regional clouds and surface radiation parameters derived from GOES data, Parts I and II", J. Atmos. Sci., in press.

Norton, C. C. et al. (1980): J. Appl. Meteor., 19, 633-644.

Platt, C. M. R. et al. (1980): Month. Wea. Rev., 108, 195-204.

Raschke, E. and H. J. Preuss (1979): Meteorol. Rsch., 32, 18-28.

Shettle, E. O. and R. W. Fenn (1979): Models for the aerosols for the lower atmosphere and the effects of humidity variations on their optical properties", AFGL-TR-79-0214, Env. Res. Paper No. 676, 94.

Tarpley, J.D. (1979): J. Appl. Meteorol., 18, 1172-1181.

Taylor, V. R. and L. L. Stowe (1984): "Reflectances of uniform earth and cloud surfaces derived from Nimbus 7 ERB", J. Geophys. Res., in press.

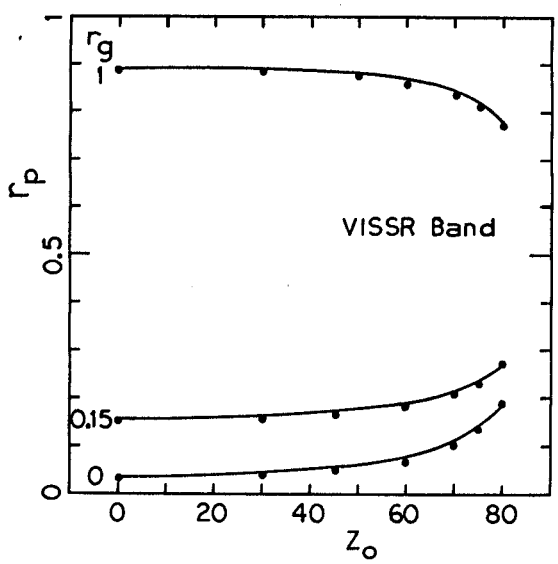

Fig. 1. *Planetary albedo, r_p, versus solar zenith angle for the VISSR band for various surface reflectances, r_g. Solid lines are from the spectral model (Justus and Paris, 1984). Dots are from the Dave (1978) model.*

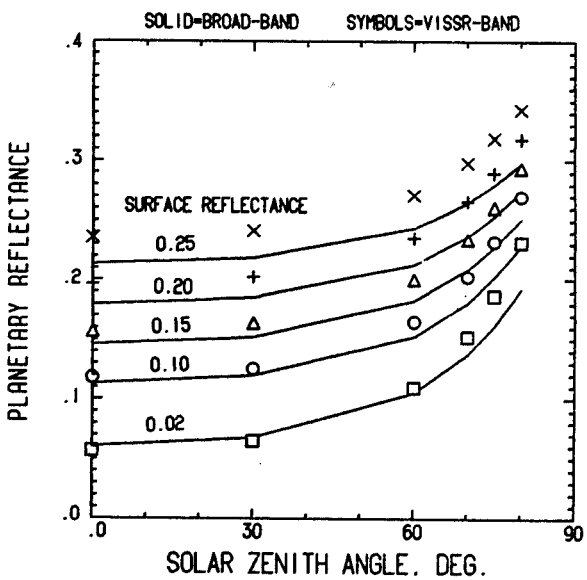

Fig. 2. *Comparison of VISSR-band (symbols) and broad-band (solid lines) planetary reflectances for various surface reflectance values.*

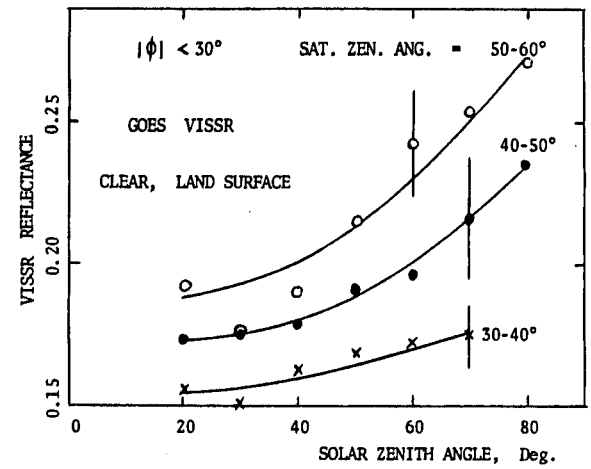

Fig. 3. *Measured directional reflectance from the GOES VDB data set for clear-sky cases.*

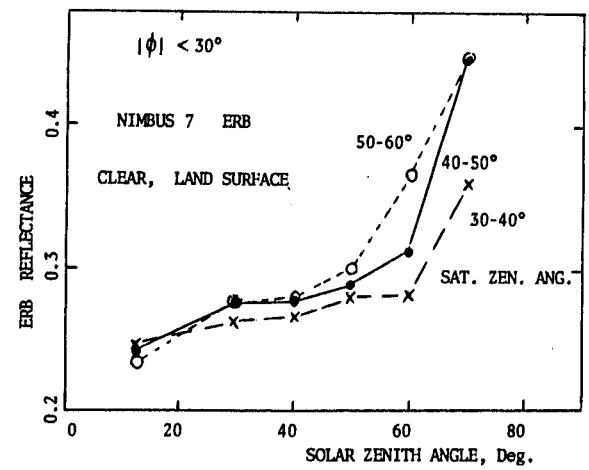

Fig. 4. *Directional reflectances from the Nimbus-7 ERB system for all clear-sky, land-surface cases (Taylor and Stowe, 1984).*

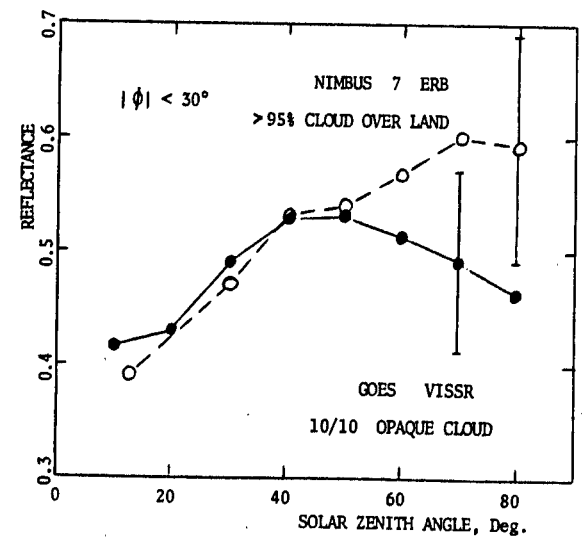

Fig. 5. *As in Figures 3 and 4 for overcast-cloud cases.*

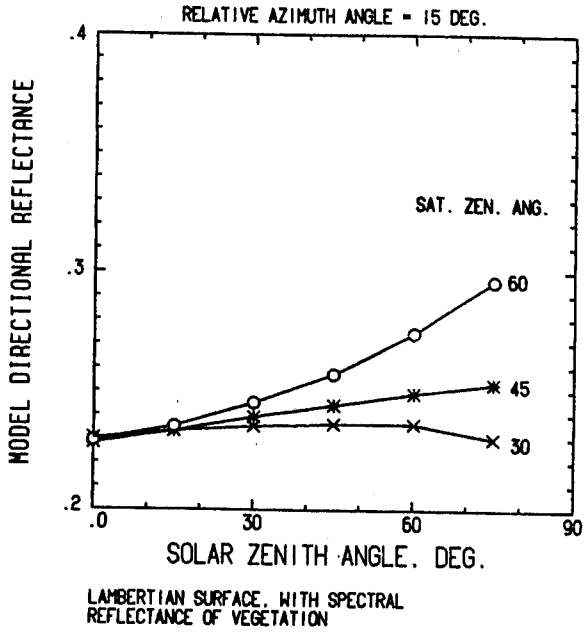

Fig. 6. *Directional reflectance from the spectral model.*

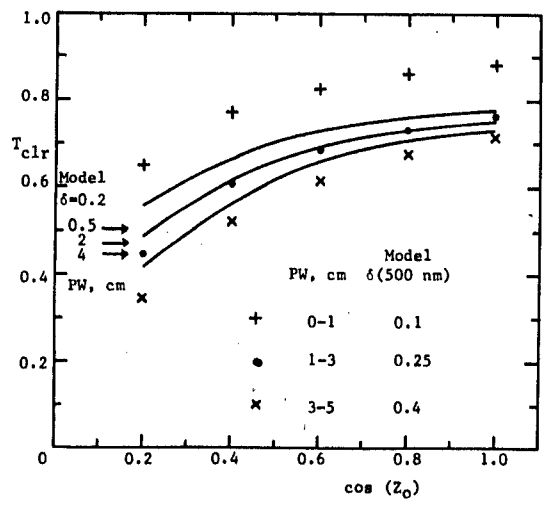

Fig. 7. *Clear-sky transmissivity, T_{clr}, versus cosine solar zenith angle, for various precipitable water ranges. Solid lines = pyranometer measurements; symbols = model values.*

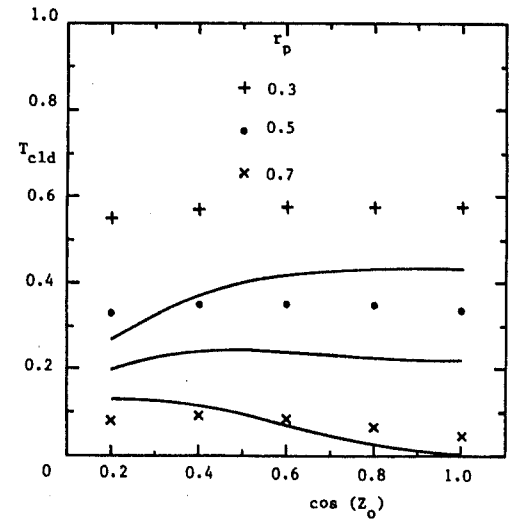

Fig. 8. *Overcast-cloud transmissivity, T_{cld}, versus cosine solar zenith angle for various planetary reflectance (cloud albedo) values.*

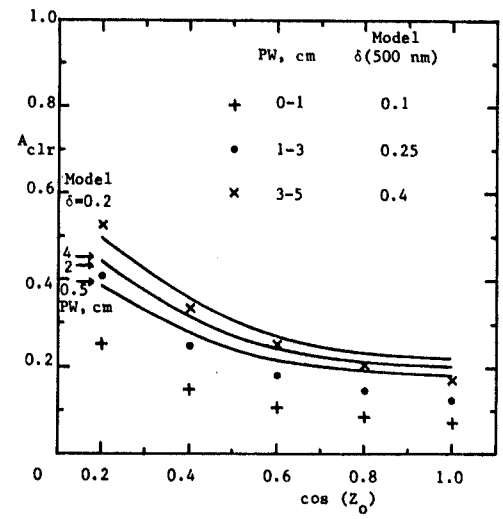

Fig. 9. *Atmospheric column absorptivity from combined satellite and ground-based data for clear-sky conditions and various precipitable water values. Solid lines = measured; symbols = modeled.*

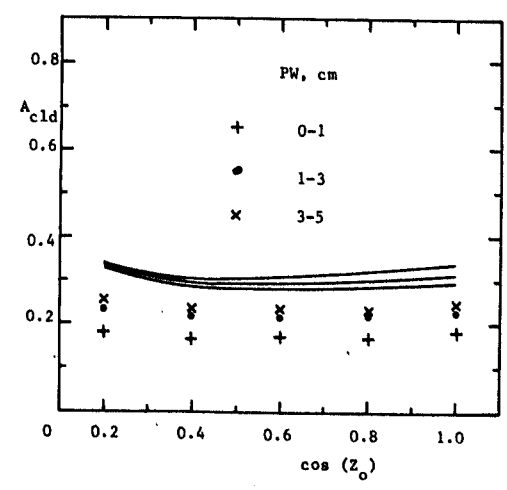

Fig. 10. *As in Figure 9 for overcast-cloud conditions.*

THE DETECTION AND LOCATION OF LIGHTNING FROM SPACE

H. J. Christian and W. W. Vaughan
NASA/Marshall Space Flight Center, AL
J. C. Dodge
NASA Headquarters/Washington, D.C.

1. Introduction

A lightning mapper sensor as presently conceived will detect and locate lightning over large areas of the earth's surface, mark the time of occurrence and measure the radiant energy. It will basically be a calibrated lightning imager. Scientific importance of these measurements include the fact that this type of information is not presently available on a large scale basis. With a mapper, scientists will, for the first time, be able to study the electrosphere from scales on the order of the earth's diameter down to the size of individual storms (10 km). They will be able to study both the spatial and temporal evolution of lightning activity on a continuous basis and relate the lightning measurements to other observables such as cloud images, radar returns, and the standard meteorological variables on both the synoptic and meso-scale. The ability to study lightning activity in continental storms will be improved because a lightning mapper will detect all types of lightning, will provide near uniform spatial coverage and detection efficiency and will disseminate the information in a readily usable form. On the larger scale, a lightning mapper will provide information that can only be obtained with a space-based instrument. Lightning detection in data sparse regions such as the tropics and ocean areas will be possible. Lightning activity will be studied on a nearly global basis. The evolution of storms as they develop and propagate will be compared on a regional basis. Lightning climatology will change from its present thunderstorm day based on audible thunder to a true measure of lightning activity based on flash density as measured in time and space.

Table 1, a summary from Davis, et al. (1983), shows a partial list of scientific activities that would be possible if a lightning mapper possessing the basic attributes of continuous large area coverage, storm system spatial resolution, high detection efficiency, high temporal resolution and a measurement of flash intensity were available. Figure 1 compares the proposed lightning mapper sensor capabilities with earlier satellite measurements. Of particular importance is (1) the capability for detecting lightning on a continuous basis rather than during very limited periods; (2) the ability to detect nearly all lightnings within the sensor field of view (90%) rather than very poor detection efficiencies; and (3) a spatial resolution on the order of 10x10 km rather than the hundreds of km that were typical of the pioneering lightning sensors.

SCIENTIFIC OPPORTUNITIES POSSIBLE WITH MAPPER IN GEOSTATIONARY ORBIT

- MAGNETOSPHERIC AND IONOSPHERIC RESEARCH
  - RELATIONSHIP BETWEEN LIGHTNING AND WHISTLERS
  - VLF–ELF ELECTROMAGNETIC NOISE
  - VLF WAVES
  - SCHUMANN RESONANCES
- EARTH'S ELECTRIC CIRCUIT
  - FAIR WEATHER ELECTRICITY
  - IONOSPHERIC CURRENTS
  - ATMOSPHERIC CURRENTS
- ATMOSPHERIC CHEMISTRY
  - NITROGEN FIXATION
  - OZONE REACTIONS
  - RADICAL AND OXIDANT FORMATION
  - HCN FORMATION
  - STRATOSPHERIC CHEMISTRY
- STORM PHYSICS
  - LIGHTNING ACTIVITY/STORM INTENSITY
  - OCEAN LAND LIGHTNING RATIO
  - HURRICANE ELECTRIFICATION
  - LIGHTNING/TORNADIC ACTIVITY
  - INITIAL ELECTRIFICATION
  - SYMPATHETIC LIGHTNING
  - WARM CLOUD LIGHTNING
- SOLAR–TROPOSPHERIC EFFECTS
  - SOLAR VARIABILITY/LIGHTNING RATES
  - ELECTRICAL CONNECTION

Table 1. Examples of scientific disciplines that require lightning mapper data.

These orders of magnitude improvements in overall sensor performance are rather difficult to achieve. The major difficulty in the detection and location of lightning from geostationary orbit, given the detection efficiency and resolution specified in Figure 1, is caused by the strong background illumination produced by sunlight reflecting from the tops of clouds. The high cloud albedo makes this background much brighter than the illumination produced by lightning. Because the lightning signal tends to be buried in the "background noise," the only way to detect lightning during daytime is to implement techniques that increase the lightning signal relative to the cloud signal. Fortunately, the character of the two signals is much different. While the lightning pulse duration is on the order of 0.5 msec, the background illumination tends to be constant on a time scale of seconds; thus one could use temporal filtering to attenuate the background "noise" relative to the lightning signal.

Another difference between the signals is that the lightning signal is composed of predomi-

SATELLITE LIGHTNING EXPERIMENTS

SATELLITE	SENSOR	ORBIT	PERIOD	LIGHTNING POWER SENSITIVITY (WATTS)	FOOTPRINT
[illegible]	PHOTOMETERS		MODULATED NIGHT	$\sim 10^{[illegible]}$	
VELA V	PHOTODIODES	$1.1 \times 10^{[illegible]}$ km	DAY – NIGHT	$10^{11} - 10^{12}$	VERY WIDE FIELD OF VIEW
[illegible]	SCANNING RADIOMETER	830 km	LOCAL MIDNIGHT	SENSITIVE*	140 km
[illegible]	12 PHOTODIODE ARRAY	830 km	LOCAL MIDNIGHT	$10^{8} - 10^{10}$	750 x 700 km
[illegible]	0.1° PHOTODIODE		DAWN/DUSK	$4 \times 10^{8} - 10^{12}$	1300 km DIA.
[illegible]	4 NARROW BAND RECEIVERS		DAY/NIGHT	NV	IONOSPHERE DEPENDENT (TYPICALLY–HUNDREDS OF km)
SHUTTLE–DOD[illegible]	PHOTOCELL PLUS FILM	100 km	SHUTTLE OPERATIONS	NA	VARIABLE
LIGHTNING MAPPER PROPOSED	CCD ARRAY	GEO–STATIONARY	CONTINUOUS COVERAGE	$10^{8} - 10^{[illegible]}$	10 km

Figure 1. Characteristics of previous satellite lightning experiments.

nately discrete emission lines, while the background illumination closely follows the black-body-like continuum of the sun; thus the requirement for an optimized spectral filter. Finally, the lightning tends to illuminate a smaller area than the background and this illuminated area tends to change with each event. A form of spatial filtering can be used which matches the field of view of each detector to the typical cloud top area illuminated by a lightning stroke.

Even after using these three filtering techniques, the ratio of background illumnination to lightning signal may still exceed 50 to 1 at the focal plane. For this reason, post-detection filtering must be implemented. Feasibility studies performed by Hughes (V. Norwood, 1983), and TRW (Eaton, et al. 1983) reviewed a number of post-detection background removal techniques. They both selected analog background subtraction schemes similar to the one illustrated in Figure 2. This approach utilizes a modified frame-to-frame subtraction or adaptive filter approach. An important point to understand is that the power of any post-detection technique is totally limited by the lightning signal to background noise ratio coming off the focal plane.

2. Sensor Components

The design of the required filtering methods is conceptionally straightforward. However, the actual implementation can be quite complex. Figure 2 is a block diagram of probable sensor components. The optics system is expected to consist of a fairly fast lens using either reflective or refractive elements and a narrow band interference filter, both of conventional design. The emission line centered filter performs the previously described spectral filtering. The lens must be fast to provide high throughput because of the weak signals arriving at geostationary altitude.

The focal plane assembly (FPA) is the heart of the lightning mapper. This is the component that detects an incident photon flux and outputs an electrical signal. Together, the lens and the focal plane array determine the spatial resolution of the mapper. The temporal filtering performance is determined by the focal plane integration time and readout rate.

The focal plane assembly will consist of a large mosaic array of either photodiodes or charge coupled devices (CCD). If the FPA is

SENSOR COMPONENTS

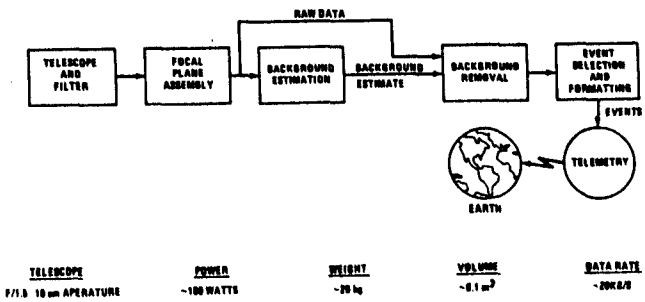

Figure 2. Block diagram of lightning mapper sensor components.

operated in the charge integration mode, then each individual sensor (or pixel) must be sufficiently large to store the charge produced by both the background and lightning signals. In addition, a physically large pixel is required to produce a big signal so that an adequate signal to noise ratio can be acheived. The requirement for large pixel size and a large number of pixels for wide area, 10 km resolution coverage, would require too large an array size to be produced economically. Hence, either multiple focal plane assemblies, each with its own lens system, or multiple mosaic array chips butted together to form a single large assembly will be required.

Independent of the specific focal plane geometry that is implemented, the major challenge in the focal plane design is the development of a high speed readout technique. As discussed previously, the background signal can be attenuated relative to the lightning signal if one takes advantage of the temporal behavior of the signals. In an integrating sensor, the only means to control this parameter is the frame integration time. The integration time specifies how long a particular pixel accumulates a signal between readouts. The lightning signal to noise ratio improves as the integration period approaches the pulse duration. However, if the integration period becomes too short, the lightning signal tends to be split between successive frames. Frame splitting actually decreases the signal to noise ratio. Instrumented U-2 measurements indicate that the median optical lightning pulse width, when viewed from above, is 400 usec, (Christian, et al., 1983). Based on this pulse width, a TRW analysis (Eaton, et al., 1983) suggests that a one msec frame time is appropriate for minimal pulse splitting and high lightning detectability.

One thousand frames per second is extremely fast for an imaging sensor. If the focal plane array contained 500,000 pixels, the total data rate coming off the focal plane would be 5×10^{8} pixels per second. No commercially available mosaic array detector is capable of clocking data out at this rate. Thus, the important technological development for a lightning mapper sensor will be a custom focal plane array that can be

accessed at the required rates and a data processor capable of compressing the data to rates that can be handled by conventional telemetry systems.

Since FPA clocking rates are presently limited to around 5 MHz, multiple output lines will be required. The data coming off the focal plane will have to be processed in parallel. If the total data rate were 5×10^8 pixels per second, then a minimum of 100 parallel output lines and data processors would be required. Since presently available solid state arrays have only one output line, any array used in the lightning mapper will require modification to include the multiple readout lines. This type of circuit modification is technically straight forward and is well within the present state-of-the-art.

Figure 3 shows a possible configuration for the data processor. This circuit, by subtracting the background and digitizing only lightning events, would reduce the transmission data rate by a factor 10^6 to a rate on the order of 20 kbits/sec. Background subtraction is performed by first generating a pixel by pixel background estimate. That is, an independent running average of the background signal of each pixel is maintained. This background estimate for a particular pixel is subtracted, using a difference amplifier, from the the signal of the same pixel as it is clocked off the focal plane. If the output from the difference amplifier is greater than a predetermined threshold, then this output is accepted as a lightning signal. The amplitude of the lightning signal is then digitized and a digital word that represents the X-Y position of the specific pixel is determined.

The final signal processing requires the multiplexing of the digital lightning signal, the event address, a time stamp and housekeeping information into an event queue. Queueing is needed to smooth the events, which may occur in bursts, into a data rate which is consistant with a larger term average. From the event buffer, the data can be formatted into a serial bit stream and transmitted to ground stations.

3. Sensor Performance

The overall performance of the lightning mapper will be determined by a number of parametric tradeoffs. The major factors that will determine the ability of the lightning mapper to detect lightning during daytime will be the overall sensor throughput and the ratio of lightning signal to background noise coming off the focal plane. The signal to noise ratio and total signal throughputs are determined by many sensor parameters including lens speed, detector quantum efficiency, filter bandwidth, frame time, spatial resolution, etc. Figure 4 lists some of the sensor parameters that extensive radiameteric analyses indicate might be resonable.

The major objective of all the tradeoff analyses is to maximize the sensor lightning detection efficiency. The goal is to detect 90% of all lightnings that occur within the sensor field of view. Figure 5 shows how changes in certain sensor parameters effect the detection efficiency which is directly related to the

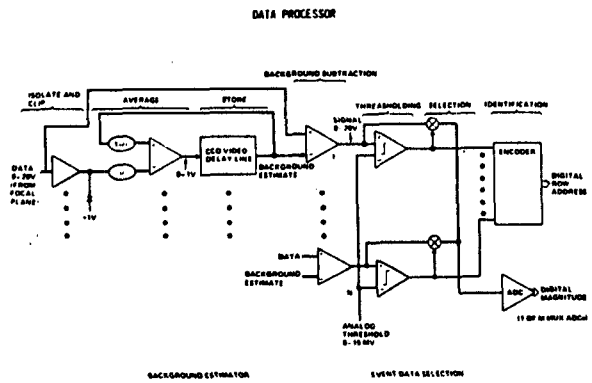

Figure 3. Lightning data processing circuit.

SENSOR PARAMETERS AND PERFORMANCE

LENS f/NUMBER	–	1.5
DIAMETER	–	10 cm
SPATIAL RESOLUTION	–	10 km
FILTER WAVELENGTH	–	8653 Å
FILTER BANDWIDTH	–	8 Å
FRAME TIME	–	1 msec
FOCAL PLANE ARRAY		
NUMBER OF PIXELS	–	650 x 650
PIXEL SIZE	–	50 μm
FULL WELL CAPACITY	–	10^8 ELECTRONS
BACKGROUND REMOVAL	–	ANALOG TIME DOMAIN FILTERING
SIGNAL TO NOISE RATIO	–	~6
LIGHTNING DETECTION EFFICIENCY	–	80–90%
DATA RATE	–	~20 k bits/sec (Buffered)

Figure 4. Example of possible sensor parameters.

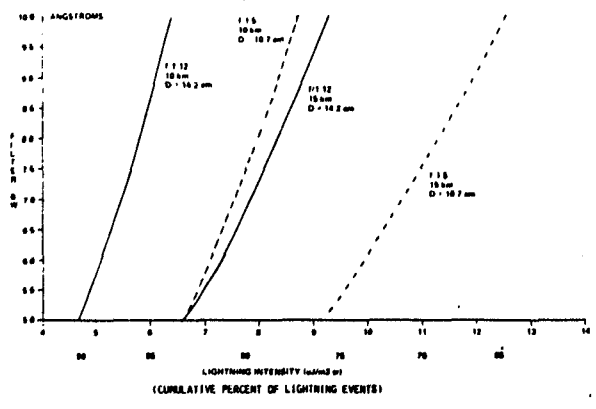

Figure 5. Lightning intensity versus filter bandwidth for constant SNR.

strength of the lightning signal. For example, a sensor with the values listed in Figure 4 should detect approximately 80% of all lightnings within its field of view. If the filter bandwidth were changed to from 8A to 5A and the lens speed were changed from F/1.5 to F/1.12, then the detection efficiency would improve to 90%. Obviously there are many variables such as weight, power, cost, filter bandpass shifts, etc. that effect the overall system design in such a way that maximum sensor performance may not be desirable.

The final design configuration of a lightning mapper will be driven by detailed scientific requirements, by specific capabilities of the platform into which the sensor is integrated and by overall economic constraints. A major result of the lightning mapper sensor feasibility studies has been the determination that the combination of modern solid state mosaic focal plane arrays with extensive onboard signal processing provides a powerful technique for the detection of weak, background contaminated, signals. The technology being applied to the lightning mapper problem should be easily adaptable for other atmospheric remote sensing applications. The resulting steering sensors would have significant advantages over present scanning systems.

References

Christian, H. J., R. L. Frost and S. J. Goodman, 1984: "Optical Characteristics of Lightning as Measured From Above Cloud Tops." Preprint Volume, VII International Conference on Atmospheric Electricity, Albany, NY.

Davis, M. H., M. Brook, H. Christian, B. G. Heckes, R. E. Orville, C. G. Park, R. G. Roble and B. Vonnegut, 1983: "Some Scientific Objectives of a Satellite-Borne Lightning Mapper." Bull. Am. Meteor. Soc., Vol 64, 114-119.

Eaton, L. R., C. W. Poon, J. C. Shelton, N. P. Loverty and R. D. Cook, 1983: "Lightning Mapper Sensor Design Study." NASA Contractor Report, NASA CR-170909, Marshall Space Flight Center, AL.

Norwood, V., 1983: "Lightning Mapping Sensor Study." NASA Contractor Report, NASA CR-170908, Marshall Space Flight Center, AL.

OBJECTIVE SCATTEROMETER WIND AMBIGUITY REMOVAL USING SMOOTHNESS AND DYNAMICAL CONSTRAINTS

Ross N. Hoffman

Atmospheric and Environmental Research, Inc.
Cambridge, MA 02139

1. INTRODUCTION

In this study a variational analysis method (VAM) is used to remove the ambiguity of the SEASAT-A Satellite Scatterometer (SASS) winds. At each SASS data point not one but 2, 3 or 4 wind vectors (termed ambiguities) are retrieved. The VAM is basically a least squares method for fitting data; the problem may be nonlinear. The VAM admits a variety of constraints, e.g., smoothness. The variational analysis is the minimizer of an objective function S which is the sum of a sum of squares due to lack of fit to the data and terms which measure how poorly other constraints are met. When one constraint is smoothness, a measure of roughness is added to the objective function. A simple measure of roughness is the integral of the square of the Laplacian. Each constraint is weighted by a factor which depends on the accuracy of the constraint. This work extends an earlier study (Hoffman, 1982; hereafter referred to as DM). In DM only surface wind data were used; here smoothness and dynamical constraints on the surface wind analysis are also used.

The method used in this study is conceptually very much like that of Wahba and Wendelberger (1980). However, the problem of analyzing the SASS data is inherently nonlinear. The constraints used require the analysis to be smooth and dynamically consistent. These constraints are expected to hold only approximately and thus enter the problem as "weak" constraints in the sense of Sasaki.

The SEASAT scatterometer actually measured radar backscatter (σ^0) at a frequency near 14.6 GHz from the ocean surface with forward and backward pointing antennas on either side of the satellite. Measurements made by the forward and backward pointing antennas at a single ocean location may be inverted to obtain surface winds; excluding nadir data locations 2, 3 or 4 wind vectors are obtained at each data location (Jones et al., 1982; Schroeder et al., 1982). At nadir locations only the wind magnitude is retrieved. Two procedures have been used to group the σ^0 measurements for inversion: (1) pairing measurements, one from each antenna and (2) binning all measurements within a small (e.g., 1° × 1°) geographic region. Examples using paired SASS winds are presented below. These data are from the GDR (Geophysical Data Record) data sets obtained from EDIS (now NESDIS-NOAA).

The ambiguity of the scatterometer winds is mostly of a directional nature. The variation of wind speed among the ambiguities (Fig. 1) is generally well within the expected errors of the scatterometer wind magnitudes (± 2 m/s or 10%). Since the variation in wind speed among the ambiguities is small, the ambiguity average or rms wind speed is representative. For convenience we have taken the scatterometer wind speed to be the ambiguity rms wind speed.

The objective function S is defined below in Section 2. Minimizing S yields the analysis. The analysis procedure was tuned and its sensitivity was examined using the QE II case as an example; the procedure is applied to a second case in Section 3. A discussion of the method and of the feasibility of applying the method to global data sets follows in Section 4.

2. THE OBJECTIVE FUNCTION

The VAM finds the best fit to the data and constraints by minimizing the objective function S. Thus S must accurately measure lack of fit to the data and constraints. Since S essentially defines what is meant by "best fit" a proper specification of S is crucial to the success of this method.

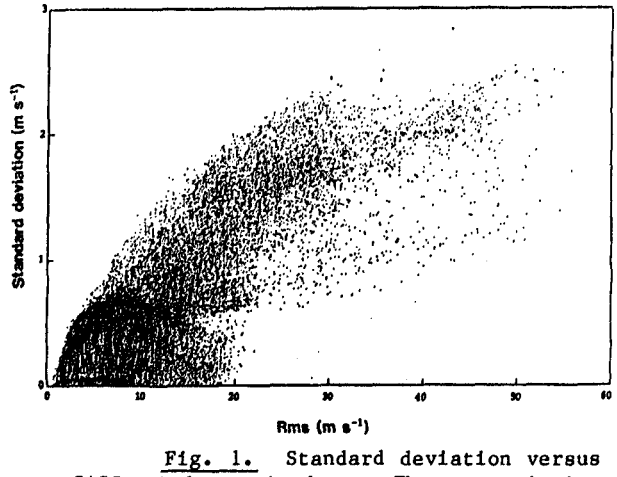

Fig. 1. Standard deviation versus rms SASS wind magnitudes. These statistics are defined in terms of an average over the SASS wind ambiguities for a single SASS data location. Data used are for 00 h - 06 h GMT 6 September.

Table 1. Measures of lack of fit. The objective function is a weighted sum of the S_i; each S_i measures lack of fit to data or a constraint. The mnemonic devices are used in the text and Table 2 in place of integer values for i.

i	Data/constraint used in S_i	Mnemonic
1	Previous forecast	FORE
2	Conventional surface wind	CONV
3	SASS wind vectors	SASS
4	SASS wind magnitudes	|SASS|
5	Velocity components	VEL
6	Velocity potential	DIV
7	Velocity stream function	VORT
8	Vorticity evolution	DYN

In this study, S is considered to be a function of the wind analysis $\underset{\sim}{V}$, and is defined as a weighted sum of lack of fits to the data and constraints:

$$S = \sum_i \lambda_i S_i$$

Given any wind analysis, each S_i measures the lack of fit (expressed in $m^2 s^{-2}$) of this analysis to the ith type of data or the ith constraint. The S_i are summarized in Table 1. Since the constraints used here are all weak constraints all the S_i may be thought of as sums of squares. The λ_i are weights which control how closely the minimizing analysis fits each type of data or constraint. One of the λ_i is arbitrary; in this work $\lambda_1 \equiv 1$.

In the text below i is allowed to be one of the mnemonic devices defined in Table 1 or to be an integer. Conceptually the S_i for $i = 1,2,3,4$ are similar to the measures of lack of fit used in DM, but a number of changes has been made for computational convenience and to avoid multiple solutions. Brief descriptions of the other S_i follow.

The velocity increments, i.e. the difference between the analysis and forecast velocities, is required to be smooth in the minimizing analysis by including in the objective function measures of the roughness of the velocity increments, velocity stream function and the velocity potential function. The simplest measure of roughness suggested by Wahba (1981) is used. The objective function also includes a dynamical constraint, defined by

$$S_{DYN} = T^2 \iint 2^{-1} \left(\frac{\partial \zeta}{\partial t}\right)^2$$

which measures how fast the vorticity of the analysis is changing. In evaluating $\partial\zeta/\partial t$ vertical advection of ζ and the solenoidal terms are neglected and friction is specified in terms of the bulk aerodynamic or drag formulation. T is a convenient time scale taken to be 10^4 s.

3. RESULTS

The VAM was tested and tuned using the QE II case at 12 h GMT 10 September 1978. This case has been studied extensively by Gyakum (1983). Gyakum (1983) used the SASS winds in his analysis and performed a subjective ambiguity removal which compares well with the objective ambiguity removals presented in DM (cf. Fig. 14, Gyakum, 1983; Fig. 7b, DM).

A case study is made here of an intense cyclone centered S of Japan at 138°E,

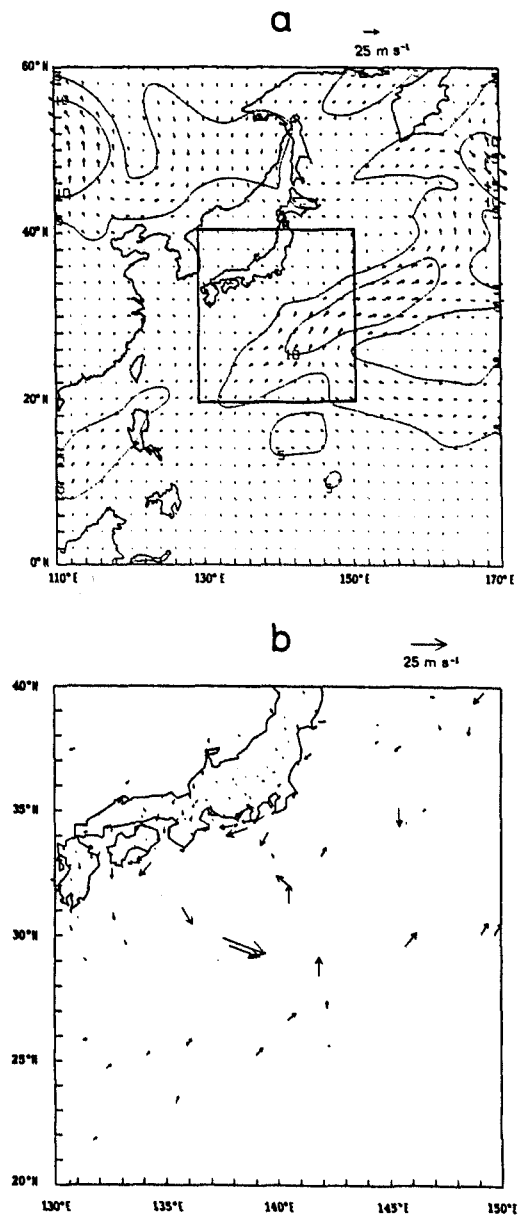

Fig. 2. Data for the case of 00 h GMT 6 September 1978. (a) The NMC analysis valid at this time. The area plotted is the analysis domain. (b) The conventional surface wind observations in a ±3 h time window centered on 00 h GMT. In (b) and subsequent plots only the central part of the analysis domain which is outlined in (a) is shown.

30°N at 00 h GMT 6 September 1978. In this case the maximum SASS wind speeds are ~20 ms^{-1} and one ship reported winds in excess of 30 ms^{-1}. Two minimizing analyses are presented here: Case A uses a 2° × 2° grid, while Case B uses a 1° × 1° grid. The forecast wind and conventional data are shown in Fig. 2. For this experiment the forecast wind is actually taken to be the NMC analysis of 1000 mb u and v interpolated to the analysis grid from the archived 2.5° × 2.5° grid (Fig. 2a). All conventional data (Fig. 2b) and SASS data within ±3h of the synoptic time are used. Presumably this conventional data was used in the NMC analysis, but the high wind speeds observed are not evident in NMC analysis. The minimizing analyses are described in Table 2 and Figs. 2-4. For the fine resolution analysis the demand for smoothness was increased.

The pattern of the resolved SASS winds seems most coherent for case B (Fig. 3). In both cases a strong vorticity maximum of ~2 × $(10^4\ s)^{-1}$ is seen but the position of the center agrees best with the conventional

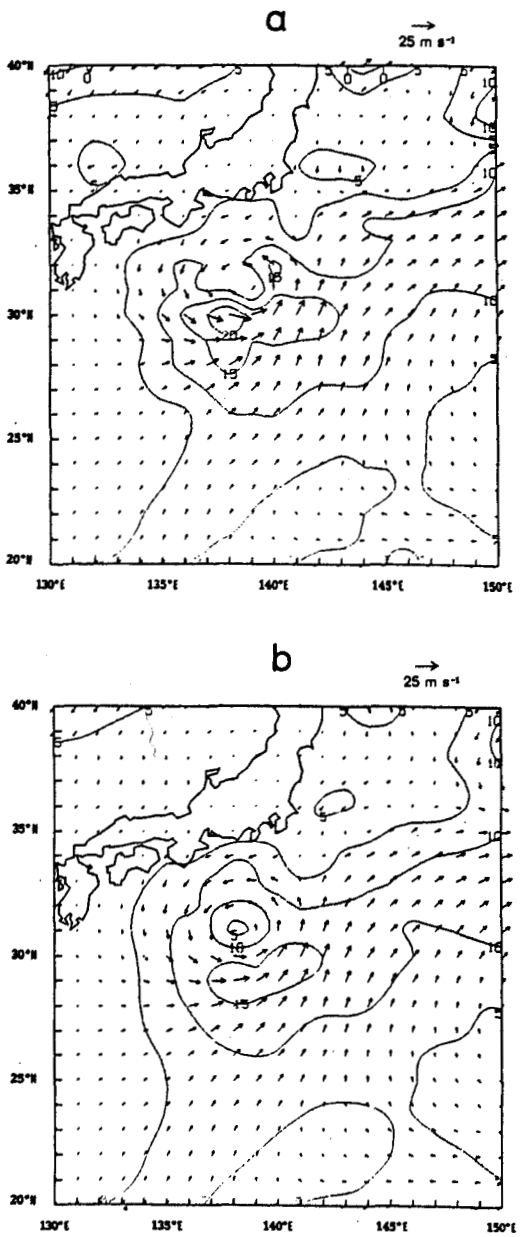

Fig. 3. Minimizing analyses for 00 h GMT 6 September 1978. Panels (a) and (b) correspond to cases A and B of Table 2. Isotachs plotted in ms^{-1}.

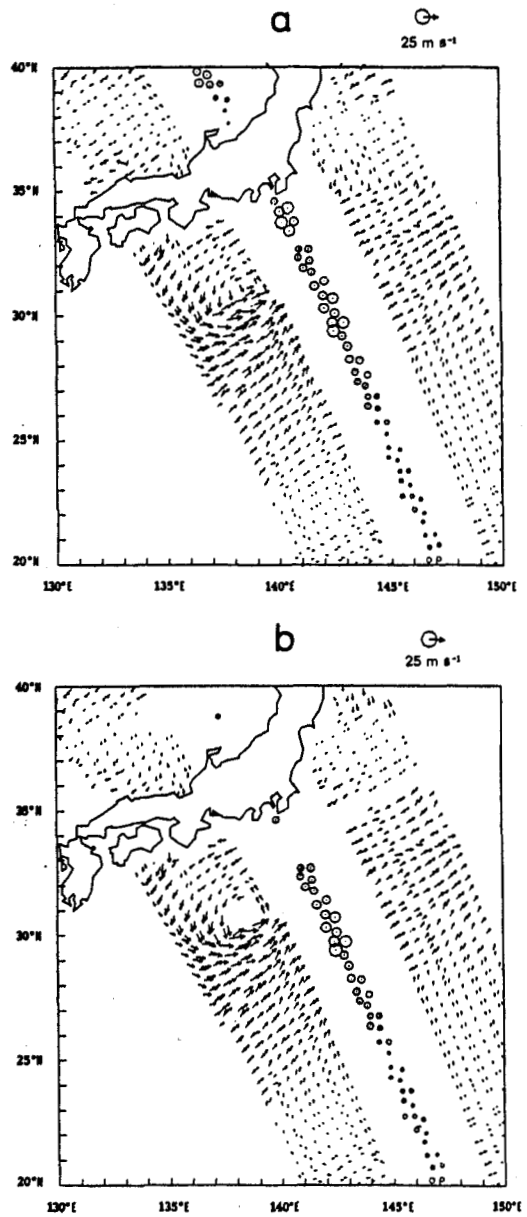

Fig. 4. Resolved SASS winds for the corresponding analyses of Fig. 2. The data for this orbit are within 1 h of the synoptic time. The ambiguity has been removed by choosing the SASS wind vector for which the vector difference between the analysis wind interpolated to the data location and the SASS wind is smallest. At nadir locations octagons proportional to the observed SASS wind speeds are plotted.

Table 2. Values of N_i, λ_i, and S_i (m^2 s^{-2}) for 00 h GMT 6 September 1978. Cases A and B correspond to panels (a) and (b) of Figures 2-4. The analysis domain is 110°-170°E and 0°-60°N. The analysis grid is 2° × 2° for A and 1° × 1° for B.

Case	A		B	
i	λ_i	S_i	λ_i	S_i
FORE	1	36367	1	21719
CONV	64	1814	64	1622
SASS	12	6786	12	6935
|SASS|	16	1308	16	1433
VEL	1	12258	4	7266
DIV	4	2409	16	777
VORT	1	6729	4	4773
DYN	16	920	64	299

data for Case B (Fig. 4, Fig. 2b). In the analysis using the 1° × 1° grid (Case B) there is a distinct secondary vorticity maximum NE of the main circulation, while case A shows a wind shift along a line oriented WSW-ENE. In this area a wind shift is evident in Fig. 3 and a front is seen in the DMSP imagery. In this area of the plots and in the SE corner of the plots the available conventional data is not sufficient to resolve the SASS ambiguities and the analysis procedure resolves the ambiguities differently in each case.

4. DISCUSSION

In this study, the VAM uses only surface wind data and constraints. Generally, to properly use other types of data and/or constraints requires a model of the boundary layer. Other data and constraints which are potentially useful and which could be included within the VAM are surface pressure observations, cloud imagery and cloud track wind vectors. In principle all the available data could be used in the analysis system. For example, within the context of numerical weather prediction, the analyzed variables might be surface pressure and temperature, and winds and water vapor mixing ratio in the lowest layer or layers of the model. Considering only oceanic areas and assuming that sea surface temperature is known, then any observed quantity in the boundary layer may be diagnosed from the values of the analyzed variables. Thus the VAM would minimize the differences between the observed and diagnosed values of all observations in the boundary layer. Potentially, this approach has some interesting and advantageous applications. For example, if the boundary layer model diagnoses cloud then the observed presence or absence of low level cloud may be used as data. Also the boundary layer model could diagnose surface stress which in turn could be used to compute radar backscatter for comparison with the SASS σ^0 values.

Global analyses are possible. The methods presented here can be used with global data sets. From a computation standpoint the limiting factor is storage for the gridded arrays and to a lesser extent for the paired SASS data. A 2° × 2° global analysis using the binned data (>10000 points) and all available conventional data (>7000 points) requires several (<10) minutes of Amdahl V-7 cpu time. In addition, the method is amenable to vectorization; there is for example no searching as in statistical (i.e. optimal) interpolation. In preliminary global experiments, there were some problems at high latitudes because of the large reflectivity of sea ice. Since these points are grouped together they colloborate themselves and pass the data screening tests.

5. ACKNOWLEDGEMENTS

This work relied heavily on resources kindly made available by others. I thank M. Halem and E. Kálnay for computer resources at the NASA GSFC Laboratory for Atmospheric Sciences. I thank R. Atlas and A. Pursch for easy to use data sets. I thank R. Atlas, W. Baker, and P. Woiceshyn for helpful discussions. I thank L. Gibson for carefully typing the manuscript and drafting the figures for this work.

This work was supported by the National Research Council Resident Research Associateship program, by NASA contract NAS-5-27297 to the Universities Space Research Association visiting scientist program and by Air Force Geophysics Laboratory contract F19628-83-C-0027.

6. REFERENCES

Gyakum, J. R., 1983: On the evolution of QE II storm. I: Synoptic aspects. Mon. Weather Rev., 111, 1137-1155.

Hoffman, R. N., 1982: SASS wind ambiguity removal by direct minimization. Mon. Weather Rev., 110, 434-445.

Jones, W. L., L. C. Schroeder, D. H. Boggs, E. M. Bracalente, R. A. Brown, G. J. Dome, W. J. Pierson and F. J. Wentz, 1982: The SEASAT-A Satellite Scatterometer: The geophysical evaluation of remotely sensed wind vectors over the ocean. J. Geophys. Res., 87(C5), 3297-3317.

Schroeder, L. C., D. H. Boggs, G. Dome, I. M. Halberstam, W. L. Jones, W. J. Pierson, and F. J. Wentz, 1982: The relationship between wind vector and normalized radar cross section used to derive SEASAT-A Satellite Scatterometer winds. J. Geophys. Res., 87(C5), 3318-3336.

Wahba, G., 1981: Spline interpolation and smoothing on the sphere. SIAM J. Sci. Stat. Comput., 2, 5-16.

Wahba, G., and J. Wendelberger, 1980: Some new mathematical methods for variational analysis using splines and cross-validation. Mon. Weather Rev., 108, 1122-1143.

A COMPARISON OF REAL-TIME SATELLITE RAIN ESTIMATES AND RADAR DATA

John A. Augustine and Cecilia Girz Griffith

NOAA/ERL Weather Research Program
Boulder, Colorado

1. INTRODUCTION

In 1979 NOAA's Environmental Research Laboratories established the Program for Regional Observing and Forecasting Services (PROFS) to incorporate the latest in computing and meteorological technologies into weather forecasting. The centerpiece of this system is a workstation consisting of a high-resolution color video display monitor and a user-interface device to accept forecaster commands (Schlatter et al., 1984). In 1982 PROFS requested that the Weather Research Program implement the Convective Infrared Satellite Technique (CIST), developed by ERL scientists (Griffith et al., 1978, Woodley et al., 1980, Augustine et al., 1981), on the workstation. The purpose was to provide ancillary estimates of convective rainfall outside the range of the local weather radars. A real time version of the algorithm was entered and tested but has not yet been incorporated into the workstation. This paper concerns the final phase of this effort - to determine the credibility of the algorithm through a comparison of rain estimates and radar reflectivity data over the eastern plains of Colorado and Wyoming. In doing so the authors hope to document the technique's successes and limitations in a real-time mode and to determine the best approach to improving it.

2. THE STREAMLINED TECHNIQUE

As originally derived and subsequently tested, CIST is a life history technique. That is, a sequence of images that cover the life history of a convective entity must be available before a rain volume can be computed. Given a large region where a number of convective entities exist at one time, the complexity of making rain estimates with this version of the technique in any time frame other than after the fact is obvious. For this reason, for the near real-time applications at PROFS, we have applied a version of the technique that does not incorporate the life history aspect. This version is herein referred to as the streamlined technique. It was first described in Waters et al., 1978 and has been applied to landfalling hurricanes since 1974. Its value lies in its utility to real-time applications of satellite rainfall.

In the streamlined version, cloud areas are measured on the satellite image at the -20°C threshold and the fractional coverage of the colder contours are determined as is done in the life history version. The rain volume equation that applies to the life history version is also used in the streamlined technique, namely,

$$R_V = I \times (A_E/A_M) \times A_M \times \sum a_i b_i \times \Delta t \qquad (1)$$

Under the life history scheme, with the exception of b_i, each term in (1) is a function of the cloud's lifecycle. In the streamlined technique, each cloud on each image is assumed to exist at its maximum area (A_M). This then specifies a value for I of 16.7×10^{-3} m^3-h^{-1}-km^{-2} and for (A_E/A_M) of 0.0667. Because no life history information is required by the streamlined technique, each image is processed individually. In making the rain estimates for an image, the algorithm isolates clouds above the prescribed threshold, and computes the necessary parameters for Eq. (1) as well as the subsequent rain volume. These rain volumes are apportioned over the cloud top area, pixel by pixel, in the manner prescribed by the apportionment function (Augustine et al., 1981). After the entire image is processed, a rainfall image results with each pixel of the satellite image having been assigned a rain depth in millimeters. In past comparisons between results generated by both version of the technique differences in the rainfall patterns derived from the streamlined and life history versions have shown that the streamlined version of the technique preserves the rain volume as computed by the life history scheme to within 10%.

An added modification to the application of this technique to the High Plains environment is a correction for environmental differences. The empirical relationships in Eq. (1) were derived for free convection in a subtropical setting. Griffith et al., (1981) discuss the application of these relationships to the U.S. High Plains and show that the convective rain estimates must be adjusted based on regional differences between the subtropics and the High Plains. The most successful correction factor used a one-dimensional cumulus cloud model to parameterize this difference. Although this correction modification was not applied for this report the results to be presented demonstrate a clear need

for such an adjustment when the technique is applied to Colorado's eastern plains.

3. DATA

3.1 Satellite data

GOES-West digital thermal infrared imagery were used in making the rain estimates used for this study. GOES-West is a geostationary satellite positioned over the equator at 135°W. The nominal resolution of its thermal infrared sensor is 8 km at the subpoint; temporally, imagery are collected on half-hour intervals at 15 minutes and 45 minutes past the hour.

The data used were collected by the NOAA/NCAR-operated ground station in Boulder. Digitization, sectorization and archiving of these data are routinely carried out at PROFS. Of the many satellite products produced, this study employed the infrared "regional scale" sector, which is centered on Colorado and is roughly 1000 km on a side. Although the area of eastern Colorado and southeast Wyoming that is under radar coverage is but a small subset of this 10^6 km^2 area, rain estimates were made over the entire regional scale so as to insure that the true cloud areas were used in the rain calculation for those convective clouds whose cloud tops were only partially within the radar coverage.

Once the regional scale rainfall image was created, a smaller area roughly corresponding to the area in Fig. 1 (but at the satellite projection) was subset for the radar comparisons. The dimensions of the subset area were 64 pixels by 64 lines, and geographically covered Colorado, southern Wyoming, southwest Nebraska and western Kansas. This area is referred to as the "eastern Colorado scale" and was the area over which all subsequent analyses and comparisons were made.

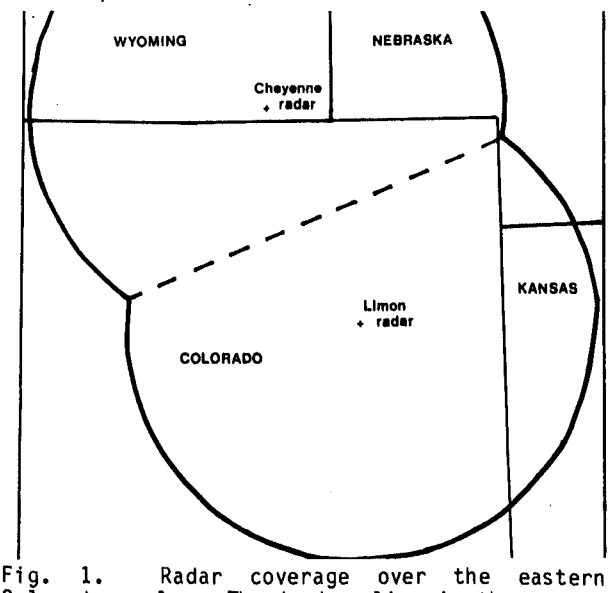

Fig. 1. Radar coverage over the eastern Colorado scale. The broken line is the merger line separating the Limon and Cheyenne radar coverages.

The time difference in the rain volume computation of Eq. (1) was assumed to be one-half hour - the nominal time between successive images. Consequently, each rainfall image represents rainfall accumulations over one-half hour, and should not be confused with the instantaneous rain rates usually displayed for radar data.

3.2 Radar data

Low level reflectivity data from the NWS Limon, Colorado (WSR-57) and Cheyenne, Wyoming (WSR-74) radars are an integral part of the PROFS data ingest system. Product generation software assumes that the range of each of these radars is 230 km. Because the distance separating the two sites is less than twice their unambiguous (radar) range, their respective coverages have a common area contained within northeastern Colorado. Before they are archived, the two fields of data are merged creating a "mosaic" product, and then mapped to a Lambert conformal projection (Fig. 1). The broken line midway between the two radars in Fig. 1 is the merger line; north of this line Cheyenne data are used, and south of it, Limon data are used. In instances when one radar is not operative, the entire coverage of the working radar is retained. The temporal frequency of this product is 15 minutes, beginning on the hour, fortuitously synchronous with the image start times of both GOES-East and GOES-West satellite imagery and presumably ideal for comparison with satellite-derived rain estimates. In reality, however, the time of the satellite data lags, by approximately seven minutes, that of the radar data. This delay accounts for the time required for the satellite sensors to mechanically reach the area of interest while in a full-disk scan.

Areas within the radar mosaic envelope not conducive to comparison with the satellite rain estimates were the ground clutter area within 20 km of the radar, areas of anomalous propagation (usually found adjacent to the 20-km ground clutter area) and return signals from the Front Range of the Rocky Mountains. Owing to the distance of Limon from the mountains, only Pikes Peak was consistently within the field of view of the radar, although other Front Range peaks were in view on occasion. Cheyenne's limitations were more severe. Its low-level beam is intercepted 70 km to the west by the Laramie Range, and to the southwest by the Front Range of Colorado. Therefore the reader should note that only a small area west of Cheyenne is covered in the analyses to follow.

In order to compare directly the satellite-derived rainfall with the radar reflectivity data on small scales, the radar data had to be (1) remapped from Lambert conformal to the satellite projection, (2) subset to the same area as the satellite rainfall comparison area and (3) reduced to the resolution of the satellite data. The remapping program uses the navigation information accompanying the satellite image on which concurrent radar data are to be remapped. This software utilizes a file which contains the latitude and longitude of every point on the radar mosaic image. By

using the satellite navigation information, the location of each radar data point is remapped either by direct navigation or interpolation, to the satellite projection over an area corresponding to the regional scale (~ 10^6 km^2). The remapped radar image is then subset from the regional scale to the eastern Colorado scale.

3.3 Error correction

The final step of colocating these two data sets was to objectively remove any errors that were incurred over the arduous remapping procedure, and also to adjust the positioning of the satellite rain estimates according to the perspective of the satellite. The perspective error results from using the cloud top temperature structure to apportion the satellite rain volume at the surface. Ideally, the rain pattern should be translated vertically through the cloud depth to the surface. However, in reality, it is translated along the line of sight of the satellite. The geometry of the case studied indicated that to correct the error due to the perspective of the satellite, the satellite rainfall grid had to be shifted by two infrared pixels southward and one pixel westward. This adjustment was applied uniformly to every image presented. However, when the radar image and perspective-corrected satellite image were overlaid, small errors, varying in magnitude and direction, were noted in the placement of the radar data. Corrective displacements for the radar images were objectively computed by bilinear interpolation of the true (latitude, longitude) location of the two radars to the correct location on the satellite grid (according to the satellite navigation information). The largest displacements computed for the radar images presented in this study were six infrared pixels meridionally and 1 infrared pixel zonally.

After these objective corrections were applied to the radar and satellite rainfall arrays, small displacement errors were still noticeable. However, because the sources of these errors were not clearly known, no further objective corrections were possible.

3.4 Data Presentation

As presented, reflectivity contours are superimposed on the satellite-inferred rain image. A two-step gray scale represents the half-hour satellite-derived rain pattern. The dark gray shade corresponds to the smallest rain accumulations (up to 1.5 mm in a half-hour period) and the light gray represents 1.5 to 6.3 mm per half hour. The contours overlaid on the gray scale image depict both the radar coverage (the elliptical outer contour) and the reflectivity. Contoured reflectivities begin at 20 dBZ (roughly equivalent to 1 $mm\text{-}h^{-1}$ at 230 km with the WSR-57) and are incremented by 20 dBZ up to 80 dBZ. The reader should note that the indicated coverage of the Limon radar, as depicted in the following figures, includes an erroneous area which ranges from the Colorado - Nebraska border to eastern Wyoming and is recognized by an ordered field of small diamond-shaped contours. (The best example of this is in Fig. 4.) This is a consequence of a software error in the radar remapping routine and the affected area should be ignored. The comparison of the two fields in the following discussion concerns the correspondence of the rain areas only; rain amounts are not considered.

4. RESULTS

4.1 The case day

June 12, 1983 was selected to test the real-time rain estimation algorithm because a relatively complete and timely data set existed in the PROFS archive, and that day's convective events were well positioned with respect to the dual radar coverage. For the time period studied, the location of the storm complex was in an area free of ground clutter and anomalous propagation with respect to Limon, however the coverage was not as clean with respect to Cheyenne, especially in the earliest images.

Examination of the sequence of satellite images over the course of the day revealed that at 1200 GMT (0500 LST), remnants of the previous day's convective storms had moved out of eastern Colorado and the skies over the eastern plains were relatively clear. Small cumulus clouds were evident forming over the foothills shortly after sunrise, and by 1800 GMT, convective storms were noticeable along the northern region of the Colorado's Front Range and over southeast Wyoming. Between 1800 and 2000 GMT the storm complex grew explosively and began moving eastward. At 2000 GMT (Fig. 2) overshooting tops were evident along the Colorado-Wyoming border, indicating vigorous updrafts. The bulk of the canopy was not extremely cold, with most of the temperatures in the -42° to -52°C range. There were a few, small overshooting tops that were colder than -52°C. This complex sustained itself as it moved eastward towards Nebraska. Confirmed reports from storm intercept teams indicated that several severe thunderstorms moved across northeast Colorado during the afternoon of 12 June, however, by 2000 GMT their anvils had merged, and appeared on the satellite imagery as one large system (indicated by "A" on Fig. 2). By 0100 GMT on 13

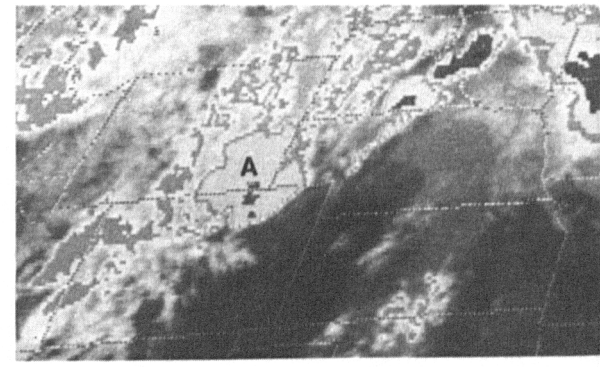

Fig. 2. Thermal infrared image (MB enhanced) for 2000 GMT on 12 June 1983. "A" indicates the northern Colorado - southeast Wyoming storm complex.

June the storm complex had moved entirely out of Colorado. The PROFS data archive for that day covered the formation, growth and eastward progress of the storm complex. The times for which concurrent radar and GOES-West digital imagery were accessible along with the radar coverage for those times are listed in Table 1.

Table 1

Archived data for June 12, 1983.

Time (GMT)	Available radar coverage
1815	Limon and Cheyenne
1845	Limon
1945	Limon and Cheyenne
2015	Limon and Cheyenne
2045	Cheyenne
2245	Cheyenne

4.2 The satellite rainfall - radar reflectivity comparison

Because these satellite rainfalls were not adjusted for environmental differences, we expected the satellite rain areas to be more extensive than the radar threshold reflectivity areas. That expectation was met; however, what was also apparent was that the most intense satellite rain areas correlated well with the reflectivity areas.

At 1815 GMT (Fig. 3) the radar reflectivity pattern indicates that the thunderstorm complex was already intense. It is made up of two predominate echo areas: one shaped like an inverted V and extending from southeast Wyoming into northeast Colorado, the other an isolated echo located immediately south of the inverted V pattern. (Radar returns to the south of the active regions represent the signal reflected from Pike's Peak to the west of Limon and anomalous propagation surrounding the Limon site on the east.) Each of these areas contains maximum reflectivities in excess of 40 dBZ. The total area of satellite estimated rainfall that is contained in the coverage of the radar is a great deal larger than the reflectivity area. However, the heaviest satellite rain accumulations (light gray) appear to be well correlated with the echo areas. Although the satellite rain cores are displaced south and east of the echo areas, the inverted V-shaped echo appears to correspond to three light gray satellite rain areas, two straddling the Colorado-Wyoming border and another to their southwest. The isolated echo in northern Colorado seems to correspond to the satellite rain core immediately to its east. In contrast, the lightest satellite rainfalls, represented by the dark gray shade, appear to have little or no correspondence to the radar rain areas. (Satellite rain areas to the west and northwest of Cheyenne are not considered because radar coverage does not exist there.)

By 1845 GMT (Fig. 4) the the large echo straddling the Colorado-Wyoming border had increased in size and merged with the isolated

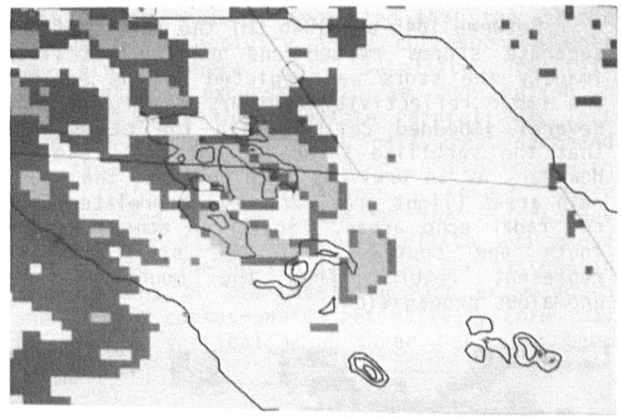

Fig. 3. Satellite-derived rainfall image (mm) with radar coverage (outer elliptical contour) and reflectivity contours (> 20 dBZ) overlaid for 1815 GMT on 12 June 1983. Anomalous propagation around Limon, and returns from Pike's Peak are evident.

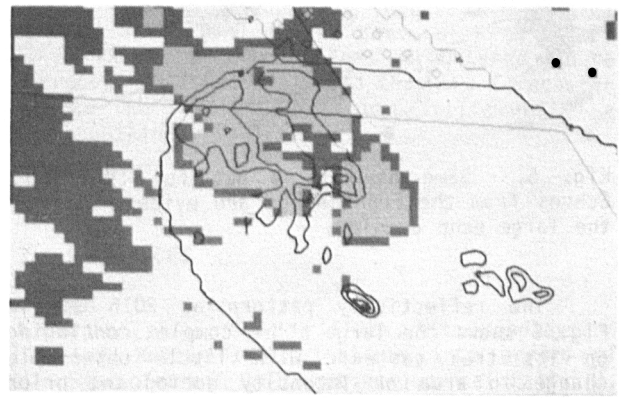

Fig. 4. Same as Fig. 3 but for 1845 GMT. Diamond-shaped reflectivity contours north of the radar coverage area should be ignored.

cell in northern Colorado. It is unknown whether or not growth occurred to the north because the Cheyenne radar was not available at this time. It is intriguing that the same association between the radar reflectivity pattern and the strongest satellite rain areas is again apparent, but also with a slight displacement between the two fields. As described in section 3.3, objective corrections have been applied for known errors which would result in offsets. The observed displacements may result from errors in the software or may be attributable to a meteorological source. An obvious physical cause would be vertical wind shear which would tilt the storm in a downwind direction. Because the satellite estimated rain volume is apportioned according to the cloud top temperature pattern, then directly translated to the surface, strong vertical wind shear could result in the placement of the isohyets downwind of the storm center. In the 12 June 1200 GMT sounding westerly winds were present from 700 mb to 300 mb with a vertical speed shear of over 40 knots. If such a wind profile was sustained through the day, it could partially account for the observed displacements.

Between 1845 and 1945 GMT the anvils of the separate storms merged and on the satellite imagery the storm was depicted as one entity. The radar reflectivity contours in Fig. 5 show several imbedded cells within the cloud mass that the satellite technique does not resolve. However, as in previous time periods, the heavy rain areas (light gray) are well correlated with the radar echo areas. Scattered echoes to the south and southwest of the storm complex represent returns from the mountains and anomalous propagation.

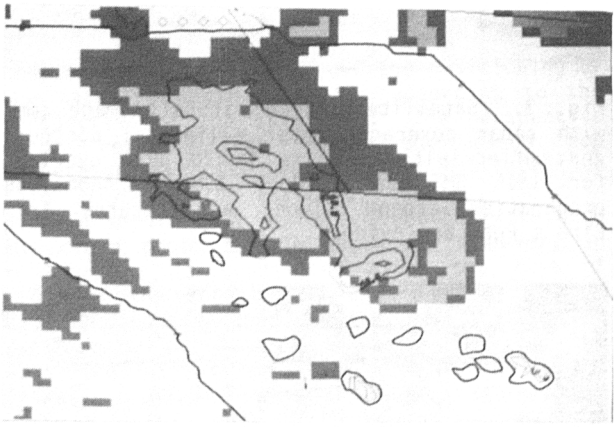

Fig. 5. Same as Fig. 3 but for 1945 GMT. Echoes from the Front Range are evident west of the large echo complex.

The reflectivity pattern at 2015 GMT in Fig. 6 shows the large storm complex continuing on its trek eastward with little observable change in area or intensity during the prior half hour. To the east of this complex a new echo appears on the Colorado-Nebraska border. The satellite rain pattern shows the heaviest rain area beginning to break down on the back side of the storm, and at the same time build on the storm's eastern flank (southwest Nebraska) where the new radar echo is forming. There remains fairly good agreement between the highest satellite rain areas and the echo areas, but with the usual displacement for which to account. Anomalous return is again observable from the Front Range and around the radar sites.

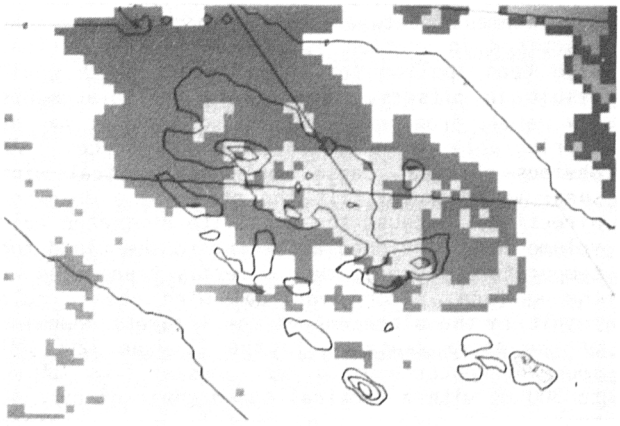

Fig. 6. Same as Fig. 3 but for 2015 GMT. Echoes from the Front Range are evident in a line north of Pike's Peak.

The radar coverage at 2045 GMT (Fig. 7) is a special case of the mosaic radar data. The Limon data are missing and the Cheyenne data are cut off at the merger line shown in Fig. 1. Consequently the southeast end of the satellite rainfall area may have contained some radar reflectivity contours as the area did at 2015 GMT when the Limon data were available.

Both the radar and satellite patterns indicate that two separate areas of precipitation exist at 2045 GMT. One is an area of widespread low reflectivity which corresponds to the storm complex that has been tracked eastward from the foothills of the Rocky Mountains and now appears to be weakening. The other corresponds to the growing cell which has formed along the Colorado-Nebraska border. Each envelope of radar reflectivity corresponds to an eastward displaced light gray region in the satellite rain image. For the first time however, the low reflectivity on the north end of the decaying storm complex lies in a satellite-derived light rain area (dark gray on the image).

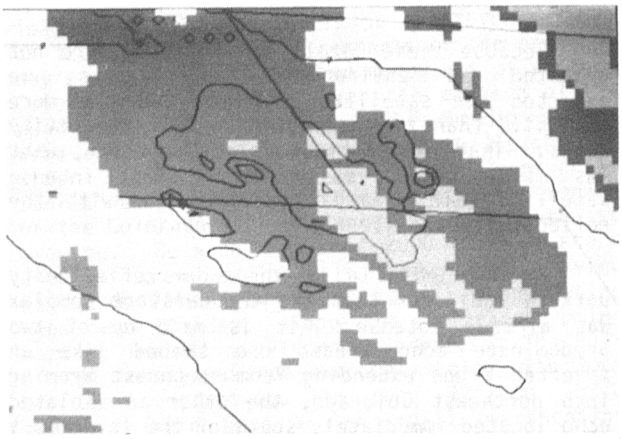

Fig. 7. Same as Fig. 3 but for 2045 GMT. In this figure radar data exist only north of the merger line of the two radars.

At 2245 GMT, (Fig. 8), two hours after the previous satellite-radar pair, the Cheyenne reflectivity pattern shows the storm complex in northern Colorado and extreme southeast Wyoming to be rather weak. In contrast, the small cell which formed less than three hours earlier on the Colorado Nebraska border appears to have gained momentum on its track into the Nebraska panhandle. It is identified by the intense reflectivity core on the eastern edge of the radar coverage. This is the first instance where the reflectivity pattern corresponds entirely to very light satellite rainfall (dark gray), even though there are imbedded cells which show radar returns in excess of 40 dBZ. The reason for this lies in the way that the satellite-estimated rain volumes are apportioned. Figure 9 shows that by 2300 GMT the canopy of the storms that had plagued northeast Colorado and southeast Wyoming during the previous four hours (indicated by "A") had merged, at least at upper levels, with a meso-β convective complex in central Nebraska (indicated by "B"). At that point the satellite technique considered the entire envelope of the

two storms as one entity and consequently computed one rain volume. Because the meso-β system was much deeper and more widespread than the northern Colorado storm, most of the rain volume was apportioned to the east over the higher cloud tops of the meso-β system, thus leaving only low rain depths for the more shallow western storm.

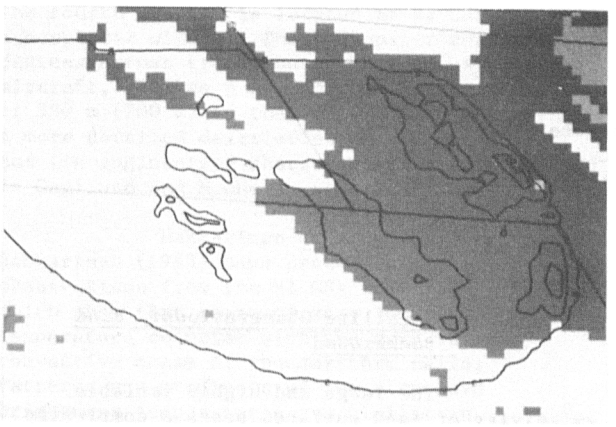

Fig. 8. Same as Fig. 3 but for 2245 GMT. Echoes from the mountains west of Cheyenne are clearly evident.

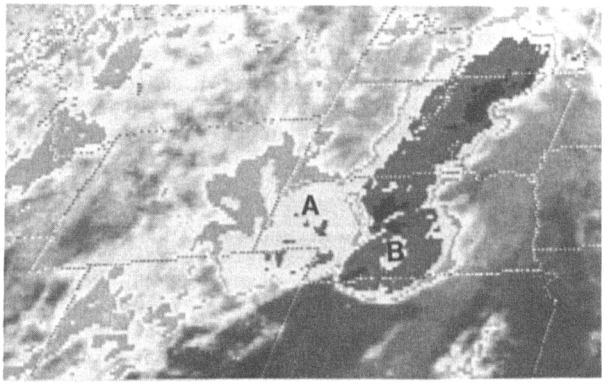

Fig. 9. Thermal infrared image (MB enhanced) for 2300 GMT on 12 June 1983. "A" indicates the northern Colorado - southeast Wyoming storm complex and "B" indicates the meso-β convective complex in central Nebraska.

5. SUMMARY AND CONCLUSIONS

A real-time version of CIST has been tested with one case for ultimate implementation on the PROFS workstation. This streamlined version of the technique does not use life history information; only cloud-top temperature and area are indexed. In this preliminary effort, satellite-derived rain areas (but not amounts) were compared to radar reflectivity data for six half-hour periods on 12 June 1983.

In comparing the total envelopes covered by the satellite rain estimates and threshold radar reflectivities, the satellite rain areas were consistently larger. However, in all but the last period, results indicated that the 20 dBZ threshold reflectivity areas corresponded well to areas where the satellite rainfall accumulations exceeded 1.5 mm per half-hour period. Where the satellite rainfall was less than 1.5 mm, the satellite rain areas exceeded the radar reflectivity regions. Problems with the rainfall apportionment scheme were hypothesized as the cause of the discrepancy between the sizes of the satellite and radar rain areas. The possibility that the systematic displacement of the satellite rain areas south and east of corresponding reflectivity cores may be due to vertical wind shear has also been discussed.

Although limited by only one case study, the authors are encouraged by these preliminary results. This work succeeded in isolating problems which should be addressed before the real-time version of CIST is tested operationally. Future research will be guided by these findings. New apportionment schemes more appropriate to High Plains convective storms will be tested, and future case studies will be stratified on the basis of wind shear. It is hoped that the problems encountered can be corrected satisfactorily and that the forecaster at the PROFS workstation soon will benefit by this additional tool.

7. REFERENCES

Augustine, J.A., C.G. Griffith, W.L. Woodley and J.G. Meitin 1981: Insights into errors of SMS-inferred GATE convective rainfall. J. Appl. Meteor., 20, 509-520.

Griffith, C.G., J.A. Augustine and W.L. Woodley, 1981: Satellite rain estimation in the U.S. High Plains. J. Appl. Meteor., 20, (1), 53-66.

Griffith, C.G., W.L. Woodley, P.G. Grube, J. Stout, D.W. Martin and D.N. Sikdar, 1978: Rain estimation from geosynchronous satellite imagery - visible and infrared studies. Mon. Wea. Rev., 106, 1153-1171.

Schlatter, T.W., P. Schultz and J.M. Brown, 1984: Forecasting convection with the PROFS system: Evaluation of the workstation and comments on a developing science. In review Bull. Amer. Meteor. Soc.

Waters, M.P.,III, C.G. Griffith and W.L. Woodley, 1978: Use of digital geostationary satellite imagery for real-time estimation of hurricane rain potential in landfalling storms. Preprint Volume: Eleventh Technical Conference on Hurricanes and Tropical Meteorology, December 13-16, 1977, Miami, FL., Am. Meteor. Soc., Boston, Mass., 198-203.

Woodley, W.L., C.G. Griffith, J.S. Griffin and S.C. Stromatt, 1980: The inference of GATE convective rainfall from SMS-1 imagery. J. Appl. Meteor., 19, 388-408.

OBSERVATIONS OF DEEP CONVECTION FROM AN AIRBORNE HIGH-FREQUENCY (92 AND 183 GHZ) PASSIVE MICROWAVE RADIOMETER

Ida M. Hakkarinen* and Robert F. Adler

Goddard Laboratory for Atmospheric Sciences
NASA/Goddard Space Flight Center
Greenbelt, MD 20771

1. INTRODUCTION

A variety of techniques have been developed over the last decade to determine precipitation amount and intensity from satellite observations. Visible/infrared methods attempt to relate visual appearance and brightness temperature characteristics of the clouds in the imagery to precipitation. Microwave radiometric observations have the advantage of being more directly related to the precipitation mechanism, since upwelling radiation at microwave frequencies is affected by rain drops and ice particles in the cloud.

1.1 Satellite Observations: Ocean Background

Wilheit et al. (1977) developed a theoretical model for microwave radiative transfer through raining clouds over an ocean surface at frequencies of 19.35 and 37 GHz (1.55 and 0.81 cm, respectively). This model was applied to brightness temperature measurements from the Electrically Scanning Microwave Radiometer (ESMR) (Wilheit, 1972) on Nimbus-5. Using WSR-57 radar observations of rain from four case study days and an independent radiometer/rain gauge ground-based test, they concluded that brightness temperatures at 19.35 GHz could be related to average rain rates (over a dynamic range of 1-20 $mmhr^{-1}$) to within a factor of 2.

More recently, Spencer et al. (1983a) have compared 37 GHz brightness temperatures from the Scanning Multichannel Microwave Radiometer (SMMR) (Gloersen and Hardis, 1978) on Nimbus-7 to rain rates derived from WSR-57 radar observations over the Gulf of Mexico. Their results indicated that the SMMR brightness temperatures explained 72% of the variance of the rain rates.

1.2 Satellite Observations: Land Background

The large and highly variable emissivity of land surfaces poses a complexity in the interpretation of microwave observations of precipitation over land. Savage and Weinman (1975) demonstrated that scattering of hydrometeors is strong enough at 37 GHz to provide at least a qualitative estimate of rain extent over land. Rodgers et al. (1979) used statistical classification techniques to analyze dual-polarized 37 GHz data from the ESMR on Nimbus-6. These authors were able to distinguish between rain, lakes, and dry ground, but found it difficult to separate rain over land from wet ground. When surface temperatures were between 5° and 15°C, the classification scheme broke down.

Two recent papers by Spencer et al. (1983b,c) have reported that very low Nimbus-7 SMMR brightness temperatures at 37 GHz over land coincide with heavy thunderstorm rainfall. Their results, which compared average brightness temperatures over the 20 km SMMR footprint to average rain rates from digitized WSR-57 radar plan position indicator (PPI) images, indicated that the relationship between 37 GHz brightness temperatures and rain rate is approximately linear, and holds up to rain rates of at least 40 $mmhr^{-1}$.

1.3 Aircraft Observations At Higher Microwave Frequencies

At microwave frequencies above 90 GHz, the scattering effect of ice associated with convective rainfall has a large enough effect to produce brightness temperatures much colder than either the land or ocean backgrounds (Savage, 1976). Wilheit et al. (1982) used an aircraft-mounted fixed-view (45° angle) radiometer operating at 92 and 183 GHz to observe convective precipitation associated with a tropical storm over the ocean. Their measurements found that brightness temperatures as low as 140 K were associated with heavy rain. Through radiative transfer modeling, they accounted for these extremely cold temperatures by scattering from precipitation-sized ice particles in the upper portion of the clouds.

---

*Also affiliated with General Software Corporation, Landover, MD 20785.

The Advanced Microwave Moisture Sounder (AMMS) is a four-channel passive scanning radiometer which is a scanning version of the instrument designed and used by Wilheit et al. (1982). It has been flown on NASA high-altitude (18 km) research aircraft. Three channels of the AMMS are centered about the 183 GHz water vapor absorption line, with sidebands of ±2, ±5, and ±9 GHz, respectively. The fourth channel is located at 92 GHz, an atmospheric window. The radiometer scans ±45 degrees across track about the roll axis of the aircraft, and has a ground resolution from 18 km of 350 m (700 m) in the 183 (92) GHz channels. A more detailed description of the instrument and its engineering characteristics can be found in Gagliano and McCheehy (1981).

Hakkarinen et al. (1982) and Hakkarinen (1983) have presented preliminary observations from the 92 GHz channel of the AMMS which show that areas of very low brightness temperature coincide with the more intense convective areas of thunderstorm cells. Patterns and gradients of the microwave brightness temperatures are similar in appearance to radar echoes. Using the radiative transfer model results of Wilheit et al. (1982), the authors inferred that an ice layer 3-5 km thick located above the freezing level in the cloud was sufficient to account for the observed brightness temperatures in the range 120-150 K. A one-dimensional dynamic cloud model (Cheng, 1981) with parameterized microphysics initialized with a representative local sounding produced values for the height and thickness of the ice layer which agreed well with the radiative transfer model calculations.

In 1984, a multi-frequency microwave imager (SSM/I) on a Defense Meteorological Satellite Program (DMSP) Block-5D polar-orbiting satellite will be launched. The SSM/I will have a dual-polarized 85.5 GHz channel that has a footprint of 15 km. Analysis of the AMMS aircraft measurments should help clarify some of the observations which this new satellite will obtain, as well as provide information about the potential utility of high-frequency passive microwave sensors on geostationary satellites.

The objective of this paper is to summarize the preliminary results of AMMS observations of convective raining clouds and to determine whether empirical relationships between rain rate and microwave brightness temperature, such as those developed for 37 GHz satellite data by Spencer et al. (1983a), can be extended to higher microwave frequencies.

2. AMMS OBSERVATIONS WITH AN OCEAN BACKGROUND

During the afternoon hours of 17 Sept 1979, a squall line formed off the eastern coast of Florida near Palm Beach (PBI), and drifted slowly southeastward during the next several hours. The NASA WB-57F aircraft flew four E-W flight lines along the major axis of this cloud system. Figure 1(a) shows the GOES visible satellite image from 1945 GMT with the aircraft position from 2006-2013 GMT marked by

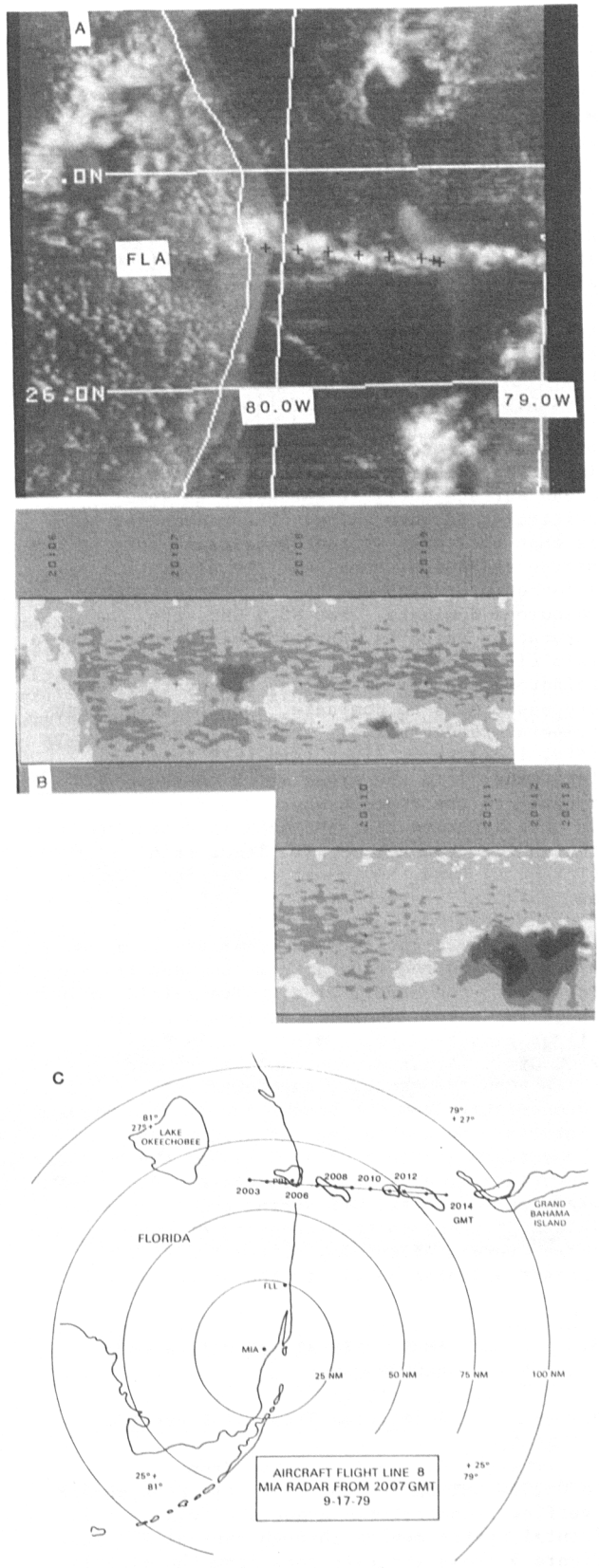

Fig. 1. a) GOES-East visible photo from 1945GMT, 17 September 1979. b) AMMS 92 GHz brightness temperatures. The temperature values (in K) for each grey level (from dark to light) are: 135-155, 156-190, 191-245, 246-255, 256-265, 266-283. c) Miami WSR-57 PPI image from 2007GMT.

the black crosses (with time increasing toward the right). The AMMS 92 GHz imagery corresponding to this portion of the line is shown in Fig. 1(b), while Fig. 1(c) displays the Miami (MIA) WSR-57 radar PPI image from 2007 GMT. The microwave imagery has a fine-scale structure, and is qualitatively similar to the radar echoes. Regions of lowest brightness temperature tend to coincide with the areas of strongest radar reflectivity, which agrees with earlier observations by Wilheit et al. (1982). However, there are several elongated regions where the brightness temperatures are warmer than the ocean background temperature (260-264 K). Huang and Liou (1983) have modeled the effects of a precipitating cloud on upwelling microwave radiation at 85.5 GHz, and have shown that the brightness temperature at this frequency increases with increasing rain rate over an ocean surface until it saturates at some critical rain rate value. The reason for this is that the ocean is radiometrically cold in the microwave region, such that the absorption and emission processes due to the precipitating raindrops dominate. For 85.5 GHz, the saturation value is approximately 2 $mmhr^{-1}$ for a rain cloud thickness of 4.7 km. With larger raindrops and ice particles, the scattering process begins to dominate, and the brightness temperature decreases. The radar image (Fig. 1(c)) shows light rain (VIP level 1=<5 $mmhr^{-1}$) in the areas which correspond roughly to the regions where $266<T_B<283$ K. It is thus inferred that the AMMS is detecting both the shallow convection with light rain ($T_B>266$ K), and the deeper convection which has an ice layer above heavy rain ($T_B<190$ K).

Figure 2 shows the satellite, aircraft, and radar data from the last track flown over the squall line. (The satellite image is approximately 30 minutes after the flight pass because of missing GOES data at 2100 GMT.) Areas of very cold microwave brightness temperatures have expanded considerably from the pass shown in Fig. 1(b). There is a noticable lack of brightness temperature gradient (Fig. 2(b)) on the southern (downwind) side of the storm cells. Upper level winds were from the NNE during the study period. This difference in the intensity of the temperature gradient may be related to the updraft orientation within the storm cells.

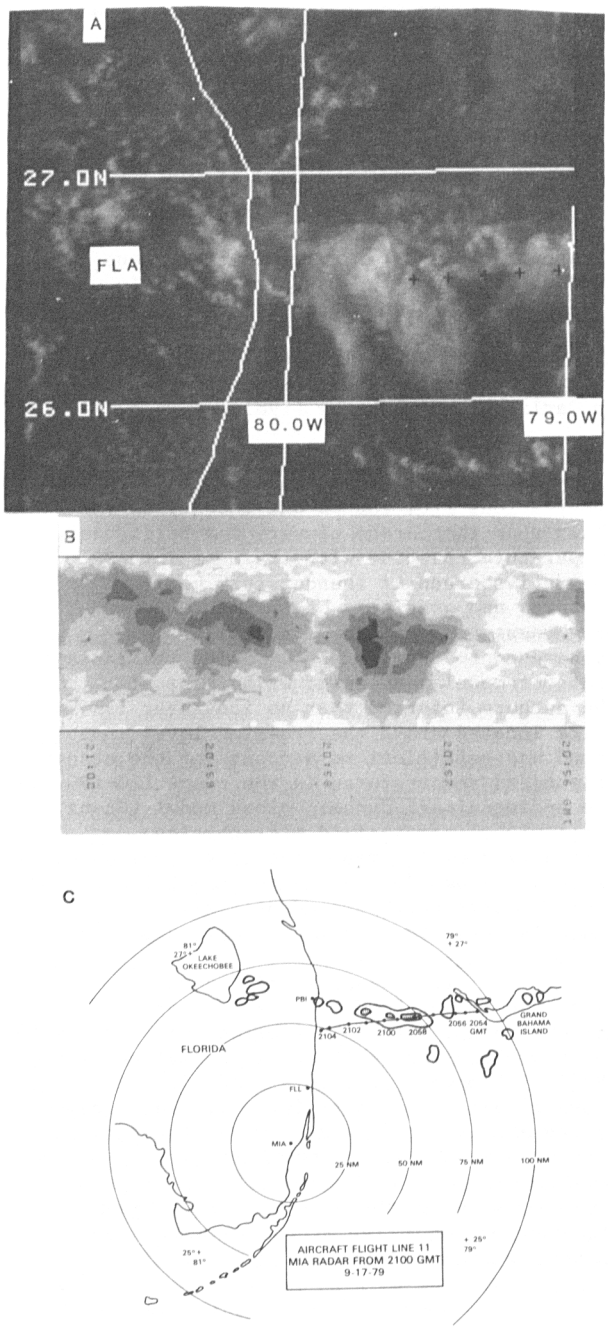

Fig. 2. a) GOES-East visible photo from 2130GMT, 17 September 1979. b) AMMS 92 GHz brightness temperatures. Values are as given in Fig. 1. c) Miami WSR-57 PPI image from 2100GMT.

3. AMMS OBSERVATIONS WITH A LAND BACKGROUND

3.1 Summertime Tropical Convection

During the period from 1800-2000 GMT on 23 Sept 1979, the NASA WB-57F overflew thunderstorms associated with a cold frontal system moving through central Florida. Figure 3 shows aircraft data from the visible (a) and 11 μm infrared (b) channels of the Cloud Top Scanner (CTS) scanning radiometer, and the corresponding 92 GHz (c) and 183 ±9 GHz (d) channels of the AMMS. Very cold microwave brightness temperatures are associated with deep convection, as found in the ocean background case. However, the small increase in brightness temperature associated with light rain cannot be detected due to the high emissivity of the land surface. There is an interesting feature in the AMMS imagery located slightly off nadir at 19:21:30 GMT. This cold point in the microwave imagery does not have a corresponding turret in the visible data or cold point in the IR channel. Lidar observations along nadir near this feature suggest the presence of two cloud layers- a small convective turret overlain by upper-level semi-transparent cirrus. The detection of this anomalous scattering feature by the microwave sensors implies that

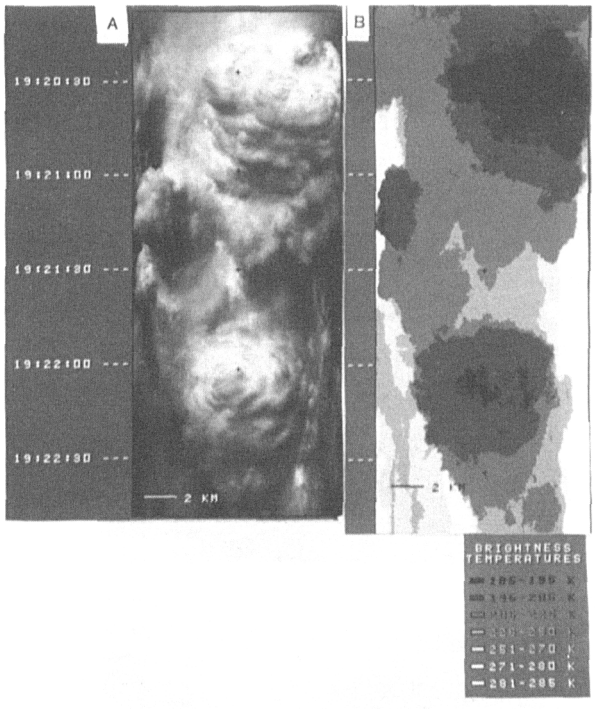

Fig. 3. *Airborne sensor images from 23 September 1979. a) visible and b) 11 μm infrared images from the CTS. c) AMMS 92 GHz and d) AMMS 183+9 GHz images. The temperature values (in K) for each grey level (from dark to light) for (d) are: 51-90, 94-120, 122-155, 157-208, 210-247, 249-280, 282-290.*

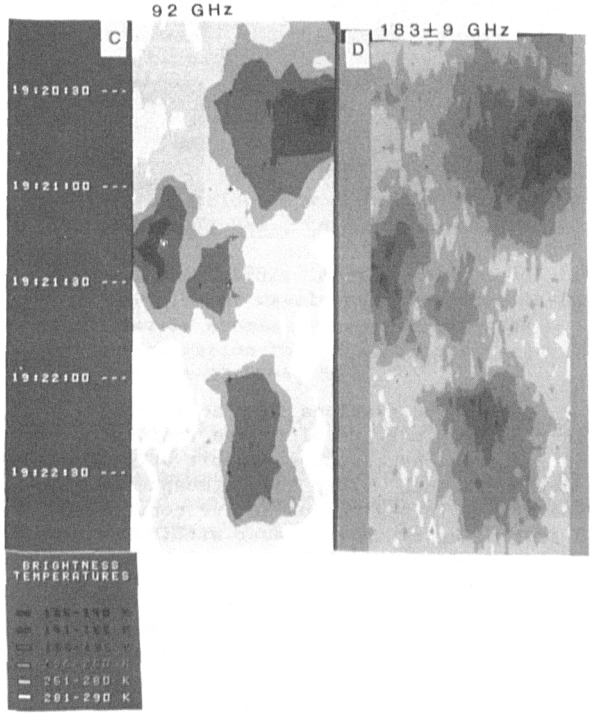

high-frequency passive microwave techniques may prove useful in delineating convection embedded within a large cirrus shield- such convection is often undetectable by conventional visible and infrared instrumentation.

3.2 Summertime Mid-latitude Convection

The NASA WB-57F participated in the Cooperative Convective Precipitation Experiment (CCOPE) held during May-June 1981 in eastern Montana. Figure 4 shows AMMS data from a portion of an overflight of developing and mature thunderstorms. (The data gap is due to the instrument operating in a "stare mode" for 6 scans for calibration purposes.) The data were remapped to an altitude of 10 km; the swath width is approximately 16 km for features at this altitude. Airborne lidar measurements along nadir indicated cloud top heights of 9-10 km (Spinhirne et al., 1983) at this portion of the flight line. Visible and window infrared imagery from the Multispectral Cloud Radiometer (MCR) show that the nadir line passed between two large convective towers that were still growing. A local sounding showed that the tropopause height was 12 km. The large convective tower in the upper left corner of the AMMS images has very cold brightness temperatures in all channels. It is likely an actively growing turret which contains a high concentration of graupel in its updraft. Radar observations from the NCAR CP-2 radar at Miles City, MT reveal maximum reflectivities at z=2.1 km of 45-60 dBZ associated with this cloud complex. Reflectivities of 35 dBZ were reported as high as 9 km in the vertical.

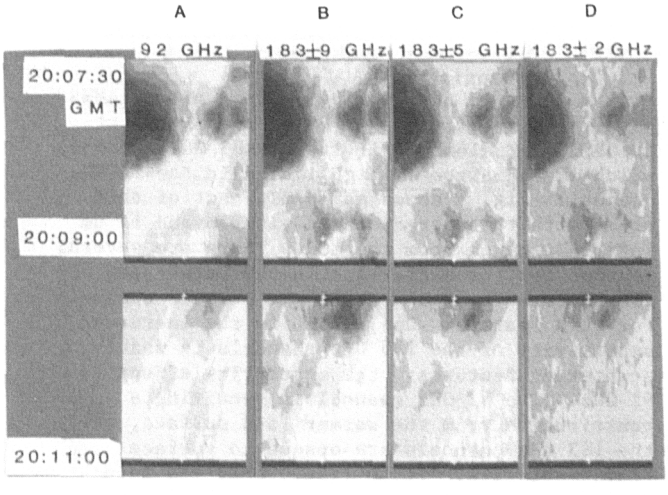

Fig. 4. *AMMS images from 2007-2011GMT, 31 May 1981. a) 92 GHz, b) 183+9 GHz, c) 183+5 GHz. The temperature values (in K) for each grey level (from dark to light) are: 138-164, 166-184, 185-208, 210-222, 224-236, 238-250, 252-263, 264-292. d) 183+2 GHz. The temperature values (in K) for each grey level (from dark to light) are: 97-127, 128-148, 150-176, 178-191, 193-207, 209-223, 225-236.*

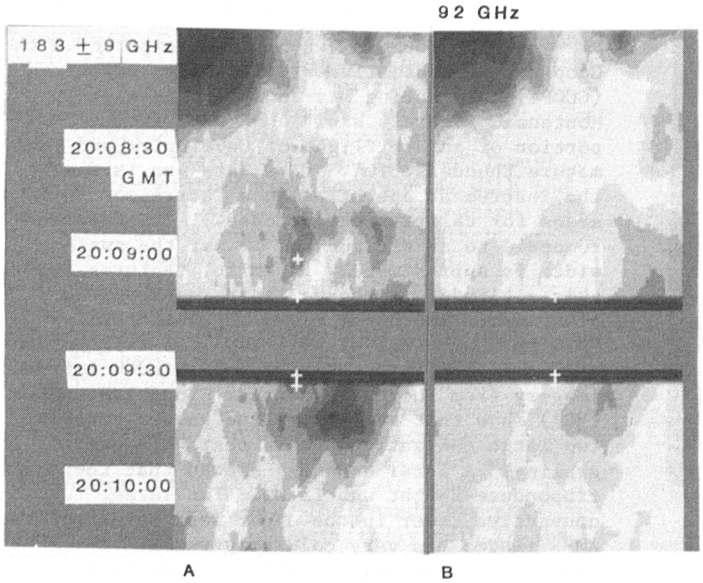

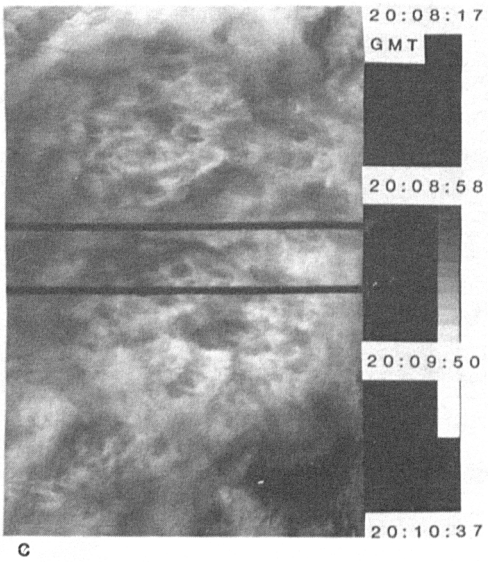

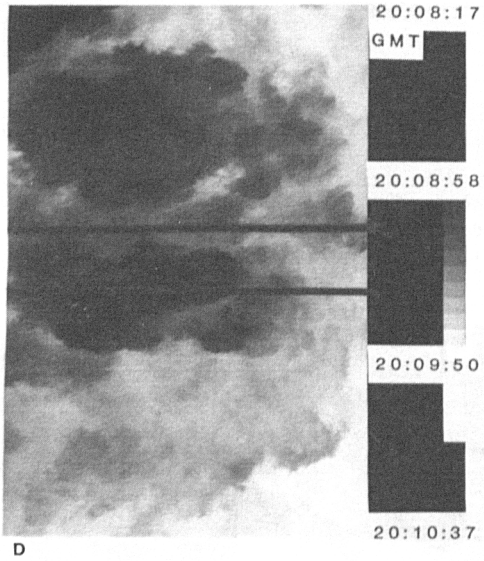

Fig. 5. *Enlargement of area in Fig. 4. a) 183±9 GHz, b) 92 GHz. Temperature ranges are as given in Fig. 4. c) MCR visible and d) 11μm infrared images. The black lines denote the approximate location of the data gap in the AMMS images.*

An interesting feature of the AMMS data is the region of minimum temperatures at 20:09:00 GMT along nadir in the 183 GHz channels which is not strongly highlighted in the 92 GHz channel. Fig. 5 shows an enlargement of this area, with the corresponding visible and 11 μm infrared images from the MCR. There are several reasons for the difference in the brightness temperatures between the 92 and 183 GHz channels for this feature. One reason is the increased sensitivity of the 183 GHz channels to weakly scattering features: the scattering effect 92 GHz. The 92 GHz channel is receiving a contribution from the warmer land surface, while the 183 GHz channels are opaque to surface characteristics. It is likely that the main reason for the difference between the 92 and 183 GHz channels is that this turret contains smaller ice particles than the largest tower in Fig. 4 (Wilheit, personal communication). Lidar measurements show that the altitude of this tower is 7.5 km, which is probably several kilometers lower than the largest tower of Fig. 4. Thus, the differences between the 92 and 183 GHz channels may provide some information about the growth stage of the storm cells. The modeling work of Nieman (1982) shows that the emissivity of an ice layer may not be the same for radiation at 92 and 183 GHz. At this stage of the analysis, it is difficult to determine conclusively the reason for the differences among the AMMS channels. However, it is clear that information is present in these images about the intensity of the convection, and that more work needs to be done to relate the cloud physical processes to their radiative effects.

4. SUMMARY

Observations from an airborne high-frequency passive microwave radiometer over land and ocean backgrounds exhibit brightness temperatures much colder than atmospheric temperatures in regions of active convection. Mie scattering by an ice layer within the clouds is postulated as the mechanism which causes the reduction in T_B (Savage, 1976; Wilheit et al., 1982; Huang and Liou, 1983). The patterns and gradients of T_B bear a strong resemblance to radar echoes.

A major difficulty in the interpretation of these observations is the determination of the depth into the ice layer from which the upwelling radiation is being scattered. This level will depend upon the size and concentration of the ice particles along the viewing path, the height and thickness of the ice and rain layers, cloud temperature and observing angle.

Work in the near future will concentrate on the CCOPE AMMS observations of convection and their relation to ground-based radar observations and cloud characteristics as determined by the airborne cloud lidar and MCR instruments.

5. REFERENCES

Cheng, C.P., 1981: Numerical simulation of the dynamics, cloud microphysics and radar echo structures of tropical and mid-latitude convection. Ph.D. Dissertation, Dept. of Atmospheric Sciences, University of Washington, 217 pp.

Gagliano, J.A., and J.J. McCheehy, 1981: Advanced microwave moisture sounder (AMMS) for WB-57F CCOPE mission. Technical report for Project A-2904, Georgia Institute of Technology, 40 pp.

Gloersen, P. and L. Hardis, 1978: The Nimbus-7 Users' Guide. NASA Goddard Space Flight Center, 213-245.

Hakkarinen, I.M., E.B. Rodgers and M.C. McCumber, 1982: The evolution of Florida thunderstorms on 23 September 1979 as observed by an airborne passive microwave radiometer. Preprints Conf. on Cloud Physics, Chicago, IL, Amer. Meteor. Soc., 504-507.

Hakkarinen, I.M., 1983: Airborne passive microwave radiometric observations of intense convection. Preprints Conf. on Severe Local Storms, Tulsa, OK, Amer. Meteor. Soc., 186-189.

Huang, R. and K.-N. Liou, 1983: Polarized microwave radiation transfer in precipitating cloudy atmospheres: Application to window frequencies. J. Geophys. Res., 88, 3885-3893.

Nieman, R.A., 1982: An ice layer model for millimeter wavelength observations in severe storms. Computer Sciences Corporation Technical Report CSC/TR-82/6004, 56 pp.

Rodgers, E.B., H. Siddalingaiah, A.T.C. Chang and T.T. Wilheit, 1979: A statistical technique for determining rainfall over land employing Nimbus-6 ESMR measurements. J. Appl. Meteor., 18, 978-991.

Savage, R.C., 1976: The transfer of thermal microwaves through hydrometeors. Ph.D. Dissertation, Department of Meteorology, University of Wisconsin, 147 pp.

Savage, R.C. and J.A. Weinman, 1975: Preliminary calculations of upwelling radiance from rainclouds at 37.0 and 19.35 GHz. Bull. Amer. Meteor. Soc., 56, 1272-1274.

Spencer, R.W., B.B. Hinton and W.S. Olson, 1983a: Nimbus-7 37 GHz radiances correlated with radar rain rates over the Gulf of Mexico. J. Climate Appl. Meteor., 22, 2095-2099.

Spencer, R.W., D.W. Martin, B.B. Hinton and J.A. Weinman, 1983b: Satellite microwave radiances correlated with radar rain rates over land. Nature, 304, 141-143.

Spencer, R.W. W.S. Olson, W. Rongzhang, D.W. Martin, J.A. Weinman and D.A. Santek, 1983c: Heavy thunderstorms observed over land by the Nimbus-7 Scanning Multichannel Microwave Radiometer. J. Climate Appl. Meteor., 22, 1041-1046.

Spinhirne, J.D., M.Z. Hansen and J. Simpson, 1983: The structure and phase of cloud tops as observed by polarization lidar. J. Climate Appl. Meteor., 22, 1319-1331.

Wilheit, T.T., 1972: The electrically scanning microwave radiometer (ESMR) experiment. Nimbus-5 Users' Guide. NASA Goddard Space Flight Center, 55-105.

Wilheit, T.T., A.T.C. Chang, M.S.V. Rao, E.B. Rodgers and J.S. Theon, 1977: A satellite technique for quantitatively mapping rainfall rates over the oceans. J. Appl. Meteor., 16, 551-560.

Wilheit, T.T., A.T.C. Chang, J.L. King, E.B. Rodgers, R.A. Nieman, B.M. Krupp, A.S. Milman, J.S. Stratigos and H. Siddalingaiah, 1982: Microwave radiometric observations near 19.35, 92 and 183 GHz of precipitation in Tropical Storm Cora. J. Appl. Meteor., 21, 1137-1145.

Relative Errors of Satellite Soundings and Radiosondes

Harold J. Brodrick and Albert Thomasell

Climate and Earth Sciences Laboratory
NOAA/NESDIS Washington, D.C. 20233

1. INTRODUCTION

A standard procedure for evaluating the accuracy of satellite temperature soundings is the direct comparison of matched pairs of radiosonde and satellite temperature profiles. This process attempts to determine satelite temperature retrieval errors by comparing two essentially different types of measurements, and ignores the 'errors' inherent in the radiosonde measurements. The desired goal is to know how well an ensemble of satellite data describe the mass structure of the atmosphere. This means, for example, how accurately does a temperature analysis from a group of a satellite reports represent the true pattern in the atmosphere. A number of problems are inherent in making this type of evaluation, among them being the difficulty of objectively measuring the differences between patterns that are discernible to the eye, and obtaining a representative standard of comparison of the desired scale of mass structure. These difficulties notwithstanding, this paper presents the results of a study assessing the relative errors of satellite temperature soundings and radiosondes in describing an analyzed state of the atmosphere.

2. APPROACH AND DATA

Radiosonde measurements are the only readily available and commonly used standard of comparison, and the errors in those measurements would include instrumental error, coding/transmission errors, and noise in the data caused by atmospheric systems smaller in scale than those being resolved by the analysis procedure and data density. It is assumed that in a region of dense radiosonde data a representative error-free analysis can be obtained, and that departure of the radiosonde data from that analysis will give a measure of the radiosonde noise. This inherent noise is calculated by analyzing a set of radiosonde data and then calculating statistics of the fit of that analysis to a subset of the radiosonde reports. The statistics of the fit, of course, will be dependent upon the type of analysis scheme used, grid spacing, and the smoothness of the fit to the data. However, the satellite sounding error is determined by similarly analyzing a set of satellite retrievals and calculating the fit of the analysis to the same subset of radiosonde reports. The mean square of the radiosonde error can then be subtracted from the mean square of the satellite fit to the radiosondes to arrive at an estimate of the 'true' satellite sounding error, when a collection of data are used to describe a thermal field.

The parameters being analyzed and compared are the 850mb and 500mb temperatures, and the 1000-500mb and 700-300mb thicknesses, over eastern North America. The latter thickness layer was chosen because it encompasses the mid-troposphere where the satellite retrievals are generally expected to produce the best results. The area was limited to eastern North America so as to avoid possible elevation problems in the retrievals. The analyses are produced using a successive approximation type analysis scheme (Cressman, 1958) on a portion of the NMC 65x65 polar stereographic grid (381 km at 60°N). A zero first guess field is used to start off the analysis cycles. Analyses are interpolated to the radiosonde locations and the differences between analyzed and radiosonde reported values are collected. To provide an additional standard against which to judge the satellite/radiosonde differences, the NMC global analysis with a data cut-off time of about 9.5 hours after synoptic time was also compared to the each selected set of radiosondes. For quality control, an initial analysis of the radiosondes and the NMC analysis were examined and any radiosonde that differed considerably from both analyses was rejected for comparison in the final samples including the satellite analyses. As a final standard of comparison, data were also collected from an analysis of the radiosondes 12 hours earlier, to estimate how well a persistence analysis compares with current satellite data in providing thermal patterns.

Samples of TIROS-N and NOAA 6 sounding data were collected individually for two periods in the winter of 1979/80; December 20-27, 1979 and January 1-9, 1980. Depending on the completeness of the satellite sounding coverage, the verification area was varied somewhat so that a region covered mutually by both satellites could be selected for comparison to the same set of radiosondes at each time. Thus, in the results presented, analyses from both satellites have been compared to the same sample of radiosonde observations.

3. RESULTS

The root mean square (RMS) of the differences between the various analyses and the radiosonde observations is presented as the statistical measure of how the one fits the other. The RMS values for the December sample are given in table 1. For all parameters it can be seen that

the value for the radiosonde only analysis is the smallest, however, for the thickness layers the NMC analysis values are very similar in the 1000-500 mb layer and only somewhat larger in the 700-300 mb layer. The values for the remaining three analysis types are markedly higher for each parameter. The analyses of 12 hour old radiosondes give the largest RMS values except for the 850 mb temperatures where the value falls between the two satellite values. The RMS values for the 500 mb temperature are clearly smaller than for 850 mb in all analysis categories, which is to be expected, however, the values are more nearly comparable between the two thickness layers.

The RMS values for the January 1980 sample are shown in table 2. The statements made concerning the RMS values in table 1 hold for the sample in table 2 as well, except the 850 mb temperature RMS for the 12 hour old radiosonde analysis is somewhat larger than either of the satellite analysis values.

The radiosonde analysis RMS values in the tables were defined previously to be the radiosonde error. If the square root of the difference between the mean square (RMS^2) of the satellite fit and the mean square of the radiosonde error is taken, we can arrive at an estimate of the 'true' satellite sounding error. Results of this operation are shown in table 3 as RMS values of the true satellite analysis errors for the two samples. There is some variability between the samples and satellite. However, for both satellites the January 80 sample yields lower values for all parameters. At 850 mb, TIROS N produces lower RMS values than NOAA 6, but for all the remaining parameters the reverse is true. The numbers in parenthesis below the thickness RMS values are the conversion to mean temperatures for the layers at a standard atmosphere. Thus, at least for the lower layer the mean temperature error is less than either of two of the individual levels that are part of the layer. This condition agrees with accepted fact that satellite layer mean temperatures are better than individual level temperatures.

4. DISCUSSION

It is interesting to compare the results in tables 1 and 2 with those in Gruber and Watkins (1982), who used radiosonde/satellite matchings. Direct comparison is complicated by the fact that their results are given in terms of mean temperatures for layers between mandatory levels. However, estimating from those winter 79 results indicates that the results in tables 1 and 2 vary from lying between their clear and cloudy values to being better than the clear values at 850 mb and 500 mb. This comparison suggests that, even though the analyses in this study were done using soundings having a combination of retrieval paths, an analysis of an ensemble of satellite data may produce a better fit to radiosonde data than individual radiosonde/satellite sounding matchings.

The RMS values in table 3 yield satellite errors of generally acceptable magnitude, particularly at 500 mb and for the thickness layers. It seems fairly clear that error values using this approach, analysis of satellite data and subtracting off radiosonde error, are comparable to or less than those obtained by accepting radiosonde observations as strict truth and making a one on one comparison with satellite soundings.

However, these values of error, as in table 3, still fail to impart a feel for how accurately an analysis using satellite data represent a mass field. As an illustration of the representativeness of a satellite data analysis, an example of 1000-500 mb thickness patterns from one of the cases in table 1 is shown in figure 1. Analyses of the data from each satellite along with the analysis of the radiosonde data is shown. The differences between each satellite analysis and the radiosonde analysis are superimposed. Considerable similarity between the patterns is apparent despite the fact that this is one of the worst cases in terms of the magnitude of the satellite analysis RMS differences with the radiosonde observations. Thus, in an area of sparse radiosonde coverage, it could be expected that analyses made from satellite soundings would depict well the broad overall temperature fields, though perhaps differing in some of the details from what might be described by good radiosonde coverage.

5. REFERENCES

Cressman, G.P., 1959: An operational objective analysis system. Mon. Wea. Rev., 87, 367-374.

Gruber, A. and Watkins, C.D., 1982: Statistical assessment of the quality of TIROS-N and NOAA-6 satellite soundings. Mon. Wea. Rev., 110, 243-252.

Analysis Type	850mb T	500mb T	1000-500mb ΔH	700-300mb ΔH
Radiosonde	1.27°	.87°	11.34m	12.69m
NMC	2.07	1.20	12.16	16.28
TIROS-N	2.99	2.03	31.14	39.46
NOAA 6	3.23	1.81	28.16	34.03
12 hr old radiosonde	3.06	2.54	44.66	51.39
Sample Size	457	457	456	446

Table 1. RMS values for each analysis type, December 20-27, 1979

Analysis Type	850mb T	500mb T	1000-500mb ΔH	700-300mb ΔH
Radiosonde	1.22°	1.01°	12.26m	13.65m
NMC	1.71	1.27	12.56	15.34
TIROS-N	2.32	1.91	26.24	28.85
NOAA 6	2.77	1.81	25.95	25.64
12 hr old radiosonde	2.92	2.66	46.13	49.31
Sample Size	455	456	450	439

Table 2. RMS values for each analysis type, January 1-10, 1980

		850mb T	500mb T	1000-500mb ΔH	700-300mb ΔH
TIROS-N	Dec 79	2.71°	1.84°	29.00m (1.43°)	37.36m (1.51°)
	Jan 80	1.98	1.62	23.20 (1.14°)	25.41 (1.02°)
NOAA 6	Dec 79	2.97	1.59	25.78 (1.27°)	31.58 (1.27°)
	Jan 80	2.49	1.50	22.87 (1.13°)	21.71 (0.87°)

Table 3. RMS values of 'true' satellite analysis error

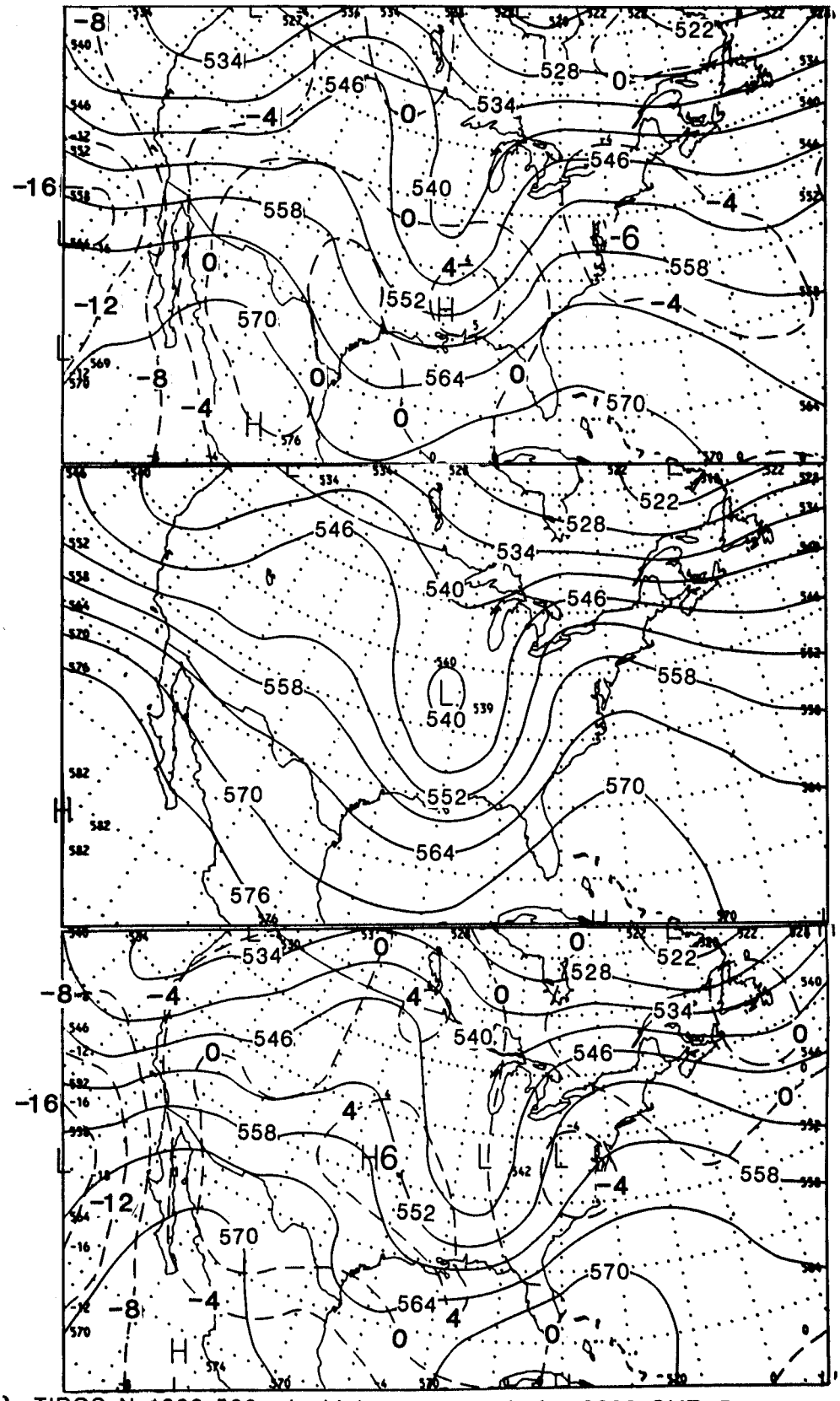

Fig. 1. a) TIROS N 1000-500 mb thickness analysis for 0000 GMT, December 25, 1979 (data about 2200 GMT over eastern U. S.). Solid lines are contours at 6 dm intervals. Broken lines are thickness analysis difference at 4 dm intervals, for analysis a) minus analysis b). b) Radiosonde 1000-500 mb thickness analysis for 0000 GMT, December 25, 1979. Contours at 6 dm intervals. c) Same format as a) for NOAA 6 thickness analysis (data about 0200 GMT).

THE ACCURACY OF MESOSCALE TEMPERATURE AND DEWPOINT FIELDS RETRIEVED FROM VAS SATELLITE AND CONVENTIONAL SURFACE DATA

D. Chesters[1], T.H. Lee[2], A. Mostek[3] and D.A. Keyser[3]

[1]Goddard Lab. for Atmos. Res., NASA/GSFC, Greenbelt, MD 20771
[2]Computer Sci. Corp., Silver Spring, MD 20910
[3]General Software Corp., Landover, MD 20785

1. GEOSYNCHRONOUS SOUNDING

The VISSR Atmospheric Sounder (VAS) is a twelve channel imaging radiometer on the operational GOES satellites. The instrument is designed to monitor the evolution of tropospheric temperature and moisture fields at mesoscale resolution (Montgomery and Uccellini, 1984). VAS multi-spectral images provide direct mesoscale information about the height and motion of clouds (Menzel et al., 1983) and about the structure and changes of clear-air moisture fields (Chesters et al., 1983; Petersen et al., 1984). Fields of VAS soundings show good horizontal and temporal continuity and can delineate potential convective instabilities (Smith et al., 1982; Petersen et al., 1983).

The absolute and relative accuracy of VAS soundings must be verified quantitatively, since their numerical qualities affect their usefulness in data assimilation and numerical forecast models. In fact, the excellent mesoscale resolution of the VAS soundings makes it difficult to verify their accuracy objectively, because of the lack of independent ground truth data with the same space-time resolution as the VAS instrument.

We present objective verification for two VAS case studies: (1) a midsummer preconvective environment over the United States, measured against the NWS radiosonde network, and (2) a springtime post-storm environment over Texas measured against a special mesoscale radiosonde network. Absolute accuracy is measured by comparing the VAS retrievals to the radiosonde values at the network sites. Relative accuracy is measured by the space-time correlations within the retrieved temperature and moisture fields. The impact of ancillary surface data, stringent colocation criteria, and careful cloud screening upon the accuracy of the VAS soundings is determined. Significant limitations in the conventional "ground truth" data are also noted.

2. RETRIEVALS WITH VAS AND SURFACE DATA

VAS retrievals are limited both by coarse vertical resolution (Chesters et al., 1982), and by noise and calibration difficulties imposed by remote operation at geosynchronous altitude (Menzel et al., 1981; Chesters and Robinson, 1983). Cloud contamination requires "man-in-the-loop" quality control, and poor resolution of the lower troposphere requires ancillary surface data.

Conditioned regression is used for VAS soundings at NASA's Goddard Space Flight Center (GSFC) (Lee et al., 1983). Variations in X (12 VAS radiances plus 2 SFC parameters) are used to predict Y (temperature and dewpoint profiles, precipitable water, thickness, etc.) based upon previous training.

$$X = R(1),..,R(12) \text{ and } T(SFC),D(SFC) \tag{1}$$

$$Y = T(P),D(P), \text{ and } PW,\phi(\Delta P),\theta e(P),\text{etc.}$$

$$x = X-\langle X\rangle, \quad y = Y-\langle Y\rangle, \quad G^2(x) = \langle N^2(x)\rangle/\langle S^2(y)\rangle,$$

$$M = \langle y^*x'\rangle * [\langle x'^*x\rangle(1+G^2(x)\delta_{x',x})\rangle]^{-1}$$

$$Y'' = \langle Y\rangle + M^*[X''-\langle X\rangle]$$

The conditioning factor G(x) serves to stabilize the regression matrix against the problems of training with a small sample set of noisy, redundant predictors. G is estimated from experience with the "signal" (variance) $S^2(y)$ and the "noise" (errors) $N^2(x)$. Values of S/N = 10/1 work well for the combination of VAS+SFC data. Values of S/N = 1/10 are used to suppress individual predictors, such as surface data or noisy VAS channels, in order to assess their impact on VAS soundings.

TABLE 1

VAS channel specifications

VAS Chan	Band (μm)	NEΔT* (±K)	Absorbing Gases	Sounding Purpose
1	14.7	5.3	CO2	temp
2	14.5	2.2	CO2	temp
3	14.3	1.8	CO2	temp
4	14.0	1.8	CO2	temp
5	13.3	1.0	CO2+H2O	temp+moisture
6	4.5	1.6	N2O	temp+cloud
7	12.7	1.0	H2O+CO2	moisture+skin
8	11.2	0.1	window+H2O	skin+moisture
9	7.3	3.4	H2O	moisture
10	6.7	1.6	H2O	moisture
11	4.4	6.7	N2O	temp+cloud
12	3.9	0.8	window	skin+cloud

The single sample noise in the brightness temperature (NEΔT*) listed in Table 1 is large for many of the VAS channels. Consequently, the radiances must be time (dwell) and space (field-of-view) averaged in order to be useful for sounding, which requires errors less than ±0.3 K in all channels. Sounding fields-of-view with 30 to 60 km resolution are commonly spaced at 50 to 150 km intervals in the cloud-free regions of radiance frames scanned at 1 to 3 hr intervals. The VAS channels are also subject to calibration and other non-random errors. For instance, the shortwave window (channel 12) is affected by reflected sunlight, especially at low latitudes during midday.

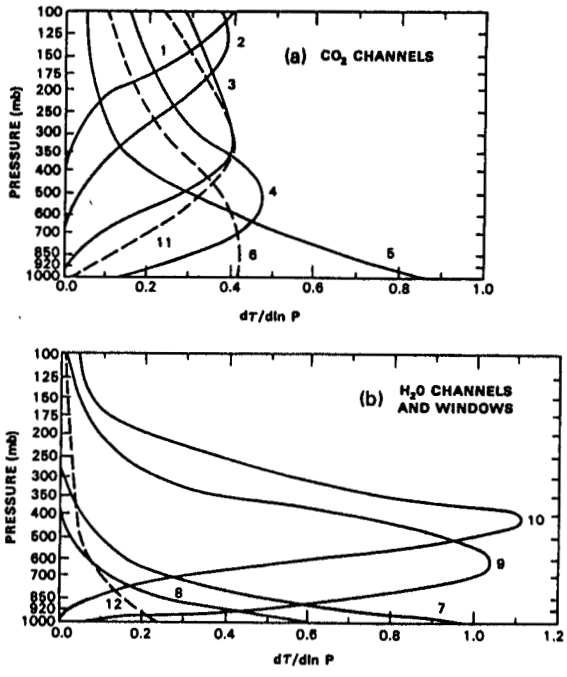

Figure 1: VAS standard weighting functions

Fig. 1 indicates that VAS is unable to resolve vertical temperature and moisture features which are less than a few km thick, especially in the lower troposphere. Fortunately, North America is serviced by hourly reports of surface (SFC) temperature and dewpoint from a network of airways stations with separations comparable to the horizontal resolution of the VAS sounding data. For statistical training over the United States, colocated VAS, SFC and RAOB data are gathered at relatively cloud-free sites, as determined from high resolution visible data and SFC reports of local cloudiness. Neighboring SFC reports are either relocated or interpolated to each VAS sounding field-of-view. Mesoscale fields of VAS soundings (without soundings in cloudy areas) are objectively analysed on a 0.5 degree (50 km) grid, using the GEMPAK-Barnes scheme (Koch et al., 1983) to make contour maps and numerical intercomparisons.

3. A MIDSUMMER PRECONVECTIVE ENVIRONMENT

On 13 and 20 July 1981, hot and humid air covered most of the central United States. These cases were used to test the VAS regression scheme (Lee et al., 1983), and to examine VAS performance in regions of convective instability (Petersen et al., 1983 and 1984; Mostek et al., 1984). On each day, 5 frames of VAS data were collected at approximately 3 hour intervals from dawn to dusk (1200 to 2300 GMT). NWS radiosonde data east of the Rockies provide training and testing datasets at synoptic times. The entire series of VAS retrievals is used to measure the relative space-time continuity throughout the diurnal cycle.

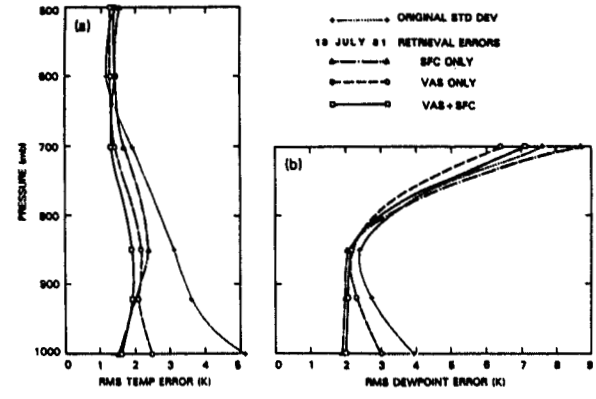

Figure 2: RMS differences among VAS-RAOB temperature and dewpoint profiles on 13 July 1981

Fig. 2 presents RMS statistics for VAS-RAOB profile differences, comparing the standard deviation in the RAOBs to the errors in the VAS-only, SFC-only and VAS+SFC retrievals. These statistics were derived for 13 July 1981, using 56 NWS sites for training and 25 independent sites for testing. Absolute accuracy is comparable to the HIRS soundings from the polar-orbiting satellites. Temperature accuracy is not really tested above 700 mb because the midsummer temperature field is quite uniform. Dewpoint profile accuracy is poor above 700 mb because the atmosphere contains many thin and variable moisture layers which VAS cannot resolve. Fig. 2 shows that the impact of SFC data is significant at 920 mb, and dominates the "1000 mb" (lowest RAOB level) retrievals. However, the substantial residual errors at the "1000 mb" level indicate that the SFC temperature and dewpoint are imperfect predictors of the RAOB temperature and dewpoint boundary layer report at a neighboring site. Even where the airways and radiosonde sites coincide, the two conventional systems have discrepancies averaging ±1.5°C. Consequently, some of the variance in the verification statistics is due to errors in the conventional data.

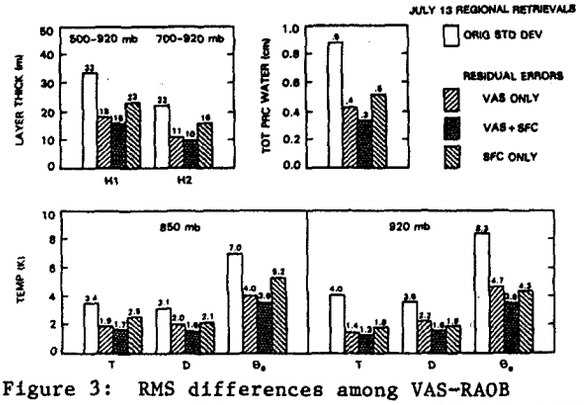

Figure 3: RMS differences among VAS-RAOB stability paramaters on 13 July 1981

Fig. 3 indicates that much of the variation among the RAOB reports is well retrieved for low level stability indicators, doing especially well for total PW (errors of ±0.3 cm in a field varying by ±0.9 cm) and θe at 920 mb (errors of ±3.6°C in a field varying by ±8.3°C). Fig. 3 also indicates that VAS-only retrievals are more accurate than SFC-only retrievals above 920 mb, where the two predictors are equally informative. Absolute accuracy in the lower troposphere is always improved by using the combined VAS+SFC predictors.

Fig. 4 presents a series of VAS retrievals of 920 mb dewpoint over the midwestern United States, performed with and without ancillary SFC data. Relative accuracy of the low level moisture is significantly superior in the VAS+SFC soundings, which clearly show: (1) a reproducible east-west moisture gradient across Nebraska-Kansas, (2) an east-to-west dry slot across central Missouri, and (3) a significant water vapor maximum in eastern Iowa and western Illinois. RAOB reports are indicated at 1200 and 2300 GMT, but they are too sparse to provide verification of the mesoscale details. Objective verification of the space-time continuity is provided by two numerical values: (1) the RMS scale length L(t) for the gradients within the field at time t, and (2) the temporal correlation C(t,t′) between successive fields.

$$\Delta T(t) = T(t) - \langle T(t)\rangle \qquad (2)$$

$$L^2(t) = \langle \Delta T^2(t)\rangle / \langle [dT(t)/dx - \langle dT(t)/dx\rangle]^2\rangle$$

$$C(t,t') = \langle \Delta T(t)\Delta T(t')\rangle / [\langle \Delta T^2(t)\rangle\langle \Delta T^2(t')\rangle]^{1/2}$$

The ensemble averages <...> are taken horizontally over the objectively gridded fields. Fig. 4 lists values of L(t) in km and C(t,t′) as %. The VAS+SFC gradient scales average 174±19 km and are smoothest at midday, while the VAS-only scale lengths average only 113±14 km and are roughest at midday. The VAS+SFC frame-to-frame correlations are consistent at 91±3%, while the VAS-only correlations are scarcely significant at 75±6%. The VAS+SFC low level moisture retrievals appear to be completely independent of side effects from the diurnal heating, while the

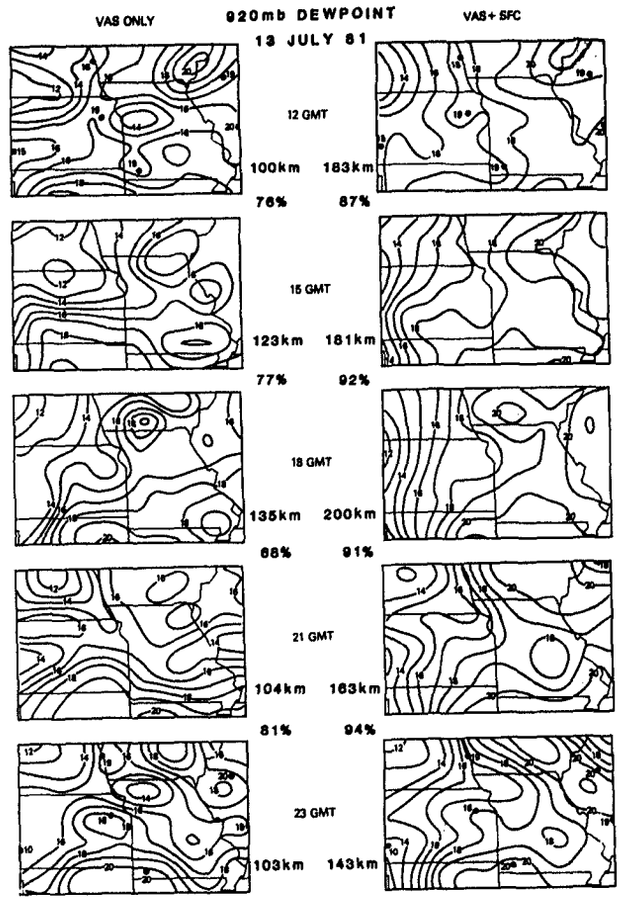

Figure 4: Continuity of VAS-only and VAS+SFC 920 mb dewpoint fields, measured by gradient scale lengths and temporal correlations

VAS-only fields show dramatic changes in structure, such as in the direction of the moisture gradient across Kansas at 1800 GMT. Further demonstrations of VAS space-time stability and of the impact by SFC data are published in Lee et al. (1983).

4. VERIFICATION WITH A MESOSCALE NETWORK

The VAS Atmospheric Variability Experiment (VAS/AVE) attempted to capture severe storm conditions by gathering simultaneous VAS and radiosonde data in the south-central Great Plains during the spring of 1982, including a separate meso-b network in central Texas. However, the VAS/AVE experiment was frustrated by generally cloudy and non-convective weather conditions during its operations (Greaves et al., 1982). The observations from 6 March 1982 are suitable for a mesoscale case study, capturing clear, cold air moving southeastward behind a snow storm pushing into warm, moist air. This

VAS/AVE case is thoroughly discussed in the final report of the VAS Demonstration (Montgomery and Uccellini, 1984).

The VAS+SFC regression soundings were trained with 50 RAOB profiles from the regional NWS network at 1200 and 2300 GMT, and with profiles estimated at 1800 GMT as a linear interpolation between the synoptic reports. The synthetic midday data was introduced in order to include diurnal effects in the statistical training. In addition, VAS channel 12 was suppressed in order to avoid diurnal effects on this window channel.

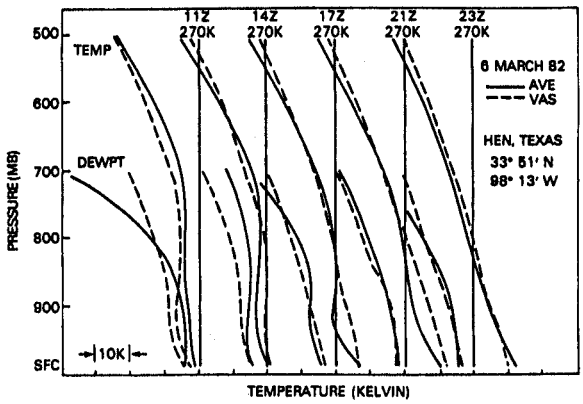

Figure 5: Time series of VAS/AVE temperature and dewpoint profiles at Henrietta, Texas on 6 March 1982

Fig. 5 displays a representative time-series of VAS and AVE temperature and dewpoint profiles retrieved at the Henrietta (HEN) site in northern Texas. This VAS/AVE comparison reveals that: (1) the VAS and AVE profiles are in general agreement, (2) the temproral changes are fairly well monitored by VAS, (3) the low level dewpoint is accurately retrieved with VAS+SFC data, (4) the temperature inversion at 920 mb is unresolved by VAS, and (5) the cold layer at 500 mb is underestimated by VAS.

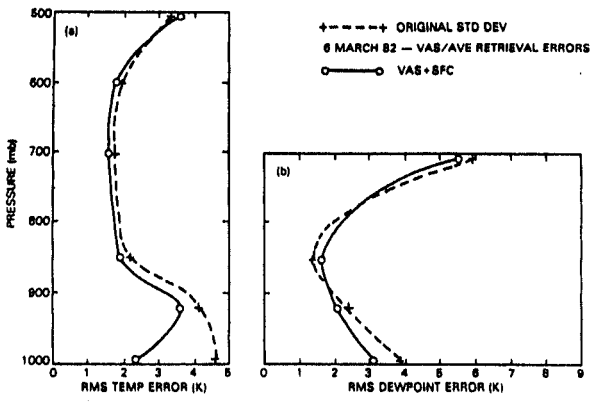

Figure 6: RMS differences between VAS-AVE profiles on 6 March 1982

Fig. 6 displays the RMS VAS-RAOB differences for the VAS/AVE profiles (214 samples). The absolute accuracy of the VAS+SFC soundings is significant only near the surface, where the ancillary SFC data are most influential. The 920 mb temperature inversion variations are unresolved, and temperature variations from 850 to 600 mb are too small to detect. The poor temperature accuracy at 500 mb is unexpected, since several VAS channels are temperature sensitive at this level. Two attempts were made to improve VAS absolute accuracy: (1) the VAS-SFC-RAOB colocation requirements were tightened, and (2) cloud rejection criteria were stiffened. Each attempt at improved quality control reduced the VAS/AVE sample size by a factor of two, but neither attempt significantly improved the VAS/AVE differences shown in Fig. 6. The surprising inaccuracy of the VAS temprature retrievals at 500 mb remains under investigation for this case.

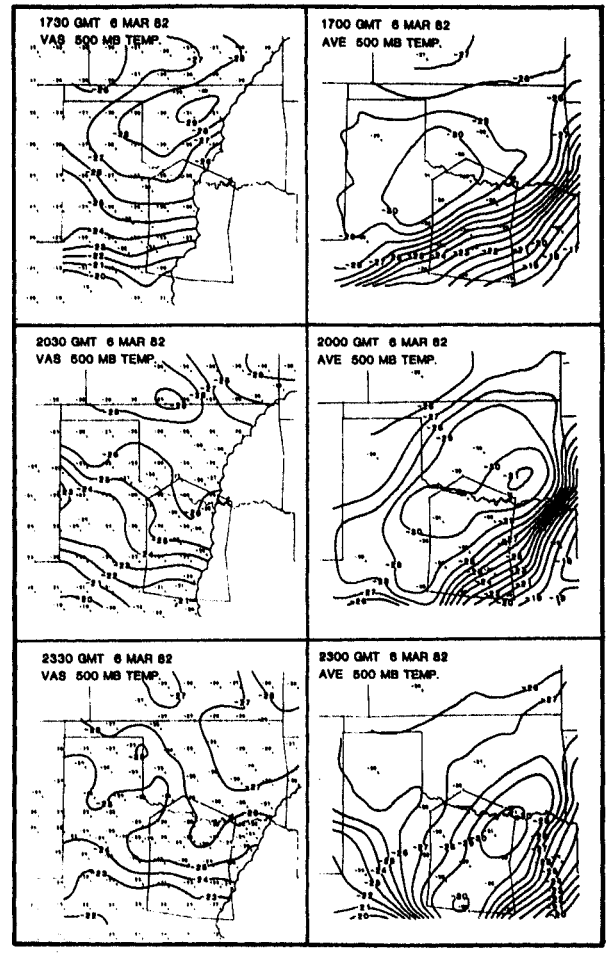

Figure 7: Time series of VAS and AVE 500 mb temperature fields on the afternoon of 6 March 1982

Fig. 7 compares VAS and AVE 500 mb temperature analyses. The RAOB fields indicate a cold bubble moving in behind the strong temperature gradient under the clouds in southeastern Texas. The VAS fields consistently indicate a cool

pocket further north, moving eastward across Oklahoma, with a weak north-south temperature gradient over the meso-b network. The apparent differences are due as much to dissimilarity in coverage as to retrieval errors. The RAOB gradients are heavily influenced by reports from stations located well outside of the displayed region, while the VAS retrievals are densely reported, but only in the cloud-free areas. A VAS/AVE comparison over the cloud-free meso-b network reveals more differences in absolute than in relative values. The cold bubble is detected as relatively colder air by both the VAS and AVE soundings, and the temparature gradient in the cloud-free section over the southern part of the meso-b network is comparable. In summary, VAS is superior for horizontal coverage in cloud-free areas, but the AVE radiosonde network in superior for vertical resolution and temperature accuracy.

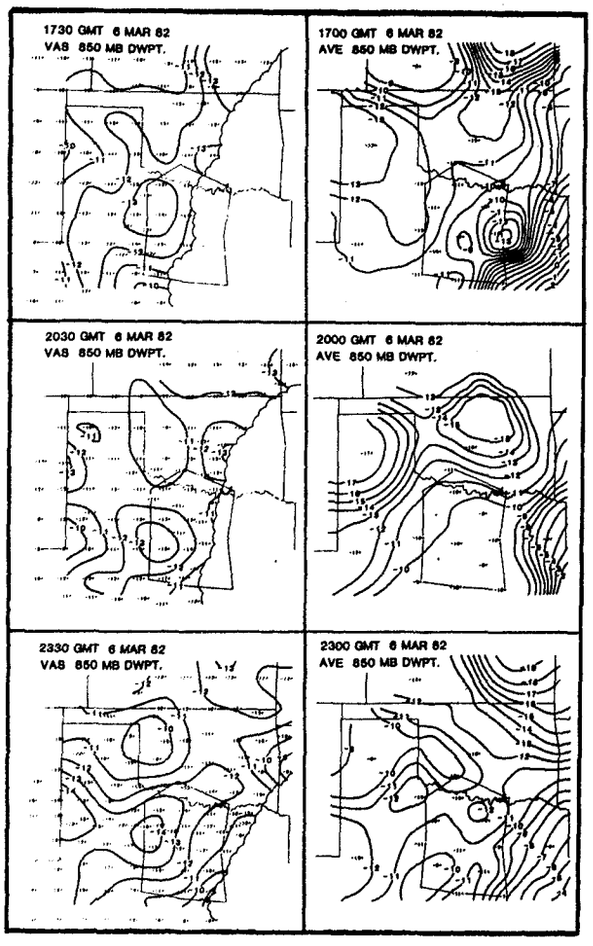

Figure 8: Time series of VAS and AVE 850 mb dewpoint fields on the afternoon of 6 March 1982

Fig. 8 compares the VAS and AVE 850 mb dewpoint analyses. The RAOB moisture fields are surprisingly inconsistent even over the meso-b network. The VAS moisture fields are very consistent, with a dry pocket imbedded over the meso-b network. The VAS low level moisture retrievals over the meso-b network are about 3°C drier than the RAOB reports, but provide more coherent spatial detail than the the AVE soundings. The retrieved moisture gradients at this level are determined mainly by the VAS "split window" (channels 7 and 8), which have been demonstrated to be a reliable measure of relative water vapor content integrated over the lower troposphere (Chesters et al., 1983). Consequently, the accuracy of the VAS 850 mb moisture retrievals in Fig. 8 appear to be superior to the AVE "ground truth" in everything except absolute value.

The AVE "ground truth" radiosonde data have some notable inaccuracies. During the experiment, mandatory levels and entire profiles were sometimes unreported. For example, three meso-b sites fail to report the 850 mb dewpoint at 2000 GMT in Fig. 8. The AVE upper air dewpoint data is error-prone. As an example which indicates the degree of RAOB self-consistency, the 2300 GMT radiosonde over Abilene failed at 500 mb, and another was launched at 0000 GMT. These repeated measurements show dewpoint discrepancies of 5°C at 700 mb and 3°C at 500 mb, while remaining in agreement by ±0.2°C for the other levels in the profile. Finally, the SFC (airways) and RAOB (lowest level) reports show temperature and dewpoint discrepancies of 2° to 3°C, and some AVE stations disagree with their neighboring airways reports by more than 10°C. Consequently, many of the discrepancies between the VAS and AVE 850 mb dewpoint fields in Fig. 8 are actually due to errors in the conventional data.

5. CONCLUSIONS ABOUT VAS ACCURACY

These two case studies provide some benchmarks for the accuracy of useful VAS mesoscale soundings in the lower troposphere:

(A) Absolute temperature accuracy is ±2°C below 500 mb.

(B) Absolute dewpoint accuracy is ±2° to ±3°C below 850 mb.

(C) Absolute accuracy in total precipitable water is ±0.3 cm.

(D) Mesoscale dewpoint fields show excellent temporal continuity (90% correlations) and spatial gradients (200 km scale lengths).

(E) Low level moisture fields are relatively independent of diurnal effects when retrievals are properly trained and conditioned.

(F) Low level stability indicators are accurately retrieved when ancillary surface data are included to suppress the undesirable influence of the skin temperature detected by the VAS window channels.

This degree of accuracy requires careful sounding techniques:

(a) A noise- and bias-resistant retrieval algorithm, such as regression conditioned by signal/noise estimates.

(b) The ability to suppress the sunlight contaminated shortwave window in order to avoid diurnal effects, especially at low latitudes.

(c) The use of ancillary surface temperature and dewpoint data in order to resolve features below 920 mb.
(d) Sufficiently varied and appropriate radiosonde training in order to encompass regional and diurnal variations.
(e) Man-interactive quality control and the use of high resolution visible data in order to detect cloud contamination.

Notable limitations uncovered by these verification studies are:
(i) Uncertain verification of VAS temperature profile soundings at 500 mb and above.
(ii) Uncertain verification of the VAS dewpoint profile soundings at 700 mb and above.
(iii) The inability to resolve detailed vertical features, such as temperature inversions and thin layers of water vapor in the middle troposphere.
(iv) The inability of VAS to sound in cloudy areas, such as those already undergoing convection.
(v) The difficulty of acquiring enough cloud-free radiosonde profiles with the appropriate space-time coverage for thorough statistical training and testing of the VAS soundings.
(vi) Significant discrepancies between radiosonde reports at the bottom of the boundary layer and surface (airways) reports from the neighboring stations, with RMS differences of $\pm 1.5^\circ$ and $\pm 2.0^\circ$C in temperature and $\pm 2.0^\circ$ and $\pm 3.0^\circ$C in dewpoint for the conventional NWS and AVE networks, respectively.

Conditioned regression retrievals are very good at suppressing difficulties, but they also sacrifice some of the information available in the satellite data. Consequently, this assessment should be regarded as a pessimistic estimate for VAS accuracy while the VAS instrumentation and ground-based processing are improved.

6. ACKNOWLEGDEMENTS

Dr. Louis Uccellini (VAS Demonstration Scientist) and Dr. Ralph Petersen provided meteorological guidance with the analysed fields. Mr. David Larko (Research and Data Systems, Inc.) assisted in the analysis of the shortcomings of the AVE radiosonde data.

7. REFERENCES

Chesters, D., L.W. Uccellini and A. Mostek, 1982: VISSR Atmospheric Sounder (VAS) simulation experiment for a severe storm environment. Mon. Wea. Rev., 110, 198-216.

Chesters, D., L.W. Uccellini and W.D. Robinson, 1983: Low-level water vapor fields from the VISSR Atmospheric Sounder (VAS) split window channels. J. of Climate and Appl. Meteor., 22, 725-743.

Chesters, D. and W.D. Robinson, 1983: Performance appraisal of VAS radiometry for GOES-4, -5 and -6. NASA TM 85125. 55 pp.

Greaves, J.R., H.E. Montgomery, L.W. Uccellini and D.L. Endres, 1982: 1982 AVE/VAS ground truth field experiment: satellite data acquisition summary and preliminary meteorological review. NASA/GSFC X-903-82-17. 27 pp.

Koch, S.E., M. DesJardins and P.J. Kocin, 1983: An interactive Barnes objective analysis scheme for use with satellite and conventional data. Accepted by J. of Climate and Appl. Meteor..

Lee, T.H., D. Chesters and A. Mostek, 1983: The impact of conventional surface data upon VAS regression retrievals in the lower troposphere. J. of Climate and Appl. Meteor., 22, 1853-1874.

Menzel, W.P., W.L. Smith and L.D. Herman, 1981: Visible infrared spin-scan radiometer atmospheric sounder radiometric calibration: an inflight evaluation from intercomparisons with HIRS and radiosonde measurements. Appl. Opt., 20, 3641-3644.

Montgomery, H.E. and L.W. Uccellini, editors, 1984: The Final Report of the VAS Demonstration, NASA Conf. Publ., in preparation.

Mostek, A., L.W. Uccellini, R.A. Petersen, D. Chesters and T.H. Lee, 1984: A case study of the impact of VAS soundings in the analysis of a pre-convective environment. In preparation for Mon. Wea. Rev..

Petersen, R.A., L.W. Uccellini, D. Chesters and A. Mostek, 1983: The use of VAS satellite data in weather analysis, prediction and diagnosis. Nat. Wea. Dig., 8, 12-23.

Petersen, R.A., L.W. Uccellini, A. Mostek and D.A. Keyser, 1984: The use of VAS moisture channels in delineating regions with a potential for convective instability. Accepted by Mon. Wea. Rev..

Smith, W.L., V.E. Suomi, F.X. Zhou and W.P. Menzel, 1982: Nowcasting applications of geostationary satellite atmospheric sounding data. Nowcasting, ed. K.A. Browning, Academic Press, New York, NY, pp 123-135.

VERIFICATION AND ANALYSIS OF TOVS SATELLITE DATA

M.E. Gelman*, F.J. Schmidlin+, and A.J. Miller*

*NOAA, NMC, Climate Analysis Center
Camp Springs, Maryland

+NASA, Goddard Space Flight Center
Wallops Island, Virginia

1. INTRODUCTION

Satellite sounder data from Tiros Operational Vertical Soundings (TOVS) are being used at the National Meteorological Center (NMC), NOAA to produce daily global fields of geopotential height and temperature at 8 pressure-levels in the stratosphere 70 to 0.4 mb (18-55 km) (Gelman et.al., 1983). At 70 to 10 mb, rawinsonde data are also used in the analyses for deriving the Northern Hemisphere fields. TOVS data are used exclusively for the 5-to 0.4-mb fields.

The NMC stratospheric fields are used for many applications. A few examples of these uses include monitoring of the stratosphere for long term changes (possible anthropogenic influences)(Geller et.al., 1983), short-term changes (stratospheric warmings), correlation of the thermodynamic and motion fields with aerosols and constituent measurements, and determining atmospheric density and wind influence on aerospace vehicles (i.e. space shuttle). For all these applications and others it is important to have estimates of the uncertainty in the fields of temperature, geopotential height, and derived winds.

Verification of these stratospheric temperature fields and winds (derived geostrophically from the height fields) has involved using radiosonde and rocketsonde data. The major interest in this study concerns not only verification of the original TOVS stratospheric temperature information and derived geopotential heights, but also the higher order derivations of wind, heat flux and momentum flux.

2. DISCUSSION

Previous work (Gelman et. al., 1983, 1980) has shown that mean differences between satellite data and rocket data vary with satellite instrument, geographic location (latitude), and pressure level. Biases of 1 to 5°C, 5-10 m/sec, and root mean square differences of 4 to 7°C and 15 m/sec are representative of these kind of comparisons.

For this study we have emphasized examination of temperature and wind changes with time. Rocketsondes were launched daily at the times of NOAA-7 overpasses of Wallops Island during 23 Feb.- 24 Mar. 1982. Resources made available by NASA were used to provide in-situ field measurements and additional analysis. Measurements, reduction methods, and other techniques attendant to obtaining the in-situ data were carefully controlled to ensure that the data were as error free as possible. The levels examined were the 50-, 30-, 10-, 5-, 2-, 1-, and 0.4-mb pressure surfaces. The special rocket soundings launched once daily for 30 days from Wallops Island have been studied to provide further insight into the nature of differences between in-situ and remotely sensed data and derived products.

The daily soundings over the month allow a continuous record of the extent to which the day- to- day changes over Wallops Island as observed from a high resolution in-situ soundings were captured from satellite data and analyses of those satellite soundings. The correlations between data sources range from .90 to .79 for west to east wind, .62 to .45 for south to north wind and .77 to .27 for temperatures at 5 to 1 mb, respectively. The high correlation in the zonal wind components suggests that the analyses may be quite adequately used to portray this aspect of the circulation. However, there was relatively low correlation of the meridional wind components and 1-mb temperatures at this location and time. This may be due to the relatively weaker south-north wind and their smaller variations. This suggests we should use some caution for calculations such as heat flux and momentum flux that use this quantity.

Data have been compared in various ways. The most straightforward way was to directly compare the TOVS satellite products from the hemispheric analyses with unsmoothed rocketsonde data, as discussed above. However, the vertical resolution of the satellite data is much broader than the finer resolution of the rocket measurement. In order to study the consistency in resolution of the two techniques, the individual rocketsonde wind and

temperature profiles were also smoothed in the vertical. Harmonic smoothing of the rocket data (available at 100 meter intervals) was accomplished between harmonics number one to ten. The fundamental vertical wavelength selected was 36 km because the 30-day rocketsonde data set was complete between 20 and 56 km. Smoothing 10 harmonics over a 36-km fundamental wavelength thus provided derivation of the wind and temperature that corresponded to vertical resolution of 36 km (harmonic number one) to 3.6 km (harmonic number ten). Analysis of the percent of the variance of the wind components explained by each harmonic indicated that for most days during the period, broad scale waves in the vertical predominated, with most variance explained by harmonics one and two. On days when there was more contribution to variations by shorter scale motions, differences between rocket and satellite data appeared no greater than on days when vertical scales were broader. No evidence could be found that supported any clear relatonsip between the degree of smoothing and the differences between the analysis values and smoothed in-situ values.

The comparisons to date have had important benefits. There is an increased awareness of satellite instrumental changes, with their attendant effects on derived data. The NOAA/NESDIS has instituted timely updates of the coefficients relating radiance to temperature to account for gradual shifts in pressure of the Stratospheric Sounding Unit (SSU) channels in each instrument and somewhat greater differences between instruments for different satellites. Such adjustments go a long way in alleviating severe jumps in the base level of derived temperatures. For longer term use of the satellite data, the comparisons have provided a much needed "calibration" or base level against which to measure average differences. Other important benefits of the comparisons arise from assessing and documenting the stratospheric scales of motion that may be captured by the remote soundings relative to the scales of motion appearing in the in-situ data. It is clear that we should not expect the same resolution from the different observing systems. However, it is very important to gain a more complete understanding of the strengths and limitations of these sounding systems.

We are continuing to study these data and we will present our latest results at the conference.

3. REFERENCES

Geller, M. A., M. F. Wu and M. E. Gelman, 1983: Troposphere-Stratosphere (Surface-55 km) Monthly Winter General Circulation Statistics for the Northern Hemisphere-Four Year Averages. J. Atmos. Sci., Vol. 40, 1334-1352.

Gelman, M. E., R. M. Nagatani, A. J. Miller, J. D. Laver, and F. G. Finger, 1980: An Evaluation of Stratospheric Meteorological Analysis Using Satellite Sounder and Rocketsonde Data. Extended Abstracts from International Symposium on Middle Atmosphere Dynamics and Transport, Edited by S. K. Avery, Urbana, Illinois, Handbook for MAP Vol. 2, 1-9.

Gelman, M. E., A. J. Miller, R. M. Nagatani, and H. D. Bowman II, 1983: Mean Zonal Wind and Temperature Structure During the PMP-1 Winter Periods. Adv. Space Res., Vol. 2, 159-162.

Smith, W., H. W. Woolf, C. Hayden, D. Wark, and L. McMillan, 1979: Bull. Amer. Meteor. Soc., Vol. 60, 1177-1187.

G.7

THE EFFECT OF WIND AND MOISTURE GRADIENTS ON THE ARBITRARY ASSIGNMENT OF CLOUD MOTIONS TO A VERTICAL COORDINATE SYSTEM IN TWO SESAME CASES

Cynthia A. Peslen, Steven E. Koch, and Louis W. Uccellini

Goddard Laboratory for Atmospheric Sciences
NASA/Goddard Space Flight Center
Greenbelt, MD 20771

1. INTRODUCTION

The increasing use of satellite-derived cloud motion "wind" vectors (CMV) in mesoscale and global analyses and in numerical models has raised questions concerning the uncertainty of the level assignment for the CMV. There are two major problems in selecting a level for the CMV. The first is related to uncertainties in assigning the motion vector to either the cloud top or base, a problem compounded by limitations in determining the actual cloud height based on infrared data. The second problem is related to the inability to transfer the "wind" derived from the CMV at individually specified heights to a standard coordinate surface (e.g., pressure level). This is due to the lack of wind shear information needed to interpolate the CMV wind to the specified levels. Given these problems, the CMV have been arbitrarily assigned to "low," "middle" or "upper" isobaric levels based upon surface reports, sounding data, or infrared emissivities (Hubert and Whitney, 1971; Wilson and Houghton, 1979; Negri and Vonder Haar, 1980; and Peslen, 1980). However, the arbitrary assignment of CMV to a single level could lead to serious errors in regions of strong vertical wind shear usually found near the strong thermal inversions which mark the pre-thunderstorm environment.

The objective of this paper is to assess if the arbitrary level assignment poses a serious obstacle to the use of cloud motion wind vectors in the meso-scale analysis of a severe storm environment. Two SESAME case studies are used in this study, each marked by different wind shear characteristics and each containing a distinct moisture discontinuity. In this analysis, comparisons are made between analyses based upon arbitrarily assigning CMV to a pressure surface and to a normalized pressure (σ) surface which are both representative of the lower troposphere. The goal is to determine (1) if there is a preference for sigma over pressure and (2) the impact of moisture gradients on the level assignment for either coordinate system. We have also analyzed the effect of interpolating the CMV to specific pressure and σ levels using a vertical wind shear vector derived from the SESAME radiosonde data base. The results of this work are discussed in a forthcoming expanded paper.

2. DATA AND METHOD

High resolution soundings acquired from the AVE-SESAME regional scale network (Alberty et al., 1979) and time-compatible 3 min interval visible GOES pictures for 2000 GMT 9 May and 1800 GMT 10 April are used to create the data sets for this study (Figs. 1 and 2). For each case, two wind sets are created; a "SESAME" wind set based solely on the radiosonde data and a "combined" wind set based on a combination of the radiosonde and satellite winds where the CMV are acquired using an interactive analysis and display system called the Atmospheric and Oceanographic Information Processing System or AOIPS (Billingsley, 1976).

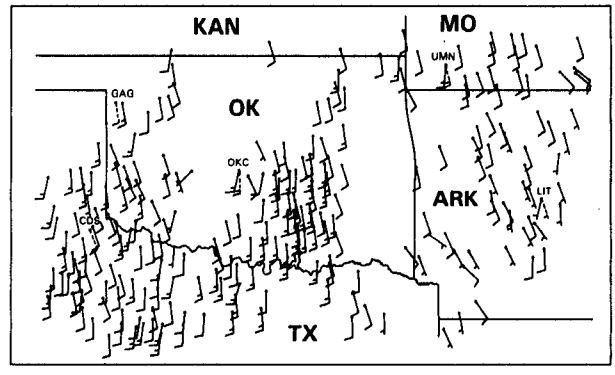

Fig. 1. *Regional scale SESAME rawinsonde wind data at 825 mb and σ=0.9 and low level cloud motion vectors for 9 May 1979. Rawinsonde data are the wind barbs at GAG, CDS, OKC, UMN, and LIT (solid barbs at 825 mb; dashed barbs at σ=0.9). All wind barbs have units of m s^{-1} where one flag ✓ = 10 m s^{-1}.*

Grid point values of the combined winds and of the SESAME winds are derived from a Barnes (1973) interpolation scheme which has been modified specifically to incorporate satellite data (Koch et al., 1983). The data spacing (Δn) [Δn=2.7° for 9 May and Δn=2.0° for 10 April] corresponds to the Δn of the regional scale in each SESAME case. To insure proper representation of resolvable features, the computed grid spacing (Δx) is Δx=1.0° for both

case studies. Grid point values of the SESAME data are subtracted from those values of the combined data resulting in vector differences between the winds which show the impact of the non-uniformly distributed cloud motion winds on the larger-scale rawinsonde wind field. The comparisons are made first assuming that the CMV are arbitrarily assigned to 825 mb, then assuming that they are assigned to σ ($\sigma = P_{vector}/P_{surface}$)=0.9.

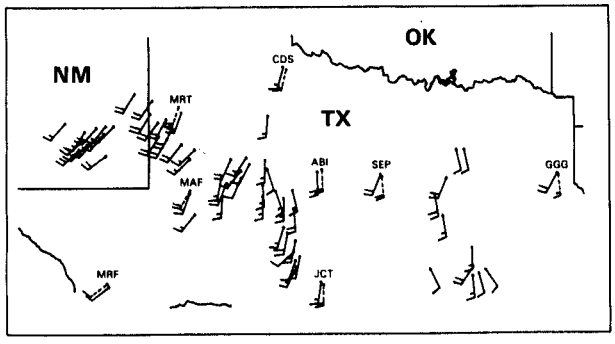

Fig. 2. *Regional scale SESAME rawinsonde wind data at 825 mb and σ=0.9 and low level cloud motion vectors for 10 April 1979. Rawinsonde data are the wind barbs at MRT, CDS, ABI, SEP, MRF, GGG, MAF, and JCT (solid barbs at 825 mb; dashed barbs at σ=0.9). All wind barbs have units of m s^{-1} where one flag ⟋ = 10 m s^{-1}.*

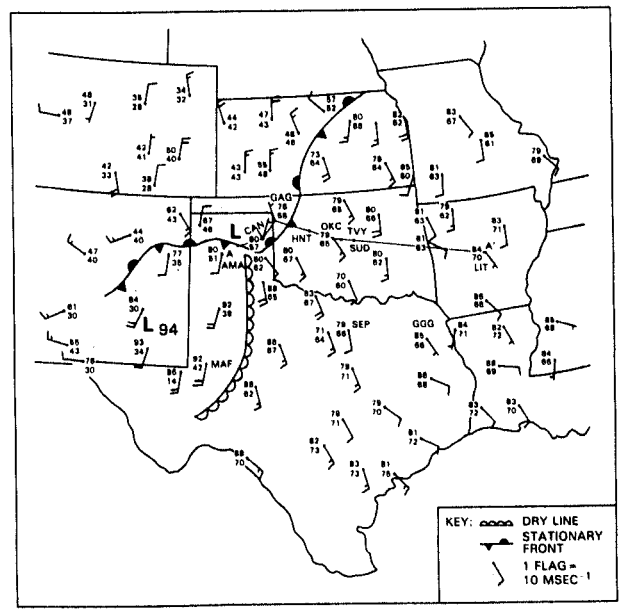

Fig. 3. *The 2000 GMT surface hourly analysis for 9 May 1979. Temperature and dew points in (°F) are plotted adjacent to each surface station. All wind barbs have units of m s^{-1} where one flag ⟋ = 10 m s^{-1}.*

3. 9 MAY 1979 CASE STUDY

3.1 Synoptic Analyses

On 9 May 1979, severe thunderstorms developed after 2100 GMT in the Texas and Oklahoma panhandles within the convectively unstable atmosphere ahead of a stationary front. The 2100 GMT surface hourly analysis (Fig. 3) shows a developing low in the Texas panhandle and a stationary front separating cool, dry northerly air from warm, moist tropical air. The area of CMV is located east and south of the front within a relatively homogeneous air mass.

Analysis of the 2000 GMT SESAME soundings shows the existence of a restraining inversion at 750 mb. The cross section (Fig. 4) between Amarillo (AMA), TX, and Little Rock (LIT), AR, (refer to line A-A', Fig. 3 for locations) shows a well-mixed layer east of GAGE (GAG), OK, between 750 mb and 600 mb. There is rather weak vertical wind shear across Oklahoma despite the presence of a strong inversion. The most significant aspects of the wind field are (1) the horizontal variation of the vertical wind shear in the plane of the cross section, (2) the stronger vertical wind shears at AMA and GAG, and (3) the considerable directional shear at LIT.

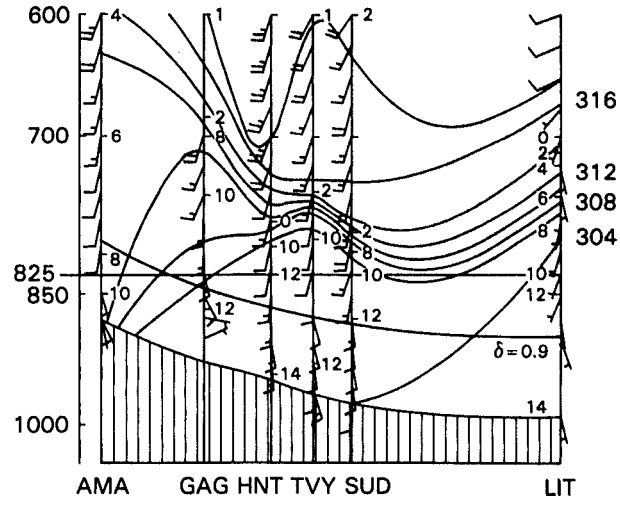

Fig. 4. *Vertical cross section from Amarillo (AMA), TX, to Little Rock (LIT), AR, along a sequence of stations (A-A' in Fig. 3) for 2000 GMT 9 May 1979. Solid lines correspond to isentropes (°K), one flag ⟋ = 10 m s^{-1}, and values of mixing ratio (in g kg^{-1}) are located adjacent to the vertical profile for each rawinsonde station.*

3.2 Results of CMV Assignment

Fig. 5 shows the vector differences in wind between combined winds and SESAME winds for CMV arbitrarily assigned to 825 mb. Arbitrary assignment of CMV to 825 mb produces vector differences ≥ 2 m s^{-1} east of central Oklahoma. A comparison of the CMV directions and speeds in Fig. 1 with the vertical profile of rawinsonde-observed winds (Fig. 4) reveals that the large vector differences in the eastern half of Fig. 5 are primarily due to assignment of CMV too high in the atmosphere in the presence of vertical wind shear. Lower level (~875-900 mb) clouds, which are embedded in a southeast flow east of Hinton (HNT), OK, are being assigned to a level of stronger southwest winds at 825 mb. The result of this assignment is to decrease the overall wind speed and to give the wind a southeasterly component at 825 mb.

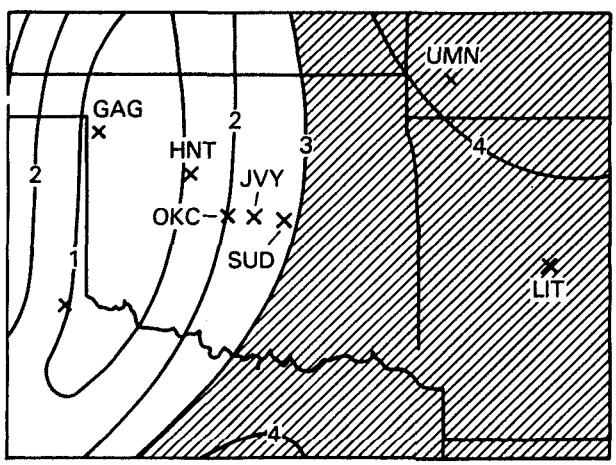

Fig. 5. *Vector differences in wind (m s^{-1}): combined (SESAME and CMV) winds minus SESAME winds at 2000 GMT, 9 May 1979 for CMV arbitrarily assigned to 825 mb. Vector differences ≥ 3 m s^{-1} are shaded.*

Arbitrary assignment of CMV to σ=0.9 (Fig. 6) shows comparatively smaller vector differences than for the 825 mb assignment case because the arbitrary assignment of CMV is made through a smaller depth of vertical wind shear. Southeasterly CMV at cloud base levels (between σ=.93 and σ=.88) are very similar to the southeasterly SESAME winds at σ=0.9. Cloud base levels appear to follow closely the slope of the σ surface and, consequently, the slope of the terrain. For the 825 mb case, the southeasterly CMV are being assigned to a level of strong southwest winds within a deeper layer of vertical wind shear between cloud base (~875-900 mb) and 825 mb. The vector differences in the wind remain large (>3 m s^{-1}) in extreme northeast Texas for two reasons. The assignment of CMV to σ=0.9 is done

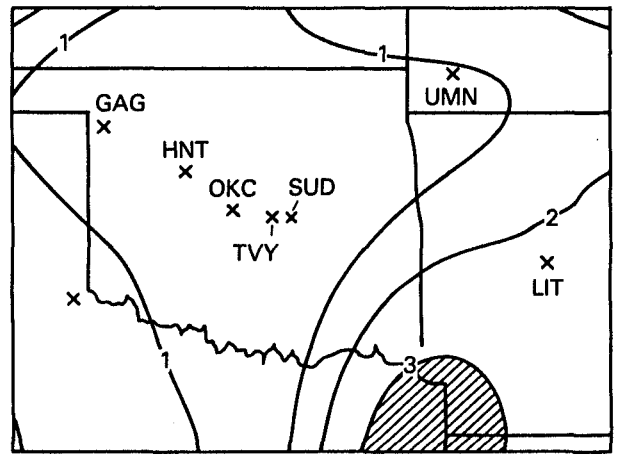

Fig. 6. *Same as in Fig. 5, except for CMV arbitrarily assigned to σ=0.9.*

through a layer of strongly veering winds located between Stephenville (SEP), TX, and Longview, TX (not shown). Although these stations are not displayed in the analysis area in Fig. 6, they are a part of a larger data area which influences the results of the objective analysis of the winds. The second reason is the existence of a strong horizontal gradient of the v component of the wind across eastern Oklahoma and Arkansas at 825 mb and σ=0.9. Consistently large vector differences could also be a reflection of increased error in the rawinsonde measurement of the wind at a point within an area of large horizontal gradient.

The results for 9 May indicate that vector differences in the wind occur between combined and SESAME wind sets due to the existence of horizontal and vertical gradients in the wind field. Since cloud bases follow closely the slope of a σ surface, CMV are being arbitrarily assigned to σ=0.9 within a smaller depth of vertical wind shear. This results in smaller vector differences at σ=0.9 than at 825 mb, except under conditions of strong horizontal gradient of the winds.

4. 10 APRIL 1979 CASE STUDY

4.1 Synoptic Analyses

On 10 April 1979, severe thunderstorms developed in the northern Texas panhandle and later in north-central Texas and southern Oklahoma between 1800 GMT and 0200 GMT. The 1800 GMT surface hourly analysis (Fig. 7) shows a cold front extending from an intense low pressure system in Colorado to the Texas-Mexico border. The initial thunderstorm activity began at 1800 GMT south of AMA, TX, and northeast of a dry line in western Texas (Alberty et al., 1979). The dry line separates warm, moist southeasterly air from hot, dry air which has its source air from over the elevated Mexican plateau (Carlson et al., 1980 and Carlson et al., 1983). The initial outbreak of severe thunderstorms moves eastward by 2100 GMT toward the weak warm front in north-central Texas where more intense storms develop in the Red River Valley.

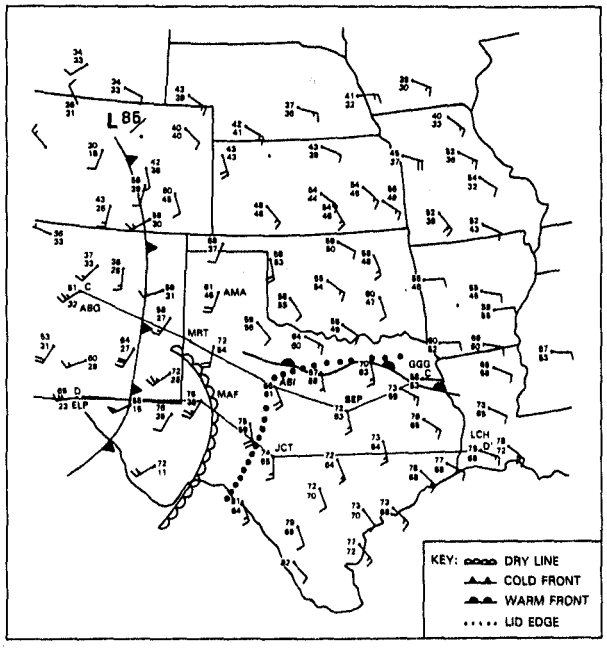

Fig. 7. *The 2000 GMT surface hourly analysis for 10 April 1979. Temperature and dew points in (°F) are plotted adjacent to each surface station. All wind barbs have units of m s^{-1} where one flag = 10 m s^{-1}.*

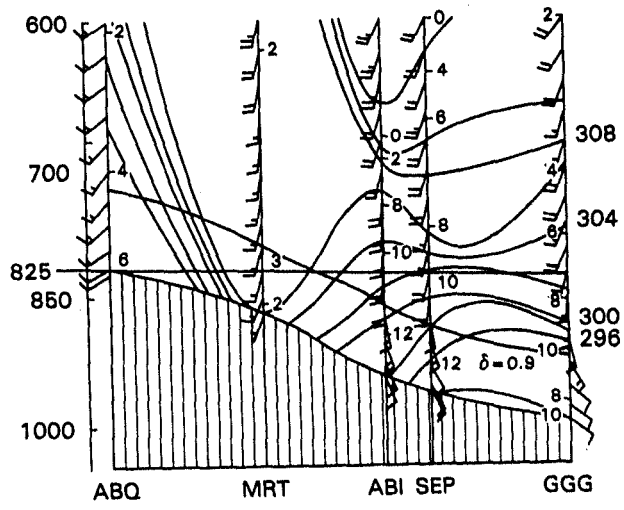

Fig. 8. *Vertical cross section from Albuquerque (ABQ), NM, to Longview (GGG), TX, along a sequence of stations (C-C' in Fig. 7) for 1800 GMT 10 April 1979. Solid lines correspond to isentropes (°K), one flag = 10 m s^{-1}, and values of mixing ratio (g kg^{-1}) are located adjacent to the vertical profile for each rawinsonde station.*

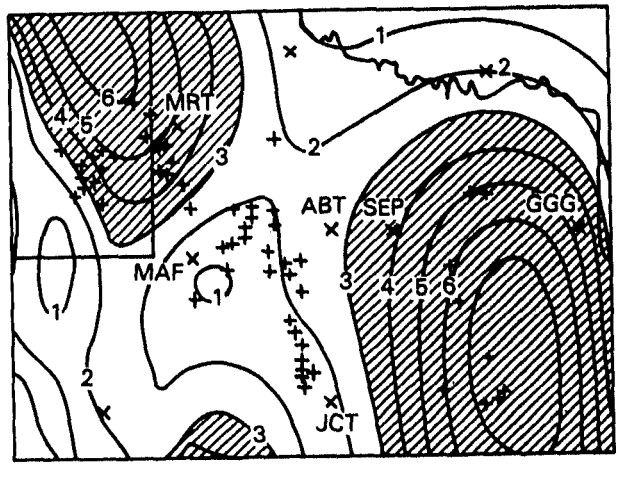

Fig. 9. *Vector differences in wind (m s^{-1}): combined (SESAME and CMV) winds minus SESAME winds at 1800 GMT, 10 April 1979 for CMV arbitrarily assigned to 825 mb. Vector differences ≥ 3 m s^{-1} are shaded.*

Analyses of the 1800 GMT SESAME regional scale soundings (Fig. 8) show southwesterly flow at all levels for stations at and west of Morton (MRT), TX, as is characteristic of a well-mixed layer. Southeasterly moist air is overlaid by southwesterly drier air at mid levels east of MRT, TX. The 10 April case is similar to 9 May in that differential advection of mid level warmer, drier air from Mexico over the cooler, moister air from the Gulf of Mexico has created an inversion over southern and eastern Texas and Louisiana. The western edge of the inversion is displayed in Fig. 7. The 10 April case is different from 9 May in that CMV are not uniformly distributed but occur in clumps of data and that there is a strong moisture discontinuity (a dryline) whose existence influences the results of the vector differences.

4.2 Results of CMV Assignment

Fig. 9 shows the vector differences in wind between the combined winds and SESAME winds for CMV arbitrarily assigned to 825 mb. Arbitrary assignment of CMV to 825 mb produces large vector differences ≥ 3 m s^{-1} in eastern Texas and New Mexico. CMV are assigned too high in the atmosphere east of Abilene (ABI), TX, in the presence of vertical wind shear. The vertical wind field is highly variable between the surface and 825 mb in eastern Texas. The vertically-averaged shear between 775 and 875 mb is 1.8 m s^{-1} 25 mb^{-1} decrease and 1.0 m s^{-1} 25 mb^{-1} decrease in the u and v components, respectively. The 900-940 mb level CMV are decreasing the wind speeds at 825 mb and are making the winds more south-southeasterly. These cloud tracers have lower bases than their counterparts west of ABI due to suppression of convection by the inversion over eastern Texas. In New Mexico, CMV are being assigned too low in the atmosphere at 825 mb. Their stronger southwesterly winds are increasing the overall wind field. Although cloud bases are horizontally interpolated to be near 700 mb, the actual values are probably higher due to the existence of dry air west of the dryline. An accurate determination of cloud bases is difficult to achieve because of sparse

rawinsonde data west of MRT and the necessity to horizontally interpolate cloud bases across a moisture discontinuity. The dryline has an interesting effect on the overall wind field. CMV are higher than 825 mb west of the dryline and, consequently, they tend to increase the scalar u component of the wind (figure not shown) in the presence of positive vertical wind shear. Farther east of the dryline, CMV are lower than 825 mb and the opposite is true. The arbitrary assignment of CMV to 825 mb in the area between Midland (MAF), TX, and Junction (JCT), TX, has little impact on the SESAME winds as vertical wind shears are small ($\sim$1 m s^{-1} 25 mb^{-1}) and cloud bases are near 825 mb.

Arbitrary assignment of CMV to σ=0.9 (Fig. 10) results in much smaller vector differences overall. Because cloud bases apparently parallel the σ=0.9 surface across eastern Texas, this surface is a better choice of level assignment than 825 mb. The persistence of vector differences > 3 m s^{-1} in New Mexico can be explained on the basis of CMV which are assigned too low at σ=0.9 in the presence of vertical wind shear. The cloud base levels jump up above the σ=0.9 surface as the dryline is crossed from east to west. This behavior is consistent with the presence of much drier air and, hence, higher condensation levels over New Mexico. Strong moisture gradients evidently impose an upper limit on the usefulness of the sigma system for CMV level assignment. The persistence of large vector differences in New Mexico could also be due, in part, to a suspected sampling problem in the rawinsonde data.

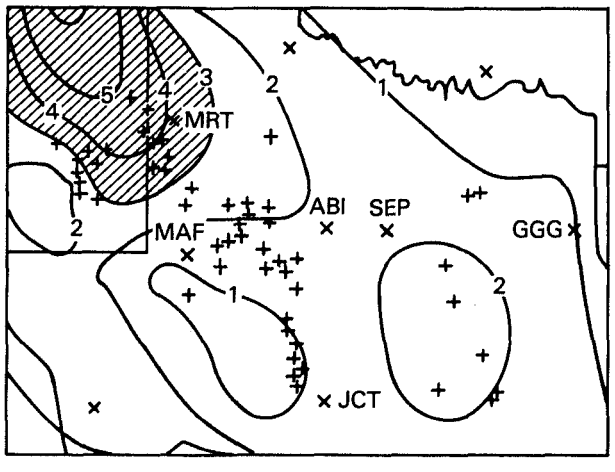

Fig. 10. *Same as Fig. 9, except for CMV arbitrarily assigned to σ=0.9.*

The results for 10 April are similar to those of 9 May except for the additional impact of the dryline on the scalar wind field. The largest vector differences in wind occur within regions of strong horizontal and vertical gradients of the wind. These differences are reduced by assignment of CMV to σ=0.9 rather than 825 mb.

5. CONCLUSIONS

The impact of satellite-derived cloud motion vectors on SESAME rawinsonde wind fields is studied in two separate cases (10 April 1979 and 9 May 1979). In addition, we assess the effect of wind and moisture gradients on the arbitrary assignment of the satellite data to coordinate surfaces in a vertically sheared environment.

The results show that systematic differences occur between the rawinsonde and combined analyses, which are primarily the result of the customary isobaric method by which cloud motions are assigned to coordinate surfaces. The largest differences occur near moisture discontinuities and in regions of strong horizontal and vertical wind shears. Arbitrary assignment of cloud motions to σ=0.9 substantially reduces these differences from the arbitrary assignment to 825 mb. This indicates that the customary method for assigning cloud motions to a single isobaric level introduces unnecessarily large assignment errors, particularly in a highly sheared environment in which severe convection typically occurs. Despite this, strong moisture gradients evidently impose an upper limit on the usefulness of the sigma system for CMV level assignment. Arbitrary assignment of CMV to a surface could possibly be improved within areas of moisture gradients by selecting σ levels appropriate to different air mass regimes from local soundings.

This work represents only an initial step in defining how satellite cloud motions have the potential to be effectively used to add information to basic wind analyses. Additional work has been done concerning the impact of arbitrary assignment of CMV on divergence and relative vorticity fields. CMV have also been interpolated to 825 mb and σ=0.9, and their impact on the overall wind field has been studied. The interpolation of CMV appears to have more of an impact at 825 mb than at σ=0.9 in producing smaller vector differences. The advantage of interpolation is in accounting for the vertical wind shear between cloud base levels and the assigned level. Additional results will be presented in forthcoming papers. Stereo cloud height data are probably desirable for more accurate cloud base determination. Where special-type wind data are not available, model output might possibly be used as the basis for providing afternoon vertical wind shear conditions for the assignment of unconventional wind data to an appropriate level for objective analysis.

6. REFERENCES

Alberty, R. L., D. W. Burgess, C. E. Hane, and J. F. Weaver, 1979: Project Severe Environmental Storms and Mesoscale Experiment SESAME 1979 Operations Summary. Environmental Research Laboratories/NOAA, Boulder, CO, 53 pp. U.S. Government Printing Office, 1979-677-072/1303, Reg. 8.

Billingsley, J. B., 1976: Interactive image processing for meteorological applications at NASA/GSFC. Preprints, 7th Conf. Aerospace and Aeronautical Meteorology and Symposium on Remote Sensing from Satellites, Melbourne, Amer. Meteor. Soc., 268-275.

Carlson, T. N., R. A. Anthes, M. Schwartz, S. G. Benjamin, and D. G. Baldwin, 1980: Analysis and prediction of severe storms environment. Bull. Amer. Meteor. Soc., 61, No. 9, 1018-1032.

_____, S. G. Benjamin, and G. S. Forbes, 1983: Elevated mixed layers in the regional severe storm environment: Conceptual model and case studies. Mon. Wea. Rev., 111, 1453-1473.

Hubert, L., and L. Whitney, 1971: Wind estimation from geostationary satellite pictures. Mon. Wea. Rev., 99, 665-672.

Koch, S. E., M. desJardins, and P. J. Kocin, 1983: An interactive Barnes objective map analysis scheme for use with satellite and conventional data. J. Clim. Appl. Meteor., 22, 1487-1503.

Negri, A. J., and T. H. Vonder Haar, 1980: Moisture convergence using satellite-derived wind fields: A severe local storm case study. Mon. Wea. Rev., 108, 1170-1182.

Peslen, C. A., 1980: Short-interval SMS wind vector determinations for a severe local storms area. Mon. Wea. Rev., 108, 1407-1418.

Wilson, T. A., and D. D. Houghton, 1979: Mesoscale wind fields for a severe storms situation determined from SMS cloud observations. Mon. Wea. Rev., 107, 1198-1208.

G.9

PREDICTION OF FROST NIGHT TEMPERATURES THROUGH USE OF GOES EAST SATELLITE DATA AND TEMPERATURE PREDICTION MODELS

Paul H. Heinemann and J. David Martsolf

Fruit Crops Department, IFAS, University of Florida, Gainesville, FL 32611.

1. INTRODUCTION

Providing users temperature predictions via computer terminal follows from the Satellite Freeze Forecast System (SFFS) (Bartholic and Sutherland, 1978; Martsolf, 1981, Martsolf and Gerber, 1981; Sutherland, et al, 1979; Martsolf, 1982; Heinemann, et al. 1984; Martsolf, et al., 1984). SFFS was developed in cooperation with NASA and NOAA to aquire and apply GOES EAST thermal infrared satellite images (both real and predicted) to National Weather Service forecasters and Florida agriculturalists.

Several models evaluate the temperature distribution near the surface and how those temperatures change with time (Georg, 1971; Blackadar, 1976; Sutherland, 1980; Miller, 1981). The original SFFS prediction model provides hourly temperature predictions but requires hourly inputs from 10 automated weather stations (Sutherland, 1980). A boundary layer model has recently been obtained and will be implemented into the SFFS system (Blackadar, 1976). None of the models utilize the GOES IR data as an input, which is available to SFFS every half hour. The purpose of this paper is to describe the incorporation of satellite data into the Sutherland model.

2. DESCRIPTION OF THE MODELS

2.1 P-Model and S-Model

Sutherland (1980) developed a model (called P-model, or physical model) to predict temperatures during radiative frost nights. The model inputs are temperatures at 1.5, 3.0, and 9.0 m; surface, 10 cm, and 50 cm below the surface; wind speed and net radiation. These parameters require hourly observations from automated weather stations. The energy balances of a subsurface layer, earth-air interface, and a 9 m air layer, are described by three differential equations. Solving for the time rate of temperature and multiplying the rate by hourly increments yields temperature predictions.

The P-model predictions were used as input to another model, called S-model (Martsolf and Gerber, 1981). The S-model used the P-model results and weighted distance coefficients to extrapolate the temperature predictions across the entire state of Florida. The results were then displayed in a map form identical to the IR maps, for any desired forecast hour up to 14 hours in advance.

2.2 Blackadar's Boundary Layer Model (BLM)

The Boundary Layer Model describes the atmospheric boundary layer and predicts how the layer changes over time and with varying inputs (Blackadar and Jersey, 1976; Blackadar, 1980). The model divides the boundary layer (including some depth into the soil) into several layers: Two soil layers, 10 m thick surface layer that includes vegetation, and 30 air layer each 100 m thick. Heat, momentum, and water vapor budgets are calculated.

3. RESULTS: SATELLITE DATA AS INPUT TO MODELS

Satellite data was used as P-model input for a sample frost night. The average temperatures of nine pixels from 10 Florida areas were calculated and supplied to the P-model as 1.5 m inputs. The P-model predictions were then supplied to a routine that extrapolates the new values across the state to create a forecast map. This new map is similar in appearance to the thermal IR map. Forecast maps can be produced up to 14 hours in advance.

The night of January 15-16, 1983 was used as a sample for satellite data input. Observations began at 1800 EST January 15 and continued until 0700 EST January 16. Satellite drift was corrected by aligning the satellite gridding data of a distinct outline (Lake Okeechobee) from one map to the next. The east-west and north-south offsets were calculated. These were included into the routine that determined the satellite pixel temperature averages from the 10 map locations.

The average temperature from each location was entered into the model as 1.5 m air temperature. The first three hours of observations provided the prediction base for the rest of the night. As each hour passed, the previous two hours plus the latest hour served as the new predictive base. In this way the model adjusted predictions as the conditions changed. Hence, the predictions become more accurate as the night progresses.

The predicted values were inputted to the S-model. S-model extrapolated the predictions across the state and processed the results into a map form. The routine that determines the average temperatures of the nine pixels from each location was again run on the forecasted map. The resulting values were compared to the observed map from the forecasted hour. The differences between the observed values and P-model predicted values are summarized in Table 1. The differences between the observed values and S-model predicted values are summarized in Table 2.

The predictions are quite acceptable in the regions with clear skies. The presence of scattered clouds in some areas created problems as can be seen at locations 7, 8, and 9. The reduction of the satellite-measured temperatures can significantly lower the accuracy of the predictions by causing the models to predict too low. Temperatures from the tenth location were not included because high percentage of cloud cover.

The S-model improved the accuracy of the predictions from the P-model as shown in the tables. This can be explained by the manner in which S-model extrapolates the data. When an anomolous value is inputted to the P-model for a single area, the predictions from that hour are less accurate. The predictions inputted to the S-model are used to determine temperature gradients across the state. Therefore, an area with an anomolous input is influenced by adjacent areas. This process tends to smooth the predictions.

Table 1

Summary of means and standard deviations of differences between observed values and P-model predicted values (predicted-observed, °C).

Prediction Base Hour	Map Location 1	2	3
3	0.5 ± 0.6	-1.7 ± 0.7	0.6 ± 0.4
4	1.7 ± 1.0	-1.0 ± 0.6	0.7 ± 0.5
5	0.5 ± 0.6	1.1 ± 1.2	-0.8 ± 0.4
6	1.2 ± 0.5	1.0 ± 1.1	0.3 ± 0.5
	4	5	6
3	1.8 ± 1.5		0.8 ± 1.0
4	3.5 ± 1.7	-0.4 ± 2.1	2.1 ± 1.6
5	-0.6 ± 1.5	-2.2 ± 1.5	1.3 ± 1.5
6	0.4 ± 1.7	2.4 ± 2.2	2.0 ± 1.2
	7	8	9
3	4.0 ± 2.3	5.2 ± 2.2	2.9 ± 1.9
4	0.4 ± 2.8	-0.3 ± 2.1	3.7 ± 1.1
5		-0.4 ± 2.5	-3.6 ± 1.8
6	-2.0 ± 3.4	-1.0 ± 2.5	-2.7 ± 1.8

Table 2

Summary of means and standard deviations of differences between observed values and S-model predicted values (predicted-observed, °C).

Prediction Base Hour	Map Location 1	2	3
3	0.1 ± 0.8	-0.2 ± 1.2	1.8 ± 0.7
4	0.1 ± 0.5	-0.3 ± 0.9	1.5 ± 0.6
5	-1.9 ± 0.5	-1.6 ± 0.5	-0.6 ± 0.2
6	-1.5 ± 0.7	-0.8 ± 0.5	-0.3 ± 0.6
	4	5	6
3	-0.2 ± 1.5	-1.2 ± 1.4	0.7 ± 1.5
4	0.1 ± 1.0	-1.0 ± 1.4	0.6 ± 1.1
5	-3.0 ± 1.8	-2.0 ± 1.8	-0.8 ± 1.2
6	-2.0 ± 2.0	-0.8 ± 2.2	1.7 ± 0.8
	7	8	9
3	4.9 ± 1.7	2.9 ± 2.2	3.3 ± 0.9
4	1.9 ± 1.3	2.3 ± 1.5	3.5 ± 1.5
5	0.7 ± 1.5	1.7 ± 3.0	-2.7 ± 1.5
6	-1.5 ± 0.4	-0.8 ± 2.6	2.5 ± 0.3

4. CONCLUSIONS AND FUTURE WORK

The results show that satellite temperatures can indeed be used as input for the model to predict temperatures, but are most effective when the air is very clear and the satellite-sensed temperatures decrease smoothly with time. Scattered clouds cause large errors in the predictions. However, conditions that permit cloud formation are those that reduce the possibility of frost.

The problem of scattered cloud cover over some areas may be alleviated by using ground station temperatures aquired from AFOS lines to supplement the satellite data. If an unusually low satellite temperature due to cloud cover is detected, the ground station temperature could be substituted.

Movement of clouds is not accounted for on the predicted maps. Clouds that appear on the initial base maps will appear at the same location on any predicted map. A provision to predict cloud movement by the model will be attempted.

The recent aquisition of the Boundary Layer Model expands the prediction capabilities of SFFS. The satellite data will be used as input to the BLM and accuracy of predictions will be compared to the P-model results.

5. REFERENCES

Bartholic, J.F. and R.A. Sutherland, 1978: Future freeze forecasting. Proc. Fla. State Hort. Soc. 91:334-336.

Blackadar, A.K., 1976: Modeling the nocturnal boundary layer. Preprint from the Third Symposium on Atmospheric Turbulence, Diffusion, and Air Quality. Raleigh, N.C. p. 46-49.

_____, and G.R. Jersey, 1980: Efficient modeling of evapotranspiration. Preprint from the Fifth Symposium on Atmospheric Turbulence, Diffusion, and Air Quality. Raleigh, 2 pp.

Georg, J.G., 1971: A numerical model for prediction of the nocturnal temperature in the atmospheric surface layer. M.S. thesis, The University of Florida, Gainesville. 121 pp.

Heinemann, P.H., J.D. Martsolf, J.F. Gerber, and D.L. Smith, 1984: Development of manually digitized radar and GOES IR composite products. Preprint from the AMS Conference on Satellite Meteorology/Remote Sensing and Applications. Tampa, Fl., June, 1984. 3 pp.

Martsolf, J.D., 1981: Satellite frost forecast system. HortSci. 16:586.

_____, 1983: Florida frost information and dissemination in Florida. Fl. Ag. Exp. St. J. no. 4638. Proceedings of the Conference on Cooperative Climate Services. Natl. Climate Program Office Workshop. March 22-24, 1983, Tallahassee, Fl. 19 pp.

_____, and J.F. Gerber, 1981: Florida satellite frost forecast system. Proc. Fla. St. Hort. Soc. Paper no. 18.

_____, P.H. Heinemann, J.F. Gerber, D.L. Smith, and F.L. Crosby, 1984: Rapid weather information dissemination in Florida. Preprint from the AMS 10th Conference on Weather Forecasting and Analysis, Tampa, Fl., June, 1984. 3 pp.

Miller, R.G., 1981: GEM: A statistical weather forecasting procedure. NOAA Technical Report NWS 28. Silver Spring, Md. 104 pp.

Sutherland, R.A., 1980: A short-range objective nocturnal temperature forecasting model. J. Appl. Meteor. 19:247-55.

_____, J.L. Langford, J.F. Bartholic, and R.G. Bill, Jr., 1979: A real-time satellite data acquisition, analysis, and display system--a practical application of the GOES network. J. Appl. Meteor. 18:355-360.

H.1

DEVELOPMENT OF MANUALLY DIGITIZED RADAR AND GOES IR COMPOSITE PRODUCTS*

Paul H. Heinemann, J. David Martsolf, and John F. Gerber, Fruit Crops Department, IFAS, University of Florida, Gainesville, FL 32611, and Daniel L. Smith, National Weather Service, Fort Worth, TX.

1. INTRODUCTION

The Satellite Frost Forecast System (SFFS) was designed with a goal of aquiring, processing, and disseminating Satellite thermal infrared (IR) data to users in the Florida agricultural community on a real-time basis (Martsolf, 1980; Martsolf and Gerber, 1981). The IR binary data was processed into maps, and the temperature values divided into color coded ranges for display on a color monitor or terminal. The maps were then disseminated through the SFFS system to users throughout Florida.

The SFFS display system used for the IR maps can be enhanced to display other products as well. Development of SFFS has led to the aquisition of several products from the National Weather Service. One of these, Manually Digitized Radar (MDR), was developed into a color display product and made available to users in Florida through SFFS. The capability of the system enabled overlay of MDR and GOES IR maps to form a new product showing rainfall patterns at a higher resolution than the MDR alone.

Some methods of measuring precipitation from satellite and radar information are mentioned in the literature. Waters and Green (1979) describe a combination IR and MDR product. Scofield (1981) and Del Beato (1981) described methods of correlating visible and infrared GOES images to precipitation levels.

Strong convection is usually accompanied by heavy precipitation in clouds. The convective processes cause the cloud tops to reach heights of 5 km and more, which appear to a satellite much colder than the surrounding areas. The correlation between cold cloud top temperatures and convection enables infrared satellite images to give an indication of where precipitation may be occuring. The addition of even a low resolution radar product such as manually digitized radar (MDR) verifies the presence of precipitation for a given region.

2. AQUISITION OF IR AND MDR DATA

The Satellite Frost Forecast System based in the Climatology Lab, Fruit Crops Department, University of Florida, provides a direct digital downlink with GOES East meteorological satellite (Martsolf, 1981, 1982, 1983). Thermal infrared scans, with 3.2 x 6.4 km (2 x 4 mile) pixel size, are received every half hour through a 5 meter satellite dish, then sectorized into an area covering the state of Florida. The binary values are processed into a map form by an HP 21 MX-E minicomputer.

Smith (1980) describes Manually Digitized Radar in detail. Radar operators place a 32 x 32 km (20 x 20 mile) grid overlay on the radar PPI. The predominant precipitation level in each grid spacing is assigned an intensity value. In the case of heavier rain, the grid spacing will receive the highest intensity value found within that space. The operator codes this data and sends it across AFOS lines.

MDR data are aquired from one Georgia and six Florida radars through a DS-1000 computer link with the National Weather Service in Ruskin, Florida. This is done every hour on the half hour. Each station transmits MDR code between 25 and 35 minutes past the hour so that reception of the radar data is within ± 5 minutes of satellite image reception. The precipitation code is collected by the Gainesville computer and combined into an array (Figure 1). This shows the regions of precipitation over the state of Florida at 32 x 32 km resolution.

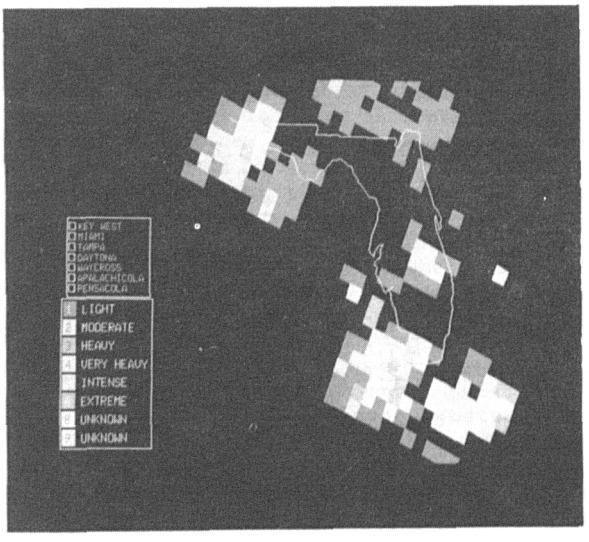

Figure 1. Black and white representation of color coded Manually Digitized Radar display from six Florida and one Georgia station.

3. DEVELOPMENT OF IR-MDR COMPOSITES

The composite map development procedure is listed in the appendix. A blank map of 180 columns by 120 lines was created to accept processed composite MDR-IR values. Satellite drift from one map to the next is partially corrected by programatic alignment of the satellite map grid patterns. The gridding is added to the satellite data after the initial transmission to Wallops Island. The gridding is not always placed correctly; however, the error of grid alignment is usually within a few kilometers of the intended placement. The maps are aligned by finding a fit between map grid points using a distinct outline, such as those surrounding Lake Okeechobee.

*USDA/Extension Grant 12-05-300-535, Florida Agricultural Service and Technology and NWS/Southern Regional Headquarters are acknowledged for support of this project.

Due to the MDR element orientation convention, the elements had to be rotated 23°. This rotation aligned the element arrays in an east-west direction to correspond to the IR pixel element arrays.

A single MDR block covers 50 IR pixels. Each MDR block is divided into an array of 50 elements so that each element can be compared to an IR pixel. It is assumed that any IR pixel with a temperature value warmer than a given threshold temperature does not represent significant cloud areas, and therefore does not contain rain. An IR pixel with a temperature greater than the threshold (set at 0 C) was automatically eliminated from the array. The coldest IR pixel temperature and the standard deviation of the remaining IR pixel temperatures were calculated for each MDR block. Within each block, the coldest pixel and all other pixels with values less than one standard deviation warmer were assigned the MDR value of that block. IR pixels with values between one and two standard deviations were assigned the next lowest MDR value, and so on (Figure 2). This process is repeated for each MDR element.

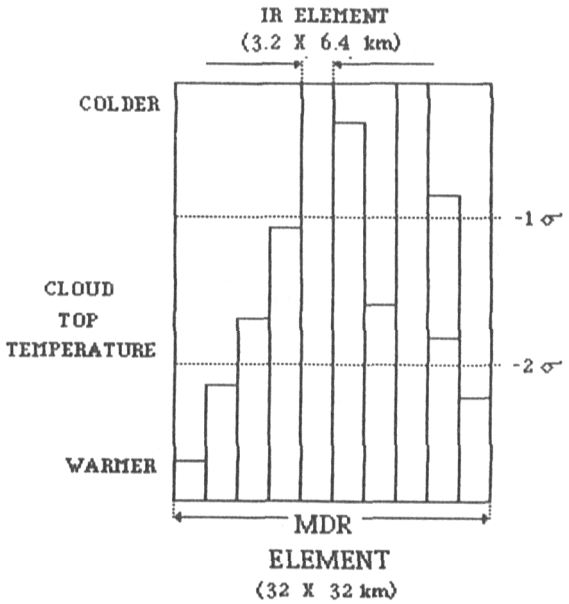

Figure 2. Schematic of IR-MDR corellation. IR pixels with temperatures less than one standard deviation from the coldest value would be assigned the original MDR value for that MDR element, IR pixels between one and two standard deviations from the coldest value would be assigned the next lowest MDR value, etc.

The new composite values are placed into the blank map as they are calculated. The values are then assigned a color coding describing the intensity of the rainfall. The processed data are displayed on a color terminal or monitor and gridding from the IR map is added (Fig. 3).

Each time a new MDR-IR composite map is processed it is called by a seperate program that adds the latest map to previous maps. This shows accumulated rainfall patterns (Fig. 4). A new accumulated rainfall map is produced daily. Other products could be developed by a similar procedure including weekly, monthly, and yearly accumulated rainfall summaries.

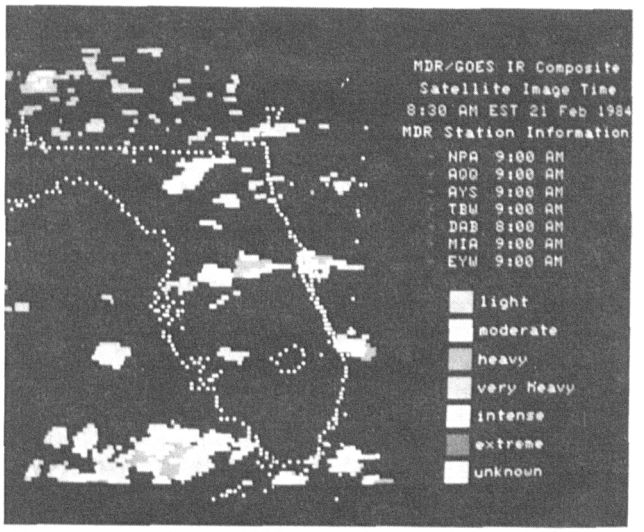

Figure 3. Black and white representation of color coded composite IR-MDR rainfall map.

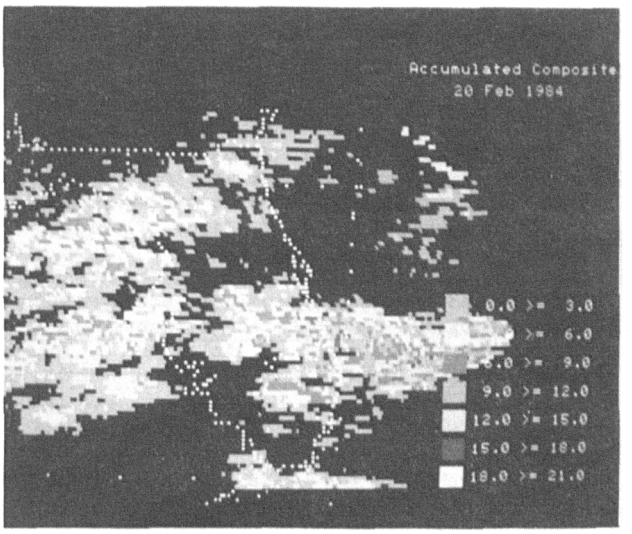

Figure 4. Black and white representation of color coded accumulated rainfall map.

4. DISSEMINATION OF COMPOSITE PRODUCTS

The composite products are disseminated on a real-time basis to the Florida agricultural community through a microcomputer network (Martsolf, et al., 1984). After the HP minicomputer processes a new map, the computer automatically transmits the map to the Institute of Food and Agricultural Sciences' VAX computer. The maps are stored in user accessible files. Agricultural users (county extension agents at this point) call the VAX with microcomputers through modems to obtain the maps at their convenience. Software is being developed to display these maps on several microcomputers, including APPLE II, DEC PRO 350, IBM PC, and Zenith Z-100. These maps will be made available to the public through a not-for-profit corporation known as Florida Agricultural Services and Technology (FAST). The dissemination process will be similar to SFFS, except that the products will be transferred to a CDC CYBER 730 operated by FAST.

5. REFERENCES

Del Beato, R., 1981: Relationship between extratropical rainfall and satellite cloud top temperatures. Aust. Meteor. Mag. 29:125-131.

Martsolf, J.D., 1980: An improved satellite frost warning system. Proc. Fla. State Hort. Soc. 93:41-44.

_____, 1981: Satellite frost forecast system. Hortscience. 16:586.

_____, 1982: Satellite thermal maps provide detailed views and comparisons of freezes. Proc. Fla. State Hort. Soc. 95:14-20.

_____, 1983: Florida frost information and dissemination system. Proceedings of the Conference on Cooperative Climate Services. National Climate Program Office. NOAA Mar. 22-24, 1983, Tallahassee, Fl. pp. 209-227.

_____ and J.F. Gerber, 1981: Florida satellite frost forecast system documents freezes of January, 1981, and is refined for future seasons. Proc. Fla. State Hort. Soc. 94:39-43.

_____, P.H. Heinemann, J.F. Gerber, F.L. Crosby, and D.L. Smith, 1984: Rapid weather information dissemination in Florida. Preprint from AMS Tenth Conference on Weather Forecasting and Analysis, June 24-27, Tampa, Florida.

Scofield, R.A., 1981: Visible and infrared techniques for flash flood, hydrological, and agricultural applications. Precipitation measurements from space workshop report. D. Atlas and O. Thiele, ed. Goddard Space Flight Center, Greenbelt, Md. p. D145-152.

Smith, D.L., 1980: Theory and practice of heavy rainfall estimation using manually digitized radar. NWS Technical Procedures Branch Report. NWS Headquarters, Silver Spring, Md. 6 pp.

Waters, M.P., III and R.N. Green. 1979: A merged satellite infrared and manually digitized radar product. Ppreprint from 1979 Machine Processing of Remotely Sensed Data Symposium. pp. 183-190.

6. APPENDIX

Procedure of composite map process:

1. aquire and process GOES IR data.
2. aquire and process MDR data.
3. combine MDR from seven stations into 30x40 element array.
4. create blank map 180 columns by 102 lines (same size as Florida IR sector.
5. call alignment routine to get x,y location of Lake Okeechobee based on grid bits.
6. compare to base map to determine offsets.

MAIN LOOP:

7. rotate MDR pixel 23 deg. to proper perspective.
8. divide MDR element into IR pixel size (divide into 50 elements).
9. create coordinates of IR pixels that map into that particular MDR element.
10. extract IR data, place into vector for that MDR element.
11. calculate minimum, maximum, and standard deviation of IR values corresponding to that MDR element.
12. correlate IR to MDR value based on statistics.
13. place new values into blank map
14. go to next MDR element.
15. display new values.

THE DIURNAL CYCLE IN COLD CLOUD IN THE TROPICS DURING 1982-83

Phillip A. Arkin
Climate Analysis Center
National Meteorological Center
NWS/NOAA
Washington, D. C. 20233

1. INTRODUCTION

The diurnal cycle in tropical cloudiness and precipitation has been extensively studied in recent years. Reed (1983) presents a review of many recent studies, including several which used satellite data in various forms. Many earlier studies were reviewed by Wallace (1975) and Gray and Jacobson (1977); the interested reader is referred to these papers for further details of the literature.

The subject of the forcing of large-scale tropical and extratropical circulations by condensation heating is the focus of much current research (Paegle et al., 1984; Arkin et al, 1984). The evolution of circulation anomalies during the El Niño/Southern Oscillation event of 1982-83 and their association with rainfall anomalies in the tropical Pacific (Arkin, 1983b) illustrate the importance of the distribution of tropical precipitation. While understanding of the relationship between the time-mean circulation and condensation heating is improving, the importance of the transient portion of the thermal forcing is much less clear. Since the diurnal signal in tropical convection is generally thought to be quite large, it might well be important to the large-scale flow.

2. DATA AND ANALYSIS

Diagnosis of the diurnal cycle in cloudiness and precipitation is extremely difficult when one is limited to conventional data. As pointed out by Reed (1983), most recent studies have utilized some form of satellite data in order to obtain the necessary density of data. Imagery from geostationary satellites is in some ways ideally suited to diagnoses of the diurnal cycle. Infrared (IR) imagery serves to define the approximate altitude of cloud tops reasonably well at intervals of 1/2 hour (for the U.S. GOES) throughout the day. In this study, statistics for large areas from such imagery will be examined to determine the diurnal variability of cloud of various heights.

In the process of computing the GOES Precipitation Index (GPI) (Arkin, 1983a), frequency distributions of the equivalent blackbody temperature (EBBT) in 2.5^{o}x 2.5^{o} areas are archived separately for each of eight times (0000, 0300, 0600, ...GMT) averaged over half-months from December 1981 through the present. The classes of the histograms are 5K wide between 210 and 270K, allowing the mean fractional coverage of each area by cloud colder than various thresholds to be easily determined for 8 times during the diurnal cycle.

The fractional coverage of such areas by cloud with EBBT colder than 235K has been shown to be highly correlated with areally averaged rainfall even for times as short as 1 hour (Arkin, 1979); Richards and Arkin, 1981). Thus, in an approximate sense, the diurnal variation of this index (which, when multiplied by an appropriate constant, is the estimate of large-scale precipitation used at the Climate Analysis Center and called the GPI) should correspond to that of precipitation. It is important to keep in mind, however, that the results presented are for clouds and not direct measurements of precipitation. In particular, there is very likely to be a lag, with maximum GPI occurring later by 1-2 hours than maximum rainfall (Richards and Arkin, 1981).

The results presented here will be for clouds with EBBT<235K, <270K and <220K, representing in a crude way the variability of raining cloud, total cloud (excluding stratus) and deep convection. Averages over the calendar seasons (DJF, MAM, JJA, and SON) from December 1981 through November 1982 will be shown for the first of these, and for DJF 1982 for the others. The diurnal cycle is computed by calculating the first harmonic of the 8 daily values.

3. RESULTS

The diurnal cycle in cloud with EBBT<235K for each 2.5^{o}x2.5^{o} area from 50°N-50°S and 175°E-25°W is shown in Figs. 1-4. A vector pointing north indicates a maximum of cloudiness at 0000 local time. The vector rotates clockwise with increasing time of day, pointing east for a maximum at 0600, south at 1200 local and so on. The length of the vector is proportional to the amlpitude of the

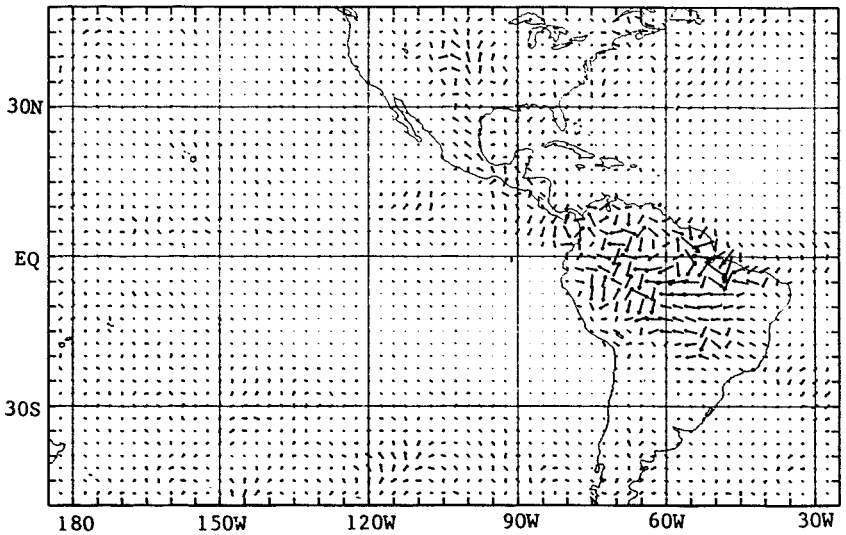

Figure 2. As in fig.1 but for MAM 1982. Maximum vector represents amplitude of 14%.

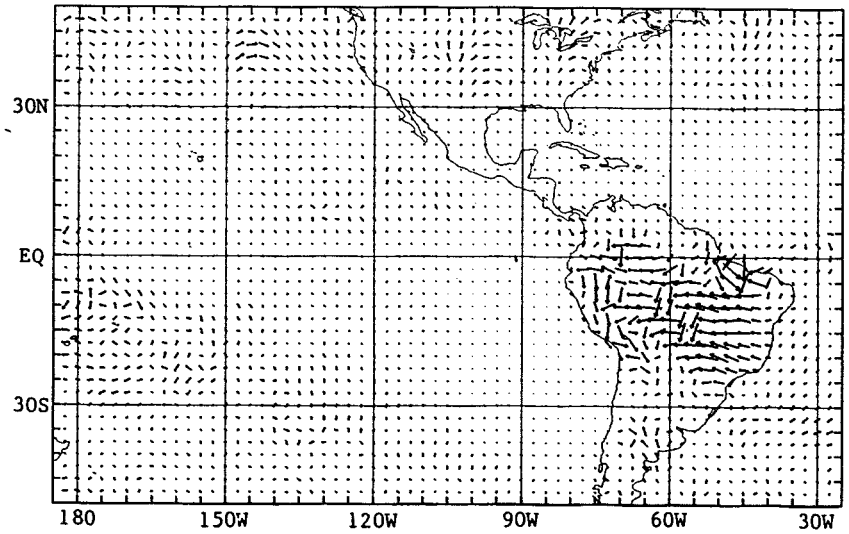

Figure 1. Vectors indicating the phase and amplitude of the first harmonic of the diurnal cycle in cloud colder than 235K for DJF 1981-82. See text for details. Maximum vector represents amplitude of 11%.

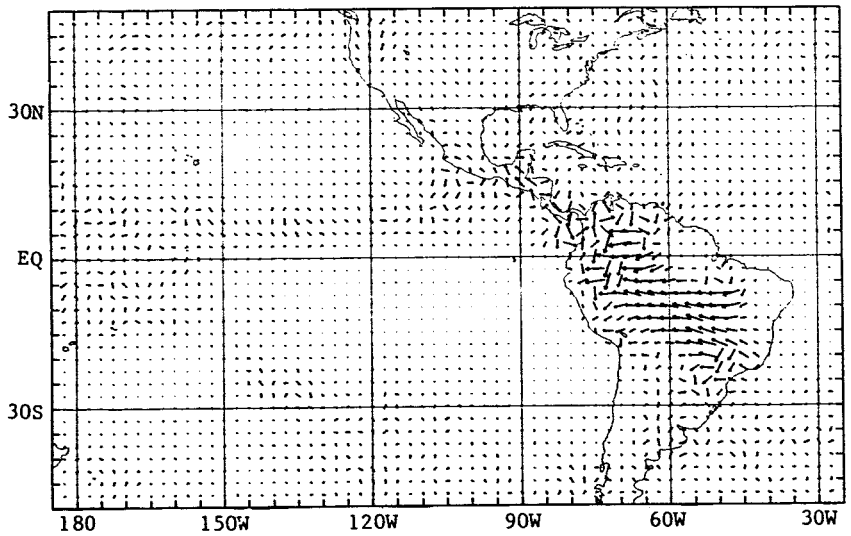

Figure 4. As in fig.1 but for SON 1982. Maximum vector represents amplitude of 11%.

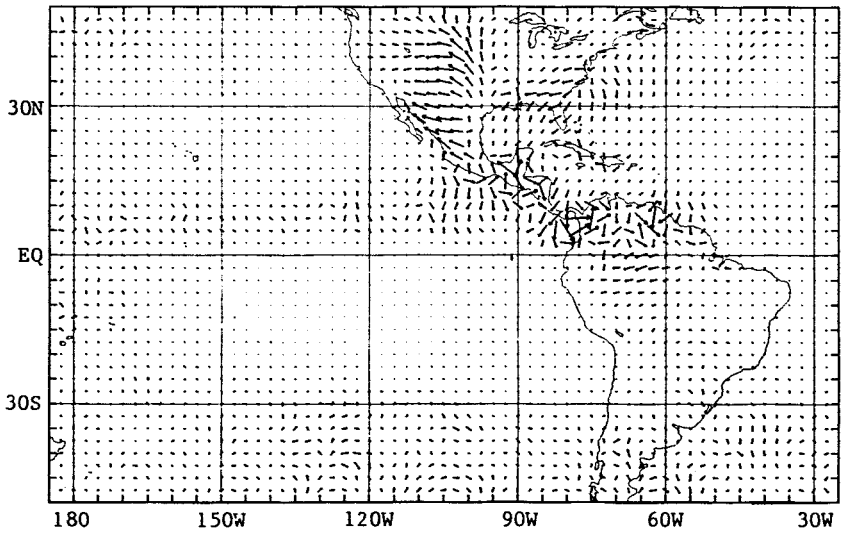

Figure 3. As in fig. 1 but for JJA 1982. Maximum vector represents amplitude of 12.5%.

diurnal cycle in fractional coverage, with a length of 2.5° (equal to the separation of the origins of adjacent vectors) indicating an amplitude of 6%. This corresponds to an amplitude of 4.3 mm/day in GPI.

The most obvious deduction to be drawn from these results is that the diurnal cycle determined in this fashion is much larger over tropical continents than oceans. This is not to say that there is no diurnal cycle over the tropical oceans. Indeed, the South Pacific Convergence Zone (SPCZ) and both Atlantic and Pacific Intertropical Convergence Zones (ITCZ's) show fairly substantial diurnal signals. However, the largest amplitudes are clearly over the summertime continents. Amplitudes of >3% are extremely rare over the tropical oceans, while values <3% are almost equally rare in the continental convective regions. While the mean fractional cloudiness over the tropical continents is somewhat greater than over the tropical oceans, the difference is on the order of 20%-40% when averaged over large areas (Arkin and Meisner, 1984), and some oceanic areas exhibit maxima nearly as large as any found over the continents. For example, during JJA 1982, largest values of fractional coverage were found near 5°N and 180° (15%) and near the Isthmus of Panama (20%). However, the diurnal signal in the latter has 4 times the amplitude (12% to 3%) found in the former. Furthermore, an area in the central U.S. with values of GPI half those found in the central Pacific has a diurnal signal of amplitude 9%, 3 times that in the central Pacific. Dorman and Bourke (1979) showed diurnal cycles for a number of locations in the Pacific Ocean north of the equator. Their diurnal signal amplitude was about .39 mm/day at 7°N and 82.5°W, near the eastern end of the Pacific ITCZ. The diurnal signal at that point (using the GPI calibration) ranges from .16 mm/day to .78 mm/day with an annual average of about .46 mm/day. This seems quite good agreement for two such disparate techniques. Their results for other locations in the north Pacific indicated much smaller amplitude diurnal cycles. The results shown here confirm this, with the only other tropical oceanic region showing large amplitudes being where the SPCZ reaches the equator.

The phase of the diurnal cycle in the tropics has been a subject of some controversy. Gray and Jacobson (1977) found an early morning maximum in most oceanic regions and night or morning maxima in many continental regions. Dorman and Bourke (1979) found an evening or very early morning maximum in the regions they examined. Albright et al. (1983) found an afternoon maximum during January-February 1979 in the SPCZ, and Gray and Jacobson (1977) and others have noted an afternoon maximum in the eastern tropical Atlantic. Minnis et al. (1983) found that deep convective activity over South America exhibits an afternoon peak, while Reed and Jaffe (1981) found a similar result for tropical Africa.

The dominance of the diurnal cycle over tropical South America, Central America and North America in the warm season, with >75% of the total diurnal variance accounted for by the first harmonic, makes determination of its phase in these areas relatively straightforward. Most areas of heavy precipitation in South America exhibit diurnal maxima near 1800 LST in each season. Coastal areas, such as near the mouth of the Amazon in DJF and MAM 1982 and in São Paulo State in SON 1982, exhibit late morning and early afternoon maxima, as do the Andes. Similar behavior was noted by Reed and Jaffe (1981). In North America, a similar set of features is seen in JJA 1982, with maxima in early afternoon near the Gulf and southeast coasts and several hours later further inland. The interior of the continent shows maxima near 1800 LST over the Rocky Mountains, with increasingly later maxima with eastward and northward distance from the mountains. Central America and northern South America show widely varying times of maximum convection, probably due to the smaller spatial scale of land/sea and orographic features there.

Since the diurnal cycle is relatively smaller in tropical ocean regions than over land, its determination there is more difficult. The Pacific, particularly at its eastern end, and the Atlantic ITCZ appear to exhibit a near noontime maximum. Dorman and Bourke (1979) found a 0900 LST maximum at 7°N, 82.5°W, while the data here show maxima at 0700, 1400, 1500, and 0900 LST during DJF, MAM, JJA, and SON, respectively. Several areas in each ITCZ show a puzzling tendency for maxima to occur later in the day closer to the equator. For example, maxima along 110°W during MAM 1982 occurred just after midnight at 12.5°N, at 0200 LST at 10°N, 0500 LST at 7.5°N, 0900 LST at 5°N, and 1000 at 2.5°N. The same behavior is seen further east and in the western equatorial Atlantic. The diurnal cycle in the SPCZ is most prominent in DJF 1982. The axis of the highest values of GPI extends from 10°S and 175°E east-southeastward to Samoa. South and west of this axis, maxima occur near 1800 LST, while mid-morning maxima are found to the north. The Gulf of Mexico and Atlantic near the southeastern U.S. both exhibit noon maxima.

The diurnal cycles during DJF 1981-82 in fractional coverage of cloud with EBBT<270K (Fig. 5) and <220K (Fig. 6) are seen to have spatial distributions of amplitude similar to those of the GPI (Fig. 1). Tropical South America and the SPCZ have large amplitudes in all three, with the ITCZ's also exhibiting relative maxima. One might reasonably conclude that the large amplitude over North America in Fig. 5 is due to the occurrence of surface temperatures <270K at night. The absolute amplitudes are greatest, excluding North America, (14% at 270K, 6% at 220K) in near equatorial South America. This is very similar to the diurnal cycle of raining cloud during this season. The phase at 270K indicates that maxima occur somewhat later than when considering only cloud colder than 235K, while the phase of cloud colder than 220K is similar to that at 235K, but with the

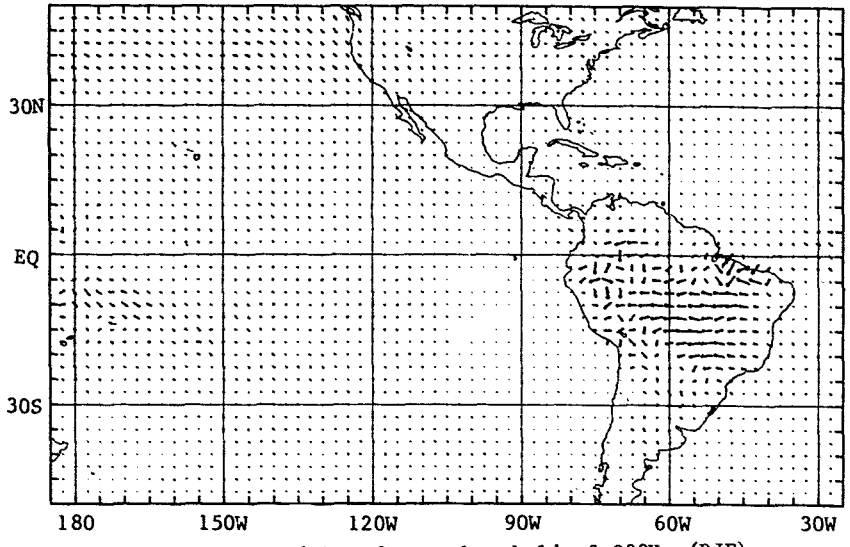

Figure 6. As in fig. 1 but for a threshold of 220K. (DJF)
Maximum vector represents amplitude of 6%.

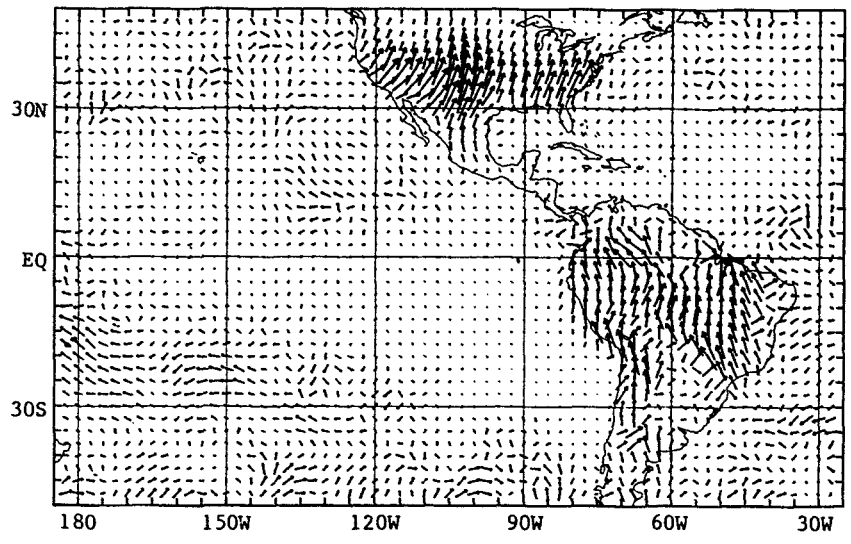

Figure 5. As in fig. 1 but for a threshold of 270K. (DJF)
Maximum vector represents amplitude of 22%.

influence of land/sea and orography somewhat less pronounced.

4. SUMMARY AND CONCLUSIONS

The data base of frequency distributions of EBBT for each of 8 daily times are used to determine the diurnal variability of cloud colder than thresholds of 270K, 235K and 220K. The first harmonic of the diurnal cycle in raining cloud (EBBT<235K) is found to have largest amplitude over the summertime continents, exceeding 3%, and to explain 75% of the diurnal variance in such regions. Maximum cloud cover in these areas occurs at about 1800 LST except in coastal and mountainous regions where earlier maxima are observed. Similar behavior was noted by Reed and Jaffe (1981). Oceanic areas exhibit smaller amplitude diurnal cycles, with earlier maxima in many areas. However, parts of the SPCZ exhibit late afternoon maxima. Use of warmer (270K) and colder (220K) thresholds yield similar results in areas of tropical convection.

It appears that the diurnal cycle in cloud colder than freezing in the tropics is dominated by the variation in precipitating cloud, with much greater diurnal variability, even when normalized by mean values, found in continental than in oceanic regions.

5. REFERENCES

Albright, M.D., 1982: A further study of the diurnal variation of the convection in the GATE B-scale region. M.S. Thesis, University of Washington, Seattle, WA 98195, 110 pp.

Arkin, P.A., 1979: The relationship between fractional coverage of high cloud and rainfall accumulations during GATE over the B-scale array. Mon. Wea. Rev., 107, 1482-1387.

_____, 1983a: A diagnostic precipitation index from IR satellite imagery. Tropical Ocean-Atmosphere Newsletter, No. 17, 1983, 5-7. Available from JISAO, University of Washington, AK-40, Seattle, WA 98105.

_____, 1983b: Tropical circulation anomalies associated with the 1982-83 ENSO event. Proceedings of the 8th Climate Diagnostics Workshop, Toronto, Canada, October 17-21, 1983.

_____, B. Meisner, 1984: Fluctuations in the large scale cloudiness and precipitation regimes in the tropical eastern Pacific and South America associated with the 1982-83 ENSO event. Postprints of the 15th Technical Conference on Hurricanes and Tropical Meteorology, AMS, Miami, FL, Janaury 9-13, 1984.

_____, J. Janowiak and G. Cressman, 1984: Rotational and divergent tropical circulations and their relationship to areas of large-scale convective activity. To be submitted to Mon. Wea. Rev.

Dorman, C.E., and R.H. Bourke, 1979: Precipitation over the Pacific Ocean, 30°S to 60°N. Mon. Rea. Rev., 107, 396-910.

Gray, W.M., and R.W. Jacobson, 1977: Diurnal variation of oceanic deep convection. Mon. Wea. Rev., 107, 1171-1188.

Minnis, P., G.G. Gibson, and F.N. Denn, 1983: Diurnal cloud variations over South America and the southeastern Pacific. Preprints of the First International Conference on Southern Hemisphere Meteorology, São Jose dos Campos, Brasil, July 31-August 6, 1983, 329-332.

Paegle, J., J.N. Paegle and F.P. Lewis, 1984: Large-scale motions of the tropics in observations and theory. Submitted to J. Pure and Appl. Geophy.

Reed, R.J., 1983: The diurnal variation of precipitation in the tropics. Preprints of the First International Conference on Southern Hemisphere Meteorology, São Jose dos Campos, Brasil, July 31-August 6, 1983, 312-319.

_____, and K.D. Jaffe, 1981: A comparison of the diurnal variation of convective activity over West Africa and the tropical eastern Atlantic during the summers of 1974 and 1978. Mon. Wea. Rev., 109, 2527-2534.

Richards, F. and P. Arkin, 1981: On the relationship between satellite-observed cloud cover and precipitation. Mon. Wea. Rev., 109, 1081-1093.

Wallace, J.M., 1975: Diurnal variations in precipitation and thunderstorm frequency over the conterminous United States. Mon. Wea. Rev., 103, 406-419.

Satellite Imagery as an Aid for Deriving 300 mb and 1000/300 mb Geopotential Heights

Steven D. Swadley

Naval Environmental Prediction Research Facility
Monterey, California

1. INTRODUCTION

During the first decade of satellite meteorology (1960-70), the operational value of satellite imagery in synoptic analysis was demonstrated. In the same period, weather forecasting was moving into the age of numerical prediction where the impact of satellite imagery has been limited (Bizzarri, 1982). This was due to the difficulty of converting imagery into information useful to the numerical analysis of the mass field.

The second and third decades of satellite meteorology have seen considerable efforts in the development of technologies and techniques for providing quantitative satellite-derived data for numerical prediction models. Although the input of satellite-derived vertical temperature profiles and cloud tracked winds have had a positive impact on numerical forecasts (Halem, et al., 1977; and Seaman and Hayden, 1979), one of the problems associated with this quantification is that the satellite data tend to reduce the amplitudes of the synoptic systems (i.e. versus those depicted by radiosonde data alone, Miller and Hayden, 1978).

The purpose of the present study is to demonstrate the potential use of the advanced Satellite Input to Numerical Analysis and Prediction (SINAP) technique (Swadley, 1983; hereinafter referred to as S83) in an operational mode. The impact of the SINAP technique on the analysis of the mass field will be demonstrated.

2. Description of the SINAP System

A quasi-objective statistical method for deriving 300 mb geopotential heights and 1000/300 mb thicknesses in the vicinity of extratropical cyclones with the aid of satellite imagery has been recently developed at the Naval Environmental Prediction Research Facility (NEPRF). The technique utilizes satellite observed extratropical spiral cloud pattern parameters in conjunction with parameters derived from the original height or thickness field. The original fields are scale separated into additive long and short wavelength component fields. Regression equations are used to specify the magnitude of the negative extrema (positive vorticity maxima) in the short wavelength field. The 300 mb heights and 1000/300 mb thicknesses are then retrieved by direct addition of the modified short wavelength component field. Adjustments can then be made to the heights at the intermediate model levels. This insures a vertically consistent mass field which is required for initialization of a multi-level primitive equation forecast model.

The operational application of this system is designed to utilize NEPRF's Satellite-Data Processing and Display System's (SPADS) unique capabilities of allowing interactive digital image processing (Schramm, Zeleny, Nagle and Weinstein, 1982). Graphic overlays of the meteorological fields superimposed upon the satellite image make this system ideal for the application of the present technique.

2.1 The Scale Separation Technique

The scale separation technique developed by Holl (1963) provides a method of decomposing geophysical fields into additive long and short wavelength component fields. The technique successively applies a smoothing operator to the subject field until the amplitude of a specified wavelength component is reduced to a predetermined percentage of its initial value. Examples of the scale separation technique applied to a 300 mb height field are shown in Figures 1, 2 and 3. Figure 1 is the initial height (Z) field; Figure 2 is the long wavelength (SR) field resulting from the smoothing process. The short wavelength (SD) field is computed by subtracting the long wavelength, SR field from the initial Z field and is shown in Figure 3. The planetary (polar) vortex (SV) field and the long wave disturbance (SL) field are also obtained by applying the scale separation technique at a greater degree of smoothing. The original field, Z, is related to the various component fields by the following relationship,

$$Z = SR + SD = SV + SL + SD. \qquad (1)$$

The short wavelength (SD) field is significant because it closely resembles the relative vorticity (ζ) field (Nagle, et. al., 1966). Although a direct proportionality of the magnitudes of the SD and ζ fields cannot be expected, the patterns and locations of the field extrema and/or zero values should be remarkably similar, as shown in Figure 4.

2.2 Satellite Analysis Scheme

The well documented (see for example Nagle and Hayden, 1971) correspondence between specific satellite observed extratropical spiral cloud patterns and synoptic features associated with upper-tropospheric relative vorticity (or SD)

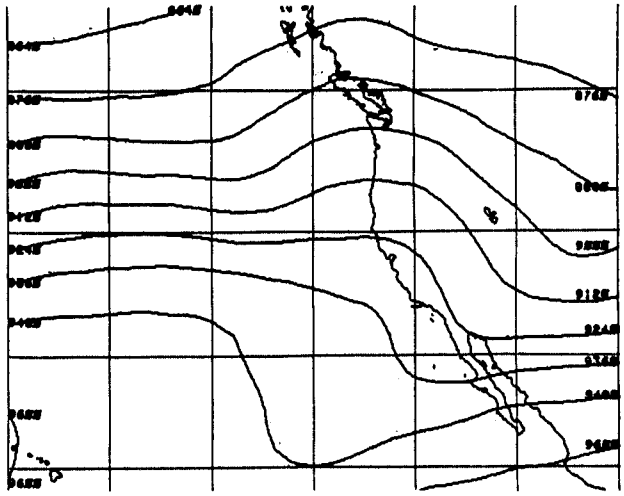

Fig. 1. Initial 300 mb height field, 12 hr forecast, valid time 000 GMT 24 February.

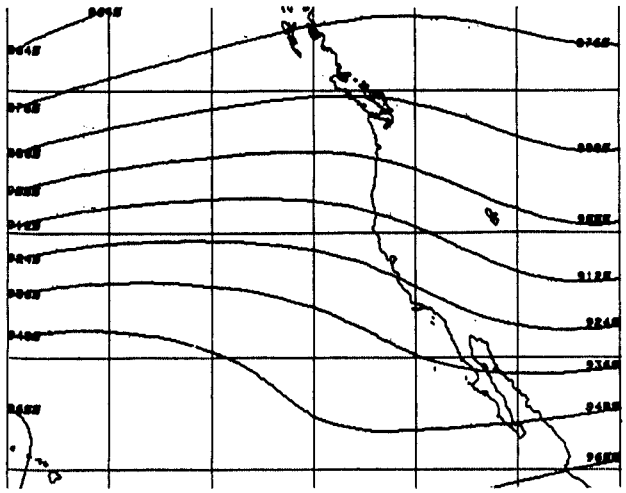

Fig. 2. 300 mb long wavelength (SR) field, 12 hr forecast, valid time 000 GMT 24 February.

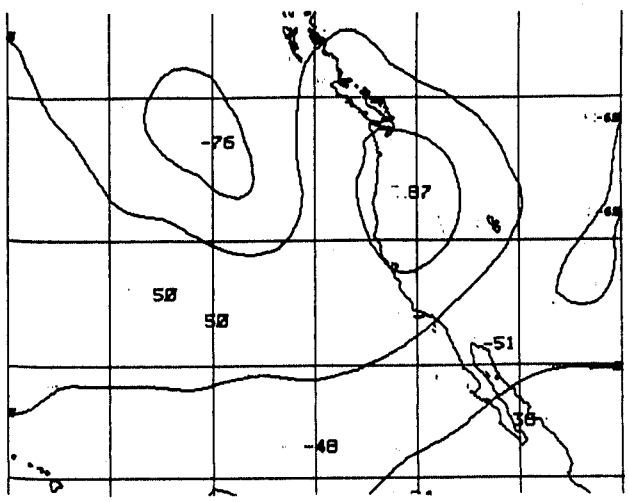

Fig. 3. 300 mb short wavelength (SD) field, 12 hr forecast, valid time 000 GMT 24 February.

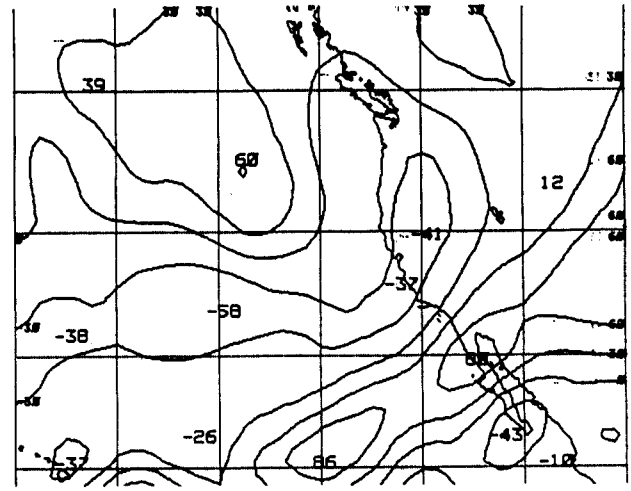

Fig. 4. 300 mb relative vorticity (ζ) field, 12 hr forecast, valid time 000 GMT 24 February.

fields permit a rather complete specification of the pattern of the SD component fields. The magnitude of the negative extrema in the SD field, however, remains to be specified.

A statistical method for specifying the magnitude of 300 mb and 1000/300 mb negative extrema has been documented and verified in S83. The satellite images are analyzed as follows: The center of the spiral system is located via the SPADS graph pen/pad. The intersection of the frontal band and the upper-tropospheric trough axis is then located in the same manner. A line orthogonal to the trough axis is then drawn passing through the system center. This line is used to define the system wavelength. An idealized schematic of the above is shown in Figure 5. Once the system amplitude (AMP) and

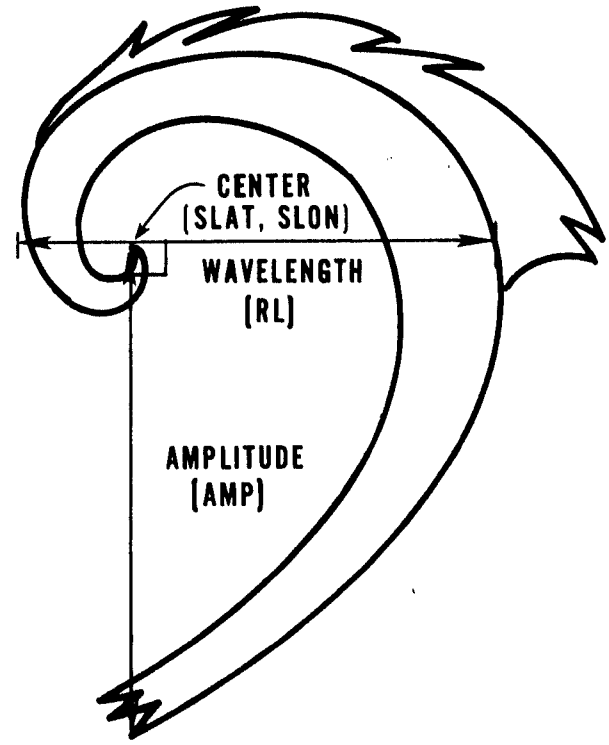

Fig. 5. Idealized SINAP satellite analysis scheme.

wavelength (RL) are known, the required long wave regression parameters are calculated at the nearest grid point to the system center. The location of the SD field zero line is then established and entered via the graph pen/pad. The SD field is then defined by the following relationship

$$Z = Z_{min} \cos(\pi r/2R), \qquad (2)$$

where Z is the value at the grid point defined by r, where r is the distance from the center to the grid point, R is the distance from the center to the zero line passing through the grid point and Z_{min} the negative SD extrema value.

Once the SD field pattern is defined, the SD values at the grid points within the region of influence when added to the SR field values, compose an array of bogus 300 mb heights. These are then blended with the rawinsonde and aircraft data used in the objective analysis. A schematic of the SINAP process is shown in Figure 6.

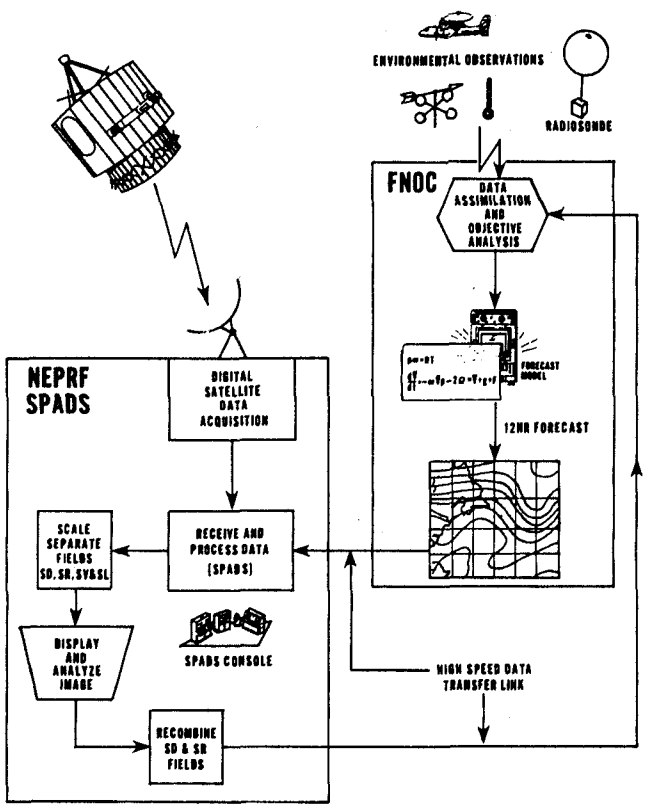

Fig. 6. Schematic flow diagram for the operational usage of the SINAP technique.

3. SINAP Case Study

Currently the NEPRF SPADS has routine access to the Fleet Numerical Oceanography Center's (FNOC) global analysis and forecast fields. The data are available on the FNOC 63 x 63 Northern Hemisphere Polar Stereographic grid points. The grid distance is 381 km, true at 60°N. Although the grid mesh is rather coarse and cannot resolve many of the small scale features the SINAP technique can provide, it is sufficient to demonstrate the impact of the SINAP technique on the 300 mb mass field.

In a realtime application of the SINAP analysis, current long wavelength analyses are not available, but rather the 12-hr forecast of the fields must be used. The critical assumption being that the 12-hr forecast (the "first guess") contains sufficient information for accurate specification of the long wavelength fields.

The figures shown in the text are 12-hr forecasts from 1200 GMT on 23 February, 1984, valid at 000 GMT on the 24th. The satellite image used for this case study was acquired from the GOES-WEST Satellite at 2345 GMT on the 23rd. The digital infrared satellite data was available at a resolution of 7 km. The 300 mb forecast field was computer processed to produce the 300 mb SV, SL, SR and SD fields. The SINAP analysis procedure is performed and the SINAP derived SD values are then processed with a Cressman type objective analysis routine to provide adjusted grid point values. The adjusted SINAP SD field is shown in Figure 7 and can be compared to the original SD field shown in Figure 3. The SINAP SD field is then added to the SR field yielding the adjusted 300 mb geopotential height field, shown in Figure 8.

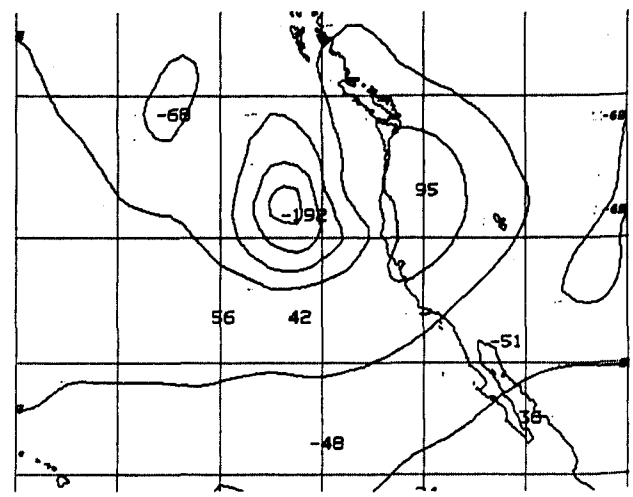

Fig. 7. 300 mb SINAP short wavelength (SD) field, 12 hr forecast, valid time 000 GMT 24 February.

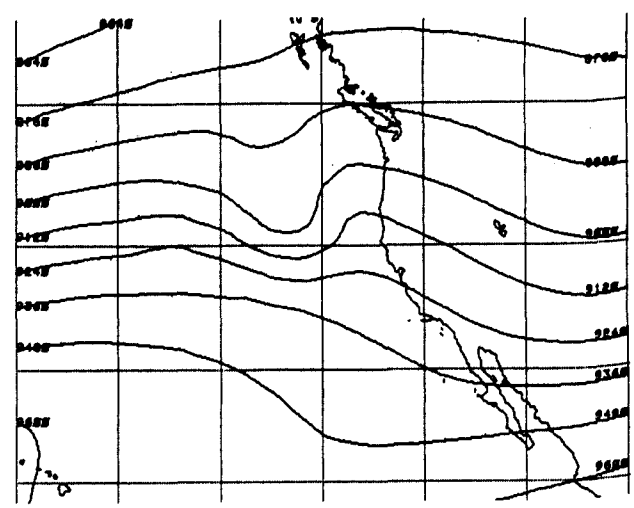

Fig. 8. SINAP 300 mb height field, 12 hr forecast, valid time 000 GMT 24 February.

4. Summary and Conclusions

The impact of the advanced SINAP technique on the analysis of the 300 mb mass field has been demonstrated. The resulting 300 mb height field reflects the qualitative characteristics observed in the satellite imagery in a quantitative manner made possible by the advanced SINAP technique. Therefore, it is concluded that the advanced SINAP technique is a viable method for improving the accuracy of the 300 mb mass field analysis in data sparse regions.

Further studies assessing the changes effected in the mass field analyses at mandatory pressure levels between 1000 and 300 mb are presently being conducted at NEPRF. The height values at the intermediate levels are adjusted by means of a weighted hypsometric equation. The standard atmosphere mean virtual temperatures for each layer are weighted by the ratio of the observed 1000/300 mb mean temperature to the standard 1000/300 mb mean temperature.

Finally, the impact of the advanced SINAP technique on the analyses and forecasts made by the Navy's Operational Regional Atmospheric Prediction System (NORAPS; Hodur, 1982) is being pursued. The ability of NORAPS' objective analysis procedure (Barker, 1982) to retain the adjustments effected by the SINAP technique will also be assessed.

5. REFERENCES

Barker, E.H., 1982: A Comparison of Two Initialization Methods in Data Assimilation. NAVENVPREDRSCHFAC Technical Report 82-06, 151 pp.

Bizzarri, B., 1982: Satellite Data for Numerical Weather Prediction. Revista Meteorologia Aeronautica, 42, 369-382.

Halem, M., Ghil, M., Atlas, R., Susskind, J. and Quirk, W.J., 1977: The GISS Sounding Temperature Impact Test. Final Report Goddard Space Flight Center, NASA 316 pp.

Hodur, R.M., 1982: Description and Evaluation of NORAPS: The Navy Operational Regional Atmospheric Prediction System. Mon. Wea. Rev., 110, 1591-1602.

Holl, M.M., 1963: Scale and Pattern Spectra Decompositions. Technical Memorandum No. 3, Contract N228-(62271) 60550, Meteorology International, Inc., Monterey, CA.

Miller, A.J. and Hayden, C.M., 1978: The Impact of Satellite-Derived Temperature Profiles on the Energetics of NMC Analyses and Forecasts During the August 1975 Data Systems Test. Mon. Wea. Rev., 106, 390-398.

Nagle, R.E. and Hayden C.M., 1971: The Use of Satellite-Observed Cloud Patterns in Northern Hemisphere 500 mb Numerical Analysis. NOAA Technical Report NESS 55, 46 pp.

Nagle, R.E., Clark, J.R., and Riegel, C.A., 1966: Objective Assembly of Meteorological Satellite Information. Final Report, Contract N62306-1775, Meteorology International Inc., Monterey, CA.

Schramm, W., Zeleny, P., Nagle, R.E., and Weinstein, A.I., 1982: The Navy SPADS, A Second Generation Environmental Display System. Ninth Conf. Weather Forecasting and Analysis, Seattle, WA.

Seaman, R.S. and Hayden C.M., 1979: Application of Quantitative Satellite Data to Numerical Analysis and Prediction. Technical Note No. 166, World Meteorological Organization. 87-99.

Swadley, S.D., 1983: The Use of Satellite Observed Cloud Patterns in Northern Hemisphere 300 mb and 1000/300 mb Numerical Analysis. M.S. Thesis, San Jose State University, 80 pp.

VAS DATA ASSIMILATION INTO A MESOSCALE MODEL

Jennifer M. Cram and Michael L. Kaplan

Systems & Applied Sciences Corporation
17 Research Dr., Hampton, VA 23666

1. INTRODUCTION

One of the problems in numerical weather prediction has always been insufficient data, especially on scales smaller than the synoptic rawinsonde network. The Visible Infrared Spin-Scan Radiometer (VISSR) Atmospheric Sounder (VAS) instrument on the Geostationary Operational Environmental Satellite (GOES) is capable of providing mesoscale vertical profiles of temperature and moisture several times over a twelve hour period. However, this data is only available over a relatively small area at any one time, not always a synoptic time. As most traditional data used in model initialization is available only at the synoptic times, the VAS data is more suited to data assimilation.

Traditionally, problems encountered in using satellite-retrieved soundings have included both random errors and large biases. Often the gradient or pattern information is more reliable than the absolute values of the data (Hillger and Vonder Haar, 1977; Chesters et al., 1981). An additional problem encountered with the VAS data is the relatively small area of data availability as compared to the model integration area (Fig. 1). To solve these problems a variational method has been developed to assimilate VAS temperature and relative humidity gradient information into a mesoscale model, the Mesoscale Atmospheric Simulation System (MASS) (Kaplan et al., 1982; Wong et al., 1983).

In this paper, the assimilation method and VAS data from one case will be discussed, that of 20-21 July 1981. Forecasts assimilating temperature gradients only and both temperature and relative humidity gradients will be compared to a non-assimilation forecast.

2. SYNOPTIC CONDITIONS

At 1200 GMT 20 July 1981 a stationary front extended from southern Michigan through Iowa to Colorado. During the day the front moved slowly southeastward through Kansas and Missouri (Fig. 2), setting off convection in northern Illinois by 1700 GMT and central Missouri at 1800 GMT. By 1800 GMT surface temperatures exceeded 35°C northeastward through Oklahoma. Cells began to develop across Oklahoma near 2000 GMT, developing eastward into Arkansas by 0600 GMT. The radar summaries for this period are shown in Fig. 3.

3. VAS DATA

The VAS soundings used in this study were processed by Goddard Space Flight Center (GSFC). Groups at both GSFC and the University of Wisconsin receive and process VAS data, although the two groups use different radiance inversion methods. Chesters et al. (1981) and Lee et al. (1983) have reported on the GSFC inversion methods. The processed VAS data included temperature and dewpoint soundings at 15 pressure levels from 1000 to 100 mb. The soundings were irregularly spaced, with an average separation near 55 km. Fig. 1 shows the locations of the soundings for 1500 GMT 20 July 1981. The soundings at 1200 and 1800 GMT covered the same area. The data from 1200, 1500, and 1800 GMT were used for the simulations described in this paper.

Using a simple Cressman (1959) weighting function, the VAS data at each pressure level were interpolated horizontally to the MASS grid, then vertically to pressure levels ranging from 1000 to 100 mb at 25 mb intervals. The vertical interpolations are logarithmic with respect to pressure. The VAS dewpoints are converted to relative humidities before the interpolations. Fig. 4 shows the 850 and 500 mb VAS temperature and relative humidity fields after this analysis at 1500 GMT 20 July 1981. Lee et al. (1983) found that VAS retrieved temperatures had errors ranging up to 2°C, while the dewpoint temperature errors at low levels were also near 2°C. Errors in cloud-contaminated areas may be larger. Fig. 5 shows the 1200 GMT 850 mb VAS analyzed temperatures and dewpoints. In this case, temperature differences up to 3°C exist in the temperature fields with larger differences in the dewpoint fields. The 850 mb temperature difference between Salem, Illinois and Topeka, Kansas is 7°C from the rawinsonde soundings, but only a little more than 2°C from the analyzed VAS data. These differences are inherent in the VAS soundings and are not a product of the analysis. Because of these differences and the smoothing in the VAS retrieved temperature and dewpoint fields, the calculated relative humidity field is also too smooth. Peterson et al. (1983) discuss the ability of VAS moisture imagery to depict strong horizontal and vertical moisture gradients. However, the retrieved moisture fields have much smoother moisture gradients.

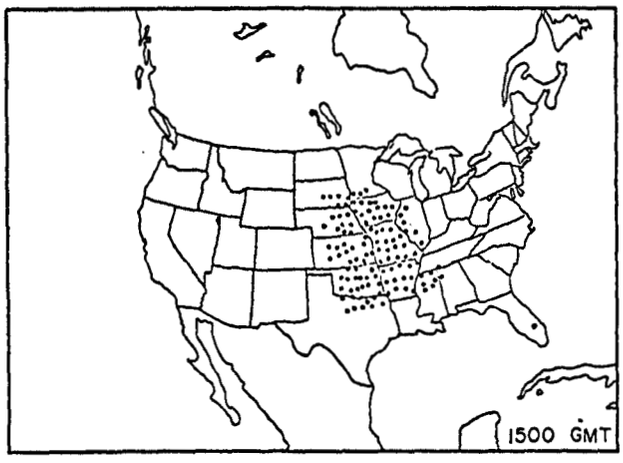

Fig. 1 - MASS area of integration and VAS sounding locations at 1500 GMT 20 July 1981.

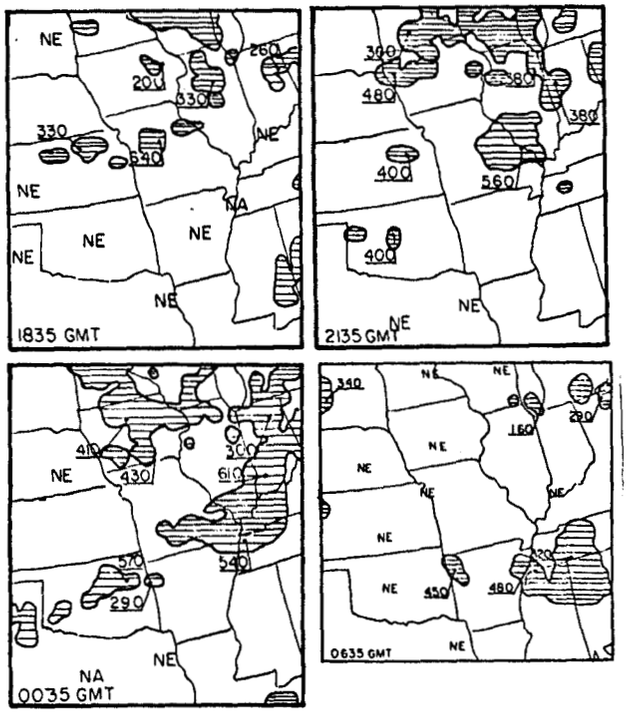

Fig. 3 - Radar summary charts.

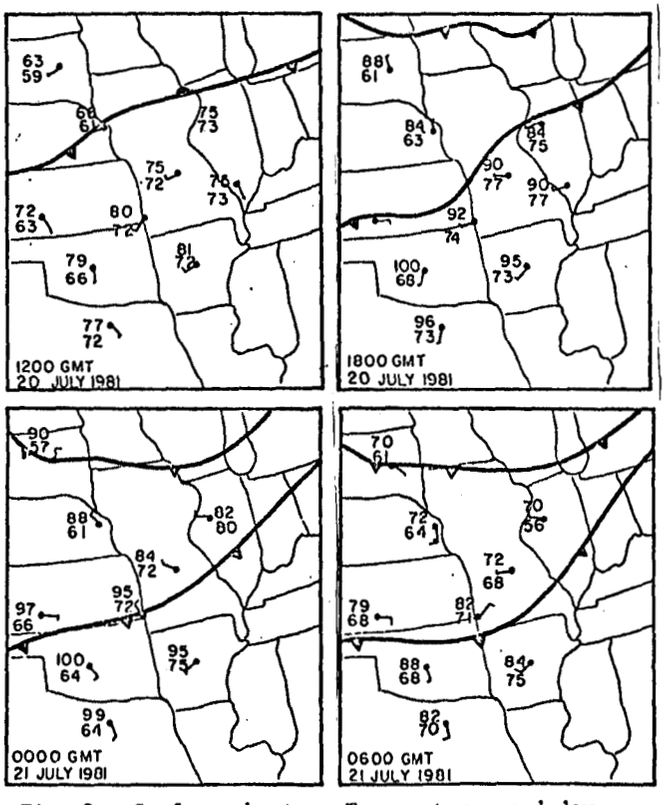

Fig. 2 - Surface charts. Temperatures and dew-point temperatures are in °F.

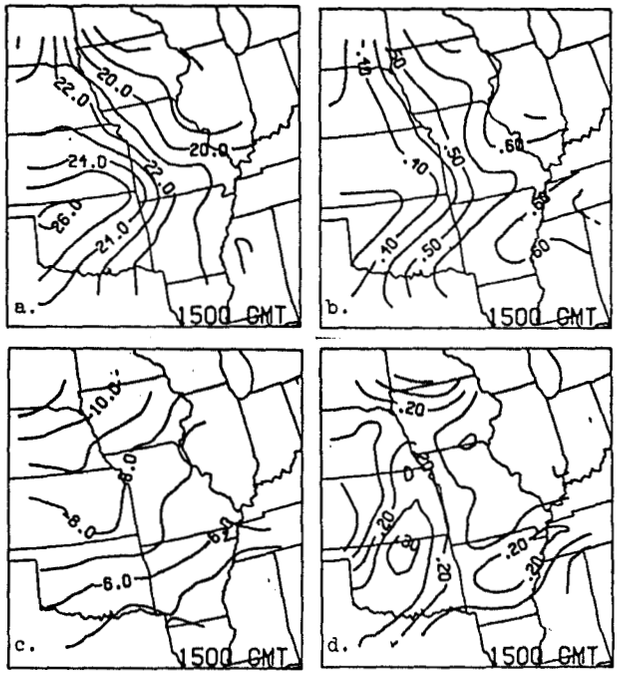

Fig. 4 - 1500 GMT 20 July 1981 analyzed VAS (a) 850 mb temperatures (°C), (b) 850 mb relative humidities (1.0 is 100%), (c) 500 mb temperatures (°C), (d) 500 mb relative humidities (1.0 is 100%).

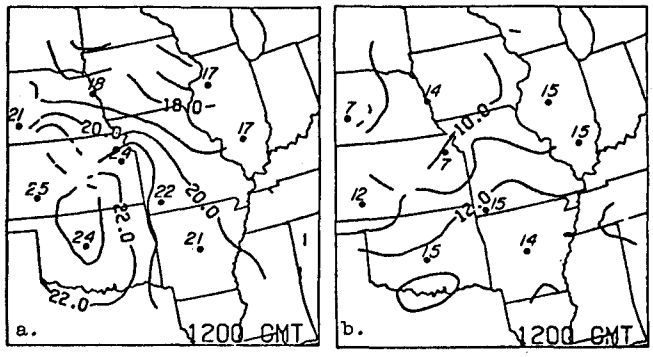

Fig. 5 - 1200 GMT 20 July 1981 850 mb VAS data (contours) and rawinsonde data (point values); (a) analyzed VAS temperatures and rawinsonde temperatures (°C), (b) analyzed VAS dewpoint temperatures and rawinsonde dewpoint temperatures (°C).

4. MASS AND VARIATIONAL ASSIMILATION METHOD

MASS version 3.0 is a primitive equation model with a 58 km grid spacing true at 90°N. There are 14 layers in the sigma-p vertical coordinate system. MASS is a comprehensive modeling system that includes a generalized similarity theory boundary layer parameterization, a surface energy budget, moist physics and a cumulus parameterization scheme (Kaplan et al., 1982; Wong et al., 1983). For the assimilation experiments described in this paper an adiabatic version of MASS was used in order to isolate the assimilation effects in the model. This adiabatic version did not include a cumulus parameterization scheme, surface heat or moisture flux, or grid-scale latent heating.

The basic principle of variational analysis is to minimize the adjustments to a field in a least-squares sense, while meeting a set of constraints on that field (Sasaki, 1955). In this case, the constraints are the VAS data gradients; the model fields are adjusted at the assimilation time to match the VAS data gradients, not the VAS data absolute values. Similar analysis schemes have been developed by Sasaki and Goerss (1982).

The variational functional to be minimized is:

$$J = \int_x \int_y \; [A(V-\tilde{V})^2 + B(\nabla_x V - \nabla_x \hat{V})^2 + C(\nabla_y V - \nabla_y \hat{V})^2]\,dxdy \qquad (1)$$

where $\tilde{V}$ is the model first-guess variable, V is the model adjusted variable, and $\hat{V}$ is the VAS data variable. ∇_x and ∇_y are the horizontal gradients in the x and y directions, and A, B, and C are the weights. The weights are assigned a constant value, estimated from the inverse of the expected variance associated with that term in the functional J. The functional is minimized, and the resulting Euler-Lagrange equation is solved using relaxation methods. There are no vertical constraints or coupling on the adjustments.

Fig. 6 shows the 850 and 500 mb temperature and relative humidity fields immediately before and after the assimilation procedure at 1500 GMT. Comparing these to the actual VAS fields in Fig. 3, the model's adjusted 850 mb temperature field shows the incorporation of the sharp tongue of

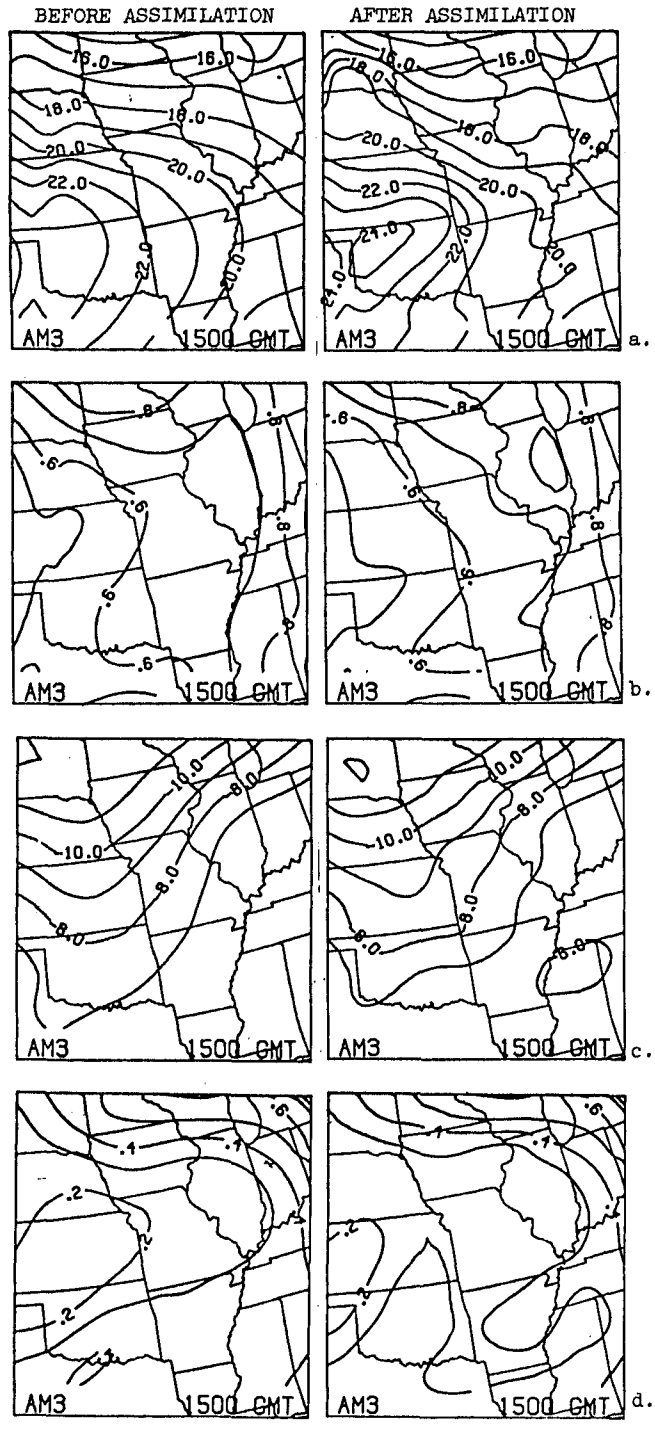

Fig. 6 - 1500 GMT MASS fields before and after assimilation of 1500 GMT VAS (a) 850 mb temperatures (°C), (b) 850 mb relative humidities (1.0 is 100%), (c) 500 mb temperatures (°C), (d) 500 mb relative humidities (1.0 is 100%).

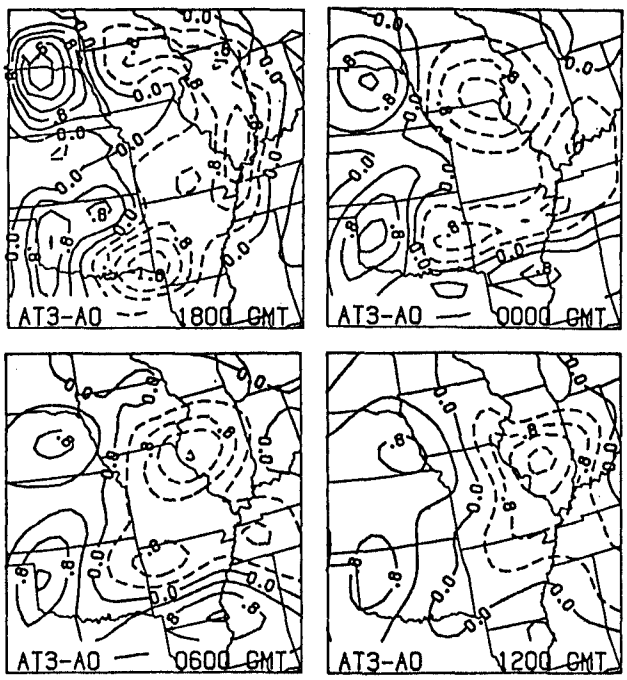

Fig. 7 - Difference between AT3 (temperature assimilation at 1200, 1500, and 1800 GMT) and A0 (control simulation) 850 mb temperature fields (°C). Solid lines are AT3 warmer, dashed lines are AT3 cooler.

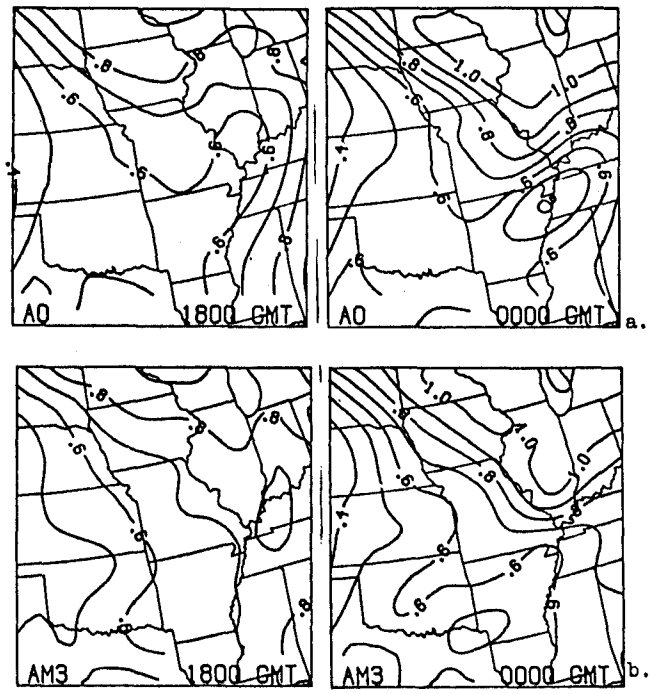

Fig. 8 - 850 mb relative humidities (1.0 is 100%) for (a) A0 (control simulation) and (b) AM3 (temperature and relative humidity assimilation at 1200, 1500, and 1800 GMT).

warm air extending eastward across northern Oklahoma. The 500 mb relative humidity field shows the incorporation of the VAS moisture extending northward through Oklahoma. The average differences between the model and VAS fields at this time were near 2°C for the temperatures and 20 percent for relative humidities. Inserting the VAS data directly into the model would have resulted in sharp discontinuities at the boundaries of the VAS data area.

5. ASSIMILATION EXPERIMENTS

Experiments comparing the assimilation of temperature gradients only (AT3) and both temperature and relative humidity gradients (AM3) to a non-assimilation forecast (A0) were conducted using the adiabatic version of MASS. All three simulations were for 24 hours, from the same initial fields at 1200 GMT 20 July 1981. VAS data were assimilated at 1200, 1500, and 1800 GMT. As noted before, the area of the VAS data for this case is relatively small, approximately 10° square. On this time and space scale very little verification data exists. The observed convection, as shown in the hourly radar summaries, will be used as an indicator of instability.

Fig. 7 shows the 850 mb temperature differences between the AT3 and A0 simulations. At 1800 GMT, immediately after the last assimilation, the AT3 850 mb temperatures are warmer by more than 1°C over northern and western Oklahoma, and cooler by 2° C over southeast Oklahoma. By 0000 GMT a cooler band extends across Arkansas while western Oklahoma is still warmer by more than 1°C. By 1200 GMT (21 July) western Oklahoma is still warmer by 1°C.

The AM3 forecast assimilated both temperature and relative humidity gradients at 1200, 1500, and 1800 GMT. The temperature difference fields in the ensuing simulation were very similar to those shown for the AT3 simulation in Fig. 7. The 850 mb relative humidity fields for this case are compared to the A0 simulation in Fig. 8. Again, at 1800 GMT the AM3 forecast has just assimilated the 1800 GMT VAS fields. By 0000 GMT, moister low level air (Fig. 8) still extends from the northeast to the southwest across Oklahoma in the AM3 simulation. At 500 mb (not shown) the differences in the AM3 and A0 fields damped more quickly, although a stronger gradient in the relative humidity does exist with the AT3 simulation across Oklahoma.

Fig. 9 shows the 500 mb lifted index (LI) fields for the A0, AT3, and AM3 simulations. The temperature-only assimilations increased the instability over northeast Oklahoma at 1800 GMT. The assimilation of both temperature and relative humidity gradients (AM3) decreased the instability in this area at 1800 GMT as drier air was assimilated at low levels and moister air at middle levels.

By 0000 GMT however, the AM3 simulation has moved the instability maximum west over north-central Oklahoma while the maximum in the A0 simulation has moved eastward into Missouri. The AM3 simulation also has a local maximum in the instability over southeast Missouri. The AT3 simulation still shows the strongest instability over northeast Oklahoma. The observed convection developed over north-central Missouri at 1800 GMT and moved through southeast Missouri by 0000 GMT. Convection also developed over western Oklahoma after 2000 GMT, and by 0000 GMT cells were spread across the state. Although the instabilities in the AM3 simulation are not as strong as in the A0

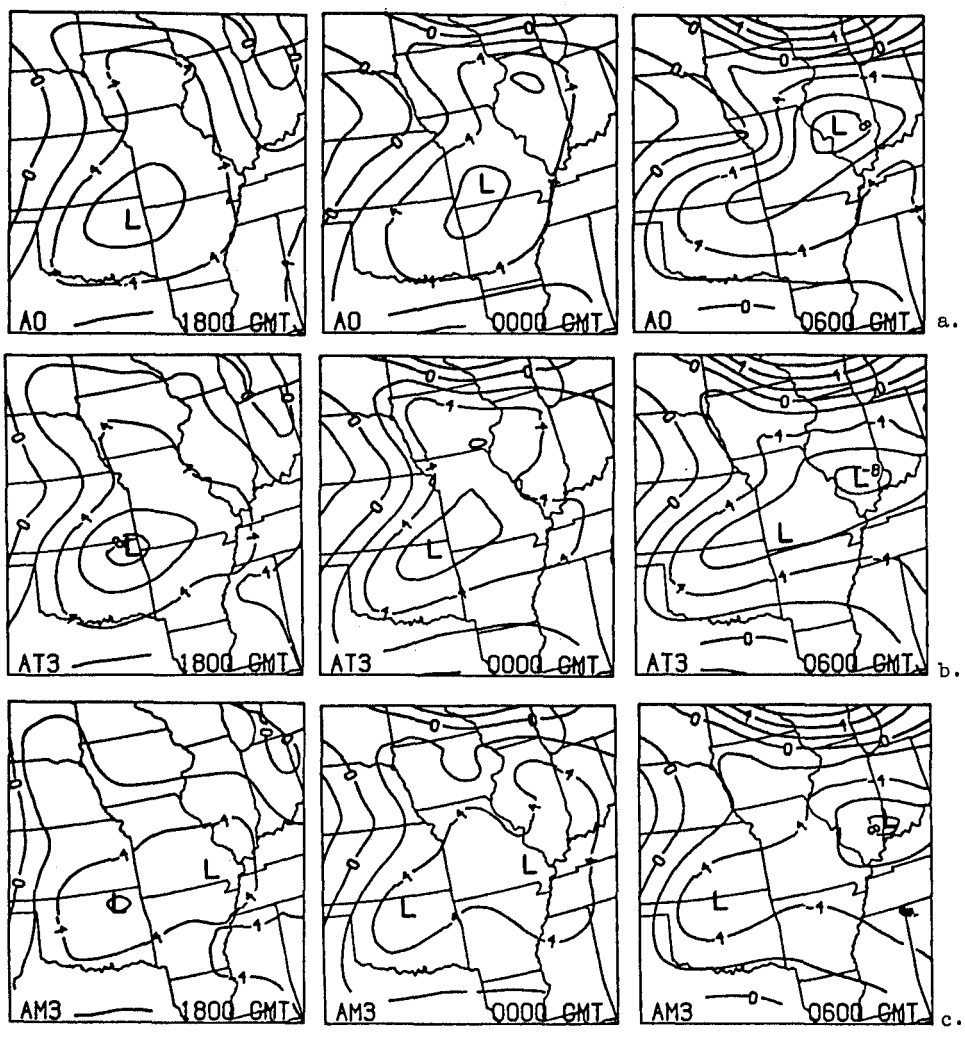

Fig. 9 - 500 mb lifted index fields (°C) for (a) AO (control simulation), (b) AT3 (temperature assimilation at 1200, 1500, and 1800 GMT), (c) AM3 (temperature and relative humidity assimilation at 1200, 1500, and 1800 GMT).

simulation, the AM3 instability pattern corresponds more closely to the mesoscale organization of the observed convection. The AT3 simulation, with greater instability over Oklahoma and a bulging of the instabilities across southern Missouri also better depicts this organization than the AO simulation.

At 0600 GMT the AM3 simulation still has an instability maximum over northern Oklahoma and the AT3 simulation has stronger instabilities from northern Oklahoma across southern Missouri. By this time the observed convection had moved out of Oklahoma and was spreading across northern Arkansas.

6. SUMMARY

A variational method for the assimilation of satellite-retrieved temperature and relative humidity gradients into a mesoscale model has been described. The variational assimilation procedure is able to smoothly introduce VAS mesoscale data into the MASS model, avoiding the problems caused by the relatively small area of available data and the biases between the model and VAS fields. Direct insertion or a local re-analysis using the VAS data would have resulted in discontinuities at the edge of the VAS data area. The variational assimilation method maintains continuity across this boundary while introducing the mesoscale temperature and moisture pattern information into the model.

A non-assimilation forecast was compared to a forecast assimilating temperature gradients at 1200, 1500, and 1800 GMT and a forecast assimilating both temperature and relative humidity gradients at all three times. The temperature gradient assimilation resulted in greater instabilities across Oklahoma, prior to the development of the observed convection. In the forecast assimilating both temperatures and relative humidities, the instability patterns more closely resembled the mesoscale organization of the convection that developed across Oklahoma and Missouri, although the actual instabilities were less than with the control simulation. The control simulation tended to merge and smooth the two separate areas of

instability over Oklahoma and Missouri into one maximum over southwestern Missouri.

To conclude, the greatest improvements to the forecast resulted when the VAS data resolved the mesoscale structure of the temperature and relative humidity fields. When this structure was assimilated into MASS, the ensuing simulations developed mesoscale patterns in the instability corresponding to the patterns of the subsequent observed convection. Assimilation experiments using the full physics version of MASS have also been conducted and will be reported on in the future.

7. ACKNOWLEDGEMENTS

This work has been supported under NASA contract NAS5-27393. Dr. James Dodge (NASA Headquarters) and Dr. Norman Crabill (NASA/LaRC) provided funding. Dr. Louis Uccellini provided the VAS data and many helpful suggestions during this study. As members of the MASS group, John Zack, Sueli Chuang, Glen Coats, Fred Proctor, and Vince Wong contributed to this work. Judy Southard drew some of the figures. Margarette Pitts typed the manuscript.

8. REFERENCES

Chesters, E., L. W. Uccellini, H. Montgomery, A. Mostek, W. Robinson, 1981: Assessment of the first radiances received from the VISSR Atmospheric Sounder (VAS) instrument. NASA TM 83827, 124 pp. [NTIS-82N19730].

Cressman, G., 1959: An operational objective analysis system. Mon. Wea. Rev., 87, 367-74.

Hillger, D. W., T. H. Vonder Haar, 1977: Deriving mesoscale temperature and moisture fields from satellite radiance measurements over the United States. J. Appl. Meteor., 16, 715-726.

Kaplan, M. L., J. W. Zack, V. C. Wong, J. J. Tuccillo, 1982: Initial results from a mesoscale atmospheric simulation system and comparisons with the AVE-SESAME I data set. Mon. Wea. Rev., 110, 1564-1590.

Lee, T., D. Chesters, A. Mostek, 1983: The impact of conventional surface data upon VAS regression retrievals in the lower troposphere. J. Climate Appl. Meteor., 22, 1853-1874.

Peterson, R. A., D. A. Keyser, A. Mostek, L. W., Uccellini, 1983: Severe storms analysis and forecasting techniques using VAS satellite data. Preprints Thirteenth Conference on Severe Local Storms, Tulsa, Amer. Meteor. Soc., 29-32.

Sasaki, Y. K., 1955: A fundamental study of the numerical prediction based on the variational principal. J. Meteor. Soc., Japan, 33, 30-43.

Sasaki, Y. K., J. Goerss, 1982: Satellite data assimilation using NASA Data System Test 6 ovservations. Mon. Wea. Rev., 100, 1635-1644.

Wong, V. C., J. W. Zack, M. L. Kaplan, G. D. Coats, 1983: A nested grid limited area model for short term weather forecasting. Preprints Sixth Conference on Numerical Weather Prediction, Omaha, Amer. Meteor. Soc., 9-15.

A DIAGNOSTIC NUMERICAL MODEL FOR THE APPLICATION OF SATELLITE DATA FOR THE STUDY OF GLOBAL WEATHER SYSTEMS

Gary L. Achtemeier and Harry T. Ochs

Illinois State Water Survey, Champaign, IL 61820

and

Stanley Q. Kidder

Dept. Atmos. Sci., University of Illinois, Urbana, IL 61820

1. INTRODUCTION

We are developing a diagnostic numerical model that will maximize the information content of data available from diverse sources, with particular emphasis on the incorporation of observations obtained by remote sensing with those from more traditional immersion techniques. Conventional and satellite data are being meshed according to measurement accuracies in a least squares variational formulation which requires the adjusted fields of meteorological variables to satisfy prescribed sets of mathematical constraints; the horizontal momentum equations, the hydrostatic equation, and an integrated form of the continuity equation. The inclusion of higher density satellite data allows for the diagnosis of the state of the atmosphere on a much finer scale over a much broader region than is presently possible and thus permits the study of the interactions and energy transfers between planetary scale and smaller scale atmospheric processes.

The model variables are presented on a staggard mesh and in a nonlinear sigma coordinate that eliminates the problem with truncation in the pressure gradient terms of the horizontal momentum equations in the middle and upper troposphere.

The diagnostic numerical model is tested with the 10-11 April 1979 cyclogenesis over the western and central United States as a case study. The NASA-AVE high temporal and spatial density rawinsonde data are used for an independent check on the analyses. Comparisons of variationally adjusted fields of meteorological quantities with and without TIROS-N mean layer temperature data will be presented.

THE UTILIZATION OF SEASAT-A DATA IN NUMERICAL WEATHER PREDICTION

Dean G. Duffy and Robert Atlas

Laboratory for Atmospheric Sciences
NASA/Goddard Space Flight Center
Greenbelt, MD 20771

1. INTRODUCTION

The lack of adequate observational data over the oceans has long been recognized as a significant gap in our current global weather data base. Currently conventional observations are limited to surface temperature and pressure reports from ships and buoys as well as a few upper-air reports from weather ships and islands. With the launch of the SEASAT-A satellite in June 1978, a new source of wind data over the world's oceans became available. From a microwave sensor on board the spacecraft, measurements of capillary-gravity wave backscatter were made. This, in turn, gave up to four possible wind vectors, one of which presumably corresponded to the actual surface wind.

An important question with regard to SEASAT wind data is their usefulness in numerical weather prediction. At present there exists only a few studies which have addressed this question. In a simulation study, Cane et al. (1981) found substantial improvement in the surface pressure and low and middle tropospheric wind forecasts in the extratropics with SASS winds. However, their results are probably too optimistic because they conducted an "identical twin" experiment in which the same model was used to generate the "nature" and the forecasts. In addition, error-free observations were inserted at the lowest model level (nominally 945 mb) which probably underestimated typical error obtained in 945 mb wind analysis from surface winds. They also did not try to simulate the ambiguity of the SASS data.

In studies with actual SASS data, Yu and McPherson (1981) used SASS winds directly in the lower wind analysis. In the Southern Hemisphere, they found large differences in a 48 h assimilation between wind and height analyses with and without SASS winds. Differences in the Northern Hemisphere were much smaller. Similarly, 72 h forecast differences were significant in the Southern Hemisphere, but very small in the Northern Hemisphere. Unfortunately they conducted the assimilation for only 48 h and performed only one 72 h forecast. Furthermore, the SASS winds were from a preliminary data set with many imperfections.

In this paper we present the results from several numerical experiments that we have made where SASS winds were either included or excluded. In the case of objective dealiased winds, we performed experiments using the 4° x 5° GLAS fourth-order model and the Navy's operational model (NOGAPS). These results are summarized in Section 2.

In the case of subjectively dealiased winds, we have employed a regional area model that is described in Section 3. In Section 4, we describe the initial conditions used in the regional model experiment. The results and conclusions will be stated in Sections 5 and 6.

2. GLOBAL SCALE EXPERIMENTS

We have made several numerical experiments using global numerical weather prediction models of the impact of SEASAT data on numerical weather prediction. Two models were used. One of the models was the 4° latitude by 5° longitude fourth-order global general circulation model described by Kalnay-Rivas et al. (1977) and Kalnay-Rivas and Hoitsma (1979). It is based on an energy-conserving scheme in which all horizontal differences are computed with fourth-order accuracy. The objective analysis, described in Baker (1983), employs a successive correction method which utilizes the first guess provided by the model 6 h forecast from the previous analysis.

The other model was the Navy's operational model, generally known as NOGAPS. The forecast model is essentially the UCLA general circulation model (see Arakawa and Lamb, 1977). The horizontal finite-differencing is second-order, enstrophy and energy conserving, with scheme C staggering of the variables in the horizontal at a resolution of 2.4° latitude by 3° longitude. The objective analysis method used in NOGAPS is a form of the successive correction technique of Barnes. The model is initialized by balancing the winds via a calculus of variation method.

The procedure used in all numerical experiments was as follows: a six hour assimilation was set up from initial conditions provided by the global operational Hough analysis of the National Meteorological Center for 0000 GMT 7 September 1978. At each subsequent six hour period, an analysis was performed using all conventional data. The first guess came from integrating the global model for six hours.

This assimilation defined the control.

A second assimilation was then run which included conventional and SASS data. In the case with the NOGAPS, it was necessary to convert the surface winds to observations at 925 and 700 mb because the NOGAPS analysis does not directly use surface winds. This was done by using the boundary layer parameterization of Randall (1976) which is used in the model. The exact method is explained in Duffy et al. (1984).

Comparison of the pressure and wind field analyses produced by the SASS and NOSASS assimilation showed larger impacts in the Southern Hemisphere than in the Northern Hemisphere. For example, in the Northern Hemisphere, small initial state differences of less than 2 mb in sea level pressure and less than 5 m sec^{-1} in surface wind cover most regions in the NOGAPS experiments. In the Southern Hemisphere, differences of 2-8 mb in sea level pressure and 10-15 m sec^{-1} in surface winds cover large portions of the extratropics.

We found that SASS winds produced a larger modification of initial states in the Northern Hemisphere in the NOGAPS analysis than the GLAS analysis. This results from the use in GLAS analysis of surface ship wind reports which were excluded from direct inclusion in the NOGAPS analysis.

In Figures 1 and 2 we present S1 skill scores over continental regions for a composite of the 72 h forecasts at 24 h intervals using the National Meteorological Center's global analysis for verification. These results show that the average impact of SASS data on sea level pressure and 500 mb forecasts is essentially negligible. When individual cases were examined, however, large impacts were found. These large impacts were both positive and negative and tended to cancel on the average.

Although the SASS winds might be useful in some instances in a global model, their high resolution suggests that they might be more useful in a higher resolution model. For this reason, we turned to a regional numerical prediction model with a resolution of 100 km. Furthermore, we shall use the best possible SASS data set available. This was a set of SASS winds that were subjectively dealiased by using all possible sources of data: conventional, satellite imagery, and continuity of systems.

3. THE REGIONAL MODEL

The regional model is essentially that described by Duffy (1981). The coordinate system used in the model is a Lambert conformed map projection which is true along 30°N and 60°N. The vertical extent of the model ranges from 100 mb

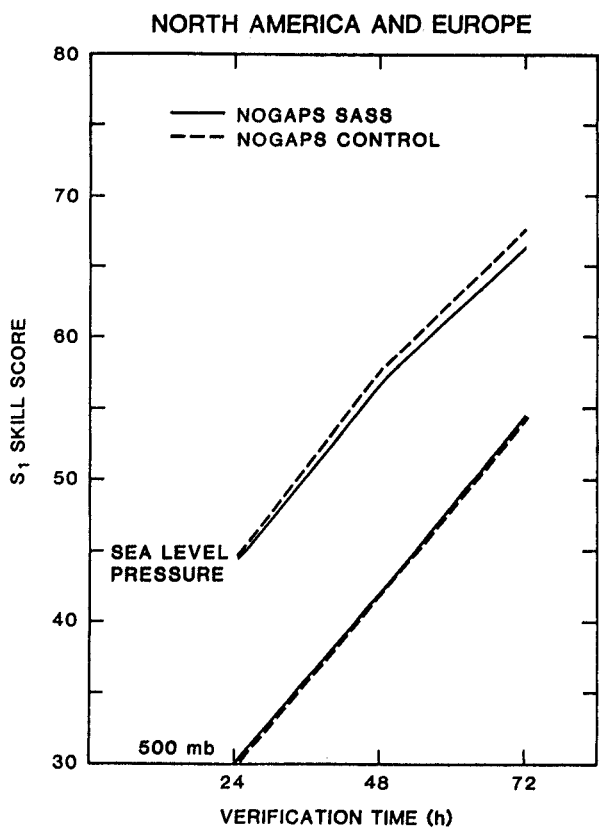

Fig. 1. S1 skill scores for all forecasts over North America and Europe for NOGAPS forecasts with and without SASS data.

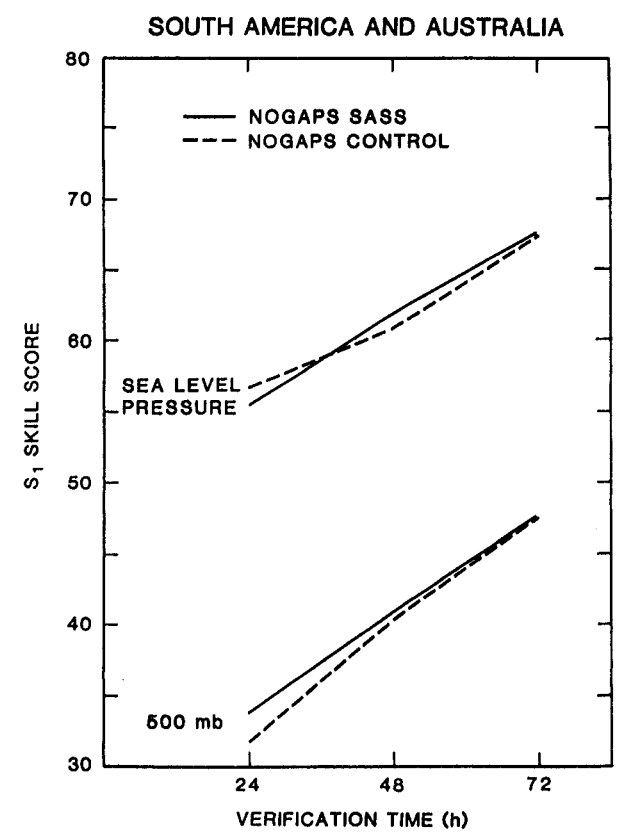

Fig. 2. Same as Fig. 1 except over South America and Australia.

to 1000 mb and has a vertical resolution of 100 mb. The horizontal resolution of the model is 100 km. All the dependent variables are located at all of the gridpoints (i.e. the A grid).

The horizontal components of the wind and geopotential heights are located at the 100, 200, ..., 1000 mb surfaces while the mixing ratio, thickness and omega are at the intermediate levels. The atmosphere is assumed dry above 300 mb.

The mathematical equations of motion, continuity, thermodynamics, and water balance are solved using a modified form of the split-explicit time-marching scheme of Gadd (1978). For the integration of those terms representing inertial-gravity waves, we used a forward-backward technique suggested by Masuda (1981). For a one-dimensional, linearized shallow water model, Masuda showed that the low frequency, meteorological wave is preserved almost perfectly, while the high frequency gravity waves were damped effectively.

The advection terms were integrated with a modified Matsuno scheme suggested by Kurihara and Tripoli (1976). By the appropriate blending of the predictive and corrective stages of the Matsuno scheme, Kurihara and Tripoli showed that the damping associated with the Matsuno scheme can be completely eliminated.

The physical parameterizations included in the model are large-scale and convective precipitation, evaporation of rain or snow as it falls through the atmosphere, and sensible and latent heat fluxes from the surface. A dry convective adjustment scheme is also present. A detailed description is given in Duffy (1981).

4. INITIAL CONDITIONS

The initial conditions for the control run was from the global analysis from the National Meteorological Center which we had archived at the resolution of 4° latitude and 5° longitude. This field was bilinearly interpolated to the model's 100 km by 100 km grid.

For the SASS experiments, the 1000 mb winds were replaced by subjectively dealiased SASS winds whenever they were available. Furthermore, SASS winds were allowed to influence the upper-level winds through the use of a vertical correlation function given by Yu and McPherson. If the upper-level winds were not modified, the effects from the upper levels soon overwhelmed the corrections that we had made.

Sea surface temperatures were taken from sea surface analysis from Fleet Numerical Oceanographic Center, valid at that time. The topography field was derived from a 1° x 1° global data set constructed by the U.S. Air Force.

In Fig. 3, we present the sea level pressure and 1000-500 mb thickness at the initial time of the experiments, 12 GMT 9 September 1978. We are primarily interested in the evolution of the nascent low located just off Nova Scotia.

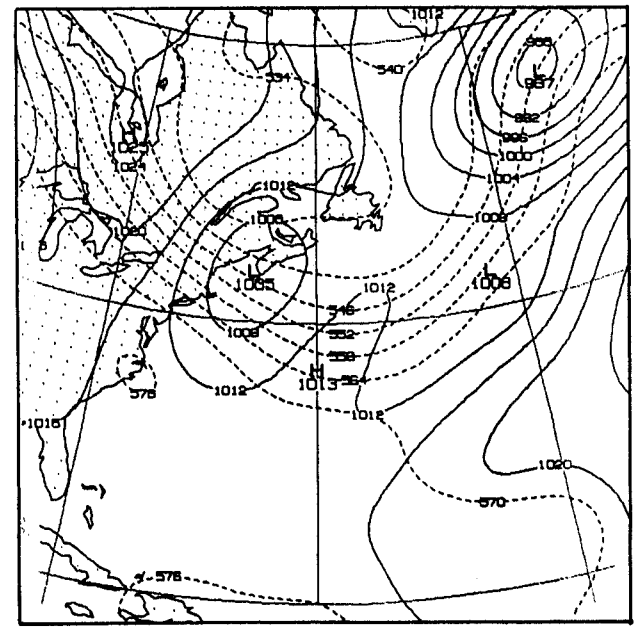

Fig. 3. The initial sea level pressure field for 12 GMT 7 September 1978.

5. RESULTS

The results from the two different experiments are presented in Figs. 4 and 5. In both cases, the low located just off Nova Scotia has moved out into the open water of the North Atlantic Ocean. In the case of the control, no intensification occurred, the pressure at 24 hr being 1005 mb. This result is consistent with the results given by the operational limited-area, fine-mesh model run at the National Meteorological Center (LFM) and the Navy's operational model. It is also consistent with the numerical results found by Anthes et al. (1983) in their numerical simulation of the QEII when only conventional data was included.

From Fig. 5 we see that the inclusion of SEASAT data has had a dramatic effect on the cyclogenesis. The difference between the SASS and NOSASS case is 11 mbs. From a preliminary study of results, the deepening of the low occurs because of larger amounts of convective precipitation in the SASS experiment than the NOSASS experiments. At the conference we will present further diagnostics which will explain why this extra precipitation occurred. Furthermore, later experiments indicate that the vertical correlation function used in this study may be an underestimate of the coupling that exists between low and upper levels of the atmosphere in this type of synoptic situation. Preliminary tests show an even greater improvement to the predicted intensification with a more realistic correlation.

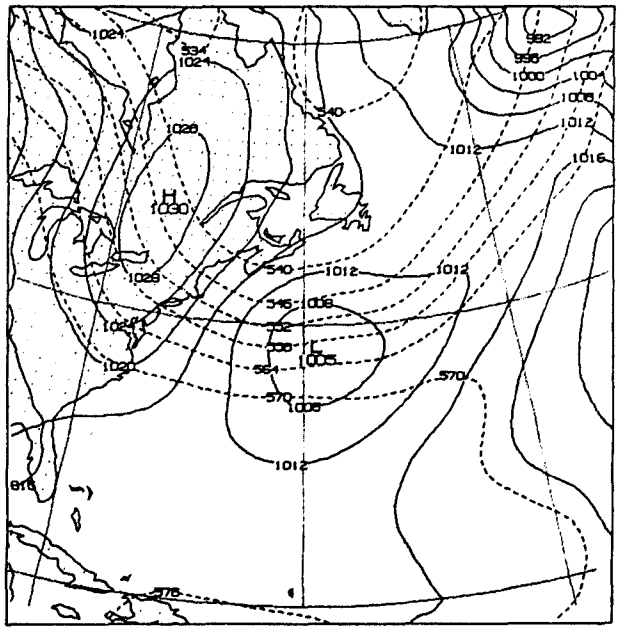

Fig. 4. The 24 h predicted sea level pressure field for the NOSASS experiments.

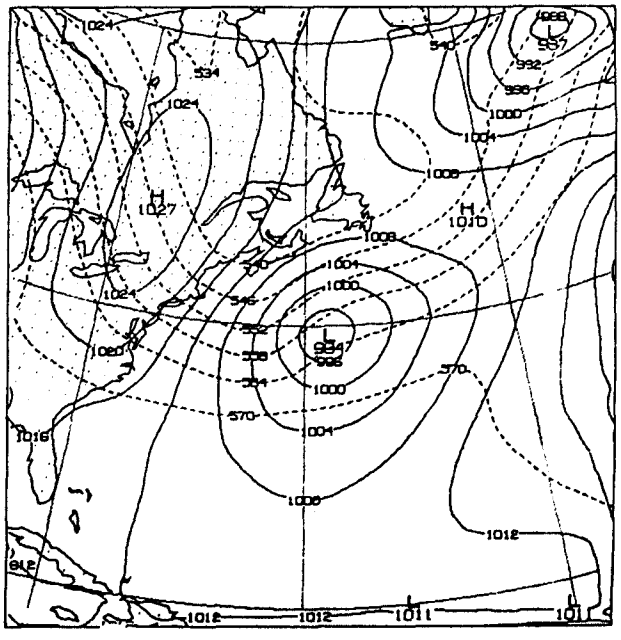

Fig. 5. The 24 hr predicted sea level pressure field for the SASS experiment

6. CONCLUSIONS

Our results show that SEASAT-A data can be important in defining the initial conditions that result in rapid maritime cyclogenesis. The best use of this data for this purpose is in a where the high resolution of the data can be best utilized. Current work is under way to develop a higher horizontal and vertical resolution global model, with an improved planetary boundary layer parameterization, to physically account for the vertical coupling between the surface and higher levels.

ACKNOWLEDGEMENTS

The authors gratefully acknowledge A. Pursch, S. Postman, J. Terry, J. Badner and R. Rosenberg for their contributions to the dealiasing of SEASAT winds at GLAS and the preparation of data sets for these experiments. The subjective dealiasing of SEASAT data was performed in collaboration with P. Woiceshyn, G. Cunningham, M. Wurtele and S. Peteherych. We thank D. Sabatino for typing the manuscript.

REFERENCES

Anthes, R. A., Y.-H. Kuo, and J. R. Gyakum, 1983: Numerical simulations of a case of explosive cyclogenesis. Mon. Wea. Rev., 111, 1174-1188.

Arakawa, A., and V. Lamb, 1977: Computational design of the basic dynamical processes of the UCLA general circulation model. Methods in Computational Physics, 17, Academic Press, Inc., New York.

Baker, W. E., 1983: Objective analysis and assimilation of observational data from FGGE. Mon. Wea. Rev., 111, 328-342.

Cane, M. A., V. J. Cardone, M. Halem, and I. Haber, 1981: On the sensitivity of numerical prediction to remotely sensed marine wind data: a simulation. J. Geophys. Res., 86, 8093-8106.

Duffy, D., 1981: A split explicit reformulation of the regional numerical weather prediction model of the Japan Meteorological Agency. Mon. Wea. Rev., 109, 931-945.

Duffy, D., R. Atlas, T. Rosmond, E. Bonker, and R. Rosenberg, 1984: The impact of SEASAT scatterometer winds on the Navy's operational model. Submitted to J. Geophys. Res.

Gadd, A. J., 1978: A split explicit integration scheme for numerical weather prediction. Quart. J. Royal Meteor. Soc., 104, 569-582.

Kalnay-Rivas, E., A. Bayliss and J. Storch, 1977: The 4th order GISS model of the Atmosphere. Beitr. Phys. Atmos., 50, 299-311.

Kalnay-Rivas, E., and D. Hoitsma, 1979: The effect of accuracy, conservation, and filtering on numerical weather forecasting. Preprints Fourth Conference on Numerical Weather Prediction, Silver Spring, AMS, Boston, pp. 302-312.

Kurihara, Y., and G. J. Tripoli, 1976: An iterative time integration scheme designed to preserve a low-frequency wave. Mon. Wea. Rev., 104, 761-764.

Masuda, Y., 1981: Economical time integration schemes with effective damping of high-frequency noise. J. Meteor. Soc. Japan, Series II, 59, 133-146.

Randall, D. A., 1976: The interaction of the planetary boundary layer with large-scale circulation. Ph.D. Thesis, Dept. of Atmospheric Sciences, UCLA.

Yu, T. W., and R. D. McPherson, 1981: Surface pressure analysis using scatterometer derived data from the SEASAT-A satellite. Preprints Fourth Conference on Numerical Weather Prediction, AMS, Silver Spring, MD.

ANALYSIS OF A 0.5 MICRON SPACEBORNE WIND SENSOR

P.B. Hays and V.J. Abreu

Space Physics Research Laboratory
The University of Michigan
Ann Arbor, Michigan 48109

J. Sroga and A. Rosenberg

RCA Astro Electronics
Princeton, NJ 08540

Abstract. A theoretical model of a doppler lidar with incoherent Fabry-Perot detection is presented. This analysis is followed by a development of the technique used for system optimization. Several near optimum systems are then discussed and evaluated to illustrate the variations which can be developed from an engineering point of view. The study is concluded with an assessment of this system in meeting meteorological requirements concerning wind measurements.

Introduction

The study of dynamics and energetics of the earth's atmosphere has a long history associated intimately with the development of instrumentation to measure pressure, temperature and winds. Lidar systems to measure atmospheric winds are presently undergoing a transition from feasibility studies to the development of operational systems.

Ground based incoherent lidar systems working in the yellow-green wavelength (0.5μ) region have been demonstrated to have the capability of measuring the vector wind with accuracy exceeding one meter per second (Benedetti-Michelangeli et al., 1972; 1974). This technique of determining the wind velocity relies on detecting the doppler shift experienced by a pulse of narrow band laser light as it is scattered by the atmosphere. The detection is done using an incoherent interferometric determination of the laser wavelength before and after reflection.

Here we investigate the implementation of a space-borne high resolution lidar to measure winds in the troposphere and stratosphere. The lidar system being considered uses a Fabry-Perot optical interferometer. The implications of carrying out such measurements from an orbital platform were first discussed by Abreu (1979), where the need for extended integration or high laser power was identified. This study extends those early investigations and includes a detailed system tradeoff assessment and analysis.

*Scientific Rationale for Space-Borne Doppler Lidar

In recent decades the advent of weather radar, weather satellites, and increasingly powerful computers has led to advances in our ability to monitor weather and to understand it. There have been, however, relatively modest gains in forecasting skills. In this area much room for improvement remains.

Weather prediction skills depend on the observational data base and on numerical prediction models. It has been realized that in order to provide improved short-range (1-2 days) predictions, fine-mesh prediction models are necessary. These models, in contrast to global models, require initial data with better accuracy and with finer spatial and temporal resolution. Also, the fine-mesh models are sensitive to factors not important for the large-scale circulation, such as vertical wind components.

The improvement of prediction models requires better horizontal wind information than is currently obtained. This is specially true in the tropics where the synoptic scale temperature and pressure gradients are weak. Also in the extratropical regions, nongeostrophic wind components near the tropopause and in the lower levels are important for the diagnosis and prediction of weather development, and these cannot be derived from the temperature field alone.

Wind information is currently derived from radiosondes launched once every 12 hours from points about 350 km apart in some countries and with much larger gaps over the oceans. Cloud motions derived from satellite photographs are another source of wind data, but this method, though very valuable, is limited as it cannot provide the wind field at cloud-free levels or locations. There are also questions regarding the possible differences between apparent cloud motions and the true wind and more fundamentally, difficulties with assigning heights to the derived cloud motion vectors. With regard to the vertical wind component there is currently no satellite method for measuring it. Table 1 lists the resolution and accuracy with which wind measurements are necessary for fundamental improvements in forecast accuracy. The parameters in the body of the table describe the needs for global or hemispheric numerical prediction models.

A space-borne doppler lidar can provide a direct measure of vertical and horizontal winds. The expected performance of a space-borne doppler lidar system and how it will satisfy the requirements of prediction models will be discussed in a later section.

Lidar Equation with Fabry-Perot Detector System

The Fabry-Perot detector system we have chosen to investigate is similar to the one developed for passive wind measurements on board the Dynamics Explorer satellite. This is a stable, high resolution system consisting of a solid plane etalon and

TABLE 1.

REQUIRED PERFORMANCE FOR LIDAR MEASUREMENTS THAT ADDRESS METEOROLOGICAL OBJECTIVES

Parameter	Global models				Fine-mesh models			
	Δt, hr	Δx, km	Δz, km	Accuracy	Δt, hr	Δx, km	Δz, km	Accuracy
Wind	12 to 24	500	2 to 4	±3 m/s	6 to 12	100	1 to 2	±3 m/s

a multiring anode detector to scan spatially the plane of the Fabry-Perot. First, we will derive the mathematical function which represents the number of laser photons backscattered from the atmosphere and which are transmitted through the Fabry-Perot to the detector system. Then, we will optimize the system parameters which minimize the error in the wind measurement.

The function used here to represent the laser lineshape is the Gaussian distribution

$$P(\lambda) = \frac{P_t}{\sqrt{\pi}\,\Delta\lambda_1} \exp\left[-\left(\frac{\lambda-\lambda_o}{\Delta\lambda_1}\right)^2\right] \qquad (1)$$

where P_t is the total laser power transmitted, λ_o is the central laser wavelength, and $\Delta\lambda_1$ is the e-folding width of the laser beam (i.e., the e-folding width is the wavelength shift at which the laser intensity has dropped to 1./e of its peak value).

The scattering cross-section can be similarly expressed by Gaussian representation of the thermal velocity distribution of the scattering medium as

$$\sigma(\lambda) = \frac{\sigma_o}{\sqrt{\pi}\,\Delta\lambda_s} \exp\left[-\left(\frac{\lambda-\lambda_v}{\Delta\lambda_s}\right)^2\right] \qquad (2)$$

where σ_o is the Rayleigh or aerosol backscatter coefficient (cm^2), λ_v is the doppler shifted reference wavelength equal to $(\lambda_o+2v\lambda_o/c)$, v is the velocity of the scattering media, c is the velocity of light, and $\Delta\lambda_s$ is the e-folding width of the scattering source, given by

$$\Delta\lambda_s = 4.3 \times 10^{-7}\,\lambda_o\,(T/M)^{1/2}$$

where T is the temperature of the scattering media (°K), and M is the molecular weight of the scatterers in amu.

The power returned per lidar pulse $P_r(\lambda,H)$ is a convolution of the transmitted signal and the broadening function associated with the scattering media, i.e.,

$$P_r(H,\lambda) = \frac{P_t Q_o A_o \beta(H,\lambda)\Delta h q^2(H,\lambda)}{4\pi H^2} \times \frac{\exp\left[-(\lambda-\lambda_v)^2/(\Delta\lambda_1^2+\Delta\lambda_s^2)\right]}{\sqrt{\pi}\,(\Delta\lambda_1^2+\Delta\lambda_s^2)^{1/2}} \qquad (3)$$

where Q_o is the product of the quantum and optical efficiencies, A_o is the telescope area, $\beta(\lambda,H)$ is the product $N(H)\sigma_o(H,\lambda)$, N(H) is the density of scatterers, H is the range, Δh is the scattering layer thickness, and $Q(H,\lambda)$ is the atmospheric transmission coefficient.

The transmission through a perfect Fabry-Perot into a detector ring of width $\Delta\theta$ is given by the expression (Hays and Roble, 1971)

$$T(\lambda) = \left(\frac{1-R}{1+R}\right)\left[1 + 2\sum_{n=1}^{\infty} R^n \operatorname{sinc}\left(\frac{n\lambda_o\theta_o\Delta\theta}{\Delta\lambda}\right) \times \cos\left(2\pi n\left[\frac{\lambda-\lambda_o}{\Delta\lambda} + \frac{\lambda_o\theta_o^2}{2\Delta\lambda} + \frac{\lambda_o}{8}\frac{\Delta\theta^2}{\Delta\lambda}\right]\right)\right] \qquad (4)$$

where R is the plate's reflectivity, $\Delta\lambda$ is the free spectral range, and θ_o is the angle corresponding to the average wavelength being transmitted through the ring. The width of the rings is chosen so the spatial scan is linear in wavelength. The detector system is taken into consideration by convolving equations (3) and (4). Then the number of photons detected in the jth ring is

$$N_j = \left(\frac{1-R}{1+R}\right) Q_o C_o \left\{1 + 2\sum_{n=1}^{\infty} R^n \operatorname{sinc}\left(\frac{n\lambda_o\theta_o\Delta\theta}{\Delta\lambda}\right) \times e^{\frac{-n^2\pi^2(\Delta\lambda_1^2+\Delta\lambda_s^2)}{\Delta\lambda^2}} \times \cos\left(2\pi n\left[\frac{\lambda-\lambda_v}{\Delta\lambda} + \frac{\lambda_o\theta_o^2}{2\Delta\lambda} + \frac{\lambda_o}{8}\frac{\Delta\theta^2}{\Delta\lambda}\right]\right)\right\} \qquad (5)$$

where $$C_o = \frac{P_t A_o \beta(H,\lambda)\cdot\Delta h\cdot q^2(H,\lambda)\lambda_o}{4\pi H^2 hc}$$

and h is Planck's constant. This expression is a good representation of the response of an incoherent lidar which has a Fabry-Perot detector.

Next a real instrument function is used where each ring anode is expanded in a Fourier series based on the instrument calibration. The response of the instrument to backscattered laser light in the presence of a continuum background is then given by an equation similar to that described above for a perfect Fabry-Perot

$$N_j = Q_o\left(\frac{1-R}{1+R}\right)\int_o^\infty \left\{A_{oj} + \sum_{n=1}^{\infty}\left[A_{nj}\cos\frac{2\pi n}{\Delta\lambda}(\lambda-\lambda_o) + B_{nj}\sin\frac{2\pi n}{\Delta\lambda}(\lambda-\lambda_o)\right]\right\} \tag{6}$$

$$\times\left\{\frac{C_o e^{-\left(\frac{\lambda-\lambda_v}{\Delta\lambda_{1+s}}\right)^2}}{\sqrt{\pi}\,\Delta\lambda_{1+s}} + B_k\right\} T_F(\lambda)\partial\lambda$$

where $$\Delta\lambda_{1+s} = (\Delta\lambda_1^2 + \Delta\lambda_s^2)^{1/2}.$$

Here N_j is the counts recorded in the jth anode channel, B_K is the continuum background intensity, and $T_f(\lambda)$ is a broadband filter transmission.

Equation (6) represents the convolution of the instrument function with a Gaussian representing the backscattered laser signal (plus background). Effecting the integration yields

$$N_j = Q_o T_{oF}\left(\frac{1-R}{1+R}\right)\left\{C_o A_{oj} + C_o\left\{\sum_{n=1}^{\infty}\left[A_{nj}\cos\frac{4\pi n V\lambda_o}{C\Delta\lambda} + B_{nj}\sin\frac{4\pi n V\lambda_o}{C\Delta\lambda}\right]\right\} e^{\frac{-n^2G^2}{4}} + \frac{B_K\overline{\Delta\lambda}_f A_{oj}}{T_{oF}}\right\} \tag{7}$$

where

$$\overline{\Delta\lambda}_f = \int_o^\infty T_F(\lambda)\,d\lambda;\quad G^2 = 4\pi^2(\Delta\lambda_1^2 + \Delta\lambda_s^2)/\Delta\lambda^2$$

and T_{oF} is the broadband filter transmission at λ_o.

The four unknowns V, T, C_o, and B_K can be determined from the spectrum using a nonlinear least squares fitting technique. However, we have chosen to linearize equation (7) in order to simplify the problem to a single matrix multiplication. We thus carry out a Taylor series expansion for a function of two variables about approximated values (V_o, T_o) of the wind and temperature, respectively. The first order terms in the expansion are only used to obtain:

$$N_j = N_j(V_o, T_o) + \frac{\partial N_j}{\partial V}\Big|_{V_o, T_o}(V-V_o) + \frac{\partial N_j}{\partial T}\Big|_{V_o, T_o}(T-T_o) + \cdots \tag{8}$$

where

$$\frac{\partial N_j}{\partial V} = Q_o T_{oF}\left(\frac{1-R}{1+R}\right) C_o \sum_{n=1}^{\infty} e^{-\frac{n^2G^2}{4}}\frac{4\pi n\lambda_o}{C\Delta\lambda} \times\left[A_{nj}\sin\frac{4\pi n\lambda_o V_o}{C\Delta\lambda} - B_{nj}\cos\frac{4\pi n\lambda_o V_o}{C\Delta\lambda}\right]$$

and

$$\frac{\partial N_j}{\partial T} = -Q_o T_{oF}\left(\frac{1-R}{1+R}\right) C_o \sum_{n=1}^{\infty} e^{-\frac{n^2G^2}{4}}\frac{n^2\pi\Delta\lambda_s}{4\Delta\lambda T_o} \times\left[A_{nj}\cos\frac{4\pi n\lambda_o V_o}{C\Delta\lambda} + B_{nj}\sin\frac{4\pi n\lambda_o V_o}{C\Delta\lambda}\right].$$

In matrix form equation (4) can be written as

$$N_j = \sum_{k=1}^{4} A_{jk}X_k,\quad j = 1\cdots N_{ring} \tag{9}$$

where

$$X_1 = C_o$$

$$X_2 = (V-V_o)C_o$$

$$X_3 = (T-T_o)C_o$$

$$X_4 = B_k$$

The method for finding the optimum fit to the data will be to minimize the variance of the squared difference between theory and the measured spectrum with respect to the four variables defined above, that is,

$$\frac{\partial\overline{\delta N^2}}{\partial X_m} = 0 \tag{10}$$

where $$\overline{\delta N^2} = \sum_{j=1}^{N_{ring}} W_j\left\{N_j - \sum_{k=1}^{4} A_{jk}X_k\right\}^2$$

and W_j is a weighing function. Taking the derivative of δN^2 in equation (10) one obtains

$$\sum_{j=1}^{N_{ring}} W_j\left\{N_j - \sum_{k=1}^{4} A_{jk}X_k\right\}A_{jk} = 0. \tag{11}$$

If we assume that the operations commute and let

$$W_j A_{jM} = S_{jM}$$

and

$$\sum_{j=1}^{N_{ring}} W_j A_{jk} A_{jM} = W_{kM}$$

the solution to equation (11) can be written as the matrix equation

$$X_k = \sum_{M=1}^{4} \left[W_{kM} \right]^{-1} \sum_{j=1}^{N_{ring}} S_{jM} N_j \quad (12)$$

or

$$X_k = \sum_{j=1}^{N_{ring}} C_{kj} N_j$$

where $C_{kj} = \sum_{m=1}^{4} [W_{kM}]^{-1} S_{jM}$, and $[\ ]^{-1}$ indicates a matrix inversion operation. One should note that the matrices $C_{kj}(T_o,V_o)$ are dependent on the reference temperature and line of sight speed, consequently the linearization only works in the immediate vicinity of (T_o,V_o). In practice, since these matrices can be precalculated, a full set of inversion matrices are computed and stored. During the data reduction process a careful initial choice is made of the starting values of (T_o,V_o) and the appropriate matrix is extracted from storage and used to determine (T_1,V_1) which are then used to refine the choice of (T_o,V_o). If the variance of matrix choice is too large, the process is repeated until the temperature and line of sight velocity determined lie in the linear range of the inversion matrix. This process is very fast and has been used effectively in the reduction of satellite wind data from the Dynamics Explorer Fabry-Perot Interferometer (Hays et al., 1981).

This technique also has the merit of providing a simple expression for the statistical error in a given measurement set. The propagation of errors theorem for a system obeying Poisson statistics states that the standard deviations of the fitted parameters are given by

$$\sqrt{\overline{\delta X_k^2}} = \left(\sum_{j=1}^{N_{ring}} C_{kj}^2 N_j \right)^{1/2} . \quad (13)$$

Optimization of Fabry-Perot Wind Detector System

The first task in the design of the lidar system is to choose the etalon-detector parameters that will minimize the uncertainty in the wind measurement. Based on the statistical principle of least uncertainty there exists an optimum combination of source and instrumental parameters, which lead to the most efficient use of a Fabry-Perot interferometer in the measurement and determination of the Doppler Shift of the line profile. The expected variation in the velocity error can be expressed as

$$\sqrt{\overline{\delta V^2}} = \frac{\Delta V_{1+s} \cdot \varepsilon}{\sqrt{C_{ph}}} \quad (14)$$

where ΔV_{1+s} is the half-width at half-height of the combined source and laser signals in velocity units, C_{ph} is the photometric signal which would be observed without the high resolution element (Fabry-Perot), and ε is a proportionality factor which varies with the instrumental design and depends upon the etalon plate reflectivity, on the number of rings in the detector, N_{ring}, on the ratio of the returned laser signal bandwidth to the Fabry-Perot free spectral range, $\Delta\lambda_{1+s}/\Delta\lambda$, and on the fraction of the free spectral range that is illuminated and covered by the N_{ring} anodes of the detector. In order to minimize the wind error for a given source function one has to determine the instrumental parameters that minimize ε. Using the technique presented in the previous section we have calculated the quantity $\sqrt{C_{ph}}\ \delta V^2/\Delta V_{1+s}$. For simulation purposes we have assumed a photometric count equal to 10^4 and we have made tables of $\varepsilon/\sqrt{C_{ph}}$, i.e., the normalized wind error as a function of etalon reflectivity and the ratio of the FWHH of the laser backscattered signal to a free spectral range ($FWHH_{1+s}/\Delta\lambda$). The results of these calculations are summarized in Table 2 which show the results for a 12 ring anode detector. A complete free spectral range has been focused on the anode.

First, let's consider the case of molecular scattering. If one assumes a laser bandwidth (FWHH) equal to 1×10^{-3}Å and a source width of 1×10^{-2}Å, then the FWHH is approximately equal to 1×10^{-2}Å, i.e., the source width dominates. The table then indicates that the minimum error in the velocity occurs when the FSR of the Fabry-Perot is equal to $10^{-2}/0.316$, or the etalon gap, t, ($t=\lambda^2/2\Delta\lambda$) is 4.0 cm. The aerosol case has a source width of $\sim10^{-4}$Å, which implies an optimum instrument with a 40.0 cm gap. It is possible to reduce the etalon gap and still maintain high accuracy in the wind

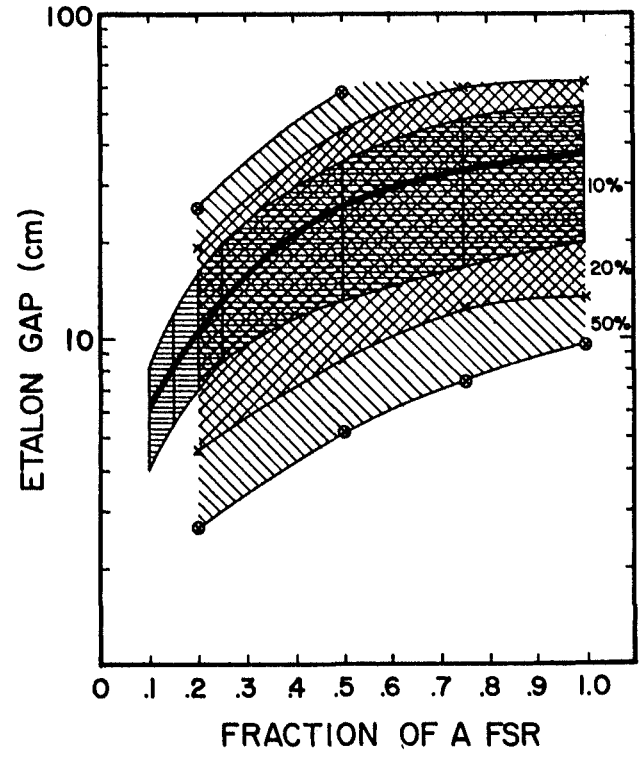

Fig. 1. Solid line indicates the combination of etalon gap and fraction of a FSR that optimizes the wind measurement. The shadowed areas indicate for a given fraction of a FSR, how much one can change the etalon gap and still remain within 10%, 20% and 50% of the minimum wind error.

TABLE 2.

SIGNAL STRENGTH	1.0000E+04
SIGNAL TO NOISE RATIO	0.1000
LASER WAVELENGTH	5000. A
FRACTION OF FSR DISPLAYED ON ANODE	1.000
LINE CENTER ON CHANNEL	6.000
NUMBER OF DETECTOR CHANNELS	12

NORMALIZED WIND ERRORS

FWHH/FSR	0.50	0.55	0.60	0.65	0.70	0.75	0.80	0.85	0.90	0.95
0.5000	0.0636	0.0620	0.0612	0.0613	0.0624	0.0647	0.0688	0.0757	0.0887	0.1203
0.3972	0.0570	0.0554	0.0546	0.0545	0.0553	0.0572	0.0606	0.0665	0.0776	0.1049
0.3155	0.0564	0.0545	0.0533	0.0528	0.0532	0.0545	0.0572	0.0622	0.0719	0.0963
0.2506	0.0589	0.0563	0.0544	0.0533	0.0530	0.0536	0.0556	0.0596	0.0680	0.0897
0.1991	0.0639	0.0602	0.0575	0.0555	0.0544	0.0542	0.0552	0.0583	0.0653	0.0847
0.1581	0.0715	0.0665	0.0625	0.0595	0.0573	0.0561	0.0562	0.0582	0.0640	0.0813
0.1256	0.0822	0.0755	0.0701	0.0657	0.0623	0.0600	0.0591	0.0601	0.0650	0.0812
0.0998	0.0968	0.0880	0.0808	0.0749	0.0702	0.0669	0.0653	0.0659	0.0709	0.0885
0.0793	0.1162	0.1050	0.0957	0.0881	0.0822	0.0782	0.0763	0.0776	0.0846	0.1081
0.0630	0.1418	0.1275	0.1158	0.1064	0.0994	0.0949	0.0937	0.0972	0.1097	0.1484
0.0500	0.1749	0.1569	0.1423	0.1308	0.1227	0.1183	0.1188	0.1271	0.1517	0.2293

REFLECTIVITY

TABLE 3.

SIGNAL STRENGTH	1.0000E+04
SIGNAL TO NOISE RATIO	0.1000
LASER WAVELENGTH	5000. A
FRACTION OF FSR DISPLAYED ON ANODE	0.5000
LINE CENTER ON CHANNEL	6.000
NUMBER OF DETECTOR CHANNELS	12

NORMALIZED WIND ERRORS

FWHH/FSR	0.50	0.55	0.60	0.65	0.70	0.75	0.80	0.85	0.90	0.95
0.5000	0.0645	0.0647	0.0607	0.0602	0.0631	0.0636	0.0676	0.0745	0.0862	0.1164
0.3972	0.0527	0.0506	0.0489	0.0486	0.0488	0.0499	0.0523	0.0568	0.0658	0.0881
0.3155	0.0472	0.0448	0.0431	0.0421	0.0419	0.0424	0.0440	0.0473	0.0542	0.0718
0.2506	0.0456	0.0428	0.0408	0.0394	0.0387	0.0388	0.0398	0.0423	0.0479	0.0629
0.1991	0.0471	0.0437	0.0412	0.0393	0.0382	0.0377	0.0382	0.0401	0.0447	0.0578
0.1581	0.0513	0.0470	0.0437	0.0412	0.0394	0.0383	0.0382	0.0393	0.0430	0.0544
0.1256	0.0580	0.0526	0.0483	0.0448	0.0421	0.0402	0.0392	0.0395	0.0422	0.0520
0.0998	0.0675	0.0606	0.0549	0.0502	0.0463	0.0434	0.0414	0.0406	0.0422	0.0505
0.0793	0.0804	0.0715	0.0640	0.0577	0.0524	0.0481	0.0448	0.0429	0.0432	0.0498
0.0630	0.0974	0.0859	0.0762	0.0678	0.0607	0.0547	0.0499	0.0465	0.0454	0.0505
0.0500	0.1194	0.1047	0.0922	0.0813	0.0719	0.0638	0.0571	0.0522	0.0499	0.0547

REFLECTIVITY

measurement by just focusing a fraction of the FSR on the anode. Table 3 shows the calculation of the wind error for a twelve ring anode detector with 50 percent of the FSR focused on the anode. We can see that the minimum appears at a different position. In general, the smaller the fraction of a FSR focused, the smaller the spacer, and the higher the reflectivity needed to optimize the measurement. For example, the etalon gap that optimizes the measurement reduces to ∿10 cm when 20% of a FSR is used. As the fraction of the FSR projected on the anode is decreased, there is some improvements in the accuracy of the wind measurement. It should be noticed, however, the minima are fairly flat and that for a given fraction of a free spectral range projected on the anode there is a range of etalon gaps over which one can operate and still maintain high accuracy in the wind measurement. This is shown in Figure 1, where we have indicated for a given fraction of a FSR, how much one can change the etalon gap and still remain within a given percentage of the minimum wind error. Here we have constrained the etalon gaps to those which do not require the plate's reflectivity to exceed 0.9. These calculations were done assuming a S/N ratio equal to .1. Calculation with S/N equal to 1., 10., and 100. show that the location of the minima does not change significantly as the S/N changes.

This section has established the trade offs among the parameters which define the Fabry-Perot interferometer that would minimize the wind error in a lidar measurement. Next, we proceed to simulate the lidar measurements.

Wind Measurement Simulations

It has been established in the previous section that there are several instrumental configurations which can produce equally accurate measurements of the wind velocity. In this section we calculate: 1) the line of sight wind error as a function of altitude for a 1 Joule laser pulse, and 2) the number of 1.0 Joule pulses to obtain a 3 m/s accuracy in the line of sight wind measurement. These calculations have been done for different instrumental configurations. In all instances we have assumed the line of sight at 45 degrees with the vertical, an altitude of 300 km and the backscatter coefficients of Elterman, 1968. The aerosol scattering phase function has been obtained using

TABLE 4.

LASER WAVELENGTH	5000.	A
LASER BANDWIDTH	1.0000E-03	A
SCATTERING BANDWIDTH(RAYLEIGH)	1.0000E-02	A
SCATTERING BANDWIDTH(AEROSOL)	1.0000E-04	A
PLATE SEPARATION GAP	10.60	cm
FRACTION OF FSR DISPLAYED ON ANODE	0.2000	
REFLECTIVITY OF ETALON PLATES	0.8800	
RECEIVER CLEAR APERTURE	100.0	cm
IMAGE PLANE DIAMETER	1.00	cm
NUMBER OF CHANNELS	12	
OPTICAL EFFICIENCY	0.2500	
QUANTUM EFFICIENCY OF DETECTOR	0.1700	
FIELD OF VIEW	4.344	mRad full cone
FOCAL LENGTH	514.8	cm
FREE SPECTRAL RANGE	1.1792E-02	A
VELOCITY FOR ONE CHANNEL SHIFT	11.78	m/sec
SATELLITE ALTITUDE	300.0	km
PULSE ENERGY	1.0	Joule

BACKSCATTERED PHOTOMETRIC SIGNAL STRENGTH

ALTITUDE	RAYLEIGH	AEROSOL	WIND ERROR FOR ONE PULSE (M SEC-1)	NUMBER OF PULSES FOR 3. M SEC-1 ERROR
20.	185.06	25.664	14.191	22.377
18.	245.34	44.271	10.018	11.151
16.	322.02	52.654	9.4423	9.9062
14.	420.62	53.974	10.019	11.153
12.	545.97	56.282	10.513	12.281
10.	696.40	55.383	11.553	14.829
8.	836.15	55.203	12.336	16.910
6.	974.94	52.719	13.538	20.365
4.	1105.9	71.739	10.888	13.172
2.	1189.4	188.01	5.0456	2.8286
0.	1030.5	668.15	1.9862	0.4383

standard theory for spherical particles. We have also assumed a detector consistent with that used on the Dynamics Explorer instrument.

The aerosol scattering lidar simulations assume the Rayleigh signal as background. Table 4 shows a sample calculation for an optimized system. The parameters used in the simulation are presented at the top of the table. Figure 2 shows the wind accuracy as a function of altitude obtained with a 1 Joule pulse when 1.0, 0.5 and 0.2 fraction of a FSR are projected on the anode. As expected, the smaller the fraction of the FSR projected, the better the accuracy.

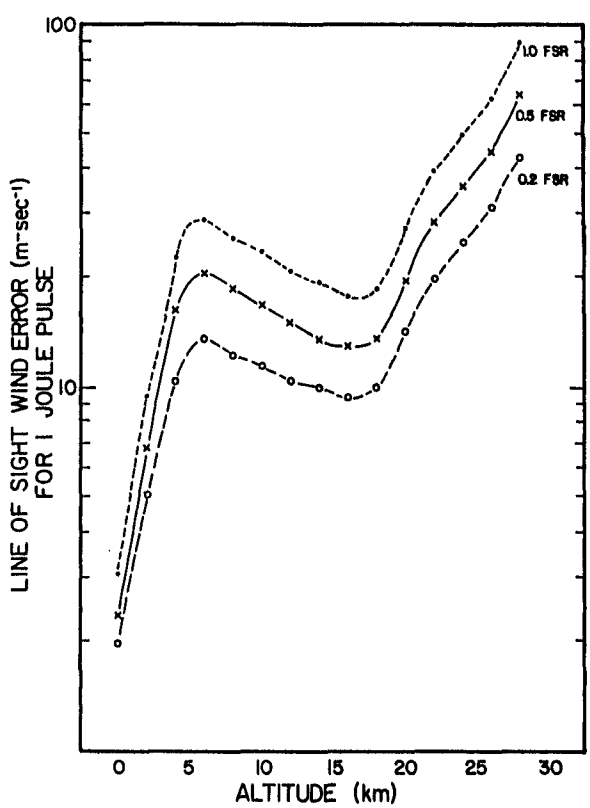

Figure 2.

These simulations indicate that the lidar performance required to satisfy the meteorological objectives outlined in Table 1 would be marginally met by a 1 watt laser. In order to fully meet these requirements a laser with a power output of approximately 10 watts is necessary. Measurements with a 1 watt laser, however, would still be very valuable since they would provide the wind at the top of clouds and in the lower troposphere with the required accuracy and resolution.

Conclusion

We have analyzed the performance of a 0.5μ doppler lidar with incoherent Fabry-Perot detection. A technique for the optimization of the system in terms of the statistical uncertainty in measuring the line of sight wind has been presented.

The result of this optimization is a class of high resolution Fabry-Perot interferometers which operate at very high order, that is, have long spacer gaps.

Near optimum systems have been discussed and evaluated to illustrate the variations which can be developed from an engineering point of view.

The optimum systems that are identified in the analysis are shown to provide global measurements which meet meteorological requirements in the lower troposphere for a 1 watt laser.

References

Abreu, V.J., Wind measurements from an orbital platform using a lidar system with incoherent detection: an analysis, Appl. Opt., 18, 2992, 1979.

Benedetti-Michelangeli, G., F. Congeduti and G. Fiocco, Measurement of aerosol motion and wind velocity in the lower troposphere by doppler optical lidar, J. Atmos. Sci., 29, 906, 1972.

Hays, P.B. and R.G. Roble, A technique for recovering doppler line profiles from Fabry-Perot interferometer fringes of very low intensity, Appl. Opt., 10, 193, 1971.

Hays, P.B., T.L. Killeen and B.C. Kennedy, The Fabry-Perot interferometer on Dynamics Explorer, Space Sci. Inst., 5, 395, 1981.

Acknowledgment

*Unpublished report "Shuttle Atmospheric Lidar Research Program" (NASA SP-433) has been used as reference for the material in this section. We would like to thank RCA Corporation for supporting this research.

OBSERVING SYSTEM SIMULATION EXPERIMENTS RELATED TO SPACE-BORNE LIDAR WIND PROFILING. PART I: FORECAST IMPACTS OF HIGHLY IDEALIZED OBSERVING SYSTEMS

M. Halem[1] and R. Dlouhy[2]

Space Data and Computation Division
NASA/Goddard Space Flight Center
Greenbelt, MD 20771

ABSTRACT

Simulation experiments are performed to determine the relative accuracy of inferred atmospheric states for an idealized LIDAR wind profiling system and then compared with idealized temperature and pressure sounding systems. The experiments are carried out for three distinct representations of the 'true' atmosphere to assess the validity of the interpretation of the results. Three fields used in this study are obtained respectively from: (i) a long general circulation integration of the GLAS 4th Order Model (4° lat x 5° lon x 9 levels), (ii) a continuous sequence of real NMC operational analysis and, (iii) a simulated long integration from the ECMWF high resolution (1.875° lat x 1.875° lon x 15 layers) operational forecast model. These fields are interpolated to the grid resolution of the GLAS model and used to simulate the observed global analysed fields of winds, temperature, moisture and surface pressure. The same interpolated fields are also used for verification of forecast impact. The effects of clouds, aerosol concentrations, and instrument accuracies on the simulated observation are discussed in Part II.

The experiments compare first, the inferred 12 h forecast fields made from an assimilation of complete, instantaneous, global fields of the primary variables, i.e., wind, temperature, and surface pressure, respectively. A subsequent series of experiments compares composite systems of the above basic variables, i.e., wind and surface pressure, temperature and surface pressure.

Results show that the LIDAR wind fields can infer most meteorological fields in the extratropics signficantly more accurately than can be inferred from temperature or pressure observing systems. The results obtained are consistent for all three "nature" fields. The 12 h forecast errors in the extratropics from wind data alone are almost as accurate as that obtained from the complete specification of all initial conditions. In tropical latitudes, only the LIDAR wind system showed the capability of inferring useful 12 h forecast winds. The experiments indicate that the accuracy of inferred states from temperature data are greatly enhanced by the addition of surface pressure data more so than are the wind data fields. The derived fields for temperatue and surface pressure are still considerably less accurate than those of an idealized LIDAR wind system alone. A by-product of these simulation studies is a measure of sensitivity to the 'nature' assumption. The identical twin experiments using the GLAS model and the GLAS 'nature' provide the most optimistic performance estimates, while the results from real NMC data and ECMWF model integration 'natures' are much more similar to each other than to the identical twin.

1. INTRODUCTION

Extended-range numerical weather prediction requires, at initial forecast times, complete global and accurate 3-dimensional fields of temperature, moisture and winds as a function of pressure throughout the troposphere, lower stratosphere and at the earth's surface. By supplementing land-based observing systems with space-borne meteorological observing systems, reasonably accurate complete, global fields of temperature analysis are currently available. The accuracies of the space-borne temperature sounders are still limited by their vertical resolution and to some extent by cloud effects. Vertical profiles of wind fields are generally available over large land masses from rawinsondes, but depend mainly on cloud-track winds from geostationary satellites to provide coverage over vast oceanic regions. The cloud-wind distributions turn out to yield essentially single level fields and moreover occur only where there are sufficient clouds (Halem et al., 1981). Like the winds, moisture fields are available over land masses from remote sensors, but only total column water vapor is currently derived with reasonable accuracies. Thus, our global observing system is still severely deficient for purposes of NWP, especially with respect to winds and moisture.

---

[1] Work formerly initiated at Laboratory for Atmospheric Sciences, NASA/GSFC.

[2] M/A COM Sigma Data Corp., NASA/GSFC.

In recent years, however, new technology has appeared which offers the potential of global space-borne systems with the accuracy of land-based radiosondes. In particular, substantial technical progress has been made in the development of coherent active CO_2 LIDAR systems (Hardesty, 1983; Pace and Lacombe, 1978), which measure the doppler shift in the backscatter from aerosols. From these measurements, it has been shown that one can infer wind motions with accuracies and vertical resolution of a rawinsonde (Hall et al., 1983). Studies have been carried out by Huffaker (1978, 1980), Lockheed (1981) and RCA (1983), indicating the feasibility of free flying space shuttle launched LIDAR wind profiling system known as WINDSAT. In addition to overcoming the significant technological problems involved in the design of instruments that have to work at the limits of quantum theory, substantial progress has been made in the signal processing and computer algorithm developments needed for the extraction of the wind information (Lawrence, 1983).

At the same time, there has been significant progress in obtaining higher vertical resolution from advanced temperature soundings through higher spectral resolutions in the wings of specific spectral lines (Kaplan et al., 1977; Reuter and Susskind, 1984). In addition, recent developments in the use of incoherent LIDAR systems (Korb et al., 1983), indicate the feasibility of obtaining pressure as a function of height with presumably very high vertical resolution and accuracy.

Since placing a LIDAR system in a space-borne operational environment will involve enormous expenditures by the national funding agencies, a compelling scientific justification on the relevant importance of wind profile data with respect to enhanced sounder system capabilities will be required before management makes such an investment. Surprisingly, there have been very few observing system studies on the effect of complete wind data relative to other systems. Many of the early simulation studies by Jastrow and Halem (1970, 1973) and Kasahara et al. (1972) were concerned mainly with the impact of sounding temperature profiles or single level wind data on forecasts. There were a number of studies on the design of the GARP Global Observing System concerned with the importance of data systems in the tropics. One such important study by Gordon et al. (1974) showed that when complete vertical wind profiles in the tropical band 10°N to 10°S are added to a global temperature sounding system, the inferred extratropical wind accuracies are improved. More recently, theoretical and statistical studies carried out by Daly (1980) and Phillips (1983) indicate that winds should greatly enhance the inferred atmospheric states in the extratropics as well. However, simulation studies with a more realistic account of atmospheric processes and structures are still required to quantify the relative performance of such systems, especially in terms of forecast improvements.

In Section 2 we present an overview of the methodology we used in performing the simulation experiments and in Section 3 we present the results from these experiments. The experiments are divided into two classes. We first study the relative performance of a primary variable to infer other primary variables, and second the effect of composite systems of variables. In Section 4, we summarize the results. In a subsequent paper in this volume, we investigate the sensitivity of the observed data by introducing some simplified atmospheric and instrumental influences.

2. GENERAL DESCRIPTION OF OBSERVING SYSTEMS SIMULATION EXPERIMENTS

The objective we have in performing these simulation experiments is to assess the effect of a particular observing system, in the context of contributing to an operational analysis. The experiments proceed in three steps. First, one attempts to assimilate a particular observing system configuration and determine its level of performance or accuracy. This requires a data set from which one can simulate observations of any degree of accuracy and a data set which can be used to statistically validate the simulated analysis. For this purpose, one can use a long simulated computer integration from a general circulation model containing detailed physical parameterizations of most of the important atmospheric processes. We customarily refer to the continuous sequence of model generated fields as 'nature'. Since the model outputs are complete in terms of all variables, any proposed observing system (with arbitrary coverage, frequency and error structure) can be derived from this 'nature' data set. For more realism, one could interpolate the model outputs to the proposed locations of an actual observing system with appropriate noise and error statistics added to conform to instrument and flight specifications.

Second, one has to convert the simulated data taken at the points of observation into a gridded field by a process called objective analysis. Thus, in addition to the 'nature' assumption, the role of the the analysis system itself is also a critical element of the assimilation. Employing an analysis system requires both a forecast model to provide first guess estimates of all simulated data at their points of observation, and the application of an appropriate objective analysis system of which there are several in operational use, (Bergman, 1979), (Lorenc, 1981), (Baker, 1983). In practice, this is very often carried out using the same GCM model for assimilations and for forecasting.

Third, one determines the improvements possible for numerical weather prediction by assessing the forecast sensitivity of the new observing systems. This is done by making forecasts from the respective analysis with and without the observing system in question and then verifying the forecasts against 'nature'. However, the most critical assumption that pervades all three elements of this study and perhaps the weakest link arguing against the realism of such simulation experiments rests on what we use as 'nature,' since it provides both the expected data and the validation.

For the purposes of this study, we have attempted to minimize these aspects of the of the problem by making simplifying assumptions and dealing only with a highly idealized observing system. We will assume that we have somehow produced a global instantaneous gridded analysis of any given meteorological field which is perfect. This is done by merely taking the field in question from the 'nature' and replacing the evolving analysis by that entire field. For example, if we are studying wind observing systems, we might replace both wind components in the assimilation cycle every 12 hours by the wind components from 'nature'. However, since we have circuited the analysis cycle by using the 'nature' field directly and plan to assess the inferred fields in terms of forecasts, this creates a dual influence of the 'nature'. In earlier experiments, it has been shown by Williamson (1973) that using the identical model to produce the 'nature' and the forecast leads to highly model dependent results.

Recognizing the serious limitations of the 'nature' assumption, we have conducted simulation experiments employing three distinct representations of 'nature' to avoid the dependence of the results on our 'nature' assumption. The three 'nature' sets are produced from long integrations made with the GLAS 4th Order General Circulation Model (Kalnay et al., 1980), the ECMWF model (Bengtsson, 1982), respectively, and a continuous sequence of real operational analysis produced by the National Meteorological Center. The respective 12 hr forecasts and analyses were kindly provided to the authors for use in this study by Drs. E. Kalnay and L. Bengtsson. The real data analysis consists of National Meteorological Operational analysis and were obtained from the National Climate Center, Asheville, North Carolina.

The simulation experiments are carried out by integrating the GLAS 4th Order GCM in all three cases for 30 days, continuously updating one or more meteorological fields every 12 hrs by the appropriate data set from 'nature.' This may involve an interpolation to the same grid as the GLAS model. The initial conditions at the start of the GLAS and ECMWF data assimilation cycle are taken from the respective 'nature' data set 30 days in advance[1]. The NMC data assimilation starts from the GLAS initial conditions. The impact of these data is presented in terms of the 12 hr rms forecast fields verified against the respective 'nature.' Figures 1a, b and c show the initial conditions of sea level pressure for the three types of 'nature' experiments. Figures 2a, b, and c show the corresponding verification fields from 'nature.' The initial

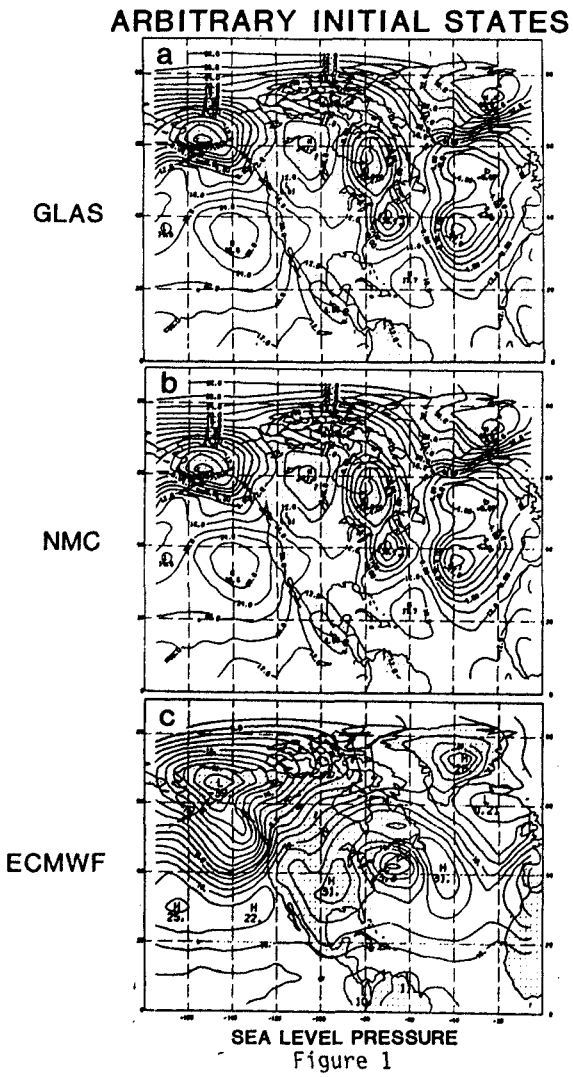

Figure 1

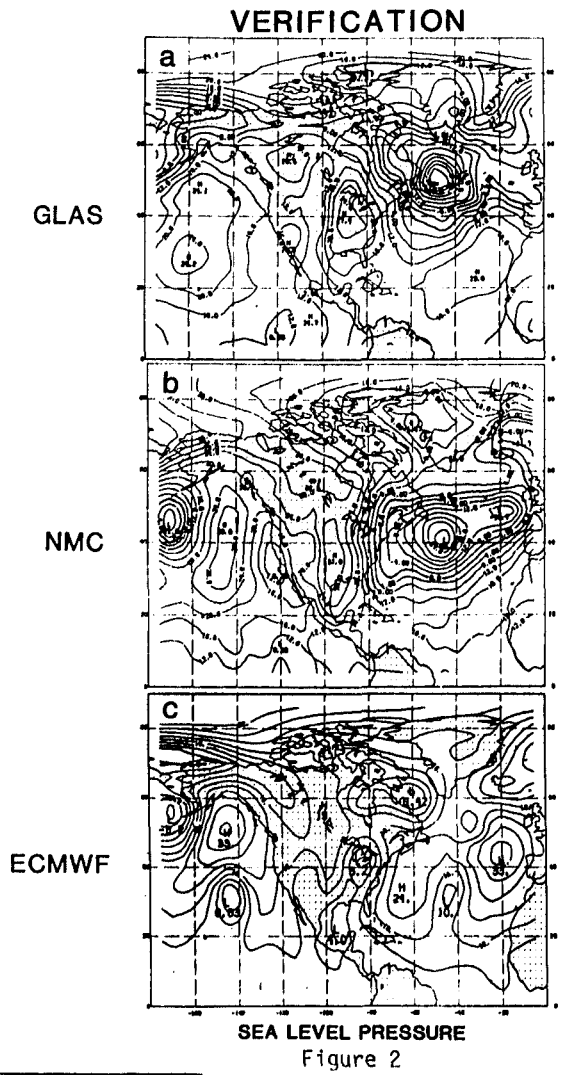

Figure 2

[1] For ECMWF only 20 days are available.

conditions are clearly seen to be relatively uncorrelated with 'nature' for the three experiments. Similar differences occur for the other variables.

3a. SIMULATION STUDY RESULTS: PRIMARY VARIABLES

Two sets of experiments are analyzed in this section. The first set of experiments are intended to study and quantify the relative forecast impact of analyses inferred from the basic meteorological fields of temperature, pressure and winds alone. The second set of experiments investigate results of composite systems and their relative forecast impact.

GLAS 'nature'. We first present results of experiments where the data are taken from the GLAS model 'nature' described earlier. Figures 3a, b, and c compare the rms 12 hr forecast errors for the synoptic assimilation of complete fields of temperature, wind and pressure data, separately. We verify the forecast rms errors for three derived fields of sea level pressure, 500 mb geopotential heights and 400 mb zonal winds, respectively. These fields were chosen to assess the ability of a single field to infer not only its own field but the other primary atmospheric states. In the upper panel of each figure, we plotted the rms errors along a typical extratropical latitude, at 50°N, every 12 hours, and in the lower panel along a tropical latitude, 2°N. For all three verification fields, the assimilation of sea level pressure data alone has only a slight effect in reducing the initial randomly correlated rms error fields in the extratropics. For example, the mean asymptotic 12 hr forecast error level of sea level pressure is reduced from 16 mb to 10 mb, 500 mb geopotential heights from 200 m to 140 m, and 400 mb zonal winds from 16 m/s to perhaps 14 m/s. The temperature data does significantly better, reducing the initial rms errors by more than 50% for all of these fields. The wind data, however, virtually eliminates the 12 hour forecast errors in all the verification fields. Moreover, the wind data has a very rapid adjustment period of less than a week to reach its asymptotic error levels, while temperature data requires several weeks. The results for these experiments in the tropics again show that pressure makes no reduction in the initial rms errors. Temperature data also shows very little influence on inferring 500 mb heights and wind data in the tropics, but does show some skill for inferring surface pressure fields. The assimilation of wind data in the tropics, however, improves the forecast of wind fields substantially, and has about the same influences as temperature data on the forecast error in 500 mb geopotential and surface pressure fields.

NMC 'nature'. Figures 4a, b and c again compare the rms 12 hr forecast impact errors of the same fields as before but for temperature and wind fields taken from the real data 'nature'. Pressure data in these experiments had no effect and is not shown on the charts. Instead, we have added a curve as a reference level which shows the 12 hour forecast of the GLAS 4th Order Model made from the full FGGE data analysis cycle as reported in (Halem et al., 1981). In the extratropics, the insertion

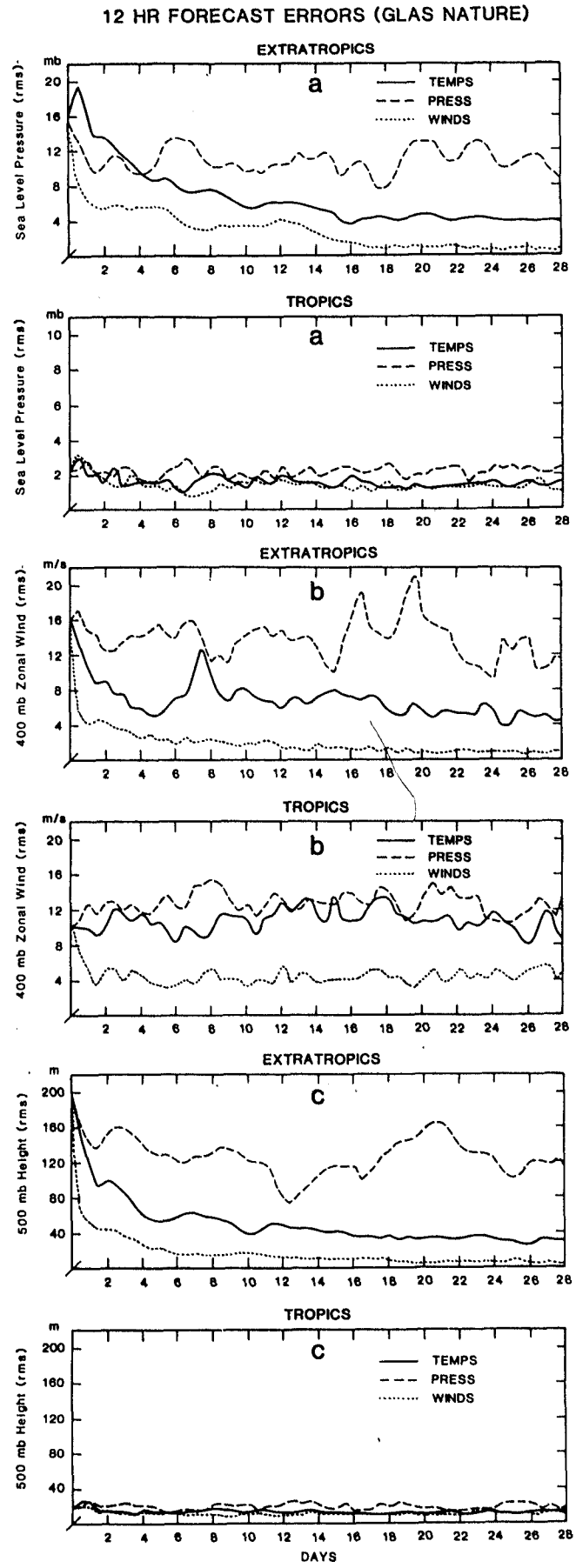

Figure 3

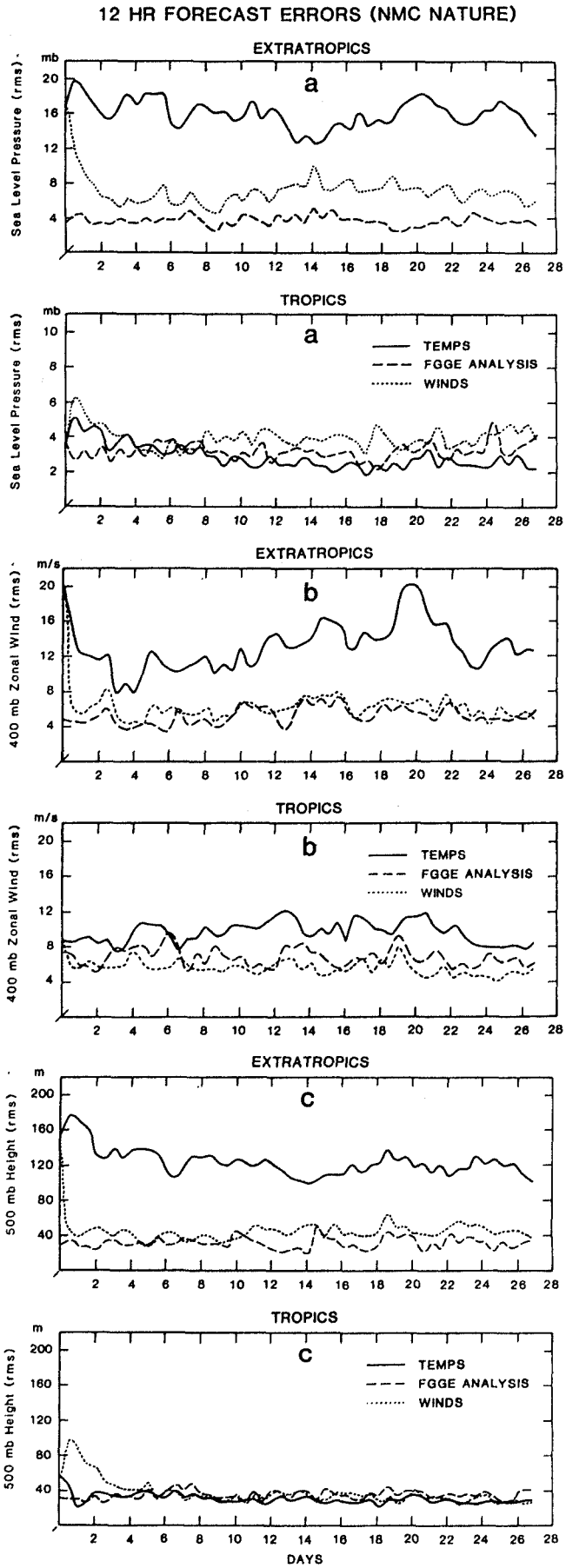

Figure 4

of temperature data shows only slight improvements in the 12 hr forecast relative to the arbitrary initial fields. For wind data alone, the 12 hr forecast 500 mb geopotential heights and zonal winds are almost as good as those obtained using the full FGGE analysis system. There is, however, about a 2-4 mb degradation in the 12 hr surface pressure forecast from the wind data alone. As before, the adjustment process of the inferred fields from wind data seems to occur in about 4 days.

In the tropics, the results are mixed and require some interpretation. For the sea level pressure 12 hr forecasts, the temperature data alone have an rms 1 to 2 mb more accurate than the FGGE reference level and wind data forecasts, respectively. The situation is reversed for the 12 hour forecast zonal wind fields where wind forecasts are 2 to 4 m/s more accurate than forecasts from FGGE and temperature data. No apparent trends are observable in the 500 mb height forecasts. A possible explanation of these results may be related to the fact that the integrated column density of the NMC height data is obtained from relatively accurate sounding systems whereas the wind data from geostationary cloud winds may have systematic errors inconsistent with the thermal fields. In comparing the accuracies of the 400 mb winds, we may be validating against a data set with the same bias thereby enhancing the wind simulation since FGGE winds have been influenced by other wind data not included in the NMC fields.

ECMWF 'nature'. In this experiment, we again show in Figures 5a, b, and c the rms 12 hour forecast impact errors of the same fields, but now we use the ECMWF 'nature' field. The rms forecast sea level asymptotic pressure error for temperature data in the extratropics is about 12-13 mb compared to 4 mb for wind data insertion. This is very similar to the results with real data. The similarity also holds for the 500 mb height fields except that the asymptotic error levels for wind data are substantially better than those with the full FGGE data. The inferred 400 mb zonal winds for the temperature data is now substantially improved to about 9 m/s while the wind data is about the same as with real data. This indicates that the consistent accurate global temperature fields can reduce the 12 hr forecast wind errors.

The results in the tropics for the ECMWF 'nature' experiment are more consistent with the idealized twin simulation experiment than obtained with the real NMC data. The two fields are comparable in the 12 hr forecast errors for sea level pressure wind 500 mb geopotential heights but wind data forecasts have half the rms zonal wind error than that from temperature data in the tropics.

3b. SIMULATION STUDY RESULTS: COMPOSITE SYSTEMS

In the following series of experiments we couple surface pressure fields with both wind and temperature data since pressure data is readily available over most of the globe from land-based stations and ship reports.

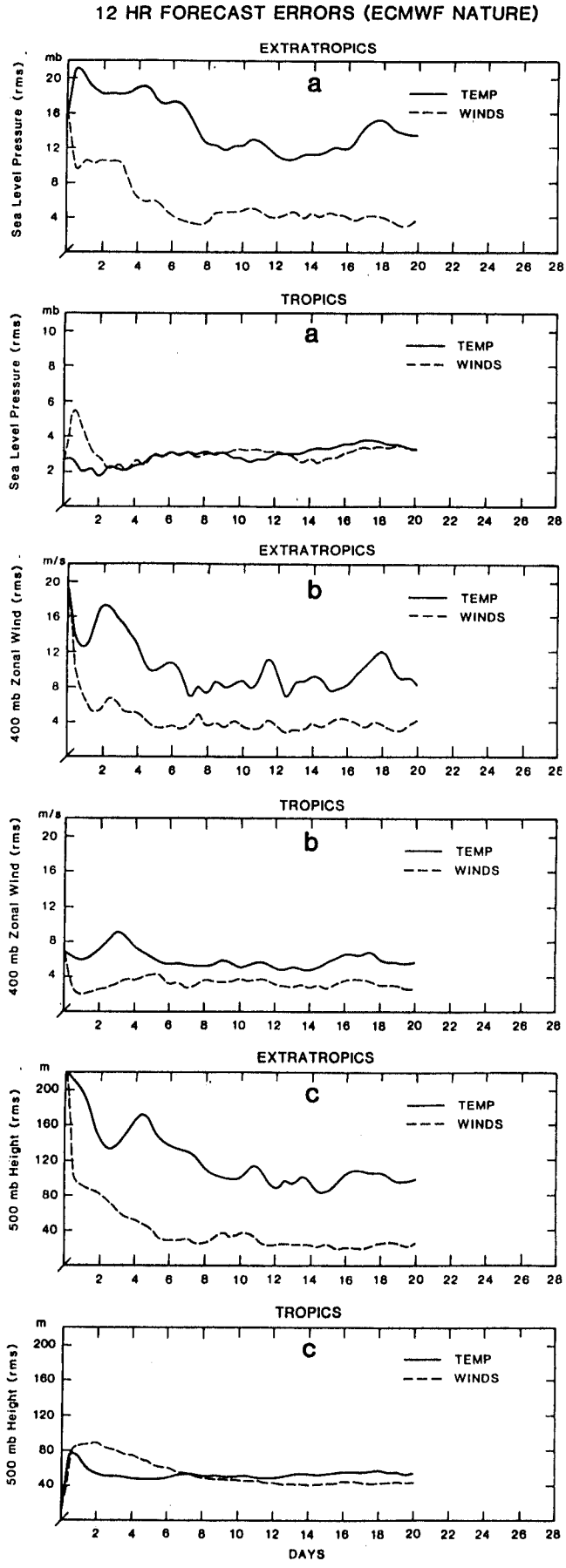

Figure 5

GLAS 'nature'. Figures 6a, b, and c compare the 12 hour forecast errors of temperature and pressure with wind and pressure data for the same basic three validation fields. The 'nature' data set for these figures is from the GLAS model. These experiments show that the composite temperature data has reduced the sea level forecast errors to 2 mb, 500 mb heights to 20 m, and zonal winds to about 3 m/s, almost 40% less than the errors obtained without the pressure data. The composite wind system had similar asymptotic errors as those without pressure. In the tropics, the use of composite systems had the same asymptotic error levels as the systems without pressure data.

NMC 'nature'. Figures 7a, b, and c show the composite system with the NMC 'nature' data set. In these experiments, we observe major reductions in forecast errors for real data composite systems relative to the earlier individual real data systems. For example, the sea level pressure asymptotic levels are 8 mb compared with 16 mb for the previous temperature only experiment, 80 m compared with 120 m for 500 mb geopotential heights and 10 m/s compared with 12 m/s. The height and wind forecast errors were about the same for the composite wind system but the sea level forecast errors were reduced in half to about 4 mb. In the tropics, the results are relatively unaffected by the addition of surface pressure for both composite systems.

ECMWF 'nature'. Figures 8a, b, and c compare the composite system for the third 'nature' data set, namely, the fraternal ECMWF model. In the extratropics, the asymptotic composite temperature system forecast error levels for sea level pressure, 500 mb heights and zonal winds are 4 mb, 40 m, and 6 m/s, respectively. These error levels are half again what the real data error levels were for the composite system and reduced the errors to more than half that of the same fraternal experiment without pressure data. In addition, the error levels are comparable to that of the wind only system for the fraternal experiment. In the tropics, the errors are also significantly reduced with the composite temperature system for sea level pressure and geopotential heights but slightly for zonal winds. Yet, the zonal wind errors at 500 mb are only 4-5 m/s compared to 2-3 m/s for the wind data system. In both cases, they are significantly better than those obtained for the real data composite systems.

4. SUMMARY

The general conclusions from the experiments using primary variables are that (i) wind data alone has a greater impact than temperature data alone for inferring the other state variables, (ii) that similar results are obtained for all three 'nature' experiments and are probably not model dependent, (iii) that atmospheric states adjust to wind data in extratropics as well as tropics, and (iv) that the adjustment times to wind data are much more rapid than to temperature data. The results of the composite system of temperature and pressure show significant improvements over those of temperature only.

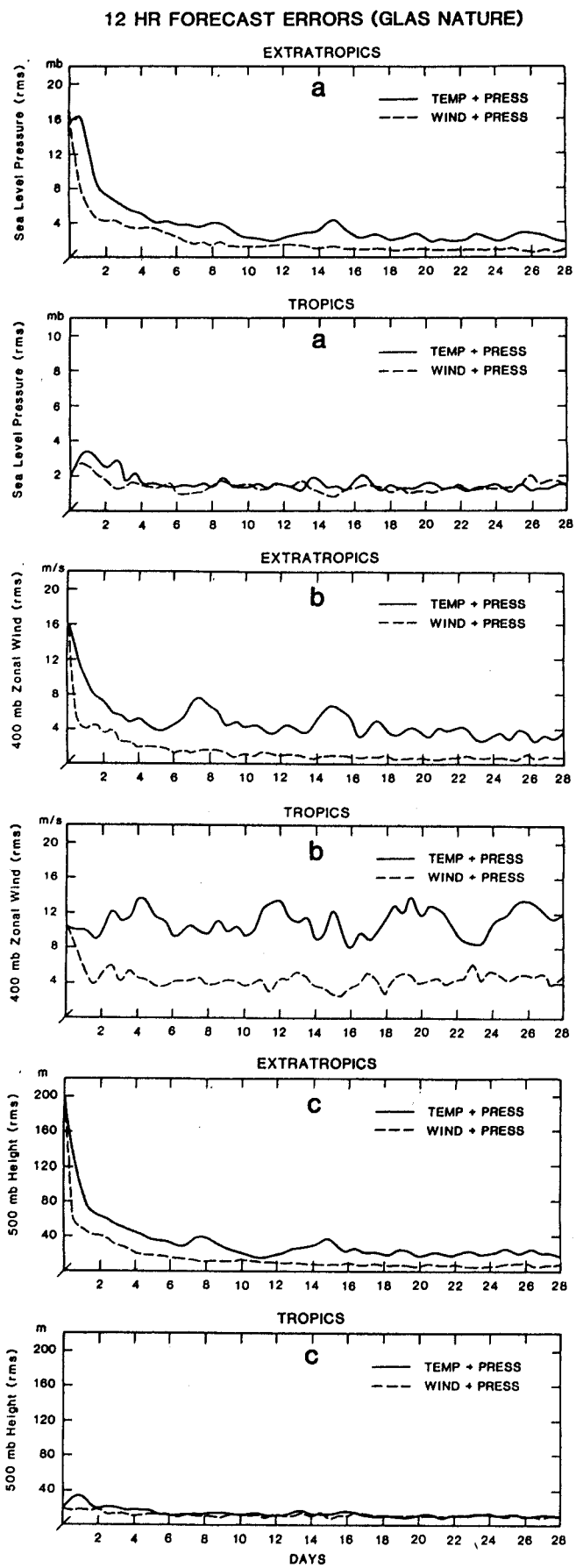

Figure 6

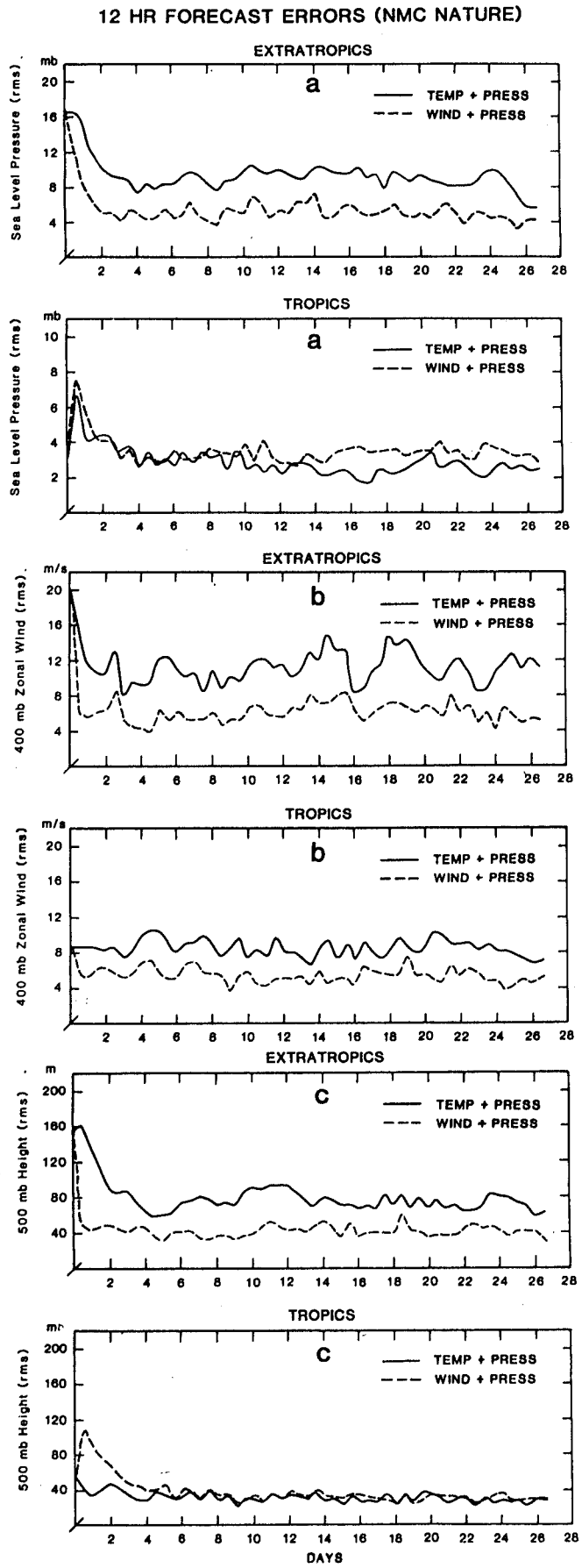

Figure 7

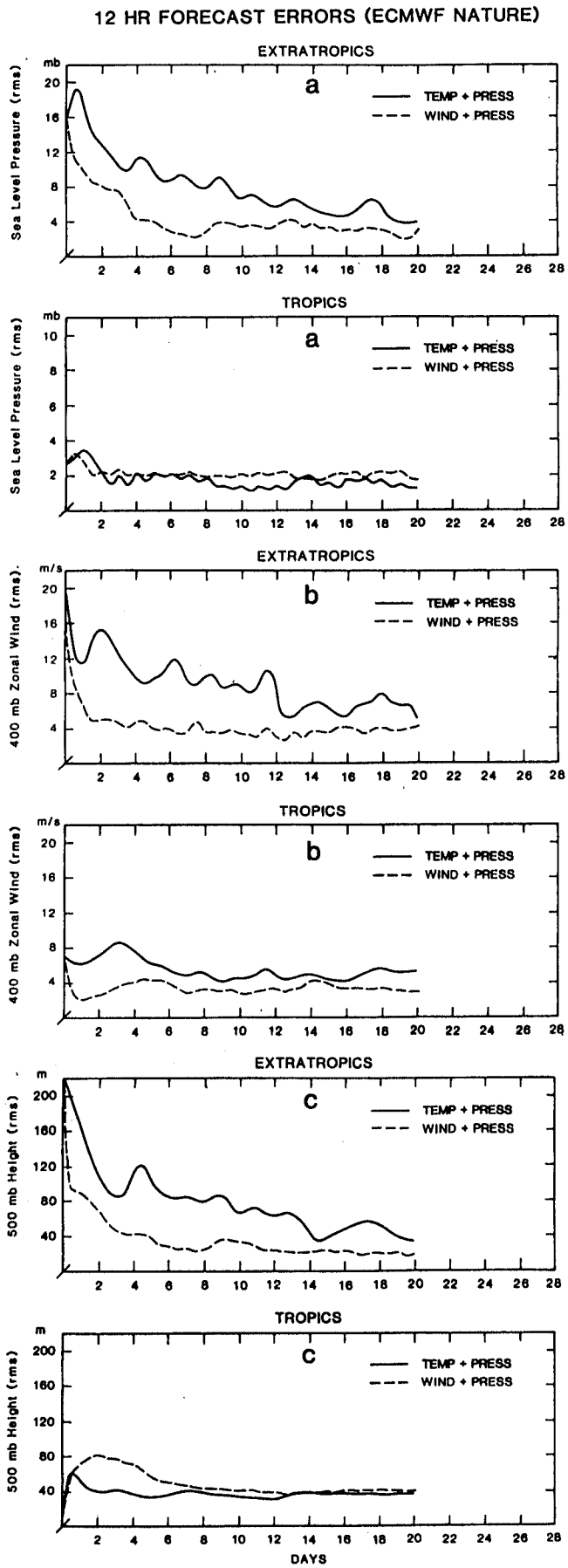

Figure 8

They also indicate that a composite wind system is neither helped nor hurt by the addition of surface pressure data. However, the most striking conclusions of the ECMWF results are that the composite system of temperature and pressure differs from the NMC results in that they provide useful inferred fields only slghtly poorer than the wind system in the extratropics and tropics as well. Thus, the importance of determining which of the three systems is most credible is a paramount issue in deciding the importance of committing major funding programs for the development of the LIDAR Windsat system.

REFERENCES

Baker, W. E., 1983: Objective analysis and assimilation of observational data from FGGE. Mon. Wea. Rev., 111, 328-342.

Bengtsson, L., M. Kanamitsu, P. Kallberg and S. Uppsala, 1982: FGGE 4-dimensional data assimilation at ECMWF. Bull. Amer. Meteor Soc., 69, 29-43.

Bergman, K. H., 1979: Multivariate analysis of temperatures and winds using optimum interpolation. Mon. Wea. Rev., 107, 1423-1443.

Daly, R., 1980: On the optimal specification o the initial state for deterministic forecasting. Mon. Wea. Rev., 108, 1719-1735.

Gordon, C., L. Umschied, and K. Miyakoda, 1972: Simulation experiments for determining win data requirements in the tropics. J. Atmos. Sci., 29, 1064-1075.

Halem, M., E. Kalnay-Rivas, W. Baker, and R. Atlas, 1981: An assessment of the state of the atmosphere as inferred from the FGG satellite observing systems during SOP-1. Bull. Amer. Meteor. Soc., 63, 407-426.

Hall, Jr., F. F., R. M. Huffaker, R. M. Hardest M. E. Jackson, T. R. Lawrence, M. J. Post, R. A. Richter, and B. F. Weber, 1983: Proceedings of 2nd Topical Meeting on Coherent Laser Radar: Technology and Applications, August 1-4, Aspen, Colorado.

Hardesty, R. M., R. W. Lee, and D. L. Davis, 1983: Real-time processes and display of coherent LIDAR returns. Proceedings of 2nd Topical Meeting on Coherent Laser Radar: Technology and Applications, August 1-4, Aspen, Colorado.

Huffaker, R. M., 1978: Feasibility study of satellite-borne LIDAR global wind monitoring system. NOAA Tech. Memo. ERL WPL-37.

Huffaker, R. M., 1978: Feasibility study of satellite-borne LIDAR global wind monitoring system: Part II. NOAA Tech. Memo. ERL WPL-63.

Jastrow, R., and M. Halem, 1970: Simulation studies related to GARP. Bull. Amer. Meteor. Soc., 51, 490-513.

Jastrow, R., and M. Halem, 1973: Simulation studies and the design of the first GARP global experiment. Bull. Amer. Meteor. Soc., 54, 13-21.

Kalnay-Rivas, E., and D. Hoitsma, 1979: Documentation of the Fourth Order Rand Model. NASA Tech. Memo. 80608.

Kaplan, L. D., M. T. Chahine, J. Susskind, and J. F. Searl, 1977: Spectral band passes for a high precision satellite sounder. Appl. Opt., 16, 322-325.

Kasahara, A., and D. Williamson, 1972: Evaluations of tropical wind and reference pressure measurements: numerical experiments for observing systems. Tellus, 24, 100-115.

Korb, C. L., and C. Y. Weng, 1983: Differential absorption LIDAR technique for measurement of the atmospheric pressure profile. Appl. Opt., 22, 3759-3770.

Lawrence, T. R., R. M. Hardesty, M. J. Post, R. A. Richter, R. M. Huffaker, F. F. Hall, Jr., 1983: Performance characteristics of the NOAA pulsed doppler LIDAR and its application to atmospheric measurements. 5th Symposium on Meteorological Observations and Instrumentation, April 11-15, Toronto, Canada.

Lockheed Missile and Space Co., 1981: Global Wind Measuring Satellite System--Windsat. Report NOAA Contract H MA 79RS600127.

Lorenc, A. C., 1981: A global three-dimensional multi-variate statistical interpolation scheme. Mon. Wea. Rev., 109, 701-721.

NOAA, 1983: Doppler Lidar-Rasinsonde Wind Comparisons. Technical Report.

Pace, D. W., and M. LaCombe, 1978: A sealed high pulsed rate TEA CO_2 laser. IEEE, J. Quantum Elect., QE-14, 263.

Phillips, N., 1983: An accuracy goal for a comprehensive satellite wind measuring system. Mon. Wea. Rev., 111, 237-239.

RCA, Astro-Electronics, 1983: Feasibility Study of a Windsat Free Flyer. U.S. Dept. of Commerce, NOAA, Contract NA82RAL00141.

Reuter, D., and J. Susskind, 1984: Comparison of AMSU temperature soundings with those produced by HIRS and AMTS. NASA Tech. Memo. 86053, pp. 28-32.

Williamson, D., 1973: The effect of forecast error accumulation on four-dimensional data assimilation. J. Atmos. Sci., 30, 537-543.

OBSERVING SYSTEM SIMULATION EXPERIMENTS RELATED TO SPACE-BORNE LIDAR WIND PROFILING. PART 2: SENSITIVITY TO ATMOSPHERIC AND INSTRUMENTAL INFLUENCES

R. Dlouhy and M. Halem[1]

M/A COM Sigma Data, Corp.
Laboratory for Atmospheric Sciences
NASA/Goddard Space Flight Center
Greenbelt, MD 20771

ABSTRACT

Three major potential sources of errors that influence the performance of the proposed LIDAR wind profiling systems are distributions and concentrations of aerosols, available power for pulsing the LIDAR and the effects of clouds and large-scale precipitations. Idealized simulation studies are performed to study their sensitivity. Two experiments are performed in which we assign random error levels of 3 m/s and 6 m/s to simulate the potential effects of errors corresponding to 2 pulses or 10 pulses per grid area. These results are then compared with the idealized LIDAR wind profile accuracies obtained in the experiments described earlier in Halem and Dlouhy, Part 1. Results from a second set of experiments introducing wind profiles only down to cloud top are also presented. The third experiment studied assumes sufficient global aerosol concentrations only in the lower troposphere and shows the resultant impact on forecast accuracy.

1. INTRODUCTION

The experience gained with space observing systems has taught us that instrument performance is greatly influenced by a wide variety of factors from atmospheric effects, space launch environment, to ground-based algorithm design. Moreover, the sensitivity to such influences varies from instrument to instrument, depending on the state of technology and real data experience. In the case of LIDAR winds, there are 3 major characteristics that are intrinsic to the system which could greatly limit the performance.

First, the coherent CO_2 laser system proposed by NOAA/ERL for the WINDSAT requires distributions of 10 μ size aerosol concentrations throughout the atmsophere to determine the doppler shifted backscatter signal. It is generally agreed that while there are probably sufficient aerosol concentrations in the lower troposphere and in the stratosphere, there may be insufficient concentrations at high latitudes and in the mid-tropospheres over oceans. Simulation experiments are presented assuming inadequate signal return for complete global wind determinations in these regions.

Second, atmospheric influences such as clouds and precipitation affect the LIDAR system's ability to obtain complete vertical wind profiles. In this study, we report on experiments in which the complete wind profiles are only available in model generated cloud-free regions down to model cloud tops.

Third, a major constraint on system performance is the available power required for the expected operational lifetime duration of a LIDAR space-borne system. The number of pulses which can be used to sample a 300 km square area gives radial velocities per model grid and is directly related to the expected errors of mean wind speed.

For this paper, we were able to conduct a number of simulation experiments again employing two of the three 'nature' experiments (GLAS and ECMWF) described in Halem and Dlouhy (1984), referred to hereafter as HD1. However, to simulate the potential sources of error, various observational assumptions are made either with regard to the distribution of the data or the quality of the data sets assimilated by the model. Section 2 describes the simulation experiments and assumptions made. In Section 3 we analyze the results separately for the different 'nature' experiments and summarize the results in Section 4.

2. DESCRIPTION OF EXPERIMENTS

The question of paramount concern in consideration of a LIDAR wind system is the distribution in space and time of the appropriate aerosol concentrations. Since time dependent accurate estimates of 10 μ aerosol distributions are not available, we made a number of gross assumptions. The initial experiment presented here assumes that aerosols of 10 μ size are always abundant up to 800 mb and that above the boundary layer are not present. Subsequent experiments assuming aerosols extending throughout the atmosphere but with much reduced concentrations in the mid to upper troposphere but

[1] Space Data and Computation Division, NASA/GSFC.

with sufficient density in the stratosphere are being carried out but will not be described in this report.

The approach we have taken to simulate the effect of clouds and precipitation of LIDAR wind profiling is to assume intense precipitation wherever model clouds are produced and that clouds are produced wherever there is upward vertical motion. We further assume that the effect of these clouds is to prevent wind profiles below the uppermost clouds over the entire grid element area. Further experiments using model simulated clouds and fractional cloud cover based on statistical cloud coverage frequencies are planned.

We also conducted a set of experiments in which we assumed that the accuracy of the profiles is a function of the LIDAR pulsing frequency. In these experiments we assumed the aerosol concentrations uniformly distributed everywhere so that the instrumental error is random and has the same absolutel value in all directions and at all atmospheric levels. Two error levels are studied, one with random wind component errors of 3 m/s and one with 6 m/s. While there is no firm basis for making these assumptions, the lower error limits correspond to prescribed GARP data requirements. By doubling those error levels, we obtain a crude range of degradation sensitivity that at least provides some information on system performance. The methodology for conducting these simulation studies is the same as that described in HD1.

3. RESULTS

We examine the effects of simulating several sources of LIDAR wind error for two different representations of 'nature', GLAS and ECMWF. They are compared with similar results obtained for perfect LIDAR wind experiments presented in HD1.

GLAS 'nature'. The dashed curve in Figures 1a, b, and c shows the effect of adding a 3 m/s random error to each wind component with perfect wind data for the GLAS 'nature.' The experiment thus far has only been carried out for 19 days. There seems to be virtually no deterioration in the 12 hour forecast errors for sea level pressure and 500 mb geopotential heights in the tropics and extratropics. However, the 12 hour forecast winds at 400 mb show a 1 m/s degradation globally. Also indicated in the same figure is a curve showing the effect of simulated cloud and precipitation that prevents the penetration of LIDAR signals. The asymptotic effect of these clouds on sea level pressure increases the 12 hour rms forecast errors from 1 mb to 4 mb in the extratropics and less than 1 mb in the tropics. In the extratropics there is a similar degradation of about 15 m in the 12 hour forecast 500 mb heights and 2 m/s in the 400 mb winds. However, in the tropics where convective clouds penetrate to high levels in the atmosphere in winter and summer, we see the 12 hr forecast error doubling to nearly 8 m/s. Distributions of mean cloud cover under the hypothesis are being obtained for presentation

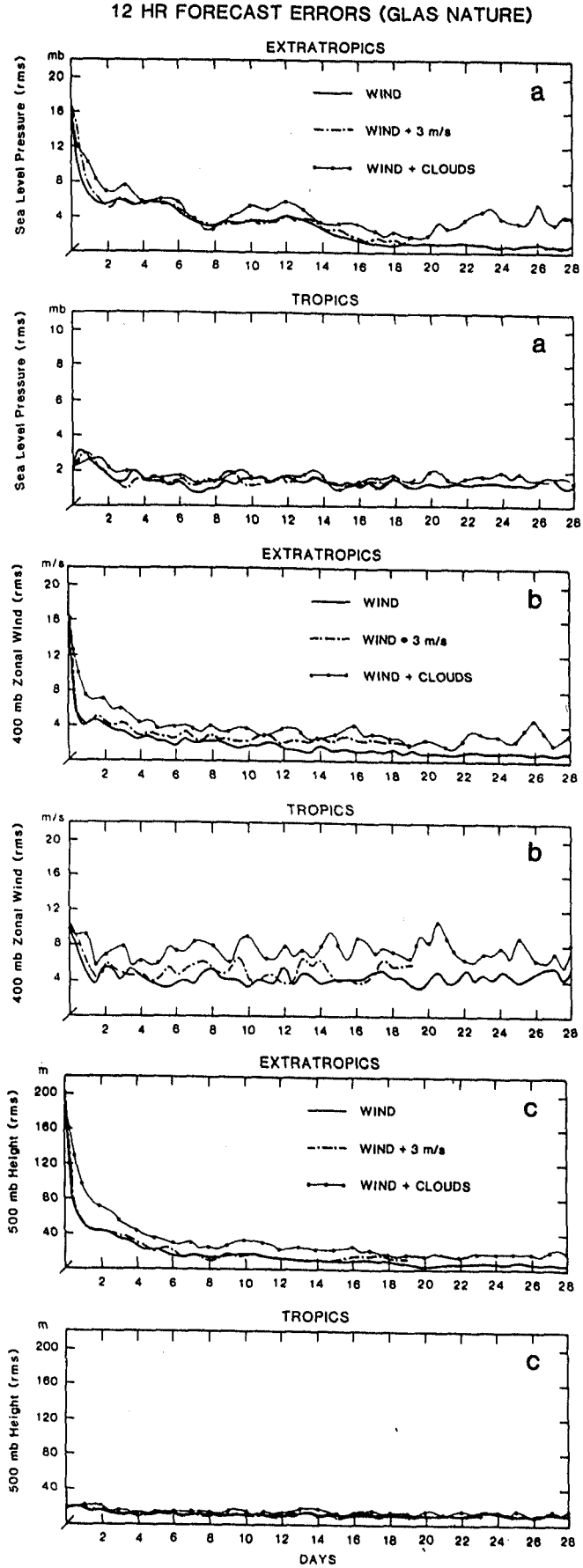

Figure 1

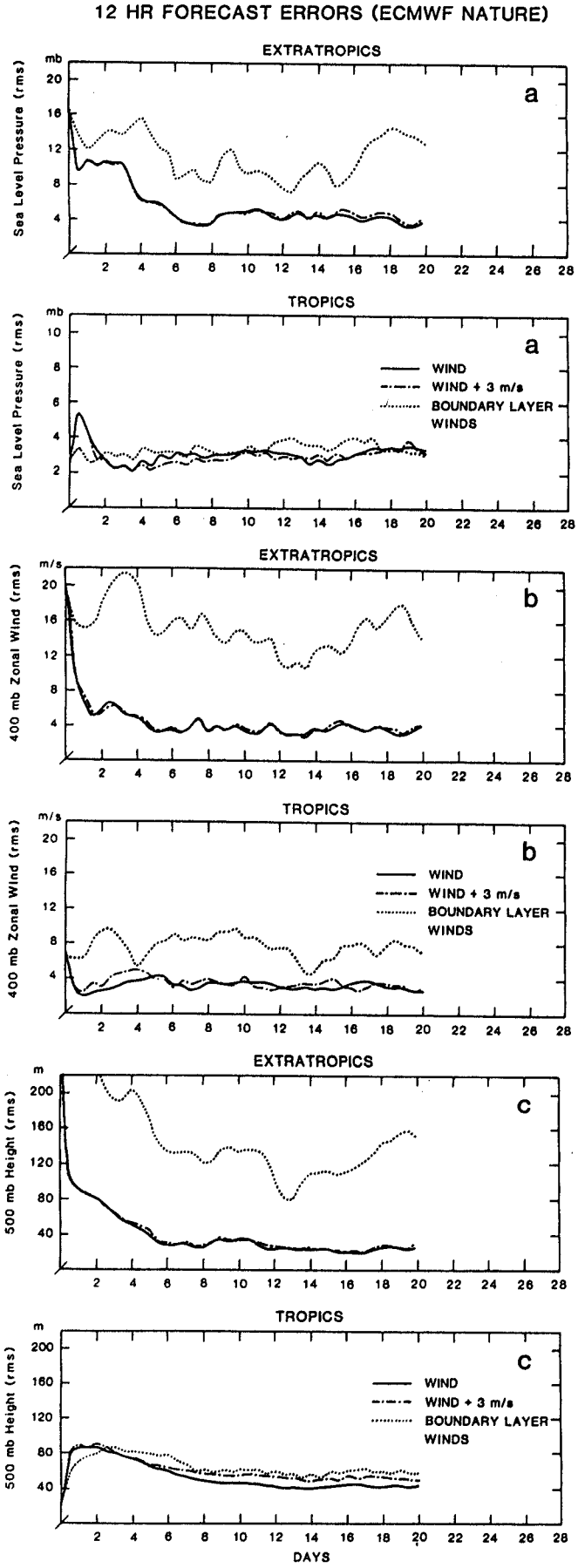

Figure 2

at the conference. Additional experiments are also planned to study the effects of insufficient aerosol concentrations in the mid- to upper troposphere.

ECMWF 'nature'. The curves in Figures 2a, b, and c show the asymptotic error levels of inferred states for the two experiments described in Section 2, concentration of aerosols only in the boundary layer and boundary global winds with random 3 m/s errors compared with perfect winds alone. It was not possible for this paper to complete a cloud experiment with ECMWF data similar to the one previously reported.

As with the GLAS experiment, the random wind errors produce negligible effects in the 12 hr forecast sea level pressure and the 500 mb geopotential globally. In contrast with the GLAS results there is also little effect in the 400 mb zonal winds producing 12 hr zonal wind forecast errors of about 4 m/s. These results suggest that random wind errors of these magnitudes are as good as perfect winds. A further experiment with double wind errors of 6 m/s is planned.

It has been suggested that there are probably adequate 10 μ aerosol concentrations globally at all times in the boundary layer but the situation in the upper troposphere is more uncertain. The remaining curve in Figure 2 shows that there is virtually no forecast skill globally if wind profiles are only available from the surface up to 800 mb. Thus, global measurements of aerosol distributions in time and space are essential to resolve the potential impact of inadequate concentrations on LIDAR wind sensing systems. More detailed studies are planned to incorporate tracer simulation of aerosol distribution.

REFERENCE

Halem, M., and R. Dlouhy, 1984: Observing system simulation experiments related to spaceborne LIDAR wind profiling. Part I: Forecast impacts of highly idealized observing systems. Preprint Volume: Conference on Satellite Meteorology/Remote Sensing and Applications of the American Meteorological Society, June 25-29, Clearwater Beach, FL.

SIMULATION STUDIES OF THE IMPACT OF ADVANCED OBSERVING SYSTEMS ON NUMERICAL WEATHER PREDICTION

R. Atlas, E. Kalnay, J. Susskind, D. Reuter, W. E. Baker, and M. Halem

Laboratory for Atmospheric Sciences
NASA/Goddard Space Flight Center
Greenbelt, MD 20771

1. INTRODUCTION

A series of realistic simulation studies is being conducted as a cooperative effort between the European Centre for Medium Range Weather Forecasts (ECMWF), the National Meteorological Center (NMC), and the Goddard Laboratory for Atmospheric Sciences (GLAS), to provide a quantitative assessment of the potential impact of proposed observing systems on large scale numerical weather prediction. A special objective of this project is to avoid the unrealistic character of earlier simulation studies. Following a brief review of previous simulation studies and real data impact tests, the methodology for the current simulation system will be described. Results from an assessment of the realism of the simulation system and of the potential impact of advanced observing systems on numerical weather prediction will be presented at the conference.

2. EARLY SIMULATION STUDIES

Since the advent of meteorological satellites in the 1960s, a considerable research effort has been directed toward the design of space-borne meteorological sensors, the development of optimal methods for the utilization of satellite soundings and winds in global-scale models, and an assessment of the influence of existing satellite data and the potential influence of future satellite data on numerical weather prediction. Observing system simulation experiments have played an important role in this research and in the planning of Data Systems Tests (DST) and the First GARP Global Experiment (FGGE). Such studies have aided in the design of the global observing system, the testing of different methods of assimilating satellite data, and in assessing the potential impact of satellite data on weather forecasting.

The earliest simulation studies proceeded according to the following sequence of steps: First, an artificial history of the atmosphere is created by numerical integration of a model. Second, simulated "data" are created from the history by addition of random variations to the history values for temperature, wind, and pressure. Third, the numerical integration that created the history is repeated, but with the meteorological variables in the model replaced by the simulated data at locations and times corresponding to the assumed pattern of observations.

For example, if the observing subsystem under study is designed to produce wind data, the winds in the history are replaced by simulated wind "data" at locations, heights, and times corresponding to the coverage expected from the observing system. If the study is directed at the performance of an observing subsystem design to yield temperature or pressure information, the temperature or pressure values in the history are replaced by the respective simulatd "data" in a similar fashion.

If the data had no errors, and therefore were identical with the history values, and was inserted at all grid points, the new integration would be identical with the history. However, when errors are present, the inserted data perturb the computed circulation, causing it to depart from the history. The difference between the history and the perturbed circulation resulting from the data insertion is a measure of the effect of the errors in the simulated data. The effect of the errors usually is expressed in terms of differences of the meteorological variables such as wind components, averaged over all points of the computing grid. These differences are considered to represent the errors in the determination of the global atmospheric states, resulting from the assumed errors in the observing system.

In order to simulate different types of data and data coverage and assess their impact on forecasting skill, a somewhat different approach has been utilized (Cane et al., 1981). In this procedure a forecast model is integrated for a long period, such as one or two months. This long run is then assumed to be "nature." "Observations" are then extracted from the nature run, following a suitable geographical and temporal distribution, and random "observational" errors are added. These simulated observations are then assimilated with an analysis cycle, and the same model is used as a "forecast model" from the analyzed fields.

Simulation studies conducted by Charney et al. (1969), Halem and Jastrow (1970), Jastrow and Halem (1970, 1973), Williamson and Kasahara (1971), Kasahara (1972), Gordon et al. (1972), and others indicated that all three of the primary meteorological variables--wind, pressure, and temperature--could be determined if a continuous time history of any one of these variables were inserted into a general circulation model. In addition, these studies provided an analysis of the GARP data requirements, the "useful" range of predictability, the need for reference level data, and the relative usefulness of asynoptic versus synoptic measurements and analysis. From the results, it was concluded that the assimilation of satellite-derived temperature profiles meeting the GARP data specifications should yield a substantial improvement to the accuracy of numerical weather forecasts.

An examination of the underlying rationale for the simulation studies as previously conducted (Jastrow and Halem, 1973), as well as a comparison of the results of the above studies with the results of subsequent real data impact tests indicates several important limitations. The most important weakness stems from the fact that the same numerical model has been used both to generate the simulated observations and to test the effectiveness of these observations. Other weaknesses relate to the model-dependence of the studies and the specification of observational errors as random.

3. REAL DATA IMPACT TESTS

In recent real data impact studies, most of the qualitative conclusions of the preceeding observing system simulation experiments have been confirmed, although in some respects the results appear to be overly optimistic. In particular, it was clear from estimates of the quality of satellite temperature soundings and cloud-track wind data obtained during the NASA Data Systems Test (DST), (Desmarais et al., 1978) that the accuracies of the FGGE satellite observing systems would be considerably poorer than were needed to infer wind profiles of the accuracy specified in the GARP data requirements. Moreover, as a result of these DST studies, expectations that the FGGE observing system would significantly improve the forecast skill and range of useful predictability also were questionable. For example, a forecast impact test by Ghil et al. (1979) with a coarse resolution second-order model showed only a modest beneficial impact of the DST-6 satellite sounding data, while a similar study by Tracton et al. (1980) revealed a slight negative impact for DST-5 and a slight positive impact for DST-6, both of which were meteorologically insignificant.

More recently, however, when the same DST-6 temperature-sounding impact test was repeated with a more accurate forecast model employing higher resolution, Atlas (1979, 1982) and Atlas et al. (1979, 1982) showed that the DST data were in certain cases capable of making modifications to the analyzed atmospheric states that produce meteorologically significant improvements in the 72 h forecasts over North America. Also, the first FGGE case studies reported by Bengtsson (1981a,b) with the ECMWF model, indicated improvements in short- and extended-range forecasts with the FGGE data. Similarly, Gustaffson (1979), employing the Swedish operational forecast/analysis system (i.e., a 300 km, quasi-geostrophic model), showed periods during the first Special Observing Period (SOP-1) in which the satellite information had a positive impact on the objective analysis which also resulted in improved numerical forecasts.

These results are supported by our recent investigation of the FGGE satellite observing system for the SOP-1 period (Halem et al., 1982). Utilizing the GLAS Fourth Order Global Atmospheric Model, an extensive series of data assimilation/forecast impact experiments have been conducted. These experiments show that although the GARP data accuracy requirements for the satellite observing systems were not met, assimilation of FGGE satellite data is capable of providing a reasonable determination of the complete atmospheric state. In general, a small improvement to forecast skill in the Northern Hemisphere and a larger improvement in the Southern Hemisphere results from the assimilation of sattellite soundings and cloud-track winds.

4. REMAINING PROBLEMS AND THE PRESENT STUDY

The results of the real data impact studies indicate that major deficiencies in the global observing system still exist and that the FGGE satellite sounders are far from optimal. Advanced passive infrared and microwave sounders and active scatterometer and lidar sounders in a variety of combinations have recently been proposed to improve the accuracy of satellite observations and extend the useful range of numerical weather prediction. Realistic observing system simulation experiments are required to determine which of the proposed instruments will provide the greatest improvements as well as the optimal design of the future global observing system.

As indicated before, previous simulation studies have been characterized by the use of the same model to simulate "nature" and observations and to produce forecasts. This "identical twin" problem may distort the conclusions derived from such studies, as discussed in the following section.

In the present study, we attempt to avoid these limitations by designing a more realistic simulation system and calibrating its results by comparison with real data experiments performed with a similar system, and by accurately simulating the expected accuracy and characteristics of observational systems. The simulation system will then be used to study the potential impact of advanced passive sounders and lidar temperature, pressure, humidity, and wind observing systems.

5. DESIGN OF THE SIMULATION SYSTEM

The analysis/forecast simulation system consists of four elements: 1) An atmospheric model integration to provide a complete record of the "true" state of the atmosphere (called nature). This record is then used to fabricate observational reports and to evaluate analyses and forecasts. 2) A conventional data assimilation cycle that is used as the "control experiment." The control experiment is like an operational forecast-analysis cycle based on conventional observations, except that it makes use of fabricated conventional data obtained from the nature run to produce the analyzed fields. 3) A satellite data assimilation that differs from the control in also including fabricated satellite data incorporated in an intermittent or time-continuous manner, in the forecast-analysis cycle. 4) Forecasts produced from both control and satellite initial conditions. Comparison of these forecasts with nature provides an assessment of the impact of satellite data.

Two important considerations are involved in the design of the control assimilation run: the nature of the initial conditions, and the forecast model used. In reality, short-range forecasts have errors stemming from three different sources: 1) inaccuracy of the initial state; 2) model errors that can be ascribed to numerical truncation (horizontal and vertical truncation errors due to insufficient resolution); and 3) model errors that can be ascribed to the "physics" of the model. The latter include parameterization of subgrid processes like radiation, cumulus convection, and friction, as well as sources of external forcing, like orography, sea/land contrast, and even the use of an artificial rigid top boundary condition, common to all numerical models. Numerical and "physical" deficiencies introduce systematic errors in the model integrations which are most evident in the differences between model and observed climatological averages. A striking example of these climatological errors is apparent in the stationary, forced planetary waves. Even though these large scale waves are numerically well resolved, they are not well simulated by numerical models. In a numerical forecast, a model tends to drift towards its own climatology, so that serious errors in the stationary waves are apparent after even a short time. For realistic simulation studies, all three sources of errors should be simulated. In previous simulation experiments, the same model was used to produce the "true" state and "forecasts." Therefore, the errors in the forecasts were due only to errors in the initial conditions. This method ("identical twin experiment") has the apparent advantage that it isolates the effect of initial data errors and avoids both numerical and "physical" errors. On the other hand, it has a very important shortcoming: since the model and "nature" have the same climatology, the accuracy of the simulated forecasts may be far superior to the accuracy of real forecasts. As a result, the external error growth due to the fact that current models are only approximations of the atmosphere is not present in the "identical twin" experiments. This has the effect of increasing the skill of conventional forecasts at low levels of data coverage, because the perfect forecast model is able to "fill up" data gaps. Consequently, at low levels of data, the impact of an observing system is overestimated, whereas the impact of high levels of data, such as provided by satellites can be underestimated. In addition, if the "nature" and "forecast" models are not realistic enough, i.e., don't possess a realistic model climatology, the data impact may be distorted. For example, a forecast model that cannot simulate the "roaring forties" regime in the Southern Hemisphere will not be helped by better low level winds in the Southern Hemisphere. The forecast model used should be sufficiently accurate that error growth should be dominated by initial data errors rather than by model dominated errors such as truncation errors. Otherwise, the experiment may overestimate the skill of the forecast and underestimate the influence of the data on the analysis.

Finally, if simulation studies are to provide an accurate indication of how simulated data will influence forecasts in the real world, it is crucial that their error characteristics be realistic. For simulated observational errors to be representative of real observational errors they should be introduced at actual observing locations and should not be just white noise. Random errors with a standard deviation of the order of GARP errors saturate the spectrum at high frequencies and their effect is mostly averaged out. Bias and horizontal and vertical correlations of errors with each other and with the synoptic situation should be introduced appropriately.

In the current simulation studies, we will attempt to minimize difficulties of earlier studies discussed previously. In order to avoid the "identical twin" character of previous studies, the high resolution (1.875° x 1.875° x 15 levels) ECMWF model will be used as nature, and the 4° x 5° x 9 levels GLAS model for assimilation and forecasting. Special care will be taken to simulate realistically observational errors.

6. SIMULATION OF OBSERVATIONS OF SPACE-BASED SOUNDING SYSTEMS

In this study, we will be simulating forecast impacts using the current passive HIRS2/MSU sounding system as well as other passive systems using the Advanced AMTS and AMSU infra-red and microwave sounders alone and in various combinations. In addition, we will simulate active lidar systems which measure pressure profile, temperature profile, and winds. The location and times of the passive soundings will be identical to those produced operationally in November 1979. In the case of the operational HIRS2/MSU sounding system, one could simulate atmospheric soundings in a manner analogous to those of the conventional observing system by using actual statistics relating accuracies of retrieved atmospheric soundings with colocated radiosonde reports. This approach has two

important drawbacks. First, this procedure cannot be used with future sounders, for which we have no error statistics. Secondly, and much more significantly, the errors of temperature profiles retrieved from passive sounders are not random, but are highly correlated in the horizontal and vertical and are dependent on the nature of the synoptic situation, including the interrelationship between atmospheric temperature-humidity profile, ground temperature, and cloud fields.

To simulate atmospheric temperatures determined from passive sounders, we therefore take the more fundamental approach of first simulating radiance observations seen by the satellite and then retrieving temperature profiles from the observations. The simulations are performed using the radiative transfer model described in Susskind et al. (1983) and temperature retrievals as in Susskind et al. (1984). In order to simulate radiances for the channels for a given observation, one needs the surface pressure, atmospheric temperature-humidity-ozone profile, the ground temperature and emissivity as a function of frequency, and the multi-layer cloud field together with the spectral properties of the clouds. In addition, one needs the viewing angle of the satellite and location of the sun. In order to simulate a sounding reported at a given time and location, the atmospheric temperature-humidity profile is taken from the "nature" run, as obtained from ECMWF, interpolated in space and time to the satellite coordinates. The surface pressure is obtained using interpolated sea level pressure values, again given by "nature," and topographical fields. The fields obtained from ECMWF did not contain information about ozone, ground temperature and emissivity, and clouds however. Of these, ozone is the least significant and was fixed as a function of latitude according to climatological values. The ground temperatures and surface emissivities were simulated according to reasonable values determined from analysis of HIRS2/MSU data for November 1979 as in Susskind et al. (1984).

In the case of ground-temperature, we generated fields of T_G-T_A, that is ground temperature minus surface air temperature, and examined their mean and standard deviation over a 2°x2° grid for the month. Ground temperatures for a given location were then defined as $T_G = T_A + \overline{T_G - T_A} + \delta$ where T_A is the interpolated surface air temperature as above, $\overline{T_G - T_A}$ is the mean ground-surface air temperature difference for the location as determined from real HIRS2/MSU data for the month, and δ is a random component consistent with the observed standard deviation. Surface emissivity, ε, at 50.3 GHz, which is an important factor affecting MSU and AMSU observations, was determined in an analogous manner, using mean and standard deviation values of ε determined for November 1979 from the real HIRS2/MSU data. It was interesting to note, looking at these maps, that the standard deviations of ε were in general small, except for those areas where the ice edge was changing during the month or in regions of variable snow cover. Surface emissivity for the infra-red channels was taken as fixed as described in Susskind et al. (1983).

Perhaps the single most important factor affecting the observations and accuracy of passive retrievals is clouds. In order to get the proper spatial correlations of errors as a function of synoptic situation, the cloud fields must be very realistically related to the synoptic situation. We used the relative humidity fields, r_j, to produce up to four levels of broken clouds at each sounding location, with pressures at 850 mb, 700 mb, 500 mb, and 300 mb. The cloud fraction α_j at a given level j, is simulated according to

$$\alpha_j = \frac{r_j - r_{cj}}{1 - r_{cj}}$$

where r_{cj} is a pressure dependent relative humidity cutoff value whose values were provided by NMC.

The radiances for channel i observed by the satellite are computed as

$$R_i = \sum \alpha_j^* R_{ij} + (1-\sum\alpha_j^*) R_{i,CLR}$$

where R_{ij} is the radiance which would be observed in channel i if the field of view were completely covered by clouds at level j. $R_{i,CLR}$ is the radiance which would be observed if there were no clouds, and α_j^* is the fraction of the sky covered by clouds at layer j as seen from above. Clearly, while α_j can be as large as 1, $\sum\alpha_j^*$ can only be between 0 and 1. To insure this, we assume the clouds in each layer are totally correlated in space and fix $\alpha_j^* = \alpha_j - \sum_k \alpha_k^*$ for layer j where α_k^* represents all layers above j, but constrain α_j^* to be no less than zero. In other words, α_j^* equals zero if α_j is less than the cloudiness above, and α_j^* is the difference between α_j and the largest cloudiness above otherwise. All cloud radiances are simulated assuming the clouds are opaque at infra-red frequencies and transparent at microwave frequencies.

The GLAS retrieval method uses two field of view to perform a cloud correction to be used on the observed infrared radiances. In the simulation of radiances, observations in two fields of view were simulated for each sounding. The radiances are simulated assuming only the cloud fractions α_j^* differ in the two fields of view. For a given level, $\alpha_{j,1}^*$ and $\alpha_{j,2}^*$, corresponding to cloud fractions in both fields of view, were simulated from α_j^* in the following way. At α_j = 0 or 100, both cloud fractions are set at 0 to 100. Otherwise $\alpha_{j,1}^*$ is less than α_j^*, varying linearly between the following points (0, 0), (20, 10), (90, 60) and (100, 100), and $\alpha_{j,2}^*$ is greater than α_j^* varying linearly between the points (0,0), (20,30) and (100,100). This allows for reasonable discrimination between the cloud fraction and radiances in both fields of view. In analysis of actual data, this discrimination, which is necessary for performing the cloud correction, is obtained by separating and then averaging observations in the warmest and coldest individual spots in an area.

As in the analysis of real HIRS2/MSU data, soundings are rejected if the radiances indicate too much cloudiness in the field of view (typically more than 70% in a sounding area) or if no atmospheric solution can be found from which computed radiances match the cloud corrected radiances to within 1°K. AMTS and AMSU observations and retrieved temperatures are produced in an analogous way.

In the case of active sounders, the errors obtained from analysis of the data are more nearly random and uncorrelated with each other. Therefore, the approach of generating random uncorrelated errors will be used in simulating retrieved quantities. To begin with, the coverage of sounding data will be taken as in the passive sounders for comparison purposes. Later, more realitic scan patterns for the active sounders will be used. Studies will be made as a function of assumed noise level and scan pattern. In all cases, signal to noise values will be attenuated at given levels according to the effective cloud cover, α_j^*, as defined above.

ACKNOWLEDGEMENTS

The authors wish to acknowledge D. Edelmann, J. Pfaendtner, G. Avesian, A. Pursch, J. Terry, and D. Wallace for their contributions to this project, and D. Sabatino for typing the manuscript.

REFERENCES

Atlas, R., 1979: A comparison of GLAS SAT and NMC high resolution NOSAT forecasts from 19 and 11 February 1976. NASA Tech. Memo. 80591. Goddard Space Flight Center, Greenbelt, Maryland 20771, (NTIS N80-17638), 6 pp.

_____, 1982: The growth of prognostic differences between GLAS model forecasts from SAT and NOSAT initial conditions. Mon. Wea. Rev., 110, 877-882.

_____, M. Halem, M. Ghil, 1979: Subjective evaluation of the combined influence of satellite temperature sounding data and increased model resolution on numerical weather forecasting. Preprints Fourth Conf. on Numerical Weather Prediction, Silver Spring, Maryland, Amer. Meteor. Soc., 319-328.

_____, 1982: The effect of model resolution and satellite sounding data on GLAS model forecasts. Mon. Wea. Rev., 110, 662-682.

Bengtsson, L., 1981a: Numerical prediction of atmospheric blocking--a case study. Tellus, 33, 19-42.

Bengtsson, L., 1981b: The impact of FGGE on global medium range forecasts. Characteristics of atmospheric planetary circulations and associated model forecast skill during FGGE case studies selected by WGNE. Proceedings of the International Conference on Early Results of FGGE and Large-Scale Aspects of its Monsoon Experiments, Tallahassee, Florida, 12-17 January, 1981.

Cane, M. A., V. J. Cardone, M. Halem, and I. Halberstam, 1981: On the sensitivity of numerical weather prediction to remotely sensed marine surface wind data: A simulation study. J. Geophys. Res., 86, 8093-8106.

Charney, J., M. Halem, and R. Jastrow, 1969: Use of incomplete historical data to infer the present state of the atmosphere. J. Atmos. Sci., 26, 1160-1163.

Desmarais, A., S. Tracton, R. McPherson, R. Van Haaren, 1978: The NMC report on the Data Systems Test. (NASA Contract S-70252-AG), U.S. Dept. of Commerce, NOAA, NWS.

Ghil, M., M. Halem, R. Atlas, 1979: Time-continuous assimilation of remote-sounding data and its effect on weather forecasting. Mon. Wea. Rev., 107, 140-171.

Gordon, C. T., L. Umscheid, Jr., and K. Miyakoda, 1972: Simulation experiments for determining wind data requirements in the tropics. J. Atmos. Sci., 29, 1064-1075.

Gustaffson, N., 1979: Use of Data from Meteorological Satellites. The Impact of Satellite Information on Short-Range Numerical Forecasts. Lannior, France, 17-21 Sept., 1979 (ESA SP-143 Oct. 1979), 113-127.

Halem, M., M. Ghil, R. Atlas, J. Susskind, W. J. Quirk, 1978: The GISS sounding temperature impact test. NASA Tech. Memo. 78063, Goddard Space Flight Center, Greenbelt, Maryland 20771.

Jastrow, R., and M. Halem, 1970: Simulation studies related to GARP. Bull. Amer. Meteor. Soc., 51, 490-513.

Susskind, J., J. Rosenfield, and D. Reuter, 1983: An accurate radiative transfer model for use in the direct physical inversion of HIRS2 and MSU temperature sounding data. J. Geophys. Res., 88C, 8550-8568.

_____, and M. T. Chahine, 1984: Remote sensing of weather and climate parameters from HIRS2/MSU on TIROS-N. J. Geophys. Res., in press.

Yu, T. W., and R. D. McPherson, 1981: Global data assimilation experimentw with scatterometer winds from SEASAT-A. Preprints, Fifth Conf. on Numerical Weather Prediction, Nov. 2-6 1981, Monterey, CA, pp. 9-13.

METHOD FOR ESTIMATING ERRORS FOR RADIATION BUDGET BASED ON A SCANNING RADIOMETER

by

G. Louis Smith, Lee M. Avis, Richard N. Green, and Bruce A. Wielicki
Atmospheric Sciences Division, Langley Research Center, NASA

1. INTRODUCTION

The Earth Radiation Budget Experiment (ERBE) project will fly three sets of instruments; each set consists of a nonscanning package and a scanning radiometer. These will fly on the NOAA F and G operational satellites and on a dedicated spacecraft, the Earth Radiation Budget Satellite (ERBS). The NOAA spacecraft are in Sun-synchronous orbits with 99° inclination orbits, and thus provide global coverage. The ERBS will be in a 57° inclination orbit and will precess around the Earth to provide sampling of the diurnal cycle of regions between ± 57° latitude. The primary function of the scanning radiometer is to provide measurements for the calculation of the Earth-emitted and absorbed solar radiation at the top of the Earth-atmosphere system, averaged over 250 x 250 km regions. A further description of the project and its scientific objectives is given by Barkstrom and Hall (1982).

This paper will treat errors in these regional averages. Error sources include instrument noise and offsets, spectral variability of the scenes, modeling of directional and bidirectional functions according to scene, and scene misidentification. Also, there are sampling errors due to spatial variability over the Earth-atmosphere system, which enter the estimate of the regional average of the radiant exitance. These errors and their propagation through the data analysis algorithms will be studied.

2. DESCRIPTION OF PROBLEM

A scanning radiometer measures the upwelling radiance L from the scene toward the instrument, as shown in figure (1). This radiance varies with the direction, which is measured by the zenith angle θ of the exiting ray and, for the reflected solar radiation, the azimuth angle ϕ of the ray relative to the Sun and the zenith angle θ_0 of the Sun at the scene. A bidirectional function $R(\theta_0, \theta, \phi)$ is defined to relate the radiance to the radiant exitance M at the top of the Earth-atmosphere system (TOA):

$$L = 1/\pi \; RM \qquad (1)$$

This bidirectional function depends upon the scene, for example whether the scene is cloud, land, etc. In practice, the bidirectional function varies from one cloud scene to another, even for the same conditions of cloud height, type, etc., so that it must be represented by a bidirectional model. The function is not deterministic, but is definable only in a statistical sense. Bidirectional models have been developed e.g., by Taylor and Stowe (1984) and Stuhlmann et al. (1983), and typical models are shown in figure (2) for cloud. In order to select the proper bidirectional model for the interpretation of the data, it is necessary to identify the scene.

The instrument ideally provides the broadband radiance measurement in each of three channels. The spectral responses of the various channels of the instrument, however, are not perfectly flat, but are rather complicated functions of wavelength, as shown in figure (3). Thus, the net response of each channel does not provide a true measure of the broadband (integrated) radiance, but a convolution of the spectral radiance of the incoming radiation with the spectral response of the channel. The resulting error associated with the spectral variability of the incoming radiance can be reduced by identifying the scene type, and then using only those spectral radiances which are appropriate to that scene type, at the given viewing angles.

It is seen that scene identification is a key function in the accurate determination of radiant exitances at the top of the Earth's atmosphere. The data flow for analysis of Scanning radiometer data is set up as shown in figure (4). Using a "global" spectral correction, approximate broadband shortwave and longwave radiances at the spacecraft are computed. The scene is then identified, and an improved spectral correction determined for the final calculation of the radiances. Also, a bidirectional model based on this scene type is used to estimate the radiant exitance for the pixel, i.e. the field of view of a single measurement, by use of a rearrangement of equation (1):

$$M = \pi \; L/R \qquad (2)$$

The instantaneous regional average is then computed by averaging all estimates of radiant exitance for pixels that fell in the region. A pixel is considered to be in the region if the pixel center falls within the region. These regional averages are then averaged throughout the month to produce a monthly-averaged radiant exitance for the region.

Each step in this analysis procedure has errors associated with it. In this paper, these errors and the way in which they propagate through the analysis will be briefly considered.

2.1 Scene Identification Procedure

The scene identification procedure for ERBE first classifies the underlying surface by its geo-

graphic type (geotype): land, ocean, or snow, desert or land-ocean mix (coastal regions). The cloud cover is defined in terms of four classes: clear (less than 5% cloud cover), partly cloudy (between 5% and 50% cloud), mostly cloudy (between 50% and 95% cloud) and overcast (more than 95% cloudy). The cloud class for a given measurement pair (shortwave and longwave radiances) is selected according to the measurement pair in a manner similar to a threshold method, but modified to account for the variance associated with each class. This technique, called the Maximum Likelihood Estimate, is illustrated in figure (5). Given that the geotype is ocean, and that the class is known, the radiance in each channel varies with cloud cover, cloud type, other atmospheric variables (haze, aerosols), sea state, etc., which cause variations within the class. There is a distribution of measurement pairs within each class, as represented by the light lines. These distributions can be partially characterized by the means and variances of the shortwave and longwave channels and their correlation. The shortwave-longwave plane is partitioned into regions according to which is the most probable scene identification for the measurement pair. The boundaries of these regions are indicated by the heavy solid lines in figure (5). Thus, e.g. if a measurement pair falls within region I, it is identified as "clear ocean."

The selection of scene classes is based on a number of considerations. For example, a finer classification of cloud cover would be desirable. However, the scatter within each class is so great that the identification would render the refinement useless. Also, the amount of data which are available for the generation of the bidirectional models is limited. The Nimbus 7 ERB-scanning radiometer collected data for 19 months. However, when one attempts to develop bidirectional models, it is necessary to "bin" the data according to viewing zenith angle, solar-zenith angle, azimuth angle, latitude, and scene class. It was found, in practice that the number of data points in some of the bins is marginal for an accurate estimation of the mean for that bin. Thus, any further subdividing would result in increased errors in the means of the bidirectional models. The result is a choice of bin size which compromises between bin-discretization errors and bin-sample mean errors.

2.2 Spectral Correction

The spectrum of the incoming radiation affects the response of each channel to the incoming radiances. In accounting for the spectral response of the instrument, the errors incurred by inferring the longwave and shortwave radiances from the measurements can be reduced by using the scene information in this calculation, which is referred to as spectral correction. The technique used for ERBE is essentially a regression method, whereby three channels (longwave, shortwave, and total) are used to estimate the broadband longwave and shortwave radiances corrected for the imperfections of the instrument spectral response. The equation is

$$\begin{Bmatrix} L^{SW} \\ L^{UN} \end{Bmatrix} = C_i \begin{Bmatrix} m^{LN} \\ m^{SW} \\ m^{TOT} \end{Bmatrix} + \begin{Bmatrix} \varepsilon^{SW} \\ \varepsilon_L^{LW} \end{Bmatrix} \qquad (3)$$

where C_i is a matrix (in general 2x3) of regression coefficients for scene class i. The term ε_L is the residual error of the regression, due to scatter about the L-m relation and is because of variability of the spectra within the scene class. This error can be reduced only by restricting the scene class so as to reduce the variation of the spectra within the class. However, the narrowing of scene classes requires the identification of the scene, which becomes increasingly difficult and results in additional errors in scene identification.

For the purpose of identifying the scene, radiances are first estimated using a global-regression matrix C_i, in which the coefficients correspond to the entire Earth with no distinction between scene classes. After the scene is identified, the shortwave and longwave radiances are computed by applying equation (3) with the appropriate C_i for the scene type.

3. ERROR ANALYSIS

The error analysis for this problem differs from the usual error analysis, in that errors in scene identification result in discrete changes in the spectral correction and bidirectional functions, or branching in the computational flow. In addition, there are the usual considerations of term errors which can be treated in a linear manner. In order to analyze the errors, we consider first the effects of the scene identification errors, after which the effects of the other errors on the radiant exitance at TOA for each pixel will be included. Finally, the error in the regional-average radiant exitance is treated.

3.1 Scene Identification Probabilities

In order to compute the probable errors due to scene identification errors, it is necessary to compute the probability that a scene which is in truth type j is identified as type i. This probability will be denoted as P_{ij}, and is

$$P_{ij} = P_j \int_{R_i} P_j(x)\, dx \qquad (4)$$

where P_j is the probability of the occurrence of scene j, $P_j(x)$ is the normalized probability distribution of $x = (L^{SW}, L^{LW})$ for scene type j , and the integration is over the region which is defined by the scene identification algorithm as being scene type i. The statistical makeup of the field, i.e. the probability of occurrence of various scene classes, enters the analysis through P_j. The $P_j(x)$ can be approximated e.g. if the means, variances, and correlations of the shortwave and longwave measurements are known for each scene type, and the type of distribution is known or assumed, e.g., Gaussian. Also, one can compute the boundaries delineating the regions R_i, for use in the scene identification procedure.

The presence of instrument noise in the data will increase the probability of making errors in scene type. This is accounted for by treating x as the sum of two random processes: the scene radiance and the instrument noise vectors. Then the covariance matrix for x will be the sum of the covariance matrices for these two processes, and would be used for the computation of the P_{ij}.

3.2 Scene Identification Error Effects

As pointed out earlier, an error in scene identification causes errors in two areas of the data analysis: first, the wrong spectral correction matrix C_j is used, and second, the wrong bidirectional model R_j is used. In this section errors induced in the radiant exitance estimate M from the measurement will be derived.

If the scene is identified as type i, but is in truth type j, the shortwave and longwave-radiant exitances at TOA, expressed as components of a two-dimensional vector, are estimated as

$$\hat{\underline{M}}_{ij} = \pi Q_i C_i \underline{m} \tag{5}$$

where Q_i is a 2x2 diagonal matrix with $1/R_i$ on the diagonal for the shortwave or longwave component, respectively. The correct radiant exitance for scene type j would be

$$\hat{\underline{M}}_j = \pi Q_j C_j \underline{m} \tag{6}$$

Thus, due to scene-identification error, there is an error in the estimate of radiant exitances:

$$\varepsilon_{Mij} = \pi(Q_i C_i - Q_j C_j)\underline{m}$$

$$= \pi(Q_i - Q_j)C_i\underline{m} + \pi Q_j(C_i - C_j)\underline{m} \tag{7}$$

The first term is the error due to the selection of the wrong bidirectional function and the second term is the error due to the selection of the wrong spectral correction. The expected error, given that the scene was identified as type i, is

$$\varepsilon_{Mi} \simeq \pi\left[\sum_j P_{ij}(Q_i - Q_j)\right] C_i\bar{\underline{m}}_i + \pi\left[\sum_j P_{ij}Q_j(C_i - C_j)\right]\bar{\underline{m}}_i \tag{8}$$

where the approximation has been made that

$$P_j \int_{R_i} d\underline{x}\, P_j(x)\underline{m} = P_{ij}\bar{\underline{m}}_i \tag{9}$$

This error, if non-zero, represents a bias in the analysis of the data. The condition for an unbiased estimator is thus

$$\sum_j P_{ij}[(Q_i - Q_j)C_i + Q_j(C_i - C_j)]\bar{\underline{m}}_i = 0 \quad \text{for all } i \tag{10}$$

Assuming that the bias is zero, the covariance matrix of the errors due to scene identification error is calculated using equation (8) to be

$$\begin{aligned}\mathrm{cov}[\varepsilon_{Mi}(\text{scene})] \simeq{}& \pi^2 \sum_j P_{ij}(Q_i - Q_j) \\ &\times \left[\bar{\underline{L}}\bar{\underline{L}}^T + \mathrm{cov}(\underline{L})(Q_i - Q_j)\right] \\ &+ \pi^2 \sum_j P_{ij}Q_j(C_i - C_j)\left[\bar{\underline{m}}\bar{\underline{m}}^T + \mathrm{cov}(\underline{m})\right] \\ &\times (C_i^T - C_j^T)Q_j + \pi^2 \sum_{ij} (K_{ij} + K_{ij}^T)\end{aligned} \tag{11}$$

where

$$K_{ij} = Q_j(C_i - C_j)[\bar{\underline{m}}\bar{\underline{m}}^T + \mathrm{cov}(\underline{m})]C_i^T(Q_i - Q_j)$$

The approximation is made that

$$\int_{R_i} d\underline{x}P(x|x\varepsilon T_j)\underline{m}\underline{m}^T = P_{ij}[\bar{\underline{m}}\bar{\underline{m}}^T + \mathrm{cov}(\underline{m})] \tag{12}$$

which is similar to the approximation of equation (9). The first term on the right-hand side of equation (11) is the error variance due to bidirectional modeling error and the second term is error variance due to spectral-modeling error, both as results of scene-identification error. The third and fourth terms are coupling terms between these two effects.

The possibility exists to modify the maximum likelihood method so as to remove biases or to make it a minimum-variance method, by adjusting the boundaries of the regions. However, this is beyond the scope of the present paper.

3.3 Total Pixel Error

The radiant exitance for each pixel is computed by use of equation (2). For a given scene, there is a great amount of variability in the bidirectional function R due to the infinite variety of Earth-atmosphere scenes within each scene class. Thus, the bidirectional reflectance function R is not known precisely, even when the scene is correctly identified, but its true value differs from the model value $\hat{R}$, which is used in the data processing, by an amount ε_R. Also, there is the error involved in the spectral correction, ε_L. Finally, the measurements themselves will have some error, ε_m. The true radiant exitance would be

$$\underline{M} = \pi QL = \pi(Q_j + \varepsilon Q_j)[C_j(\underline{m} + \underline{\varepsilon}_m) + \varepsilon_L] \tag{13}$$

and the estimate for the radiant exitance would be

$$\hat{\underline{M}}_j = \pi Q_j C_j \underline{m} \tag{14}$$

If the scene is incorrectly identified as type i, the estimate for M will be

$$\hat{M}_{ij} = \pi Q_i C_i m \tag{15}$$

The error is

$$\underline{\varepsilon}_{Mij} = \hat{\underline{M}}_{ij} - \underline{M} = (\hat{\underline{M}}_{ij} - \hat{\underline{M}}_j) + (\hat{\underline{M}}_j - \underline{M}) \tag{16}$$

The first parenthetical expression is the error due to scene-identification error and the second is due to bidirectional function and spectral-correction variations from the nominal and to instrument errors. The first part is due to branching in the data flow, whereby errors cause selection of differing R_j's and C_j's, and the second part is linear in the errors. A vector $\underline{u}_k$ will be defined, whose components are the quantities which enter equation (14). From equation (16), the bias can be written as

$$E(\underline{\varepsilon}_{Mi}) = \sum_j P_{ij}\underline{\varepsilon}_{ij}(\text{scene}) + \sum_j P_{ij}\left(\frac{\partial \hat{M}_j}{\partial u_k}\right)\varepsilon_{uk} \tag{17}$$

The variance of the radiant-exitance errors for the pixels can be computed next as

$$\sigma^2_{\varepsilon\bar{M}_i} = \mathrm{cov}[\underline{\varepsilon}M_i(\mathrm{scene})]$$

$$+ \sum_j P_{ij}\left(\frac{\partial\hat{M}_j}{\partial u_k}\right)\cos(\underline{\varepsilon}_{uk})\left(\frac{\partial\hat{M}_j}{\partial u_k}\right)^T$$

$$+ \sum_j (H_{ij} + H^T_{ij}) \qquad (18)$$

where

$$H_{ij} = \varepsilon_{ij}(\mathrm{scene})\left[\int_{R_i} d\underline{x}P(\underline{x}|\underline{x}\varepsilon T_j)\varepsilon^T_{uk}\right]\left(\frac{\partial M_j}{\partial u_k}\right)^T$$

The first term on the right-hand side is the variance due to scene identification as computed in the last section. The second term is the variance due to bidirectional and spectral-correction variations and instrument noise. The third term is the cross term between the branching and the linear terms, and accounts for errors in the radiant exitance due to scene-identification errors caused by variability in bidirectional function, spectral correction, or instrument noise.

3.4 Errors Due to Regional Averaging

After each measurement has been used to estimate a radiant-exitance value at the top of the Earth-atmosphere system, the measurements for which the center of the "footprint" or pixel lies within a given region are then averaged to produce an average for the region. Because of spatial variations of radiant exitance over the region, there will be a sampling error associated with this regional average value. Because of the characteristics of the optical and electronic systems, there is a variation of the response of the instrument to points within the footprint of the pixel. This spatial variation of the response is described by the point-spread function, shown in figure (6) in an instrument coordinate system. As the radiometer scans from nadir to the horizon, there is a growth in the area covered at the TOA, as illustrated by figure (7). The resulting coverage of the regions by the pixels near nadir and at large nadir angles is shown schematically in figure (8), where the pixels are represented by contours of 50% of peak value of the point-spread function. The error due to this effect is treated theoretically by Smith et al. (1983). For the present analysis, it is assumed that this sampling error is independent of the other errors. Thus, the error in the regional average is given by

$$\varepsilon_{\bar{M}} = \varepsilon_{\hat{M}}(\mathrm{sampling}) + \frac{1}{J}\sum_{j=1}^{J}\varepsilon_{Mj} \qquad (19)$$

where N is the number of measurements in the region. The first term is the sampling error and the second is the error in the average radiant exitance due to the measurement errors. The variance of the regional-average radiant exitance error, assuming its bias to be zero, is

$$\sigma^2_{\varepsilon\bar{M}} = \sigma^2_{\hat{M}}(\mathrm{sampling}) + \frac{1}{J^2}\sum_{j=1}^{J}\sigma^2_{\hat{M}_j} \qquad (20)$$

or, assuming that all $_M{}^2$ are equal over the region,

$$\sigma^2_{\varepsilon\bar{M}} = \sigma^2_{\hat{M}}(\mathrm{sampling}) + \frac{1}{J}\sigma^2_{\hat{M}} \qquad (21)$$

The error variance due to sampling is computed in terms of the spatial spectrum of the radiant exitance field, the transfer function of the instrument which describes its optics and time response of the instrument and electronics, and the sampling pattern (Smith and Bess, 1978; Smith et al., 1983).

4. CONCLUDING REMARKS

This paper has formulated an error analysis for the radiant exitance at the top-of-the-atmosphere as computed from scanning radiometer data. In addition to providing a measure of the quality of the estimated radiant exitance, the numerical evaluation of these errors will provide a basis for trade-offs of various parameters involved in the analysis of the data. For example, the nadir angle beyond which data becomes more misleading than useful can be estimated by this procedure. Also, this paper provides a conceptual framework for understanding results from simulation studies of Earth radiation budget experiments.

5. REFERENCES

Barkstrom, B.R. and J.B. Hall: Earth Radiation Budget Experiment (ERBE): An Overview, J. Energy, Vol. 6, No. 2, March-April, 1982, pp 141-146.

Smith, G.L. and T.D. Bess: System Considerations for an Earth Radiation Budget Scanning Radiometer, Proceedings of the Fourth Symposium on Meteorological Observations and Instrumentation of the American Meteorological Society, April 10-14, 1978, Denver, Colorado, pp 179-184.

Smith, G. L., T.D. Bess and P. Minnis: Sampling Errors in Regional Radiation Results Based on Satellite Radiation Measurements, Proceedings of Ninth Conference on Aerospace and Aeronautical Meteorology of the American Meteorological Society, June 6-9, 1983, Omaha, Nebraska.

Stuhlmann, R., P. Minnis and G. L. Smith: A Comparison of Experimental and Theoretical Bidirectional Reflectance Functions, Proceedings of Fifth Conference on Atmospheric Radiation of the American Meteorological Society, Oct. 31-Nov. 4, 1983, Baltimore, Maryland.

Taylor, V. R. and L. L. Stowe: Reflectance Characteristics of Uniform Earth and Cloud Surfaces Derived from Nimbus-7 ERB. Accepted for publication, Journal of Geophysical Research.

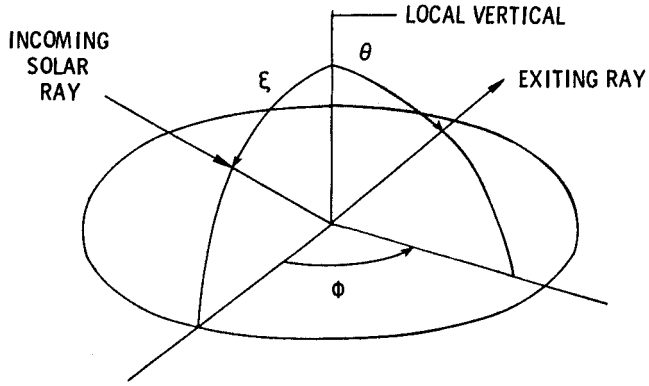

Figure 1. Viewing geometry.

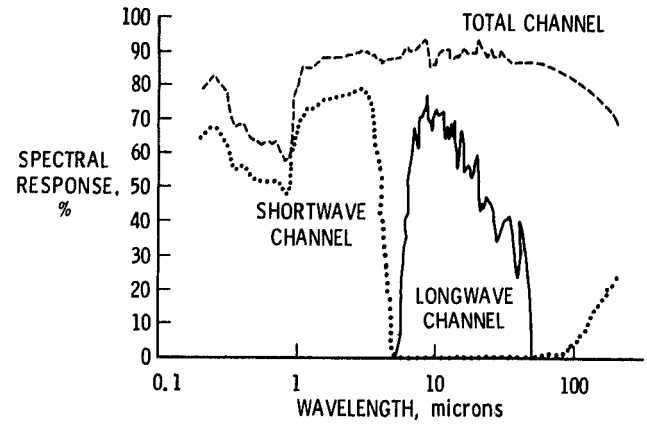

Figure 3. Spectral response of scanning radiometer channels.

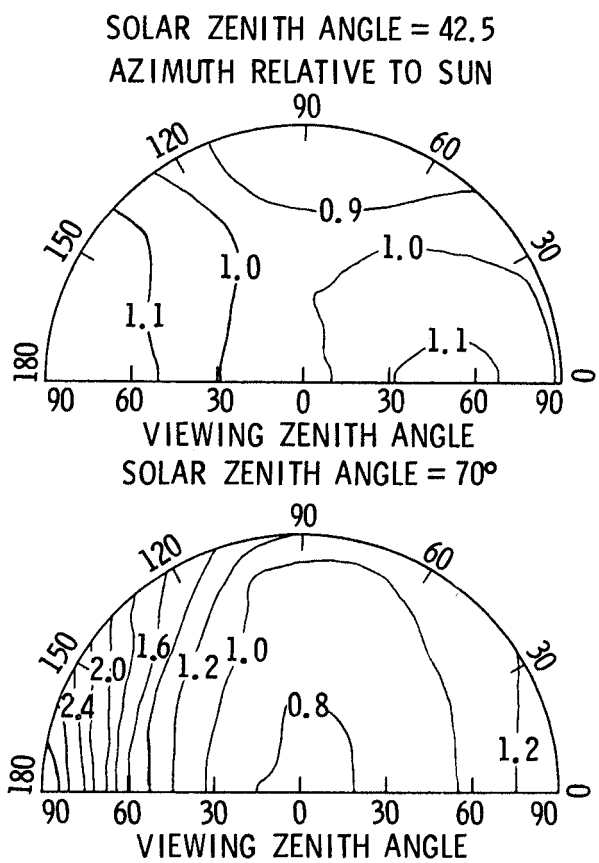

Figure 2. Shortwave bidirectional models for cloud, from Nimbus 7 ERB data.

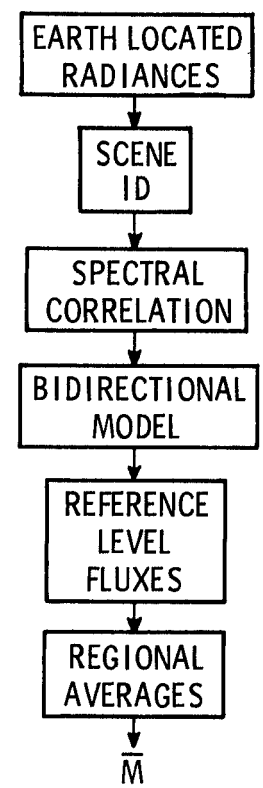

Figure 4. Scanner data analysis.

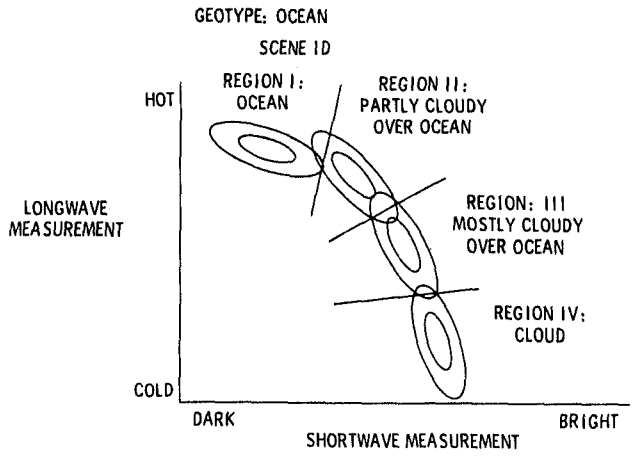

Figure 5. Schematic representation of scene identification algorithm.

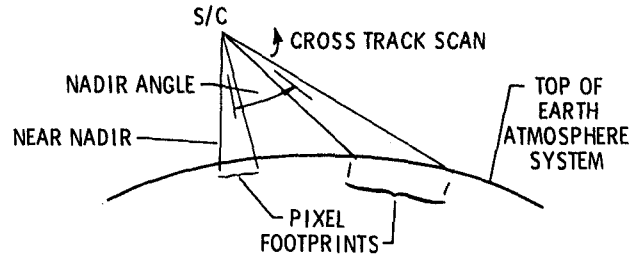

Figure 7. Growth of pixel footprint with nadir angle.

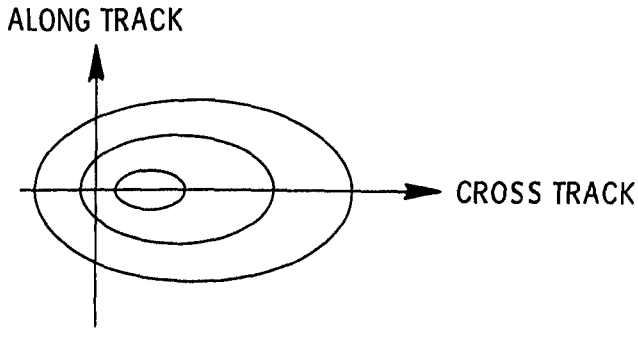

Figure 6. Schematic representation of point spread function of scanner channels.

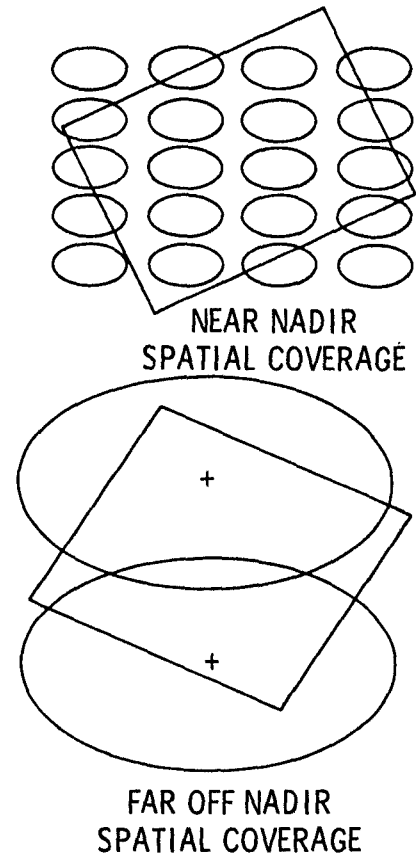

Figure 8. Coverage of regions by pixels.

A CLOUDINESS STUDY OF THE EASTERN EQUATORIAL PACIFIC USING GEOSTATIONARY SATELLITE DATA

Chi-Fan Shih, Thomas H. Vonder Haar
and G. Garrett Campbell

Cooperative Institute for
Research in the Atmosphere
and
Department of Atmospheric Science
Colorado State University
Fort Collins, Colorado 80523

1. INTRODUCTION

The Eastern Equatorial Pacific (EEP), defined here as the region between 20°N, 20°S and 85°W, 145°W, is well known for its large scale sea surface temperature (SST) warming event. Such a SST warming event is termed 'El-Nino' which, together with the surface pressure seesaw of Pacific and Indian Ocean (Southern Oscillation), is called 'ENSO'. The ENSO phenomenon has recently been accepted as one of the strongest signals of short-term climate change. The teleconnections between ENSO and floods in South America, drought in India, southward shift of jet stream position over the USA, etc., are under study (Horel and Wallace, 1981; Hoskins and Karoly, 1981). In this aspect, the extraordinary 1982-83 El-Nino event is an excellent case to study because of its strong intensity, long lasting and double peaking features. Many studies have been published to discuss the onset and peak stages of this last event, but to understand the meteorological characteristics of this unusual case completely, we also need to know more details about its decaying stage. In this study, we analyzed the July and August geostationary (GOES-W) satellite data of 1983 over the EEP region to estimate the variations of outgoing longwave radiation (OLR), albedo and cloudiness at monthly time scales. The data were obtained from the new International Satellite Cloud Climatology Project (ISCCP) of the World Climate Research Program (Schiffer and Rossow, 1983).

2. DATA ANALYSIS

The cloud estimates and related parameters used in this study are extracted from GOES-W data sets collected at Colorado State University for the ISCCP. Although detailed specifications of ISCCP data quality is referred to The Preliminary Implementation Plan of ISCCP (Schiffer, 1982), related information to the present study is as follows. The raw satellite data is processed after being received to generate two (B1 and B2) data sets. B1 data are averaged and sampled from the raw data while B2 data are sampled from B1 set. B1 has a subsatellite resolution of 8 x 12 km. B2 pixels have the same resolution but have been sampled to 32 x 36 km. We have used the larger data set, B1, for this study. Since the ISCCP data are collected every three hours, we analyzed images at 8 and 20 GMT (near local midnight and local noon in the EEP). As for the navigation, fixed earth locations were used as the boundaries of the target sector during data extraction to make sure all data are of the same area. The study area for this paper is shown in Figure 1. In order to use the 2-channel (or bispectral) threshold technique to derive cloudiness, background maps were constructed first by accumulating minimum albedo and maximum brightness temperature for a period of 10 days over the study region. Monthly 'relative' OLR maps and background maps were accumulations of 10-day maps of that month. Monthly cloudiness distributions were obtained from the combination of background temperature, albedo and OLR maps. To eliminate the possible nonuniform background temperatures over the study area, the whole region was subdivided into 16 small sectors. The threshold temperature and albedo of each sector where chosen from a frequency histogram (not shown here).

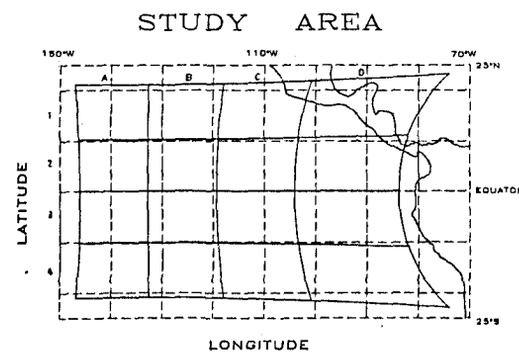

Fig. 1. The Eastern Equatorial Pacific (thick line) defined for this study with corresponding longitutde-latitude grid as the background (dash line). The EEP region is subdivided into 16 sectors (1A, 1B, 1C, 1D, etc.).

For the 8 GMT image, since it has only infrared data, a single threshold method was used to derive cloudiness, but the threshold temperature was compared to the 20 GMT threshold temperature to make sure that the sea surface temperature did not vary unreasonably. After

cloudiness is derived for each sector and each image, the average of that sector for a month gives the monthly cloudiness.

To obtain the mean OLR maps, brightness counts of infrared data are first converted to irradiance according to the Stefan-Boltzmann law without any limb darkening or frequency response corrections. Then the irradiances are averaged for a month to get the monthly outgoing longwave radiation field. The mean of July and August results in the bi-monthly average.

3. RESULTS

3.1 Background Features

Figures 2 and 3 are infrared background maps for July and August at 8 GMT. The warm region during July has an effective black body temperature warmer than 26° C. Over the EEP, it is obviously larger than that of August. We note that if no clouds stay over the same location longer than 10 days, the background maps should also represnt the ocean surface conditions. Therefore, the decrease of warm area from July to August is consistent with the changes of SST indices of 1982-83 El Nino (Arkin, et al., 1983). Our infrared background maps of 20 GMT also show similar large scale features. However, if we compare our background maps with the mean SST map of Summer 1983 (Arkin, et al., 1983), Figure 3, a difference appears in that the isotherms in our maps do not extend to the coast of South America. This difference is probably caused by the limb darkening effect of the large viewing angle. .

Fig. 2. The July backround map at 8 GMT derived from GOES-W data. The brightest region has brightness temperature over 26°C and the darkest represents regions of brightness temperature colder than 12°C.

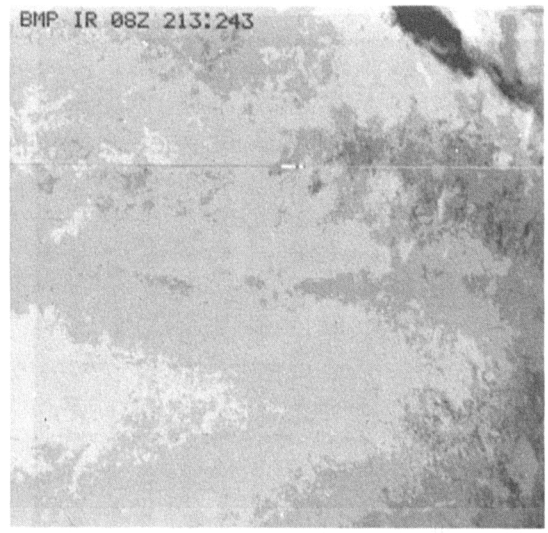

Fig. 3. The August background map at 8 GMT derived from GOES-W data. The brightest region has brightness temperature over 26°C and the darkest represents regions of brightness temperature colder than 12°C.

3.2 Outgoing Longwave Radiation (OLR)

At the conference we will contrast our higher space-time outgoing longwave radiation maps for Summer 1983 with those used by the Climate Analysis Center (1983) for the same time and region.

3.3 Cloudiness

The very preliminary results of our cloudiness analyses are discussed briefly in this section. At the conference we will show additional quantitative cloudiness summaries. In Figures 4 and 5, enhanced cloudy-clear maps of July and August are shown. The bright regions are clear areas and the dark regions are cloudy. The bottom row of the study region (Region 4A, B, C, D) is now completely shown in the map. From Figures 4 and 5, we note the cloudy areas shifted northward between July and August. Our explanation is that in August, cold water moved north of the equator and cooled the SST to about 1°C less than the average temperature of the summer. In association with this change, the minimum cloudiness region moved as well and increased clear areas along the equator.

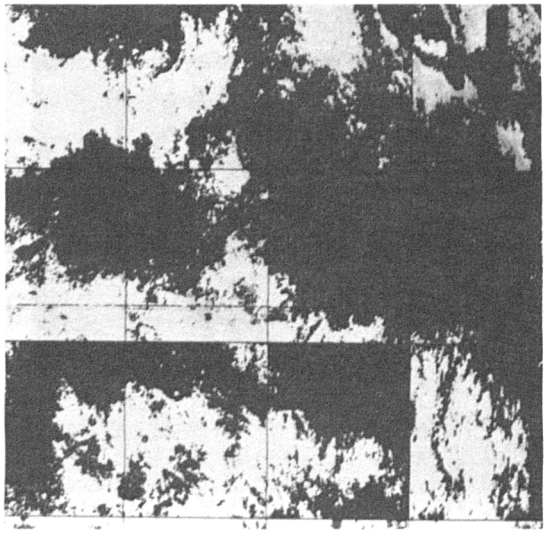

Fig. 4. Enhanced cloud-clear maps of July at 20 GMT. The bright regions are clear and the dark regions are cloudy.

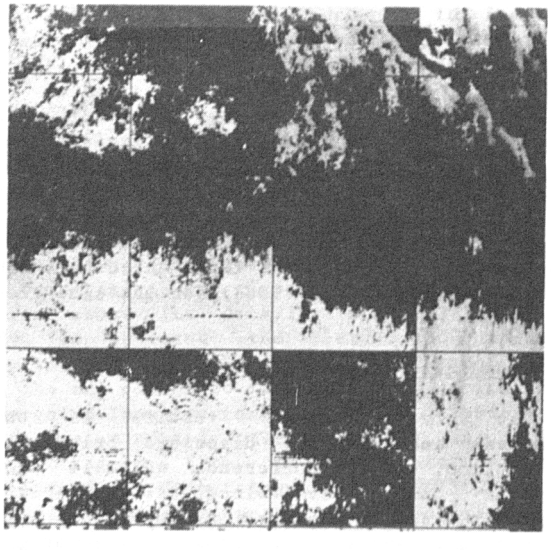

Fig. 5. Enhanced cloud-clear maps of August at 20 GMT. The bright regions are clear and the dark regions are cloudy.

4. SUMMARY

Using new ISCCP GOES-W satellite data collected at CSU, we have studied the decay of the 1982-83 El Nino event at 30-day time scales for two months. Our background maps and OLR fields are compared to the seasonal maps of the US Climate Analysis Center. With simple threshold techniques, we detected the variations of cloudiness in response to SST changes. In addition, since this study has used two separate algorithms to derive (a) cloud amount and (b) total outgoing longwave radiation, we will use the data sets in future research on the cloud/radiation feedback problem - a key element in climate study and model development. Eventually, outputs such as that presented in this study which are derived from the same data set (eg. ISCCP), will be tested and augmented by sets where the cloud data and total radiation from earth are measured by separate instruments.

5. ACKNOWLEDGEMENTS

Mr. Richard Peek and Mr. William Davis assisted with the ISCCP data acquisition at the ISCCP Sector Processing Center at Colorado State Uniersity. This research has been supported in part by NOAA, through CIRA, under contract number NA8/AA-D-00058, and by the National Science Foundation.

6. REFERENCES

Arkin, P.A., J.D. Kapman, and R.W. Reynolds, 1983: 1982-1983 El Nino/Southern Oscillation Event Quick Look Atlas. NOAA/NWS, National Meteorological Center, Climate Analysis Center, Washington, D.C.

Climate Analysis Center, 1983: Climate diagnostics bulletin. August, 1983. NOAA/NWS, National Meteorological Center, Climate Analysis Center, Washington, D.C.

Horel, J.D., and J.M. Wallace, 1981: Planetary-scale atmospheric phenomena associated with the Southern Oscillation. Mon. Wea. Rev., 109, 813-829.

Hoskin, B.J., and Karoly, 1981: The steady linear response of a spherical atmosphere to thermal and orographic forcing. J. Atmos. Sci., 38, 1179-1196.

Rasmusson, E.M., and J.M. Wallace, 1983: Meteorological aspects of the El Nino/Southern Oscillation. Science, 222, 1195-1202.

Schiffer, R.A., 1982: The international satellite cloud climatology project (ISCCP): Preliminary implementation plan. Washington, January, 1982. pp. 77.

Schiffer, R.A., and W.B. Rossow, 1983: The international satellite cloud climatology project (ISCCP): the first project of the world climate resarch programme. Bull. Amer. Meteor. Soc., 64, 779-784.

Second Conference on Coastal Meteorology

January 30–February 1, 1980
Los Angeles, Calif.

The Second Conference on Coastal Meteorology, sponsored by the American Meteorological Society, was held 30 January-1 February 1980 in Los Angeles, Calif. A session on "Coastal and Ocean Studies" was held jointly with the 60th AMS Annual Meeting and the Third Conference on Ocean-Atmosphere Interaction. The volume contains more than 60 papers arranged under the following session topics:

- *Coastal and Ocean Studies*
- *Pollution, Power Plant Siting, and Societal Needs*
- *Data and Forecasting*
- *CEWCOM-76, 78 and Marine Aerosols*
- *Sea and Lake Breeze*
- *Mesoscale Circulation*
- *Climatology, Synoptic-Scale Circulation, and Insolation*
- *Low-Level Wind and Gravity Waves*
- *MABLES WC and California Inversion*
- *Stratus/Fog and Marine Boundary Layer Structure*
- *Sea Surface and Subsurface Behavior*

307 pages

*10**
$~~15~~ AMS Members
*15**
$~~20~~ Nonmembers
(plus $2.00 postage/handling)

**while available*

Send order and remittance to:

AMERICAN METEOROLOGICAL SOCIETY
45 Beacon St., Boston, MA 02108

Second Conference on Flash Floods

March 18–20, 1980
Atlanta, Ga.

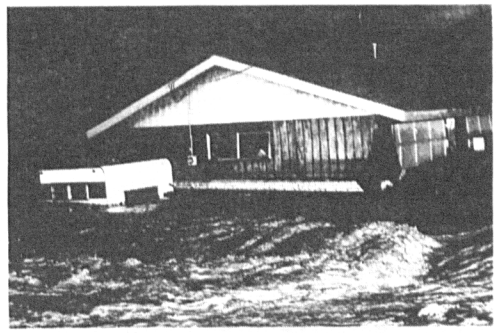

The Second Conference on Flash Floods, sponsored by the American Meteorological Society, was held 18–20 March 1980 in Atlanta, Ga. The volume contains 45 papers arranged under the following session topics:

Case studies of recent flash floods • Human response • Climatology • Satellite and radar applications • Forecasting techniques • Operations • Warning systems • Forecast delivery and utilization systems

258 pages

10*
$~~15~~ AMS Members
15*
$~~20~~ Nonmembers
(add $2.00 postage)

*while available

Send order and remittance to:

AMERICAN METEOROLOGICAL SOCIETY
45 Beacon St., Boston, MA 02108

PREPRINTS

SEVENTH CONFERENCE

ON

PROBABILITY AND STATISTICS IN ATMOSPHERIC SCIENCES

NOVEMBER 2-6, 1981 ***MONTEREY, CALIFORNIA***

Session Topics:

- Principal Components
- Weather Modification
- Climate Modeling
- Satellite Applications
- Atmospheric Systems
- Numerical Weather Prediction
- Evaluation and Verification
- Clouds and Visibility
- Markov Models
- Autoregressive Models
- Probability Models
- Radar
- Spatial Considerations
- Prediction of Continous Variables

235 Pages

$15 AMS Members
$20 Nonmembers

(plus $2 postage/handling)

Send order & remittance to:

American Meteorological Society
45 Beacon St.
Boston, MA 02108

PUBLICATIONS OF THE AMS

Nonmember Prices Effective August 1, 1983*

BOOKS

Compendium of Meteorology, 1951—Out of Print
Dynamic Meteorology and Weather Forecasting, 1957—Out of Print
Glossary of Meteorology, 1959; third printing, 1980—$25.00
Vilhelm Bjerknes Memorial Volume, 1962—$12.00
A Century of Weather Progress, 1970—$10.00
Workshop on Micrometeorology, 1973—$35.00
Atmospheric Science and Public Policy, 1976—$6.00
Workshop on the Future of National Atmospheric Research, 1977—$6.00
Curricula in the Atmospheric and Oceanographic Sciences, 1982—$10.00
Workshop on the Planetary Boundary Layer, 1980—$25.00
Lectures on Air Pollution and Environmental Impact Analyses, 1975; second printing, 1982—$30.00

Distributed by AMS:

Weather Modification in the Public Interest, 1974—$10.50
Clouds and Storms, 1980—$57.50
A Field Guide to the Atmosphere, 1981—$13.95
The American Weather Book, 1982—$14.95

METEOROLOGICAL MONOGRAPHS (ISSN 0065-9401)

No. 1 Wartime Developments in Applied Climatology, 1947—$12.00
No. 2 The Observations and Photochemistry of Atmospheric Ozone, 1950—$12.00
No. 3 On the Rainfall of Hawaii, 1951—$12.00
No. 4 On Atmospheric Pollution, 1951—$12.00
No. 5 Forecasting in Middle Latitudes, 1952—Out of Print
No. 6 Thirty-Day Forecasting, 1953—$12.00
No. 7 The Jet Stream, 1954—$12.00
No. 8 Recent Studies in Bioclimatology, 1954—$12.00
No. 9 Industrial Operations under Extremes of Weather, 1957—$12.00
No. 10 Interaction of Sea and Atmosphere, 1957—$12.00
No. 11 Cloud and Weather Modification, 1957—$12.00
Nos. 12-20 Meteorological Research Reviews, 1957. Review of Climatology; Meteorological Instruments; Radiometeorology; Weather Observations, Analysis and Forecasting; Applied Meteorology; Physics of the Upper Atmosphere; Physics of Clouds; Physics of Precipitation; Atmospheric Electricity. (In 1 vol.)—$24
No. 21 Studies of Thermal Convection, 1959—$12.00
No. 22 Topics in Engineering Meteorology, 1960—$12.00
No. 23 Atmospheric Radiation Tables, 1960—$12.00
No. 24 Fluctuations in the Atmospheric Inertia, 1961—$12.00
No. 25 Statistical Prediction by Discriminant Analysis, 1962—$12.00
No. 26 The Dynamical Prediction of Wind Tides on Lake Erie, 1963—$12.00
No. 27 Severe Local Storms, 1963—$20.00 Paperbound.
No. 28 Agricultural Meteorology, 1965—$20.00 Paperbound; $22.00 Clothbound.
No. 29 Scattered Radiation in the Ozone Absorption Bands at Selected Levels of a Terrestrial, Rayleigh Atmosphere, 1966—$20.00 Paperbound; $22.00 Clothbound
No. 30 The Causes of Climatic Change, 1968—$20.00
No. 31 Meteorological Investigations of the Upper Atmosphere, 1968—$18.00
No. 32 On the Distribution and Continuity of Water Substance in Atmospheric Circulations, 1969—$18.00
No. 33 Meteorological Observations and Instrumentation, 1970—$25.00
No. 34 Long-Period Global Variations of Incoming Solar Radiation, 1971—$20.00
No. 35 Meteorology of the Southern Hemisphere, 1972—$25
No. 36 Alberta Hailstorms, 1973—$18.00
No. 37 The Dynamic Meteorology of the Stratosphere and Mesosphere, 1975—$35.00
No. 38 Hail: A Review of Hail Science and Hail Suppression, 1977—$35.00
No. 39 Solar Radiation and Clouds, 1980—$35.00
No. 40 METROMEX: A Review and Summary, 1981—$35.00
No. 41 Tropical Cyclones—Their Evolution, Structure, and Effects, 1982—$40.00

* Add $2.00 per item for postage and handling. Prices subject to future changes without notice.

HISTORICAL MONOGRAPHS

The History of American Weather (All 4 vols.—$40.00)
Early American Hurricanes (1492-1870), 1963—$12.00
Early American Winters (2 vols.—$22.00)
(1604-1820), 1966—$12.00
(1821-1870), 1967—$12.00
Early American Tornadoes (1586-1870), 1970—$12.00
The History of Meteorology (to 1800), 1977; second printing, 1983—$20.00
The Thermal Theory of Cyclones: A History of Meteorological Thought in the Nineteenth Century, 1979—$35.00

TRANSLATIONS

No. 76 Problems of Dynamic Meteorology and Climatic Theory—Out of Print
No. 82 Question of Physics of the Atmosphere—$5.00
Studies of Clouds, Precipitation, and Thunderstorm Electricity—$10.00

CONFERENCE PREPRINTS/PROCEEDINGS

$20.00 each (unless other price is given)

Second National Conference on Weather Modification, 1970
Seventh Conference on Severe Local Storms, 1971
International Conference on Weather Modification, 1971
Second Symposium on Meteorological Observations and Instrumentation, 1972
Third Conference on Weather Modification, 1972
Conference on Atmospheric Radiation, 1972
Third Conference on Probability and Statistics in Atmospheric Science, 1973
International Tropical Meteorology Meeting, 1974 (2 vols.)—$25
Second International Conference on the Environmental Impact of Aerospace Operations in the High Atmosphere, 1974
Sixth Conference on Aerospace and Aeronautical Meteorology, 1974
Fourth Conference on Weather Modification, 1974
Third Symposium on Meteorological Observations and Instrumentation, 1975
Fourth Conference on Probability and Statistics in Atmospheric Sciences, 1975
Conference on Hydrometeorology, 1976
International Conference on Cloud Physics, 1976—$35.00
Third Conference on Numerical Weather Prediction, 1977
Sixth Conference on Planned and Inadvertent Weather Modification, 1977
10th Conference on Severe Local Storms, 1977
Second Conference on Hydrometeorology, 1977
Fifth Conference on Probability and Statistics in Atmospheric Sciences, 1977
Joint Conference on Applications of Air Pollution Meteorology, 1977
11th Technical Conference on Hurricanes and Tropical Meteorology, 1977—$25.00
Fifth Joint Conference on Fire and Forest Meteorology, 1978
18th Conference on Radar Meteorology, 1978
Conference on Flash Floods: Hydrometeorological Aspects, 1978
Conference on Climate and Energy: Climatological Aspects and Industrial Operations, 1978
Conference on Sierra Nevada Meteorology, 1978
Third Conference on Atmospheric Radiation, 1978 (Abstracts)
Conference on Cloud Physics and Atmospheric Electricity, 1978—$25.00
Conference on Weather Forecasting and Analysis and Aviation Meteorology, 1978
Conference on Atmospheric Environment of Aerospace Systems and Applied Meteorology, 1978

Nonmember Prices Effective August 1, 1983*

(continued)

Conference and Workshop on Wind Energy Characteristics and Wind Energy Siting, 1979—$25.00
Third Conference on Hydrometeorology, 1979
11th Conference on Severe Local Storms, 1979
Seventh Conference on Inadvertent and Planned Weather Modification, 1979 (Extended Abstracts)
Sixth Conference on Probability and Statistics in Atmospheric Sciences, 1979
Second Conference on Coastal Meteorology, 1980
Second Conference on Flash Floods, 1980
Second Joint Conference on Applications of Air Pollution Meteorology and Second Conference on Industrial Meteorology, 1980—$32.00
Eighth Conference on Weather Forecasting and Analysis, 1980
13th Technical Conference on Hurricanes and Tropical Meteorology, 1980
Fifth Symposium on Turbulence, Diffusion, and Air Pollution, 1981 (Extended Abstracts)
15th Conference on Agriculture and Forest Meteorology and Fifth Conference on Biometeorology, 1981 (Extended Abstracts)
Fourth Conference on Atmospheric Radiation, 1981
Eighth Conference on Inadvertent and Planned Weather Modification, 1981 (Extended Abstracts)
Fourth Conference on Hydrometeorology, 1981
Fifth Conference on Numerical Weather Prediction, 1981
Seventh Conference on Probability and Statistics in Atmospheric Sciences, 1981
Second Conference on Mountain Meteorology, 1981
20th Conference on Radar Meteorology, 1981—$25
12th Conference on Severe Local Storms, 1982—$25
Third Joint Conference on Applications of Air Pollution Meteorology (Extended Abstracts), 1982
First International Conference on Meteorology and Air/Sea Interaction of the Coastal Zone, 1982—$25
Second Symposium on the Composition of the Nonurban Troposphere (Extended Abstracts), 1982
Ninth Conference on Weather Forecasting and Analysis, 1982
Conference on Cloud Physics (Extended Abstracts), 1982
Proceedings of the International Conference on the Aviation Weather System, 1981 (published 1982)—$25
Proceedings of the International Conference on Climate and Offshore Energy Resources, 1980 (published 1982)—$25
Sixth Symposium on Turbulence and Diffusion (Extended Abstracts), 1983
Fifth Symposium on Meteorological Observations and Instrumentation, 1983—$25
16th Conference on Agriculture and Forest Meteorology and Sixth Conference on Biometeorology (Extended Abstracts), 1983
Seventh Conference on Fire and Forest Meteorology, 1983
Sixth Conference on Numerical Weather Prediction, 1983
Ninth Conference on Aerospace and Aeronautical Meteorology, 1983
First International Conference on Southern Hemisphere Meteorology (Extended Abstracts), 1983
21st Conference on Radar Meteorology, 1983—$32
13th Conference on Severe Local Storms (Extended Abstracts), 1983—$25
Fifth Conference on Hydrometeorology, 1983
Fifth Conference on Atmospheric Radiation (Extended Abstracts), 1983
Eighth Conference on Probability and Statistics in Atmospheric Sciences, 1983

* Add $2.00 per item for postage and handling. Prices subject to future changes without notice.

BIBLIOGRAPHIES ON OCEANOGRAPHY

Physical Oceanography of the Indian Ocean, 1965—Out of Print
Collected Bibliographies on Physical Oceanography (1953–1964), 1966—Out of Print
Marine Corrosion, 1967—$5.00
Marine Seismics, 1967—$5.00
Oceanography of the Tropical Atlantic, 1967—Out of Print
Marine Atlases, 1968—$10.00

AMSnewsletter

Volume 5, 1984. Monthly Calendar year subscription: $60.00*

Brief, timely reports on happenings on the Washington scene and throughout the U.S. and the world meteorological communities. The affairs of government, industry, academe, and national and international bodies as they affect the atmospheric and related hydrospheric sciences and their practitioners are reported under the following headings: News; Opportunities; Dates to Note; Congressional Happenings; Government Publications; Personalities; and Contracts and Grants.

* Add $15 for postage and handling of subscriptions mailed outside U.S.A. and Canada.

For further information, write to:

AMERICAN METEOROLOGICAL SOCIETY

45 Beacon Street, Boston, Massachusetts 02108 U. S. A.

TROPICAL CYCLONES
Their Evolution, Structure and Effects
by Richard A. Anthes

Tropical cyclones and hurricanes, long feared for the death and destruction that often accompanies them, are among the most fascinating of atmospheric phenomena. Created by thermodynamic processes, they unleash vast amounts of energy and influence a wide variety of natural processes along their paths.

In *Tropical Cyclones—Their Evolution, Structure and Effects*, the author, Richard A. Anthes, tells the story of their creation and destruction, of meteorology's successes in understanding, modeling and predicting their behavior, and of the attempts to modify them.

Chapter Topics Include:

- *Structure and Life Cycle of Tropical Cyclones*
- *Physical Processes in Tropical Cyclones*
- *Simulation of Tropical Cyclones by Numerical Models*
- *Hurricane Modification*
- *Oceanic Response to Tropical Cyclones*
- *Tropical Cyclone Forecasting*

208 Pages
11 Pages of References
17 Photos, 99 Figures
Hardcover

A unique feature of this book, which may be used in the home, laboratory, or classroom, is a thorough treatment of the interactions between storm and ocean, with both observations and theory being integrated to provide a complete description.

$30 AMS Members
$40 Nonmembers
(plus $2 postage/handling)

Send order and remittance to:

AMERICAN METEOROLOGICAL SOCIETY
45 Beacon St.
Boston, Mass. 02108

Meteorological Monographs, Vol. 19, No. 41
American Meteorological Society

ISBN: 0-933876-54-8
ISSN: 0065-9401